



Measurement of the W boson mass with the ATLAS detector

Oleh Kivernyk

► To cite this version:

Oleh Kivernyk. Measurement of the W boson mass with the ATLAS detector. High Energy Physics - Experiment [hep-ex]. Université Paris Saclay (COmUE), 2016. English. NNT : 2016SACLS590 . tel-01502465

HAL Id: tel-01502465

<https://theses.hal.science/tel-01502465>

Submitted on 5 Apr 2017

HAL is a multi-disciplinary open access archive for the deposit and dissemination of scientific research documents, whether they are published or not. The documents may come from teaching and research institutions in France or abroad, or from public or private research centers.

L'archive ouverte pluridisciplinaire **HAL**, est destinée au dépôt et à la diffusion de documents scientifiques de niveau recherche, publiés ou non, émanant des établissements d'enseignement et de recherche français ou étrangers, des laboratoires publics ou privés.

NNT : 2016SACLS590

THÈSE DE DOCTORAT
de l'Université Paris-Saclay
préparée à Université Paris-Sud
au sein de l'IRFU/SPP

Ecole doctorale n° 576
Particules, Hadrons, Énergie, Noyau, Instrumentation, Imagerie,
Cosmos et Simulation (PHENIICS)

Spécialité de doctorat: Physique des particules

par

M. Oleh Kivernyk

**Measurement of the W boson mass
with the ATLAS detector**

Thèse présentée et soutenue à Saclay, le 19 Septembre 2016

Composition du jury :

M. Martin Aleksa

M. Reza Ansari

M. Maarten Boonekamp

M. Daniel Froidevaux

M. Luca Malgeri

M. Fulvio Piccinini

Directeur de Recherche, CERN, Examineur

Professeur, Université Paris-Sud, Président du Jury

Directeur de Recherche, CEA/Irfu, Directeur de thèse

Directeur de Recherche, CERN, Rapporteur

Senior Scientist, CERN, Rapporteur

Senior Scientist, Université de Pavie, Examineur

Abstract

This thesis describes the W boson mass measurement with the ATLAS detector based on the 2011 data-set recorded by ATLAS at a centre-of-mass energy of $\sqrt{s} = 7$ TeV, and corresponding to 4.6 fb^{-1} of integrated luminosity. Measurements are performed through template fits to transverse momentum distributions of charged leptons as well as to transverse mass distributions of the W boson in electron and muon decay modes in various kinematic categories. All the individual measurements are found to be consistent and their combination leads to a value of

$$m_W = 80371.1 \pm 18.6 \text{ MeV},$$

The measured value of the W boson mass is compatible to the current world average of $m_W = 80385 \pm 15 \text{ MeV}$. The uncertainty is competitive to the current most precise measurements performed by the CDF and D0 collaborations.

Keywords : LHC, ATLAS, W boson mass, Standard Model.

Résumé

Motivation. Après la découverte des bosons W et Z au collisionneur SPS du CERN, les particules massives qui sont responsables de la force faible, les efforts ont été orientés vers la détermination précise de leurs propriétés. Les masses des bosons W et Z sont des paramètres clés du modèle standard de la physique des particules. Le modèle standard possède 25 paramètres libres pour décrire les masses des quarks, des leptons et des neutrinos, du boson de Higgs, ainsi que les paramètres de la matrice de mélange des quarks et les couplages entre particules. Certains d'entre eux sont mesurés directement, parfois avec grande précision; les autres sont contraints par la mesure de grandeurs physiques reliées par la théorie. De telle manière, grâce aux corrections radiatives, la valeur de M_W est reliée aux masses du Z , du boson de Higgs et du quark top qui sont les particules les plus massives du modèle standard. La masse du Z a été mesurée avec une grande précision au LEP et apporte une contrainte fondamentale au modèle standard. Avant la découverte du boson de Higgs, la sensibilité intrinsèque de M_W à M_H et m_t permettait d'imposer des contraintes sur la valeur de la masse du Higgs. Maintenant, le boson de Higgs est découvert et donc la masse du W peut être prédite. Autrement dit, la mesure des masses M_W , M_H et m_t peut être utilisée pour valider la cohérence du modèle standard. Si les valeurs prédite et mesurée de M_W sont en accord, il est possible de placer des limites sur l'existence de nouvelles particules qui se couplent au boson W .

La première mesure de la masse du boson W a été effectuée lors de la découverte grâce au collisionneur proton-antiproton au CERN, avec une valeur de $M_W = 81 \pm 5 \text{ GeV}$. Plus tard, sa valeur a été mesurée avec une erreur relative mieux que 1% par les plusieurs expériences dans le collisionneur electron-positron LEP au CERN et dans le collisionneur proton-antiproton au Tevatron de Fermilab. Les mesures effectuées avec les expériences des collisionneurs LEP et Tevatron ont permis de diminuer la précision considérablement. Maintenant, la valeur combinée est $M_W = 80370 \pm 15 \text{ MeV}$ qui correspond à une précision relative de 0.02%. La valeur la plus précise est obtenue avec le détecteur CDF à Fermilab. D'un autre côté, la valeur M_W est prédite avec une précision de l'ordre de 0.01%, ce qui dicte la précision souhaitée pour les mesures directes pour pouvoir tester le modèle standard.

Cette thèse présente les résultats de la première mesure de M_W avec le détecteur ATLAS au collisionneur proton-proton du CERN, le LHC, exploitant 4.7 fb^{-1} de données collectées en 2011 à $\sqrt{s} = 7$ TeV. Au LHC, les bosons W sont produits principalement par la réaction d'annihilation d'un quark et d'un antiquark. Contrairement à la production des W en collisions proton-antiproton au Tevatron, où un antiquark de valence participe, au LHC seulement les antiquarks de la mer, issus de la séparation de gluons, peuvent produire des W . La connaissance des fonctions de structure du proton (PDFs) pour les quarks de la mer, et particulièrement des quarks de la seconde

génération, est donc d'une importance particuliere. Pour atteindre une precision de mesure similaire au TeVatron, il est necessaire de contraindre les incertitudes correspondantes en utilisant les données du LHC.

Une autre difficulté sur la mesure de m_W est liée au grand nombre d'interactions inélastiques simultanees ayant lieu a chaque croisement de faisceaux au LHC. Ces interactions additionnelles compliquent considérablement la reconstruction des particules dans le detecteur, et seules les désintégrations leptoniques du W peuvent être reconstruites avec une efficacité suffisante et un bruit de fond réduit. Les produits de désintégration leptoniques utilisés pour la presente mesure sont un électron ou un muon accompagné d'un neutrino. En fait, le neutrino échappe à la détection, mais sa présence est signalée par un déséquilibre d'impulsion dans le plan transverse aux faisceaux. Son impulsion transverse, p_T^ν , peut alors être mesurée indirectement à partir du lepton et du système hadronique qui recule face au W.

Méthodologie. Trois variables cinématiques sont sensibles à M_W : l'impulsion transverse du lepton chargé, p_T^ℓ , l'impulsion transverse du neutrino, p_T^ν , et la masse transverse construite comme $m_T^W = \sqrt{2p_T^\ell p_T^\nu (1 - \cos\Delta\phi)}$. Les distributions d'impulsions transverse du lepton et du neutrino sont maximales à la valeur de $M_W/2$, tandis que la distribution de la masse transverse est maximale à M_W . La distribution en impulsion transverse du W elargit ces distributions. La valeur de M_W peut être extraite de ces distributions dand les données, par la méthode des '*templates*'. Dans cette méthode, des échantillons sont simulés en supposant des valeurs différentes de M_W . Les distributions sensibles à M_W sont comparées aux données, et l'échantillon en meilleur accord avec les données donne la valeur mesurée de M_W .

Cette methode est sensible a diverses sources d'incertitude. Des exemples typiques sont l'efficacité de reconstructions des leptons, la calibration de la mesure de l'impulsion transverse des leptons et de l'impulsion manquante, le bruit de fond, et les mécanismes de production et de désintégration de bosons W. Ces effets peuvent introduire un biais dans la mesure et doivent être suffisamment maîtrisés.

Les corrections expérimentales. Expérimentalement, la distribution de p_T^ℓ est principalement affectée par la calibration des leptons chargés, tandis que la distribution de p_T^{miss} est également sensible à la calibration du recul hadronique u_T . La distribution de m_T^W est construite en utilisant p_T^ℓ et p_T^{miss} , et est par conséquent également affectée par les deux effets. Un bon accord entre les valeurs de M_W extraites des différentes distributions valide les corrections appliquées.

En raison d'incertitudes liées à l'alignement et à la résolution du détecteur, au champ magnétique, et à la quantité de matériau passif dans le détecteur, il faut corriger les simulations utilisées dans cette analyse. La procédure de calibration est basée sur les événements $Z \rightarrow \ell\ell$, qui ont l'avantage de contenir peu de bruit de fond (moins de 0.1% pour les électrons). Les corrections d'énergie des électrons et d'impulsion des muons sont obtenues en exploitant la position du pic de la distribution de masse invariante des paires des leptons dans l'état final autour de la mass M_Z qui est connue très précisément. De plus, la résolution en énergie des électrons et en impulsion des muons est corrigée en exigeant une description exacte des données par la simulation.

Une autre quantité qui doit être calibrée est le recul hadronique dans le plan transverse. Le recul hadronique est défini comme la somme vectorielle de tous les dépôts d'énergie dans le calorimètre, à l'exception des depots associés aux leptons : $\vec{u}_T = \sum \vec{E}_{T,i}$. Le recul est calibré en utilisant l'égalité attendue entre u_T et l'impulsion transverse $p_T^{\ell\ell}$ des leptons de désintégration du boson Z. En particulier, les projections parallèle ($u_{||}^Z$) et perpendiculaire (u_{\perp}^Z) à la ligne de vol du Z sont sensibles respectivement à la réponse et la résolution du détecteur. Les corrections sont ensuite transférées à simulation du boson W.

La sélection des leptons chargés tend rejeter les particules de bruit de fond et à maximiser l'efficacité pour le signal. Tout d'abord, les muons et les électrons doivent déclencher l'acquisition du détecteur. Ensuite, les traces reconstruites associées aux leptons chargés doivent être isolées, c'est-à-dire qu'aucune d'activité importante ne doit être observée autour de la trace. Dans le

cas des électrons, des sélections d'identification sont définies afin de rejeter davantage le bruit de fond venant des hadrons. Ces selections utilisent des coupures sur neuf variables qui caractérisent le développement latéral et longitudinal de la gerbe électromagnétique des électrons dans le calorimètre, et certains critères reliés à la qualité de la trace associée. Les désaccords entre données et simulation sur l'efficacité de sélection, en particulier si elles dépendent de p_T^ℓ , peuvent introduire un biais dans la mesure. Dans cette analyse les corrections ont été calculées séparément dans des catégories en pseudo-rapacité des candidats et en p_T afin de faire correspondre données et simulation avec suffisamment de précision.

Étude du calorimètre électromagnétique. La description latérale des gerbes électromagnétiques des électrons dans la simulation est imparfaite. En particulier, les profils latéraux de dépôt d'énergie des électrons simulés dans le code GEANT4, utilisé pour la simulation du détecteur, sont plus étroits que dans les données. En conséquence, cette différence perturbe les distributions des variables d'identification, qui à leur tour augmentent l'incertitude dans la mesure des corrections d'identification des électrons. De plus, la différence observée entre données et simulation peut être une source d'augmentation d'incertitude systématique sur la calibration d'énergie des électrons et des photons. Une explication potentielle est liée à l'effet de la diaphonie dans le calorimètre électromagnétique, qui a été étudiée en détail dans cette thèse. La diaphonie est une perturbation du signal électronique à cause des couplages parasites présents dans les électrodes. Ces couplages sont des trois types: capacitif, résistif et inductif. À cause de cette diaphonie, une partie de l'énergie déposée dans la cellule "fuit" dans les cellules voisines. De par la symétrie du calorimètre, la diaphonie doit être uniforme le long de ϕ , mais peut changer en fonction de η . Si l'effet de la diaphonie est sous-estimé dans la simulation, le corriger peut mener à élargir les profils latéraux et donc à une meilleure description des données.

La diaphonie a été mesurée en étudiant la réponse du calorimètre électromagnétique à des muons d'événements $Z \rightarrow \mu\mu$. Cette méthode s'appuie sur la connaissance précise de la trace mesurée dans le détecteur interne. Presque toute l'énergie perdue par les muons est déposée dans la cellule traversée. La mesure des dépôts d'énergie dans les cellules voisines permet donc de quantifier la modélisation de la diaphonie. La méthode est testée en utilisant des échantillons simulés avec et sans diaphonie. Cependant, cette mesure demande des connaissances précises de la position réelle des cellules. Plusieurs effets peuvent causer un déplacement des cellules: la rotation et le déplacement global du calorimètre, la contraction du calorimètre en raison de la température, et la déformation du calorimètre sous son poids. Dans cette thèse, on présente une méthode pour la détermination précise de la position des cellules de la première couche du calorimètre avec des muons. Après correction de la position des cellules, la diaphonie est mesurée dans les première et seconde couches du calorimètre tonneau ($|\eta| < 1.4$) dans les données et comparée avec simulation. Les valeurs moyennes de la diaphonie sont en accord entre les données et la simulation pour $|\eta| < 0.8$ (environ 8%), tandis qu'une différence est observée pour $0.8 < |\eta| < 1.4$ (environ 4% dans la simulation, 7% dans les données) et dans la seconde couche (environ 1% dans MC, 1.5% dans les données).

Les corrections théoriques. L'étude de la production des bosons vecteurs W et Z est affectée par des complications significatives liées à l'interaction forte. L'impulsion transverse des bosons W et Z est non nulle à cause l'émission de quarks et de gluons dans l'état initial. La majorité des événements sont à faible valeur d'impulsions transverse. Dans ce domaine, les logarithmes divergents doivent être éliminés et les effets non-perturbatifs doivent être inclus dans les prédictions QCD soit à l'aide des modèles de *parton shower*, soit à l'aide des calculs basés sur une approche analytique. Simultanément, les corrections QCD affectent la polarisation des bosons vecteurs et introduisent une asymétrie dans les distributions angulaires des leptons. En résumé, la distribution de p_T^ℓ est élargie par la distribution en p_T du boson, et est sensible aux états d'hélicité du W , à leur tour influencés par les PDFs du proton.

Les échantillons utilisés dans cette analyse sont simulés avec le code Powheg+Pythia. Afin d'inclure les effets d'ordre supérieur QCD, les distributions de rapidité du boson vecteur et les

distributions angulaires des leptons de l'état final sont corrigés à l'aide des prédictions d'ordre NNLO basées sur les PDF CT10nnlo. De plus, les simulations sont corrigées à l'aide du code PHOTOS pour prendre en compte les effets de QED affectant l'état final. Les incertitudes liées aux corrections électrofaibles d'ordre supérieur ont été estimées à l'aide du code WINHAC.

La modélisation de la distribution en impulsion transverse $p_T^{W,Z}$ est basée sur Pythia 8. Les paramètres QCD décrivant cette distribution dans Pythia 8 sont contraintes en utilisant la distribution de p_T^Z mesurée avec les données à 7 TeV. Ces prédictions sont utilisées pour la modélisation de p_T^W . L'ensemble complet des coefficients angulaires peut être mesuré précisément pour la production de bosons Z . La prédiction NNLO des coefficients angulaires est validée par comparaison à la mesure dans les événements Z et extrapolée à la production de bosons W .

Les échantillons des signaux et du bruit de fond utilisent les PDF CT10nnlo. Ces fonctions décrivent les distributions en impulsion des partons dans le proton, et jouent un rôle important dans l'analyse. La connaissance des PDFs est limitée par les incertitudes théoriques et expérimentales. Ces incertitudes sont améliorées en utilisant des mesures précises des sections efficaces différentielles Z et W mesurées avec ATLAS.

Estimation du bruit de fond QCD. Après la sélection d'événements de grande impulsion transverse manquante et contenant un lepton de grande impulsion, l'échantillon est composé d'événements signal $W \rightarrow \ell\nu$ et d'une part significative de bruits de fond, processus autres que la production du boson W . Ces processus incluent la production du boson Z , des dibosons WW, WZ, ZZ , des quarks top t ou de paires $t\bar{t}$, ainsi que des événements multijet avec un jet identifié comme lepton ou à cause de désintégrations semi-leptoniques de hadrons. Ces distributions diffèrent de celles du signal et doivent donc être correctement modélisées. Les contributions des bruits de fond électrofaible et top peuvent être simulées précisément, mais le bruit de fond multijets est difficile à simuler et des techniques d'estimation de ce bruit de fond à partir des données sont utilisées. Dans cette méthode, la forme des distributions est extraite des données dans une région d'espace des phases dominée par les événements multijet, où les critères d'isolation des leptons doivent échouer mais les coupures cinématiques sont inchangées. La normalisation des distributions correspondant au bruit de fond multijets est estimée grâce à une méthode de *template fit* dans une région basée sur des sélections d'événements où les coupures cinématiques sont relâchées. Les normalisations relatives des événements contenant un vrai lepton venant du signal W ou du bruit de fond multijets sont ajustées pour reproduire les distributions observées dans les données. Simultanément, la contribution des événements du signal et des bruits de fond simulés sont pris en compte par la simulation. La corrélation entre les variables cinématiques et l'isolation du lepton est prise en compte en découplant les échantillons par critères d'isolation des leptons. Enfin, l'évolution de la forme des distributions multijet liée à la corrélation entre isolation et distributions cinématiques est prise en compte.

Validation de la méthode sur M_Z . Les corrections théoriques et expérimentales sont vérifiées avec les événements de $Z \rightarrow \ell\ell$ en effectuant des mesures de M_Z par la même méthode que celle utilisée pour déterminer la masse du W . La détermination de M_Z à partir de la masse invariante des paires de lepton fournit un premier test de l'étalonnage en énergie des leptons. De plus, la détermination de M_Z à partir de la distribution de p_T^ℓ teste les corrections d'efficacité, la modélisation de l'impulsion transverse du Z et de sa polarisation. Un test de l'étalonnage du recul hadronique peut également être réalisé en utilisant des observables m_T^Z et E_T^{miss} , qui peuvent être définies en traitant un des leptons de désintégration comme un neutrino. La compatibilité entre les valeurs de m_Z extraites à partir des distributions $m_{\ell\ell}$, p_T^ℓ et m_T^Z valide la procédure de mesure qui est appliquée à la mesure de M_W . La précision de cette procédure de validation est limitée par la taille finie de l'échantillon de bosons Z , qui est environ dix fois plus petit que l'échantillon de bosons W .

Resultats. La valeur finale mesurée de M_W est obtenue à partir de la combinaison de mesures différentes effectuées dans les canaux de désintégration des électrons et des muons, séparés par charge, et dans des catégories de pseudo-rapacité des leptons. Les mesures de M_W utilisées dans la combinaison sont basées sur les distributions p_T^ℓ et m_T^W , qui sont partiellement corrélées.

Les mesures de M_W basées sur les distributions E_T^{miss} sont utilisées afin de tester la méthode. La cohérence des résultats dans les canaux électron et muon fournit un test des étalonnages expérimentaux, tandis que la cohérence des résultats mesurés dans les catégories en pseudo-rapacité $|\eta_\ell|$ et en charge des leptons teste la modélisation théorique. D'autres tests sont effectués en mesurant de M_W dans des catégories du nombre moyenne d'interactions inélastiques simultanées, dans deux intervalles du recul hadronique, ainsi que sans appliquer de coupure sur E_T^{miss} . Ces tests permettent de vérifier la calibration du recul hadronique et la modélisation de la distribution en impulsion transverse du boson W .

L'avantage de la catégorisation de la mesure est qu'elle permet une réduction significative des incertitudes théoriques en comparaison avec une mesure inclusive, grâce aux impacts différents des incertitudes des PDF dans les différentes catégories et distributions utilisées pour la mesure. Toutes les mesures individuelles sont compatibles et leur combinaison conduit à une valeur de

$$\begin{aligned} m_W &= 80371.1 \pm 6.7 \text{ MeV(stat.)} \pm 10.7 \text{ MeV(exp.sys.)} \pm 13.6 \text{ MeV(mod.sys.)} \\ &= 80371.1 \pm 18.6 \text{ MeV,} \end{aligned}$$

La valeur mesurée est compatible avec la prédiction du modèle standard, avec les valeurs mesurées aux collisionneurs LEP et TeVatron et avec la moyenne mondiale. Cette mesure est la plus précise à ce jour. Cette analyse a été effectuée avec les seules données enregistrées en 2011. L'analyse de plus de données permettra de réduire l'incertitude statistique (actuellement 7 MeV) et certaines incertitudes systématiques expérimentales.

Contents

1	Theoretical background	1
1.1	Introduction	1
1.2	The Standard Model	1
1.2.1	Elementary Particles	1
1.2.2	Fields and Interactions	3
1.2.3	The EW symmetry breaking	5
1.3	W boson mass	7
1.3.1	Prediction in the SM	7
1.3.2	W boson mass beyond the SM	8
1.3.3	Direct measurements	9
1.4	W and Z production at hadron colliders	11
1.4.1	Structure of the proton	11
1.4.2	W and Z boson production and rapidity distributions	12
1.4.3	Boson transverse momentum	15
2	The Large Hadron Collider and the ATLAS detector	17
2.1	LHC	17
2.1.1	Accelerator complex	18
2.1.2	Luminosity	19
2.2	The ATLAS detector	20
2.2.1	Coordinate system	21
2.2.2	The Inner Detector	22
2.2.3	Calorimetry	24
2.2.4	Muon Spectrometer	27
2.2.5	Trigger system and data acquisition	30
3	Event reconstruction and selection	31
3.1	Muon reconstruction and identification	31
3.2	Electron reconstruction and identification	33
3.3	Hadronic recoil reconstruction	34
3.4	W and Z boson selection	37
3.4.1	Muon selection	37
3.4.2	Electron selection	38
3.4.3	W and Z boson selection	38
4	Calibration of the EM calorimeter	39
4.1	Introduction	39
4.2	Methodology	39
4.2.1	Data and MC samples	39
4.2.2	Method description	40
4.2.3	Muon selection	41
4.2.4	Energy spectra fits	43
4.3	Crosstalk analysis	44
4.3.1	Energy MPV distributions	44
4.3.2	Athena crosstalk rederivation	45
4.3.3	Pile-up subtraction	47
4.3.4	Data/MC calibration. Intercalibration of first and second layers	49

4.4	Calorimeter alignment and deformation	51
4.4.1	Introduction	51
4.4.2	Overview of the possible effects	51
4.4.3	Methodology	52
4.4.4	ϕ –independent effects: contraction and z –shifts	54
4.4.5	ϕ –dependent effects: rotation and pear-shape deformation	55
4.5	Results	56
4.5.1	Crosstalk in data	56
4.5.2	Uncertainties	59
4.6	Summary	61
5	Calibration of the reconstructed objects	63
5.1	Muon momentum corrections	63
5.1.1	Methodology	63
5.1.2	Sagitta correction	64
5.1.3	Momentum scale and resolution	65
5.1.4	Momentum calibration as a function of muon azimuth	66
5.1.5	Uncertainties and impact on the m_W	67
5.2	Muon selection efficiency	67
5.3	Electron calibration corrections	70
5.3.1	Electron energy pre-corrections	70
5.3.2	Energy scale and resolution corrections	71
5.3.3	Energy calibration as a function of electron azimuth	73
5.3.4	Impact of energy tails	74
5.3.5	Impact of the LAr hole	77
5.3.6	Uncertainties and impact on the m_W	79
5.4	Electron selection efficiency	81
5.5	Hadronic recoil calibration	82
5.5.1	Pile-up correction	83
5.5.2	Correction of the $\Sigma E_T - u$ distribution	83
5.5.3	u_Y correction	86
5.5.4	Residual Recoil Corrections	86
5.5.5	Validation of the corrections	90
5.5.6	Propagation of the corrections to $W \rightarrow \mu\nu$ and $W \rightarrow e\nu$	90
5.5.7	Uncertainty and impact on the m_W	90
6	Production and decay model	95
6.1	Introduction	95
6.2	Resonance parameterisation	95
6.3	Electroweak corrections	96
6.3.1	Final state photonic QED corrections	96
6.3.2	Final state fermion pair emissions	98
6.3.3	Effect of $O(\alpha)$ electroweak corrections	101
6.4	Rapidity distribution and angular coefficients at $O(\alpha_S^2)$	110
6.4.1	Differential predictions as function of rapidity with CT10, CT14, and MMHT PDFs	111
6.4.2	Angular coefficients in POWHEG, DYNLLO	111
6.5	Transverse momentum distribution	113
6.5.1	Baseline prediction	115
6.5.2	Uncertainties on the p_T^W distribution with PYTHIA	116
6.6	Propagation of QCD uncertainties to m_W	121

6.6.1	Rewighting in (p_T, y, A_i) space	121
6.6.2	PDF uncertainties	122
6.6.3	Non-PDF uncertainties on the p_T^W distribution	123
6.6.4	Non-PDF polarization uncertainties	124
6.7	Summary	125
7	Event selection and background determination	131
7.1	Data samples and Monte Carlo simulations	131
7.2	Definition of the signal region	133
7.3	EW and top backgrounds	134
7.4	Multijet background estimation	137
7.4.1	Methodology	137
7.4.2	Fits to kinematical distributions in the muon channel	138
7.4.3	Fits to kinematical distributions in the electron channel	144
7.4.4	Independent cross-check of the multijet background estimates with W and Z cross section analysis at $\sqrt{s} = 7$ TeV	146
7.4.5	Multijet background estimation for W cross section measurement at $\sqrt{s} = 8$ TeV	150
7.4.6	Multijet fractions in the measurement categories	152
7.4.7	Correction of the multijet background shapes	152
7.4.8	Impact of multijet background uncertainty on M_W	156
7.5	The distributions	159
8	W boson mass measurement	171
8.1	Methodology	171
8.1.1	Introduction to the template fit method	171
8.1.2	Consistency Test	173
8.2	Measurement strategy	173
8.2.1	Introduction	173
8.2.2	Measurement categories	175
8.3	Validation on Z boson mass measurement	176
8.3.1	Z boson selection	176
8.3.2	Lepton-pair distributions	177
8.3.3	Lepton momentum, W-like recoil and transverse mass distributions	177
8.3.4	Z boson mass fit results	177
8.4	Uncertainty determination	181
8.5	Blinded fit results	184
8.5.1	Correlations between W boson observables	184
8.5.2	Combination Procedure and Correlations	187
8.5.3	Results with initial fitting range	188
8.5.4	Stability of m_W measurement with different fitting ranges	193
8.5.5	Results with optimal fitting range	198
8.5.6	Additional Cross-Checks	198
8.6	Unblinding	202
	Summary and conclusions	207
	Bibliography	209

A	Cross-talk calculations	215
A.1	Middle-Strip crosstalk	215
A.2	Strip-strip crosstalk	215
A.3	Middle-Middle crosstalk	216
B	PDF profiling	217
C	Distributions in lepton η categories	223

Theoretical background

1.1 Introduction

The dream of all particle physicists is to understand how the Universe works from the most fundamental principles. The first attempts to describe nature with axioms is referred to ancient Greek philosophers. In particular, Democritus introduced the concept of atoms as small indivisible objects, called particles, that constitute matter. This has been allowed to describe all phenomena observed at that time as motion and collision of atoms in empty space. The huge amount of progress has been made since that time and now the Universe is proven to be much richer than makes it even more interesting to explore. As far as we understand it now, all of the matter around us is mostly composed of a few lightest elementary particles: the electron, the up quark and the down quark. There is also a slew of other elementary particles, but they are massive, and therefore forced to transform (or ‘decay’) into less-weight particles. The need to consider such heavy particles as fundamental arises from the fact that they can be distinguished by unique characteristics, called quantum numbers. These particles interact through three fundamental forces - electromagnetic, strong and weak. The fourth known elementary force, the gravitational, is far too weak to cause a measurable effect at microscopic scale.

A continuing collaboration between theorists and experimentalists brought us to a small set of fundamental laws and two simple theories upon which all modern physics is based. The Standard Model (SM) of particle physics describes the electromagnetic, strong and weak interactions of particles. The General Relativity focuses only on gravity for understanding the Universe in regions of large scale. Up to now, the SM has been successfully explained almost all experimental results within its appropriate domain of applicability. Scientists tried to fit gravity into the framework of the SM, but this came out to be a difficult challenge. Besides the omission of the gravity, the SM contains no candidate for dark matter or dark energy, evidence of which comes from astrophysical observations. In order to construct a single all-encompassing theory able to explain all phenomena, more experimental inputs are needed.

1.2 The Standard Model

1.2.1 Elementary Particles

In the Standard Model there are two kinds of particles: fermions and bosons. Fermions obey Fermi-Dirac statistics and thus they respect Pauli exclusion principle, i.e. two fermions in the same quantum state can not exist in the same place at the same time. Such particles have half-integer spin in units of reduced Planck constant \hbar . Bosons, on the other hand, obey Bose-Einstein statistics and due to spin-statistics theorem they have integer spin values. Within the SM, all the matter is composed of fermions and all force carrying particles are bosons.

▷ Fermions

The modern particle physics was born after discovery of electron, the first elementary particle, as well as the proton and neutron, the building blocks of the nuclei. With the construction of large particle accelerators, the world exploded with hundreds newly discovered particles, called hadrons.

In order to properly classify such particles, Murray Gell-Mann and George Zweig have proposed a model in which hadrons are composed of even smaller particles, named quarks. Existence of quarks has been experimentally confirmed from proton's structure studies. Originally the model contained only three quark flavours, the *up*(u), *down*(d) and *strange*(s). But after discovery of J/ψ and Υ mesons it was extended with *charm*(c) and *bottom*(b) quarks. The arrangement of the quark flavours in doublets led to prediction, and later to discovery, of the *top*(t) quark, which has been found to be extremely heavy that prevents it to form hadrons.

	1 st Generation	2 nd Generation	3 rd Generation	Charge [e]
Quarks	up (u) $m = 2.3^{+0.7}_{-0.5}$ MeV	charm (c) $m = 1.275 \pm 0.025$ GeV	top (t) $m = 173.2 \pm 0.7$ GeV	+2/3
	down (d) $m = 4.8^{+0.5}_{-0.3}$ MeV	strange (s) $m = 95 \pm 5$ MeV	bottom (b) $m = 4.18 \pm 0.03$ GeV	-1/3
Leptons	Electron e^- $m = 511$ keV	Muon μ^- $m = 105.7$ MeV	Tau τ^- $m = 1.8$ GeV	-1
	Electron neutrino ν_e $m < 2$ eV	Muon neutrino ν_μ $m < 0.19$ MeV	Tau neutrino ν_τ $m < 18.2$ MeV	0

Table 1.1: Generations of quarks and leptons with their masses and charges.

The model also contains a set of six other elementary particles, called leptons. Such leptons include the electron (e), muon (μ), tau (τ), and their complemented partners, the neutrinos (ν). In general, the quarks and leptons are grouped in pairs, or doublets, and each doublet is arranged in generations as shown in Tab.1.1. Within each generation, the quarks are classified into one has charge +2/3 (up-type) and one has -1/3 (down-type), while the leptons are classified into one has electric charge -1 (electron-like) and one is neutral (neutrino). Each of higher generations has particles with higher mass and thus tends to decay to lower generation. This explains why the ordinary matter is made of the first generation particles.

Except the electric charge, the quarks have other intrinsic quantum numbers, called ‘colour charge’. This notion was proposed to the model to allow the same-flavour quarks coexist in hadrons, i.e. Δ^{++} baryon, without violating the Pauli principle. Within the SM each quark has one of three colours, commonly denoted *red*, *green* and *blue*. The number of unique colour charges was experimentally confirmed in the $\pi^0 \rightarrow \gamma\gamma$ decay rate measurement as well as the ratio R of total e^+e^- hadronic cross-section to the cross-section for the $\mu^+\mu^-$ production.

All leptons and quarks have spin 1/2 and are thus fermions. For each lepton and quark exists an associated antiparticle with the same mass but opposite charge. Most familiar example of anti-matter particle is positron which is antiparticle of the electron. This type of particles is known to form anti-matter. If a particle collides with its respective antiparticle, they will annihilate. Why the Universe has more matter than antimatter remains one of the most important questions facing the SM.

▷ Bosons

Additionally to the elementary fermionic particles, experiments also established the existence of 12 elementary bosonic particles. One of such particles is the *photon* (γ), known in some form since Isaac Newton's times. The experimental investigations of the properties of the photon gave a push to the development of the quantum physics, the theory used to describe the micro world and on which the SM is based. The photon has zero rest mass and it does not carry a charge.

Another set of elementary bosonic particles are gluons that ‘glue’ quarks together forming hadrons. Unlike the quarks, the gluons carry colour and anticolour pairs. Due to colour confinement

hypothesis, stating that only colourless particles can be found individually, eight independent combinations and, therefore, eight gluons exist. The mass of the gluons is known to be strictly zero.

In order to explain ‘weak’ processes, such as nuclear β decays, a new theory was proposed by Yang and Mills [1] and then improved by Glashow, Weinberg and Salam [2–4]. The Glashow-Weinberg-Salam electroweak model predicted existence of three massive W^+ , W^- and Z spin-1 bosons, as well as the spin-0 Higgs boson. The masses of the predicted bosons happened to be so large that it took many years to build accelerators powerful enough to produce them. The W and Z bosons have been discovered at CERN in 1983 by the UA1 and UA2 collaboration [5, 6] and their masses were found to be about 80 GeV and 91 GeV respectively. The Higgs boson has been discovered at CERN in 2012 by the ATLAS and CMS collaborations [7, 8] and its mass is measured to be about 125 GeV.

Boson	Mass	Charge [e]	Spin	Interaction	Range	Act on
photon	0	0	1	Electromagnetism	∞	charge
8 gluons	0	0	1	Strong	10^{-15} m	colour
W^+	80.4 GeV	+1	1	Weak	10^{-18} m	isospin
W^-	80.4 GeV	-1	1			
Z	91.2 GeV	0	1			
Higgs	125 GeV	0	0			

Table 1.2: The Standard Model bosons with their masses and ‘charges’, and corresponding interaction types.

1.2.2 Fields and Interactions

In our modern understanding, the particles that carry ‘charge’ are sources of quantum fields. The fields, such as electric field, give rise to forces that act on elementary particles. The forces are transmitted by the exchange of related particles, which are ‘quanta’ of the fields. So the elementary particles and their interactions are governed by quantized, relativistic and locally interacting fields. There are three conventionally taken fundamental forces (other than gravitation) - electromagnetic, weak and strong. They are successfully described by a class of quantum field theories constrained by various symmetry principles and by condition of infinity cancellations (renormalizable). The electroweak theory unifies the electromagnetic and weak forces, while the quantum chromodynamics is used to describe the strong forces. The mediators of the electromagnetic force are the photons and the strong force is mediated by eight gluons that act on the colour charge. In contrast, the weak force is mediated by massive W and Z bosons as summarized in Tab.1.2.

▷ Electromagnetism

In the same spirit as in classical field theory, each quantum field theory is formulated using Lagrangian formalism. For example in QED, for a freely propagating fermion the Lagrangian is a function of fermion field $\psi(x, t)$ and its derivative $\partial\psi(x, t)$ in time and space:

$$L_0 = \bar{\psi}i\gamma^\mu\partial_\mu\psi - m\bar{\psi}\psi \quad (1.1)$$

where γ^μ are gamma matrices, ∂_μ is differential operator and m is the mass of the particle. It is assumed that the Lagrangian depends on only the field value and its first derivative but not the higher derivatives. Then the Hamilton’s principle leads to the classical Dirac equation of motion for the fermion fields. A transformation that changes the field configuration but does not change

the observable quantities is called gauge transformation. The quantum electrodynamics is gauge theory, so the Lagrangian should be invariant under the $\psi \rightarrow e^{i\alpha}\psi$ gauge transformation of the field. The requirement of the Lagrangian to be invariant under the local gauge transformation, where $\alpha(x)$ is a general function of space-time, leads to additional terms in the Lagrangian and a new gauge field A_μ that represents the photon

$$L = \bar{\psi}i\gamma^\mu\partial_\mu\psi - m\bar{\psi}\psi - e\bar{\psi}\gamma^\mu\psi A_\mu - 1/4F_{\mu\nu}F^{\mu\nu} \quad (1.2)$$

which is the free Dirac Lagrangian plus an interaction term that couples the vector gauge field and the fermion field with strength (e), plus the kinetic term that describes the propagation of the new gauge field. Here

$$F_{\mu\nu} = -F_{\nu\mu} = \partial^\nu A^\mu - \partial^\mu A^\nu \quad (1.3)$$

is the field-strength tensor for the electromagnetic force, as described by Maxwell equations. As a mass term of a form $m^2 A_\mu A^\mu$ would spoil the gauge invariance, it is not added to (1.3). This is in agreement with the observation that the photon is massless. Under such local $U(1)$ phase rotation, the photon field transforms as $A_\mu(x) \rightarrow A_\mu(x) - \partial^\mu \alpha(x)$. Thus the coordinate-dependent $U(1)$ gauge symmetry leads to the existence of massless photon.

▷ Strong interactions

Additionally to $U(1)$ symmetry with only one related transformation (or generator) of the field, the SM also has $SU(2)$ and $SU(3)$ gauge symmetries with three and eight generators respectively. The requirement of local invariance for each of $SU(2)$ and $SU(3)$ symmetries leads to the existence of additional gauge bosons, number of each turns out to correspond to the number of generators. The strong force respects the $SU(3)$ symmetry and has eight generators constructed with Gell-Mann matrices that correspond to eight gluons. The expression for the locally gauge invariant Lagrangian of QCD which describes interactions of quarks of mass m and massless gluons is

$$L_{QCD} = \sum_{flavours} \bar{\psi}_a(i\gamma^\mu\partial_\mu\delta_{ab} - g_s\gamma^\mu t_{ab}^C A_\mu^C - m\delta_{ab})\psi_b - 1/4F_{\alpha\beta}^A F^{A\alpha\beta} \quad (1.4)$$

where the $\psi_a(x)$ are quark-field spinors for a quark with mass m , with a color-index $a = 1, 2, 3$. The A_μ^C are the gluon fields with $C = 1, 2, \dots, 8$ that transform under the adjoint representation of the $SU(3)$ group. The t_{ab}^C are the generators of the $SU(3)$ group, the quantity g_s corresponds to strong coupling constant that determines the strength of interactions between coloured objects. The strong field tensor is defined as

$$F_{\mu\nu}^A = \partial_\mu A_\nu^A - \partial_\nu A_\mu^A - g_s f^{ABC} A_\mu^B A_\nu^C \quad (1.5)$$

where f^{ABC} are the structure constants of the $SU(3)$ group satisfying $[t^A, t^B] = if^{ABC}t^C$. Because of non-Abelian nature of $SU(3)$ group, in contrast to QED, the field tensor of the QCD includes the gluon triplet and quartic self-interactions, ultimately leading to the property of asymptotic freedom. This property predicts that the coupling of quarks and gluons is large at large distances. so that neither quarks nor gluons are observed as free particles. At the same time the coupling is predicted to be small at short distances so that quarks behave as free particles within hadrons as probed by deep inelastic photon. The effect of running coupling forces to consider separately the QCD at sufficiently large energy scale using perturbative expansions in the coupling (pQCD), leading to Feynman rules of QCD. For the non-perturbative regime, the methods of lattice QCD are extensively used.

▷ Electroweak interactions

In the electroweak theory, the electromagnetic and weak interactions are unified and can be derived from the combined $U(1) \times SU(2)$ symmetry, following the same strategy as for QED. The $U(1)$ group has one generator Y , which is called 'weak hypercharge', and the $SU(2)$ isospin algebra has three generators T_1, T_2 and T_3 constructed with Pauli matrices. Then the Lagrangian of the theory can be written as

$$L = L_0 - eY\bar{\psi}\gamma^\mu B_\mu\psi - g_W\bar{\psi}\gamma^\mu(\mathbf{T} \cdot \mathbf{W}_\mu)\psi - 1/4F_{\mu\nu}F^{\mu\nu} - 1/4W_{\mu\nu}^i W^{i\mu\nu} \quad (1.6)$$

where g_W is the weak coupling to the fermionic fields. The field strength tensor for the weak gauge fields W^i is defined as

$$W_{\mu\nu}^i = \partial_\mu W_\nu^i - \partial_\nu W_\mu^i - g_W \varepsilon_{ijk} W_\mu^j W_\nu^k \quad (1.7)$$

The third non-Abelian term in Eq.(1.7), similar as in QCD model, gives rise to the weak boson self-interactions.

Need to note that experimental observations [9] require to decompose the fermions into left-handed and right-handed chirality types. For massless fermions, the definition of chirality is the same as helicity and refers to the relation between a particle's spin and direction of motion. For massive fermions the chirality is trickier to define. Remarkably, the weak force interacts only with left-handed particles and right-handed antiparticles, violating the P-symmetry. Thus, only left-handed leptons and left-handed neutrinos can form weak isospin doublets

$$\psi_L = \gamma_L \begin{pmatrix} \nu_e \\ e^- \end{pmatrix}, \gamma_L \begin{pmatrix} \nu_\mu \\ \mu^- \end{pmatrix}, \gamma_L \begin{pmatrix} \nu_\tau \\ \tau^- \end{pmatrix} \quad (1.8)$$

where $\gamma_L = 1/2(1 - \gamma_5)$ in the limit of massless leptons. Similarly the quarks form three left-handed doublets

$$\psi_L = \gamma_L \begin{pmatrix} u \\ d' \end{pmatrix}, \gamma_L \begin{pmatrix} c \\ s' \end{pmatrix}, \gamma_L \begin{pmatrix} t \\ b' \end{pmatrix} \quad (1.9)$$

The primed quarks q' differ from mass eigenstates by a transformation $q'_i = \sum_j V_{ij} q_j$, and matrix V is known as Cabibbo-Kobayashi-Maskawa (CKM) matrix. The magnitudes of the CKM elements determine couplings of W boson to physical up and down-type quarks. It is convenient to assume that right-handed neutrinos do not exist and the right handed leptons and quarks $\psi_R = 1/2(1 + \gamma_5)\psi$ are all $SU(2)$ singlets. But in this representation the fermion mass term $-m_f \bar{\psi}\psi$ of the Lagrangian links left-handed and right-handed components $\bar{\psi}_L \psi_R + \bar{\psi}_R \psi_L$ that transform differently under $SU(2)$ and $U(1)$. This term does not respect the local gauge invariance and is forbidden. So one can see that the model still can not describe the real world as we know experimentally that fermions have mass. Moreover, it contains four massless bosons while in reality only a photon is massless. The addition of explicit mass terms to Lagrangian would break the local gauge invariance.

1.2.3 The EW symmetry breaking

In the SM, the $SU(2) \times U(1)$ symmetry is broken to the remaining $U(1)_{EM}$ symmetry by introducing a doublet of complex fields ϕ_h which interacts with all the SM particles, including EW bosons, and generates their masses. The Higgs potential is chosen to be of the form

$$V(\phi_h) = -\mu^2 \phi_h^\dagger \phi_h + \lambda (\phi_h^\dagger \phi_h)^2 \quad (1.10)$$

With parameters $\lambda, \mu^2 > 0$ this potential has minimum not at zero, but equal to the vacuum expectation value $|\phi| = \sqrt{\mu^2/2\lambda} = v/\sqrt{2}$, where $v \approx 246$ GeV. Redefinition of the new ground state $\phi = (v + H)/\sqrt{2}$ spontaneously breaks the $SU(2)$ symmetry, and only one neutral scalar field

H remains giving rise to the physical Higgs boson. Three other degrees of freedom are used up in giving mass to gauge bosons. At low energies the value of Higgs field can be replaced by the constant value, allowing fermions to have mass, $m_f = g_f v / \sqrt{2}$, through the Yukawa term in the Lagrangian:

$$L_Y = -g_f \bar{\psi} \psi \phi_h \rightarrow -g_f \bar{\psi} \psi \frac{v}{\sqrt{2}} \quad (1.11)$$

This appears only after EW symmetry breaking. The g_f is Yukawa coupling and represents the strength of H to ψ coupling. Note that the property of the Higgs field is that it flips handedness of the fermion fields. The fact that right-handed neutrinos do not exist, therefore the left-handed neutrinos can not interact with Higgs field and are, thus, massless.

It is convenient to redefine the electroweak fields in terms of electrically neutral and charged electroweak fields corresponding to charge and mass eigenstates:

$$\begin{aligned} A_\mu &= B_\mu \cos \theta_W + W_\mu^3 \sin \theta_W \\ Z_\mu &= -B_\mu \sin \theta_W + W_\mu^3 \cos \theta_W \\ W_\mu^\pm &= (W_\mu^1 \mp i W_\mu^2) / \sqrt{2} \end{aligned} \quad (1.12)$$

Then the interaction Lagrangian after symmetry breaking can be expressed in terms of these physical fields:

$$\begin{aligned} L_{EW} &= \sum_f \bar{\psi}_f (i \gamma^\mu \partial_\mu - m_f - g_W \frac{m_f H}{2 M_W}) \psi_f \\ &\quad - \frac{g_W}{2\sqrt{2}} \sum_f \bar{\psi}_f \gamma^\mu (1 - \gamma^5) (T^+ W_\mu^+ + T^- W_\mu^-) \psi_f \\ &\quad - e \sum_f Q_f \bar{\psi}_f \gamma^\mu \psi_f A_\mu - \frac{g_W}{2 \cos \theta_W} \sum_f \bar{\psi}_f \gamma^\mu (V_f - A_f \gamma^5) \psi_f Z_\mu \end{aligned} \quad (1.13)$$

where the angle θ_W is the Weinberg angle, fixed by the ratio of $SU(2)$ and $U(1)$ coupling constants $\theta_W = \tan^{-1}(g'_W/g_W)$. The Weinberg angle is determined from experiment to be $\sin^2 \theta_W = 0.23$. Due to the coupling of the photon to fermion has to be equal to that in QED, the g_W and g'_W couplings are related to the elementary charge through $e = g_W \sin \theta_W$. The second term in (1.13) represents the V-A charged-current interaction, where $T^+ = T^1 + iT^2$ and $T^- = T^1 - iT^2$ are the weak isospin raising and lowering operators. The third term describes electromagnetic interactions with pure vector couplings. The last term is the weak neutral-current interaction with a mix of vector and axial vector couplings of the fermions to the Z boson that depend on the quantum numbers of the fermion

$$V_f = T_f^3 - 2Q_f \sin^2 \theta_W, A_f = T_f^3 \quad (1.14)$$

Here T_f^3 and Q_f are the weak isospin and charge of the fermion respectively.

After the rotation defined in (1.12), the boson masses can be obtained from the quadratic terms in the vector boson fields in terms of vacuum expectation value v and the coupling constants g_W and g'_W :

$$\begin{aligned} M_W &= \frac{1}{2} g_W v \\ M_Z &= \frac{1}{2} \sqrt{g_W^2 + g'^2_W} v = \frac{M_W}{\cos \theta_W} \\ M_H &= \sqrt{2\lambda} v \end{aligned} \quad (1.15)$$

Note that these relations are given at low energies (i.e. at lowest order). The photon remains massless as there are no terms quadratic in the field A_μ . At low energies the Fermi model works well that allows us to make the relation $\frac{g_W^2}{8M_W^2} \equiv \frac{1}{2v^2} = G_F/\sqrt{2}$, where the value $G_F = 1.66 \cdot 10^{-5} \text{ GeV}^{-2}$ is the Fermi constant which is derived from the muon lifetime measurement. This yields to the vacuum expectation value of the Higgs field $v = 246 \text{ GeV}$.

As a consequence of spontaneous symmetry breaking, the charged and neutral gauge bosons get masses M_W and M_Z respectively, the fermions acquire masses through the corresponding Yukawa couplings. While masses of the weak bosons are predicted in the SM, the mass of the Higgs boson is not predicted and could have any value.

1.3 W boson mass

1.3.1 Prediction in the SM

As shown above, the fundamental parameters of the EW sector of the SM after spontaneous breakdown of the symmetry are the mass of the Higgs boson, the large number of charged lepton and quark masses as well as quark mixing matrix, together with two coupling constants g_W and g'_W and vacuum expectation value of the Higgs field. At low energies the effect of Higgs mass on the physical observables is small. Thus, neglecting the fermion masses, only three independent input parameters remain to make predictions with the SM. It is convenient to choose those parameters which are measured with a high precision. These are taken to be the value of fine-structure constant, $\alpha_{em} = e^2/4\pi$, the Fermi constant G_F , and the mass of the Z boson M_Z determined with high accuracy from Z lineshape scan at LEP1:

$$\begin{aligned}\alpha_{em}^{-1} &= 137.035999074(44) \\ G_F &= 1.1663787(6) \times 10^{-5} \text{ GeV}^{-2} \\ M_Z &= 91.1876(21) \text{ GeV}\end{aligned}\tag{1.16}$$

At this level, the W boson mass in eq.(1.15) can be rearranged via these parameters

$$M_W^2 = M_Z^2 \left(\frac{1}{2} + \sqrt{\frac{1}{4} - \frac{\alpha_{em}\pi}{\sqrt{2}G_F M_Z^2}} \right)\tag{1.17}$$

that predicts $M_W = 80.939 \pm 0.0026 \text{ GeV}$. However, the W mass measurement can be performed at sufficiently large energy scale $Q^2 = M_W^2$. Thus, the predictions should be calculated at these energies in order to describe precision experiments adequately. The standard procedure is to define the running $\alpha_{em}(Q) = \frac{\alpha_{em}}{1 - \Delta r(Q)}$, and calculate $\alpha_{em}(Q^2 = M_W^2)$ by including radiative corrections arising from higher order loop contributions to W boson propagator and vertices, which enter via Δr . The expression (1.17) takes then form

$$M_W^2 = M_Z^2 \left(\frac{1}{2} + \sqrt{\frac{1}{4} - \frac{\alpha_{em}\pi}{\sqrt{2}G_F M_Z^2 (1 - \Delta r)}} \right)\tag{1.18}$$

The complication is that in perturbation theory the calculation of loops results in divergences. The way to cancel them is through renormalization procedure for couplings, fields and masses. When these corrections are renormalized in the 'on-shell' scheme, the one-loop contributions to Δr can be decomposed as

$$\Delta r = \Delta\alpha - \frac{\cos^2 \theta_W}{\sin^2 \theta_W} \Delta\rho + \Delta r_{rem}\tag{1.19}$$

where $\Delta\alpha$ is the fine-structure shift due to light fermionic loop corrections $\Delta\alpha \sim \log m_f$, the $\Delta\rho$ is the shift of classical ρ parameter that contains the weak part of the one-loop contributions, including the quadratic dependence on the top quark mass, as a consequence of a large mass splitting in the isospin doublet [10]. The ρ parameter is defined as

$$\rho = \frac{M_W^2}{M_Z^2 \cos^2 \theta_W}\tag{1.20}$$

and should be equal to unity at tree level according to relation (1.15). The Δr_{rem} collects the remaining contributions from higher order expansions, where the dependence on the Higgs mass enters. In practice, the hadronic contributions to the $\Delta\alpha$ can not be precisely calculated, as masses of the light quarks are not well-known (and/or non-perturbative regime at low Q). Therefore, the fine-structure shift is usually divided in two categories: from leptonic loops $\Delta\alpha_{lep}$ and light quark loops $\Delta\alpha_{had}$. The hadronic part is best determined from experiments by analysing e^+e^- annihilation and τ decay data.

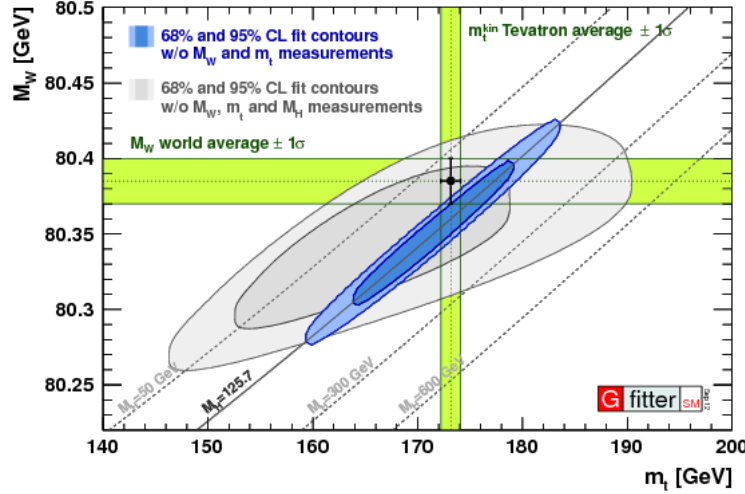


Figure 1.1: Prediction of M_W as a function of m_t as obtained from electroweak fit, including (blue contour) and excluding (grey contour) Higgs boson mass M_H , as compared to the direct measurement (vertical and horizontal green bands and black dot).

In summary, the quantity $\Delta r = \Delta r(\alpha_{em}, M_Z, M_W, m_t, M_H)$ includes the top quark and Higgs masses which are not present at the tree level expression. The Higgs loops enter to the Δr with a contribution proportional to the logarithm of the M_H , with positive sign. On another hand, the heavy-light (top-bottom) doublet loop results to Δr with a term proportional to $-m_t^2$ and leads to sizable dependence on the top quark mass. The Δr also depends on the W boson mass itself, thus the numerical calculations are done with iteration procedures. In practice, the procedure converges quickly and only a few iterations are required.

The size of one-loop contributions results to $\Delta r^{(\alpha)} \approx 0.03$, indicating that even more higher order corrections are needed to satisfy the current level of experimental precision. At present, the corrections are calculated at full two-loop order $O(\alpha^2)$ and $O(\alpha\alpha_s)$, and partially for three and four-loop at order $O(\alpha\alpha_s^2)$, $O(\alpha^2 m_t^2 \alpha_s^2)$, $O(\alpha^3 m_t^3)$ and $O(\alpha m_t \alpha_s^3)$. The contributions from unknown higher-order corrections are estimated using well-tested assumption that the perturbation series follow a geometric growth. The largest correction is expected to be from unknown $O(\alpha^2 \alpha_s)$, $O(\alpha^3)$ and $O(\alpha_s^3)$ terms and these are taken as sources of theoretical uncertainties. The overall theoretical uncertainty amounts to $\delta_{theo} M_W = 4$ MeV [11].

The prediction of the W boson mass results from a global least-square fit to all experimental data that enter in eq.(1.20). The experimental uncertainty of each input parameter is additional source of uncertainty on the M_W . The fit determines the W mass to be [12]

$$\begin{aligned}
 M_W &= 80.3584 \pm 0.0046_{m_t} \pm 0.0030_{\delta_{theo} m_t} \pm 0.0026_{M_Z} \pm 0.0018_{\Delta\alpha_{had}} \\
 &\quad \pm 0.0020_{\alpha_s} \pm 0.0001_{M_H} \pm 0.0040_{\delta_{theo} M_W} \text{ GeV} \\
 &= 80.358 \pm 0.008_{tot} \text{ GeV}
 \end{aligned} \tag{1.21}$$

which is more precise than the direct measurement (see Section 1.3.3). At present, the largest uncertainties are due to m_t , both theoretical and experimental, following by the theory and M_Z uncertainties.

1.3.2 W boson mass beyond the SM

The SM cannot be a fundamental theory of the particle physics as there are questions that cannot be answered satisfactory within its framework. For example, the SM does not include the gravity, it has no solution to the hierarchy problem, it does not explain the dark matter. In order to answer at least some of these question, a number of new physics models are studied, in particular the Minimal Supersymmetric Standard Model (MSSM). Supersymmetry is an extension

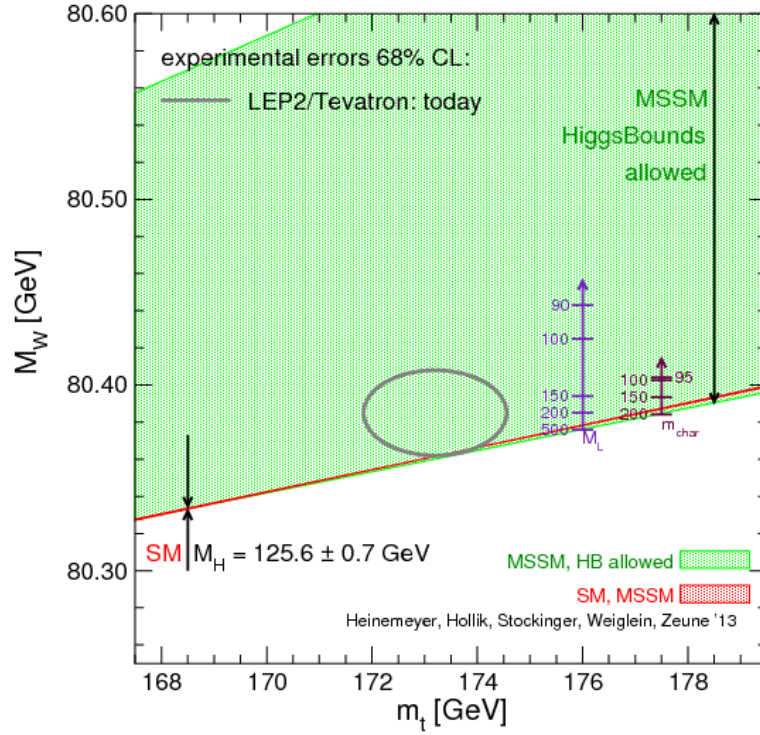


Figure 1.2: Prediction of M_W as a function of m_t . The green region corresponds to parameter scan within MSSM model. The red strip indicates the overlap region of the SM and the MSSM, with $M_H^{SM} = 125.6 \pm 0.7$ GeV.

of the SM. It predicts that for each fermionic particle exists a bosonic supersymmetric partner and vice versa. It turns out that superpartner particles are out of the SM and they are so massive that are not directly detected yet. Although the current energy regime in the experiments is too low, the effect of a new physics can be present via virtual effects of not yet discovered particles. Various models predict different radiative correction Δr due to different particle content and their interactions. The precision measurement of the SM observables, in particular the W mass, provides a powerful probe of a new physics. A deviation of the experimental measurement of the M_W from its prediction in the SM implies the existence of other undiscovered particles that enter either through loop contributions or are heavy resonances, such as heavy W' . However this requires high precision of both the experimental results and the theoretical predictions.

In the MSSM, the radiative corrections to the M_W also contain contributions from sfermions, charginos, neutralinos and the Higgs bosons that enter at one-loop level and can give significant contributions. As the masses of these particles are unknown, it is practical to scan the MSSM parameter space for comparison of M_W prediction and its experimental result. The variation range of SUSY parameters is wide, the masses of unknown particles are usually varied within 100 GeV-2000 GeV independently of each other. The evaluation of M_W prediction is currently done for full one-loop contributions and partially for higher order corrections. It turns that the largest one-loop contributions arise from the stop-sbottom doublet, similar to top-bottom doublet in the SM, as well as from single squark loops. In general, the lighter the squark masses and the larger stop-sbottom mass splitting, the larger contribution to the W mass. The total radiative correction in the supersymmetric sector can reach several hundred MeV [13], as shown in Fig.1.2.

1.3.3 Direct measurements

The W boson has been discovered by UA1 and UA2 collaborations in proton-antiproton collisions at the SPS collider in 1983. The detector was tuned to look for energetic electrons. Out of the several thousand million collisions which had been collected, the UA1 and UA2 announced only

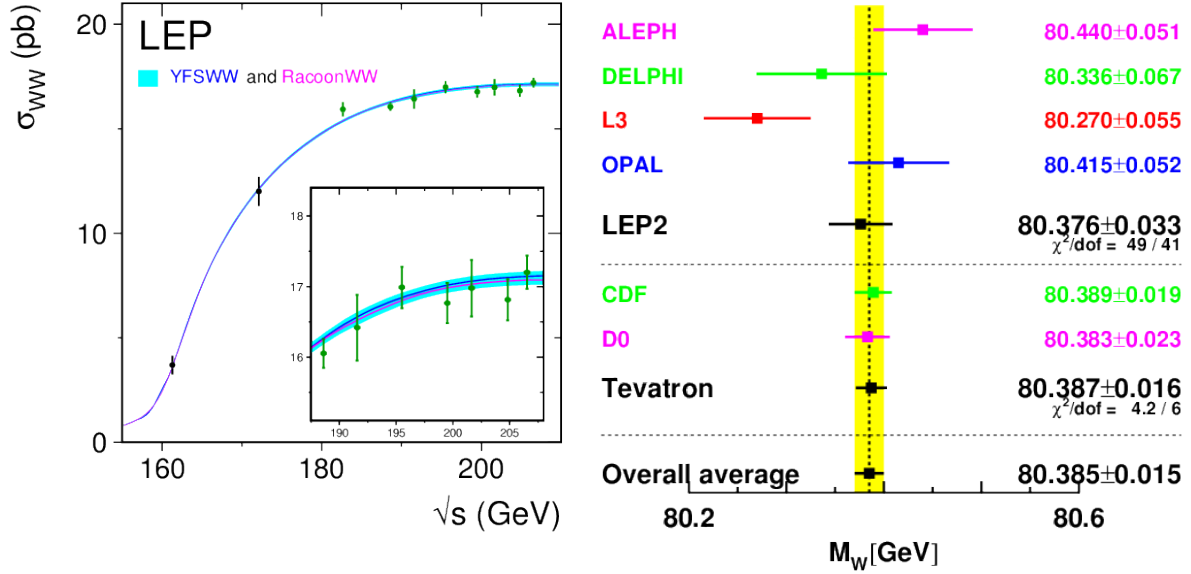


Figure 1.3: *Left*: combined LEP W^+W^- cross-section measurements as a function of the center-of-mass energy compared with the SM predictions using $M_W = 80.35$ GeV. *Right*: Measurements of the W -boson mass by the LEP and Tevatron experiments. The world-average uncertainty (15 MeV) is indicated by the yellow band.

six and four W candidates respectively. The energy imbalance of particles around a W decay point indicated about presence of a neutrino. Despite such a low statistics, both teams could already obtain values for the W mass of 81 ± 5 GeV [5] and $80 + 10 - 6$ GeV, that agrees with the SM prediction.

Later, the W boson mass has been also measured in the Large Electron-Positron Collider (LEP) at CERN. The LEP has been constructed in 1989 and it was designed to accelerate electrons and positrons to a total energy of about 45 GeV each, aiming to produce Z bosons. Later it was upgraded and from 1995 to 2000 its collision center-of-mass energy, \sqrt{s} , was gradually increased from Z pole up to 209 GeV. During 1996-2000 the LEP operated above the threshold for W^+W^- production and recorded significant number of events for precision measurements. The W^+W^- decay modes are measured to be fully hadronic $q\bar{q}q\bar{q}$ (45%), mixed hadronic-leptonic $q\bar{q}l\bar{\nu}_l$ (44%) and leptonic $l^+\nu_l l^-\bar{\nu}_l$ (11%). The clear W -pair decay topology at LEP allowed to identify these events with a high purity.

The scan of the $e^+e^- \rightarrow W^+W^-$ cross-section with energy has shown the threshold behavior close to $\sqrt{s} = 161$ GeV that corresponds to two times of the W mass (see Fig.1.3 (*left*)). In the threshold region the cross-section is dominated by the t -channel (ν exchange diagram) that is proportional to the W velocity:

$$\sigma(W^+W^-) \sim \sqrt{1 - 4M_W^2/s} \quad (1.22)$$

This allows to determine directly the W mass by fitting data points with this function. The combined result of this method from ALEPH, DELPHI, L3 and OPAL experiments [14] is

$$M_W^{LEP}(\text{threshold}) = 80.42 \pm 0.20_{\text{stat}} \pm 0.03_{\text{syst}} \text{ GeV} \quad (1.23)$$

where the systematic uncertainty is dominated by imperfect knowledge of the beam energy. However, the LEP operated mostly at energies significantly above the W -pair production threshold, which is less sensitive to the M_W . At these higher energies, the four LEP experiments recorded data that corresponds to about ten thousand W^+W^- events each. Here the W invariant mass

was directly determined with high precision by reconstructing the W-pair decay products mainly in fully hadronic and semileptonic decay channels. The $W^+W^- \rightarrow q\bar{q}q\bar{q}$ events are reconstructed from hadronic jets associated with particle tracks and energy deposits in the calorimeter. In case of semileptonic decay channel, the W mass is determined by reconstructing hadronically decaying W boson. The mass of the second leptonically decaying W can also be determined as the neutrino momentum can be calculated through the momentum balance. This method is limited by energy resolution of reconstructed jets. The combined LEP W mass value from direct reconstruction method [15] is

$$M_W^{LEP}(direct) = 80.376 \pm 0.025_{stat} \pm 0.022_{syst} \text{ GeV} = 80.376 \pm 0.033 \text{ GeV} \quad (1.24)$$

and is indicated in Fig.1.3.

The mass of the W boson has been also measured in Tevatron collider at Fermilab. The two detectors, CDF and D0, recorded proton-antiproton collisions during two periods 1987-1996 (Run-I) and 2002-2011 (Run-II) at center-of-mass energy of $\sqrt{s} = 1.8 \text{ TeV}$ and $\sqrt{s} = 1.96 \text{ TeV}$ respectively. At the Tevatron, the W bosons are produced mainly in quark-antiquark annihilation processes. The W mass is determined from comparisons of kinematical distributions of subsequent $W \rightarrow l\nu$ decay products reconstructed in data with those ones that are simulated with different assumption of the m_W value. As the longitudinal component of the neutrino momentum cannot be measured in hadron colliders, all the kinematic variables are considered in the transverse plane with respect to the beam direction. These distributions depend not only on the detector effects, which must be accounted for the simulations, but also are sensitive to the W boson kinematics and parton distribution functions (PDFs) of the interacting hadrons. In contrast to the lepton colliders, imperfect knowledge of these quantities limits the precision of the W mass determination in hadron colliders. However, in high-energy hadron colliders the W production rate is high. That allowed both CDF and D0 to measure the M_W with higher precision than the combined LEP result. The combined value of the W mass from both Tevatron experiments is [16]

$$M_W^{Tevatron} = 80.387 \pm 0.016 \text{ GeV} \quad (1.25)$$

The uncertainty here is equally dominated by the detector calibration, physics modeling and statistics. The combination with LEP result (1.24) leads to the world average value

$$M_W = 80.385 \pm 0.015 \text{ GeV} \quad (1.26)$$

1.4 W and Z production at hadron colliders

1.4.1 Structure of the proton

One of the ways to produce vector bosons, W or Z, is through quark-antiquark annihilation processes $q\bar{q}' \rightarrow W$, $q\bar{q} \rightarrow Z$, but the quarks are confined in colourless hadrons and cannot be observed freely. Thus, in hadron colliders like the LHC and Tevatron, the vector bosons V are produced by colliding hadrons h_1 and h_2 , which are more complicated objects composed of the quarks and gluons (commonly called 'partons')

$$h_1(p_1) + h_2(p_2) \rightarrow V + X \quad (1.27)$$

where p_1, p_2 are the momenta of incoming hadrons, and X represents the accompanying final state. In order to study the physics (properties and characteristics) of the produced W bosons at hadron colliders, one needs to understand the physics starting from protons.

The protons are known to be made up of two up and one down quarks uud . They are called *valence* quarks and together determine the quantum numbers of the proton. The valence quarks strongly interact between each other through the gluon exchange. Due to non-Abelian nature of

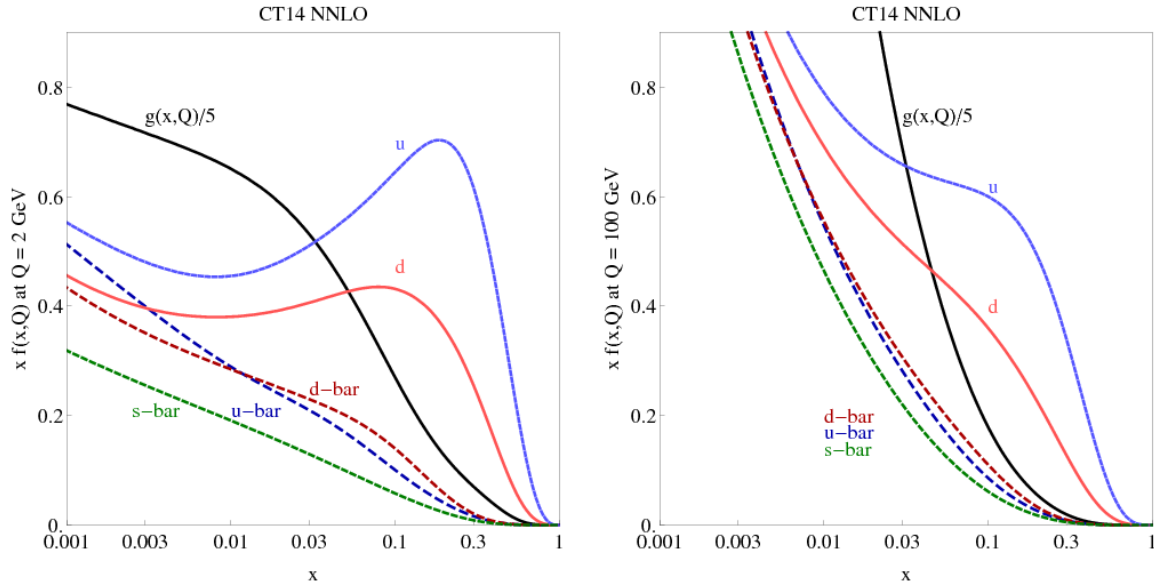


Figure 1.4: The CT14 parton distribution functions at $Q = 2$ GeV and $Q = 100$ GeV for $u, \bar{u}, d, \bar{d}, s = \bar{s}$ and g [17].

the QCD, the gluons can self-interact and produce more gluons. Moreover, each gluon can produce a pair of *sea* quarks that can also contribute to the W boson production in proton collisions. So the dynamics of products of two colliding protons is determined by the dynamics of partons inside each proton. The additional complication is that it involves the non-perturbative regime of the QCD.

The structure of the proton has been extensively studied in deep inelastic lepton-proton scattering (DIS) experiments. Measurements of DIS structure functions allowed to determine how the proton's momentum is distributed among the partons. The momentum distribution functions $f_i(x, Q^2)$ of parton $i = u, d, \dots, g$ within the proton are called Parton Distribution Functions (PDFs) and represent the probability density to find a parton carrying momentum fraction x at energy scale Q . In general, the PDFs are solutions of DGLAP evolution equations providing the Q^2 dependence, but only in the perturbative domain. The x dependence at a given Q^2 cannot be calculated analytically but rather are extracted from global fits to data from many experiments, including deep inelastic scattering, vector boson production and inclusive jet production. Examples of parton distributions in the proton is shown in the Fig.1.4 at two energy scales $Q = 2$ GeV and $Q = 100$ GeV. There are different PDF sets which use different fitting methods and experimental data.

1.4.2 W and Z boson production and rapidity distributions

The processes that appear in collisions of hadrons in general involve both 'hard QCD' and 'soft QCD' regimes. The hard QCD processes, such as vector boson production, correspond to large momentum transfers Q^2 of interacting partons and can be calculated perturbatively. In contrast, the soft processes correspond to low Q^2 and large $\alpha_s(Q)$ that makes perturbative treatment impossible. However, the parton density functions $f_i(x, Q^2)$ considered at sufficiently large energy scale $Q^2 = \mu_F^2$ can absorb divergencies of non-perturbative processes. According to the *factorization theorem*, the total cross section of the hard scattering process in Eq.(1.27) can be obtained by weighting the sub-process cross section $\sigma_{q\bar{q} \rightarrow V}$ with the PDFs:

$$\sigma_V(h_1(p_1), h_2(p_2)) = \sum_{a,b} \int_0^1 dx_a dx_b f_{a/h_1}(x_a, \mu_F^2) f_{b/h_2}(x_b, \mu_F^2) \times \sigma_{ab \rightarrow V}(x_a p_1, x_b p_2, \mu_F^2) \quad (1.28)$$

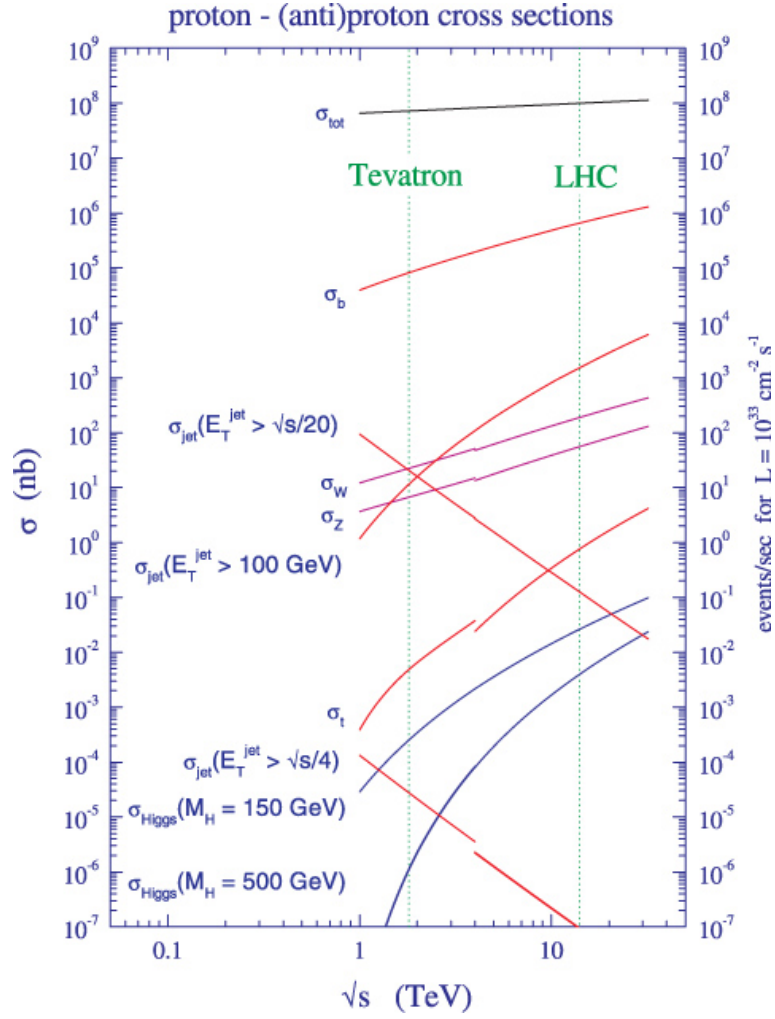


Figure 1.5: Standard model cross sections as predicted at the Tevatron (first vertical green line) and LHC (second vertical green line) colliders. The second vertical line corresponds to designed LHC energy of $\sqrt{s} = 14$ TeV.

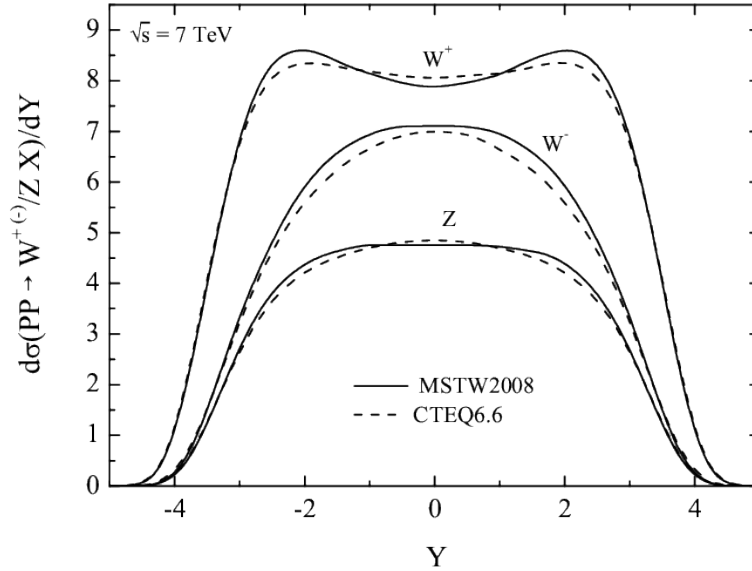


Figure 1.6: The rapidity distribution of the differential cross sections for W^+ , W^- and Z boson productions at $\sqrt{s} = 7$ TeV.

where μ_F is the factorization scale that separates hard and soft QCD regimes. The sum runs over all partons that can contribute to the process. The partonic cross section can be expanded in terms of α_s as

$$\sigma_{ab \rightarrow V} = \sigma_0 + \alpha_s(\mu_R^2)\sigma_1 + \alpha_s^2(\mu_R^2)\sigma_2 + \dots \quad (1.29)$$

Here the μ_R is the renormalization scale of the running coupling. In general, the cross section calculated at all orders of perturbative expansion does not depend on choice of the μ_F and μ_R parameters. But the processes of lepton pair production through mechanism of quark-antiquark annihilation are known only up to next-to-next-to-leading order (NNLO). In this case it is necessary to make a specific choice of μ_F and μ_R values to the cross section predictions. For such processes the standard choice is $\mu_R = \mu_F = M_W, M_Z$, the mass of the vector boson [18]. Figure 1.5 shows the predictions for some important Standard Model cross sections at pp and $p\bar{p}$ colliders, calculated using the above formalism at NLO.

In the center-of-mass frame of the two colliding hadrons, the four-momenta of the incoming partons can be assumed collinear with the colliding hadrons

$$\begin{aligned} p_a &= \frac{\sqrt{s}}{2}(x_a, 0, 0, x_a) \\ p_b &= \frac{\sqrt{s}}{2}(x_b, 0, 0, -x_b) \end{aligned} \quad (1.30)$$

where \sqrt{s} denotes the center-of-mass energy of the colliding hadrons h_1 and h_2 . The partonic collision energy is related to the overall hadronic collision energy by $\hat{s} = (p_a + p_b)^2 = x_a x_b s$. With this approximation, the hadronic cross section for vector boson production in equation (1.28) can be rewritten at lowest order of perturbative expansion and at threshold energy with mass M as

$$\sigma(h_1 h_2 \rightarrow V + X) = \int_0^1 dx_a dx_b \delta(x_a x_b s - M^2) \times \sum_{a,b} \sigma_0^{ab \rightarrow V}(M) f_a(x_a, M^2) f_b(x_b, M^2) \quad (1.31)$$

where the partonic cross sections for vector boson $V = W, Z$ production have form [18]

$$\begin{aligned} \sigma_0^{q\bar{q}' \rightarrow W} &= \frac{\sqrt{2}\pi G_F M_W^2}{3} |V_{qq'}|^2 \\ \sigma_0^{q\bar{q} \rightarrow Z} &= \frac{\sqrt{2}\pi G_F M_Z^2}{3} (g_V^2 + g_A^2) \end{aligned} \quad (1.32)$$

where $V_{qq'}$ is the appropriate Cabibbo-Kobayashi-Maskawa matrix element, and g_V (g_A) is vector (axial vector) coupling of the Z to the quarks.

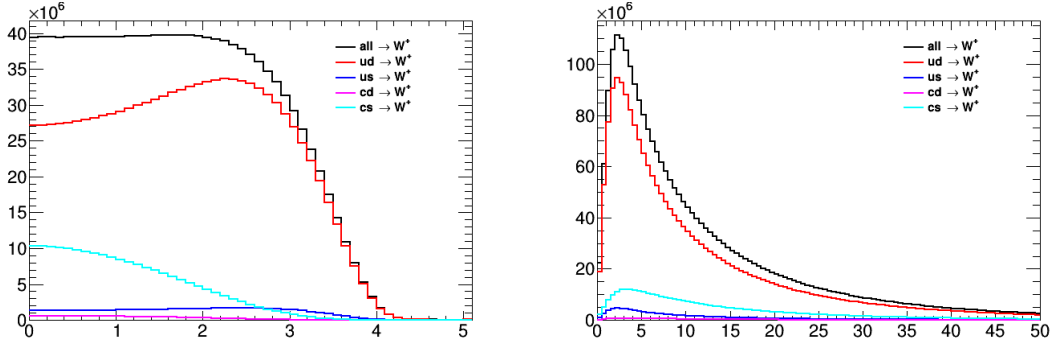


Figure 1.7: Differential cross section as a function of rapidity (*left*) and transverse momentum (*right*) for W^+ boson for different initial parton flavours.

The rapidity of the vector boson with energy E and longitudinal momentum p_z is defined as

$$y = \frac{1}{2} \log \frac{E + p_z}{E - p_z} \quad (1.33)$$

Using (2.2.1), the latter can be represented in terms of the parton momentum fractions by $y = \frac{1}{2} \log(\frac{x_a}{x_b})$, and hence

$$x_a = \frac{M}{\sqrt{s}} e^y, x_b = \frac{M}{\sqrt{s}} e^{-y} \quad (1.34)$$

Therefore, the differential cross section as a function of boson rapidity distribution is

$$\frac{d\sigma}{dY} = \frac{1}{s} \sum_{a,b} \sigma_0^{ab \rightarrow V}(M) f_a(x_a, M^2) f_b(x_b, M^2) \quad (1.35)$$

with x_a, x_b given by (1.34). As can be seen, the vector boson rapidity distribution at leading order directly depends on parton distribution functions of the colliding hadrons. By measuring the rapidity distribution at energy scales $Q^2 = M^2$, one can constrain the PDFs for different values of parton x . At the LHC, the accessible rapidity range is $|y| < 4.3$ for $\sqrt{s} = 7$ TeV and expected to be $|y| < 5$ for $\sqrt{s} = 14$ TeV, that allows to probe the parton $x = 1.7 \cdot 10^{-4}$ and $x = 4.2 \cdot 10^{-5}$ respectively.

Figure 1.6 shows the rapidity distributions of the differential cross sections for W^+, W^- and Z boson production at $\sqrt{7}$ TeV [19]. The difference between W^+ and W^- rapidity distributions are due to the difference of the $u(x)$ and $d(x)$ parton density distributions seen in Fig.1.4 (*right*). Therefore, in particular, the charge asymmetry can be used to constrain the ratio $u(x)/d(x)$. Figure 1.7 (*left*) shows the expected rapidity distributions for W^+ boson production for different initial parton flavours. As can be seen, processes involving only sea quarks generate on average more central rapidity distributions, while the processes involving a valence quark are more forward. If a particular PDF set mis-models the partonic fractions, it can result in a mis-modeling of the overall rapidity distribution. Such discrimination between W boson rapidity distributions produced by sea and valence quarks could also provide an additional constraining power for the parton density functions. Similarly, Figure 1.7 (*right*) shows the expected W boson momentum distributions p_T^W transverse to the beams direction for different initial parton flavours. The processes involving heavy quarks generate on average a harder boson p_T than those involving only first generation quarks.

1.4.3 Boson transverse momentum

At leading order calculations for W and Z production cross section the momentum of the vector boson in transverse plane with respect to the beam axis is expected to be zero if momenta

of incoming partons are defined as in equation (2.2.1). However, the intrinsic non-perturbative motion of partons inside the colliding hadrons can also give a contribution. This effect has been studied in fixed-target proton-neutron collisions and it was determined that the average intrinsic transverse momentum is $k_T \approx 0.76$ GeV [20]. In addition, the processes from higher order QCD corrections that lead to radiation of additional quarks and gluons in transverse plane can generate large transverse momentum of produced boson. Low p_T is generated dominantly by multiple soft or almost collinear partons, while higher p_T spectrum is dominated by emission of one or more hard partons. The relevant next-to-leading processes are $q\bar{q} \rightarrow Vg$ and $qg \rightarrow Vq$ etc. The amplitudes of these processes can be easily obtained from Feynman diagrams and the resulting partonic cross sections for W production are expressed by the Mandelstam variables

$$\begin{aligned}\sigma_1^{q\bar{q}' \rightarrow Wg} &\sim \alpha_s \frac{t^2 + u^2 + 2sM_W^2}{tu} \\ \sigma_1^{qg \rightarrow Wq'} &\sim \alpha_s \frac{s^2 + u^2 + 2tM_W^2}{-su}\end{aligned}\quad (1.36)$$

The NLO results for partonic cross section of the Z boson production are similar. The transverse momenta distributions $d\sigma/dp_T$ then can be obtained by convoluting (1.36) with parton density functions. In a similar way the NNLO perturbative corrections can be obtained from gluon emission processes like $q\bar{q}' \rightarrow Vgg$. At present, the corrections up to NNLO order, including virtual loop corrections, have been calculated [21].

For $p_T \gg M$, the (1.36) leads to the differential cross section of the form $\frac{d\sigma}{dp_T^2} \sim \alpha_s/p_T^2$. However, the poles at $t = 0$ and $u = 0$ in (1.36) lead to divergencies in the cross section at small p_T . These divergencies are of the form $\alpha_s^n \log^{2n-1}(M^2/p_T^2)$ for n -th order. When $\alpha_s \log^2(M^2/p_T^2)$ become close to one, the high order terms cannot be neglected. Fortunately, the leading logarithms can be resummed to all orders in perturbation theory. The resummed procedure for the W boson gives

$$\frac{d\sigma}{dp_T^2} = \sigma \frac{d}{dp_T^2} \exp\left(-\frac{\alpha_s C_F}{2\pi} \log^2 M_W^2/p_T^2\right) \quad (1.37)$$

This describes the basic shape of p_T^W distribution but it does not include the case when the multiple gluons are emitted with $k_T \sim p_T$ or $\sum \vec{k}_{T,i} \sim \vec{p}_T$. The RESBOS generator [22–24] is tuned to model low p_T regime by resumming the leading order contributions up to the next -to-next-to-leading logarithms (NNLL).

Another numerical approach is provided by parton showers which are implemented in programs such as PYTHIA [25], HERWIG [26] and SHERPA [27]. In this approach the energy scale of partons that participate in hard interaction (vector boson production) can be related to an energy scale of the protons Λ_{QCD} . This is possible because of the parton shower approach provides such evolution of the parton fragmentation functions through the DGLAP formalism. Free parameters of such parton shower algorithms can be tuned to match p_T distributions measured in data. As an example, a parton shower algorithm in PYTHIA has been tuned to match p_T^Z data from the Tevatron [28].

The p_T^W distribution has been measured at the Tevatron using $\sqrt{s} = 1.8$ TeV data collected by both CDF [29] and D0 [30], as well as at the LHC using ATLAS detector [31].

The Large Hadron Collider and the ATLAS detector

2.1 LHC

The Large Hadron Collider (LHC) is a circular accelerator of hadrons with a circumference of 27 kilometers. The LHC was designed to accelerate and collide proton beams with a center-of-mass (CM) energy up to 14 TeV as well as heavy ions, in particular lead nuclei, at 2.3 TeV per nucleon. In principle, a collider can be designed for different particle species with their own advantages and disadvantages. The choice of the particles depends on the key objective of the collider project. The lepton colliders, such as LEP, are better suited for high precision measurements as the CM energy of collided leptons is precisely defined. In hadron colliders, such as Tevatron and LHC, the collisions occur between pairs of quarks and gluons that carry only a certain fraction of the hadron energy and therefore the CM energy can vary. On another hand, the hadrons are heavy and lose only a small fraction of energy during acceleration in form of the synchrotron radiation that allows to accelerate them to high CM energies. In addition, the interaction rate at hadron colliders is much higher with respect to lepton colliders. These features offer good discovery potential that satisfies the key objectives of the LHC.

The LHC has been built in already existing LEP tunnel at a depth varying from 50 to 170 meters underground. Approximately 22 km of the LHC ring consists of curved sections. The remaining 5 km of the tunnel consist of 8 straight sections that provide space for the experiments, elements for the injection and extractions of the beam, acceleration and beam cleaning devices. The bending of accelerated beams in arcs is ensured by 1232 dipole magnets of 15 meters in length each. In addition, 392 quadrupole magnets, each 3-7 meters long, provide a strong reflection of stray particles of the beam towards the designed orbit. The strength of the focusing magnets is required to be high to squeeze the transverse beam sizes and, thus, increase the chances of collisions. The balance between the maximal beam energy and the transverse beam size is reflected in the trade between maximising space for the dipoles and keeping sufficient space for quadrupoles. The adopted design at the LHC is approximately 80% of the arcs is filled with dipole magnets. Dipoles are also equipped with sextupoles, octupoles and decapoles, function of which is to correct non-linear dynamics of the beams.

Inside the LHC accelerator two counter rotating proton beams are used. They are accelerated in two separate vacuum beam pipes that require opposite dipole magnetic fields. The only option to avoid the construction of two separate beam pipes and use opposite dipole fields would be the use of protons and anti-protons, as this has been implemented at the Tevatron. However, the current production rate of the anti-protons is too low for the LHC.

In circular proton machines the maximum energy is limited by the strength of the bending magnets. Keeping 7 TeV proton energy beam on the designed orbit implies the use of magnetic bending fields of 8.4 T. Generation of such field requires to use superconducting magnets at the limit of the existing technologies. Approximately 96 tonnes of liquid helium is needed to maintain the superconductivity of the magnets at operational temperature of 1.9 K (-271.3°C), making the LHC the largest cryogenic facility in the world. The LHC dipoles, made of niobium-titanium (NbTi), are constructed with novel 2-in-1 design where the two magnetic coils share a common cryostat. Such dipoles allow the compact installation of two separate beam apertures into the

existing tunnel. To protect the superconducting magnets from the spray particles, there are two dedicated cleaning sections in the ring, where the absorbers remove protons significantly deviated from the reference orbit before they reach the sections with magnets.

2.1.1 Accelerator complex

The acceleration of proton beams to their maximum energies is performed through several steps. Before they reach the LHC, the protons are sped up in a series of interconnected linear and circular accelerators. The accelerator complex is illustrated in Figure 2.1. The protons are derived from the hydrogen gas using an electric field to strip electrons. The process of the acceleration starts from the linear accelerator Linac 2, which accelerates the protons up to 50 MeV. The beam is then injected into the Proton Synchrotron Booster (PSB). The PSB accelerates the protons to 1.4 GeV and feeds the Proton Synchrotron (PS), where the protons are further accelerated to 25 GeV. The next chain is the Super Proton Synchrotron (SPS), which is 6.9 km long. Here the protons reach the energy of 450 GeV before they are transferred to two beam-pipes of the LHC main ring. It takes several minutes to fill the LHC ring and about 15 minutes to accelerate beams to their maximum energy of 3.5 TeV. Eight radio frequency (RF) cavities, oscillating voltage at $f_{RF} = 400$ MHz along the beam axis, are used to accelerate the beams within the LHC. They are placed in straight sections in four cryomodules which keep the RF cavities working in a superconducting state. In this way, the particle beam is sorted into discrete packets called *bunches* spaced with 50 ns.

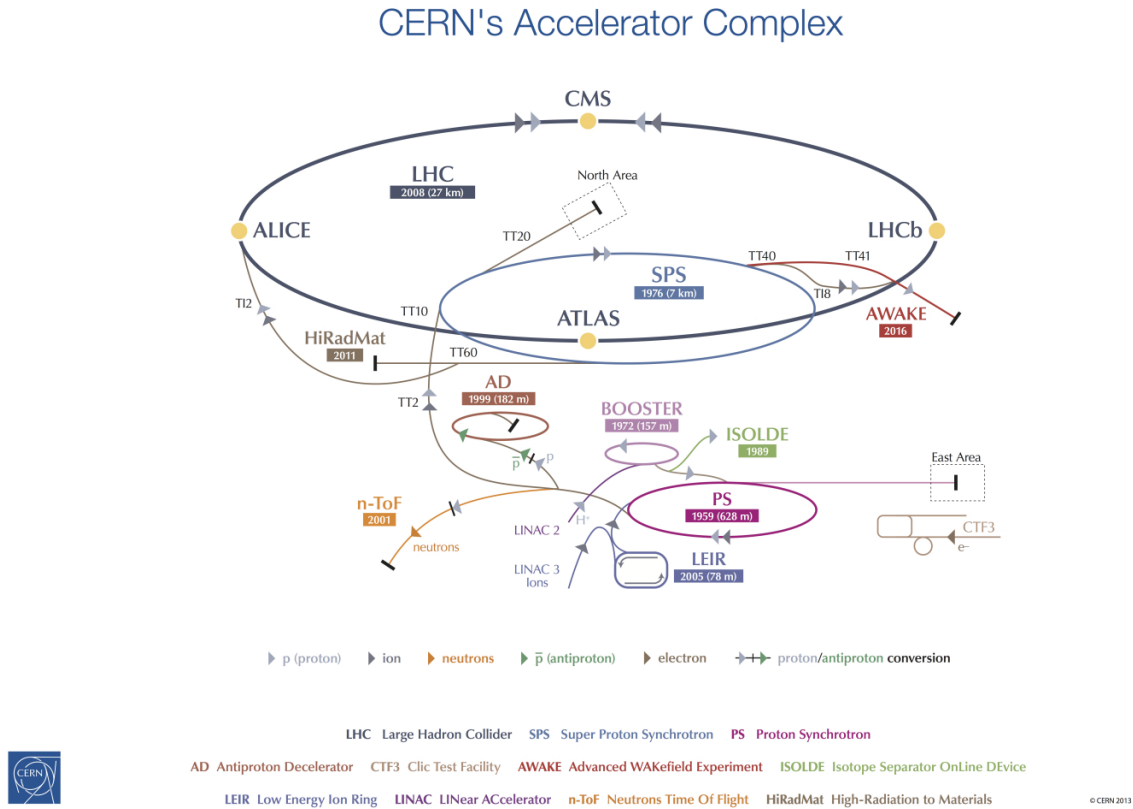


Figure 2.1: Illustration of the LHC accelerator complex.

The two beams are brought into collision in four straight sections of the LHC ring where four detectors are placed - ATLAS, CMS, LHCb and ALICE. Two of them, ATLAS and Compact Muon Solenoid (CMS), are general purpose detectors, focusing on looking for sign of new physics and Higgs boson hunt and studies. LHCb is focused on the precise b-physics studies. The ALICE detector is designed to study the physics of strongly interacting matter at extreme energy densities,

where quark-gluon plasma is formed.

2.1.2 Luminosity

An important characteristic of the LHC machine is the luminosity L , which defines the number of collision events that can be delivered to the experiments

$$\frac{dN_{pp \rightarrow X}(t)}{dt} = L(t) \cdot \sigma_{pp \rightarrow X}, \quad (2.1)$$

where $\sigma_{pp \rightarrow X}$ is a production cross section for an inelastic process $pp \rightarrow X$. The luminosity is process independent quantity, which is entirely determined by the proton beam parameters:

$$L = \frac{f_{rev} \cdot n_b \cdot N_b^2}{2\pi\sigma_x\sigma_y} \cdot F(\phi, \sigma_{x,y}, \sigma_s). \quad (2.2)$$

Here f_{rev} denotes the revolution frequency of the accelerated protons (11245 Hz) synchronized with f_{RF} ; n_b is the number of bunches per beam; N_b is the number of particles per bunch; σ_x and σ_y are the transverse RMS beam sizes at the interaction point (IP) and $2\pi\sigma_x\sigma_y$ represents the effective transverse area in which collision takes place assuming the particles in a beam are Gaussian distributed. The F is the geometrical reduction factor that depends on the crossing angle ϕ between two beams, transverse beam sizes and the bunch length σ_s . It is convenient to express the transverse beam size in terms of the normalized transversed emittance ε_n and the betatron function β^* at the IP as $\sigma_{x,y} = \sqrt{\varepsilon_n \beta_{x,y} / \gamma_r}$, where γ_r is relativistic gamma factor. The LHC luminosity can be then parametrized as:

$$L = \frac{f_{rev} \cdot n_b \cdot N_b^2 \cdot \gamma_r}{2\pi\varepsilon_n\beta^*} \cdot F \quad (2.3)$$

Several factors limit the maximum luminosity that can be achieved at the LHC:

- ▷ **Beam-beam effect** is electromagnetic interaction between bunches of two beams as well as the interaction between particles of the same bunch. This can lead to beam distortions from the orbit and results in an increase of the emittance.
- ▷ **Crossing angle** is introduced to avoid unwanted collisions outside the interaction point. Due to the crossing angle θ_c the luminosity is decreased by factor $F = \sqrt{1 + (\theta_c \sigma_s / 2\sigma_{x,y})^2}$.
- ▷ **Beam offset** can result from the beam-beam effects, quadrupole misalignment and appears if the beams are colliding with a small transverse offset. Such beam offsets induce a loss of luminosity at the interaction point.
- ▷ **Hourglass effect** appears when beams are colliding at a point which is away from the IP. As the beams are focused to the interaction point, the beam sizes and the betatron function are increased.

An accurate measurement of the delivered luminosity is crucial for the ATLAS physics program. For cross-section measurements, the uncertainty on the delivered luminosity is often one of the major systematic uncertainties. The precise knowledge of the luminosity is also important for evaluation of backgrounds to beyond SM searches. The instantaneous luminosity is determined from measuring the average number of interactions per bunch crossing times an efficiency of the luminosity algorithm for the certain detector μ_{vis} , and the effective cross section σ_{vis} which is luminosity calibration constant:

$$L = \frac{f_{rev} \cdot n_b \cdot \mu_{vis}}{\sigma_{vis}} \quad (2.4)$$

There are several methods for the luminosity measurement.

- ▷ **Luminosity monitoring algorithms.** The LHC luminosity is determined in real time approximately once per second using a variety of detectors and algorithms for measuring μ_{vis} . The following devices are used to measure the interaction rate μ (only ATLAS specific devices are listed): Minimum Bias Trigger Scintillators, Cerenkov detector LUCID, EM/Forward calorimeter [32]. They use the event-, hit- or track-counting algorithms. The basic time unit for storing luminosity information for later use is the *Luminosity Block* (LB). The length of a LB is approximately two minutes. Luminosity information is stored as delivered luminosity. Corrections for data acquisition dead-time and other sources of data loss are performed when the integrated luminosity is calculated.
- ▷ **Absolute luminosity determination from the beam parameters.** This method used to determine the σ_{vis} and requires a good measurement of the lateral beam sizes outside of the IP. This can be done using wire scanners or synchrotron light monitors. To obtain reliably the beam size in the IP, one needs to know precisely the betatron function. The betatron function at the IP can be determined using so-called K-modulation of the nearest quadrupoles. The typical uncertainty of this method is up to 5%. A more precise method, known as *van Der Meer scans*, allows to directly measure the effective beam sizes $\sigma_{x,y}$ and shape by recording the relative interaction rates μ_{vis} as a function of the transverse beam separation $\delta_{x,y}$ [33]. However, an assumption that the luminosity profile is factorisable $L(\delta_x, \delta_y) = f_x(\delta_x)f_y(\delta_y)$ is often the dominant uncertainty. An independent *beam-gas imaging* method allows to extract directly the density distributions by reconstructing beam-gas interaction vertices. The visualizing gas used is a residual gas in the vacuum beam-pipe or a specially injected one. The beam-gas imaging method is limited by vertex resolution, especially when the beam sizes become smaller than the resolution.
- ▷ **Absolute luminosity determination from the SM processes.** The processes that have well-known cross sections can be used for luminosity determination by measuring the corresponding production rate. The relatively clean $Z \rightarrow ll$ and $W \rightarrow l\nu$ processes are suited for this purpose. Their theoretical cross section are known with precision of about 5%. In addition, other processes such as muon pair production via two photon exchange $pp \rightarrow pp\mu\mu$ can also be used but this is limited statistically.

In 2011 the maximal instantaneous luminosity at the LHC was $3.5 \times 10^{33} \text{ cm}^{-2}\text{s}^{-1}$, whereas the design luminosity is $10^{34} \text{ cm}^{-2}\text{s}^{-1}$. The parameters of the LHC accelerator were different during the data acquisition. The Figure 2.2 shows the integrated luminosity delivered to the ATLAS experiment in 2011 that is about $L_{int} = 4.58 \text{ fb}^{-1}$. Knowing the cross section of the W boson production, one can evaluate the number of events available for the analysis as $N_{W \rightarrow l\nu} = L_{int} \cdot \sigma_{pp \rightarrow W} \cdot BR(W \rightarrow l\nu)$ that leads to about 8M events in each channel.

An accurate knowledge of the integrated luminosity is important for the W boson mass determination. It plays a significant role of the data-driven multijet background estimates that will be discussed in Section 7.

2.2 The ATLAS detector

The ATLAS (A Toroidal LHC ApparatuS) experiment at the LHC is a multi-purpose particle detector [34] with a forward-backward symmetric cylindrical geometry with respect to the IP. It consists of an inner tracking detector (ID) surrounded by a thin superconducting solenoid, electromagnetic and hadronic calorimeters, and a muon spectrometer (MS) incorporating three large superconducting toroid magnets. The aim of the tracking detector is to track charged particles by detecting their interactions with medium at discrete points. The calorimeters measure the

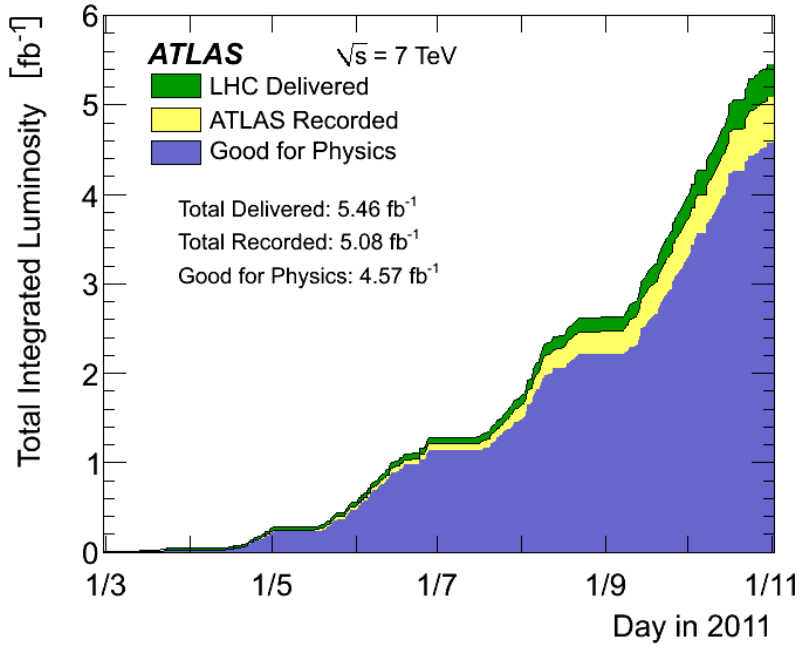


Figure 2.2: The total integrated luminosity recorded by ATLAS detector during 2011 data-taking period.

energy and direction of those particles that are stopped in the calorimeter. The MS is designed for additional measurements of the muons penetrating through the calorimeter. The two magnet systems bend the charged particles in the ID and MS allowing their momenta to be measured and the corresponding charge to be identified.

2.2.1 Coordinate system

The nominal interaction point is defined as the origin of the coordinate system, while the beam direction defines the z -axis and the $x-y$ plane is transverse to the beam direction. The positive x -axis is defined as pointing from the interaction point to the center of the LHC ring and the positive y -axis is defined as pointing upwards. The side-A of the detector is defined as that with positive z and side-C is that with negative z . The azimuthal angle ϕ is measured as usual around the beam axis, and the polar angle θ is the angle from the beam axis. The *pseudorapidity* is defined as

$$\eta = -\ln[\tan(\theta/2)]. \quad (2.5)$$

In case of massive particles such as W and Z bosons the *rapidity* y introduced in equation (1.33) is used instead. The pseudorapidity is Lorentz invariant under longitudinal boosts. It is also preferred to be used instead of θ because of distribution of particles recorded is approximately flat with respect to η . The transverse momentum p_T , the transverse energy E_T and the missing transverse energy E_T^{miss} are defined in the $x-y$ plane. The distance ΔR between particles is usually measured in the pseudorapidity-azimuthal angle space as

$$\Delta R = \sqrt{\Delta\eta^2 + \Delta\phi^2} \quad (2.6)$$

which is also Lorentz invariant if the involved particles are massless. Once the transverse momentum, the polar angle and pseudorapidity of a particle are measured, the cartesian momenta can be obtained from

$$\begin{aligned} p_x &= p_T \cos(\phi) & p_y &= p_T \sin(\phi) \\ p_z &= p_T \sinh(\eta) & p &= p_T \cosh(\eta) \end{aligned} \quad (2.7)$$

2.2.2 The Inner Detector

The ATLAS Inner Detector (ID) [35] is designed to provide hermetic and robust pattern recognition, excellent momentum resolution and both primary and secondary vertex measurements for charged tracks above approximately 0.5 GeV. Its acceptance covers the pseudorapidity range $|\eta| < 2.5$. It also provides electron identification over $|\eta| < 2.0$. The physics goals at the LHC impose the requirements on the ID to operate at very large track density environment, so the high-precision measurements must be made with fine detector granularity. The ID consists of three types of tracking components listed from innermost one: Silicon Pixel Detector (PIX), SemiConductor Tracker (SCT) and Transition Radiation Tracker (TRT). The outer radius of the tracker is about 115 cm, fixed by the inner dimension of the cryostat containing the liquid argon EM calorimeter. The total length of the ID is 7 m, limited by the position of end-cap calorimeters. The ID is divided into the barrel part ($|z| < 80$ cm) and two end-caps. The magnetic field of 2 T is provided by a solenoid inserted between the ID and the EM calorimeter. The positions of signals, called *hits*, caused by charged particles traversing the ID are used to reconstruct particle trajectories inside the tracker. Each track is expected to be reconstructed with 3 hits in Pixel Detector, 8 hits in SCT and 36 hits in TRT on average. The ID layout is illustrated in Figure 2.3.

The semi-conductor pixel detector is situated the closest to the beryllium beam-pipe and has the highest granularity. The main limitation of the pixel detector is the radiation hardness as the expected fluence is at the tolerable limit. Here wide sensors $400 \times 50 \mu\text{m}$ of n^+/n silicon type 250 μm thick are used. The PIX consists of three layers in the barrel region at $R = 50.5$, 88.5 and 122.5 mm, and three discs in the end-cap regions on each side positioned at $|z| = 495$, 580 and 650 mm. The first layer of the pixel detector with highest granularity, so-called B-layer, plays a crucial role in finding of short-lived particles such as b-quarks and τ -leptons as well as photons converting to electron-positron pair. In total there are about 80 million readout channels in the whole Pixel Detector. The intrinsic spatial resolution of individual Pixel Detector modules is 10 μm in $R\phi$ and 115 μm in z .

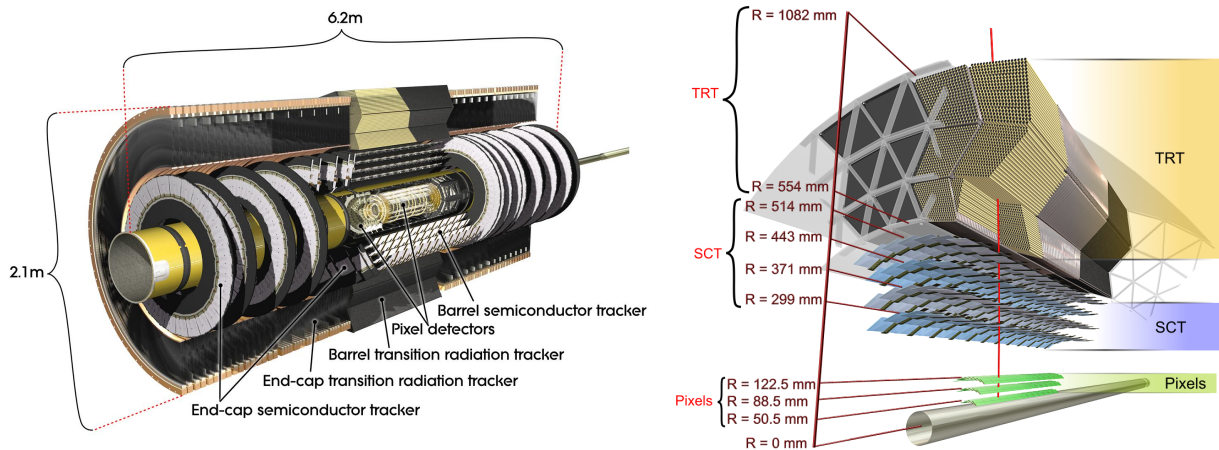


Figure 2.3: *Left:* Cut-away view of the ATLAS inner detector. *Right:* Illustration of the ID sensors and structural elements traversed by a charged track in the barrel inner detector ($|\eta| = 0.3$)

The SCT is a silicon detector with micro-strips which surround the Pixel Detector layers providing four space point measurements and contributing to the measurement of momentum, impact parameter and vertex position. It has coarser granularity as the track density decreases with increasing the radius. The silicon p/n single-sided strips are 80 μm wide and 12 cm long leading to the resolution of 16 μm in $R\phi$ and 580 μm in z (R) in barrel (end-cap). The barrel SCT consists of four layers to provide precision points in $R\phi$ and has small stereo angle to measure z . The four complete barrels at radii of 300, 373, 447 and 520 mm are linked together. The forward modules are mounted onto nine end-cap wheels on each side. The tracks can be distinguished if

separated by more than $\sim 200 \mu\text{m}$. There are 6.3 millions readout channels for the SCT.

The TRT component is composed of gaseous proportional counters (straws), 4 mm in diameter and 1.44 m long. The straws are filled with gas mixture of 70% Xe , 27% CO_2 and 3% O_2 . The xenon gas provides an electron identification capability by detecting transition-radiation photons created by radiator between the straws. This yields to much larger signal amplitudes from electrons than from minimum-ionizing charged particles which are detected by high-threshold discriminator in the radiation-hard front-end electronics [36]. To keep the TRT performance to be constant, the close-loop gas system is used maintaining the correct gas fractions. Possibility to use argon-based mixture instead of xenon, which is much cheaper, is also studied since recent times. The straws are arranged to be parallel to the beam-pipe in the barrel and perpendicular in the end-cap region. The intrinsic radial resolution is about $130 \mu\text{m}$. There are about 50k straws in the barrel and 320k straws in the end-cap providing a large number of measurements for each track.

The Figure 2.4 shows the coverage of each Inner Detector components with their active positions.

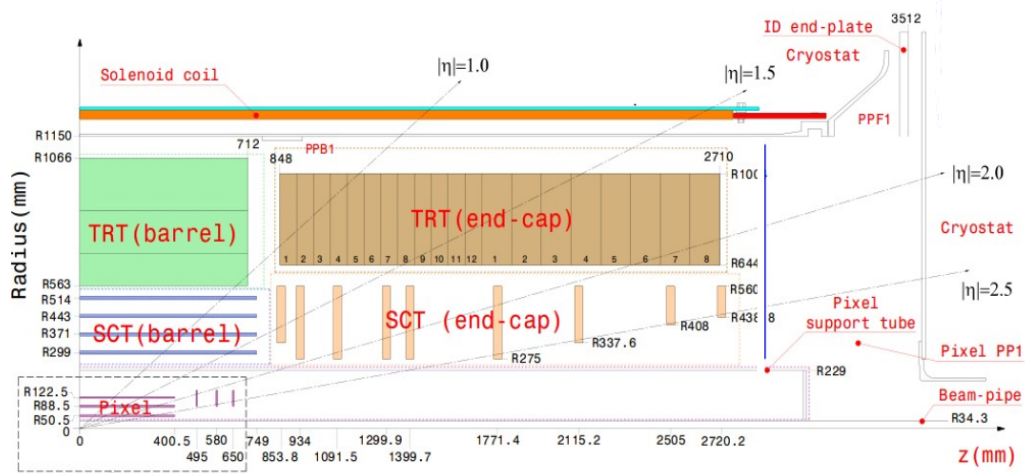


Figure 2.4: The $R - z$ view of individual ATLAS Inner Detector components

Sub-detector	Element size	Resolution [μm]	Hits per track
Pixel	$50\mu\text{m} \times 400\mu\text{m}$	100×15	3
SCT	$80\mu\text{m}$	17	8
TRT	80mm	130	30

Table 2.1: Summary of the main characteristics of the three ATLAS ID sub-detectors [37].

Tracks are described using the parameters of a helical trajectory at the point of closest approach to the z -axis: the transverse impact parameter, d_0 , the z coordinate, z_0 , the angles of the momentum direction, θ and ϕ , and the inverse of the particle momentum multiplied by the charge, q/p , as illustrated in Figure 2.5 (left). The typical track resolution of these parameters is summarized in Table 2.2. The tracks are reconstructed using special algorithms such as global- χ^2 and Kalman-filter techniques. The global- χ^2 fitter finds the track among all possible candidates by solving a set of linear equations. The Kalman method is used in the search for compatible measurements in the next detector layer when track is extrapolated from a seed. The track finding algorithms also include the corrections for interactions with material. The ID is designed with effort to keep the material in the tracking volume to a minimum. For example, the photons can convert inside the tracker. The material also provokes bremsstrahlung in electrons and affects both the energy measurement in the calorimeter and the track momentum measurement. The multiple scattering of hadrons and muons also degrades the impact parameter resolution. All these examples allow to

make improvements to the ATLAS material simulation. An estimated amount of material budget before the calorimeter is shown in Figure 2.5 (*right*).

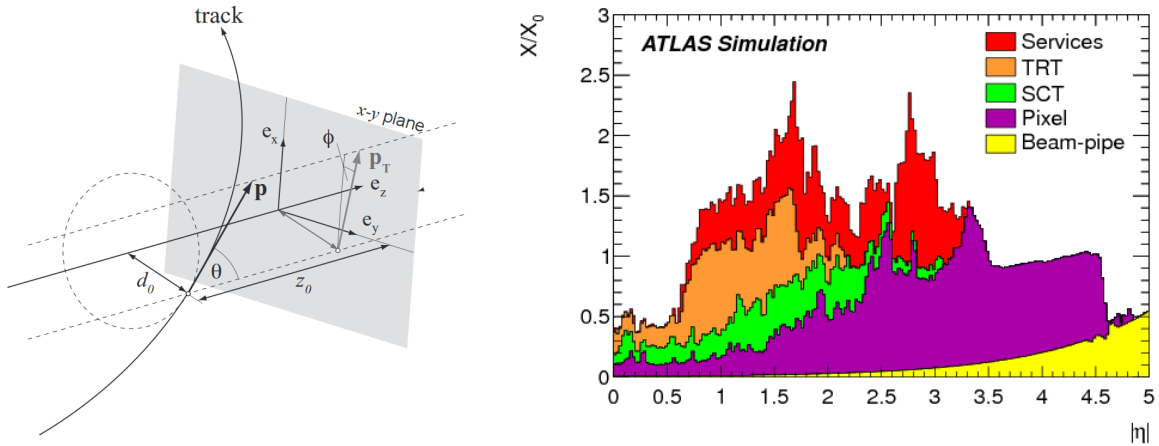


Figure 2.5: *Left*: Illustration of the parameterised track [38]. *Right*: Amount of material traversed by a particle, in units of radiation length X_0 , as a function of $|\eta|$.

The ID provides a transverse momentum resolution of $\sigma_{p_T}/p_T = 0.05\% p_T \text{ GeV} \otimes 1\%$ in central η region.

Parameter	d_0	z_0	ϕ_0	θ	q/p
Units	$[\mu\text{m}]$	$[\mu\text{m}]$	$[\text{mrad}]$	$[\text{mrad}]$	$[\text{GeV}^{-1}]$
Typical resolution	20	110	0.15	0.9	$5 \cdot 10^{-4}$

Table 2.2: Typical resolutions for track parameter with $p_T > 30 \text{ GeV}$ [36].

2.2.3 Calorimetry

The aim of the calorimeter in ATLAS is to measure accurately the energy and position of electrons and photons as well as jets. It also allows to measure the missing transverse energy and provides the separation of electrons and photons from hadrons and jets. The ATLAS Calorimeter system consists of an EM calorimeter covering the rapidity region $|\eta| < 3.2$, barrel hadronic calorimeter covering $|\eta| < 1.7$, hadronic end-cap calorimeter covering $1.5 < |\eta| < 3.2$, and forward calorimeter covering $3.1 < |\eta| < 4.9$ (Figure 2.6). The calorimeter system is contained in a cylinder of outer radius 2.25 m and has the total length between $|z| < 6.65 \text{ m}$. The Tile calorimeter system has an outer radius of 4.23 m and a length spanning $\pm 6.10 \text{ m}$.

2.2.3.1 EM calorimeter

The ATLAS electromagnetic (EM) calorimeter is a sampling calorimeter with accordion shaped Kapton electrodes and lead absorbers as shown in Figure 2.8. The accordion geometry provides a very high granularity, full azimuthal symmetry without cracks and fast signal read-out. Liquid argon (LAr) is used as an active material for the signal collection. The advantages of LAr calorimetry, such as radiation hardness, intrinsic linear behavior, cheapness comparing to other noble gases, have been considered to outweigh the difficulties associated with the need of cryostats and signal feedthroughs.

The EM calorimeter is divided into two identical half-barrels ($|\eta| < 1.475$) and two endcaps ($1.375 < |\eta| < 2.5$) and is segmented in three longitudinal layers called respectively strip, middle and back. The thickness of each layer changes with $|\eta|$ as illustrated in Figure 2.7. The two barrels area separated by a small gap (4 mm) at $z = 0$. The middle layer in the barrel region is equipped

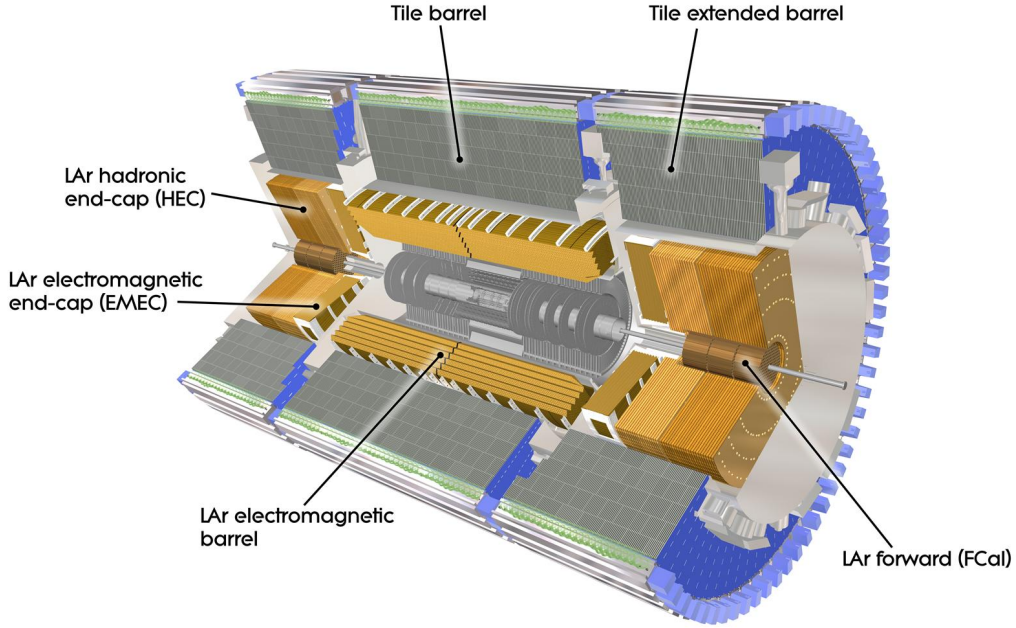


Figure 2.6: Three-dimensional view of the ATLAS calorimetry.

with $\Delta\eta \times \Delta\phi$ cells of size 0.025×0.025 while the strip layer has 8 times finer granularity in the $|\eta|$ direction, as shown in Figure 2.8, providing a precise η measurement of incident particles. In addition, the strip sampling is used to enhance the particle identification, such as γ/π^0 , e/π separation. On the other hand, there is no need to have fine lateral strips size as the shower is smeared in ϕ by the magnetic field. The back layer has a twice coarser granularity in η and the same ϕ segmentation as in the middle layer. Each calorimeter cell is designed to point towards the interaction point. Before the EM barrel calorimeter there is a presampler (PS) LAr detector, covering range $|\eta| < 1.8$ and placed just behind the cryostat cold wall. It is placed to start the shower before the calorimeter and is used to correct for the energy lost in the material upstream the calorimeter. The thickness of LAr material in the presampler is 1.1 cm in the barrel and 0.5 cm in the end-cap.

Each end-cap calorimeter is mechanically divided into two coaxial wheels: an outer wheel covering the region $1.375 < |\eta| < 2.5$, and an inner wheel covering the region $2.5 < |\eta| < 3.2$. The boundary between inner and outer wheel is 3 mm wide and is located at $|\eta| = 2.5$. The external and internal radii of the wheels are 2098 mm and 330 mm respectively. The end-cap calorimeter also divided into longitudinal segments and has granularity of cells that vary with $|\eta|$ as explicitly given in Table 2.3. The lead thickness in the absorber plates has been chosen as a function η to achieve optimized the EM calorimeter performance in terms of energy resolution. The lead plates in the barrel are 1.53 mm thick for $|\eta| < 0.8$ and 1.13 mm thick for $|\eta| > 0.8$. In the end-cap the lead plates have thickness of 1.7 mm for $|\eta| < 2.5$ and 2.2 mm for $|\eta| > 2.5$. The amplitude of accordion waves increases with radius. Since the thickness of absorbers is constant, the LAr gap also increases with radius.

The particles entering the EM calorimeter develop EM showers through their interactions with absorbers. The ionization electrons drift to the electrode under electric field generated by the high voltage of 2000 V. The size of the drift gap on each side of the electrode is 2.1 mm. The induced current on the electrode has triangular shape and is initially proportional to the deposited energy in the cell. The time of charge collection has order of 400 ns. The physical triangular signal is then amplified, shaped by bipolar shaper and digitized every 25 nanoseconds. If signal is accepted by trigger, the signal amplitude is determined from signal samples and transformed to the cell energy.

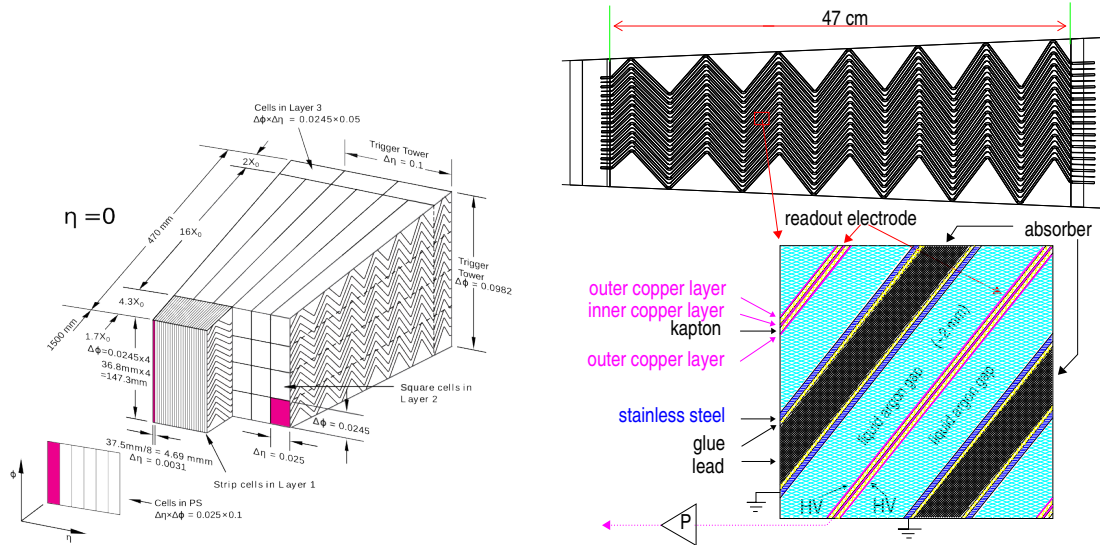


Figure 2.8: Read-out granularity and accordion shape of the EM calorimeter.

extended barrel Tile calorimeters in the range $1.5 < |\eta| < 4.9$ the LAr is used. The important parameter for the hadronic calorimeters is the thickness. It has to be large enough to contain the hadronic showers and reduce the punch-through hadrons penetrating to the muon system. The total thickness is chosen to be about 11 interaction lengths that allows to have good performance on resolution for high energy jets.

The Tile calorimeter is situated behind the EM barrel calorimeter. The signal is provided by scintillating tiles as active material while the iron is used as an absorber. The tiles are placed perpendicular to the beam-pipe and are 3 mm thick. The total thickness of iron in each period is 14 mm. It is composed of barrel and two extended barrel components. It has inner radius of 2.28 m and outer radius of 4.23 m. The Tile calorimeter is longitudinally sampled into three layers. The granularity corresponds to $\Delta\eta \times \Delta\phi = 0.1 \times 0.1$ in first two layers and $\Delta\eta \times \Delta\phi = 0.2 \times 0.1$ in the last layer. A vertical gap of 68 cm wide between the barrel and extended barrel regions is used for passage of cables from the ID and the EM calorimeter. The electronic noise in the cells is about 20 MeV.

The Liquid Argon calorimeters cover end-cap and forward regions with $1.5 < |\eta| < 4.9$. Each end-cap calorimeter (HEC) consists of two independent wheels of equal diameter: one is built with 25 mm absorber plates and another has 50 mm absorber plates. The copper is used as an absorber material. The gap is equipped with 3 electrodes that split it in four drift spaces of 1.8 mm each. The end-cap calorimeter is divided into front, middle and back longitudinal segments. The values of electronic noise are about 250, 350 and 800 MeV in the respective segments. The outer radius of the copper plates is 2.03 m, while the inner radius is 0.475 m. The forward calorimeter (FCAL) is placed at a distance of about 5 meters from the interaction point. It is high density detector consisting of three longitudinal sections. The first section is made of copper, while the other two are tungsten. The sensitive material is LAr with the gap of 250, 375 and 500 microns in first, second and third sections respectively. Such gaps ensure the fast signal collection in the forward region where the pileup effects are expected to be large. The granularity of the hadronic LAr calorimeter is $\Delta\eta \times \Delta\phi = 0.1 \times 0.1$ for $1.5 < |\eta| < 2.5$ and 0.2×0.2 for $2.5 < |\eta| < 3.2$ while the forward calorimeter has 0.2×0.2 . The forward calorimeters are also capable to reconstruct electrons.

2.2.4 Muon Spectrometer

The Muon Spectrometer (MS) is the outermost part of the ATLAS detector. It is designed to detect muons exiting the calorimeter and measure their momentum in the pseudorapidity range

of $|\eta| < 2.7$. In addition, it is used to trigger on the muons in the region of $|\eta| < 2.4$. The MS consists of the large superconducting air-core toroid magnets, instrumented with separate-function trigger and high-precision tracking chambers. The conceptual layout of the spectrometer is shown in Figures 2.9. Over the range $|\eta| < 1.4$, magnetic bending is provided by the large barrel toroid. For $1.6 < |\eta| < 2.7$ region muon tracks are bent by two smaller end-cap magnets inserted into both ends of the barrel toroid. Over $1.4 < |\eta| < 1.6$, usually referred to as the transition region, magnetic deflection is provided by a combination of barrel and end-cap fields. This magnet configuration provides a field that is mostly orthogonal to the muon trajectories, while minimizing the degradation of resolution due to multiple scattering

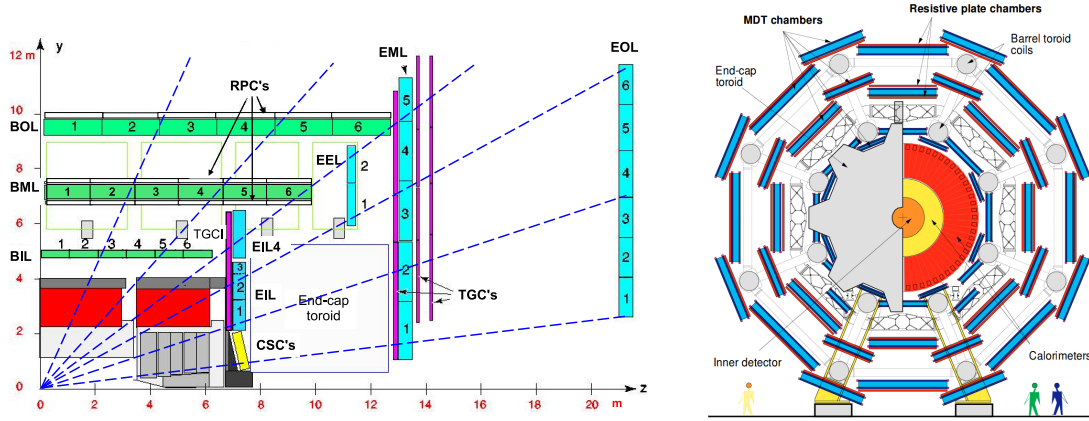


Figure 2.9: Side view of one quadrant (*left*) and transverse view (*right*) of the muon spectrometer.

Cost, performance requirements and the radiation tolerance lead to implementation of four different technologies for the muon chambers. In the barrel region, tracks are measured in chambers arranged in three cylindrical layers around the beam axis at radii of approximately 5 m, 7.5 m, and 10 m; in the transition and end-cap regions, the chambers are installed vertically forming large wheels and located at distances of $|z| \approx 7.4$ m, 10.8 m, 14 m, and 21.5 m from the interaction point. Over most of the pseudorapidity range, a precision measurement of the track coordinates in the principal bending direction of the magnetic field is provided by Monitored Drift Tubes (MDTs). At large pseudorapidity and close to the interaction point, Cathode Strip Chambers (CSCs) with higher granularity are used to sustain the demanding rate and background conditions. Resistive Plate Chambers (RPCs) in the barrel and Thin Gap Chambers (TGCs) in the end-cap region are used as a trigger system. Both trigger chambers also provide a “second-coordinate” measurement. The driving performance goal is a stand-alone transverse momentum resolution of approximately 10% for 1 TeV tracks, which translates into a sagitta along the z axis of about $500 \mu\text{m}$, to be measured with a resolution of $50 \mu\text{m}$. In the center ($\eta \approx 0$) of the MS a gap is made to allow for services for the toroid magnet, the calorimeter and the ID.

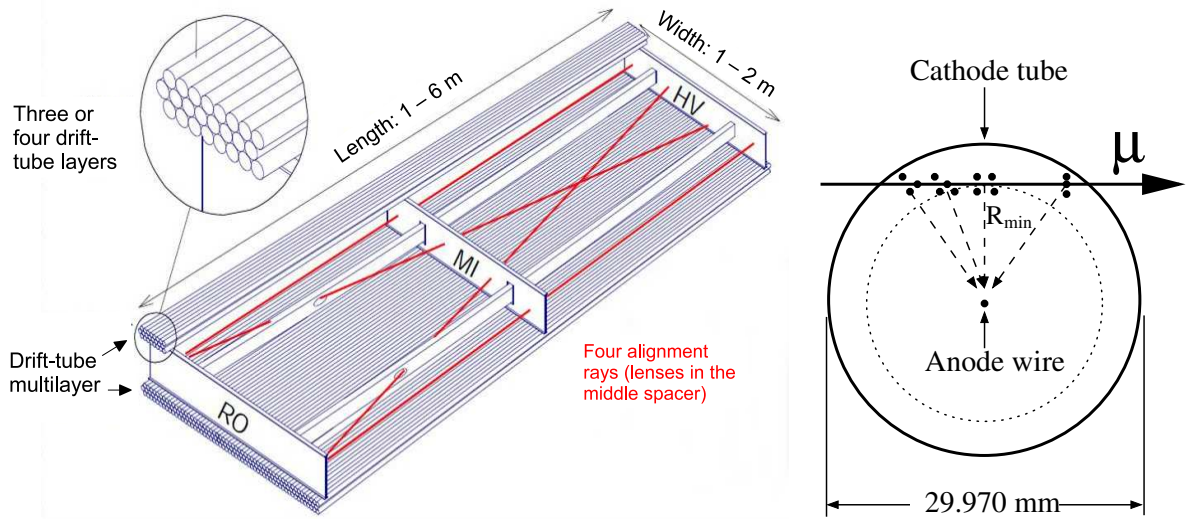
The toroid magnets. The barrel toroid magnet system is situated around the calorimeters with inner diameter of 9.4 m, outer diameter of 20.1 m and its length is 25.3 m. It consists of eight flat coils assembled radially and symmetrically around the beam axis. The end-cap toroid coils are rotated in azimuth by an angle of 22.5° with respect to the barrel coils to optimize the bending performance in the overlap region. The magnetic field varies with η and provides for typical bending powers of 3 Tm in the barrel and 6 Tm in the end-cap regions. Owing to the finite number of coils, the field configuration is not perfectly toroidal and presents a regularly rippled profile. The regions with low bending power in the overlap region exist leading to degraded momentum resolution.

The Monitored Drift Tube chambers are aluminum drift tubes with a diameter of 29.970 mm, operating with Ar/CO_2 gas (93/7) at 3 bar as shown in Figure 2.10. Each chamber consists of two sections with three (inner station) or four (middle and outer station) layers of the drift tubes.

Type	Function	RMS in			measurement/track	
		z/R	ϕ	time	barrel	end-cap
MDT	tracking	$35 \mu\text{m} (z)$	—	—	20	20
CSC	tracking	$40 \mu\text{m} (R)$	5 mm	7 ns	—	4
RPC	trigger	10 mm (z)	10 mm	1.5 ns	6	—
TGC	trigger	2-6 mm (R)	3-7 mm	4 ns	—	9

Table 2.4: Parameters of the four sub-systems of the muon detector.

The electrons resulting from ionization are collected at the central tungsten-rhenium wire with a diameter of $50 \mu\text{m}$, at a potential of 3080 V. The maximum drift time can reach about 700 ns. The signal is amplified, shaped and discriminated. The arrival time is interpreted as a drift-distance providing the single hit resolution of about $80 \mu\text{m}$ per tube, or about $35 \mu\text{m}$ per chamber. The main parameters are summarized in Table 2.4. The overall layout of MDTs is projective, i.e. the layer dimensions and the chamber sizes increase with distance from the IP.

Figure 2.10: Mechanical structure of a MDT chamber (*left*) and transverse cross section of the MDT tube (*right*).

The Cathode-Strip Chambers are multiwire proportional chambers with cathode planes segmented into strips in orthogonal directions. This allows both coordinates to be measured from the induced-charge distribution. The CSC are used in the innermost tracking layer due to their higher rate capability and time resolution. Each chamber is arranged in 4 layers with 5 mm gap filled with $Ar/CO_2(80\%/20\%)$. The resolution of a chamber is $40 \mu\text{m}$ in the bending plane and about 5 mm in the transverse plane. Other important characteristics are small electron drift times (≤ 30 ns) and good time resolution (7 ns).

The Resistive Plate Chambers are gaseous detectors which provide the triggering and the measurement of the second coordinate in a direction orthogonal to the one measured in the precision chambers. The basic RPC unit is a narrow gas gap of 2 mm formed by two parallel resistive electrodes, separated by insulating spacers. The gap is filled with a mixture of $C_2H_2F_4$ /Iso- $C_2H_2F_4$ / SF_6 (94.7/5/0.3). The electric field between electrodes is about 4.9 kV/mm allows avalanches to form along the ionising tracks towards the anode. The signal is read out via capacitive coupling by metal strips on both sides of the detector. The RPCs are arranged into three concentric cylindrical layers around the beam axis. Figure 2.9 shows their position relative to MDTs. Typical space-time resolution of the RPCs is about $1 \text{ cm} \times 1 \text{ ns}$.

The Thin Gap Chambers provide the muon trigger capability in the end-cap and determine azimuthal coordinate to complement the measurement of the MDTs. The TGCs are arranged in

seven layers in each side: one triplet (M1) and two doublets (M2, M3) placed at $|z| = 13.5$ m, 14.7 m and 15 m respectively. EI ($|z| = 7$ m) and FI ($|z| = 7.3$ m) are the innermost TGCs, which are used to suppress the fake hits and low momentum background tracks. Each TGC is a multiwire proportional chamber filled with highly quenching gas mixture $CO_2/n - C_5H_{12}$ (55%/45%) that permits to operate in saturated mode. Wire-to-cathode distance of 1.4 mm and wire-to-wire distance of 1.8 mm lead to good time resolution.

In addition, there are a **specialized detectors** such as Beam Conditions Monitor (BCM) that consists of two stations containing diamond sensors at $|z| = 1.84$ m; forward LUCID Cerenkov detector covering $5.4 < |\eta| < 5.9$. Both are used to luminosity determination. Also there is forward Zero Degree Calorimeter (ZDC) covering $|\eta| > 8.3$ and the Minimum Bias Trigger Scintillators (MBTS) covering $2.1 < |\eta| < 3.8$.

2.2.5 Trigger system and data acquisition

The purpose of the ATLAS trigger system is to reduce the input rate of the events generated in pp collisions with 40 MHz bunch crossing rate to an output rate of about 200 Hz in order to record them for further analysis. The system has three levels. The first level ($L1$) is a hardware-based system using information from the calorimeter (L1Calo) and muon (L1Muon) subdetectors. At this stage, the regions of interest (ROI) are identified and a decision to reject the background events is made by specialized electronics within $2.5 \mu s$ after a collision occurred. The decision is based on hit coincidences in different subdetector layers within certain windows. The accepted events are read out from the front-end electronics into readout drivers (ROD) and then transmitted into readout buffers (ROB), the starting points for the data acquisition (DAQ). The L1 trigger system is responsible for reducing the rate to at least 75 kHz.

The second ($L2$) and third (Event Filter, EF) levels are software-based systems using information from all subdetectors. For each bunch crossing, the trigger system verifies if at least one of hundreds of conditions is satisfied. The triggers are based on identifying combinations of candidate physics objects (*signatures*) such as electrons, photons, muons, jets, jets with b -flavour tagging (b -jets) or specific B -physics decay modes. In addition, there are triggers for inelastic pp collisions and triggers based on global event properties such as missing transverse energy and summed transverse energy. Events selected by the EF are then sent to mass storage [39]. An average processing time is about 4 s. Often the final output rate cannot be made small enough. In this case only random events are selected and stored. Such triggers are called "prescaled triggers". In principle, there are two types of triggers: primary and supporting. Primary triggers are main triggers with tightly applied cuts needed for sufficient selection of electrons, muons, etc. Such triggers cannot be prescaled. Supporting triggers are used to collect a sample of unbiased objects with looser cuts. They are needed to build background-enriched regions that can be used in an analysis.

This thesis describes the analysis performed with proton-proton collision data collected at center-of-mass energy of $\sqrt{s} = 7$ TeV with the ATLAS detector during 2011. In addition, the calorimeter studies described in Section 4 is performed using data collected at $\sqrt{s} = 8$ TeV during 2012, which benefits from higher statistics. If there was a mechanical or a read-out problem in a part of the detector during the data acquisition, the reconstructed object which is used in the analysis could be affected. The data was used for the analysis only if relevant sub-detectors were operational and magnet systems were on. The state of the detector (data quality) was monitored during data acquisition and stored into the condition database according to corresponding data-taking period or luminosity block. The detection of many problems is not fully automated and manual input is required [40]. The high quality of data is guaranteed with Data Quality group recommendations. After application of data quality requirements, the total integrated luminosity corresponds to $4.59 \pm 0.08 \text{ fb}^{-1}$ for 7 TeV data and $20.3 \pm 0.6 \text{ fb}^{-1}$ for 8 TeV data, respectively.

Event reconstruction and selection

3.1 Muon reconstruction and identification

Muons are identified and reconstructed in ATLAS by exploiting the Inner Detector and Muon Spectrometer in order to cover wide range of p_T and pseudorapidity η . The passage of muon in each subdetector allows to measure its local position and direction, and thus providing the information about a segment of its track. The global trajectory of muons cannot accurately be described by an analytical model so a high precision numerical approximation is needed.

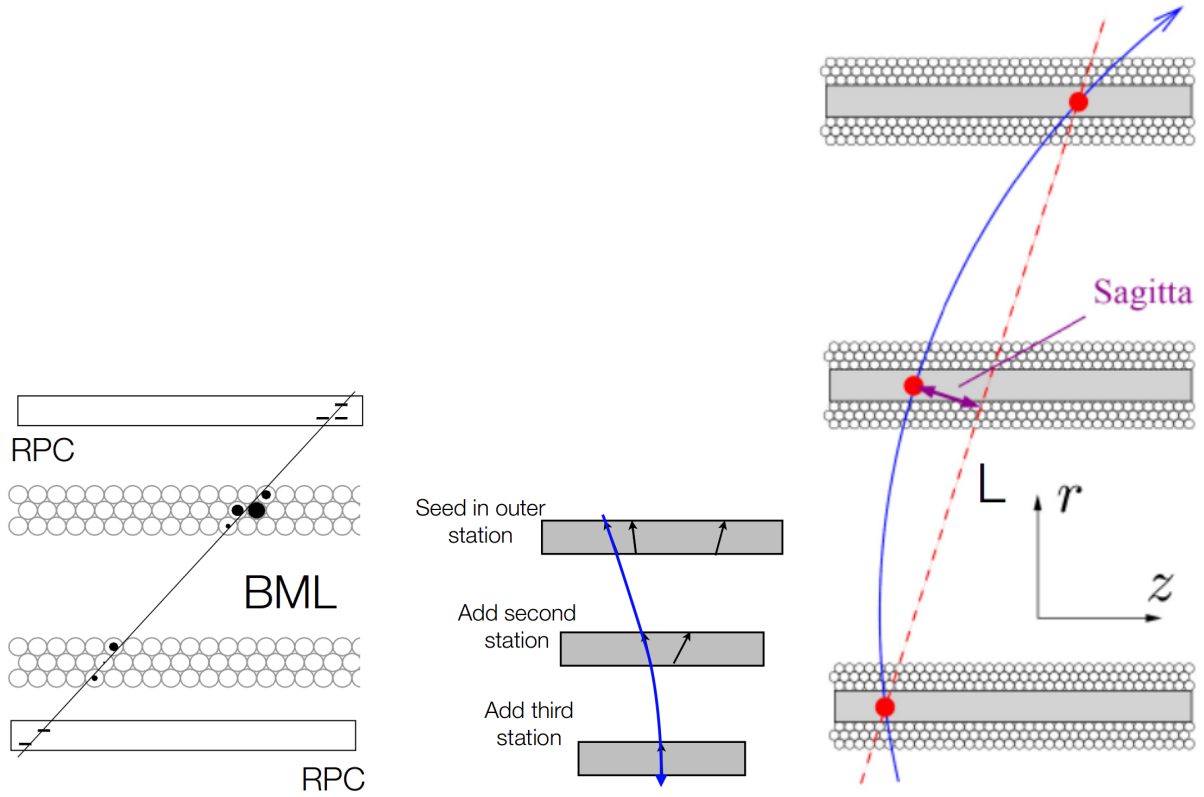


Figure 3.1: Illustration of the muon track reconstruction and sagitta definition in the Muon Spectrometer.

In the first step of the reconstruction in the MS, the muons are triggered in RPC/TGC if at least one hit exists (see Figure 3.1), defining the region of activity (ROA). All the muon chambers intersecting with the ROA are then selected as muon track candidates. In the next step, the track segments are formed through the two-dimensional fit of the associated hits in MDT multilayers of the same chamber. The χ^2 -fit takes into account the tubes with missing signal. Here the bending of muons above few GeV is sufficiently small and their trajectories can be approximated by a straight line. The fitted segments are required to point loosely towards the IP, in order to reject background events and random hit combinations. In the final step, the muon track finding is performed by extrapolation each of these segments to the other (i.e. to inner or outer if starting from a middle one) stations using tracking in the magnetic field and taking into account the traversed material that causes multiple scattering and energy loss. In the non-bending transverse (xy) plane of the

spectrometer the trajectory of the muons is close to a straight line. Among all possible candidate segments forming the track those are chosen that best satisfy the global χ^2 fit.

An important parameter measured in the MS is "sagitta" (S) as it directly determines the particle momentum. The sagitta measurement is defined as the distance from the segment point in the middle layer to the straight line connecting the two outer segments as shown in Figure 3.1. The inverse momentum can be determined as

$$1/p = \frac{8S}{BL^2}, \quad (3.1)$$

where B is magnetic field. Thus, the sagitta resolution is crucial for the precise momentum determination.

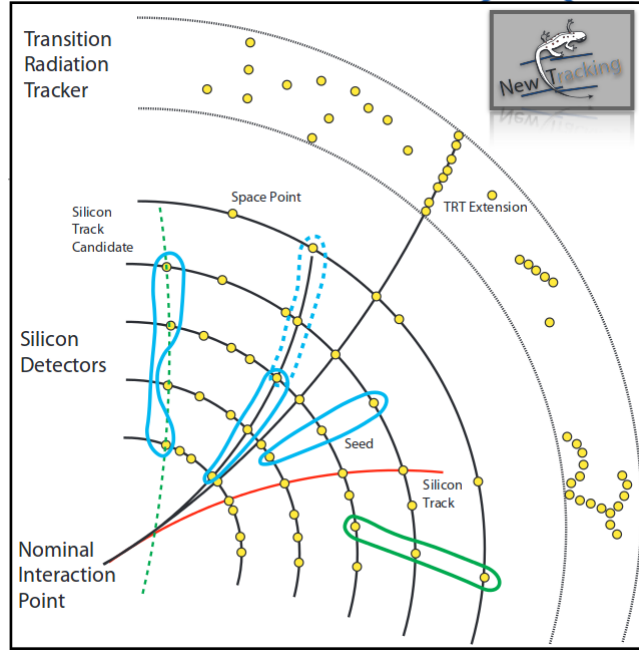


Figure 3.2: Illustration of the track reconstruction in the Inner Detector

In the Inner Detector the muons are reconstructed using a similar approach. When a particle, in particular muon, traverses a tracking detector, it will generate points ("hits") in individual detector elements as shown in Figure 3.2. Among a big number of recorded hits, the tracks of charged particles can be formed using pattern recognition algorithms. The task of the pattern recognition is to determine which point belongs to which track, and ultimately to estimate the track parameters. There are two modes of pattern recognition. In the first mode, the tracks are seeded in the pixel and SCT detectors and then extrapolated to the TRT. An amount of passive and active material of the detector is accurately accounted in the track extrapolation.

The second mode in which the track finding starts from the TRT can be used when no track is found in the silicon detectors. This information is then given to the track fitting algorithm, which tries to produce a track trajectory that is as close to the true trajectory as possible. The track fitting is based on the χ^2 -minimization of the track-to-hit mismatching. The accuracy of the track reconstruction is limited by the resolution of the detector elements, the knowledge of the magnetic field and amount of the material in the detector. In addition, the possible misalignment can affect the measured momentum and the measured impact parameter.

Muons used in this analysis are reconstructed independently in the ID and MS. A combined track is formed from the successful combination of a MS track with an ID track based on a statistical combination (*staco* algorithm) of the track parameters. This combination improves the momentum resolution and provides better rejection of muons from secondary interactions and from π/K decaying in-flight, collectively called as fake-muons. The reconstruction efficiency for

combined muons is affected by acceptance losses in the MC due to lack of muon chambers in $\eta \sim 0$ and problematic transition region ($1.1 < |\eta| < 1.3$) between barrel and end-cap. For the definition of the reconstructed muon kinematics, the ID measurement is retained as sole input, as the MS measurement has a significant impact on the momentum reconstruction performance for transverse momenta above 100 GeV. This choice allows a simpler calibration procedure, as it avoids complications related to the above-mentioned energy loss; the cost in terms of resolution is negligible in the transverse momentum range relevant for the present measurement.

3.2 Electron reconstruction and identification

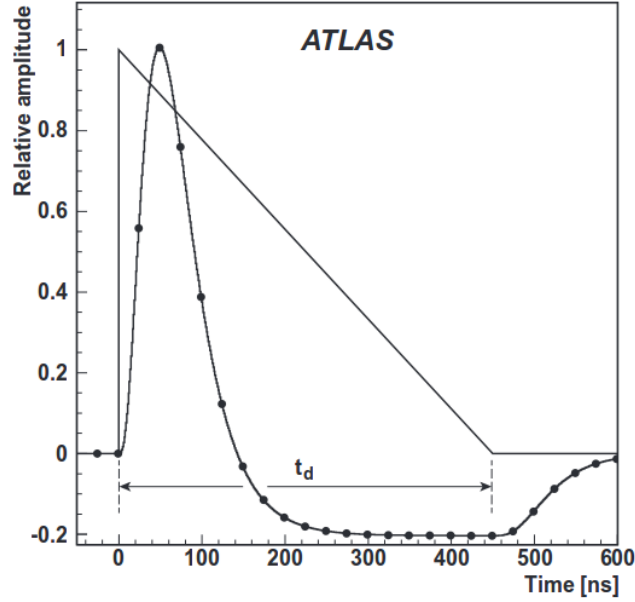


Figure 3.3: The pulse shape in the ATLAS LAr calorimeters. The unipolar triangular pulse is the current pulse in the liquid argon generated by fast ionising particles. t_d represents the drift time. The shaped pulse is superimposed with circles indicating 25 ns intervals. [41].

The electrons and photons are reconstructed using the ATLAS EM calorimeter (see Section 2.2.3). When these particles enter the calorimeter, they develop the EM showers through their interaction with matter. The showers initiated by electrons and photons are quite wide, therefore they deposit energy in many calorimeter cells of each sampling. The EM showers ionise the active material and the ionisation electrons induce an electrical signal on the electrodes which is proportional to deposited energy in the active volume of the calorimeter. The induced signal has triangular shape due to charge collection time of about 450 ns as illustrated in Figure 3.3. It is then amplified, shaped by bipolar shaper and digitized every 25 nanoseconds. The signal amplitude is then determined from signal samples and transformed to the cell energy as

$$E_{cell} = F \times \sum_{i=1}^{N_{samples}} a_i (s_i - p), \quad (3.2)$$

where s_i are the samples of the shaped ionisation signal in $N_{samples} = 5$ time slices spaced by 25 ns; p is the read-out electronic pedestal measured in the dedicated calibration runs; the a_i weights are the optimal filtering coefficients derived from the predicted shape of the ionisation pulse and the noise autocorrelation. The noise in the cell is a combination of an electronic noise, which is about 10 MeV in strip layer and about 30 MeV in middle and back layers, and the contribution from *pile-up* particles. The pile-up contributions can be either due to particles coming from

the same bunch crossing (in-time pile-up) or particles coming from previous bunch crossing (out-of-time pile-up). The factor F which converts the collected signal into MeV and is determined experimentally for each cell of the calorimeter in dedicated calibration runs.

In order to measure the total energy deposited in the EM calorimeter, the cells are grouped into the EM clusters. To reconstruct the EM clusters, the EM calorimeter is divided into a grid of $N_\eta \times N_\phi$ towers of size $\Delta\eta \times \Delta\phi = 0.025 \times 0.025$, corresponding to the granularity of the calorimeter middle layer. Inside each of these elements, the energy of all cells in all longitudinal layers is summed into the tower energy. These clusters are seeded by towers with total transverse energy above 2.5 GeV and searched for by a sliding-window algorithm, with a window size of 3×5 towers. Then, if the reconstructed cluster can be associated with at least one well-reconstructed track in the ID, the candidate is classified as an electron. If several tracks are matched with the EM cluster, tracks with silicon hits are preferred, and the track is chosen which is closest in terms of $\Delta R = \sqrt{\Delta\eta^2 + \Delta\phi^2}$. In order to reject the electrons coming from photon conversions (a photon with energy above 1 GeV interacts with tracker material predominantly via e^+e^- production), the track is required to be close to the IP. The track-to-cluster association accounts for the presence of the solenoidal magnetic field and for the effect of bremsstrahlung losses due to electron bending in this field. In the absence of a matching track, the cluster is classified as an unconverted photon candidate.

After a successful track-cluster matching, the electron clusters are rebuilt using an area of calorimeter cells corresponding to 3×7 in the barrel and 5×5 in the end-cap in units of $\Delta\eta \times \Delta\phi = 0.025 \times 0.025$. Such lateral sizes are taken to contain the electron shower while minimizing the pile-up and noise contributions. The larger size in ϕ in the barrel is needed because of magnetic field causing the bremsstrahlung radiation smears the shower in ϕ .

The clusters associated with electron candidates must satisfy a set of identification criteria, requiring their longitudinal and transverse profiles to be consistent with those expected for EM showers induced by such particles. Three reference sets of cut-based selections, labeled *loose*, *medium* and *tight*, have been defined for electrons with increasing background rejection power. The variables used in these selections are summarized in Table 3.1. They include shower shape variables, tracking variables and track-cluster matching variables. The information from hadronic calorimeter is also used to veto particles giving rise to significant hadronic activity.

After the clusters are reconstructed, the electron position and energy are calculated. The EM cluster properties, including its longitudinal development, and additional information from the ID, are used to correct to the original electron and photon energy in simulated MC samples using multivariate techniques. The calibration constants are determined using a multivariate algorithm (MVA); a dedicated optimisation is performed for electrons. The main inputs to this calibration procedure are $E_{ps}, E_{str}, E_{mid}, E_{back}$, the energies measured in a given cluster of cells in the corresponding calorimeter sampling. The total energy is also affected by the lateral leakage outside the cluster (crosstalk effect) and is studied in Section 4. Corrections are made for the energy deposited in front of the calorimeter and outside of the cluster, as well as for the variation of the energy response as a function of the impact point on the calorimeter. The inputs to the energy calibration algorithm are the measured energy per calorimeter layer, including the presampler, η of the cluster and the local position of the shower within the second-layer cell corresponding to the cluster centroid. The reconstructed electron kinematics are defined from the energy measured in the EM calorimeter, and from the associated track angles η and ϕ .

3.3 Hadronic recoil reconstruction

While the charged leptons from the W or Z boson decays can be detected by the MS or calorimeter as described in previous sections, the neutrino leaves the detector unseen. Thus the neutrino transverse momentum \vec{p}_T^ν is determined from the missing transverse energy \vec{E}_T^{miss} , which can be calculated using the charged lepton transverse momentum \vec{p}_T^ℓ and the recoil in transverse

Type	Description	Name
Loose selection		
Acceptance	$ \eta < 2.47$	
Hadronic leakage	Ratio of E_T in the first layer of the hadronic calorimeter to E_T of the EM cluster	R_{had1}
	Ratio of E_T in the hadronic calorimeter to E_T of the EM cluster	R_{had}
Middle layer of EM calorimeter	Ratio of the energy in 3×7 cells over the energy in 7×7 cells centered at the electron cluster position	R_η
	Lateral shower width $\sqrt{\sum E_i \eta_i^2 / \sum E_i - (\sum E_i \eta_i / \sum E_i)^2}$ where E_i is the energy and η_i pseudorapidity of cell i and sum is within 3×5 cells	$w_{\eta 2}$
Medium selection		
	includes loose	
Strip layer of EM calorimeter	Shower width, $\sqrt{\sum E_i (i - i_{max})^2 / \sum E_i}$, where i runs over all strips in a window of 0.0625×0.2 , and i_{max} - index of a strip with highest energy	w_{stot}
	Ratio of the energy difference between the largest and second largest energy deposits in the cluster over the sum of these energies	E_{ratio}
Track quality	Number of hits in the pixel detector (≥ 1)	n_{pix}
	Number of total hits in the pixel and SCT detectors (≥ 7)	n_{Si}
	Transverse impact parameter ($ d_0 < 5$ mm)	d_0
Track-cluster matching	$\Delta\eta < 0.01$ between the cluster position in the strip layer and the extrapolated track	$\Delta\eta$
Tight selection		
	includes medium	
Track-cluster matching	$\Delta\phi < 0.02$ between the cluster position in the middle layer and the extrapolated track	$\Delta\phi$
	Ratio of the cluster energy to the track momentum	E/p
	Tighter $\Delta\eta$ requirement ($ \Delta\eta < 0.005$)	$\Delta\eta$
Track quality	Tighter transverse impact parameter requirement ($ d_0 < 1$ mm)	d_0
	Total number of hits in the TRT	n_{TRT}
	Ratio of the number of high-threshold hits to the total number of hits in the TRT	f_{HT}
Conversions	Number of hits in the b-layer (≥ 1)	n_{BL}
	Veto electron candidates matched to reconstructed photon conversions	

Table 3.1: Definition of variables used for loose, medium and tight electron identification cuts.

plane \vec{u}_T . As shown in Section 1.4.3, the vector boson transverse momentum $p_T^{W,Z}$ is expected to be zero at LO calculations. The situation changes for higher order calculations and Parton Shower models, which lead to a significant transverse momentum, peaking at 5 – 10 GeV. This results from quark or gluon radiation in the initial state, which are then fragmented into multiple hadrons and detected in the calorimeter. Thus, the transverse momentum of the vector boson has to be balanced in the transverse plane by such hadrons, as the initial sum of transverse momenta before the collision was zero (neglecting the Fermi motion):

$$\vec{p}_T^{W,Z} = \vec{p}_T^{lepton1} + \vec{p}_T^{lepton2} = - \sum \vec{p}_T^{ISRquarks,gluons} \quad (3.3)$$

where the \vec{p}_T^{lepton} denote the transverse momenta of the decay leptons. The term $\sum \vec{p}_T^{ISRquarks,gluons}$ accounts for all transverse momenta of the partons from initial state radiation, also called *hadronic recoil*, which is denoted by \vec{u}_T . Hence, the transverse momentum of the neutrino can be indirectly determined via

$$\vec{p}_T^\nu := \vec{E}_T^{miss} = -(\vec{u}_T + \vec{p}_T^{\perp\pm}) \quad (3.4)$$

Similar to the transverse momentum of the charged lepton $\vec{p}_T^{\perp\pm}$, also the hadronic activity \vec{u}_T can be accessed experimentally, by measuring the reconstructed (topo-)clusters¹ in the ATLAS calorimeters and/or the reconstructed tracks in the ATLAS. The physical quantities are therefore not \vec{E}_T^{miss} and $\vec{p}_T^{\perp\pm}$, but \vec{u}_T and $\vec{p}_T^{\perp\pm}$.

The basic performance quantity is the projection of the hadronic recoil vector \vec{u}_T along the transverse momentum vector of the vector boson as illustrated in Figure 3.4. This projection results in a parallel component $u_{||}$ and a perpendicular component u_{\perp} . An ideal measurement of the hadronic recoil would results in $\vec{u}_{||} = -\vec{p}_T^{W,Z}$ and $u_{\perp} = 0$. However, the finite experimental resolution of the hadronic recoil measurement leads to relatively wide distributions for the parallel

¹ There are two calorimeter clustering algorithms in ATLAS. The "sliding window" algorithm clusters the calorimeter cells within fixed-size rectangles and it is used for electrons, photon and τ -lepton reconstruction. The "topological algorithm" clusters those neighboring cells around a seed, which have large signal-to-noise ratio. The latter algorithm is used for jet and missing transverse energy reconstruction in ATLAS [42].

and perpendicular components. In addition, the reconstructed energies in the detector are not only due to one proton-proton collision, but also include contributions from underlying event as well as the residual energy in the detector from previous bunch crossings (out-of-time pileup). For 2011 data-set, where the pileup environment is not too high, the simple cluster-based approach is taken for the recoil derivation. In later data-sets with higher pileup environment the combined track/cluster based algorithm is planned to be used.

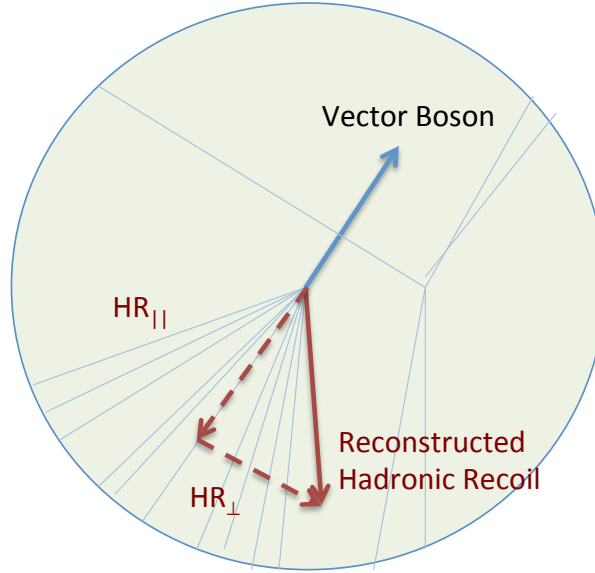


Figure 3.4: Projection of Hadronic Recoil on vector boson for the definition of $u_{||}$ and u_{\perp} .

As a basic concept of cluster-based approach, the hadronic recoil is computed by the vector sum of all energy deposited in the calorimeters (sum of the reconstructed topo-clusters):

$$\vec{u}_T = \sum \vec{E}_T^{topo}. \quad (3.5)$$

Another informative quantity is scalar sum of all transverse energies of topo-clusters

$$\sum E_T = \sum E_T^{topo} \quad (3.6)$$

that represents the hadronic activity of the event. With this simple approach, the transverse energy of decay electrons will be counted twice, as well as the energy deposited in calorimeters by showering muons. To solve this problem, the clusters falling inside a cone of size ΔR around the lepton are excluded. While a cone size of $\Delta R = 0.05$ still is too small to exclude all double counting effects, a cone size of $\Delta R = 0.2$ leads to a complete exclusion of the energy deposited by signal leptons. However, the energy resolution of the hadronic recoil starts to degrade when more and more information is removed from the recoil measurement.

In order to recover the recoil energy, the excluded clusters coming from the underlying event have to be compensated. The situation is illustrated in Figure 3.5. For each event, two components can be identified: the part of hadronic recoil in a cone around the lepton, that we will call for simplicity the “removed cone” and is indicated as “zone B” in figure; and the hadronic recoil in the rest of the calorimeter, that we will call “raw recoil” and is indicated as “zone A”. Two strategies are used for the compensation: if the lepton is isolated, the magnitude of the removed cone is estimated in a zone C which has the same surface, but is not overlapping with the removed cone self. We will call the zone C “replacement cone”. The replacement cone is defined by a cone at the same pseudo-rapidity of the removed lepton, but at different ϕ direction. The replacement cone cannot overlap with the removed cone and has to be far from the direction of the raw recoil ($\Delta\phi > 0.6$).

If the lepton is not isolated, the value of the lepton isolation (the calorimetric isolation in a cone of the same size of the removal cone) is used as estimate of the energy in the “removed cone”. In Summary, the cluster-based hadronic recoil measurements involves three steps: 1) first summing vectorially the p_T of all topo-clusters deposited in calorimeters; 2) then removing clusters in a big enough cone around the lepton to avoid the double counting problem; 3) finally compensating the underlying event excluded in the cone to correct the recoil energy. The recoil energy correction is especially needed for the recoil behavior in Z and W to be similar since the number of exclusion cones which is equal to the number of leptons in the final states are different in W and Z samples.

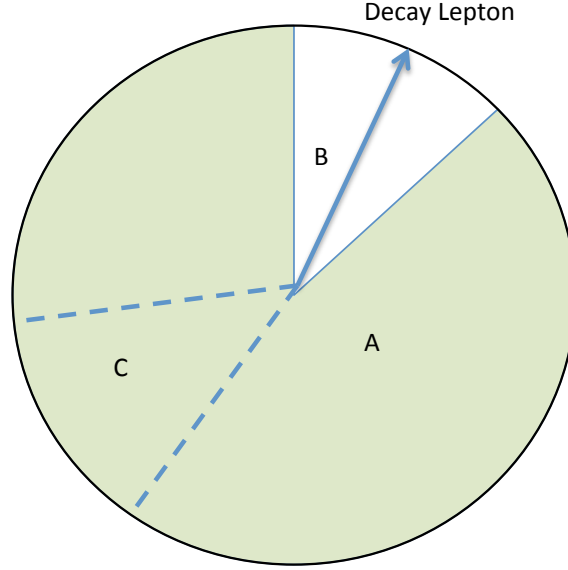


Figure 3.5: Definition of different zones in the calculation of the cluster-based hadronic recoil.

3.4 W and Z boson selection

3.4.1 Muon selection

Muon candidates are formed from tracks reconstructed in the ID combined with MS. They are required to have $|\eta| < 2.4$ due to muon trigger system coverage and $p_T > 15$ GeV. Beside this, selection requirements on the ID track kinematics are imposed as follows:

- require at least one expected B-layer hit if it is geometrically expected: $N_{pixel} > 1$;
- expected pixel hits: $N_{pixel} + N_{pixel\ dead\ sensors} > 1$
where N_{pixel} is the number of pixel hits and $N_{pixel\ dead\ sensors}$ is the number of crossed dead pixel sensors;
- expected SCT hits: $N_{SCT} + N_{SCT\ dead\ sensors} > 5$
where N_{SCT} is the number of SCT hits and $N_{SCT\ dead\ sensors}$ is the number of crossed dead SCT sensors;
- Si holes: $N_{pixel\ holes} + N_{SCT\ holes} < 3$;
- TRT quality cuts:
for $|\eta| < 1.9$: $N_{TRT} + N_{TRT\ outliers} > 5$ and $N_{TRT\ outliers} < 0.9 \cdot (N_{TRT} + N_{TRT\ outliers})$;
for $|\eta| \geq 1.9$ and $N_{TRT} + N_{TRT\ outliers} > 5$: $N_{TRT\ outliers} < 0.9 \cdot (N_{TRT} + N_{TRT\ outliers})$;

where N_{TRT} is number of TRT hits on the muon track and $N_{TRT\text{ outliers}}$ is the number of TRT outliers on the muon track.

In addition, muon candidates are required to have a longitudinal impact parameter $|z_0| < 10$ mm with respect to the primary vertex to reduce muons arising from cosmic and other non-collision backgrounds. The candidates are also required to satisfy an ID-based isolation criteria in order to be isolated from other particles and to suppress background from heavy-flavour decays and decaying in-flight pions and kaons. The isolation requires the scalar sum of momenta of ID tracks within a cone $\Delta R = \sqrt{\Delta\eta^2 + \Delta\phi^2} < 0.2$ around the muon candidate (excluding the muon candidate itself) to be less than 10% of the muon p_T .

$$I_\mu = \frac{p_T^{\text{cone20}}}{p_T^\mu} < 0.1 \quad (3.7)$$

3.4.2 Electron selection

Electron candidates are built from clusters of energy deposited in the electromagnetic calorimeter that are associated with at least one well-reconstructed track in the ID. They are required to have $p_T > 15$ GeV and $|\eta| < 2.4$ excluding the region $1.2 < |\eta| < 1.82$. The electrons are required to pass the tight identification criterion of a cut-based discriminating variables. In order to achieve even better background rejections, a requirement on absence of an activity around electron tracks is applied. The isolation cuts are imposed on the track-based p_T^{cone40} and calorimeter-based E_T^{cone20} electron isolation variables, defined as

- track-based electron isolation p_T^{cone40} defined as the scalar sum of the p_T of tracks in a cone of $\Delta R < 0.4$ around the electron track, minus the p_T of the electron.
- calorimeter-based electron isolation E_T^{cone20} determined by the total E_T of energy deposits in the calorimeter within $\Delta R < 0.2$ around the electron track (centroid of EM cluster), minus E_T of EM cluster.

The electron isolation cuts are p_T - and η -dependent maintaining a uniform isolation efficiency of 97% for track- and 98% for calorimeter-based variables across a wide range of p_T and η . In general, these cuts vary in the range of $p_T^{\text{cone40}} < 2.0..3.0$ GeV and $E_T^{\text{cone20}} < 2.5..4.5$ GeV.

In addition, the LAr calorimeter had a few smaller problems in the 2011 run with dead Front End Boards, noise bursts, as well as dead or noisy cells. The cuts were applied to remove the affected regions.

3.4.3 W and Z boson selection

In order to further reduce the contributions from non-signal backgrounds, the W and Z boson selections were tightened requiring the following cuts on the corresponding kinematical distributions:

- **W boson:** $p_T^l > 30$ GeV and $E_T^{\text{miss}} > 30$ GeV in order to reject high-background region; $p_T^W < 30$ GeV and $m_T^W > 60$ GeV in order to have more sensitive region for the m_W measurement².
- **Z boson:** $p_T^l > 25$ GeV cut is decreased as the background level is much lower; dilepton momentum cut is $p_T^l < 30$ GeV in order to be consistent with the W selection; tight invariant mass cut is applied $81 \text{ GeV} < m_{ll} < 101 \text{ GeV}$ to minimize the background and the impact of QED FSR on the signal acceptance (see Section 6) as well as to be consistent with the mass window used to extract calibration scales in the electron channel. For muons, this range is smaller and therefore a tighter mass range $84 \text{ GeV} \leq m_{ll} \leq 98 \text{ GeV}$ is used for the mass fits.

²Tighter cut on p_T^W sharpens the Jacobian peak used for the M_W extraction (see Section 8.1.1)

Calibration of the EM calorimeter

4.1 Introduction

The minimum ionizing particle, traversing the calorimeter, creates electron-ion pairs along its track in the liquid argon gaps. The ionization electrons drift to the electrode under electric field generated by the high voltage. The induced current on the electrode has triangular shape and is initially proportional to the deposited energy in the cell. The time of charge collection has order of 400 ns. The physical triangular signal is then amplified, shaped by bipolar shaper and digitized every 25 nanoseconds. If signal is accepted by trigger, the signal amplitude is determined from signal samples and transformed to the cell energy. The energy response of the calorimeter needs to be calibrated in advance. The energy deposited in the absorber can be taken into account by knowing the sample fraction of the calorimeter.

The value of reconstructed energy in an individual cell of the ATLAS electromagnetic calorimeter is affected by signal leakage from or to its neighbour cells. This effect is called crosstalk. The crosstalk is caused by capacitive (strip-strip), resistive (strip-middle) or inductive coupling between calorimeter cells. It can be observed as a pulse distortion in the cell, leading to the change of the signal amplitude, and treated as an energy sharing between neighbouring cells. The crosstalk effect has significant impact not only in the calibration runs, when a signal is injected in one individual cell, but also can lead to wrong cluster energy, especially in the strips layer.

Detailed crosstalk studies have been performed in the calibration runs by investigating the signal shape distortions. A complete map of the crosstalk was provided and implemented into the reconstruction step of the MC simulation. Furthermore, the crosstalk tests with electron beams were carried out and a discrepancy between Data and MC longitudinal development of electron showers reconstructed in the EM calorimeter was observed. This discrepancy is assumed to be caused by mis-modeling of the crosstalk effect in the calorimeter. Hence, additional crosstalk studies are performed in this section using muons from $Z \rightarrow \mu\mu$ decays recorded by ATLAS detector with $\sqrt{s} = 8$ TeV 2012 collision data and results are reported here.

4.2 Methodology

The muons produced in $Z \rightarrow \mu\mu$ decays are minimum ionizing particles and their energy deposits are insensitive to amount of crossed material in front of the calorimeter. Such muons initiate very localised shower along the trajectory and significant part of the energy is deposited in the traversed cell of the electromagnetic calorimeter. In middle layer, almost full energy deposit is localised in 3 cells along η direction, while in strip layer, where the granularity is finer, it is enough to take into account 5 cells as shown in Figure 4.1. The approach of the irradiation of the calorimeter cell with muons and reading the energy deposits in neighbouring cells provides a direct sensitivity to the crosstalk and other effects caused by calorimeter miscalibration.

4.2.1 Data and MC samples

The goal of the analysis is to determine an amount of energy leakage between the calorimeter cells by using muons from collision data. Hence, arises a need to study effects that could contribute to energies measured in each cell. First of all, the pile-up noise has to be taken into account as it can increase (in-time pile-up) or decrease (out-of-time pile-up) the energy deposits in calorimeter

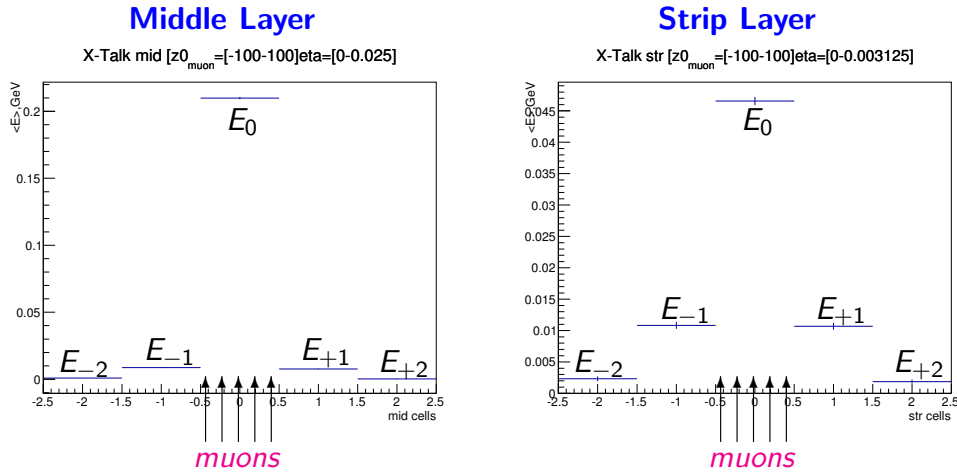


Figure 4.1: Average energies in central cell and its neighbour cells deposited by muons traversing central cell of middle (*left*) and strip (*right*) layer.

cells. The understanding of average pile-up contribution is crucial especially in neighbouring cells where energies left by muons are small. The electronic noise in the calorimeter cells is assumed to be well simulated in MC samples. In addition, the measured energy can be biased due to not perfect electronic calibration of the cell. Thus the $L1/L2$ (here $L1$ and $L2$ denote the strip and middle layers) corrections are needed in data to adjust this effect.

This analysis uses the following Data and MC samples:

- Proton-proton collision data sample collected in 2012 at $\sqrt{s} = 8$ TeV, containing muons from $Z \rightarrow \mu\mu$ decays. The data sample contains about 33 M muons.
- Official Monte Carlo sample with muons from $Z \rightarrow \mu\mu$ decays corresponding to $\sqrt{s} = 8$ TeV pp collisions. The simulation includes the pile-up noise and already injected map of the crosstalk effect between calorimeter cells obtained in previous crosstalk studies. This sample contains ~ 8 M muons.
- MC sample of single muons with $p_T^\mu = 40$ GeV with flat $|\eta| < 2.5$ and $-\pi < \phi < \pi$ distributions. The pile-up effect in such sample is not present, while a map of the crosstalk is applied to calorimeter simulation as well as the electronic noise in calorimeter cells. This sample contains about 9 M muons.
- Similar MC sample of $p_T^\mu = 40$ GeV single muons, with crosstalk effect in the calorimeter is disabled, providing the energies directly deposited by muons in the calorimeter cells. This sample contains about 9 M muons.

4.2.2 Method description

This analysis is divided into three main steps. In the first step, the analytical model of the energy leakage between cells of the same layer (strip \rightarrow strip, strip $\rightarrow 2^{nd}$ strip, middle \rightarrow middle) and between layers (middle \rightarrow strip) is developed. The analytical expressions for the corresponding crosstalks are derived and presented below. The use of both single muons MC samples with disabled and enabled crosstalk effect allows to re-derive the crosstalk map already added to ATLAS calorimeter simulation. The comparison of the athena¹ crosstalk map and rederived one allows to conclude if the analytical model works well and is applicable to data. In the second step, the

¹The athena framework for data processing and analysis is an enhanced version of the Gaudi framework [43] that was originally developed by the LHCb experiment but is now a common ATLAS-LHCb project.

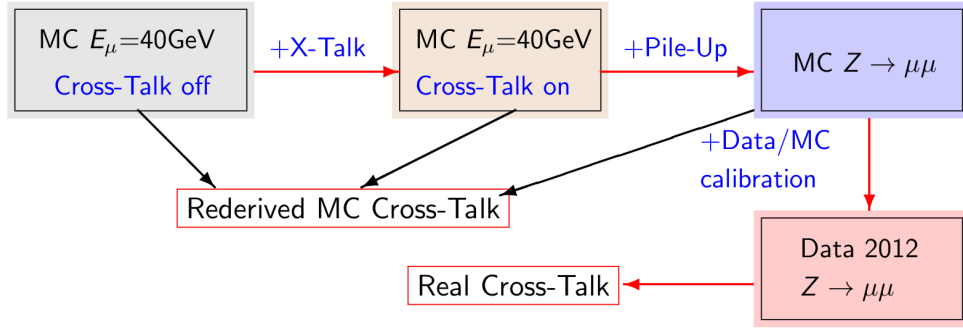


Figure 4.2: Block-scheme showing the strategy used for the crosstalk analysis.

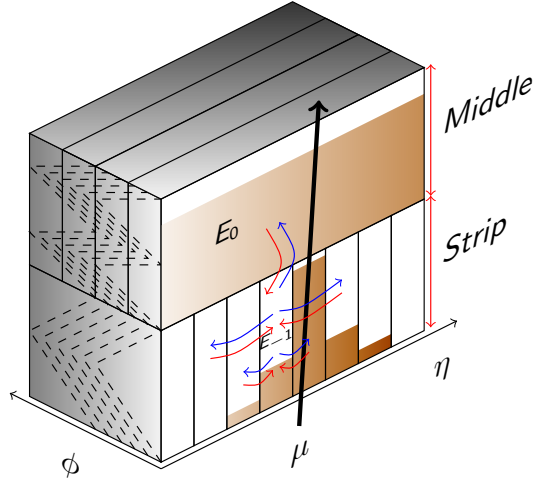


Figure 4.3: Schematic illustration of muon energy deposits in cells of strip and middle layers of the EM calorimeter.

crosstalk model is applied to the official $Z \rightarrow \mu\mu$ MC sample that differs from the $p_T^\mu = 40$ GeV single muons simulation by presence of pile-up. Effects caused by different p_T^μ distributions are assumed to be negligible. An average pile-up contribution to the calorimeter cells is then studied and properly subtracted in order to re-derive already known crosstalk map. Finally, the developed procedure of pile-up subtraction and crosstalk derivation can be applied to the data. To account for not perfect electronic calibration of the calorimeter cells, the layer $L1/L2$ intercalibration corrections must be applied in advance. The block-scheme in Figure 4.2 summarizes the strategy for the derivation of the crosstalk in the EM calorimeter.

4.2.3 Muon selection

In this analysis the muons from $Z \rightarrow \mu\mu$ decays requiring $p_T^\mu > 25$ GeV are used. The muon's track can be reconstructed by inner detector and muon spectrometer. The calorimeter cells traversed by a muon are determined extrapolating the track to the entrance of the corresponding calorimeter layer. The extrapolation procedure takes into account the magnetic field seen by muon in the calorimeter.

To reach a satisfying precision of the crosstalk determination, the eta-projective muons are required, i.e. the muons emanating near the interaction point in rapidity plane. The muon eta-projectivity can be achieved by placing requirements on track impact parameter z_0 with respect to the IP. In current crosstalk studies the cut on muon projectivity $|z_0| < 100\text{mm}$ was applied which is sufficient for middle layer. Given that the energy deposit of a muon is proportional to path

length in active medium, the muon eta-projectivity ensures bigger energy deposit in the crossed (central) cell and smaller energy deposits in its neighbour cells. This provides higher sensitivity to the crosstalk effect. The z_0 impact parameter distributions in data and MC are shown in Figure 4.4. To ensure that modeled muons have similar conditions in MC and data, the corresponding impact parameter z_0 has been reweighted in all MC simulations.

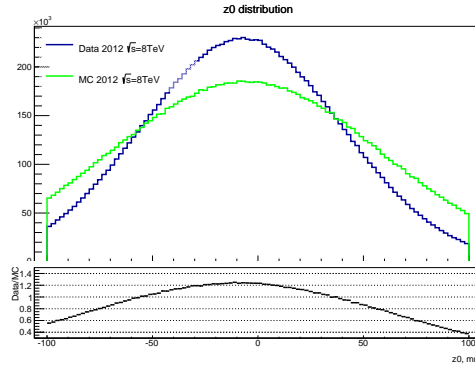


Figure 4.4: Comparison of the z_0 impact parameter distributions of selected muons in data and MC.

If condition of muon eta-projectivity to the interaction point is fulfilled, five cells (central cell, neighbour and second neighbour cells) of strips and middle layer that are close to the reconstructed track are considered. But even these cells require additional cleaning cuts. In particular, the energy deposit in crossed cell has to be above the electronic noise. In addition, muon track is not perfectly reconstructed and uncertainty on muon rapidity is observed in data to be of order $\Delta\eta \approx 0.001$ for $\eta = 0$ direction that is compatible with strip width ($\Delta\eta^{strip} \approx 0.003$). Also possible calorimeter misalignment can lead to the selection of non-projective muons. To guarantee that muon is projective, crosses the central cell and deposits significant energy there, an additional requirement was applied: energy deposit in central cell of strip layer should be larger than energy deposit in its neighbouring cells.

Because this analysis is sensitive to the pileup effect, there is the need to reweight the Monte Carlo pileup conditions to what is observed in Data. The current data is collected using pp collisions with bunch separation of 50ns, so the convenient variable for reweighting is the average number of pileup interactions μ . The μ distributions observed in data and simulated in MC are shown in Figure 4.5. The ratio plot corresponds to weight applied to official MC sample.

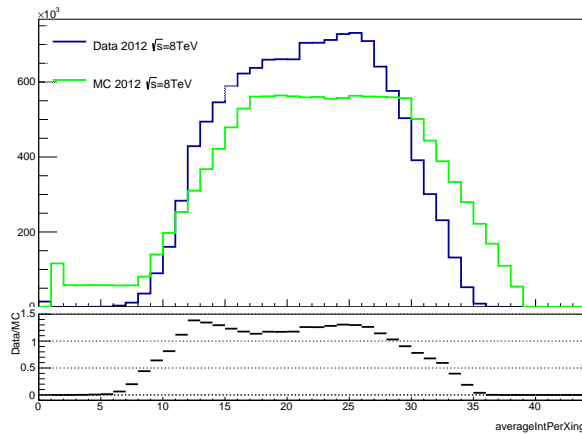


Figure 4.5: Average number of pileup interactions μ in data and MC.

4.2.4 Energy spectra fits

The muons fulfilling selection requirements deposit a certain amount of energy in the calorimeter that can be described by a Landau distribution. The observed energy distributions in the crossed cell and its neighbours is given by the convolution of the Landau distribution with a gaussian distribution corresponding to the electronic noise. The convolution model was used for the E_0 , $E_{\pm 1}$ and $E_{\pm 2}$ energy spectra fits of strips and middle layers and the most probable values (MPV) were extracted. The following notations are taken

- E_0 denotes the energy deposited by muon in the crossed (central) cell.
- E_{-1} and E_{+1} are energy deposits in the neighbour cells which are closer to $\eta = 0$ and further from $\eta = 0$, respectively.
- E_{-2} and E_{+2} are energy deposits in the second neighbour cells which are closer to $\eta = 0$ and further from $\eta = 0$, respectively.

Examples of E_0 , E_{-1} and E_{-2} fits for the middle layer requiring muon's rapidity to be $0 < \eta < 0.025$ and for the strips layer requiring $0 < \eta < 0.003$ are shown in Fig.4.6 and Fig.4.7 respectively. The center of the Gauss distribution that represents the electronic noise is fixed at zero. In the E_0 distribution of strip layer a low energy tail is due to strip displacement with respect to its expected position. Therefore, a fraction of Gauss-Landau convolution determined from $\eta - 1$ cell was added to fitting function of strip E_0 distribution. After applying the corrections of the calorimeter deformation (see later) the low energy tail disappears.

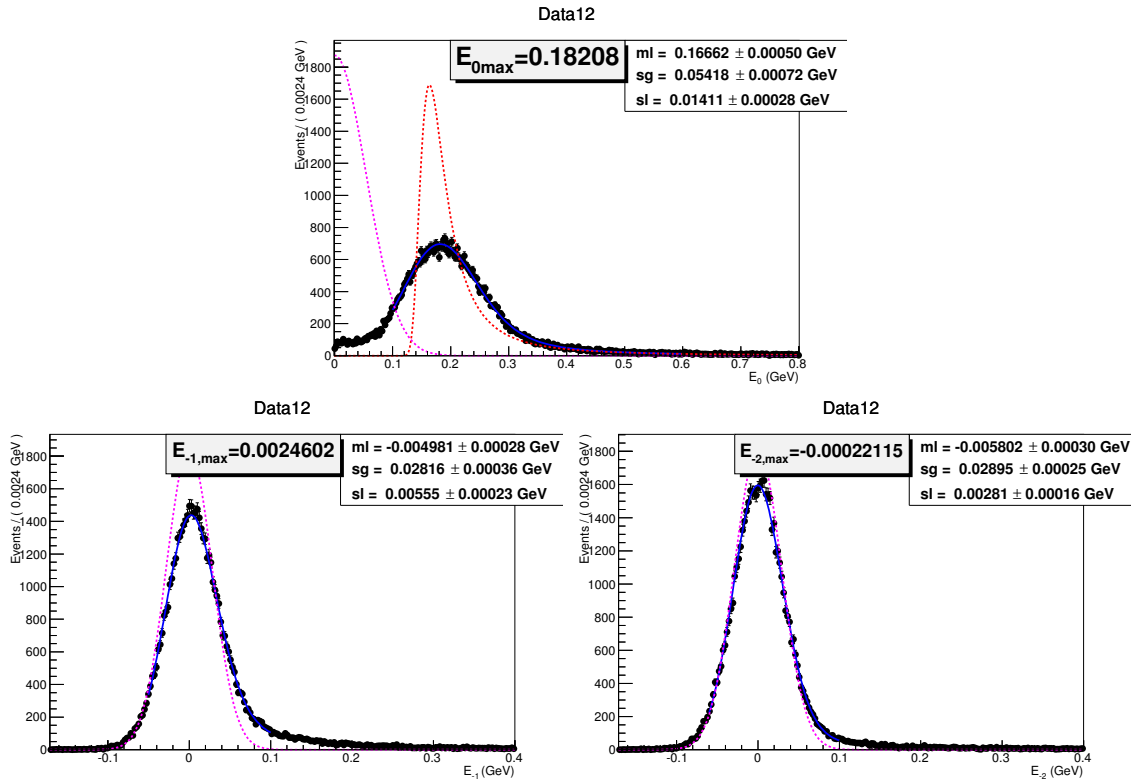


Figure 4.6: Energy spectra deposited by muon in crossed cell E_0 , in the left neighbouring cell E_{-1} and in second neighbouring cell E_{-2} of middle layer in data. The central cell corresponds to $0 < \eta < 0.025$. Energy distributions are fitted with Gauss-Landau convolution. The center of the Gauss distribution (magenta colour) that corresponds to the noise is fixed at zero. The landau distribution (red line, shown only for central cell) represents the energy deposited by muon.

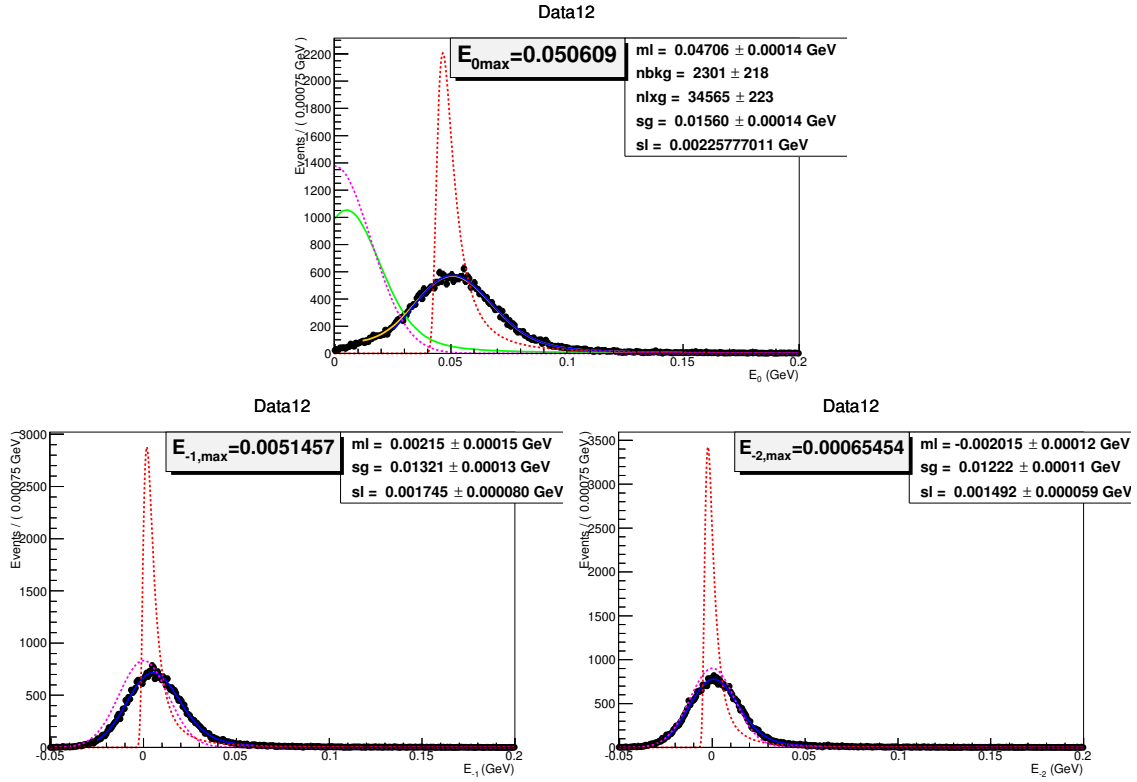


Figure 4.7: Energy spectra deposited by muon in crossed cell E_0 , in the left neighbouring cell E_{-1} and in second neighbouring cell E_{-2} of strip layer in data. The central cell corresponds to $0 < \eta < 0.003$. Energy distributions are fitted with Gauss-Landau convolution (plus additional gauss term in central cell). The center of the Gauss distribution (magenta colour) that corresponds to the noise is fixed at zero. The Landau distribution (red line) represents the energy deposited by muon. The additional Gaussian term in central cell (green) is needed to model the low energy tail caused by strip displacement (taken as distribution from the left strip).

In order to perform the fits of energy spectra and precisely extract muon's most probable energy deposits in the calorimeter cells, a uniformly distributed $[-5\text{MeV}, 5\text{MeV}]$ smearing of energy deposit of the selected muon was applied. This smearing smoothes out energy distributions and helps to avoid a digitization problem in the cells of the calorimeter. It makes distribution wider but does not change its maximum position.

4.3 Crosstalk analysis

4.3.1 Energy MPV distributions

Once the central cell for each muon is determined in the corresponding layers, the energy response is then read out in this cell as well as in two neighbour cells on each side along η . The observed muon energy distributions are fitted with the Gaussian-Landau convolution model and the MPV values of the deposited energy are extracted as described in Section 4.2.4. The crosstalk analysis is performed in terms of such MPV values. The MPV values of E_0 , E_{-1} , E_{+1} , E_{-2} and E_{+2} of energy spectra as a function of muon pseudorapidity η_μ are shown in Figures 4.8 and 4.9 for strip and middle samplings respectively. The distributions are shown for data and all MC samples introduced in Section 7.1. The comparisons of *red-green*, *green-black* and *black-blue* distributions already allows to get size of cross-talk and average pile-up contributions.

Because the selected muons are minimum ionising particles, the $MPV(E_0)$ value extracted from central cell is proportional to the length of the muon track in active material. Thus, the

MPV distributions corresponding to central cell reflect the geometrical depth of each cell in the sampling.

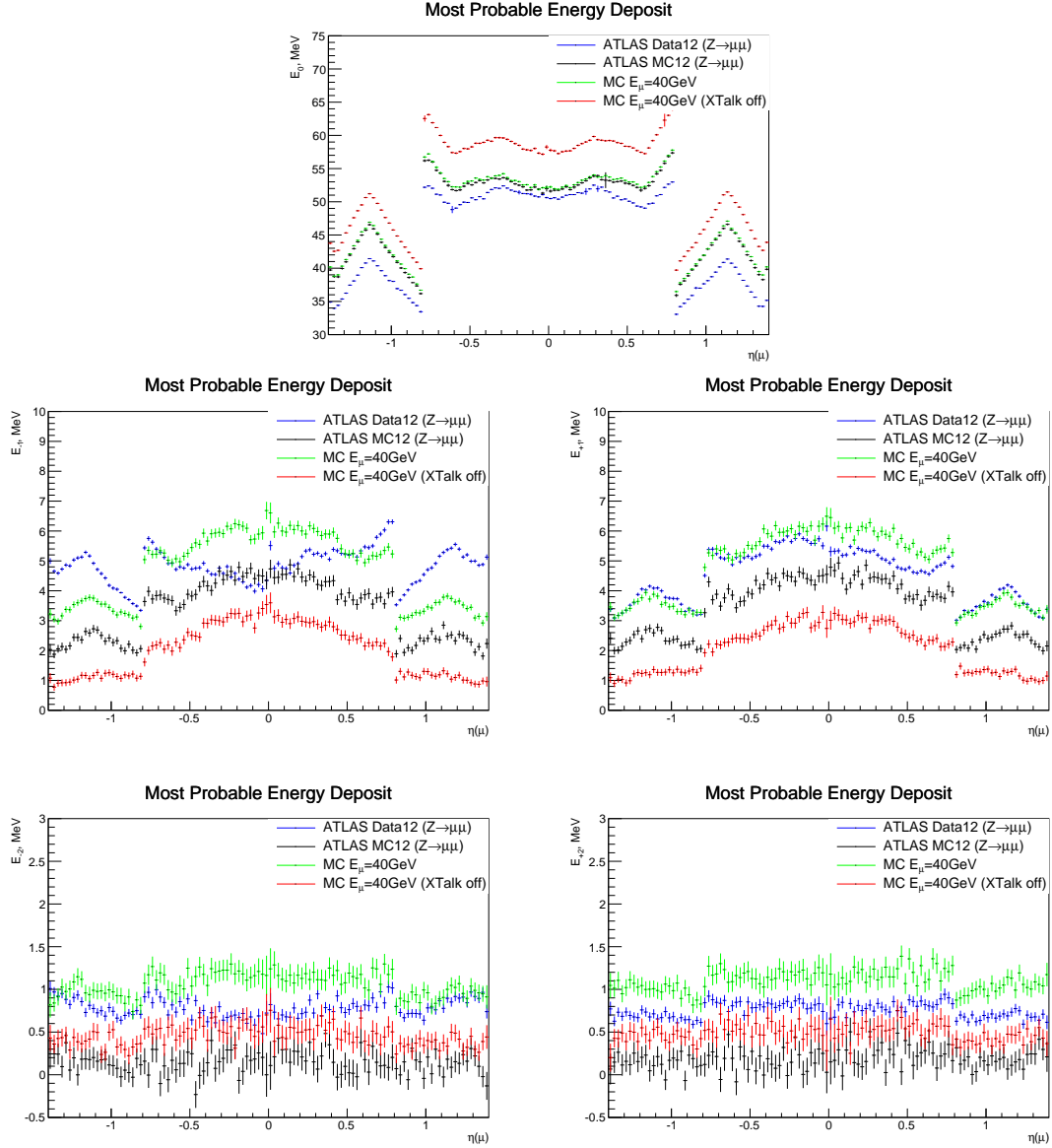


Figure 4.8: Most probable energy distributions E_0 , E_{-1} , E_{+1} , E_{-2} and E_{+2} of strip layer in muon's rapidity bins respectively. The distributions are shown for data and all MC samples. The error bars correspond to the statistical uncertainty.

In addition, the MPV values of total muon energy deposits in five cells $S = MPV(E_{-2} + E_{-1} + E_0 + E_{+1} + E_{+2})$ of each sampling are also useful to consider as here the effect of horizontal crosstalk along η is canceled out (the muon shower is fully localised in five strips of the strip layer). These distributions are shown in Figure 4.10.

4.3.2 Athena crosstalk rederivation

4.3.2.1 Previous measurements

As already mentioned above, the cross-talk between the cells in each sampling of the EM calorimeter has been studied during the calibration runs [44], [45]. The sources of the crosstalk effect are highlighted to be

- **Capacitive crosstalk** — Capacitive coupling between adjacent electrodes in all samplings.

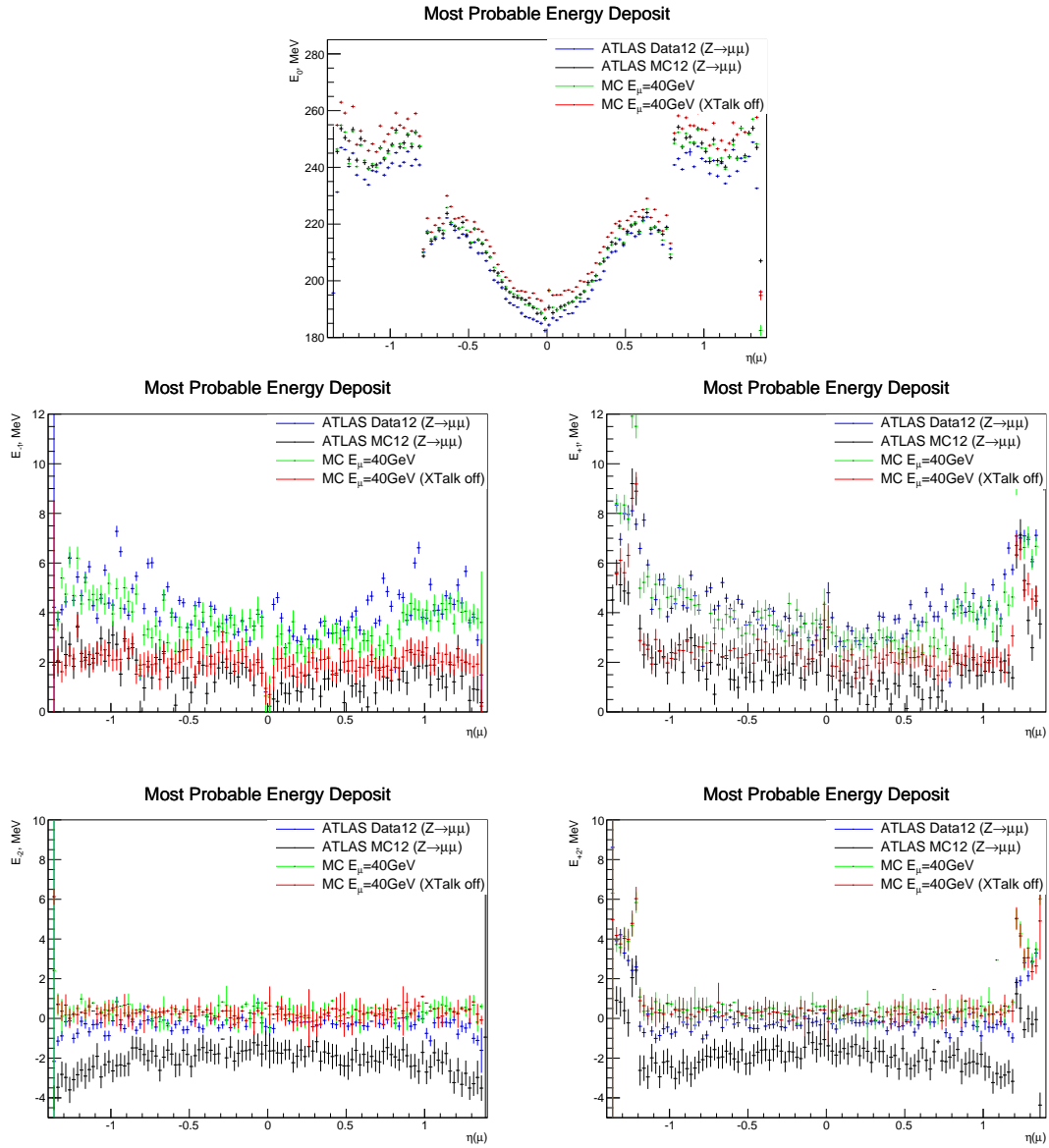


Figure 4.9: Most probable energy distributions E_0 , E_{-1} , E_{+1} , E_{-2} and E_{+2} of middle layer in muon's rapidity bins respectively. The distributions are shown for data and all MC samples. The error bars correspond to the statistical uncertainty.

- **Resistive crosstalk** — High voltage resistor between strip and middle samplings.
- **Inductive crosstalk** — Inductive effects in middle layer coming from mother boards.

During the calibration runs the calorimeter cells were pulsed individually and the reconstructed signal was studied. Each source of the crosstalk makes distortions of the readout signal shape in a different way. The study of the readout signal in pulsed cell allows to estimate the crosstalk quantitatively as the reconstructed amplitude becomes smaller due to signal leakage to the neighbours. A complete map of the crosstalk was provided and implemented in the ATLAS simulation. It is illustrated in Figures 4.11 as a function of η (barrel region) for strip and middle layers. As shown, the fraction of signal leaking from a middle cell to its horizontal neighbours is about 1-1.5%. The crosstalk from strip cell to its closest neighbours is much larger and corresponds to about 8%. Moreover, the total signal leakage from strip cell to second neighbours is not negligible amounting to about 1%. The total crosstalk from middle cell to strip layer is expected to be about 0.6% and has to be also taken into account in this analysis.

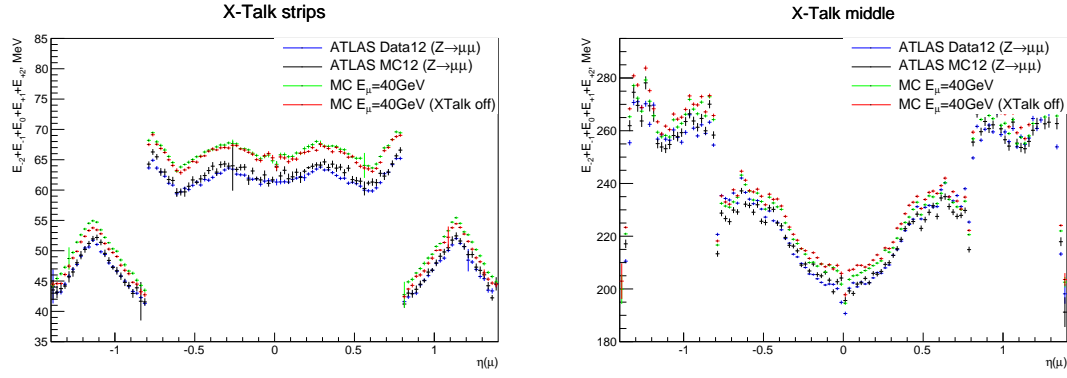


Figure 4.10: Most probable energy distributions $S = MPV(E_{-2} + E_{-1} + E_0 + E_{+1} + E_{+2})$ in middle and strip samplings as a function of muon η . The distributions are shown for data and all MC samples. The error bars correspond to the statistical uncertainty.

The cross-talk analysis performed here benefits from the fact that the studies are performed with physical signal from muons, while the previous results are based on the electrical pulses.

4.3.2.2 Rederivation of the crosstalk in MC

The crosstalk measurement using muons is based on the same principle as used in previous studies with electronic pulses. The crosstalk map derived from studies of electronic pulses is currently used in athena reconstruction software. In this approach each cell of the calorimeter is irradiated with muons and energy response of five cells along η is read independently. The advantage of this method is that it operates directly with physical data.

In order to derive the crosstalk in the EM calorimeter, the analysis starts with two Monte Carlo samples (see Section 7.1) in which muons with constant energy $E_\mu = 40$ GeV are used. One of these samples has crosstalk disabled, so the comparison of energy responses in terms of MPVs in each of five cells allows to derive the crosstalk. The analytical model for energy sharing due to crosstalk is developed and described in Section 8.6. The main analytical results are

- **Middle→Strip** crosstalk can be obtained using equation (A.3). It is derived by comparing the total muon energy deposits reconstructed in strip layer with crosstalk effect On/Off.
- **Strip→Strip** and **Strip→^{2nd}Strip** crosstalks can be obtained using equations (A.7) and (A.8) respectively. It is derived by comparing the muon energy deposits reconstructed each cell of strip layer with crosstalk effect On/Off. The values of Middle→Strip crosstalk are here as input.
- **Middle→Middle** crosstalk can be obtained using equation (A.11) which is derived in a similar way as above.

An assumption of these derivations is that the energy flows between cells equally in both directions. The results of reconstructed crosstalk in MC are compared with values injected in the simulation and shown in Figure 4.11. Good agreement is observed meaning that the analytical model works well.

4.3.3 Pile-up subtraction

Without the pile-up the energy distribution is given by the convolution of Landau distribution describing the muon energy deposit, and a Gauss distribution that corresponds to electronic noise

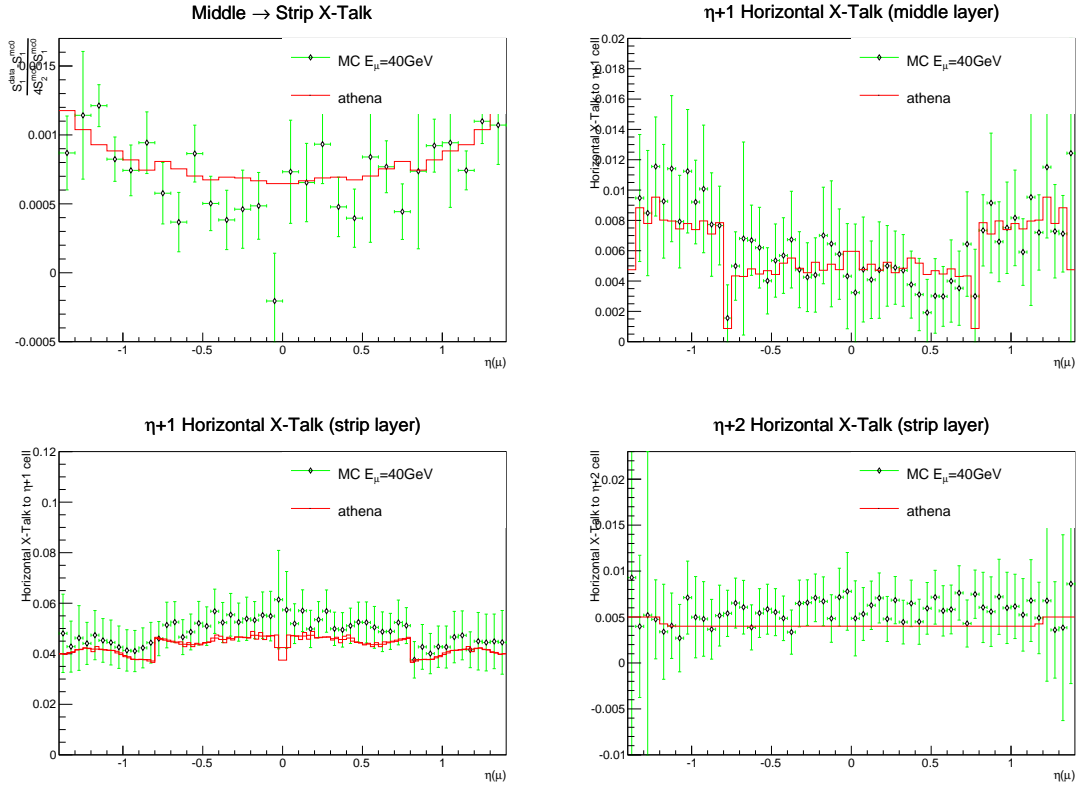


Figure 4.11: The crosstalk map in barrel EM calorimeter used in athena and reconstructed from MC $E_\mu = 40$ GeV simulations. The *middle* \rightarrow *strip*, *middle* \rightarrow *middle* + 1, *strip* \rightarrow *strip* + 1 and *strip* \rightarrow *strip* + 2 crosstalks are shown. The results for *middle* \rightarrow *middle* - 1, *strip* \rightarrow *strip* - 1 and *strip* \rightarrow *strip* - 2 are similar and thus omitted here. The error bars correspond to the statistical uncertainty.

in the cell. In presence of pile-up the energy spectra E_i ($i = 0, \pm 1, \pm 2$) reconstructed in cells of strip or middle sampling become

$$P(E_{dep}) \otimes \text{Landau}(E_{dep}) \otimes \text{Gauss}(\text{mean} = 0, \sigma_{noise}) \quad (4.1)$$

where $P(E)$ corresponds to pile-up energy spectrum reconstructed in a cell. Therefore, the pile-up can affect the MPV of the energy reconstructed in a cell and this effect will be different in central cell, first and second adjacent cells. Note, that the ATLAS calorimeter read-out is designed to cancel such pile-up contribution for large number of events. However, this seems to not work for small energies deposited by muons. For current studies we choose the following parametrization which describes the MPV transformation under the pile-up:

$$\begin{aligned} E_{\pm 2} &\rightarrow E_{\pm 2} + \text{PileUp} \\ E_{\pm 1} &\rightarrow E_{\pm 1} + W_1 * \text{PileUp} \\ E_0 &\rightarrow E_0 + W_0 * \text{PileUp} \end{aligned} \quad (4.2)$$

Here *PileUp* is a reference parameter. Natural choice is to extract it from $E_{\pm 2}$ second neighbour cells where the pile-up contribution is dominant. The W_0, W_1 are parameters which depend on pseudorapidity region η as muon energy deposits are η -dependent. To account for remaining contribution from muon energy shower in these cells, the MC sample of single muons (crosstalk is On) can be used:

$$\text{PileUp} = \frac{\Delta E_{-2} + \Delta E_{+2}}{2}, \quad (4.3)$$

where $\Delta E = E(\text{PU on}) - E^{MC}(\text{PU off})$. The estimated pile-up contribution in MeV in data and MC as a function of η is shown in Figure 4.12. Mismodeling of the pile-up contribution is observed

to be about 3 MeV in middle and about 0.6 MeV in strip layers. The ratio of these values is close to 4 that corresponds to ratio of cells in strip and middle layers. While the *PileUp* can be obtained separately in MC and in data, the correction values W_0, W_1 are estimated from Monte Carlo and applied to data for the pile-up subtraction. The W_0, W_1 parameters in η bins are shown in Figure 4.13 for strip layer and Figure 4.14 for middle layer.

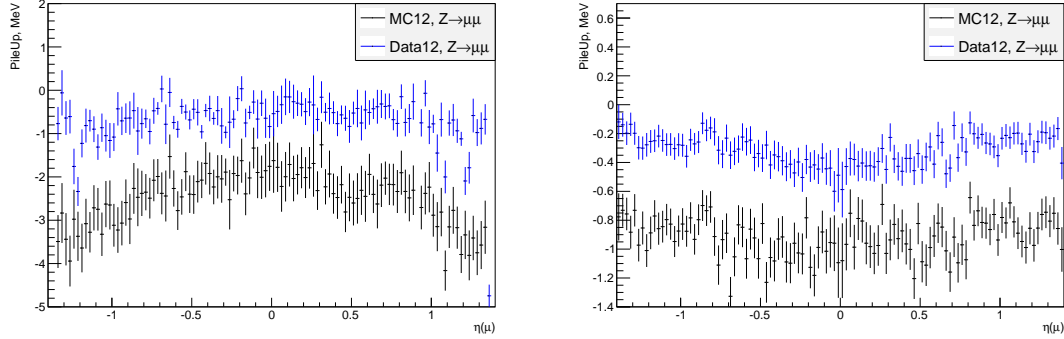


Figure 4.12: The estimated pile-up contribution using Eq.(4.4) in MeV in data and MC as a function of η observed in second neighbour cells (low signal) of middle (*left*) and strip (*right*) layers. Mismodeling of the pile-up contribution is observed to be about 3 MeV in middle and about 0.6 MeV in strip layers.

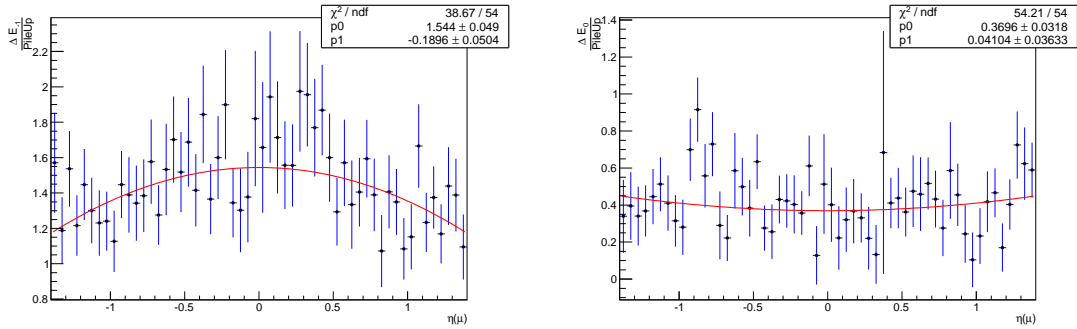


Figure 4.13: The W_1 (*left*) and W_0 (*right*) pile-up correction factors in strip layer extracted from MC (see Eq.(4.2)).

4.3.4 Data/MC calibration. Intercalibration of first and second layers

The cells of the EM calorimeter can be not perfectly calibrated. This could affect the current analysis results, thus additional correction has to be applied. An assumption can be used that the ratio of reconstructed energies deposited by muon in strip and middle samplings of the calorimeter is well modeled in MC. In addition, the total reconstructed energy should be equal in data and MC. To account for the total muon energy profile in η , the two following cases are considered:

- $E_{tot} = MPV(E_{-2} + E_{-1} + E_0 + E_{+1} + E_{+2})$
- $E_{tot} = MPV(E_{-2}) + MPV(E_{-1}) + MPV(E_0) + MPV(E_{+1}) + MPV(E_{+2})$

In the first step, the ratios of the MPVs of total energy in five cells in data and MC are shown in Figure 4.15 for strip and middle layers. The corresponding L1/L2 intercalibration scale factor,

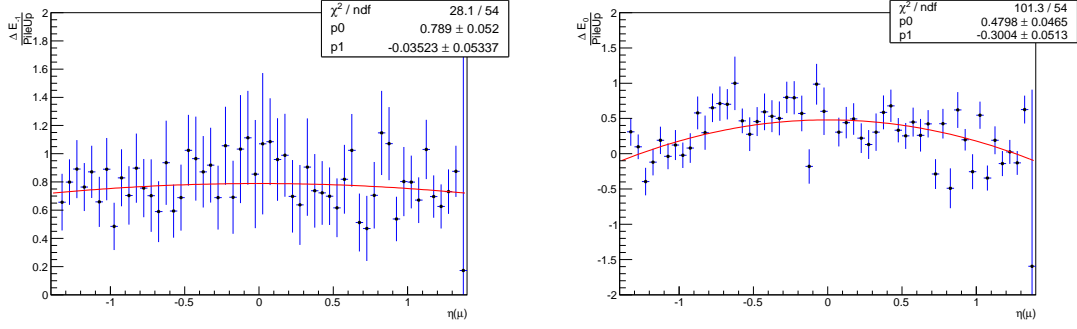


Figure 4.14: The W_1 (left) and W_0 (right) pile-up correction factors in middle layer extracted from MC (see Eq.(4.2)).

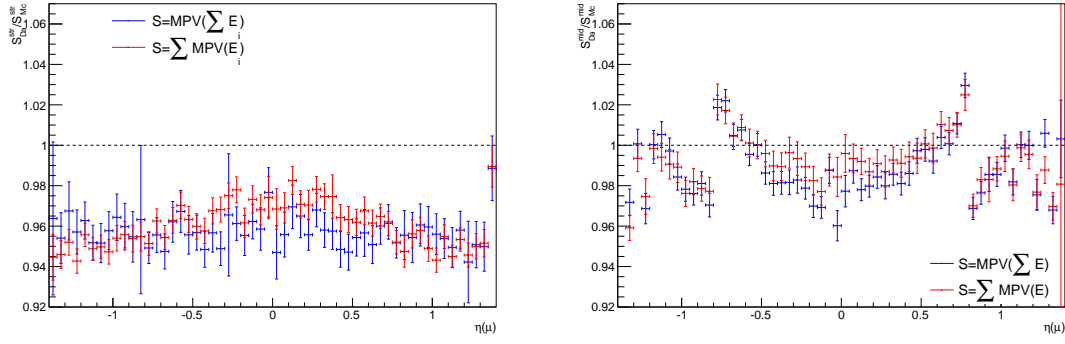


Figure 4.15: Ratio $E_{data/MC} = MPV(E_{data})/MPV(E_{MC})$ as a function of η in strip (left) and middle (right) layers.

$\alpha_{1/2}$, defined as the ratio $E_{data/MC}^{strip}/E_{data/MC}^{middle}$ is presented in Figure 4.16. Both definitions of the energy summation provide the same result. The estimated distribution agrees with the one obtained in [46]. Due the fact that the pattern observed in Figure 4.16 comes from middle layer, the intercalibration correction is applied to L2 sampling as $E_{middle}^{corr} = E_{middle}/\alpha_{1/2}$.

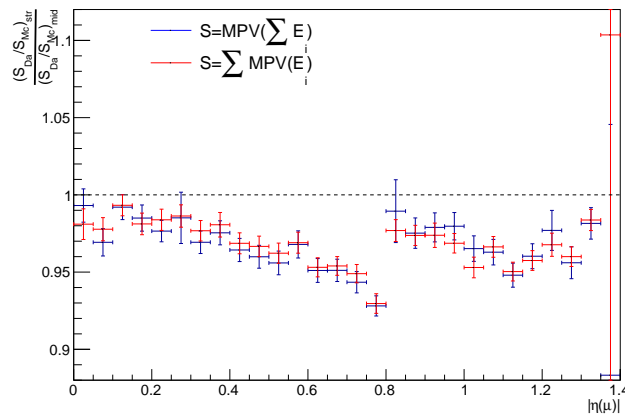


Figure 4.16: The L1/L2 layer intercalibration scale factor $\alpha_{1/2}$.

In the next step, the total deposited energy by muon in strip and middle layers has to be equalized in data and MC. Such global energy scale factor is shown in Figure 4.17. This correction is defined from data and MC after pile-up subtraction as

$$g = \frac{(S_{tot}^{strip} + S_{tot}^{middle}/\alpha_{1/2})_{data}}{(S_{tot}^{strip} + S_{tot}^{middle})_{MC}} \quad (4.4)$$

and data corrected as $E^{corr} = E/g$.

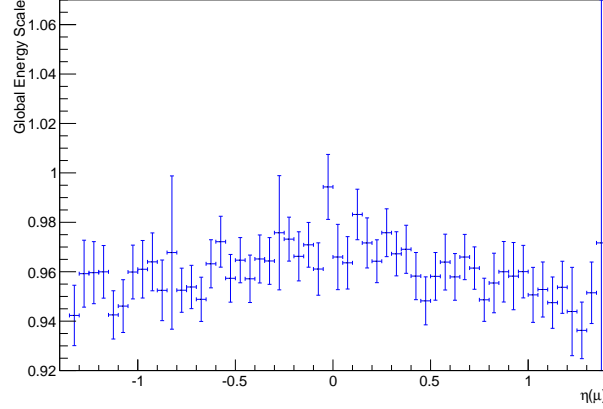


Figure 4.17: The global energy correction applied to data to equalize the total muon energy deposits in Data and MC.

4.4 Calorimeter alignment and deformation

4.4.1 Introduction

After applying the pile-up subtraction and the energy scale corrections discussed in previous section, the crosstalk can be directly extracted from data in the same way as this is done in MC. But an issue has been observed in data. In this analysis we assume that the horizontal energy leakage due to crosstalk in the electronics is the same in both directions from a given cell. This actually has been confirmed in previous measurements and the crosstalk values used in the Monte Carlo are symmetric. Consequently, the MPV distributions in first neighbour cells extracted from strip layer are compatible in MC as shown in Figure 4.18(right). In contrast, the similar distributions extracted from data (see Figure 4.18(left)) show asymmetric behavior and this is not expected to be from the crosstalk.

4.4.2 Overview of the possible effects

4.4.2.1 z_0 reweighting as test of muon projectivity

Obviously, a muon originating from the z_0 position far away from interaction point becomes non-projective with respect to orientation of calorimeter cells. The balance between average energy deposits in first neighboring strips of such muons is not kept anymore. To assess the size of this effect, the additional reweighting that corresponds to significant z_0 impact parameter shifts of 10 mm, 30 mm and 70 mm has been performed. The impact was verified on the MPV distribution in first neighbour strip as shown in Figure 4.19. No significant change is observed at relatively small shifts. To change average energy deposit in this cell by 1% need to shift z_0 by ~ 30 mm that is large value.

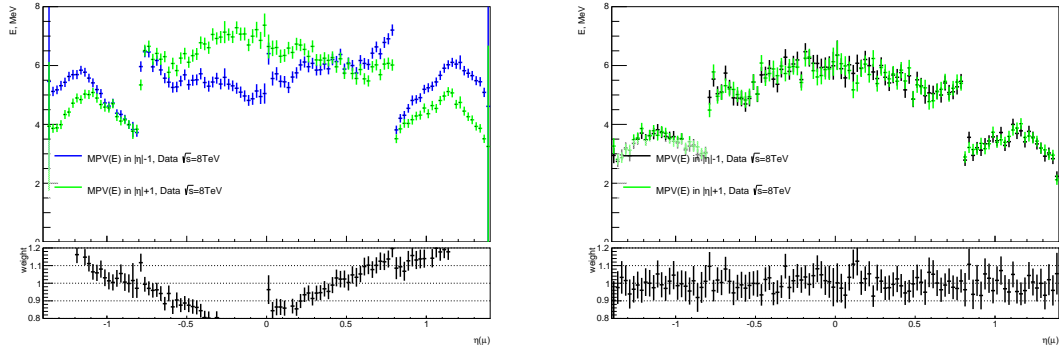


Figure 4.18: The comparison of the MPV distributions in first neighbour cells extracted from strip sampling. The left side corresponds to data and the right side corresponds to MC. Distributions are shown after pile-up subtraction and energy scale corrections in data.

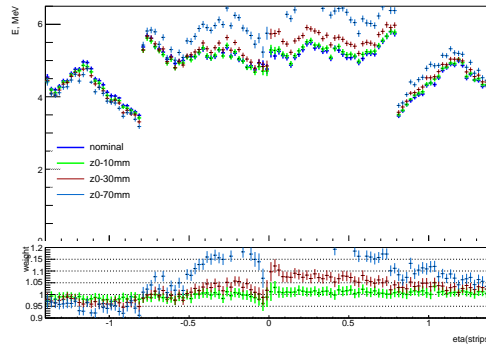


Figure 4.19: Impact of muon z_0 impact parameter shifts on the energy deposits in neighbour cell of strip layer.

4.4.2.2 Displacement of calorimeter cells

Another effect that could cause such asymmetry of energy distributions in neighbour cells is connected with displacements of cells from their expected position (see Figure 4.20). If due to such displacement the muon crosses the neighbour cell instead of central one, the energy deposit is then decreased in the expected central cell and increased in the neighbouring one. The opposite neighbouring cell collects lower energy deposit in this case and the mentioned asymmetry appears. While the energy deposits in individual cells change due to such displacements, the total energy in five cells almost does not change. This means that the impact on layer intercalibration is negligible.

The following sources of the cell displacements are considered:

- The contraction of the calorimeter due to temperature
- Global translations of the calorimeter compartments along z axis or in perpendicular plane X, Y
- Rotation of the calorimeter
- Deformation of the calorimeter under its own weight

4.4.3 Methodology

A global survey of the calorimeter position and its deformations have been performed during the installation. However these measurement have been done at a warm temperature and the

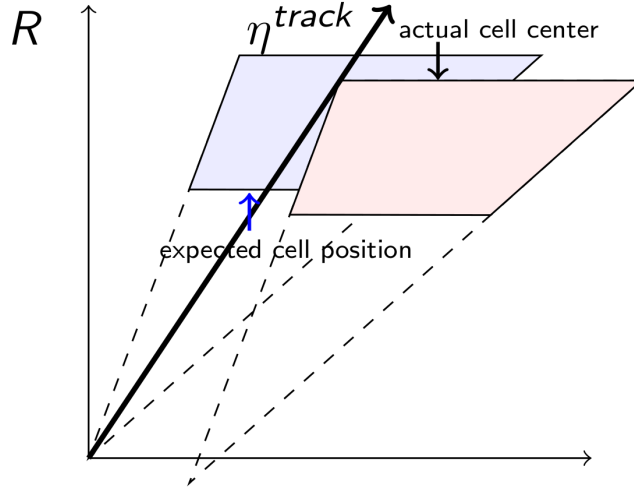


Figure 4.20: Schematic illustration of cell displacement. Black arrow represents a muon direction crossing the calorimeter.

precision of some measurements is limited. In addition, a study of the calorimeter alignment with respect to the Inner Detector (ID) has been performed using electrons [47]. In this section a new *in-situ* method is introduced that allows to scan the calorimeter using muons. Due to the muon shower in the calorimeter is narrow, the position of each cell can be tested individually.

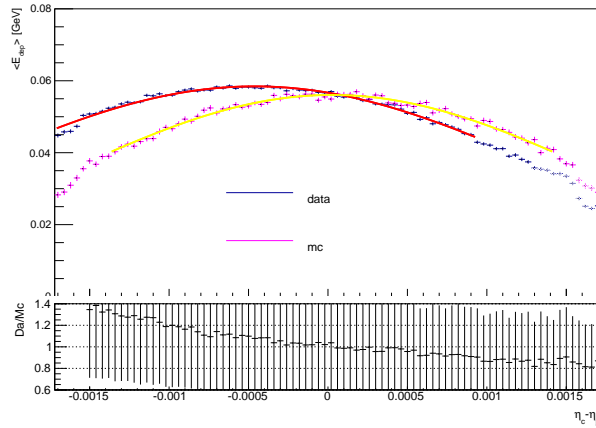


Figure 4.21: Profile of the deposited energy in strip cell crossed by muon as a function of $\Delta\eta$ between muon track and expected cell center position in data and MC. The muon pseudorapidity is required to have $-0.15 < \eta_\mu < -0.10$.

This method is based on the scanning of the energy response of each cell by irradiating it with muons with different η . The energy deposited by muon in a cell is defined by the track length in the active LAr volume. Due to the projectivity of cells the energy response as a function of muon η is expected to be an isosceles trapezoid. However, the muon η is one of muon track parameters measured in the ID and it has an uncertainty. Moreover, the value η extrapolated to the calorimeter is additionally smeared due to multiple scattering. Size of $\sigma(\eta)$ is expected to be about 0.001 in $\eta = 0$ direction that is quite large comparing to strip width ~ 0.003 . The resulting energy response of the cell as a function of muon eta is then given by convolution of gauss and trapezoid. The position of center of the cell corresponds to maximum energy deposit and it is used in the method. Example of energy profile as a function of $\Delta\eta$ between muon track and expected

cell center position is shown in Figure 4.21 for data and MC in strip layer. The distributions are fitted by a Gaussian and the position of maximum is extracted. In the MC the center of cell matches the expected position, while in data the maximum is displaced. The extracted difference $\Delta\eta$ between muon track and expected cell center position is treated as displacement of the strip cell and used to study further the contributions of each source of the displacement.

It is convenient to separate the sources into ϕ -dependent and ϕ -integrated categories. The ϕ -integrated shifts $\Delta\eta$ can be due to

- Longitudinal and radial contraction of the calorimeter
- Translations of the calorimeter compartments along z

The ϕ -dependent shifts $\Delta\eta$ are caused by

- Translations of the calorimeter in (X, Y) plane
- Calorimeter rotations
- Deformation of the calorimeter under its own weight

4.4.4 ϕ -independent effects: contraction and z -shifts

The extracted displacements of the strip cells from data and MC are shown in Figure 4.22 in η bins, including end-cap for completeness. As expected the result is zero for MC in barrel region but $|\Delta\eta| \sim 0.0002$ shifts are observed in end-cap region. In case of data, the six different parts are seen which correspond to different compartments of the EM calorimeter.

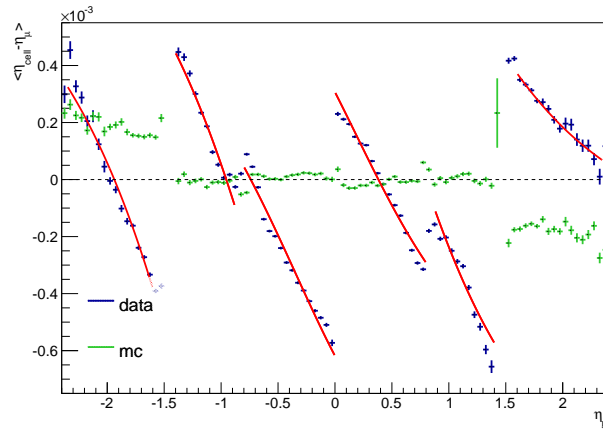


Figure 4.22: Observed displacement of strip cells in terms of $\Delta\eta$ with respect to expected position as a function of η . The displacements are parametrized using Eq.4.9 and summarized in Table 4.1.

In order to derive the model which describes such displacements, we start with well-known relation:

$$z = R \cdot \sinh(\eta) \quad (4.5)$$

Contraction of the calorimeter. Assume the contraction is allowed to be longitudinal and radial. Then from (4.5) we get

$$\Delta z = \Delta R \cdot \sinh(\eta) + R \cdot \cosh(\eta) \Delta\eta \quad (4.6)$$

After reorganizing the latter we have

$$\Delta\eta = (a_z - a_R) \tanh(\eta) = a \cdot \tanh(\eta) \quad (4.7)$$

where $a_z = \Delta z/z$ and $a_R = \Delta R/R$ are longitudinal and radial temperature expansion coefficients.

Constant z -shifts. From the relation (4.5), the impact on $\Delta\eta$ displacements of strips ($R = 1500$ mm) from calorimeter z -shifts is expected to be

$$\Delta\eta = \frac{Z_C}{1500 \text{ mm} \cdot \cosh(\eta)} \quad (4.8)$$

where Z_C is a value of calorimeter z -shift. The data distribution in Figure 4.22 is then fitted with

$$\Delta\eta = \frac{Z_C}{1500 \text{ mm} \cdot \cosh(\eta)} - a \cdot \tanh(\eta) \quad (4.9)$$

that combines both effects. The fit is performed for each of six η regions independently: four barrel subregions $-1.4 < \eta < -0.8$, $-0.8 < \eta < 0$, $0 < \eta < 0.8$, $0.8 < \eta < 1.4$ and 2 endcap subregions $-2.4 < \eta < -1.4$ and $1.4 < \eta < 2.4$. The observed discontinuity of the distribution is due to different z -shifts of separated parts of the calorimeter. The extracted temperature expansion coefficient and shifts along z are summarized in Table 4.1. The estimated values a are equal in symmetric regions with respect to $\eta = 0$. Differences between extracted contraction coefficients in the inner and outer barrels can be due to different Pb thickness (1.5 mm and 1.1 mm respectively). Note, the results of the fits in the endcap require more careful treatment as the orientation of the absorbers is horizontal. While the orientation of absorbers in the barrel suppresses the radial contraction, the horizontal orientation of endcap absorbers suppresses the longitudinal contraction. However, this parametrization can be used for the corrections of the strip displacements in the endcap. In addition, the MC also shows constant $\Delta\eta = 0.0002$ displacements in the endcap regions. This can be due to wrong definition of the cell positions in the endcap.

η range	-2.4 – -1.4	-1.4 – -0.8	-0.8 – 0	0 – 0.8	0.8 – 1.4	1.4 – 2.4
a	0.00096	0.00120	0.00076	0.00078	0.00119	0.00213
$Z_C[\text{mm}]$	-4.9	-1.99	-0.93	0.46	1.55	2.20

Table 4.1: The temperature expansion coefficients in the calorimeter and z -shifts of different compartments extracted from the fit of data.

4.4.5 ϕ -dependent effects: rotation and pear-shape deformation

To account for ϕ -dependent effects, each η bin in Figure 4.22 is scanned against ϕ . Example the extracted $\Delta\eta$ displacement of strip cells as a function of ϕ as shown in Figure 4.23 for $0.55 < \eta < 0.6$. The highest point at negative ϕ corresponds to the bottom of the calorimeter. The observed pattern of the distribution seems to be mainly due to the deformation of the calorimeter under the gravitation. However, the rotations and displacements in (X, Y) plane must be also considered and quantified. For this we do the following parametrization:

$$\begin{aligned} \Delta\eta = & A_0 + \\ & A_1 \cos(\phi) + B_1 \sin(\phi) + \\ & A_2 \cos(2\phi) + B_2 \sin(2\phi) + A_3 \cos(3\phi) + B_3 \sin(3\phi) + A_4 \cos(4\phi) + B_4 \sin(4\phi) \end{aligned} \quad (4.10)$$

where first term includes the all ϕ -integrated effects; the second term describes the calorimeter constant X_c, Y_c -shifts and tilts; and the last term describes the calorimeter deformation. Examples of fits are shown in Figure 4.24. Two models of pear-shaped deformation are considered: asymmetric and symmetric, where B_2, A_3, B_4 are dropped. As the gravity acts in vertical direction, the symmetric model is preferable.

The comparisons of ΔR calorimeter deformation observed in survey and extracted from $Z \rightarrow \mu\mu$ analysis are shown in Figure 4.25. In the survey the measurements have been performed on P-wheel(C-side) and M-wheel(A-side). In the current analysis the ΔR values were extracted from

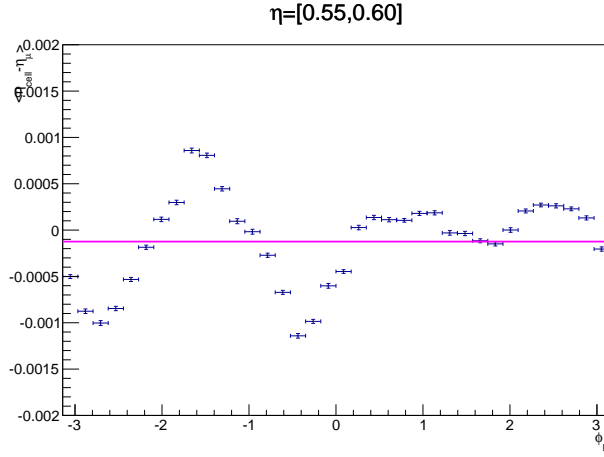


Figure 4.23: Observed displacement of strip cells in terms of $\Delta\eta$ as a function of azimuth in $0.55 < \eta < 0.6$ region. The horizontal line indicates the ϕ –integrated $\Delta\eta$ displacement that corresponds to Figure 4.22.

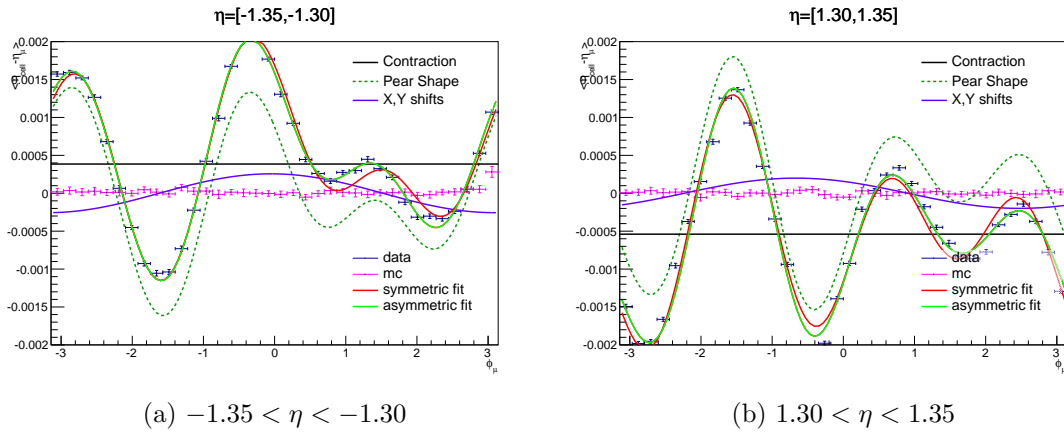


Figure 4.24: Example of fits with ϕ –dependent model introduced in equation (4.12). The following components are shown: *black* line represents ϕ –integrated A_0 coefficient; *blue* line represents effect of X_c, Y_c –shifts and tilts(A_1, B_1); *green-dashed* line represents the pear-shape deformation.

$\eta = -1.375$ and $\eta = +1.375$ bins which are close to the survey measurements. Both results are compatible.

The pear-shape deformation in (X, Y) plane in different η regions is shown in Figure 4.26. An impact of the pear-shape deformation of the calorimeter on the W boson mass extraction is illustrated in Figure 4.27.

4.5 Results

4.5.1 Crosstalk in data

Once the actual position of each strip cell is estimated, the correction is applied to η of muons in data as

$$\eta_\mu^{corr} \rightarrow \eta_\mu + \Delta\eta \quad (4.11)$$

in order to point them to correct position of cell. The correction is applied in η bins, inclusive in ϕ , using $\Delta\eta$ from equation (4.9). The (η, ϕ) –dependent correction using (4.12) provides the same result. The central cell has to be redefined accordingly to new pseudorapidity of the muons. This

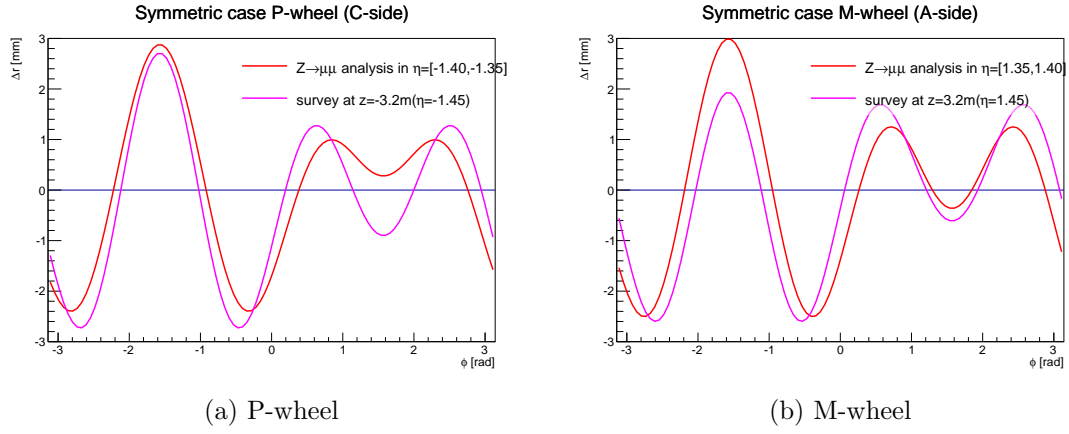


Figure 4.25: Comparisons of ΔR calorimeter deformation observed in survey and extracted from $Z \rightarrow \mu\mu$ analysis. The survey has been performed at a warm temperature.

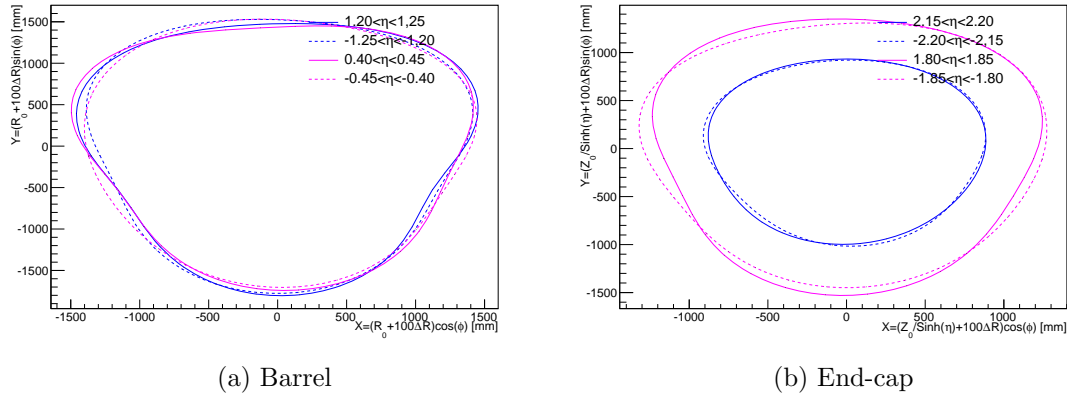


Figure 4.26: The pear-shape deformation in (X, Y) plane in different η regions.

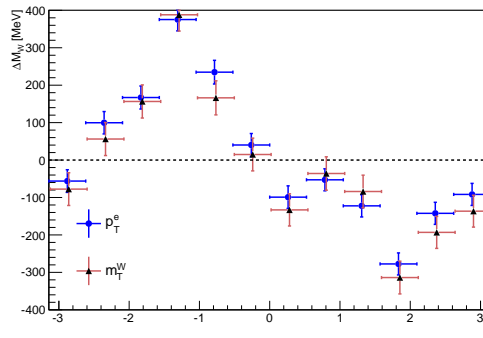


Figure 4.27: Impact of the pear-shape deformation of the calorimeter on the W boson mass extraction using electrons. The M_W values are plotted with respect to reference value.

is done with

$$\begin{aligned} if(\eta_c - \eta_\mu^{corr} > \frac{0.025}{16} - a \cdot |\eta_\mu|) &\rightarrow E_i = E_{i-1}, i = 0, \pm 1 \pm 2 \\ if(\eta_c - \eta_\mu^{corr} < -\frac{0.025}{16} + a \cdot |\eta_\mu|) &\rightarrow E_i = E_{i+1}, i = 0, \pm 1 \pm 2 \end{aligned} \quad (4.12)$$

where $a \approx 0.00065$ is the temperature expansion coefficient (see Table 4.1) to account for the contraction of the calorimeter cells.

After such correction is applied to data, the comparison of the MPV distributions in first

neighbour cells extracted from strip sampling becomes compatible as shown in Figure 4.28. But they differ from corresponding distributions in MC shown in Figure 4.18(right) that makes the L1-L1 crosstalk to be different. The extracted *middle* \rightarrow *strip* crosstalk values as a function of η from data are shown in Figure 4.29. The agreement between data and MC is a consequence of L1/L2 layer intercalibration.

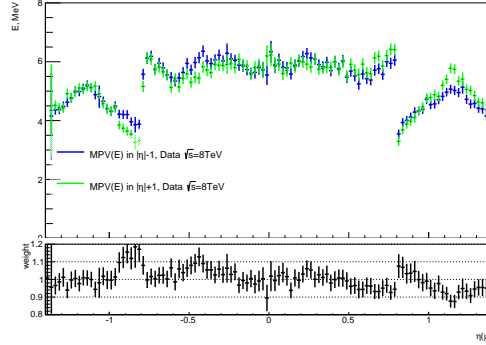


Figure 4.28: The comparison of the MPV distributions in first neighbour cells extracted from strip sampling after correction of the position of strip cells.

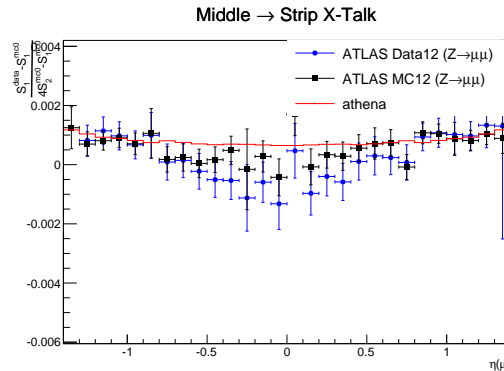


Figure 4.29: The *middle* \rightarrow *strip* crosstalk in barrel EM calorimeter used in athena, reconstructed from MC $Z \rightarrow \mu\mu$ simulation and from data after all corrections are applied. The errors are statistical only.

The *middle* \rightarrow *middle* ± 1 , *strip* \rightarrow *strip* ± 1 and *strip* \rightarrow *strip* ± 2 crosstalks are shown in Figure 4.30. The extracted crosstalk in middle layer is within 1σ . The crosstalk to second neighbour strips shows also good agreement with MC. However the crosstalk to neighbouring cells in data and in MC are different especially at high η .

For the cross-check, the difference between MPV values in data and MC of strip layer are extracted and shown in Figure 4.31. The difference between data and MC for total energy deposits in strip layer is zero as a consequence of the layer intercalibration and global data/MC calibration of the calorimeter. As can be seen, at the calorimeter region $|\eta| < 0.6$ the Data agrees well with MC and muon energy profiles in the strip layers are well modeled. But in the region of $|\eta| > 0.6$ the shower profile in Data is broader than in MC, that can be either due to discrepancy of the crosstalk modeling (*strip* \rightarrow *strip* crosstalk in Figure 4.30) or due to problems of the modeling of the shower in the MC.

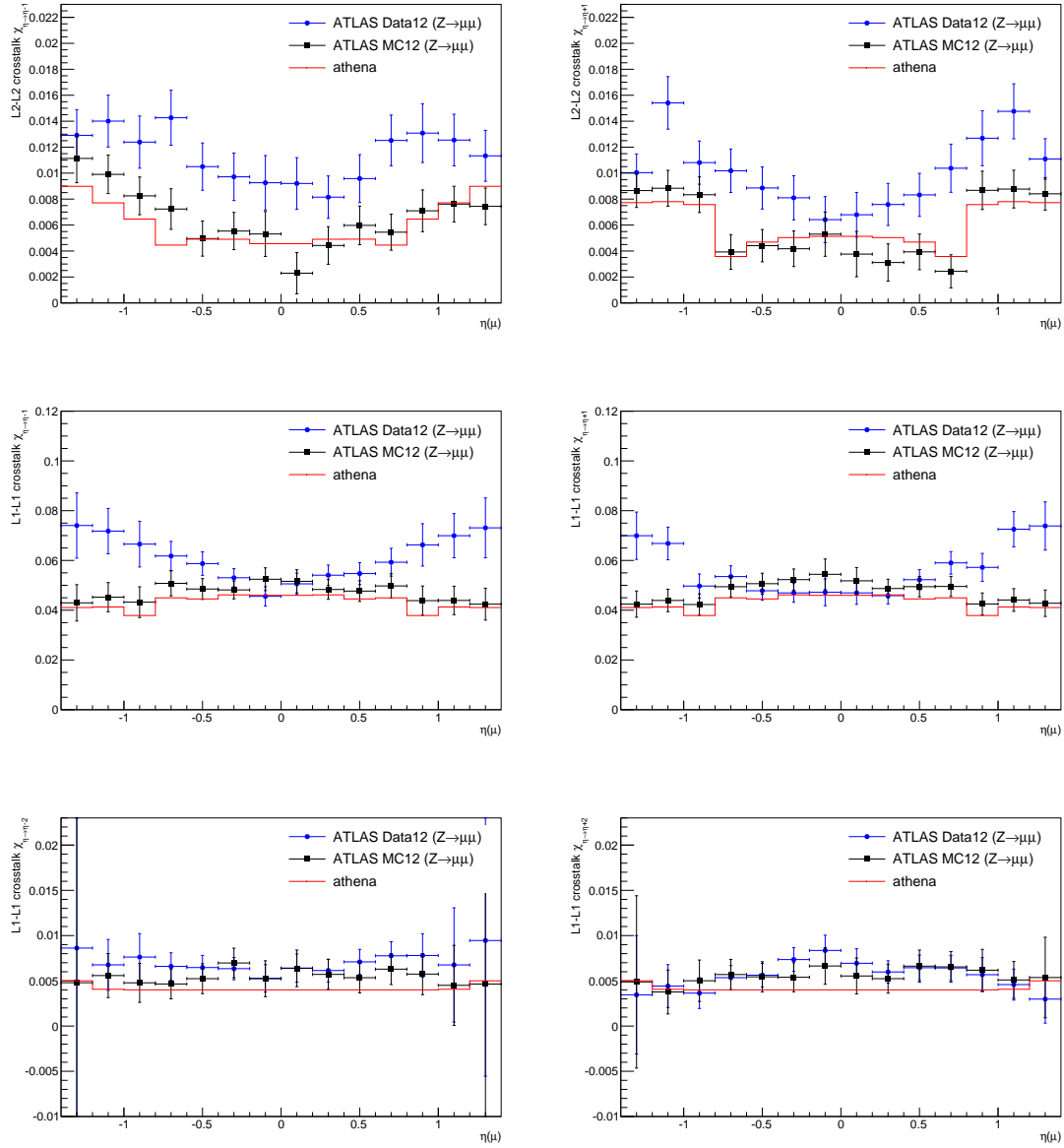


Figure 4.30: The crosstalk map as a function of η in barrel EM calorimeter used in athena, reconstructed from MC $Z \rightarrow \mu\mu$ simulation and from data after all corrections are applied. The *middle* \rightarrow *middle* -1 , *middle* \rightarrow *middle* $+1$, *strip* \rightarrow *strip* -1 , *strip* \rightarrow *strip* $+1$, *strip* \rightarrow *strip* -2 and *strip* \rightarrow *strip* $+2$ crosstalks are shown. The errors are statistical only.

4.5.2 Uncertainties

One of the possible sources of the uncertainty on the crosstalk estimations is an uncertainty coming from muon energy scale variation. This was tested by varying the muon energies deposited in strip αE_{str} and middle αE_{mid} layers of the EM calorimeter. The energy scale variations were taken to be $0.95 < \alpha < 1.05$ and $0.95 < \alpha < 1.05$. The impact of these variations on the *middle* \rightarrow *middle*, *strip* \rightarrow *strip* and *strip* \rightarrow 2^{nd} *strip* cross-talk was tested on the MC sample and results are shown in Figure 4.32.

Other systematic uncertainties on the cross-talk estimates can be due to:

- Possible contribution from third layer (no impact on the *strip* \rightarrow *strip* results is expected)
- Uncertainty on the extraction of strip cell position in η (expected to be small)

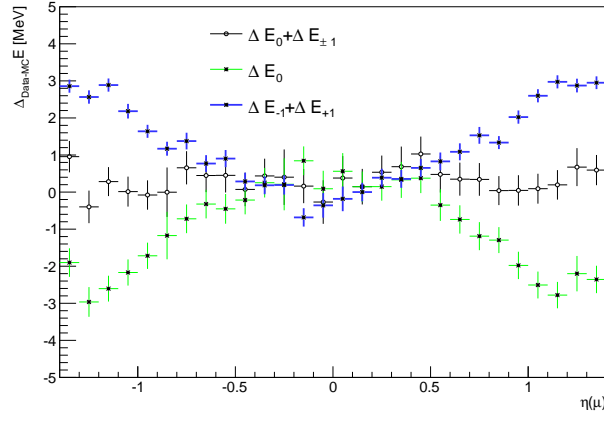
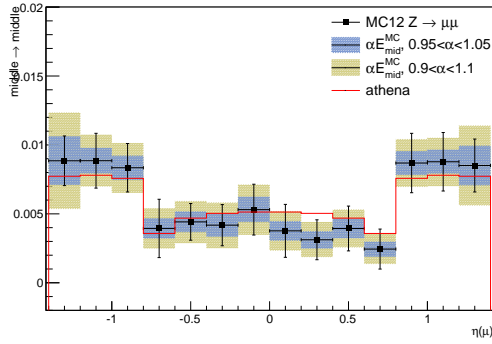
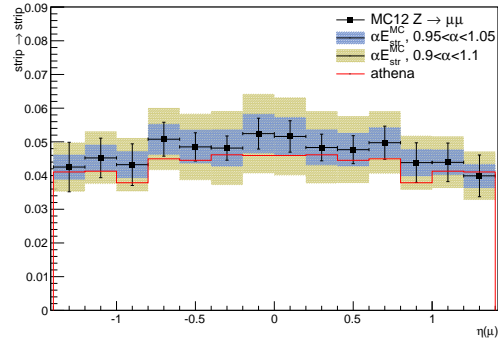


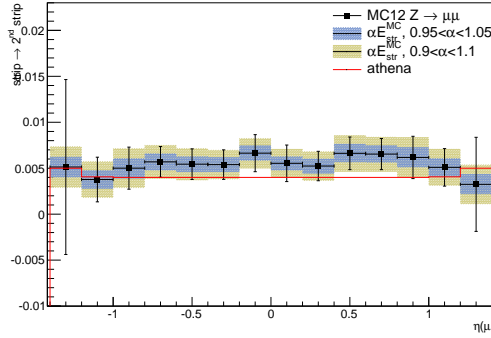
Figure 4.31: Difference $Data - MC$ of energies collected in three strips, in central strip only and in neighbour strips only.



(a) $middle \rightarrow middle$ cross-talk



(b) $strip \rightarrow strip$ cross-talk



(c) $strip \rightarrow 2^{nd} strip$ cross-talk

Figure 4.32: Impact of muon energy scale variation on the $middle \rightarrow middle$, $strip \rightarrow strip$ and $strip \rightarrow 2^{nd} strip$ cross-talk derivation in MC as a function of η .

- Contraction of strips due to temperature (width of cell)
- Pile-up subtraction model

These uncertainties still need to be estimated.

4.6 Summary

This chapter summarizes the studies on the response of the EM calorimeter to muons. The results presented here have a perspective to improve a mismodeling of electron energy tails (see Section 5.3.4), energy response as a function of azimuth (see Section 5.3.3). In addition, these results have a potential to improve the modeling of the shower shape variables, and as a consequence, to improve the electron and photon identification, as well as their energy scale and resolution.

Calibration of the reconstructed objects

The knowledge of the lepton energy and momentum response, in particular the energy and momentum scale, has a significant impact on the m_W measurement, as it directly affects the peak position of the kinematic distributions. A relative precision on the scale of about 0.1% leads to an uncertainty of about 20 MeV on the m_W using the p_T^ℓ distribution [48]. The ATLAS simulation already includes the knowledge of the detector geometry, material distribution, and physics model of the lepton interactions with detector, which were studied during previous years. However, additional corrections are needed to compensate the remaining mis-modelings at the highest possible level of precision. The lepton momentum scale and resolution obtained from the reconstruction of MC simulated events need to be corrected to precisely reproduce the characteristics of the lepton momentum reconstructed in real data. The corresponding correction factors can be derived from studying the mass distribution of dilepton resonances $J/\psi \rightarrow l^+l^-$ ($m_{ll} \approx 3.1$ GeV) and $Z \rightarrow l^+l^-$ ($m_{ll} \approx 91.2$ GeV) which are available with high statistics.

The efficiency of the detector to trigger and reconstruct leptons, in particular the dependence on the lepton momenta and pileup conditions, has to be also taken into account in the modeling. This is implemented in additional class of corrections: *efficiency corrections*. These are obtained with so-called *Tag-and-Probe method* described in this section.

5.1 Muon momentum corrections

5.1.1 Methodology

The mass of a reconstructed $X \rightarrow \ell\ell$ candidate (X being Z or J/ψ for example) is computed as:

$$m_{\ell\ell} = \sqrt{2E_1E_2(1 - \cos(\theta_{12}))}, \quad (5.1)$$

where E_1 and E_2 are the energies of the two leptons measured by the detector and θ_{12} is the opening angle between two leptons. Residual mis-calibration, due to imperfect detector modeling are parametrised in the following way for a given region:

$$p_T^{\text{meas}} = p_T^{\text{reco}}(1 + \alpha_i), \quad (5.2)$$

where p_T^{meas} is the measured lepton transverse momentum, p_T^{reco} is the reconstructed transverse momentum of the perfectly calibrated muons, and α_i represents the "departure" from a perfect calibration, in a given phase space region (for example pseudorapidity range) labeled i . The factor $1 + \alpha$ reflects imperfect knowledge of radial dimensions of the detector, magnetic field in the ID and material distribution. Neglecting second-order terms and assuming that the opening angle between the two leptons is perfectly measured, the effect on the di-lepton invariant mass is:

$$m_{ij}^{\text{meas}} \simeq m_{ij}^{\text{reco}}(1 + \frac{\alpha_i + \alpha_j}{2}) = m_{ij}^{\text{reco}}(1 + \frac{\alpha_{ij}}{2}), \quad (5.3)$$

where m^{meas} is the measured di-lepton mass, m^{reco} is the di-lepton mass computed from the true perfectly calibrated lepton momentum.

As described in Ref [49], the muon fractional momentum resolution $\frac{\sigma(p_T)}{p_T}$ can be parametrised by the quadratic sum of three terms:

$$\frac{\sigma(p_T)}{p_T} = p_0/p_T \oplus p_1 \oplus p_2 \cdot p_T, \quad (5.4)$$

each term accounts for a physics effect influencing the experimental resolution: fluctuations of the energy loss in the traversed material produce the first term (proportional to $1/p_T$), multiple scattering and any other angular deviation effect along the muon trajectory introduces the second term (constant in p_T), whilst the third term (proportional to p_T) describes the intrinsic resolution caused by the spatial resolution of the detector components and by any residual misalignment. Equation 5.4 is valid for a wide range in p_T , from $O(1)$ GeV to $O(1)$ TeV.

The following equation shows the parametrization of the correction procedure:

$$p_T^{\text{meas}} = p_T^{\text{reco}} \times (1 + \alpha(\eta)) \times (1 + \beta_{\text{MULT}}(\eta)G_1(0, 1) + \beta_{\text{CURV}}(\eta)G_2(0, 1)p_T^{\text{reco}}), \quad (5.5)$$

where p_T^{reco} is the uncorrected muon transverse momentum as obtained from the simulation, $G_1(0, 1)$ and $G_2(0, 1)$ are normally distributed random variable with mean 0 and width 1, and the correction factors $\alpha(\eta)$, $\beta_{\text{MULT}}(\eta)$ and $\beta_{\text{CURV}}(\eta)$ are defined in 24 η regions of the detector. With respect to the resolution parametrization described by Equation 5.4, no correction term is associated to p_0/p_T (i.e. energy loss fluctuation contribution) because of the low material density before the ID. For simplicity it is assumed that muon resolution is dominated by the multiple scattering term in $J/\psi \rightarrow \mu^+\mu^-$, and intrinsic resolution term in $Z \rightarrow \mu\mu$ events (and consequently for $W \rightarrow \mu\nu$ events). Hence in the fit only one type of the resolution is considered. The intrinsic resolution term will be referred to as curvature in the text.

5.1.2 Sagitta correction

Deformations parametrised with Eq. 5.2 describe the ones that are charge independent. Apart from the radial scale one has to consider charge dependent momentum corrections, referred to as sagitta bias corrections in the text. These classes of deformations consist of detector movements orthogonal to the track trajectory, and hence affect the reconstructed track curvature oppositely for positively and negatively charged particles. The simplest example of the sagitta bias deformation is the curl distortion typical for systems with a concentric cylindrical layout. It consists of azimuthal rotation of detector layers proportional to their radius. Another example is the linear twist of the detector around the z-axis which is likely to occur in the disk detector layout found in forward regions of the tracking systems. These deformations are parametrised in the following way:

$$p_T^{\text{meas}} = p_T^{\text{reco}} / (1 + q \times \delta_{\text{sagitta}} \times p_T^{\text{reco}}). \quad (5.6)$$

The δ_{sagitta} is a universal bias parameter for all measured momenta and uniquely defines the deformation, and q is muon charge. The absolute momentum bias due to a sagitta deformation is proportional to the square of the transverse momentum (Eq. 5.6) and for that reason high- p_T tracks are more suitable to detect them. Sagitta bias is of high relevance for m_W measurement at the LHC due to different amount of W^+ and W^- produced.

Two methods are used for the determination of the sagitta biases. The first one **exploits the $Z \rightarrow \mu\mu$ events** to simultaneously determine the radial scale corrections and the sagitta bias differentially in η :

$$p_{T,i}^{\text{meas}} = p_{T,i}^{\text{reco}} \cdot (1 + \alpha_i) / (1 + q \times \delta_{\text{sagitta}} \times p_{T,i}^{\text{reco}}). \quad (5.7)$$

Such a differential modeling is obtained by dividing the $Z \rightarrow \mu\mu$ events into categories according to charge and η (50 bins in η). For each of these categories, the Z mass peak position was determined for both data and simulation, and the ratio of these $\alpha_{\text{mZ}}^{\text{data/MC}} = m_Z^{\text{data}}/m_Z^{\text{MC}}$ is estimated. The

minimisation of the χ^2 yields a simultaneous determination of the radial α_i and sagitta δ_{sagitta} biases. The correlation between the sagitta and radial bias is found to be negligible.

The second method uses the EM calorimeter as a reference system, so-called **E/p method**. This allows to probe sagitta bias measured in the ID by using the ratio of the measured energy deposited in the calorimeter (E) and of momentum as measured by the ID (p) of electrons and positrons from $W \rightarrow e\nu$ decays. This measurement is performed under the assumption that the calorimeter response is independent of the charge of the incoming particle. Charge-dependent momentum biases introduced by the alignment procedure in the ID are expected to be seen as differences in the mean value of E/p distribution for electrons and positrons. Since the energy of the electron and positron does not depend on the charge, the difference of the E/p mean values is used to extract sagitta bias correction using the following equation

$$\delta_{\text{sagitta}} = (\langle E/p \rangle^+ - \langle E/p \rangle^-) / 2 \times \langle E_T \rangle. \quad (5.8)$$

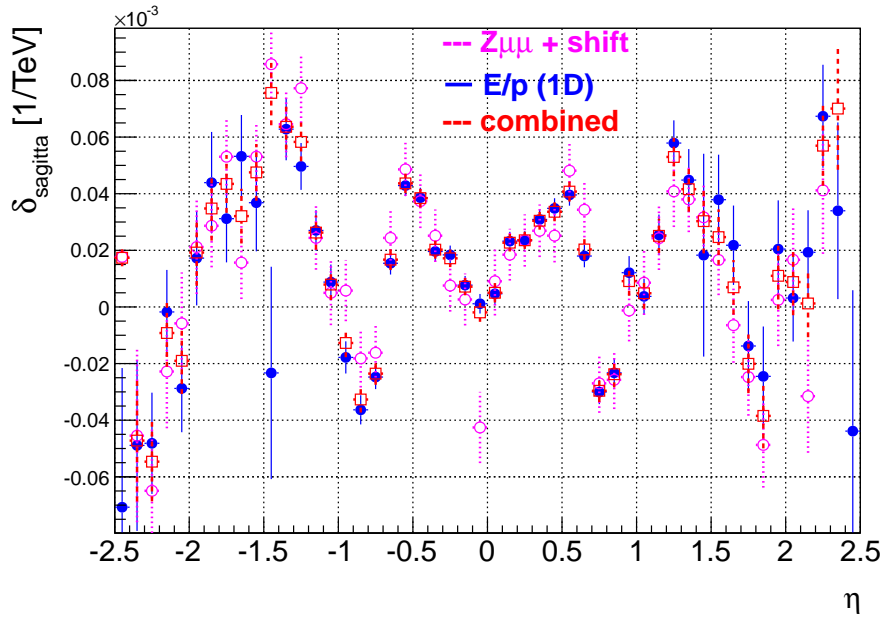


Figure 5.1: Combined values of δ_{sagitta} from E/p and $Z \rightarrow \mu\mu$ measurements.

As one is interested only in the difference between e^+ and e^- , the majority of other effects (material effects, energy and momentum resolution, and fit model) cancel. For this purpose a clean sample of $W \rightarrow e\nu$ events with tightly identified electrons are selected. The advantage of this method comes from higher statistics of $W \rightarrow e\nu$ events with respect to $Z \rightarrow \mu\mu$, which allows probing the charge dependent corrections not just as a function of η but also along ϕ coordinate. Another important advantage of E/p method is that it is sensitive to the global bias that could be present in the ID measurement of the track p_T . This bias would cancel out in the $Z \rightarrow \mu\mu$ measurement. The corrections are derived in 40 η and 40 ϕ bins. Measurement of δ_{sagitta} in $Z \rightarrow \mu\mu$ events is not sensitive to the global bias, appearing as a constant shift between the values measured with two methods.

The measurements using both methods are combined in order to decrease uncertainty especially in high η region. The uncertainty is found to be dominated by the statistical uncertainty. The combined corrections and uncertainties vs η and integrated in ϕ is shown in Figure 5.1.

5.1.3 Momentum scale and resolution

For the muon momentum scale and resolution determination the template method is used. It exploits the sensitivity of the invariant mass peak of a dilepton resonance (J/ψ , Z) to the

momentum scale of the leptons originating from resonance decay. At the LHC such events are available with a high statistics. The method allows to extract the radial scale and resolution correction simultaneously by taking into account correlation between the two fitted parameters. Template histograms are created from the simulation, adding scale and resolution perturbations to the reconstruction-level quantities, in a range covering the expected uncertainty in narrow steps. Templates are built separately for the various lepton pseudo-rapidity configurations (η_i, η_j). Analogous distributions are built from the data. Each template is then compared to data and the best- χ^2 configuration determines the muon momentum scale and resolution parameters.

The corrections are extracted in narrow pseudorapidity bins for 24 detector regions defined to maintain an uniform structure (and therefore similar momentum resolution) of the ID components within each segment. These bins have uniform width of 0.2, in range $-2.4 < \eta < 2.4$. Muons in the bin $2.4 < |\eta| < 2.5$ are discarded. The results of the $Z \rightarrow \mu\mu$ scale and smearing are shown in Figure 5.2, assuming that ID is uniform in ϕ . The results extracted from the J/ψ resonance are similar. Although the J/ψ sample has four times higher statistics comparing to $Z \rightarrow \mu\mu$, it was chosen to use the Z -based calibration for W analysis, since the muon p_T is significantly closer leading to smaller extrapolation uncertainties. After the extracted corrections are applied to the Z decay muons, the modeled dilepton invariant mass distribution becomes in a good agreement between data and MC as shown later in Fig.8.4 of the W mass analysis section.

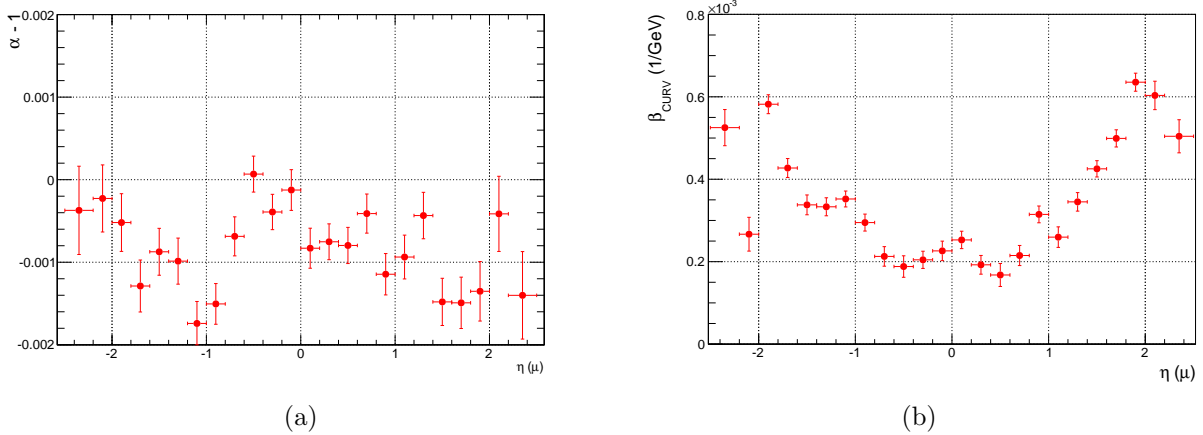


Figure 5.2: Muon momentum scale corrections (a) and additional curvature resolution term (b) obtained from the $Z \rightarrow \mu\mu$ events. The resulting scale corrections are shown as function of η . The shown uncertainties are statistical.

5.1.4 Momentum calibration as a function of muon azimuth

The momentum measurement corrections performed above are functions of muon η only. This assumes that all physics and detector effects can be integrated over ϕ in a way that does not depend on the physics process. However, this is not perfectly true: although the muon azimuthal distribution is nearly perfectly uniform in the $Z \rightarrow \mu\mu$ channel (50% of muons have $\phi > 0$, and 50% have $\phi < 0$), the $W \rightarrow \mu\nu$ channel is less balanced, with 53% of muons having $\phi > 0$ and 47% having $\phi < 0$. Hence the ϕ averaged momentum calibration measured in Z events does not perfectly apply to the W sample.

A second calibration iteration vs ϕ was performed to verify the impact of this asymmetry. An example of this study is illustrated in Figure 5.3. As can be seen, before correction the ϕ dependence of the calibration has an amplitude of maximally 0.1%. After corrections, no significant difference remains. It was verified that this procedure does not change the overall momentum scale, which remains constant within about 10^{-5} , well within the momentum scale systematic uncertainties discussed in the previous section.

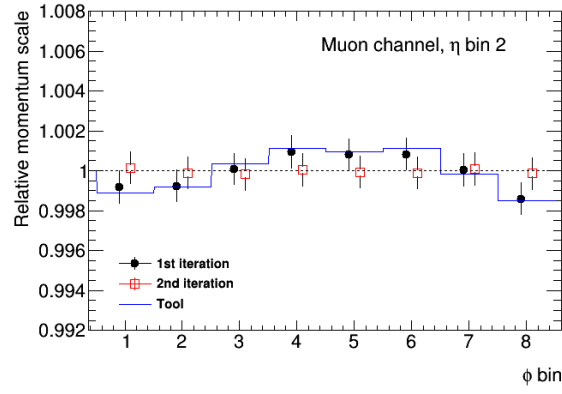


Figure 5.3: Azimuthal dependence of the momentum calibration, before and after the ϕ -dependent correction. The plot corresponds to $-2.0 < \eta < -1.4$ bin.

$ \eta $ range	$0.0 < \eta < 0.8$		$0.8 < \eta < 1.4$		$1.4 < \eta < 2.0$		$2.0 < \eta < 2.4$		Inclusive	
Fitting observable	p_T^ℓ	m_T	p_T^ℓ	m_T	p_T^ℓ	m_T	p_T^ℓ	m_T	p_T^ℓ	m_T
δm_W [MeV]										
Momentum scale	9.0	9.0	14.4	14.5	27.5	27.6	114.0	114.0	8.6	8.6
Momentum resolution	1.4	1.4	1.0	1.0	1.1	1.1	1.7	1.7	1.0	1.0
Curvature bias	1.0	1.2	2.8	2.8	3.8	1.7	4.8	10.5	1.8	1.8
Reconstruction and										
isolation efficiencies	4.0	3.6	5.1	3.7	4.8	3.5	6.4	5.5	4.3	3.6
Trigger	5.6	5.0	7.1	5.0	11.8	9.1	12.1	9.9	6.2	4.9
Total	11.5	11.0	17.1	16.1	30.6	29.3	114.9	115.0	11.6	10.7

Table 5.1: Impact of muon performance corrections on the m_W measurement uncertainties.

The bias on the mass fit is typically $\delta m_W/m_W \sim \delta f \times \delta \alpha$, where δf is the difference between the event fractions with $\phi > 0$ and $\phi < 0$ in W events, and $\delta \alpha$ the average calibration difference between these two regions. Injecting $\delta f \sim 6\%$ and $\delta \alpha \sim 0.05\%$, averaged over η_μ , yields an effect of about 3 MeV on the mass fit result.

5.1.5 Uncertainties and impact on the m_W

Possible sources of systematic uncertainties on the radial scale and resolution are those due to backgrounds and physics modeling of the Z production, the fitting range of the dilepton invariant mass, non-linearity, uncertainties due to the method, and those due to material distribution in the ID. The largest systematic uncertainty is due to extrapolation from the Z boson mass scale to the W boson mass. Table 5.1 summarizes the effect of the momentum scale and resolution uncertainties on the determination of m_W .

5.2 Muon selection efficiency

The accuracy of the ATLAS detector simulated in Monte Carlo to model the lepton measurement efficiency plays a crucial role on the W mass analysis. In particular, the dependence of the detector efficiency on the lepton momentum can introduce a bias to the m_W measurement. Thus, in order to obtain the reliable result, the MC predictions should be corrected to reproduce efficiencies measured in data.

The selection of muon candidates in $W \rightarrow \mu\nu$ and $Z \rightarrow \mu\mu$ events requires an isolated track, which is reconstructed in both the inner detector and the muon spectrometer. In addition, these

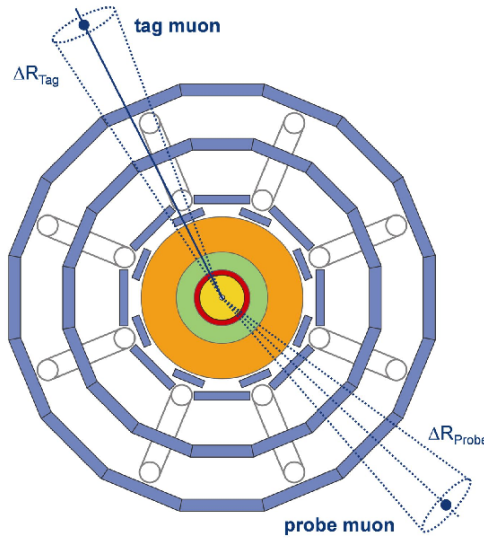


Figure 5.4: Illustration of the Tag-and-Probe method. One strongly selected muon candidate in a $Z \rightarrow \mu\mu$ event is used as tag, while the other is used as a probe to investigate the reconstruction, trigger and isolation efficiencies, respectively.

events are required to pass a single muon trigger. Measurement of the efficiency to find and select such muons is divided into three components, namely reconstruction, isolation and trigger efficiencies. The total efficiency for muons is then calculated as

$$\varepsilon_{tot} = \varepsilon_{reconstruction} \cdot \varepsilon_{isolation} \cdot \varepsilon_{trigger} \quad (5.9)$$

The reconstruction efficiency here means the efficiency of a muon already reconstructed as a track in the inner detector to be reconstructed as a combined *Staco* muon. The trigger efficiency is the probability for a muon, having passed the offline reconstruction and isolation requirements, to also fire the trigger. The isolation cut efficiency is the efficiency of a signal muon to pass a detector-based isolation requirement.

The muon reconstruction, trigger and isolation efficiencies are estimated using the **Tag-and-Probe method** (see Figure 5.4) on data and MC sample. The method employs events containing well-known resonance decays $Z \rightarrow \mu\mu$. Such events are selected requiring two muon candidates which are likely to originate from a Z decay. At least one of them has to be always a combined, isolated muon candidate, which fired the corresponding single muon trigger, thereby acting as tag for the event. The other muon candidate is used as probe and its reconstruction, trigger or isolation efficiency is measured. In order not to bias the selected probe sample, all possible tag-probe pairs in the event are considered, so that the same muon can be a tag in one pair, but the probe in another pair. The standard approach is then to correct the MC using the correction factors, called **scale factors (SF)**, given by the ratio of data and MC efficiencies:

$$SF(\eta, \phi, p_T, u_{||}^\ell) = \frac{\varepsilon_D(\eta, \phi, p_T, u_{||}^\ell)}{\varepsilon_{MC}(\eta, \phi, p_T, u_{||}^\ell)}. \quad (5.10)$$

The efficiencies are derived simultaneously in three dimensions, p_T , $u_{||}^\ell$ and the detector region. The $u_{||}^\ell$ is defined as the parallel component of the projection of the hadronic recoil onto the transverse momentum of the decay lepton. The detector region is defined by certain regions in the η, ϕ plane of the muon spectrometer and takes into account special features of the detector geometry like the crack or transition regions. It was found that the efficiencies dependence vs. $u_{||}^\ell$ is modeled very well by MC, i.e. the resulting SF are constant. Therefore only the p_T and region dependence is taken into account for the W boson mass analysis. All SFs are derived inclusively for the full

data-set, with the exception of the trigger SFs, which are derived independently for two different run periods. The muon reconstruction, trigger and isolation efficiencies measure in data and MC are illustrated in Figures 5.5, 5.6 and 5.7 respectively. The corresponding ratios represent the scale factors.

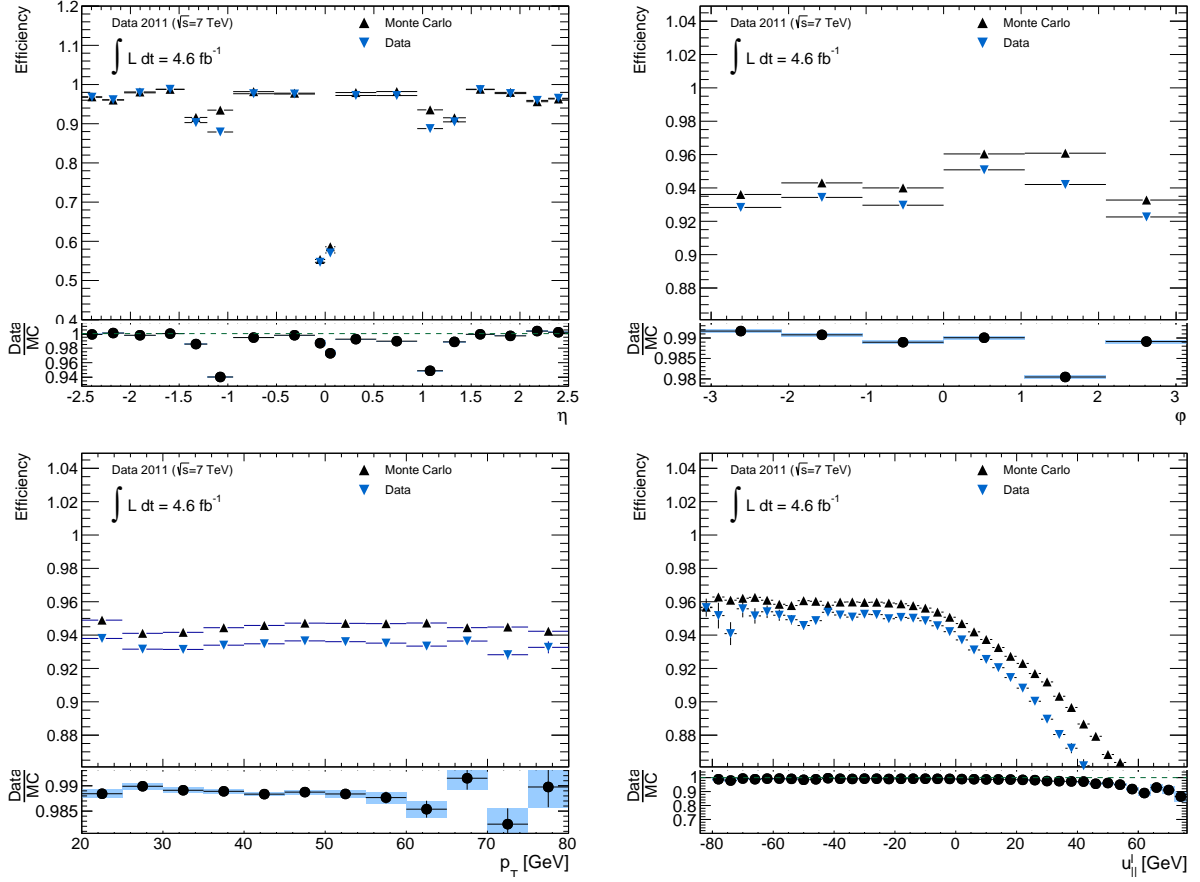


Figure 5.5: Determined reconstruction efficiency by the tag- and probe-method for Data and MC. From left to right, top to bottom: $\eta, \phi, p_T, u_{\parallel}^l$. Only statistical uncertainties are shown.

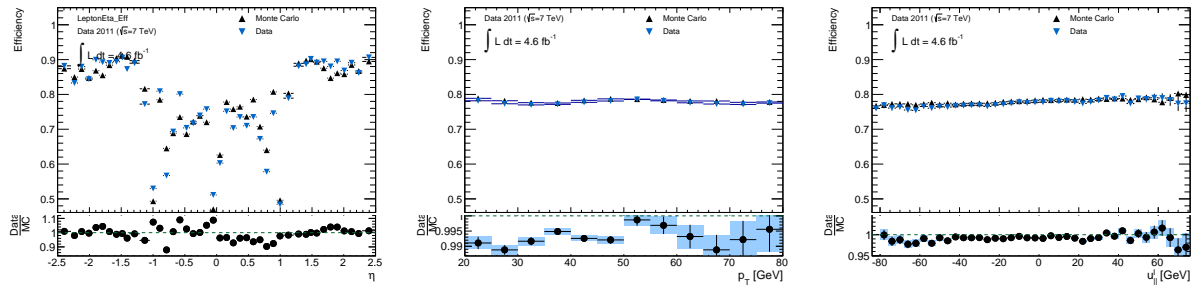


Figure 5.6: Determined trigger efficiency by the tag- and probe-method for Data and MC. From left to right: $\eta, p_T, u_{\parallel}^l$. Only statistical uncertainties are shown.

Reapplying the derived corrections to $Z \rightarrow \mu\mu$ MC sample is a first closure test of the described methodology. After correcting the MC efficiencies in $Z \rightarrow \mu\mu$ MC sample, the muon η and ϕ distributions, which are not sensitive to physics modeling uncertainties, are in good agreement between data and MC as shown in Figure 5.8.

The dominant uncertainty for all derived scale-factors in each bin is from the limited statistics of the selected Z boson events in data. The largest systematic uncertainties are due to uncertainties in

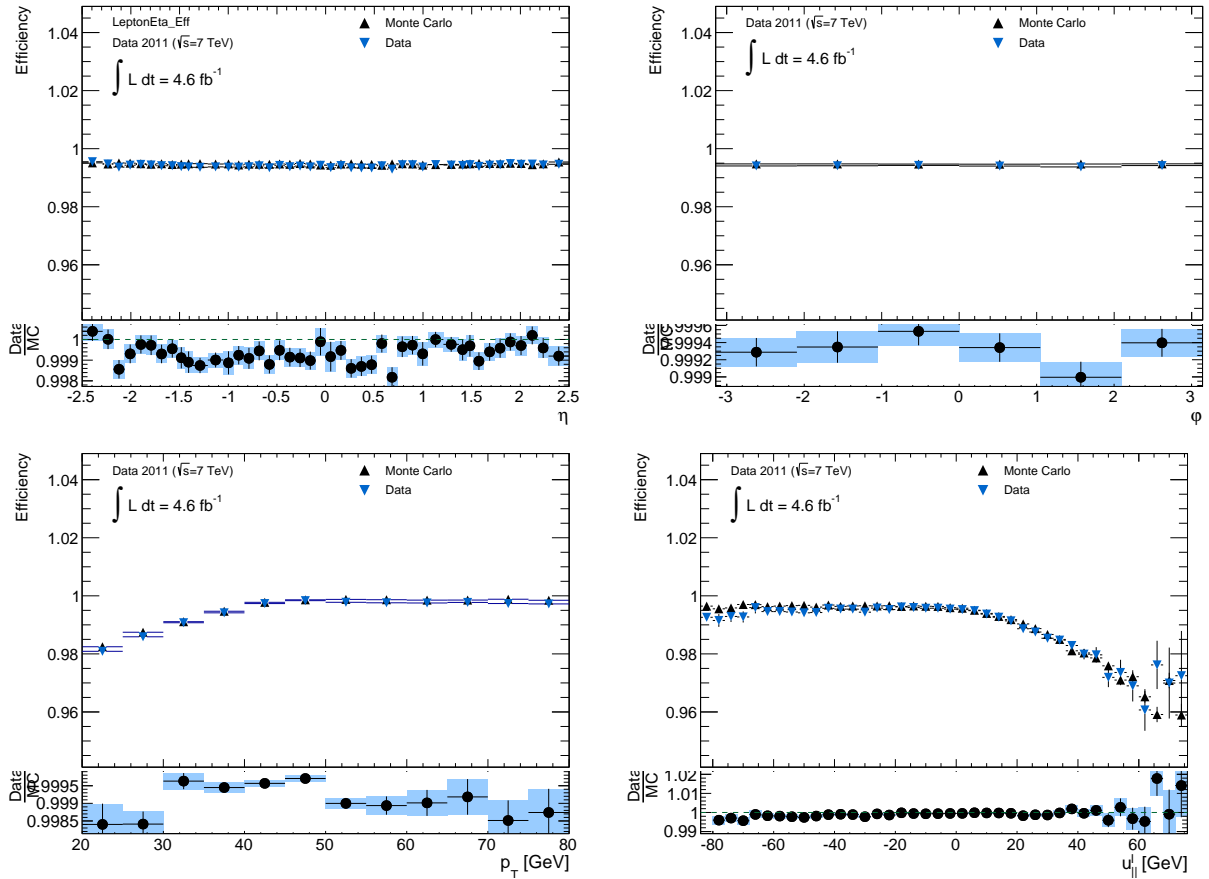


Figure 5.7: Isolation efficiencies for Powheg, $p_T^{\text{cone}20}/p_T < 0.1$. From left to right, top to bottom: η , ϕ , p_T , $u_{||}^l$.

multijet background contribution and momentum scale uncertainties. No significant p_T dependence of the SFs in each detector region could be observed, leading to a modest uncertainty on the m_W measurement in the order of 5 MeV. It should be noted that ID tracking efficiencies for muon candidates are found to be above 99.5% without any significant p_T dependence in data and detector simulation. No associated uncertainties are therefore assigned. An overview of all uncertainties associated to the muon efficiency corrections is shown in Table 5.1.

5.3 Electron calibration corrections

5.3.1 Electron energy pre-corrections

The electron energy calibration used in this analysis is based on the electron and photon calibration paper [46]. The reconstruction of electron energies, briefly described in Section 3.2, is optimised using multivariate MVA algorithms. Some steps of the calibration procedure have been repeated in the Section 4. A brief overview of the calibration correction procedure is given below.

- 1) The starting point of the calibration corrections procedure is the intercalibration of the strip and middle layers of the EM calorimeter. These corrections are needed in data to adjust residual effects not perfectly accounted for by the cell electronic calibration. The intercalibration procedure uses muons from $Z \rightarrow \mu\mu$ decays as shown in Section 4.3.4. The L1/L2 layer intercalibration scale factor $\alpha_{1/2}$ are determined as a function of detector pseudorapidity region η (see Figure 4.16) and used to correct the energy response of the middle layer. No dedicated intercalibration of the back layer is carried out, as its contribution is negligible.

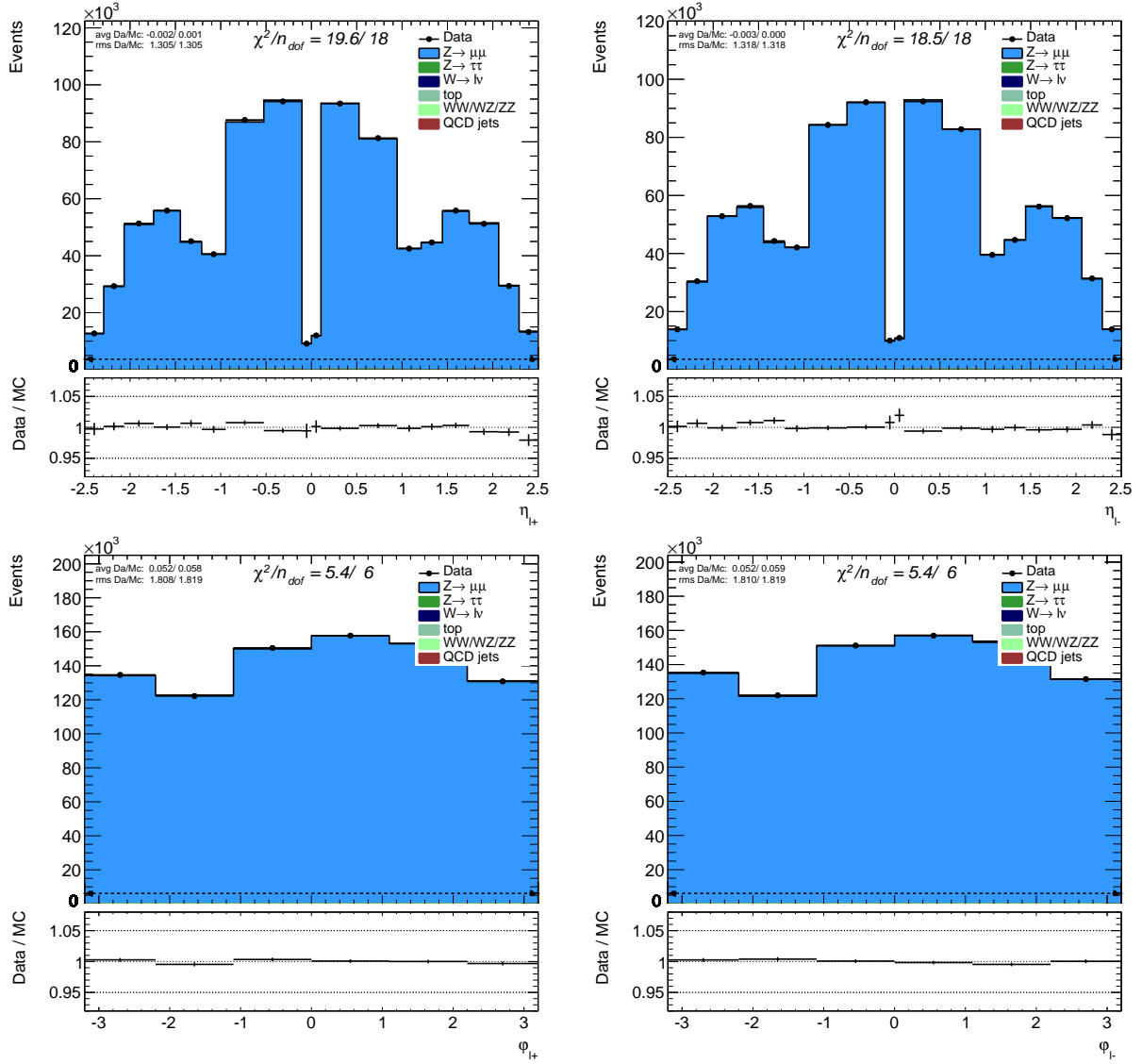


Figure 5.8: Comparison of the data and MC distribution for positive (left) and negative (right) charged muons vs. η (top) and ϕ (bottom) in $Z \rightarrow \mu\mu$ events with applying all corrections factors to the muon reconstruction, muon isolation cut and muon trigger efficiencies.

- 2) The amount of passive material upstream of the presampler is corrected in the MC exploiting the expected correlation between energy deposited by electron in presampler E_0 and the ratio of energies E_1/E_2 deposited in strip and middle layers. As such material initiates the electron shower development, the difference of the passive material between data and MC will cause the different energy deposits in each layer. The correlation is studied by adding extra material in the simulation.
- 3) The determination of the PS energy scale $w_{PS} = E_0^{data}/E_0^{MC}$ exploits the PS energy distributions of electrons in data and simulation, after effective corrections for possible mis-modeling of the upstream passive material. The measured PS energy scale w_{PS} defines the correction factor that is applied to the data.

5.3.2 Energy scale and resolution corrections

After all pre-corrections, the $Z \rightarrow ee$ resonance is used to determine the absolute energy scale correction as in bins of electron pseudorapidity η_e . The methodology is similar to muons as

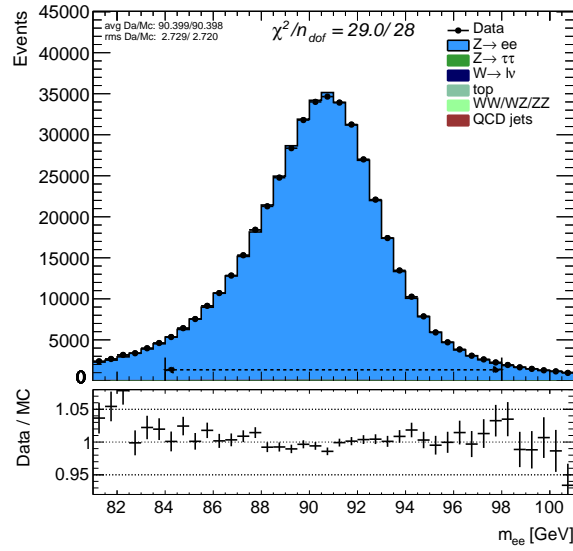


Figure 5.9: The dielectron invariant mass distributions reconstructed in data and MC after complete electron calibration procedure.

described in Section 5.1.1.

The mass of a reconstructed $Z \rightarrow ee$ candidate is computed as :

$$M = \sqrt{2E_1 E_2 (1 - \cos(\theta_{12}))} \quad (5.11)$$

where E_1 and E_2 are the energies of the two electrons measured by the calorimeter and θ_{12} is the angle between the electrons measured by the tracker. Residual mis-calibration, due to calorimeter inhomogeneities or imperfect simulation of passive material, are parametrised in the following way for a given zone:

$$E^{meas} = E^{true} (1 + \alpha_i) \quad (5.12)$$

where E^{meas} is the measured electron energy, E^{true} is the true electron energy and α_i represents the departure from a perfect calibration, in a phase space region (in practice, a range in pseudorapidity) labeled i . The derived factors are used to correct data energies.

The expected resolution (divided by energy) for the electromagnetic calorimeter can be written as:

$$\frac{\sigma(E)}{E} = \frac{a}{\sqrt{E}} \oplus \frac{b}{E} \oplus c \quad (5.13)$$

A smearing correction is derived for the MC under the assumption that the sampling term a is well modeled by the simulation. The noise term b used in the simulation is taken from calibration runs, so that any additional resolution correction must be proportional to the energy, as an additional constant term c_i in a range in pseudorapidity labeled i Ref [50].

$$\sigma_{corr} = \sigma_{MC} \oplus c_i \times E \quad (5.14)$$

An overall energy scale correction is determined as a function of electron pseudorapidity η_e from $Z \rightarrow ee$ decays, comparing the reconstructed mass distributions in data and simulation. Simultaneously, an effective constant term for the calorimeter energy resolution is extracted by adjusting the width of the reconstructed dielectron m_{ee} in simulation to match the distribution in data. After applying the complete calibration procedure the dielectron invariant mass distributions reconstructed in data and MC are compatible as shown in Figure 5.9

5.3.3 Energy calibration as a function of electron azimuth

The electron energy measurement corrections performed above are functions of electron η only. Due to reasons explained in Section 5.1.4, the ϕ_e dependency has to be taken into account.

A dependence of the energy calibration on ϕ_e can be caused by several effects: spatial variations of the LAr temperature; absorber sagging in the endcap; cylinder deformation in the barrel; and passive material variations coming from global calorimeter displacements within the cryostat. The mechanical deformation of the EM calorimeter has been also studied in Section 4.4.5. Disentangling these effects is beyond the scope of this work, and only an effective calibration is performed here.

Two methods were attempted to improve on this situation: the first based on an extension of the Z invariant mass method in (η, ϕ) space, and the second using the measured electron energy/momentum ratio, E/p . As a first attempt, a second calibration iteration was performed on top of existing one, including the ϕ_e dependency. The result of this procedure is illustrated in Figure 5.10(a) for one region of electron pseudorapidity. As can be seen, before correction the ϕ dependence of the calibration has an amplitude of typically 0.15% in the barrel. In the end-cap it reaches 0.5-0.6%. After correction, this is reduced to less than 0.05%. It was verified that this procedure does not change the overall energy scale.

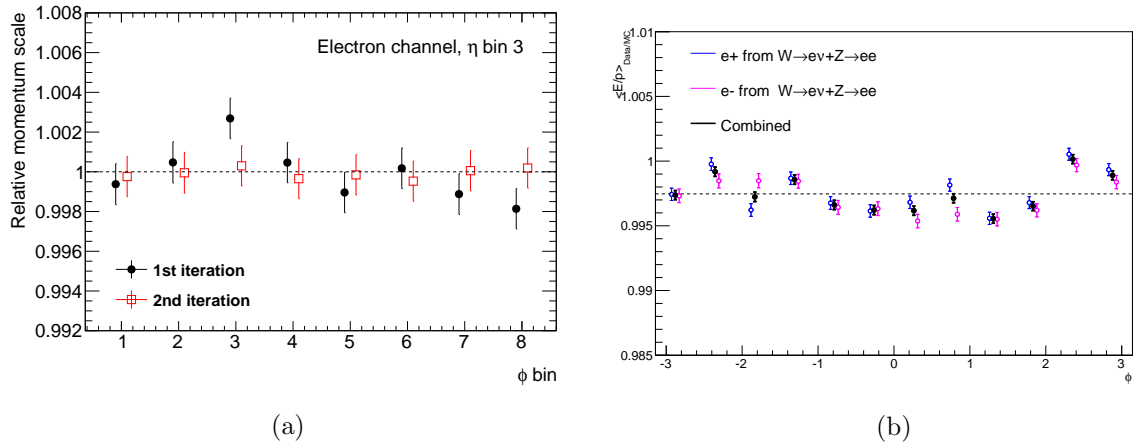


Figure 5.10: (a) Azimuthal dependence of the energy calibration in $-1.2 < \eta_e < -0.6$ region, before and after the m_{ee} -based correction described in the text; (b) Azimuthal dependence of the E/p distribution mean in $-1.2 < \eta_e < -0.6$ region, after the m_{ee} -based correction described in the text.

However, after this calibration iteration, analyzing the E/p profile shows remaining modulations, as illustrated in Figure 5.10(b). This is qualitatively understood as coming from the fact that Z decay electrons are typically back to back, and that the period of the energy response modulation is roughly 2π ; as a result, the modulations approximately cancel in the Z invariant mass, and their effect is only seen *via* boosted events; this leads to an underestimation of the actual effect. Therefore, the preferable method for the energy inter-calibration is from the E/p profile. This method presents the additional advantage that the electrons from $W \rightarrow e\nu$ decays can be used, with significantly enlarged statistics compared to the Z sample used above.

However, the E/p method requires corrections p for the momentum scale and sagitta bias discussed in Sections 5.1.2 and 5.1.3. The sagitta bias correction is responsible for the e^+/e^- differences observed in Figure 5.10(b). The effect of this correction is illustrated in Figure 5.11.

The intercalibration is estimated from the ratio of the means of the E/p distribution in data and MC. Because of the large tails at high E/p , the distributions are truncated, requiring $0.6 < E/p < 1.5$. Probing a scaling of the energy response using the mean of a truncated distribution however underestimates the effect. Therefore an iterative correction procedure is applied; the procedure converges after 3 iterations. The resulting corrections are illustrated in Figure 5.12. As expected,

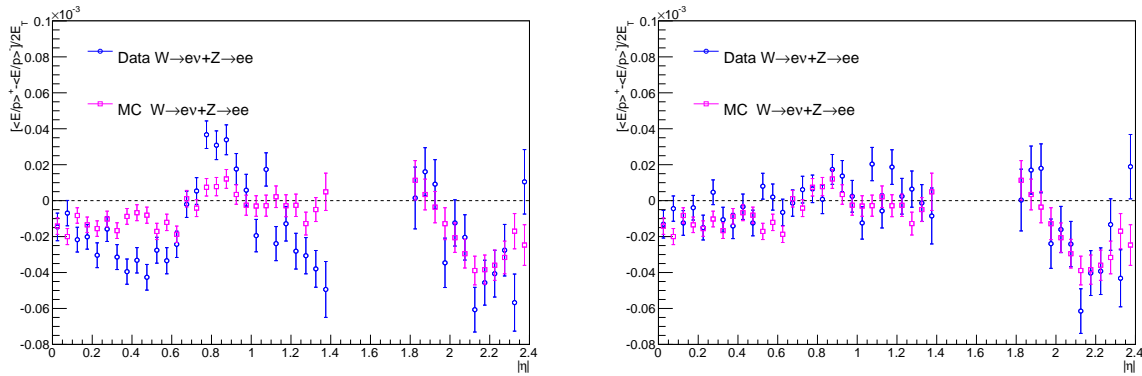


Figure 5.11: Relative difference between the E/p profiles for positrons and electrons, as a function of $|\eta|$, before (*left*) and after sagitta bias corrections (*right*). The empty region $1.4 < |\eta| < 1.82$ corresponds to the crack region in the calorimeter.

the correction is found to be larger with this method than with the m_{ee} method, with a relative increase of about 25% especially in the endcaps. An overall scaling is applied to the corrections, in each η bin, in order to preserve the ϕ -averaged energy scales

Although the impact of this ϕ_e dependence is obviously as large as the miscalibration itself when performing W boson mass fits at given ϕ_e , it is much smaller when performing a ϕ integrated measurement: the bias on the ϕ -integrated mass fit is typically $\delta m_W / m_W \sim \delta f \times \delta \alpha$, where δf is the difference between the event fractions with $\phi > 0$ and $\phi < 0$ in W events, and $\delta \alpha$ the energy calibration difference between these two regions. Injecting $\delta f \sim 4\%$ and $\delta \alpha \sim 0.2\%$, averaged over η , yields an effect of about 6 MeV, which corresponds to the expected impact of the present correction on the mass fit result. As shown in Figure 5.13, the intercalibration correction significantly improves the m_W measurement uniformity.

5.3.4 Impact of energy tails

To complement the assessment of the energy scale and resolution uncertainties, checks are performed on possible tails in the energy response. The checks are prompted by the discrepancy between data and simulation observed at low values of E/p distribution and illustrated in Figure 5.14. For values below $E/p \simeq 0.98$, the data-to-simulation ratio grows to about 1.3, very similarly in W and Z events.

As high values of this observable are essentially associated to electrons with large bremsstrahlung and underestimated momentum, this behavior suggests a mis-modeling of tails in the energy response. To verify this assumption, the comparison is repeated, for Z events, separating the electrons according to the number of TRT hits attached to the track, i.e. not outliers. While the presence of TRT hits is part of the Tight identification requirements, these hits are by default allowed to be outliers; the categorization performed here imposes at least (respectively less than) 15 TRT hits actually attached to the track. As can be seen in Figure 5.15, while this cut visibly reduces the high tails of the E/p distribution, the mis-modeling at low values is not affected, confirming that it reflects a mis-measurement of the energy rather than the track.

A possible reason for this behavior is mis-modeling of detector material in the ID or in front of the calorimeter. The E/p distribution is compared in simulation for various detector geometries representing the current uncertainty on the modeling of the passive material in front of the calorimeter. Figure 5.16 uses the following simulation tags:

- s1748 (ATLAS-GEO-21-02-02): nominal ATLAS geometry;
- s1814 (ATLAS-GEO-21-04-02): 5% increase Inner Detector passive material (full η range);

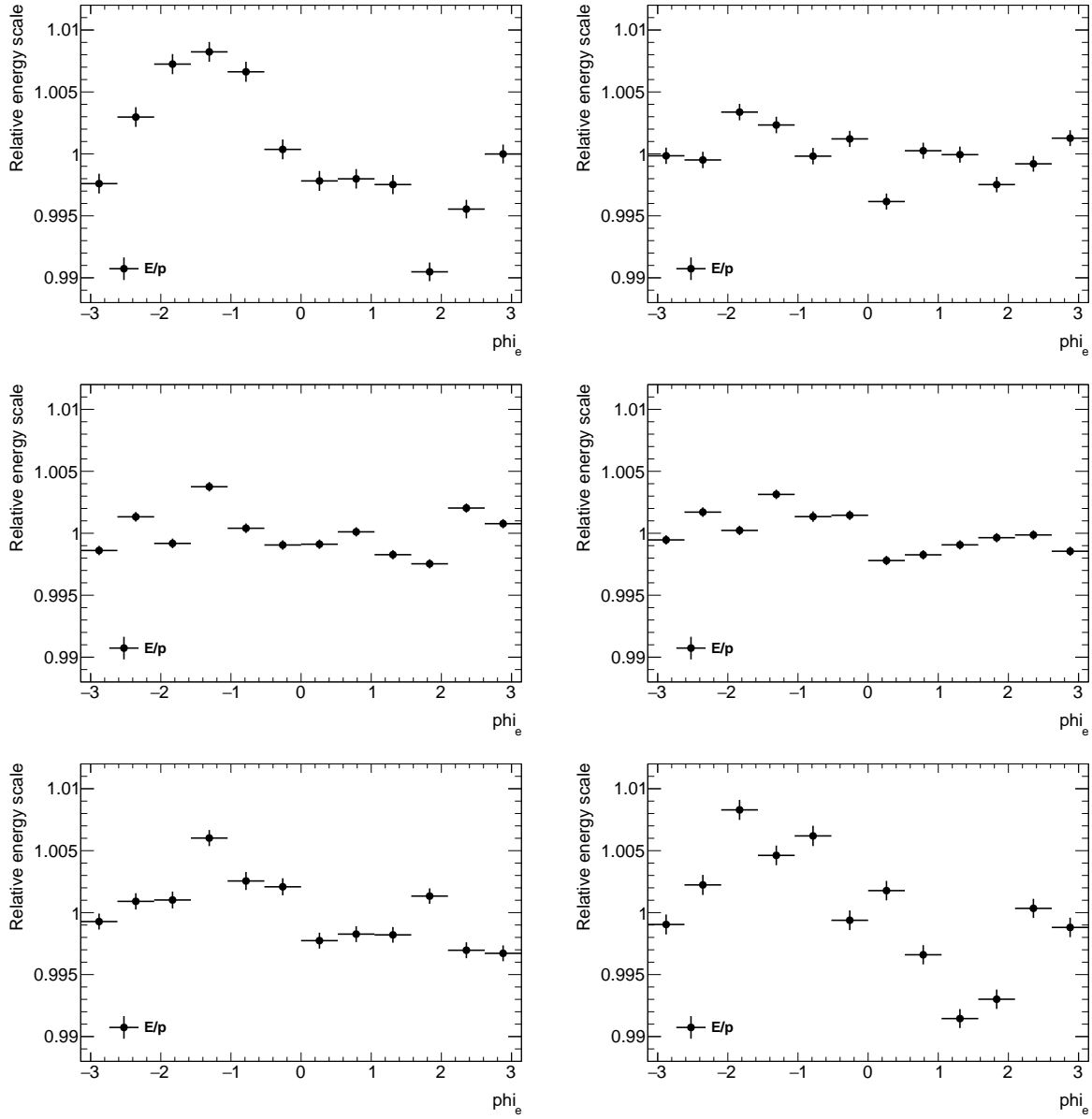


Figure 5.12: Azimuthal dependence of the E/p distribution mean, used to define the ϕ intercalibration correction. The points represent the mean of the E/p distribution, calculated within the range $0.6 < E/p < 1.5$ for $Z \rightarrow ee$ events. The 12 ϕ bins cover $-\pi < \phi < \pi$ in bins of size $\pi/6$. The η bins are, from top left to bottom right, $-2.4 < \eta < -1.8$, $-1.2 < \eta < -0.6$, $-0.6 < \eta < 0$, $0 < \eta < 0.6$, $0.6 < \eta < 1.2$, $1.8 < \eta < 2.4$.

- **s1816** (ATLAS-GEO-21-12-02): 5% X_0 added between ID and presampler (barrel); 7.5% X_0 added at SCT/TRT endcap;
- **s1895** (ATLAS-GEO-21-19-02): Beam pipe material changed from Beryllium to Aluminum;
- **s1818** (ATLAS-GEO-21-14-02): Extra material in barrel: +5% X_0 between the barrel presampler and calorimeter; +5% X_0 between ID and presampler. Extra material in the barrel-end cap crack. 5% increase of Inner Detector passive material; 15% relative increase of SCT and Pixel services; 7.5% X_0 at SCT/TRT endcap; 7.5% X_0 at ID endplate.

As can be seen, none of these geometry distortions reproduces the observed discrepancy. One partial exception is **s1818**, which conservatively sums all material distortions simultaneously; the impact on the E/p distribution matches the pattern observed in data, but only about 30% of

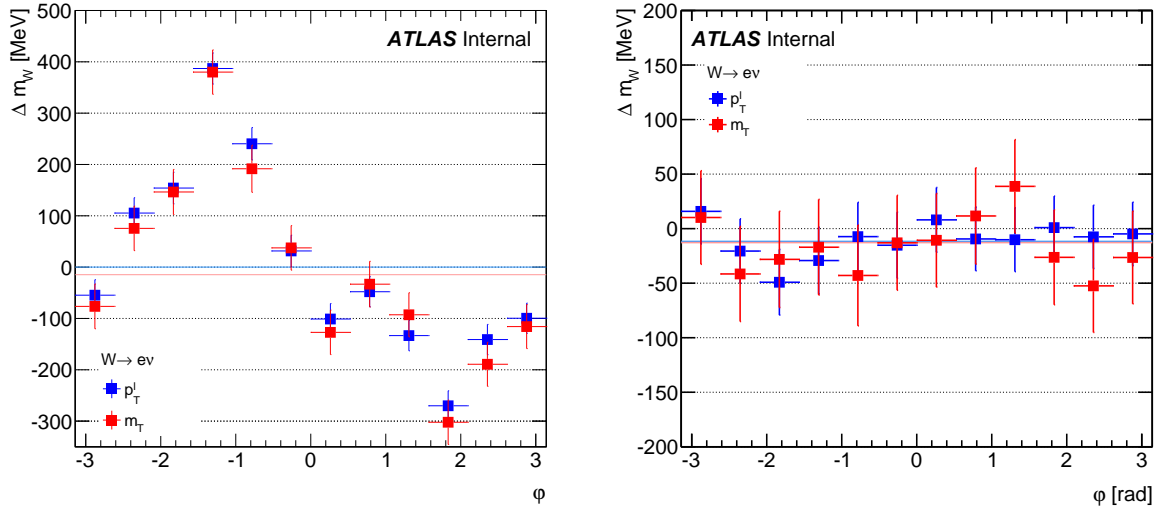


Figure 5.13: Measured value of m_W as a function of ϕ_e , before (left) and after (right) the intercalibration correction based on E/p .

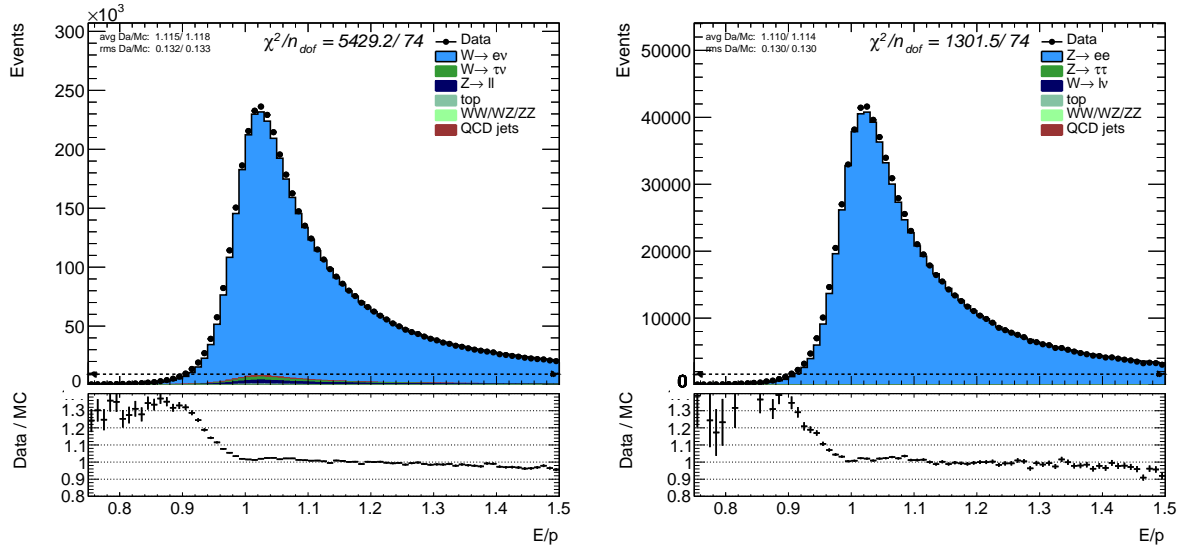


Figure 5.14: Comparison of the E/p distribution in data and simulation, for $W \rightarrow e\nu$ and $Z \rightarrow ee$ events.

its magnitude. As larger distortions are strongly disfavored, we conclude that passive material uncertainty can not explain the bulk of the observed discrepancy.

A plausible hypothesis is that the observed E/p tails reflect the mis-modeling of the lateral shower shapes in the calorimeter. Electromagnetic showers are wider in data than in simulation, which leads to slightly worse containment. Verifying this assumption is left for future work.

To quantify the impact of this mis-modeling on the W boson mass measurement, mass fits were performed including a cut $E/p > 0.98$, to remove the problematic region of this variable, and the results were compared to the nominal result. This cut has an efficiency of 93.5% per electron in data, i.e. 93.5% for W events, and 87.4% for Z events.

The fits are performed for Z events using the electron pair invariant mass distribution (i.e. this is the same analysis as the energy scale determination discussed in Section 5.3.2), and for W events using the p_T^e and m_T^W distributions. The results are shown in Table 5.2. We observe that the $E/p > 0.98$ cut induces a positive shift of order 15-20 MeV on all fits, which clearly indicates the correlation of these tails with the electron energy measurement. The uncertainties

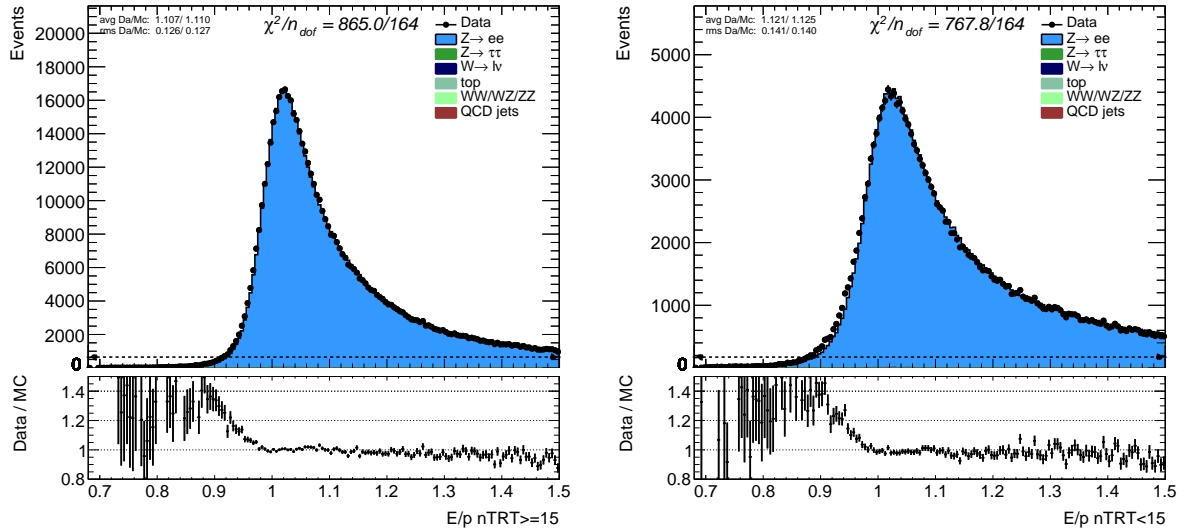


Figure 5.15: Comparison of the E/p distribution in $Z \rightarrow ee$ data and simulation, for electrons with and without TRT hits associated to the nominal track.

Selection	m_Z fit (m_{ee})	m_W^+ fit (p_T^e)	m_W^- fit (p_T^e)	m_W^+ fit (m_T^W)	m_W^- fit (m_T^W)
No E/p cut	2.6 ± 5.0	-9.1 ± 11.6	30.5 ± 12.9	-21.2 ± 16.8	16.2 ± 18.9
$E/p > 0.98$	21.3 ± 5.4	7.1 ± 12.0	50.4 ± 13.4	-4.5 ± 17.3	23.3 ± 19.4
Difference, no recal.	$+18.7 \pm 1.9$	$+16.2 \pm 3.1$	$+19.9 \pm 3.4$	$+16.7 \pm 4.4$	$+7.5 \pm 4.9$
Difference, with recal.	0.0 ± 1.9	-0.7 ± 3.1	$+3.0 \pm 3.4$	-0.2 ± 4.4	-9.4 ± 4.9

Table 5.2: Comparison of Z and W boson mass fit results with and without E/p cut, before and after the corresponding recalibration. The shown results are differences with respect to a blinded reference value of m_W , and are given in MeV.

on the differences account for the correlation between the complete samples and the sub-samples verifying $E/p > 0.98$. With the selection efficiencies given above, this correlation is $\rho = 0.967$ for W events, and $\rho = 0.935$ for Z events.

However, repeating the calibration for electrons with $E/p > 0.98$ absorbs the Z mass shift in the effective energy scale, with a shift of $\delta\alpha = (21 \pm 2) \times 10^{-5}$ (α defined as in Equation 5.12). The last line in Table 5.2 reports the mass shifts after this recalibration. The E/p mis-modeling leaves an effect on m_W of about 1 MeV on average when using p_T^e , and about 5 MeV when using m_T^W . No significant effect is seen within the statistical accuracy of this test. Since the underlying effect is not fully understood, we take the statistical accuracy of the test as a measure of the systematic uncertainty to be assigned, giving 2.3 MeV for p_T^e , and 3.3 MeV for m_T^W , combining the $W^+ \rightarrow e\nu$ and $W^- \rightarrow e\nu$ statistical uncertainties.

5.3.5 Impact of the LAr hole

For the 2011 data taking periods denoted here as E-H, corresponding to about 20% of the data, the LAr calorimeter suffered from 6 dead front end boards. This situation was reflected in the simulation, for a corresponding fraction of the simulated events. This section presents some basic checks of the modeling of the feature of the data.

As can be seen in Figure 5.17, top row, which represents the reconstructed electrons $\eta \times \phi$ distribution during periods E-H, the failure affects the region $0 < \eta < 1.475$ and $-0.9 < \phi < -0.5$. As can be seen in the middle and bottom rows, the electron η and ϕ distributions in data are equally well modeled by the simulation for data taken during periods E-H and outside of these

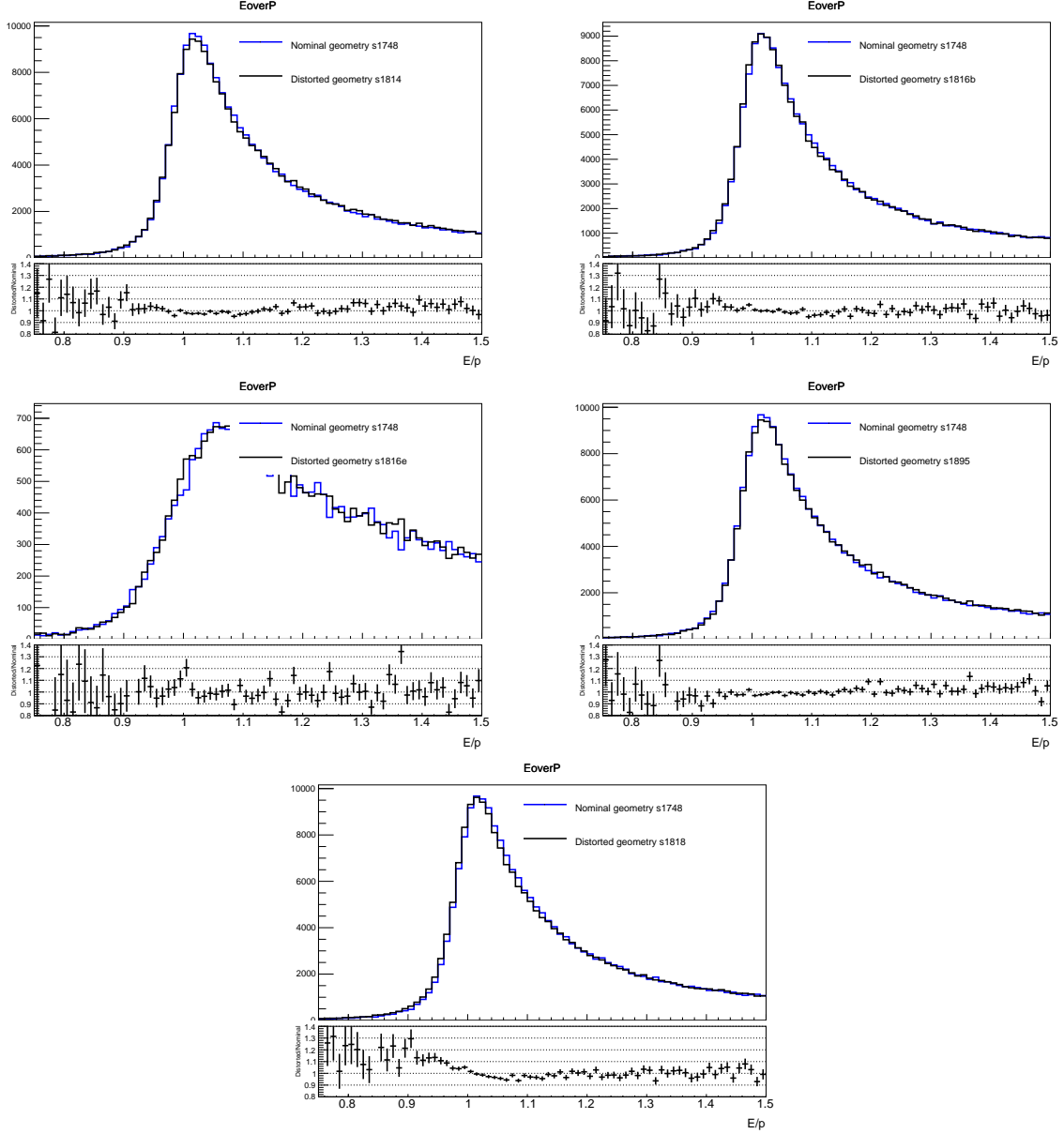


Figure 5.16: E/p distributions in $Z \rightarrow ee$ simulation, for the nominal ATLAS geometry (s1718) and geometries with Inner Detector material distortions described in the text (from top left to bottom right: s1814, s1816 barrel region, s1816 endcap region, s1895 and s1818). Since s1816 contains two independent material variations located in the barrel and in the endcap respectively, the comparison with the nominal geometry is performed separately for barrel and endcap electrons. The ratio panels show the ratio between the distorted geometry and the nominal geometry.

periods. The fraction of affected events is 20.1%, agreeing in data and simulation within 0.1%.

The impact of this defect is quantified by comparing W boson mass fit results obtained separately for the data taken during and outside periods E-H (this selection is applied consistently on data and simulation). As can be seen in Table 5.3, the p_T^e fits differ by less than one standard deviation. For the transverse mass fits, the difference is about -0.8 standard deviations for the W^+ sample, and +1.8 standard deviations for the W^- sample. The deviations are opposite in direction, and the charge-averaged difference is 18.3 ± 28.2 MeV. Since the effect is clearly identified and taken into account in the simulation, we conclude that the LAr failure is well modeled and has no significant impact on the measurement.

Data	m_W^+ fit (p_T^e)	m_W^- fit (p_T^e)	m_W^+ fit (m_T^W)	m_W^- fit (m_T^W)
All data	-9.1 ± 11.6	30.5 ± 12.9	-21.2 ± 16.8	16.2 ± 18.9
Periods E-H	-4.3 ± 25.0	14.0 ± 27.6	-9.7 ± 32.7	-41.1 ± 36.0
Other periods	-22.5 ± 12.9	36.5 ± 14.5	-39.3 ± 19.3	36.3 ± 22.0
Difference (other periods – E-H)	-18.2 ± 28.1	22.5 ± 31.2	-29.6 ± 38.0	77.4 ± 42.2

Table 5.3: Comparison of the W mass fit results for data taken during periods E-H and outside of these periods. The shown results are differences with respect to a blinded reference value of m_W , and are given in MeV.

5.3.6 Uncertainties and impact on the m_W

The electron energy resolution uncertainty has been assessed in the electron calibration paper [46] and applied to the W mass analysis without modification. In short, the resolution uncertainties receive contributions from

- the effective corrections measured using Z events. Includes the statistical and systematic uncertainties derived as a correction to the resolution constant term (c in Eq. 5.13);
- the pile-up uncertainty. Corresponds to a variation of the resolution noise term (b in Eq. 5.13) by ± 100 MeV;
- passive material uncertainties. Derived from variation the passive material in the detector geometry of the simulation;

All these uncertainties lead to the uncertainty on the m_W measurement of about 3 MeV.

The dominant uncertainties on the energy response are found to be from

- finite statistics of the $Z \rightarrow ee$ sample
- physics modeling of the $Z \rightarrow ee$ resonance (missing higher-order EW corrections)
- algorithm of the energy scale determination itself - estimated by varying the m_{ee} mass window in which the fitting is performed and from closure test

The impact coming from the backgrounds is negligible. The overall impact of the energy scale uncertainty on the W mass measurement is found to be about 8 MeV.

Besides the Z -based energy scale correction uncertainties, possible differences in the energy response between electrons from Z and W decays are taken into account. The response linearity is affected by uncertainties on the layer intercalibration, passive material and calorimeter read-out. The impact of these uncertainties on the m_W is assessed to be about 4 MeV.

The impact of the electron energy calibration of the m_W measurement is summarized in Table 5.4.

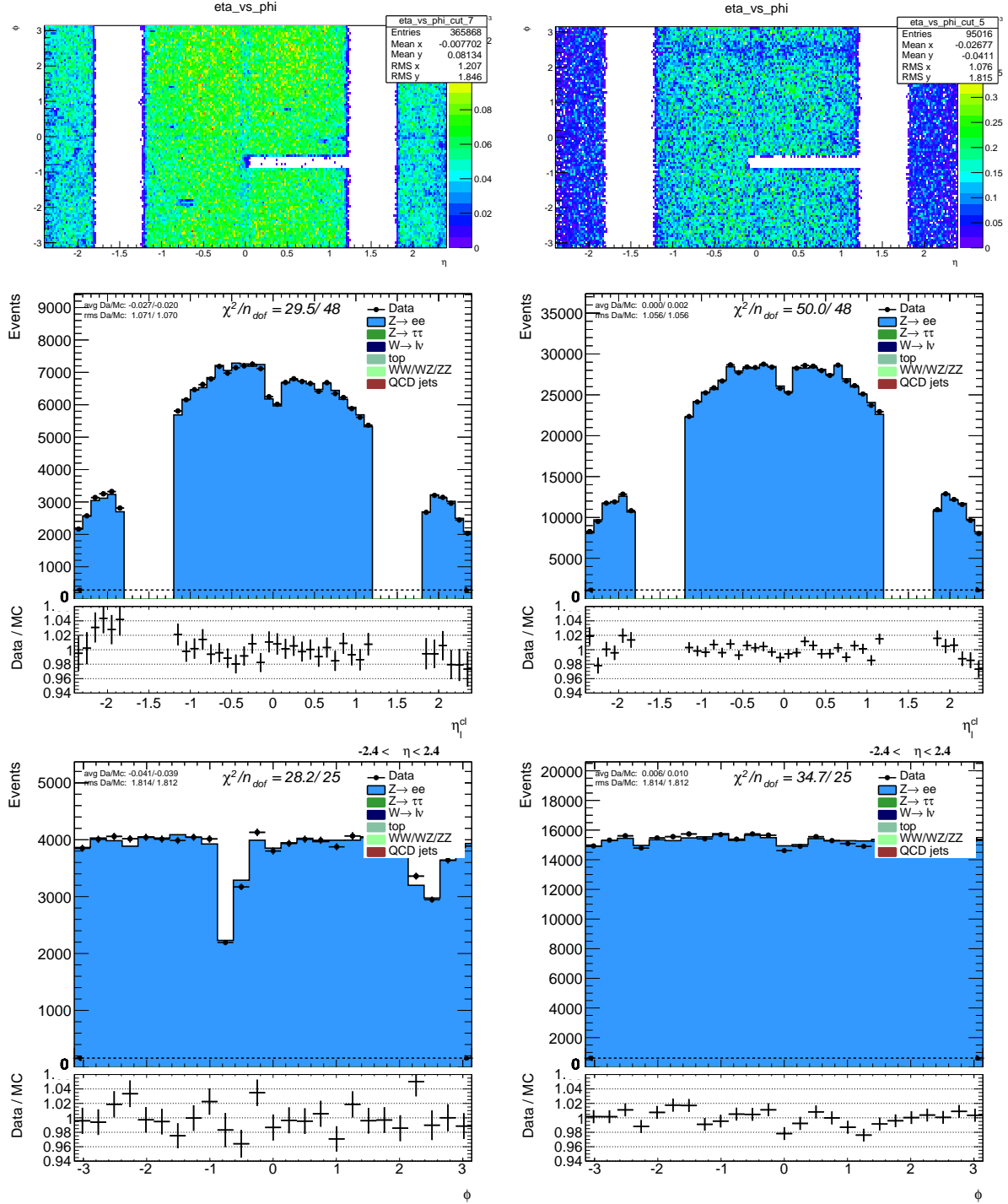


Figure 5.17: Top row: geometrical view of the “LAR hole” in W events (left) and Z (right) events taken during periods E-H. Middle and bottom rows: electron η and ϕ distributions for the data affected (left) or not (right) by the EM calorimeter failure.

$ \eta $ range	$0.0 < \eta < 0.6$		$0.6 < \eta < 1.2$		$1.82 < \eta < 2.4$		Inclusive	
Fitting observable	p_T^ℓ	m_T	p_T^ℓ	m_T	p_T^ℓ	m_T	p_T^ℓ	m_T
δm_W [MeV]								
Energy scale	10.3	10.3	10.9	10.9	16.0	16.0	8.0	8.0
Energy resolution	3.9	3.9	7.0	7.0	16.0	16.0	3.1	3.1
Energy linearity	4.9	5.4	7.4	7.2	4.6	5.1	4.2	4.5
Energy tails	2.3	3.3	2.3	3.3	2.3	3.3	2.3	3.3
Reco. efficieniy	8.5	7.4	9.2	7.8	12.4	10.6	6.8	6.0
ID efficieniy	9.2	7.8	10.6	8.5	12.2	11.3	6.7	5.7
Trigger & Isolation efficieniy	0.2	0.5	0.3	0.5	2.0	2.2	0.8	0.9
Total	17.5	16.6	20.6	19.1	29.1	28.2	13.7	13.2

Table 5.4: Impact of electron performance corrections on the m_W measurement uncertainties.

5.4 Electron selection efficiency

The electron selection efficiencies matter for the m_W measurement as they can be dependent on the electron energy used for the m_W extraction. Their dependence on the electron energy E_T induces a direct experimental uncertainty on the lepton E_T distribution, and to a lesser extent on the m_T^W distribution, due to the averaging of the E_T -dependent efficiencies at given m_T . In addition, they have an impact on the multijet background estimation that will be explained in Section 7. For these reasons, it is important to correct the MC predictions to reproduce efficiencies measured in data.

Similar to muons, the electron efficiency measurement is divided into components, namely reconstruction, identification, isolation and trigger efficiencies. The procedure of the electron triggering, reconstruction and identification are described in details in Section 3.2. The total efficiency for electrons is then calculated as

$$\varepsilon_{tot} = \varepsilon_{reconstruction} \cdot \varepsilon_{identification} \cdot \varepsilon_{isolation} \cdot \varepsilon_{trigger} \quad (5.15)$$

The reconstruction efficiency is defined as the probability for an electron to pass the reconstruction algorithm, given the existence of an EM cluster. The **loose**, **medium** and **tight** identification efficiencies are defined as the probability for an electron passing the reconstruction step to also pass the corresponding identification cuts. The trigger efficiency corresponds to the probability of reconstructed electron candidate passing the identification criteria to pass also the trigger. The variable $\varepsilon_{isolation}$ denotes the electron isolation efficiency with respect to the electrons satisfying the identification criteria.

The inputs to this analysis are taken from the published 7 TeV electron efficiency measurement results [51]. Here the electron efficiency corrections are determined using **Tag-and-Probe** method on the samples of $W \rightarrow e^\pm \nu$, $Z \rightarrow e^+ e^-$ and $J/\phi \rightarrow e^+ e^-$, and measured separately for electron reconstruction, identification and trigger efficiencies [51], as a function of electron pseudorapidity η and E_T . No ϕ dependency of the electron selection is assumed. In case of $W \rightarrow e^\pm \nu$, the missing transverse energy has been used as a tag and an electron probed the corresponding efficiencies.

As explained in Section 3.4.2, the electron isolation requirement consists on cuts applied to the track-based p_T^{cone40} and calorimeter-based E_T^{cone20} variables. These cuts are E_T - and η -dependent maintaining a uniform isolation efficiency of 97% for track- and 98% for calorimeter-based, leading to the total isolation efficiency of $\varepsilon_{isolation} = \varepsilon_{track} \cdot \varepsilon_{calo} = 0.95\%$.

In the $E_T > 30$ GeV range relevant for the W mass analysis, the total electron efficiency corrections are at the accuracy level of 0.1-0.2% in the barrel and 0.3% in the endcap. This leads to the total systematic uncertainty on the m_W measurement of about 8 MeV for both E_T and m_T^W fits. The corresponding uncertainties on m_W due to the electron-efficiencies corrections are shown

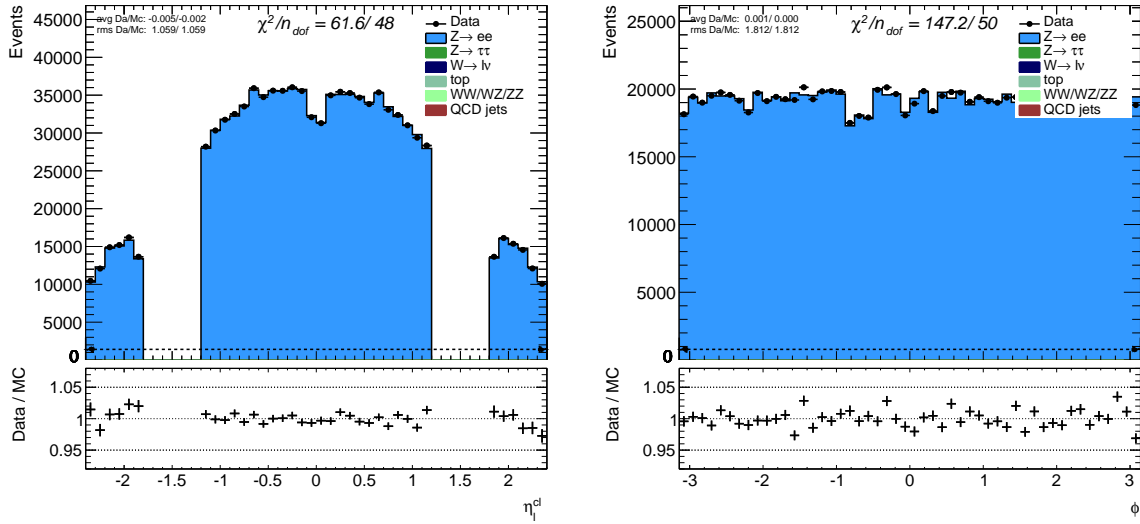


Figure 5.18: Comparison of the data and MC distribution as a function of electrons pseudorapidity η (left) and ϕ (right) in $Z \rightarrow ee$ events after applying all efficiency correction factors. The calorimeter crack region $1.2 < |\eta| < 1.8$ has been excluded.

in Table 5.4. After applying these corrections, good agreement between data and MC is achieved for electron η and ϕ distributions from $Z \rightarrow e^+e^-$, as shown in Figure 5.18.

5.5 Hadronic recoil calibration

The hadronic recoil affects the m_W measurement via its direct impact on the E_T^{miss} and m_T^W distributions. In addition, the decay lepton transverse momentum p_T^ℓ is also sensitive to the recoil due to migration effect of E_T^{miss} and m_T^W cuts.

In contrast to the decay lepton, the hadronic recoil \vec{u} to the W or Z boson is more complex quantity, involving many particles. In order to perform reliable m_W measurement, the predicted recoil system has to be calibrated to data with a high precision. Instead of precise calibration of the calorimeter response to each particle individually, it is preferable to calibrate the recoil effectively as a whole system. The reason of this is that additional energy from the underlying event and pileup activity which is measured in the calorimeter is easier to disentangle. It is also easier to address the systematic uncertainties from the recoil system instead of jet energy scale and resolution. As was introduced in Section 3.3, the hadronic recoil \vec{u} can be decomposed into parallel \vec{u}_\parallel and perpendicular \vec{u}_\perp components with respect to the boson p_T . The parallel component corresponds to "hard" recoil that balances the boson transverse momentum. The perpendicular component contains "soft" contributions including underlying event activity, pileup, electronic noise etc.

The W and Z bosons are produced at a similar Q^2 and thus they have similar recoils. Since the transverse momentum of the Z boson can be determined via the hadronic recoil measurement, but also via the precise measurement of the 4-vectors of its decay leptons, a data-driven calibration of the hadronic recoil measurements is possible. The typical energy resolution of the measured hadronic recoil in a $p_T^V \approx 20$ GeV event is in the order of ≈ 15 GeV, while the direct reconstruction of the vector boson p_T via its decay leptons is roughly 1 – 2 GeV. Hence the reconstruction of the Z-Boson p_T via the decay leptons allows for a precise determination of the expected hadronic recoil. After the calibration of the hadronic recoil measurement *via* Z boson events, the derived corrections can be transferred to W boson events ensuring the systematics of this transfer are evaluated carefully.

The hadronic recoil correction procedure consists of four main steps. At a first step, a standard reweighting as a function of average interactions per bunch crossing $\langle \mu \rangle$ is performed to equalise

the amount of pile-up present in data and MC. The second step is to correct residual discrepancies of the $\Sigma E_T - u$ distribution, by defining the Smirnov transform for $\Sigma E_T - u$ distribution in MC so it matches the Data. The next step is correcting the modulation of the φ distribution of hadronic recoil. The final step is defining additional correction for the mean and resolution of the hadronic recoil distribution. All these steps are performed in the muon decay channel only and tested in the electron channel afterwards.

5.5.1 Pile-up correction

Pile-up has significant impact on reconstruction of \vec{u} and ΣE_T (Eq.3.6). The MC samples are simulated taking into account *in-time* and *out-of-time* pile-up conditions. The pile-up is modeled by overlaying simulated hits from events with exactly one signal collision per bunch crossing with hits from minimum bias events that are produced with Pythia 8 with the appropriate ATLAS tune. Then, all generated particles are propagated through the ATLAS detector using GEANT4. However, the detector condition can change over the data-taking period, so the simulated pile-up can differ from the one in data. Regulation of the pile-up in the MC is best to perform by adjusting the average number of additional proton-proton collisions per bunch crossing $\langle \mu \rangle$. In order to account for mismodeling of the pile-up in Data and MC, a scale factor α should be applied on $\langle \mu \rangle$. The optimal value of $\alpha = 1.10^{+0.04}_{-0.03}$ has been found providing the best data/MC agreement of distributions relevant to m_W analysis, such as ΣE_T , $\Sigma E_T - u$, u_\perp and u_\parallel , as well as number of primary vertices N_{PV} . The $\langle \mu \rangle$ distribution in Data is continuous, while in MC is discrete, therefore the rescaling of $\langle \mu \rangle$ is done on Data (simply by dividing the distribution $\langle \mu \rangle / 1.1$). The distribution of $\langle \mu \rangle$, N_{PV} , ΣE_T and $\Sigma E_T - u$ after rescaling by 1.10 are shown in Figure 5.19.

5.5.2 Correction of the $\Sigma E_T - u$ distribution

After the $\langle \mu \rangle$ rescaling, residual corrections are needed to correct for the remaining differences between data and MC in the scalar sum of the hadronic activity ΣE_T and $\Sigma E_T - u$. One method to correct them is through the transformation applied to the $\Sigma E_T - u$ in MC in order to match the Data. This transformation (*Smirnov transform*) is extracted from the Smirnov inverse probability integral transform [52]. It goes beyond a simple Gaussian smearing correction and can in principle transform one histogram to another (barring issues with numerical stability, empty bins, low statistics). If a given variable x is distributed according to the probability distribution function $h_{\text{Data}}(x)$ in Data, and according to $h_{\text{MC}}(x)$ in MC, the respective cumulative distribution functions are:

$$\begin{aligned} H_{\text{Data}}(x) &= \int_{-\infty}^x h_{\text{Data}}(t) dt; \\ H_{\text{MC}}(x) &= \int_{-\infty}^x h_{\text{MC}}(t) dt \end{aligned} \quad (5.16)$$

The Smirnov transform function is mapping, in MC, the $\Sigma E_T - u$ variable to a transformed variable $(\Sigma E_T - u)^{\text{tr}}$, that is by construction distributed as $\Sigma E_T - u$ in data. It is defined as:

$$(\Sigma E_T - u)^{\text{tr}} = H_{\text{Data}}^{-1}[H_{\text{MC}}(\Sigma E_T - u)], \quad (5.17)$$

and the distribution h' of this variable satisfies

$$h'_{\text{MC}}((\Sigma E_T - u)^{\text{tr}}) \equiv h_{\text{Data}}(\Sigma E_T - u) \quad (5.18)$$

Figure 5.20 shows an example of this procedure for $\Sigma E_T - u$. The result of the transformation, for $\Sigma E_T - u$ distribution is shown on Figure 5.21.

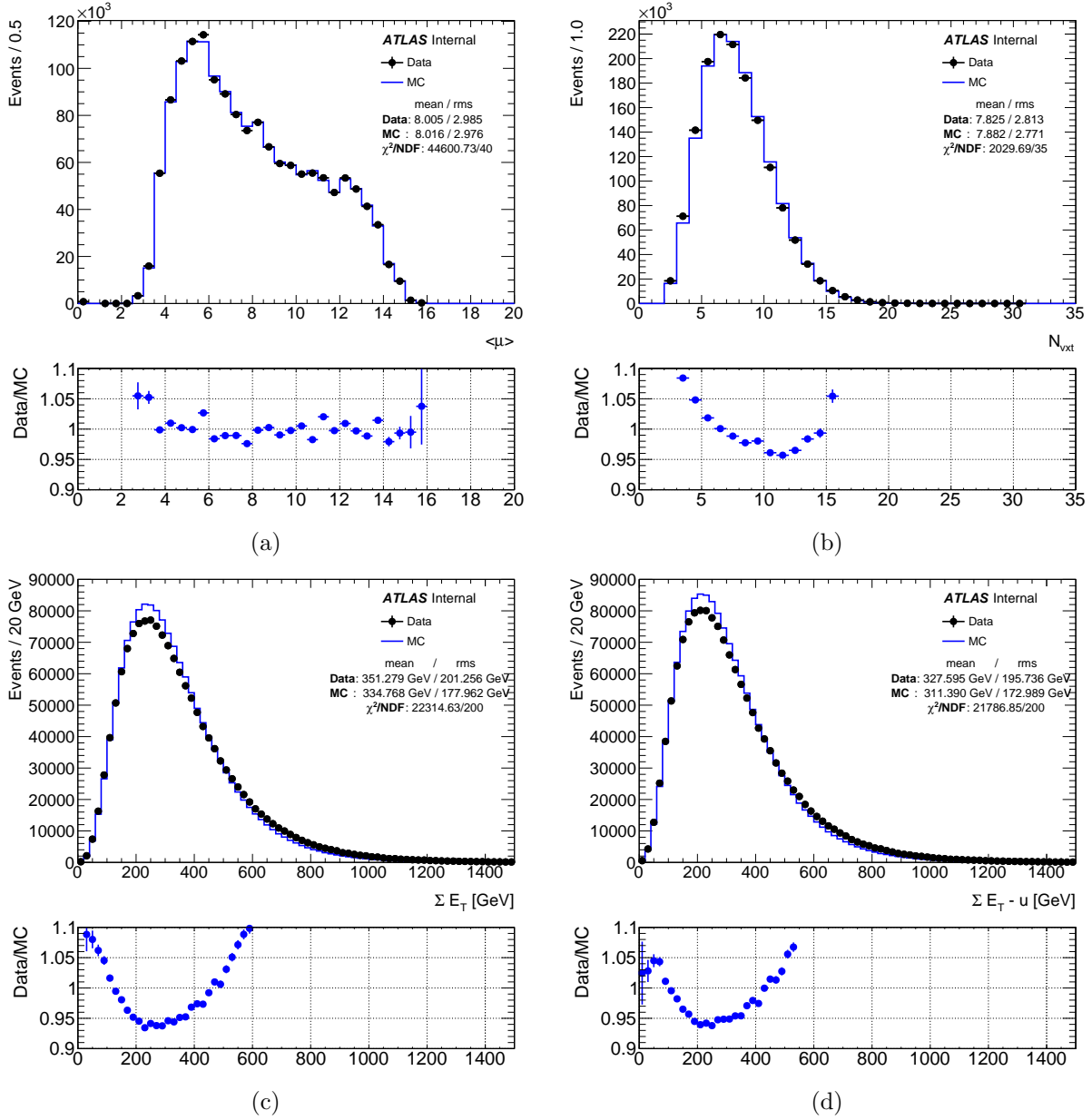


Figure 5.19: (a) Mean number of interactions per bunch crossing, (b) number of vertices, (c) ΣE_T distribution and (d) $\Sigma E_T - u$ distribution in Data (points) and MC (solid line) after pile-up reweighting and rescaling the $\langle \mu \rangle$ distribution by 1.1.

The transform can be defined inclusively or in bins of boson p_T . In Z events, the $\Sigma E_T - u$ data/MC discrepancy is observed to depend on p_T^Z , and incorporating this dependence results in better performance of the correction.

The p_T -independent Smirnov transform can be defined directly on W events, comparing Data and MC:

$$h_{\text{MC}}^W(\Sigma E_T - u) \rightarrow h_{\text{MC}}^W((\Sigma E_T - u)^{\text{tr}}) \equiv h_{\text{Data}}^W(\Sigma E_T - u), \quad (5.19)$$

but a p_T -dependent Smirnov transform on W 's has to be defined indirectly from Z events, since the boson p_T is measured with poor resolution in the W events. For this purpose the following approximation is used:

$$\tilde{h}_{\text{Data}}^W(\Sigma E_T - u; p_T) \equiv h_{\text{Data}}^Z(\Sigma E_T - u; p_T) \times \frac{\frac{h_{\text{Data}}^W(\Sigma E_T - u)}{h_{\text{MC}}^W(\Sigma E_T - u)}}{\frac{h_{\text{Data}}^Z(\Sigma E_T - u)}{h_{\text{MC}}^Z(\Sigma E_T - u)}}, \quad (5.20)$$

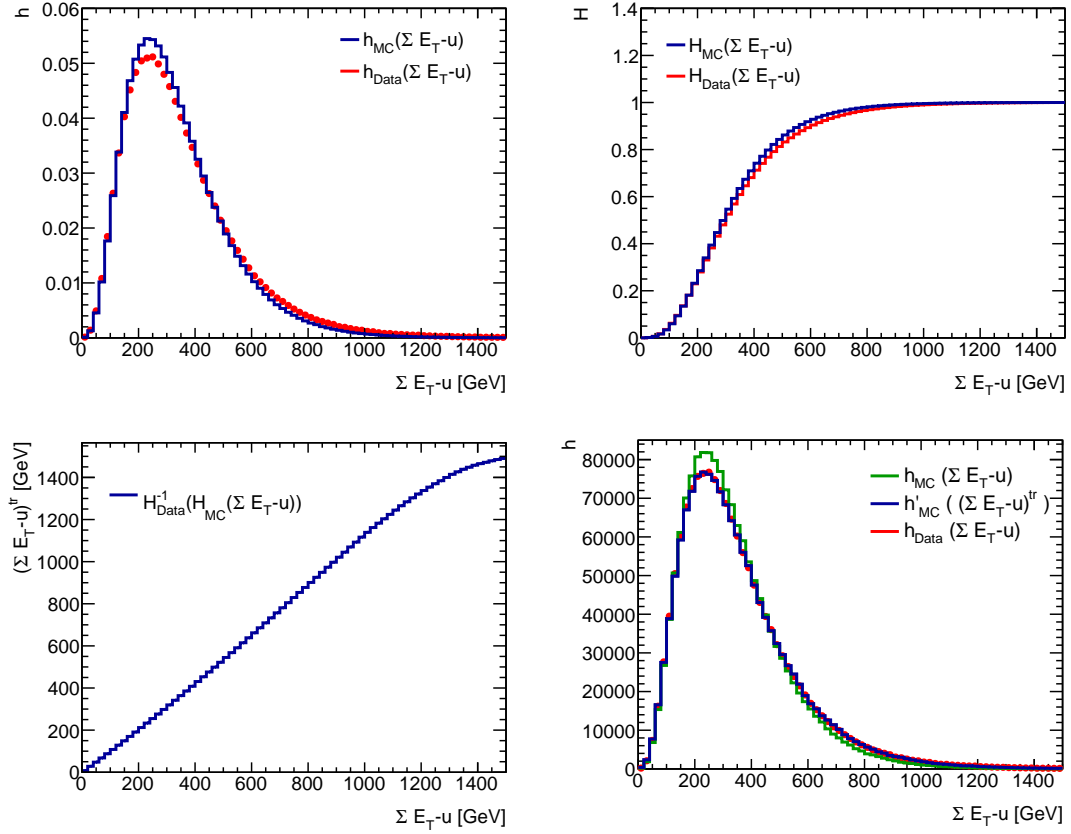


Figure 5.20: An example of the Smirnov transform procedure for $\Sigma E_T - u$ distribution for the bin $10 < p_T(Z) < 20$ GeV.

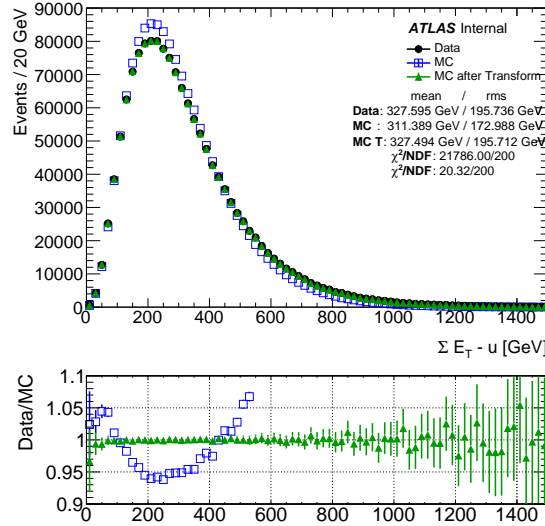


Figure 5.21: $\Sigma E_T - u$ distribution in Data and MC before and after the transformation as described in the text, where MC T in the legend denotes the transformed $\Sigma E_T - u$ distribution. The transformation is defined in bins of p_T^Z .

where the double ratio accounts for the overall data/MC difference between W and Z events, but assumes the p_T dependence of the discrepancy follows the behavior seen in Z events. The

p_T -dependent transform is defined such that

$$h_{MC}^W(\Sigma E_T - u; p_T) \rightarrow h_{MC}^W((\Sigma E_T - u)^{tr}; p_T) \equiv \tilde{h}_{Data}^W(\Sigma E_T - u; p_T). \quad (5.21)$$

5.5.3 u_Y correction

The hadronic recoil vector is expected to have no preferred φ direction. However, due to calorimeter non uniformity - there are places where the density is lower or higher than the average, the beam position - any an offset from the detector center is resulting that some clusters which are closer to the interaction point have a larger averaged measured energy, mismodeling of φ distribution of the hadronic recoil is observed. Figure 5.22 shows x and y component of the hadronic recoil, as well as φ distribution.

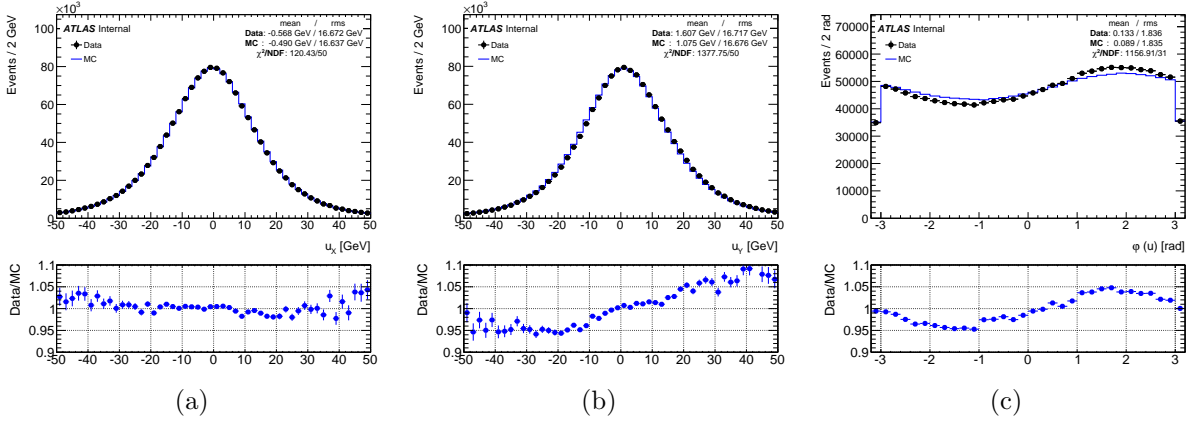


Figure 5.22: Hadronic recoil distribution in Data (points) and MC (solid line) in $Z \rightarrow \mu^+\mu^-$ events: (a) x -component of the hadronic recoil, (b) y -component of the hadronic recoil, (c) φ distribution of the hadronic recoil. Distributions are obtained after the pile-up reweighting and rescaling the $\langle \mu \rangle$ distribution by 1.1.

This mismodeling of the $\varphi(u)$ distribution can be corrected by shifting the mean of u_X and u_Y distributions. The corrections are obtained by studying the slopes of the mean of u_X and u_Y distributions as a function of $\Sigma E_T - u$ and $\varphi_{\mu\mu}$ in $Z \rightarrow \mu\mu$ events which is illustrated on Figure 5.23.

The corrections are applied to the u_X and u_Y distributions in MC according to Data to MC difference shown on Figure 5.23 (a) and (b) as a function of $\Sigma E_T - u$:

$$u'_X = u_X + (\langle u_X \rangle_{Data} - \langle u_X \rangle_{MC}) \quad u'_Y = u_Y + (\langle u_Y \rangle_{Data} - \langle u_Y \rangle_{MC}) \quad (5.22)$$

As can be seen, there is a constant shift in $\langle u_Y \rangle$ vs ϕ of about 0.6 GeV between data and MC, which is equivalent to the slope in $\Sigma E_T - u$ distribution.

5.5.4 Residual Recoil Corrections

The hadronic recoil is difficult to model, from detector and physics point of view. After rescaling the $\langle \mu \rangle$ distribution by 1.1, the transform of the $\Sigma E_T - u$ distribution and correction of the $\varphi(u)$ mismodeling, there are still differences between Data and MC for hadronic recoil in Z events (which can be seen in Figure 5.24). The recoil distributions as well as their projections are not affected by the Smirnov transform of the $\Sigma E_T - u$ distribution. In order to improve simulation to better match the data, additional correction to the hadronic recoil is defined.

The mean and the width of the projection of hadronic recoil with respect to boson p_T are corrected in bins of boson p_T and $\Sigma E_T - u$. Since the boson p_T and ΣE_T are correlated, it is better to derive the corrections as a function of $\Sigma E_T - u$ instead of ΣE_T . Corrections are derived from

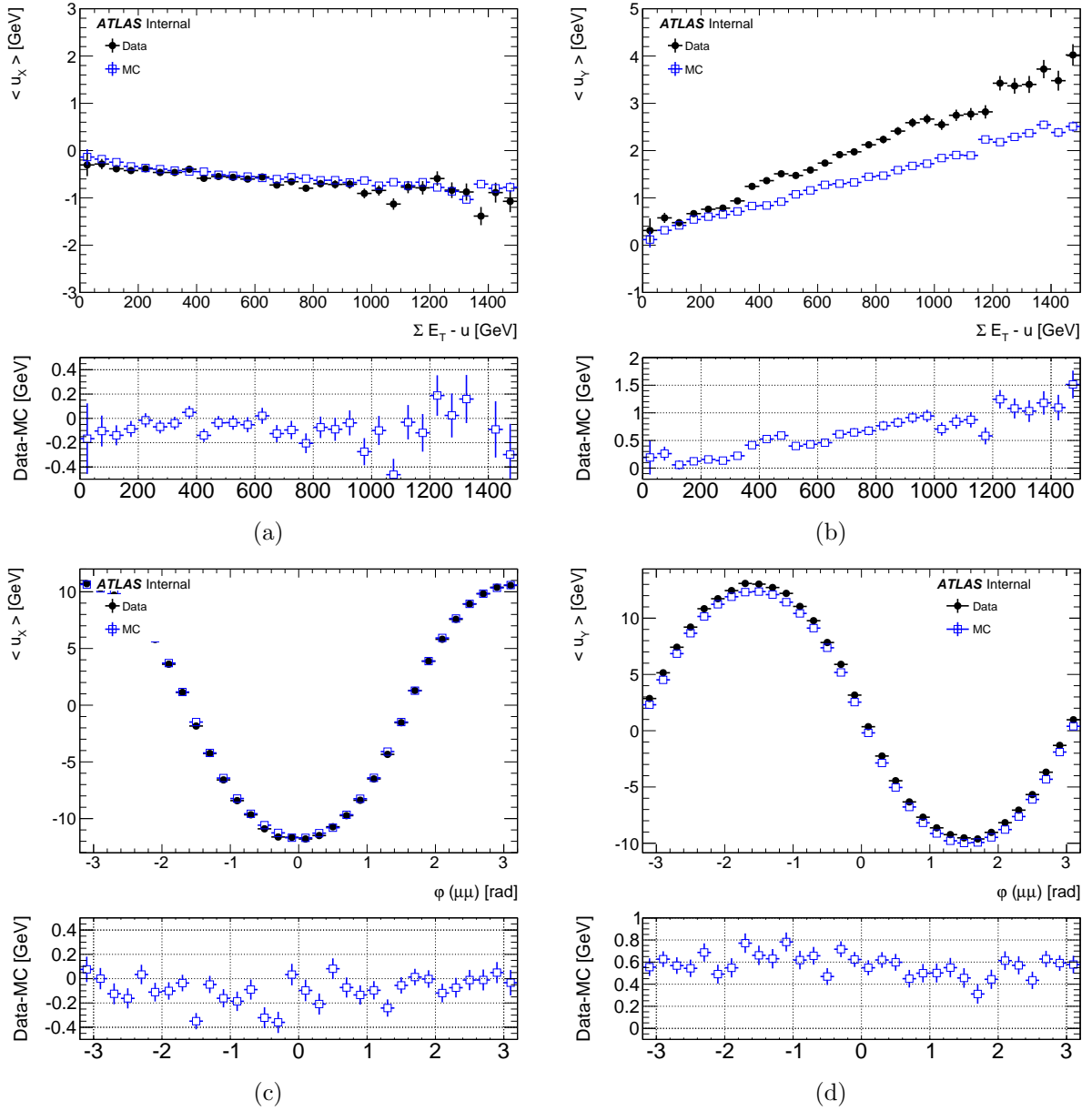


Figure 5.23: Mean of u_X and u_Y distributions in Data (black points) and MC (blue points) in $Z \rightarrow \mu^+\mu^-$ events: (a) and (b) as a function of $\Sigma E_T - u$, (c) and (d) as a function of φ of the di-muon system. Distributions are obtained after the pile-up reweighting and rescaling the $\langle \mu \rangle$ distribution by 1.1.

$Z \rightarrow \mu\mu$ events. By using correction factors that depend explicitly on boson p_T and $\Sigma E_T - u$, all remaining differences between Z and W boson events are taken into account and therefore the derived residual correction factors can be applied directly on simulated W boson events. Remaining differences between Data and MC for $p_T(W)$ and $\Sigma E_T - u$ in W boson events can be corrected independently from the residual hadronic recoil corrections. This correction is applied on MC to the mean and width of parallel and perpendicular projection of the hadronic recoil with respect to true boson p_T , in this way the correction is universal and can be applied to both, Z and W events.

The correction procedure is schematically shown on Figure 5.25. The first step is to define different resolution curves as a functions of $\Sigma E_T - u$ and p_T (Figure 5.25 is showing only as a function of $\Sigma E_T - u$) for Data, MC and $(\Sigma E_T - u)^{\text{tr}}$ in MC. One part of the difference in resolution between Data and MC comes from mismodeling of the $\Sigma E_T - u$ distribution, this is accounted for with the transform (step from (1) to (2) on Figure 5.25). Therefore, the correction for the resolution

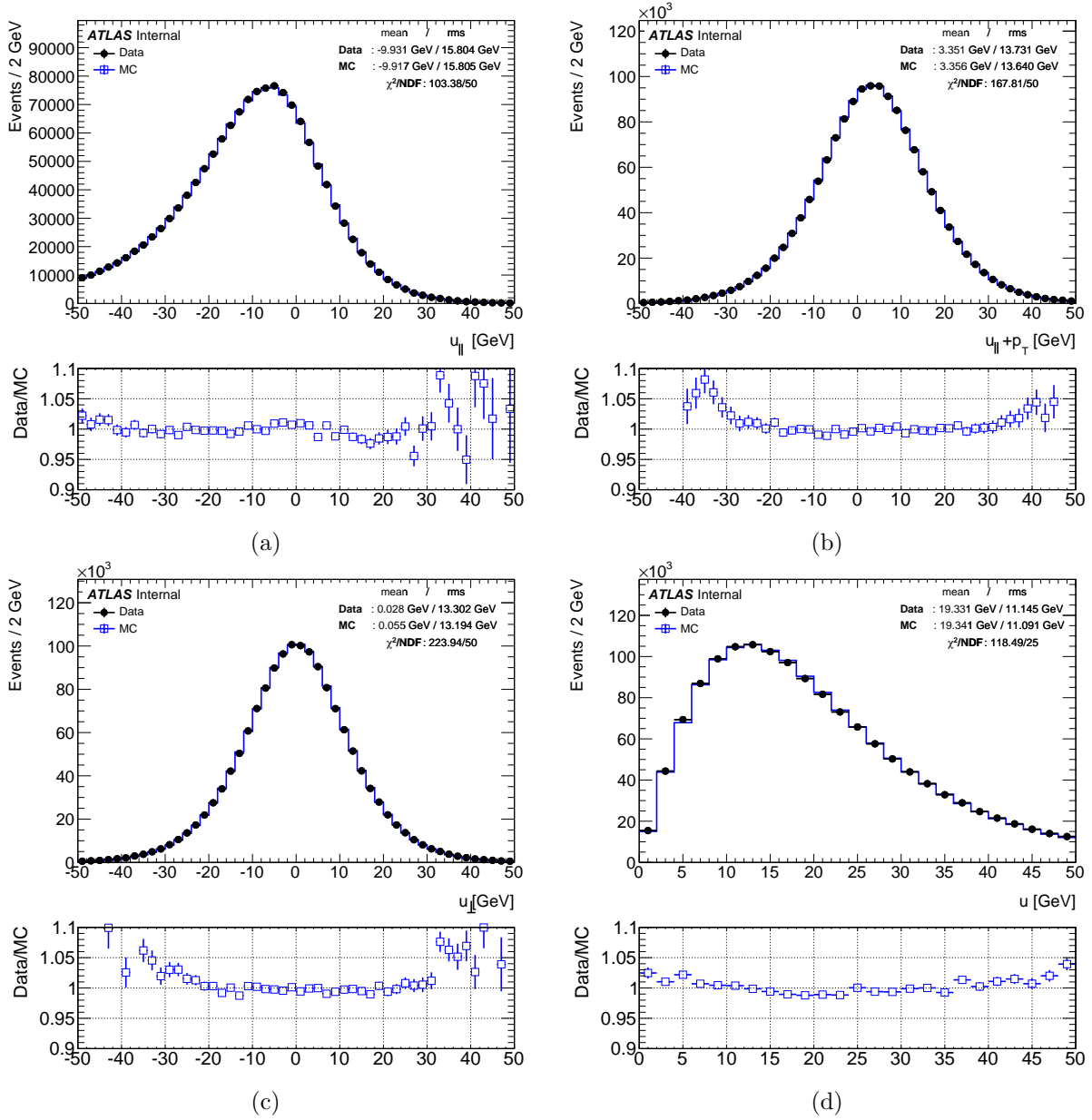


Figure 5.24: Hadronic recoil distribution in Data (points) and MC (solid line) in $Z \rightarrow \mu^+\mu^-$ events: (a) parallel projection of the hadronic recoil on the transverse momentum of the vector boson, (b) sum of parallel projection of the hadronic recoil and the vector boson p_T^Z , (c) perpendicular projection of the hadronic recoil on the transverse momentum of the vector boson, (d) hadronic recoil distribution. Distributions are obtained after the pile-up reweighting, rescaling the $\langle \mu \rangle$ distribution by 1.1 and applying the u_X and u_Y correction.

is defined from the difference in resolution between Data and MC evaluated at $(\Sigma E_T - u)^{\text{tr}}$, for a given $\Sigma E_T - u$ value (difference between (2) and (3) on Figure 5.25):

$$r = \frac{(3)}{(2)} = \frac{\sigma_{u_\perp}^{\text{Data}}((\Sigma E_T - u)^{\text{tr}})}{\sigma_{u_\perp}^{\text{MC}}((\Sigma E_T - u)^{\text{tr}})}, \quad \sigma_{u_\perp}^{\text{MC}}((\Sigma E_T - u)^{\text{tr}}) \equiv \sigma_{u_\perp}^{\text{MC}}(\Sigma E_T - u) \quad (5.23)$$

This procedure accounts for data/MC differences in the resolution curves as a function of $\Sigma E_T - u$, and for differences in the $\Sigma E_T - u$ distribution itself.

The correction for the mean is defined the same way from the difference in mean for $u_\parallel + p_T$ in Data and transformed MC. This method allows the mean and resolution to be evaluated at the same value of $\Sigma E_T - u$. It is possible to use a different approach for this method, instead of

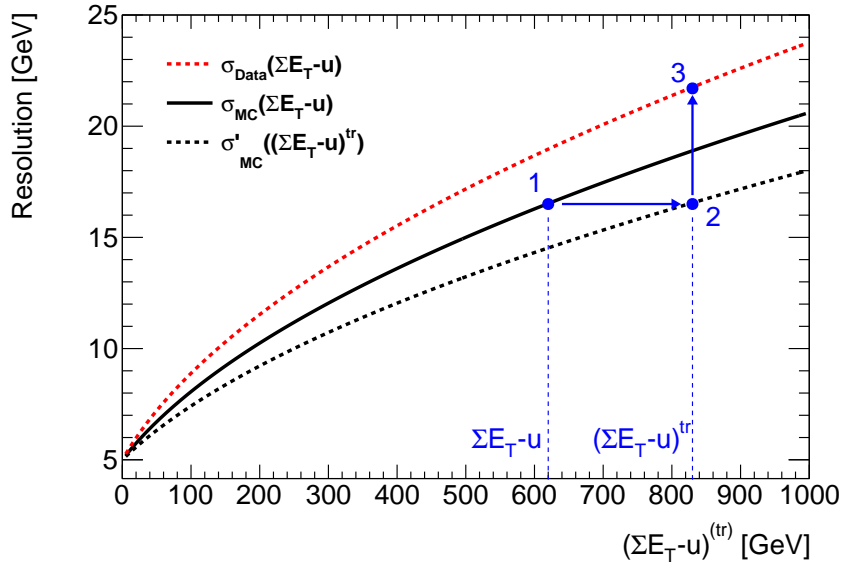


Figure 5.25: Schematic view of the correction procedure: resolution of u_{\perp} as a function of $\Sigma E_T - u$. There are three resolution curves: Data in dotted red (σ_{Data}), MC in solid black (σ_{MC}) and MC as a function of $(\Sigma E_T - u)^{tr}$ in dotted black (σ'_{MC}). Step 1 \rightarrow 2 represents the transformation of $\Sigma E_T - u$ in MC; step 2 \rightarrow 3 is the actual resolution correction (difference in resolution between Data and MC for a given value of $(\Sigma E_T - u)^{tr}$).

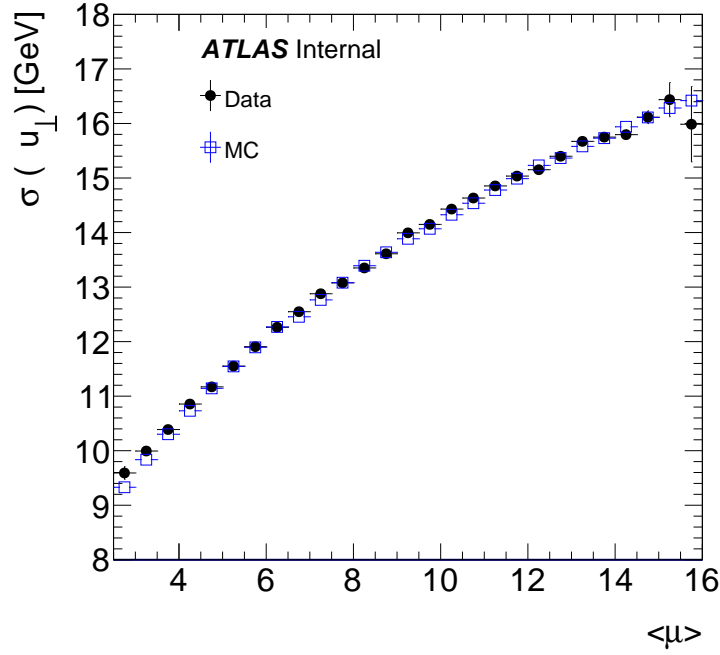


Figure 5.26: The RMS of u_{\perp} as a function of $\langle \mu \rangle$ in Z boson events for Data and MC.

calculating additional resolution curve, calculate the difference between Data and MC but for two different values of $\Sigma E_T - u$ and transformed $\Sigma E_T - u$. These two approaches are equivalent and give the same result.

In order to derive correction factors for mean and resolution for parallel and perpendicular component of the hadronic recoil, mean and RMS of the corresponding distributions are extracted from Data and MC in bins of $\Sigma E_T - u$ and p_T . The parallel component of the hadronic recoil

is corrected for mean and resolution, while the perpendicular component is corrected only for resolution. Parallel and perpendicular component of the hadronic recoil (w.r.t. boson p_T) are corrected in MC according to the equations:

$$u'_{\parallel} = b(p_T, (\Sigma E_T - u)^{\text{tr}}) + \langle u_{\parallel} \rangle_{\text{Data}} + (u_{\parallel} - \langle u_{\parallel} \rangle_{\text{Data}}) \cdot r(p_T, (\Sigma E_T - u)^{\text{tr}}), \quad (5.24)$$

$$u'_{\perp} = u_{\perp} \cdot r(p_T, (\Sigma E_T - u)^{\text{tr}}), \quad (5.25)$$

where correction for the mean is the difference in the means for $u_{\parallel} + p_T$ in Data and MC:

$$b = \langle u_{\parallel} + p_T \rangle^{\text{Data}} - \langle u_{\parallel} + p_T \rangle^{\text{MC}}, \quad (5.26)$$

and the resolution correction $r(p_T, (\Sigma E_T - u)^{\text{tr}})$ is the ratio of the u_{\perp} distributions RMS in Data and MC, as defined in Equation 5.23.

The correction for the resolution is derived from u_{\perp} and applied to both parallel and perpendicular component of the hadronic recoil. The mean is only corrected for the u_{\parallel} component of the recoil. The correction presented with previous equations is applied event by event.

The resolution of u_{\perp} depends on the pile-up and therefore the $\langle \mu \rangle$ distribution. The resolution of u_{\perp} as a function of $\langle \mu \rangle$ is illustrated in Figure 5.26. In order to gain sensitivity, this correction procedure is defined in three $\langle \mu \rangle$ bins, i.e. for low pile-up for $\langle \mu \rangle \in (2.5, 6.5)$, medium for $\langle \mu \rangle \in (6.5, 9.5)$ and high pile-up for $\langle \mu \rangle \in (9.5, 16.0)$, the sample approximately corresponds to 40%, 30% and 30% of the events for the 3 $\langle \mu \rangle$ bins respectively.

5.5.5 Validation of the corrections

The hadronic recoil distribution and its parallel and perpendicular projection for $Z \rightarrow \mu\mu$ events are shown on Figure 5.27 inclusively in $\langle \mu \rangle$.

The recoil corrections derived from $Z \rightarrow \mu\mu$ were applied to $Z \rightarrow ee$ events. The hadronic recoil distribution and its parallel and perpendicular projection for $Z \rightarrow ee$ events are shown on Figure 5.27 inclusively in $\langle \mu \rangle$. As can be seen, the impact of the hadronic recoil corrections on Z boson events is quite small.

5.5.6 Propagation of the corrections to $W \rightarrow \mu\nu$ and $W \rightarrow e\nu$

Since the $\Sigma E_T - u$ distribution itself is different among Z, W^+ and W^- events, the overall corrections derived from Z are not fully applicable to W. There is approximately 20 GeV difference in mean and about 10 GeV difference in RMS between $\Sigma E_T - u$ in Z's and W's. Furthermore there is a difference between W^+ and W^- . Thus, when applying the recoil corrections to W boson, a new $\Sigma E_T - u$ transformation is defined (as explained in Section 5.5.2), one for W^+ and one for W^- . After the transformation $\Sigma E_T - u$, the distributions in Data and MC agree by construction. The result of applying this correction on $W \rightarrow \mu\nu$ is shown in Figure 5.29 with the hadronic recoil (p_T^W) distribution.

5.5.7 Uncertainty and impact on the m_W

The uncertainties associated to the recoil calibration procedure include the uncertainty on the $\langle \mu \rangle$ rescaling value, uncertainty due to Smirnov transformation of the $\Sigma E_T - u$ distribution, statistical uncertainties in the residual correction factors and their dependence on the boson p_T , uncertainty on the $u_{X,Y}$ distribution correction, and expected differences in the hadronic response between Z- and W-boson events.

As the $\langle \mu \rangle$ rescaling value is chosen to be 1.10, the values of 1.07 and 1.14 are taken to be upper and lower variations. An impact of this uncertainty on the M_W is estimated to be below 1 MeV. The Smirnov transform of $\Sigma E_T - u$ is defined separately for W^+ and W^- in order to take into account the charge dependent p_T^W distributions. The systematic uncertainty related to the

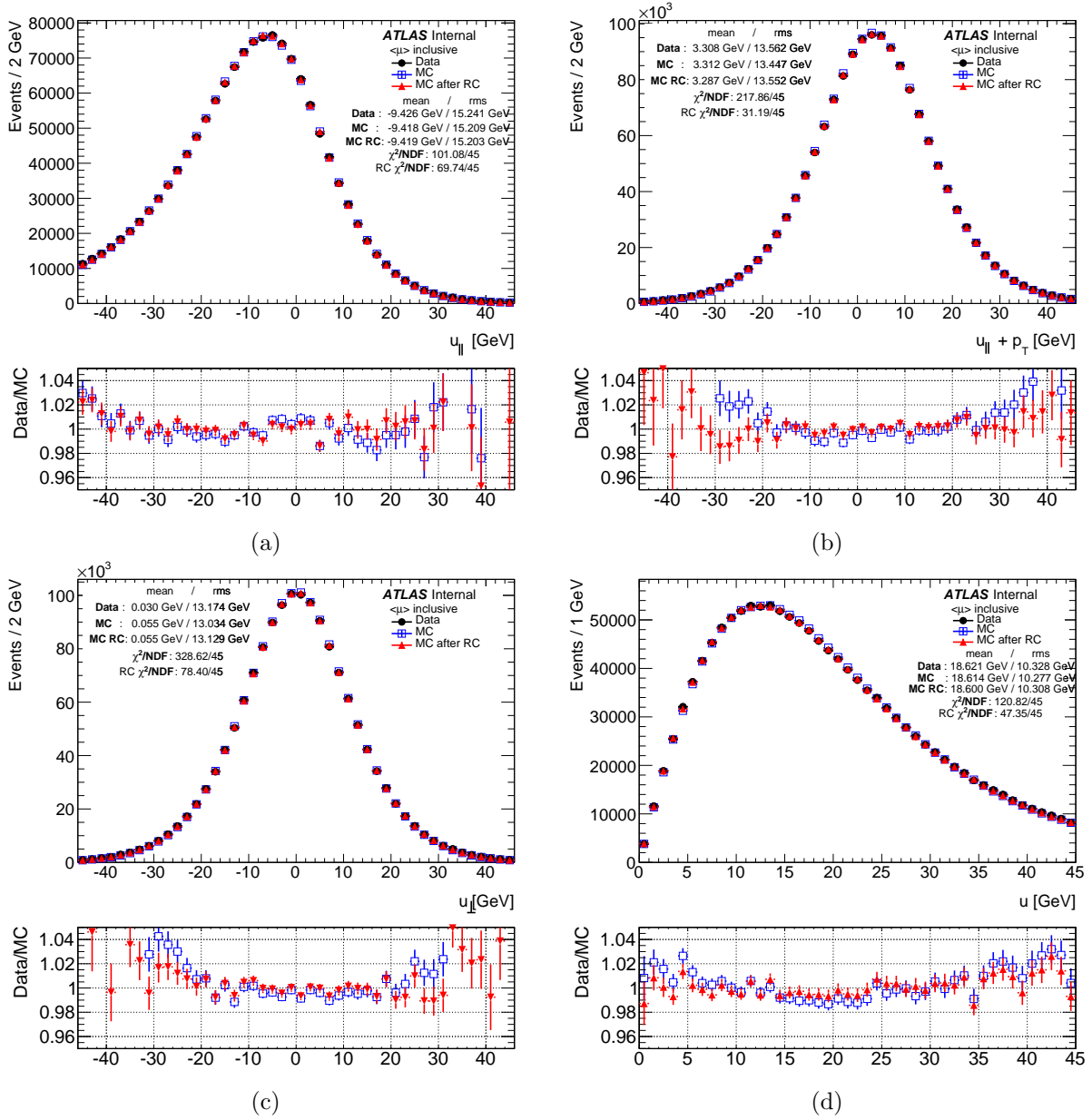


Figure 5.27: Hadronic recoil distribution in Data and MC before and after the hadronic recoil corrections in $Z \rightarrow \mu^+\mu^-$ events inclusive in $\langle \mu \rangle$. (a) Projection of the hadronic recoil to the parallel to the transverse momentum of the vector boson. (b) Sum of parallel projection of the hadronic recoil to the transverse momentum of the vector boson and the transverse momentum of the vector boson. (c) Projection of the hadronic recoil to the perpendicular to the transverse momentum of the vector boson. (d) Hadronic recoil distribution.

dependence of this correction on p_T is estimated by comparing with the results of a p_T -inclusive correction. It is estimated to contribute to M_W uncertainty of about 1 MeV using p_T^ℓ fits and of about 11 MeV using m_T^W fits. As the momentum scale and resolution corrections in Eq.(5.24) and Eq.(5.25) are derived from Z and applied to W , the difference in the response between both bosons is considered as uncertainty. The resolution can be compared, after $\Sigma E_T - u$ reweighting between Z , W^+ and W^- in simulation on Figure 5.30. This difference in recoil resolution can originate from 'genuine' differences in the boson kinematic between Z and W events, or can be the consequence of different selection criteria and reconstruction biases. Systematic uncertainties in the corrections of the $u_{X,Y}$ distributions are found to be small compared to the other systematic uncertainties and are neglected.

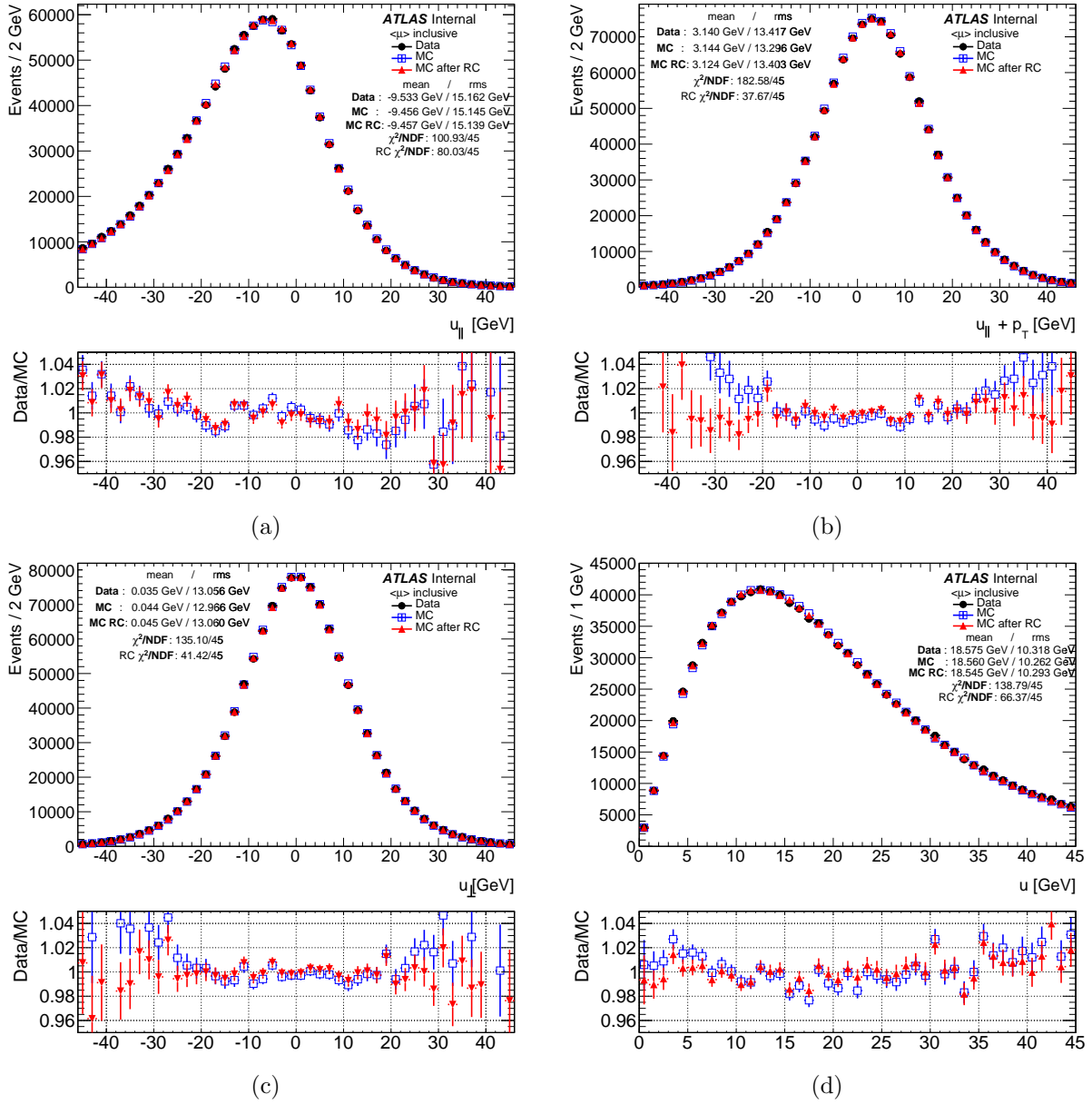


Figure 5.28: Hadronic recoil distribution in Data and MC before and after the hadronic recoil corrections in $Z \rightarrow e^+e^-$ events inclusive in $\langle \mu \rangle$. (a) Projection of the hadronic recoil to the parallel to the transverse momentum of the vector boson. (b) Sum of parallel projection of the hadronic recoil to the transverse momentum of the vector boson and the transverse momentum of the vector boson. (c) Projection of the hadronic recoil to the perpendicular to the transverse momentum of the vector boson. (d) Hadronic recoil distribution.

The impact of the uncertainties of the recoil calibration on the extraction of the W -boson mass from the p_T^ℓ and m_T^W distributions are summarised in Table 5.5. As expected, the determination of m_W from the p_T^ℓ distribution (typically 3 MeV) is marginally affected by the uncertainties of the recoil calibration, whereas larger uncertainties are estimated for the distribution (about 13 MeV). The largest uncertainties are induced by the $\Sigma \vec{E}_T$ corrections and by the extrapolation of the recoil momentum-scale and momentum-resolution corrections from Z - to W -boson events.

Table 5.6 summarizes the total systematic uncertainty of the recoil calibration in different $\langle \mu \rangle$ bins using p_T^ℓ , m_T^W or E_T^{miss} distribution for the m_W extraction. The systematic uncertainty has been added to the Figure 5.29 for the recoil distributions of the W boson.

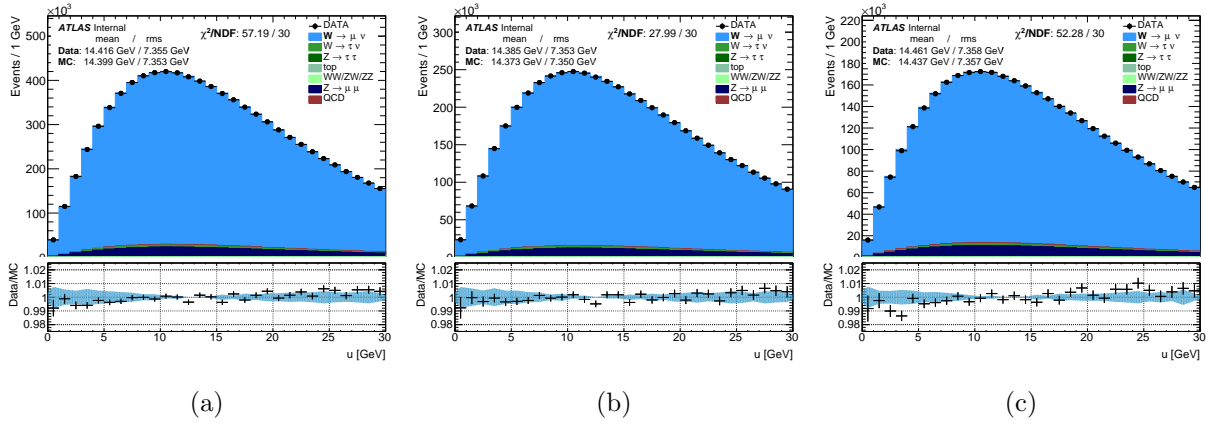


Figure 5.29: Hadronic recoil distribution in W^\pm (a), W^+ (b) and W^- (c) for inclusive $\langle \mu \rangle$ after recoil corrections with systematics uncertainties due to variation of all corrections.

$ \eta $ range	W^+		W^-		W^\pm	
Fitting observable	p_T^ℓ	m_T	p_T^ℓ	m_T	p_T^ℓ	m_T
δm_W [MeV]						
μ scale factor	0.2	1.0	0.2	1.0	0.2	1.0
$\Sigma \bar{E}_T$ correction	1.1	12.6	1.2	9.0	1.2	11.4
Effective corrections (stat.)	2.0	2.7	2.0	2.7	2.0	2.7
Effective corrections ($Z \rightarrow W$ extrap.)	0.1	5.8	0.1	4.3	0.1	5.1

Table 5.5: Impact of recoil performance corrections on the m_W measurement uncertainties.

Bin	$p_T^{\ell+}$	$p_T^{\ell-}$	$p_T^{\ell\pm}$	m_T^{W+}	m_T^{W-}	$m_T^{W^\pm}$	$E_T^{\text{miss}+}$	$E_T^{\text{miss}-}$	$E_T^{\text{miss}\pm}$
MuBin1	2.6	2.7	2.7	21.0	12.2	17.9	52.4	24.6	41.1
MuBin2	2.4	2.4	2.4	14.1	14.1	14.1	29.2	29.2	29.2
MuBin3	3.4	3.4	3.4	9.0	9.0	9.0	26.3	26.3	26.4
Inclusive	2.7	2.7	2.7	14.5	10.8	13.2	34.8	23.8	28.5

Table 5.6: Summarised results of total uncertainty from the hadronic recoil corrections. The systematics on m_W are given in MeV.

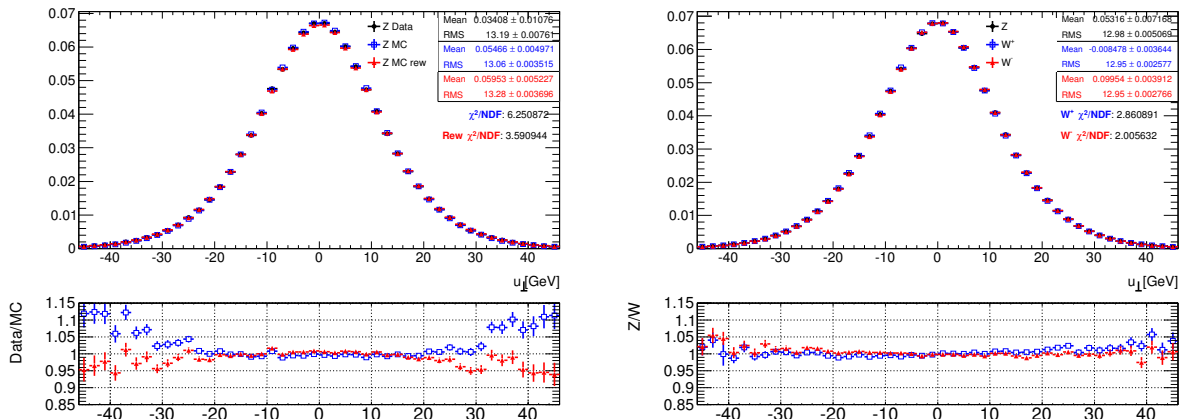


Figure 5.30: Perpendicular component of hadronic recoil distribution in (left) data and MC for Z events and (right) MC for Z , W^+ and W^- events, after ΣE_T reweighting.

Production and decay model

6.1 Introduction

Physics corrections to the final state distributions predicted by the Monte Carlo samples are based on the ansatz of the factorization of the cross section [53] in four pieces, according to the following formula:

$$\frac{d\sigma}{dp_1 dp_2} = \left(\frac{d\sigma(m)}{dm} \right) \left(\frac{d\sigma(y)}{dy} \right) \left(\frac{d\sigma(pt; y)}{dpt} \frac{1}{\sigma(y)} \right) \left(\Sigma_i A_i(y, pt) P_i(\cos \theta, \phi) \right) \quad (6.1)$$

where p_1 and p_2 are the lepton and anti-lepton 4-momenta, m , p_T , and y , are the invariant mass, transverse momentum, and rapidity of the dilepton system, $\cos \theta$ and ϕ are the polar and azimuthal angle of the lepton in a given rest frame of the dilepton system, A_i are angular coefficients, and P_i are spherical harmonics.

Variations of $\frac{d\sigma(m)}{dm}$ with respect to the value of the pole mass of the W -boson are modeled with a Breit-Wigner distribution, including EW corrections. The differential cross section $\frac{d\sigma}{dy}$, and the $A_i(y, pt)$ angular coefficients are modeled with perturbative QCD fixed order predictions. The transverse momentum spectrum at given rapidity, $\frac{d\sigma(pt, y)}{dpt} \frac{1}{\sigma(y)}$, is modeled with predictions including parton shower or analytic resummation [54].

Various ancillary measurements of W - and Z -boson production are used to validate and constrain the modelling of the fully-differential leptonic Drell-Yan cross section. The PDF central values and uncertainties, as well as the modelling of the differential cross section as a function of boson rapidity, are validated by comparing to the 7 TeV W - and Z -boson rapidity measurements [55], based on the same data sample. The QCD parameters of the parton shower model are determined by fits to the transverse-momentum distribution of the Z boson measured at 7 TeV. The modelling of the $A_i(p_T, y)$ coefficients is validated by comparing the theoretical predictions to the 8 TeV measurement of the angular coefficients in Z -boson decays [56].

6.2 Resonance parameterisation

As the baseline Monte Carlo program, POWHEG+PYTHIA, used in the m_W analysis includes EW contributions only at LO, corrections have to be applied to its description of the W and Z lineshapes.

Defining the gauge interactions and couplings according to

$$\begin{aligned} \mathcal{L}_{\text{NC}} &= \sum_{i=\gamma, Z} \alpha_i \bar{f} \gamma_\mu (v_{f_i} - a_{f_i} \gamma^5) f V_i^\mu, \\ \mathcal{L}_{\text{CC}} &= \alpha_W V_{f\bar{f}'} \bar{f}' \gamma_\mu (1 - \gamma^5) f W^\mu, \end{aligned} \quad (6.2)$$

the parton-level $q\bar{q} \rightarrow l\bar{l}$ and $q\bar{q}' \rightarrow l\nu$ cross sections can be generically written as follows, at leading order:

$$\begin{aligned} \hat{\sigma}(\hat{s}) &\propto \sum_{i,j} \alpha_i \alpha_j V_i V_j B_{ij} P_{ij}(\hat{s}); \\ B_{ij} &= (v_i v_j + a_i a_j)_{\text{in}} (v_i v_j + a_i a_j)_{\text{out}}; \\ P_{ij}(\hat{s}) &= \hat{s} \frac{(\hat{s} - m_i^2)(\hat{s} - m_j^2) + m_i m_j \Gamma_i \Gamma_j}{[(\hat{s} - m_i^2)^2 + (m_i \Gamma_i)^2][(\hat{s} - m_j^2)^2 + (m_j \Gamma_j)^2]}; \end{aligned} \quad (6.3)$$

where the sum runs over the exchanged gauge bosons in the s -channel. The indices i, j only take one value (W) in charged-current interactions, and two (γ, Z) in neutral-current interactions. The diagonal terms $i = j$ represent the squared amplitude corresponding to the exchange of a given boson; the cross-terms, $i \neq j$, describe the $\gamma - Z$ interference. The mass and width of gauge boson i are denoted m_i and Γ_i , and \hat{s} is the available energy for the parton-level process. The gauge coupling constants α_i , the generation-mixing terms V_i and the vector and axial couplings v_i, a_i for the incoming and outgoing fermions are summarised in Table 6.1.

i	$\gamma f \bar{f}$	$Z f \bar{f}$	$W f \bar{f}'$
α_i	α_{em}	$G_\mu m_Z^2 / (2\sqrt{2}\pi)$	$G_\mu m_W^2 / (\sqrt{2}\pi)$
v_i	Q_f	$I_{3f} - 2Q_f \sin^2 \theta_W$	I_{3f}
a_i	0	I_{3f}	I_{3f}
V_i	1	1	$V_{ff'}$

Table 6.1: Gauge coupling constants, fermion vector and axial-vector coupling factors, and generation mixing terms in the Standard Model.

The expression above corresponds to the fixed-width Breit-Wigner parametrization. In the running-width form, every factor of $m\Gamma$ is replaced by $\frac{\hat{s}}{m}\Gamma$, and primed quantities are used to clarify that running masses and widths differ from their fixed-width values:

$$P'_{ij}(\hat{s}) = \hat{s} \frac{(\hat{s} - m_i'^2)(\hat{s} - m_j'^2) + \frac{\hat{s}^2}{m_i' m_j'} \Gamma_i' \Gamma_j'}{[(\hat{s} - m_i'^2)^2 + (\frac{\hat{s}}{m_i'} \Gamma_i')^2][(\hat{s} - m_j'^2)^2 + (\frac{\hat{s}}{m_j'} \Gamma_j')^2]}. \quad (6.4)$$

While the fixed-width form is most often used in generators, the running-width form was used at LEP for the measurement of m_Z . It was observed in Ref. [57] that equations 6.3 and 6.4 are equivalent upon a redefinition of the resonance parameters, following:

$$m_i = m_i' / \sqrt{1 + (\Gamma_i' / m_i')^2}; \quad (6.5)$$

$$\Gamma_i = \Gamma_i' / \sqrt{1 + (\Gamma_i' / m_i')^2}. \quad (6.6)$$

which allows to translate the former parametrization into the latter. In particular, Z boson exchange according to Eq. 6.4 should be described using the values measured at LEP, $m_Z' = 91.188$ GeV and $\Gamma_Z' = 2.495$ GeV, or equivalently according to Eq. 6.3 with $m_Z = 91.154$ GeV and $\Gamma_Z = 2.494$ GeV. The W boson mass measured in earlier experiments is also defined in the running-width parametrization.

6.3 Electroweak corrections

6.3.1 Final state photonic QED corrections

The formalism described above holds in the absence of real photon emission corrections. For most samples used in ATLAS, such corrections are applied with the help of PHOTOS [58], analysing the event record returned by the generators above, generating photon emissions and modifying the final state lepton kinematics accordingly.

Starting from the Born-level final state (no QED radiation), PHOTOS generates multiple photon radiation in the full available phase space. The emission of each photon is calculated according to the corresponding QED matrix element; the algorithm is applied iteratively, updating the available phase space after each emission and using the same perturbative accuracy for each iteration. The iteration ends when the photon energy is smaller than 10^{-7} times the energy of the parent in the decay rest frame. The approach is illustrated in Figure 6.1. The ATLAS samples are generated

using an exact NLO QED matrix elements [59]. The systematic uncertainties on the present analysis are evaluated comparing these two settings. This study is performed by generating events using POWHEG+PYTHIA and PHOTOS as done for the main analysis samples, only changing the settings in PHOTOS.

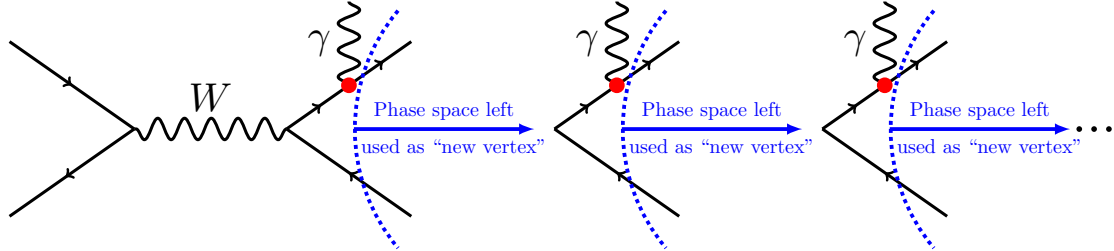


Figure 6.1: FSR treatment as applied in ATLAS using PHOTOS. The dot represents the matrix element for a single photon emission. After each photon emission, the outgoing lepton lines (right of the dashed line) are considered by PHOTOS again for further photon emissions, in an interactive way.

Illustrative kinematic distributions are shown in Figure 6.2, with and without FSR corrections, to show the overall size of this effect. Muon kinematics are presented “bare”, i.e. after FSR-induced momentum loss. The electron kinematics are presented “dressed”, recombining the bare electron with all photons emitted within $\Delta R < 0.1$, as a naive emulation of the collection of collinear photons within the electron calorimeter cluster. For dressed electrons, the height of the invariant mass peak is reduced by about 8%, and the tails are enhanced accordingly at low mass. A similar effect is seen on the Jacobian peak for bare muons, with a reduction of the peak by about 5%. The difference between the two PHOTOS settings studied below is not visible on this scale.

In figures 6.3-6.4, the settings used for the simulated samples and the optimal mode are compared. The comparisons are performed applying pseudo-rapidity cuts on the charged leptons ($|\eta| < 2.4$), and an invariant mass cut in the lepton pairs ($66 < m_{\ell\ell} < 116$ GeV). No transverse momentum cuts are applied. The effect of the correction to the exact one-photon matrix element for each photon emission is visible, and largely universal between electrons and muons. It was also verified that for each lepton flavour, the size of the correction does not depend on whether the leptons are considered bare or dressed. For W production, the effect is larger than 0.1% only for $p_T < 15$ GeV. For $p_T > 30$ GeV, the effect is very small. Similarly, no significant effect is visible in the transverse mass spectrum, for $m_T > 40$ GeV. These effects contribute to the W modeling uncertainty and directly affect the mass determination.

For Z production, the effect is larger, and exceeds 0.1% already for $p_T < 25$ GeV. In the electron channel, the recombined invariant mass distribution shows a 0.3% step for $m_{ee} < 85$ GeV. An effect of similar size, but with a smoother mass dependence is observed in the muon channel. These effects are counted as contributions to the Z modeling uncertainty and affect the electron energy scale and muon momentum scale determinations.

PHOTOS, as used in mc11, only handles the final-state photonic corrections (FSR), which dominate the overall higher order electroweak corrections to W and Z production. While the PYTHIA parton shower addresses photon radiation in the initial state, the interference of these with the FSR emissions is neglected, as is fermion-pair production *via* the radiation of virtual photons, and interference between successive FSR photon emissions. The size of the uncertainty due to these missing effects is estimated in Sections 6.3.2 and 6.3.3.

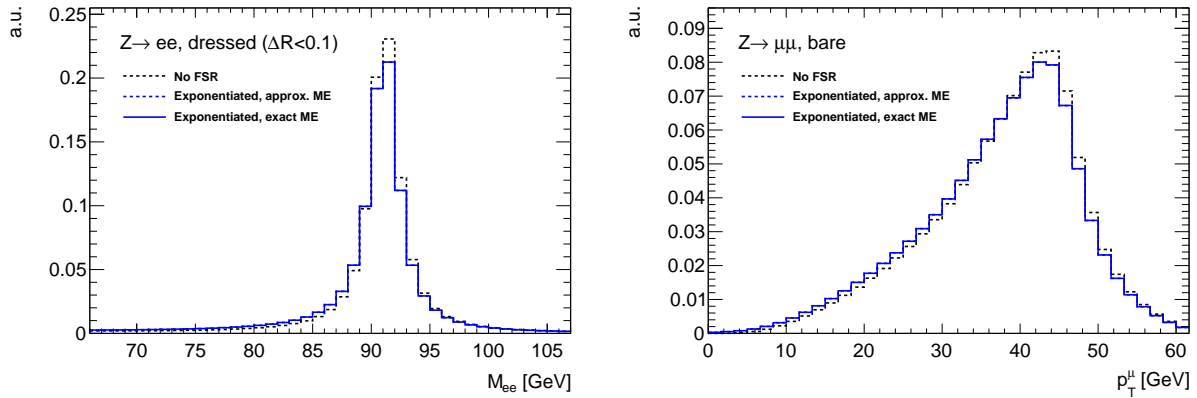


Figure 6.2: Comparison of the electron pair invariant mass distribution (left) and the muon transverse momentum distribution (right) at various levels of QED corrections. “No FSR” refers to Born-level leptons; “approx ME” and “exact ME” refer to the implementations of references [60] and [59] (see text).

6.3.2 Final state fermion pair emissions

A new version of PHOTOS under development adds the emission of at most one fermion (electron or muon) pair to the photon radiation described above. Version 3.60 was tested interfaced to PYTHIA8.175. Half a billion events were generated for each of the four channels under study, $W \rightarrow \ell \nu (n\gamma, \ell^+ \ell^-)$ and $Z \rightarrow \ell^+ \ell^- (n\gamma, \ell^+ \ell^-)$, in two configurations: PHOTOS with only exponentiated photon radiation (Exp) or PHOTOS with exponentiated photon radiation and pair emission (Exp+PE). For W events generated with Exp+PE, for instance, an additional electron pair is emitted in $1.2 \cdot 10^{-3}$ of the events and a muon pair is radiated in $1.4 \cdot 10^{-4}$ of the events.

In figures 6.5-6.6, a comparison between the setting used for the analysis (Exp) and the setting including final state lepton pair emission (Exp+PE) is performed. In the case of W decays (figure 6.5), the charged lepton is the leading one in p_T among the ones with $|\eta| < 2.4$. In the case of Z decays (figure 6.6), the positively and negatively charged leptons are chosen among the ones with $|\eta| < 2.4$ as the leading ones in p_T and the pairs are kept only if their invariant mass lies between 66 and 116 GeV. In this way, figures 6.5-6.6 are directly comparable to figures 6.3-6.4. In W leptonic decays, the effect of final state pair emission is of the order of 0.1 % on charged lepton p_T except at very low p_T (below 10 GeV) and of the order of 0.1 % on W transverse mass. In Z leptonic decays, the effect is less than 0.2 % all over the p_T range except below 10 GeV. The structure of the invariant mass ratio (figure 6.6, bottom line) cannot be explained, neither by acceptance cuts nor by recombination of electrons with nearby photons (for dressed leptons, the transverse momentum of all photons emitted in a cone of radius $\Delta R = 0.1$ around the lepton is added to the lepton p_T). In fact, the dips around 70 and 85 GeV and the threshold at 90 GeV are also present in figure 6.4, so it might be a feature of correction implementation in PHOTOS.

The theoretical uncertainty on the effect of final state lepton pair emission may be estimated by comparing PHOTOS to SANC [61] which implements the complete NLO QED radiative corrections whereas PHOTOS uses kernel approximations and only takes into account the diagrams of figure 6.7 (no ISR and no interference between ISR and FSR). Figure 6.8 shows for $Z \rightarrow \mu^+ \mu^-$ events the relative difference between bare muons after the eventual radiation of an electron pair and born muons as a function of the μ^- p_T . The photon emission has been switched off to give the pair emission effect alone. From this comparison, the two implementations differ by about 30%. Since PHOTOS predicts the largest effect, it will be used to evaluate the systematic uncertainty from not including this process in the simulated samples.

An impact on the vector boson mass extraction has been assessed for the different definitions of charged leptons (bare or dressed) and is reported in Table 6.2. Results in both electron and

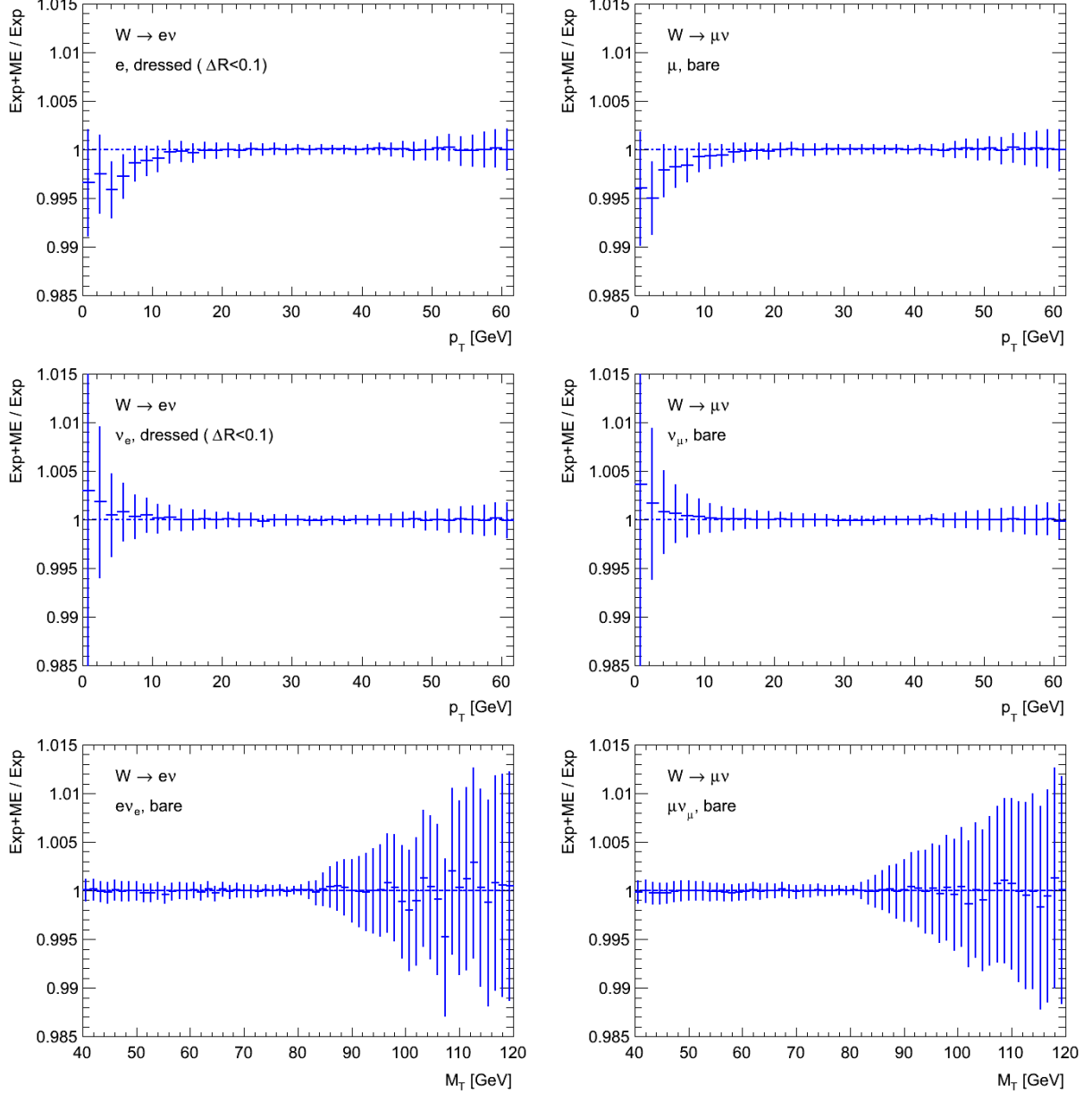


Figure 6.3: Ratios between the “exact ME” and “approx ME” predictions (“Exp+ME/Exp” in the plots), for $W \rightarrow e\nu$ (left) and $W \rightarrow \mu\nu$ (right). The observables shown are charged lepton p_T (top), neutrino p_T (middle), and transverse mass (bottom). Events were generated using POWHEG+PYTHIA, interfaced to PHOTOS.

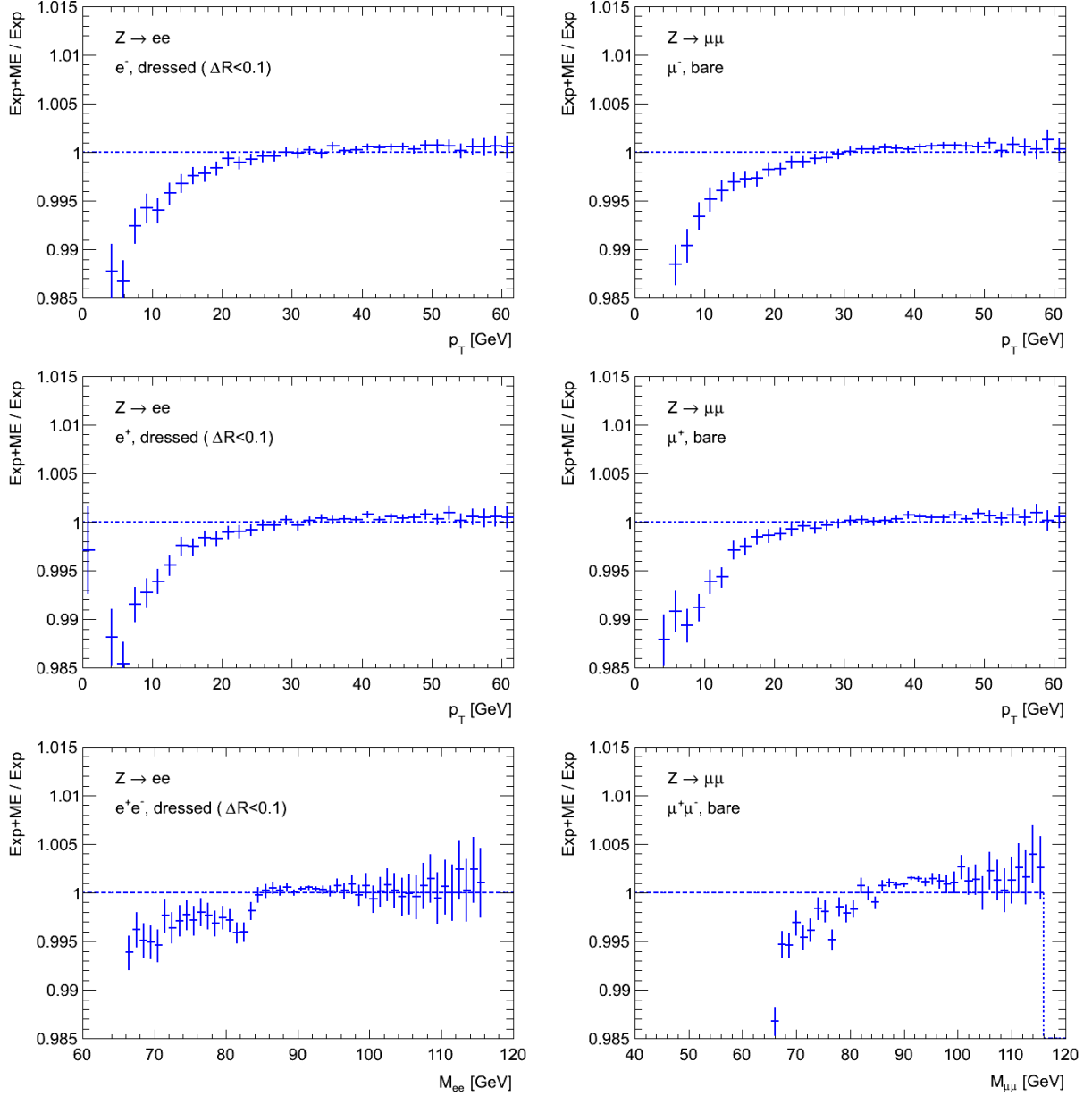


Figure 6.4: Ratios between the “exact ME” and “approx ME” predictions (“Exp+ME/Exp” in the plots), for $Z \rightarrow ee$ (left) and $Z \rightarrow \mu\mu$ (right). The observables shown are negatively charged lepton p_T (top), positively charged lepton p_T (middle), and lepton pair invariant mass (bottom). Events were generated using POWHEG+PYTHIA, interfaced to PHOTOS.

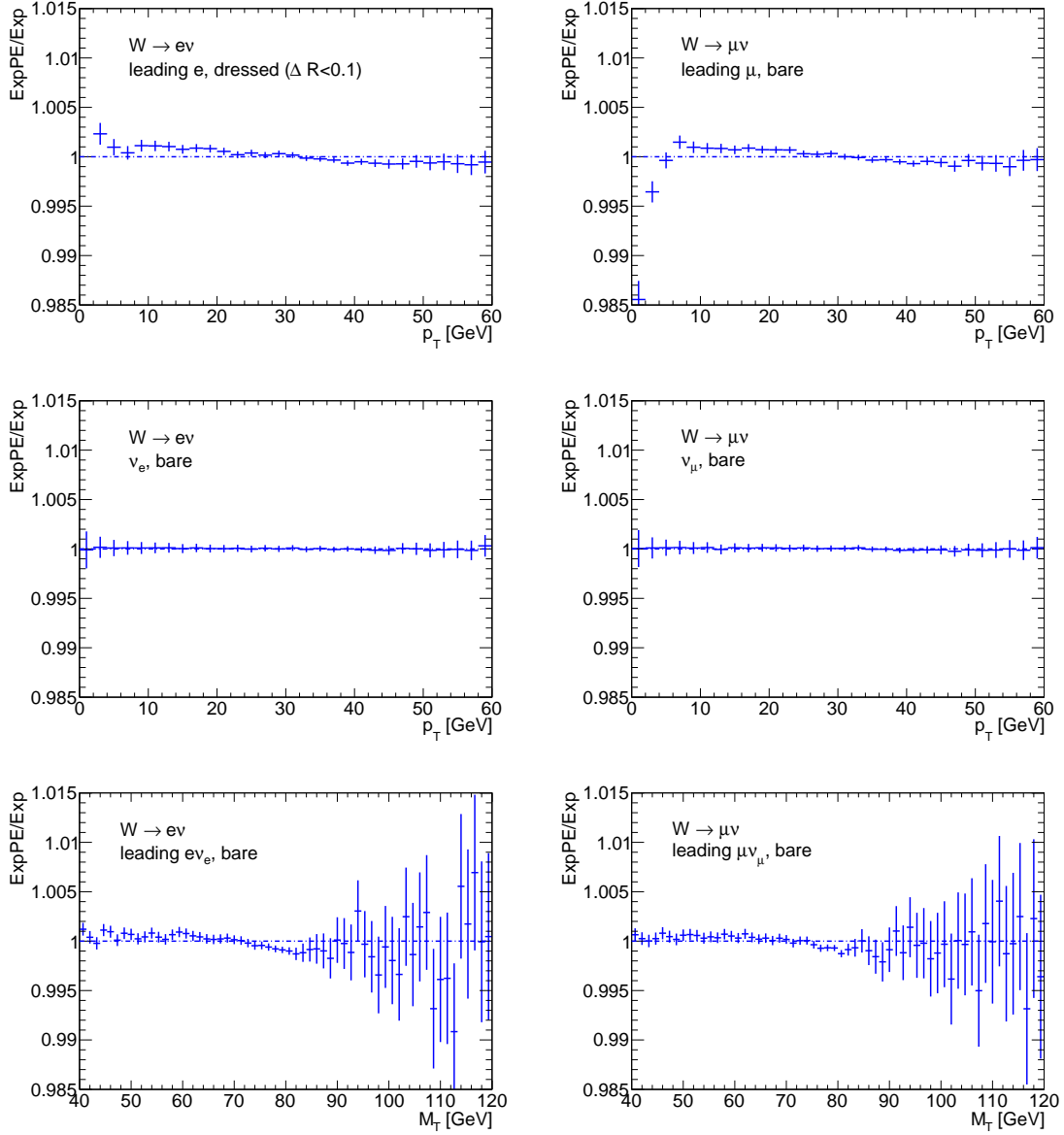


Figure 6.5: Ratios between the "Exp+PE" and "Exp" predictions, for $W \rightarrow e\nu$ (left) and $W \rightarrow \mu\nu$ (right). The observables shown are leading charged lepton p_T (top), neutrino p_T (middle) and transverse mass (bottom). No selection is applied except to require that $|\eta| < 2.4$ for the leading charged lepton. Events were generated using PYTHIA+PHOTOS.

muon channels respect universality of behaviour between leptons and the presented results are the weighted averages of the results in each individual channel. The shifts are always negative which corresponds to the loss of energy of the final state leptons because of lepton pair emission. Not taking into account final state lepton pair emission induces a bias of a 4.4 MeV on the W mass if the chosen distribution is the charged lepton p_T and a bias of less than 1 MeV in the case of m_T . The results are comparable for bare and dressed leptons. These shifts have to be decreased by the constraint coming from energy calibration on the Z dilepton mass, i.e. around 1 MeV for bare leptons and 2 MeV for dressed leptons.

6.3.3 Effect of $O(\alpha)$ electroweak corrections

An evaluation of the remaining higher-order EW effects is presented. The effects not addressed by the above studies include the interference between initial and final state photon radiation, and

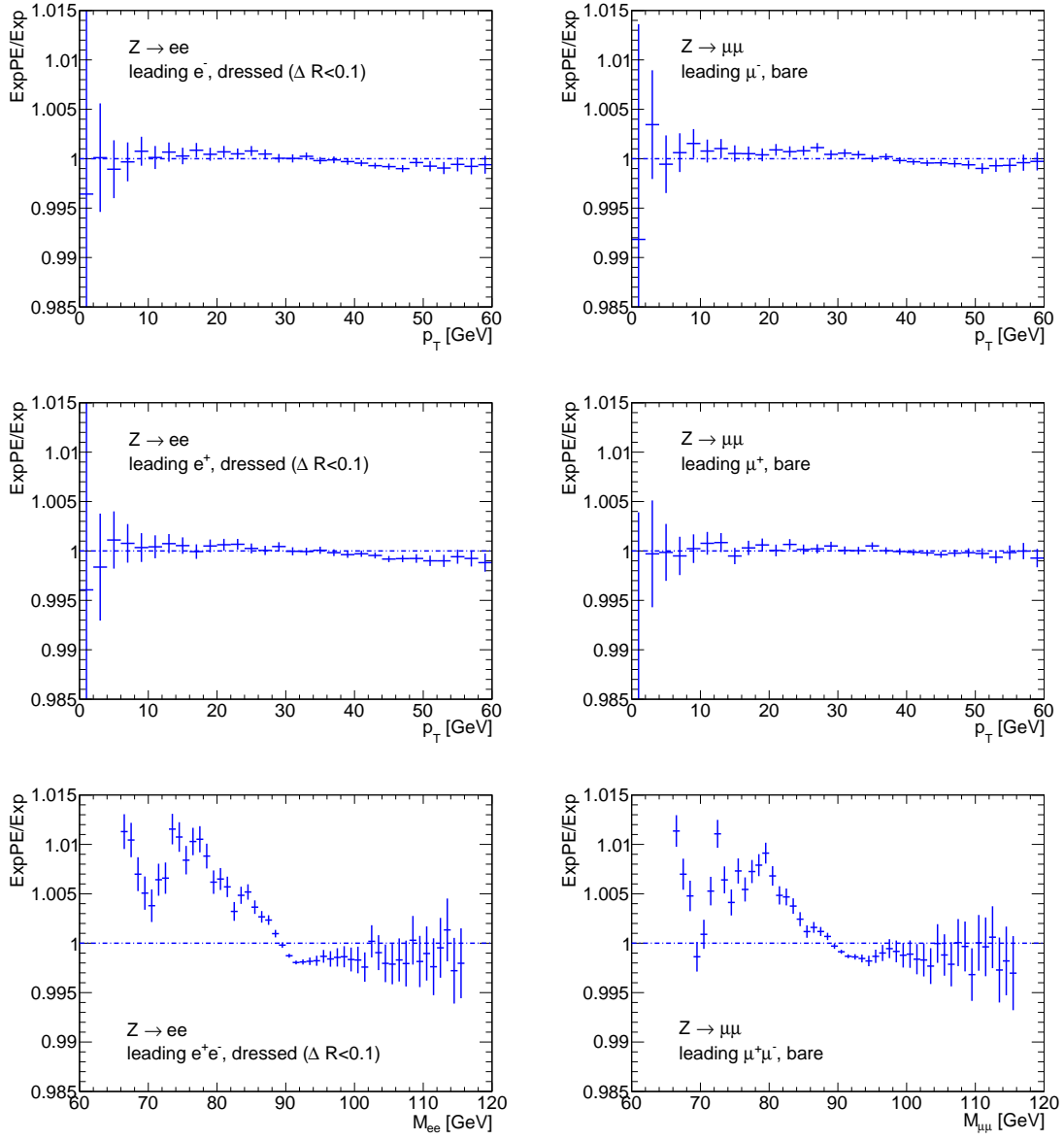


Figure 6.6: Ratios between the "Exp+PE" and "Exp" predictions, for $Z \rightarrow ee$ (left) and $Z \rightarrow \mu\mu$ (right). The observables shown are leading negatively charged lepton p_T (top), leading positively charged lepton p_T (middle) and leading lepton pair invariant mass (bottom). No selection is applied except to require that $|\eta| < 2.4$ for the leading charged leptons. Events were generated using PYTHIA+PHOTOS.

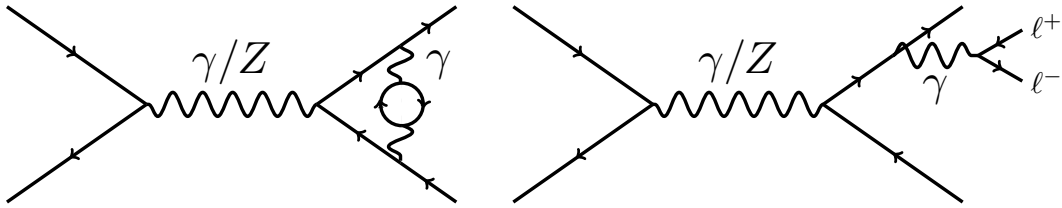


Figure 6.7: Examples of pair emission in Drell-Yan process: virtual pair (left) or real pair (right) NLO correction.

genuine weak corrections such as vertex and box diagrams.

Two programs were used to study this effect. They are briefly described below:

- POWHEG EW [62, 63]: a program combining $O(\alpha_S)$ and $O(\alpha)$ corrections to W and Z

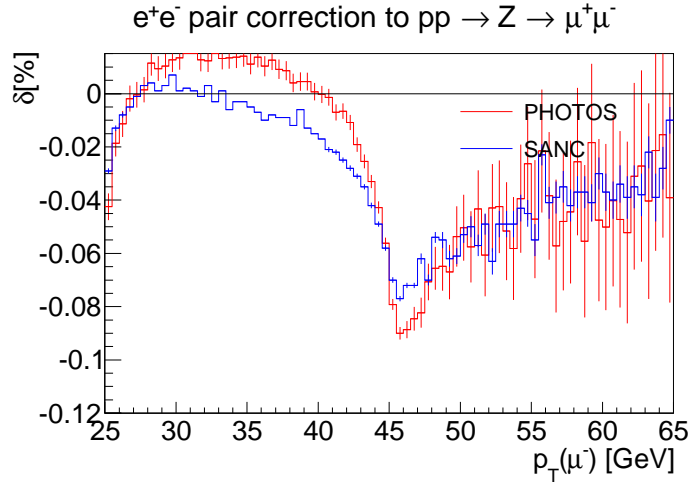


Figure 6.8: Contribution of pair emission to the NLO QED corrections shown as $\delta = \frac{\sigma^{NLO} - \sigma^{Born}}{\sigma^{Born}}$ as a function of the μ^- p_T in $Z \rightarrow \mu^+\mu^-$ events. For the estimation of σ^{NLO} the electron pair emission only has been switched on, there is no photonic radiation.

	Shift on the vector boson mass [MeV]	
	Bare leptons	Dressed leptons
$W \rightarrow \ell\nu, p_T$	$-(4.4 \pm 1.4)$	$-(3.6 \pm 1.4)$
$W \rightarrow \ell\nu, m_T$	$-(0.8 \pm 0.3)$	$-(0.8 \pm 0.3)$
$Z \rightarrow \ell\ell, p_T$	$-(2.3 \pm 1.2)$	$-(3.6 \pm 1.2)$
$Z \rightarrow \ell\ell, m_{\ell\ell}$	$-(0.9 \pm 0.1)$	$-(1.8 \pm 0.1)$

Table 6.2: From the comparison between Exp and Exp+PE versions of PHOTOS, shift on the vector boson mass induced by not taking into account final state lepton pair emission, for the different tested distributions and with the two definitions of boson decay leptons, either bare or dressed. The uncertainties are from the finite size of the generated samples.

production; the PYTHIA parton shower for further initial state parton and photon emissions; and PHOTOS for further final state photon emissions. The PYTHIA and PHOTOS emissions are “vetoed”, i.e. avoid double counting with the emissions from the hard matrix element;

- WINHAC [64], based on SANC [61] for W production described at $O(\alpha)$, PYTHIA for initial state parton and photon emissions; and two implementations of final state radiation: PHOTOS

as above, and the YFS formalism widely used at LEP.

Starting from a set of well-measured fundamental constants, electroweak corrections can be computed in several schemes. Two schemes are used below:

- the α_0 scheme: the Born-level predictions are expressed in terms of the W and Z boson masses m_W , m_Z , and of $\alpha_{\text{QED}}(Q^2 = 0) \sim 1/137$;
- the G_μ scheme: the predictions are expressed in terms of m_W , m_Z and G_μ , implying a tree-level QED effective coupling constant given by $\alpha_{G_\mu} = \frac{\sqrt{2}G_\mu \sin^2 \theta_W m_W^2}{\pi} \sim 1/133$.

The latter is generally considered more accurate, as the initial value of the electromagnetic coupling constant already accounts for part of its evolution between $\alpha(Q^2 = 0) \sim 1/137$ and $\alpha(Q^2 = m_Z^2) \sim 1/128$, therefore incorporating a subset of corrections formally beyond $O(\alpha)$.

In the following sections, we present a study of the decomposition of the EW corrections using WINHAC, a comparison of the POWHEG EW and WINHAC predictions, and finally an evaluation of the impact of these corrections on the measurement. All distributions are shown at the generator level and without any cuts, to maximize the sample statistics and the size of the observed effects.

6.3.3.1 Decomposition of the NLO EW corrections

WINHAC provides handles to study separately the effect of FSR, full QED (ie FSR, ISR, and ISR/FSR interference), and full $O(\alpha)$ corrections (i.e. QED + remaining weak corrections). Figure 6.9 illustrates the various contributions, for the $m_{\ell,\nu}$, m_T , p_T^ℓ and p_T^ν distributions. The QCD parton shower is switched off, ie $p_T^W \sim 0$; the $O(\alpha)$ corrections are computed in the G_μ scheme. Comparing to the Born prediction (left column) shows, as expected, that the FSR corrections dominates the full correction, representing about 99% of the overall effect. The effect is largest on the $m_{\ell,\nu}$ distribution.

Removing the Born prediction (Figure 6.9, right column), and comparing the remaining predictions to the FSR distributions obtained using YFS shows that

- the YFS and PHOTOS FSR predictions match perfectly, in agreement with the small uncertainty on this component discussed in Section 6.3.1;
- non-FSR QED effects represent about two thirds of the total remaining corrections; pure weak effects are sub-leading;
- the corrections are largest in the p_T^ℓ distribution and minimal in the p_T^ν distribution. The m_T distribution, built from the previous two, is in between.

The study is repeated in Figure 6.10, with the QCD parton shower switched on. As expected, the $m_{\ell,\nu}$ and m_T predictions are unaffected, as the QCD emissions typically have low p_T compared to the invariant mass of the final state, and hardly limit the phase space available for the hard process. In contrast, the effect on p_T^ℓ and p_T^ν distributions are washed out due to the non-trivial p_T^W distribution.

The differences between the FSR- and EW-corrected distributions in the presence of the parton shower, i.e. the right columns in Figure 6.10, are relevant to quantify the effects missing in the MC samples. The relative differences are at the level of 0.1% or below, with a smooth behavior around the Jacobian peaks.

6.3.3.2 Comparison of NLO EW corrections in WINHAC and POWHEG

Similar distributions were produced using POWHEG. Although the FSR-level distributions agree perfectly with WINHAC, very different results were obtained for the full EW corrections.

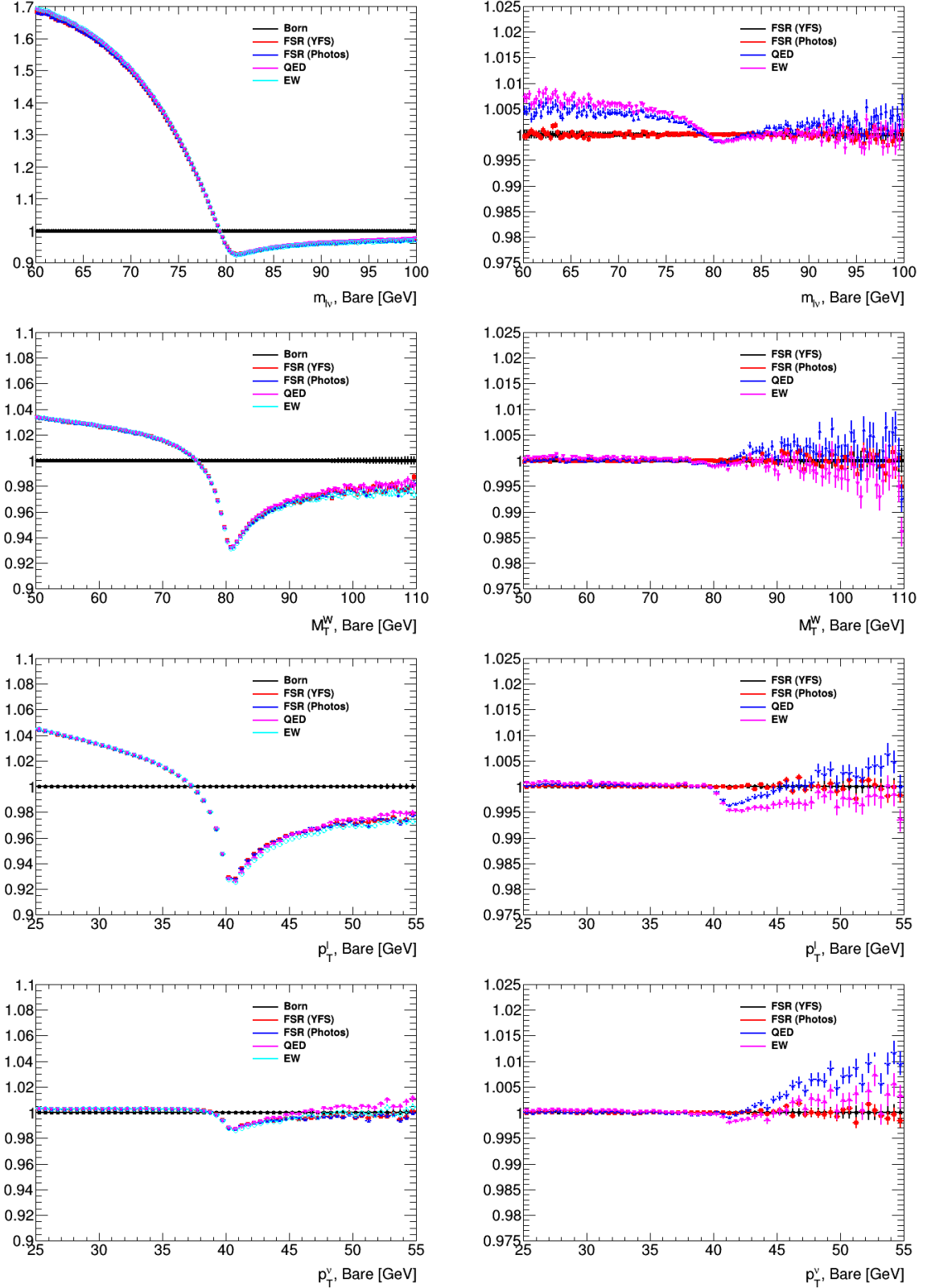


Figure 6.9: FSR, full QED and full NLO EW corrections from WINHAC, in absence of QCD radiations effects (i.e. the parton shower is switched off), for $W \rightarrow \mu\nu$ events using bare kinematics. Left column: the ratios are taken to the Born distributions; right column: the ratio is taken to the FSR-corrected distribution.

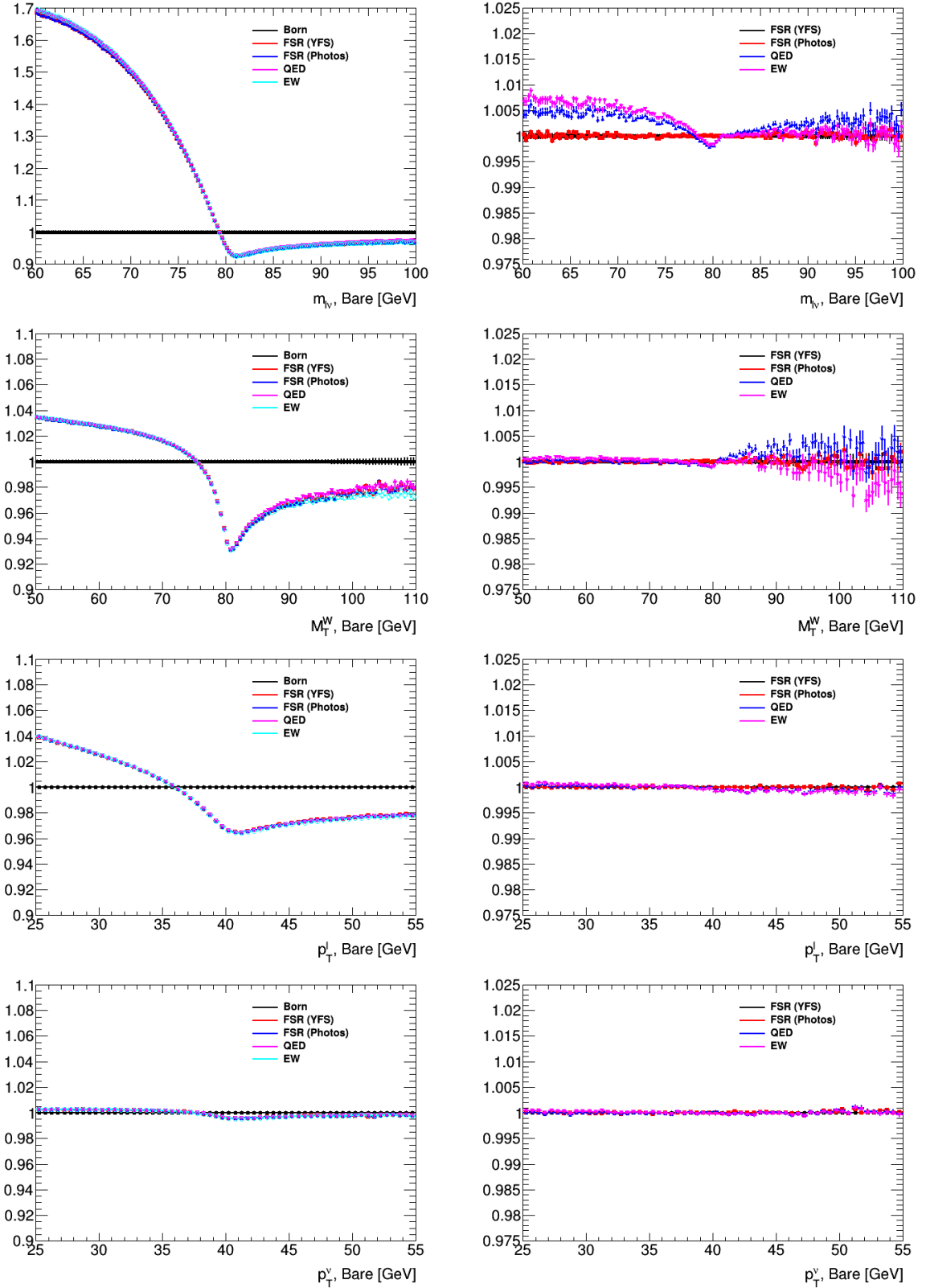


Figure 6.10: FSR, full QED and full NLO EW corrections from WINHAC, with QCD corrections from the PYTHIA parton shower, for $W \rightarrow \mu\nu$ events using bare kinematics. Left column: the ratios are taken to the Born distributions; right column: the ratio is taken to the FSR-corrected distribution.

Investigations on this effect are summarized in Figure 6.11, where the effect of QCD corrections on the distributions is studied at various levels of the electroweak corrections. The Born, FSR and full $O(\alpha)$ distributions are compared in absence and presence of QCD corrections as provided by both programs. The $m_{l\nu}$ distribution is used as main probe, as it is most sensitive to EW corrections and least sensitive to QCD corrections.

In the case of WINHAC, the invariant mass distributions are compared with and without parton shower, separately at the Born level, after FSR and at full $O(\alpha)$. As expected and discussed above, the impact of this variation is very small in all cases.

For POWHEG, the parton shower is applied in both cases, and the QCD variation consists of switching on and off the $O(\alpha_S)$ correction. That is:

- without the $O(\alpha_S)$ correction, only the parton shower is run and the prediction is equivalent to WINHAC from the QCD point of view;
- with the $O(\alpha_S)$ correction, the first parton emission is generated by POWHEG, and the parton shower handles additional radiation, which is constrained to have lower p_T than the parton generated by POWHEG.

In practice, both treatments are very close in terms of the resulting p_T^W distribution, and the main effect is on the process cross section, which is now normalized to NLO in QCD. The impact of the QCD variation applied in POWHEG is thus much smaller than the one applied in WINHAC, as far as the final state distributions are concerned.

Nevertheless, as shown in Figure 6.11, the QCD correction in POWHEG has a 1.5% effect on the low side of the $m_{l\nu}$ distribution, only when EW corrections are applied. As the pattern of the initial state emissions are essentially identical in all cases, it is at present hard to understand what justifies this behavior. Discussions with the authors of both programs are ongoing on this issue. At this stage, the most likely situation is that the interplay of NLO QCD and EW corrections leads to unnatural behavior in the case of POWHEG, and we base the rest of this study on WINHAC only.

6.3.3.3 Scheme dependence and impact on the m_W measurement

Similar distributions are shown in Figure 6.12, comparing the EW-corrected distributions to the FSR-level ones, with and without parton shower. The latter represent the missing effects in the full simulation samples, as mentioned above. The $O(\alpha)$ -corrected predictions are shown in the G_μ and α_0 schemes. For the relevant distributions (p_T^ℓ , p_T^ν and m_T , with parton shower corrections), the scheme dependence of the corrections is comparable to the value of the correction itself, and typically at the level of 0.1% or below.

To evaluate the impact on the m_W measurement, pseudo-data are generated including full $O(\alpha)$ corrections, and templates are generated for different values of m_W and including only FSR corrections. The W boson mass is then fitted and the difference between the fitted and injected values is taken as systematic uncertainty related to this effect. This exercise is repeated for both schemes, with parton shower switched on.

The results are summarized in Table 6.3. The effects are generally found larger for G_μ , with typically 3.5 MeV for the p_T^ℓ distributions, 2.5 MeV for m_T , and 0.6 MeV for p_T^ν . The statistical accuracy on these estimates is about 0.2 MeV. As these effects are absent from the full simulation samples, the full size of the effect found for G_μ is taken as uncertainty estimate.

6.3.3.4 Summary of uncertainties from higher-order EW corrections

This section summarizes the quality of the IBA in the context of the m_W measurement. The systematics are estimated by applying the template fit method which is used for W mass extraction and is described later in Section 8.1.1. The signal regions are defined as follows:

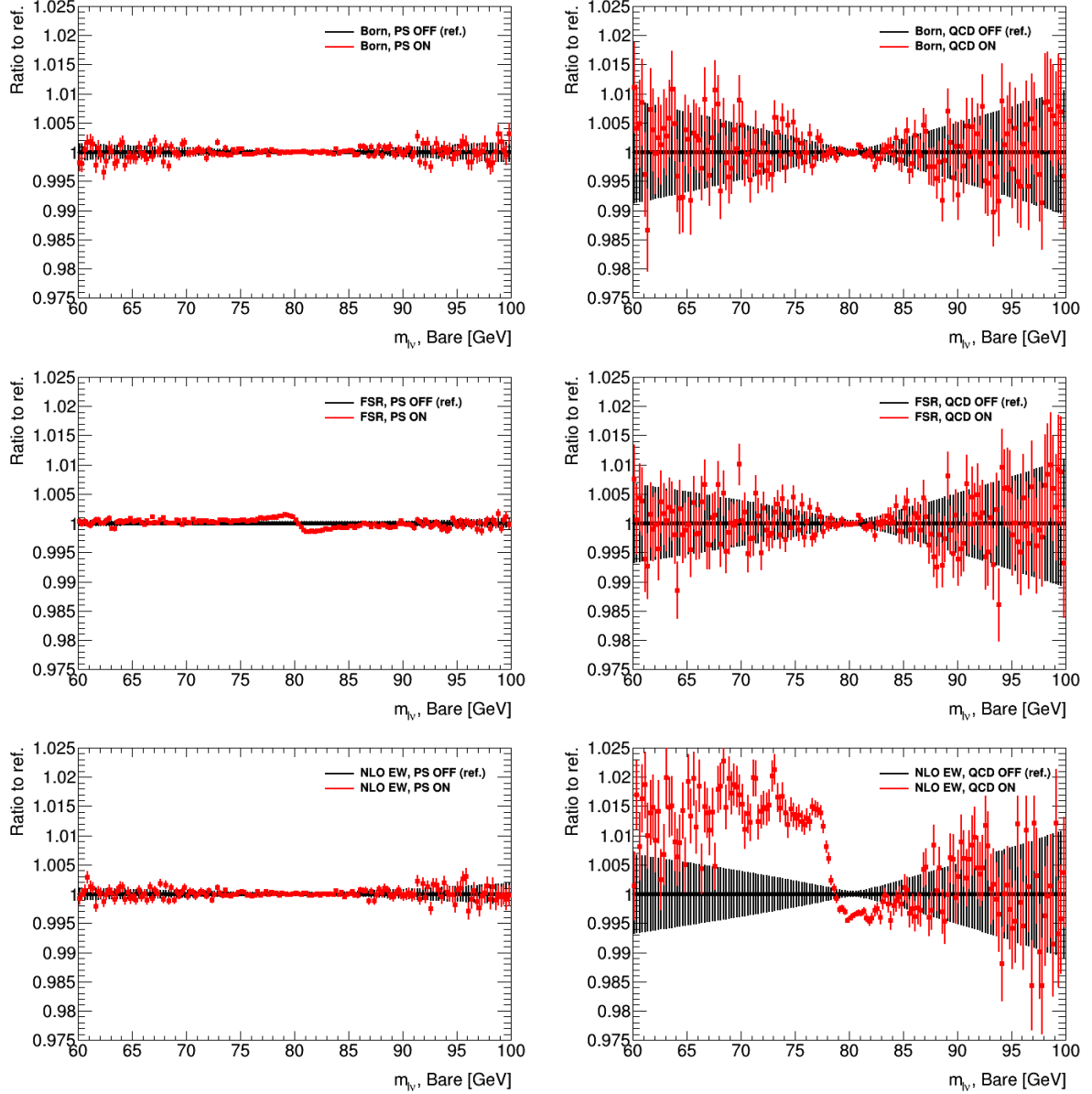


Figure 6.11: Effect of QCD corrections on the muon-neutrino invariant mass distribution. Left column: effect of switching the parton shower on and off in WINHAC, on the Born-level distribution (top), on the distribution after FSR (middle), and for the NLO EW distribution (bottom). Right column: effect of switching the $O(\alpha_S)$ correction on and off in POWHEG, while keeping the parton shower active. Born-level distribution (top), distribution after FSR (middle), and NLO EW distribution (bottom).

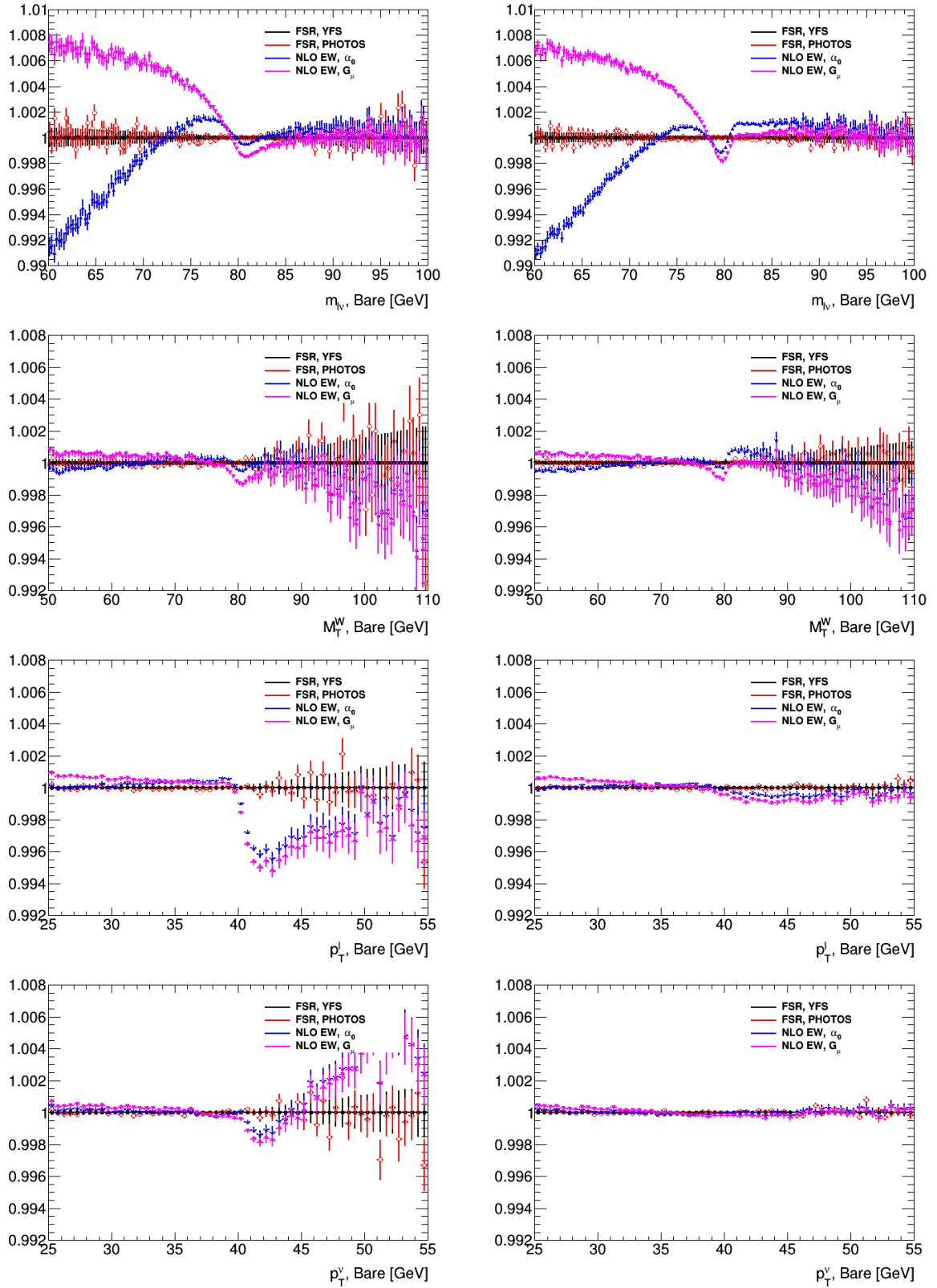


Figure 6.12: Comparison of the EW-corrected kinematic distributions, in the G_μ and α_0 schemes, to the FSR-corrected predictions, using WINHAC. Left: without parton shower; right: with parton shower.

Scheme	p_T^e	$m_T^{e\nu}$	p_T^ν	p_T^μ	$m_T^{\mu\nu}$
G_μ	3.3	2.5	0.6	3.5	2.5
α_0	2.4	0.8	< 0.1	0.8	0.5

Table 6.3: Systematic effect on the m_W measurement (in MeV) from EW corrections beyond FSR, in the G_μ and α_0 schemes.

- W : $|\eta| < 2.4$; $p_T^\ell > 30$ GeV; $p_T^\nu > 30$ GeV; $m_T^W > 60$ GeV; $p_T^W < 30$ GeV;
- Z : $|\eta| < 2.4$; $p_T^\ell > 25$ GeV; $66 < m_{\ell\ell} < 116$ GeV.

Using the reweighting technique described there, p_T^l , m_T and $m_{\ell\ell}$ distributions are produced for different W and Z boson masses. Minimizing the χ^2 between the templates and the pseudodata yields the fitted W boson mass, and the difference between the injected mass and the fitted mass for each pseudo-data sample defines the corresponding uncertainty. The fitting ranges are, for W events, $30 < p_T^l < 50$ GeV, $60 < m_T < 100$ GeV; and for Z events, $25 < p_T^l < 55$ GeV, $80 < m_{\ell\ell} < 100$ GeV.

This procedure is applied to the Z process, to estimate modeling uncertainties affecting the energy and momentum scale determination, and to the W process to estimate the impact on the m_W measurement itself. For the Z analysis, an additional uncertainty contribution is induced by the experimental accuracy on m_Z , $\delta m_Z = 2.1$ MeV. The results are summarized in Tables 6.4 and 6.5. The pair emission uncertainties result from Section 6.3.2, and the $O(\alpha)$ uncertainties from Section 6.3.3.

Source	m_{ee}	p_T^e	$m_{\mu\mu}$	p_T^μ
FSR (real)	0.4×10^{-5}	3.0×10^{-5}	0.3×10^{-5}	3.0×10^{-5}
FSR (pair production)	2.0×10^{-5}	4.0×10^{-5}	1.0×10^{-5}	2.5×10^{-5}
Weak + interf. corrections	—	—	—	—
δm_Z	2.3×10^{-5}	2.3×10^{-5}	2.3×10^{-5}	2.3×10^{-5}
Total	3.1×10^{-5}	5.5×10^{-5}	2.5×10^{-5}	4.5×10^{-5}

Table 6.4: Relative systematic uncertainties on the energy and momentum scale measurement, from higher-order EW corrections in $Z \rightarrow \ell\ell$ events. The table entries express relative energy scale uncertainties. The dashes indicate cases where the effect is negligibly small.

Source	p_T^e	$m_T^{e\nu}$	p_T^ν	p_T^μ	$m_T^{\mu\nu}$
FSR (real)	—	—	—	—	—
FSR (pair production)	3.6	0.8	—	4.4	0.8
Weak + interf. corrections	3.3	2.5	0.6	3.5	2.5
Total	4.9	2.6	0.6	5.6	2.6

Table 6.5: Systematic uncertainties on the m_W measurement (in MeV), from higher-order EW corrections in $W \rightarrow l\nu$ events, in MeV. The dashes indicate cases where the effect is negligibly small.

6.4 Rapidity distribution and angular coefficients at $O(\alpha_S^2)$

The differential cross section as a function of boson rapidity, $\frac{d\sigma}{dy}$, and the angular coefficients as a function of boson y and p_T , $A_i(y, p_T)$, are modeled with fixed order perturbative QCD predictions, at $O(\alpha_S^2)$ in the perturbative expansion of the strong-coupling constant.

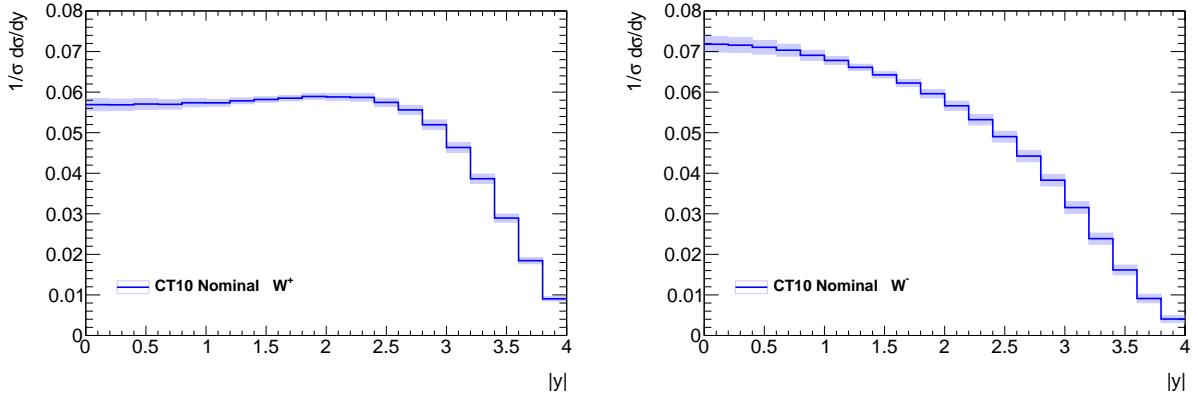


Figure 6.13: Differential cross section of W^+ (left) and W^- (right) production as a function of rapidity for the CT10nnlo PDF set. The blue line and the red line show predictions to the W - and Z -boson rapidity measurements, respectively. The shadowed bands correspond to the PDF uncertainty.

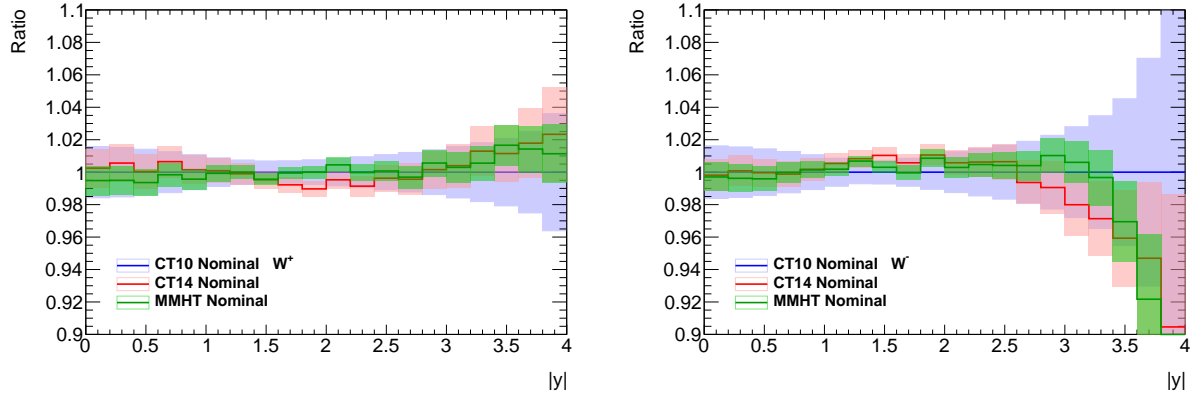


Figure 6.14: Ratio of differential cross section of W^+ (left) and W^- (right) production as a function of rapidity for the CT10nnlo (blue), CT14nnlo (red), and MMHT2014nnlo (green) PDF sets. The shadowed bands correspond to the PDF uncertainty.

6.4.1 Differential predictions as function of rapidity with CT10, CT14, and MMHT PDFs

Figure 6.13 shows the differential cross section of W^+ and W^- production as a function of rapidity at NNLO, for the CT10nnlo PDF and for the CT10nnlo PDF profiled to the W - and Z -boson rapidity measurements.

Figure 6.14 shows the comparison of CT10nnlo, CT14nnlo [65] and MMHT2014nnlo [66] PDF sets.

To validate the theoretical predictions used for the modeling in the current analysis, Figure 6.15 illustrates the comparisons of predicted Z -boson differential cross-section as a function of rapidity and W -boson differential cross-section as a function of lepton pseudorapidity to the corresponding measurements using $\sqrt{s} = 7$ TeV data. Agreement between experimental measurements and theoretical predictions is observed.

6.4.2 Angular coefficients in POWHEG, DNNLO

The angular distribution of the W and Z decay leptons are determined by the boson polarization state. In amplitudes at higher order than tree level, initial-state QCD interactions of the colliding partons provide transverse momentum to the W or Z , in turn affecting the polarization

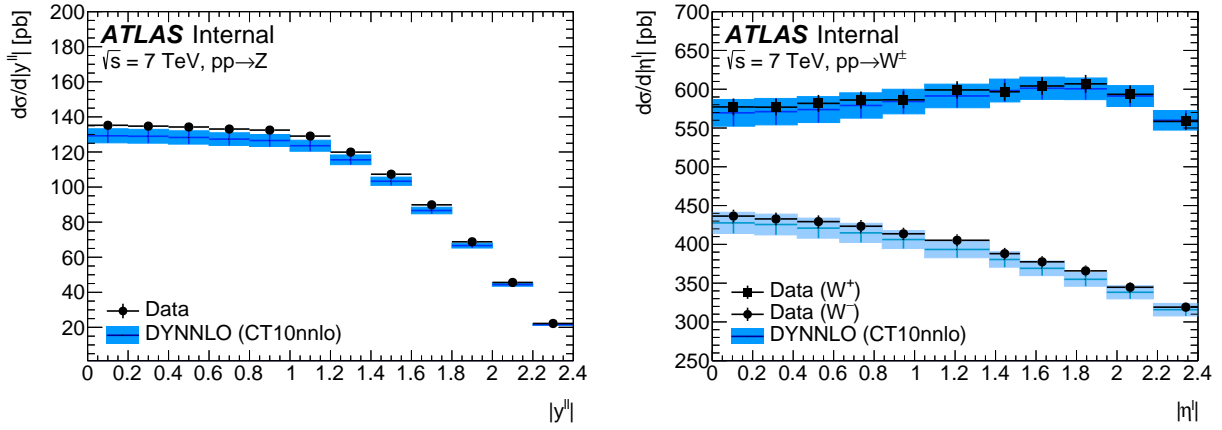


Figure 6.15: (a) Differential Z -boson cross-section as a function of boson rapidity, and (b) differential W^+ and W^- cross-sections as a function of charged decay-lepton pseudorapidity at $\sqrt{s} = 7$ TeV [55]. The measured cross sections are compared to the DYNLO predictions using the CT10nnlo PDF set. The vertical bars show the total experimental uncertainties, including luminosity uncertainty, and the bands show the PDF uncertainties of the predictions.

states. The full five-dimensional differential cross-section describing the kinematics of the leptons from the boson decay can be decomposed as a sum of nine harmonic polynomials, which depend on the polar $\cos\theta$ and azimuthal ϕ angles of the lepton in the rest frame of the boson, multiplied by corresponding helicity cross-sections that depend on the boson transverse momentum p_T , rapidity y and invariant mass M . It is a standard convention to factorise out the unpolarised cross-section and to present the five-dimensional differential cross-section as an expansion into nine harmonic polynomials $P_i(\cos\theta, \phi)$ and dimensionless angular coefficients A_i , which represent ratios of helicity cross-sections with respect to the unpolarised one and are functions of the boson kinematic variables.

$$\begin{aligned} \frac{d\sigma}{dp_T^2 dy dM d\cos\theta d\phi} &= \frac{3}{16\pi} \frac{d\sigma}{dp_T^2 dy dM} \times [(1 + \cos^2\theta) + A_0 \frac{1}{2}(1 - 3\cos^2\theta) \\ &\quad + A_1 \sin 2\theta \cos \phi \\ &\quad + A_2 \frac{1}{2} \sin^2\theta \cos 2\phi \\ &\quad + A_3 \sin \theta \cos \phi \\ &\quad + A_4 \cos \theta \\ &\quad + A_5 \sin^2\theta \sin 2\phi \\ &\quad + A_6 \sin 2\theta \sin \phi \\ &\quad + A_7 \sin \theta \sin \phi] \end{aligned} \quad (6.7)$$

The A_i coefficients nearly vanish towards $p_T = 0$, except for A_4 , which is sensitive to the electroweak mixing angle $\sin^2\theta_W$ and responsible for the forward-backward lepton asymmetry in $\cos\theta$. The $A_5 - A_7$ coefficients appear at second order in α_S and are expected to be small; they are therefore not considered here.

To extract the A_i coefficients from simulated Monte-Carlo samples, one can calculate moments of each harmonic polynomial as:

$$\langle P_i(\cos\theta, \phi) \rangle = \frac{\int P_i(\cos\theta, \phi) \sigma(p_T, y, M, \theta, \phi) d\cos\theta d\phi}{\int \sigma(p_T, y, M, \theta, \phi) d\cos\theta d\phi} \quad (6.8)$$

where $\sigma(p_T, y, M, \theta, \phi)$ is a shorthand for the l.h.s of Equation 6.7; $P_0(\cos\theta, \phi) = 1 - 3\cos^2\theta$,

$P_1(\cos\theta, \phi) = \sin 2\theta \cos \phi$, etc. The integration is performed over the full angular phase space, leading to:

$$\begin{aligned}
A_0 &= \frac{2}{3} + \frac{10}{3} \langle (1 - 3 \cos^2 \theta) \rangle \\
A_1 &= 5 \langle \sin 2\theta \cos \phi \rangle \\
A_2 &= 10 \langle \sin^2 \theta \cos 2\phi \rangle \\
A_3 &= 4 \langle \sin \theta \cos \phi \rangle \\
A_4 &= 4 \langle \cos \theta \rangle \\
A_5 &= 5 \langle \sin^2 \theta \sin 2\phi \rangle \\
A_6 &= 5 \langle \sin 2\theta \sin \phi \rangle \\
A_7 &= 4 \langle \sin \theta \sin \phi \rangle
\end{aligned} \tag{6.9}$$

In general, these coefficients are a function of p_T , y and M . The mass dependence is however negligible, and we map them only as a function of p_T and y . Angular coefficients obtained from POWHEG and DYNNLO [67], a program for fixed-order W and Z cross section calculation at NLO and NNLO, are shown in Figure 6.16 for Z , W^+ and W^- events, as a function of $p_T(W, Z)$. The coefficients are computed in the Collins-Soper (CS) rest frame. The CS rest frame is reached from the laboratory frame via a Lorentz boost along the laboratory z axis into a frame where the z component of the lepton pair momentum is zero, followed by a boost along the transverse momentum of the pair. At $p_T = 0$, the CS and laboratory coordinate systems are the same. DYNNLO is shown for comparison to the baseline Monte-Carlo used in this analysis, POWHEG+PYTHIA8 (ME+PS NLO generator). DYNNLO provides an inclusive fixed-order pQCD predictions at NLO and at NNLO with the CT10 pdf NLO and NNLO configurations. The polarisation coefficients A_3 and A_4 from DYNNLO at NLO and NNLO have been scaled, in Z events, by a factor 0.65 to account for radiative corrections to the weak mixing angle, modifying these coefficients with respect to the LO value used by default in this program. Significant differences are observed in the coefficients. For A_0 , POWHEG differs from DYNNLO at low p_T . For other coefficients, NNLO effects are large when compared to the NLO predictions. This is particularly true for A_1 and A_2 .

The effect of these differences are potentially large on the final state kinematics distributions. This is illustrated in Figure 6.17 where, using a reweighting in full (p_T, y, A_i) space, the POWHEG angular coefficients are transformed to the DYNNLO prediction. The effect of this change on the lepton p_T spectrum is very significant, with a $\sim 1\%$ distortion near the Jacobian peak ($p_T \sim 40$ GeV). The p_T^Z distribution is unaffected, as expected. This corresponds to a shift of about 90 MeV in the mass measurement.

The validity of the modeling of the angular coefficients in Z -boson events is tested by comparing the predictions of A_i as a function of p_T to the ATLAS measurement at $\sqrt{s} = 8$ TeV. Figure 6.18 shows the comparison for A_0 and A_2 as a function of the transverse momentum of the Z boson.

6.5 Transverse momentum distribution

Predictions of the vector boson p_T spectrum for the extraction of the mass of the W -boson cannot rely solely on fixed order perturbative QCD. The majority of the W -boson events used for the analysis are at low values of boson transverse momentum, $p_T^W < 30$ GeV, where large logs of the type $\log(m_V/p_T)$ need to be resummed, and non-perturbative effects must be included, either with parton showers or predictions based on analytic resummation. The modeling of the transverse-momentum spectrum of vector bosons at given rapidity is based on the parton shower MC generator PYTHIA8. The predictions of vector-boson production in the PYTHIA8 MC generator employ leading order matrix elements for the $q\bar{q}' \rightarrow W, Z/\gamma^*$ processes, complemented by a reweighting of the first parton shower emission to the leading order V +jet cross section, with $V = W, Z/\gamma^*$. The resulting prediction of the boson transverse-momentum spectrum is comparable in accuracy

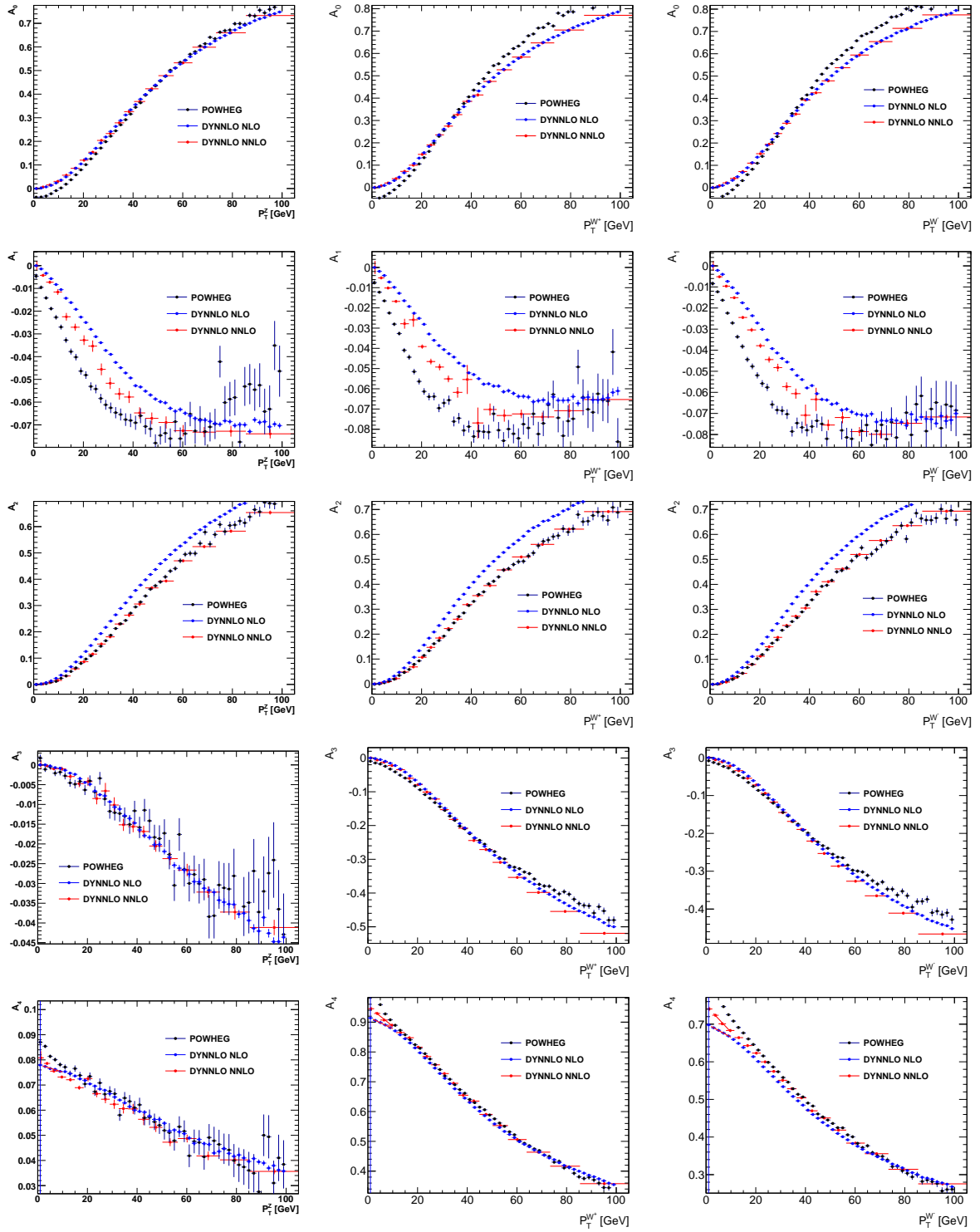


Figure 6.16: Angular coefficients for the Z , W^+ and W^- bosons for POWHEG+PYTHIA8, DYNLO NLO and DYNLO NNLO .

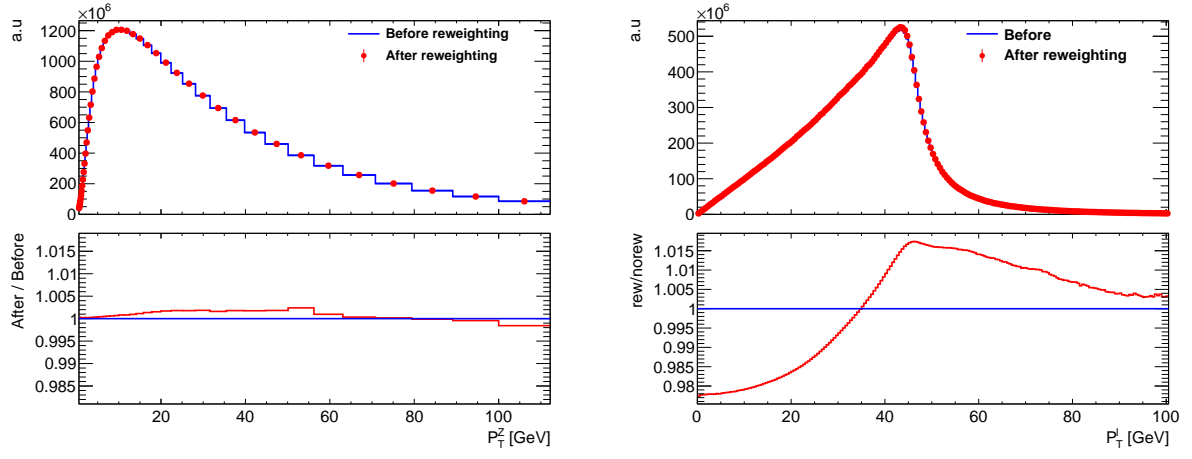


Figure 6.17: p_T distributions of the Z boson (left) and decay lepton (right) at the truth level before and after polarisation reweighting of the angular coefficients from POWHEG to DYNNLO.

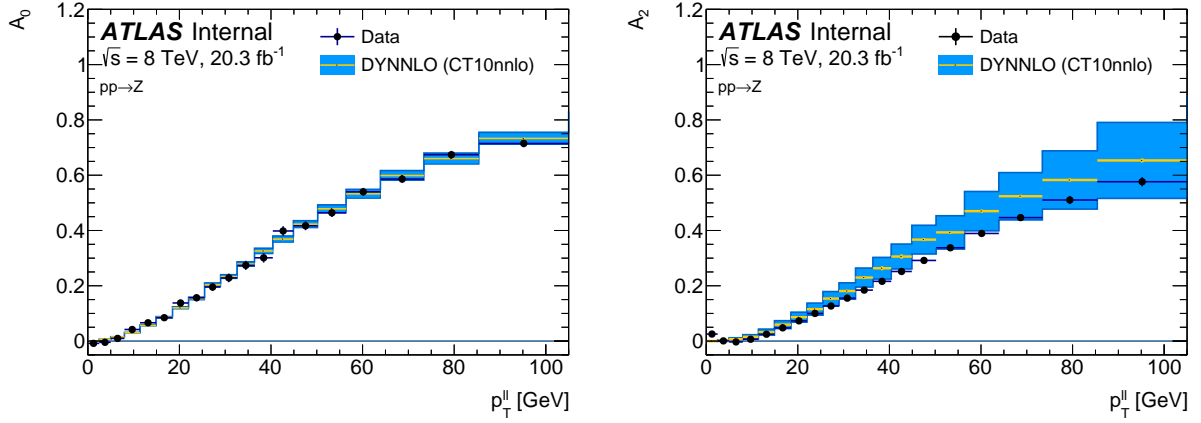


Figure 6.18: The (a) A_0 and (b) A_2 angular coefficients in Z -boson events as a function of p_T . The measured coefficients are compared to the DYNNLO predictions using the CT10nnlo PDF set. The vertical bars show the total experimental uncertainties, and the bands show the uncertainties assigned to the theoretical predictions.

to those of NLO parton shower generators as POWHEG, and of resummed predictions at next-to-leading logarithmic order [68].

6.5.1 Baseline prediction

The optimal values for the QCD parameters used in PYTHIA8 were determined by fitting the predictions to the Z -boson transverse momentum distribution measured with the ATLAS detector at a centre-of-mass energy of $\sqrt{s} = 7$ TeV. Three QCD parameters were considered in the fit: the intrinsic, or primordial, transverse momentum of the incoming partons, the value of the strong-coupling constant at the Z -boson mass used for the QCD ISR, and the value of the ISR infrared cut-off. The resulting values of the PYTHIA8 parameters constitute the AZ tune, and they are used for predicting the p_T^W spectrum. The modelling of the transverse-momentum spectrum is validated by comparing the Z -boson p_T distribution from the simulated samples to the measurement used to determine the AZ tune.

The modelling of the transverse-momentum spectrum is validated by comparing the Z -boson p_T distribution from the simulated samples to the measurement used to determine the AZ tune. As

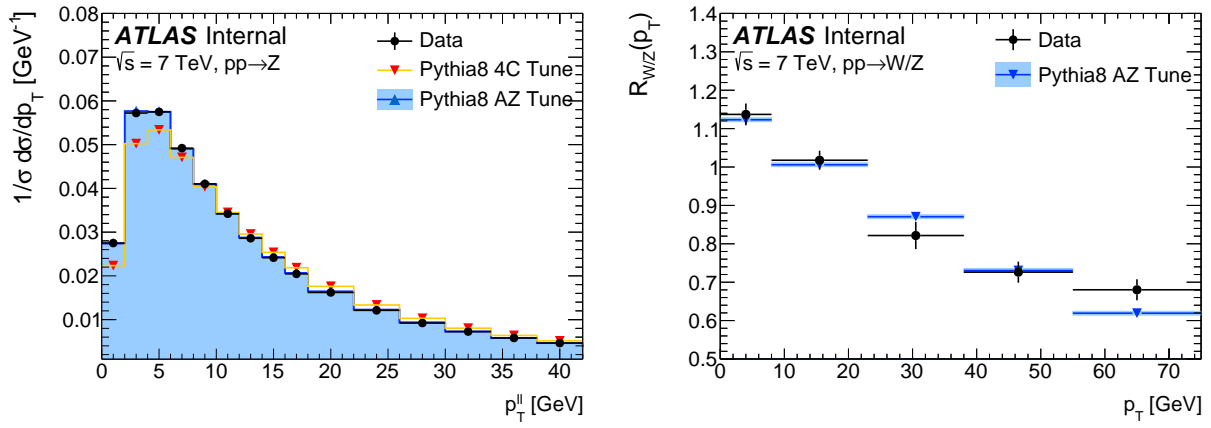


Figure 6.19: Measured differential cross section of $p_T(Z)$ (left) and the differential cross-section ratio of $\sigma(W)/\sigma(Z)$ vs. $p_T(V=W,Z)$ (right) compared to the POWHEG+PYTHIA prediction, reweighted to the AZ tune. Statistical and experimental systematic uncertainties are indicated.

a further validation, the predicted differential cross-section ratio

$$R_{W/Z}(p_T) = \left(\frac{d\sigma_W(p_T)}{dp_T} \cdot \frac{1}{\sigma_W} \right) \left(\frac{d\sigma_Z(p_T)}{dp_T} \cdot \frac{1}{\sigma_Z} \right)^{-1}$$

is compared to the corresponding ratio of ATLAS measurements of vector-boson transverse momentum. The comparisons are shown in Figure 6.19, the theoretical predictions are in agreement with the experimental measurements.

6.5.2 Uncertainties on the p_T^W distribution with PYTHIA

Since the p_T^Z distribution is constrained using data, and the W distribution is predicted with corresponding parton shower parameters, the modeling uncertainty on the p_T^W distribution gets three contributions:

- the accuracy of the Z data, which translates into an uncertainty on the parton shower parameters which directly applies to p_T^W ;
- the uncertainty on the p_T^W/p_T^Z distribution ratio, under variation of the model parameters that are assumed fixed in the Z tune;
- the uncertainty on the p_T^W/p_T^Z distribution ratio under variation of the PDF used in the matrix element. This contribution is actually part of the PDF uncertainty on the description of the process (the rapidity and polarization uncertainties are evaluated using fixed-order QCD, as discussed above), but included here.

The first contribution is evaluated using the eigentune variations illustrated in Figure 6.20. For each variation, an uncertainty of about 0.3% is obtained in the low p_T^W region. Summing in quadrature, 0.5% is found.

The following parton shower model parameters were assumed fixed for the AZ' tune, and varied here:

- the factorization scale, $\mu_F = k \cdot p_T$, within a factor 2 around its default value $k = 1$;
- the charm quark mass, varied between 1 and 2 GeV for a default value of 1.5 GeV;
- the bottom quark mass, varied between 4 and 5.5 GeV for a default value of 4.8 GeV;

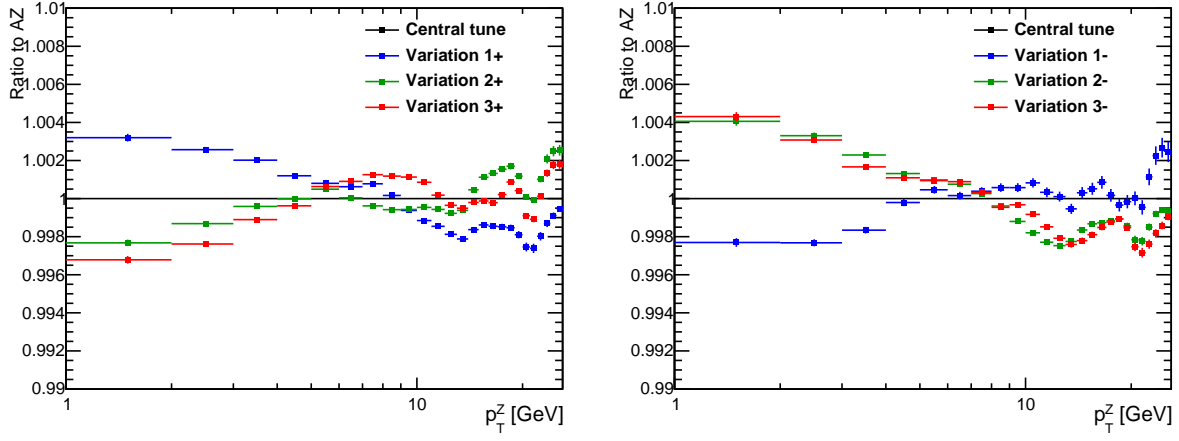


Figure 6.20: Ratio between the p_T^W distribution obtained from the tune variations ($1\pm$, $2\pm$, $3\pm$) and the nominal tune.

- the LO PDF used in the parton shower to determine the evolution. Following the previous section, CTEQ6L1, CT14LO [65] and NNPDF2.3LO [69] are used as variations with respect to MMHTLO [66].

The results of these variations are shown for the separate processes in Figures 6.21-6.24.

The charm quark mass variation has a $\sim 0.5\%$ effect at low p_T , specifically for W . The b mass variations has negligible impact on all processes. The effects of the quark mass variations are found to be very similar for W^+ and W^- and shown only for W^\pm .

The LO PDF choice also has a correlated impact on W and Z production, but differences of about 1% are visible; as shown in Figure 6.23, the W^+/Z differences tends to be opposite in direction to the W^-/Z ones.

The effect of the μ_F variations is very similar for W and Z production, and the uncertainty on the W/Z transverse momentum distribution ratio appears very small when the effect of the μ_F variations is assumed fully correlated between the two processes. This can be questioned, as the involved partonic sub-processes differ, notably in the fractions of incoming heavy quarks. To test this a decorrelation model was designed with independent μ_F variations for four categories of process: heavy flavour Z production (cc and bb), heavy flavour W production and light flavours (W and Z together).

Separate histograms of the boson p_T were produced using PYTHIA for each combination of the initial state quarks. These were:

- $u\bar{u}, d\bar{d}, s\bar{s}, c\bar{c}$ and $b\bar{b}$ (Z)
- $u\bar{d}, u\bar{s}, c\bar{d}, c\bar{s}$ (W^+)
- $d\bar{u}, s\bar{u}, d\bar{c}, s\bar{c}$ (W^-)

Bottom initiated W production is neglected. Each of these histograms were produced for up and down variations of μ_F , as well as for the nominal value. Note in the following the contributions from W^+ and W^- are summed together and referred to as W .

The four sub-process categories for which independent variations are performed are:

- Light quark induced production: $uu \rightarrow Z$, $dd \rightarrow Z$, $ss \rightarrow Z$, and $ud \rightarrow W$, $us \rightarrow W$
- Charm-induced Z production: $cc \rightarrow Z$
- Bottom-induced Z production: $bb \rightarrow Z$

Source	Typical size
Eigentune variations	0.5% (three independent contributions)
Factorization scale	1.3%
Charm mass	0.5%
Parton shower PDF	+1.5% (W^+), -1% (W^-)
Total	2.1% (W^+), 1.8% (W^-)

Table 6.6: Summary of the sources of uncertainty in the p_T^W distribution.

- Charm-induced W production: $cx \rightarrow W$

The quantity of interest is the ratio of the W p_T spectrum to the Z p_T spectrum. The W and Z spectra are normalised before the ratio is taken. The nominal (nom) ratio is given in Equation 6.10.

$$\text{Nom} = \frac{ud(\text{nom}) + us(\text{nom}) + cd(\text{nom}) + cs(\text{nom})}{uu(\text{nom}) + dd(\text{nom}) + ss(\text{nom}) + cc(\text{nom}) + bb(\text{nom})} \quad (6.10)$$

The ratio definitions for the μ_F up variations are given in Equations 6.11 to 6.14. To obtain the μ_F down variations replace (up) with ($down$).

$$\text{LightUp} = \frac{ud(up) + us(up) + cd(\text{nom}) + cs(\text{nom})}{uu(up) + dd(up) + ss(up) + cc(\text{nom}) + bb(\text{nom})} \quad (6.11)$$

$$\text{ccZUp} = \frac{ud(\text{nom}) + us(\text{nom}) + cd(\text{nom}) + cs(\text{nom})}{uu(\text{nom}) + dd(\text{nom}) + ss(\text{nom}) + cc(up) + bb(\text{nom})} \quad (6.12)$$

$$\text{bbZUp} = \frac{ud(\text{nom}) + us(\text{nom}) + cd(\text{nom}) + cs(\text{nom})}{uu(\text{nom}) + dd(\text{nom}) + ss(\text{nom}) + cc(\text{nom}) + bb(up)} \quad (6.13)$$

$$\text{cxWUp} = \frac{ud(\text{nom}) + us(\text{nom}) + (cd(up) + cs(up))/2}{uu(\text{nom}) + dd(\text{nom}) + ss(\text{nom}) + cc(\text{nom}) + bb(\text{nom})} \quad (6.14)$$

The total up and $down$ variations are defined as follows:

$$\text{TotalUp} = \sqrt{(\text{LightUp-Nom})^2 + (\text{ccZUp-Nom})^2 + (\text{bbZUp-Nom})^2 + (\text{cxWUp-Nom})^2} \quad (6.15)$$

$$\text{TotalDown} = \sqrt{(\text{LightDown-Nom})^2 + (\text{ccZDown-Nom})^2 + (\text{bbZDown-Nom})^2 + (\text{cxWDown-Nom})^2} \quad (6.16)$$

The total uncertainty is taken as symmetric around the nominal and defined as $(\text{TotalUp} + \text{TotalDown})/2$. This is displayed in the bottom plot of Figure 6.24, as well as the contributions from the individual component uncertainties. The size of the uncertainty is approximately 2.5% at very low p_T and at higher p_T values. In the region from 5 to 10 GeV the uncertainty decreases to around 0.5%.

The parton shower sources of uncertainty in the p_T^W distribution are recapitulated in Table 6.6. The uncertainty sizes are evaluated in the low- p_T region and are typical numbers, given for reference only; the induced uncertainty in m_W is evaluated by reweighting the p_T distribution over the entire range relevant for the measurement. For the baseline fitting ranges of $30 < p_T^\ell < 50$ GeV and $65 < m_T < 100$ GeV, the induced systematic on m_W is 19.6 MeV for p_T^ℓ fits, and 14.0 MeV for m_T fits.

Finally, the impact of PDF uncertainties in the hard process is discussed here. These uncertainties are evaluated by reweighting the PYTHIA distribution according to the incoming parton flavour and momentum fraction:

$$w = \frac{f'_{q1}(x, Q^2) f'_{q2}(x, Q^2)}{f_{q1}(x, Q^2) f_{q2}(x, Q^2)}, \quad (6.17)$$

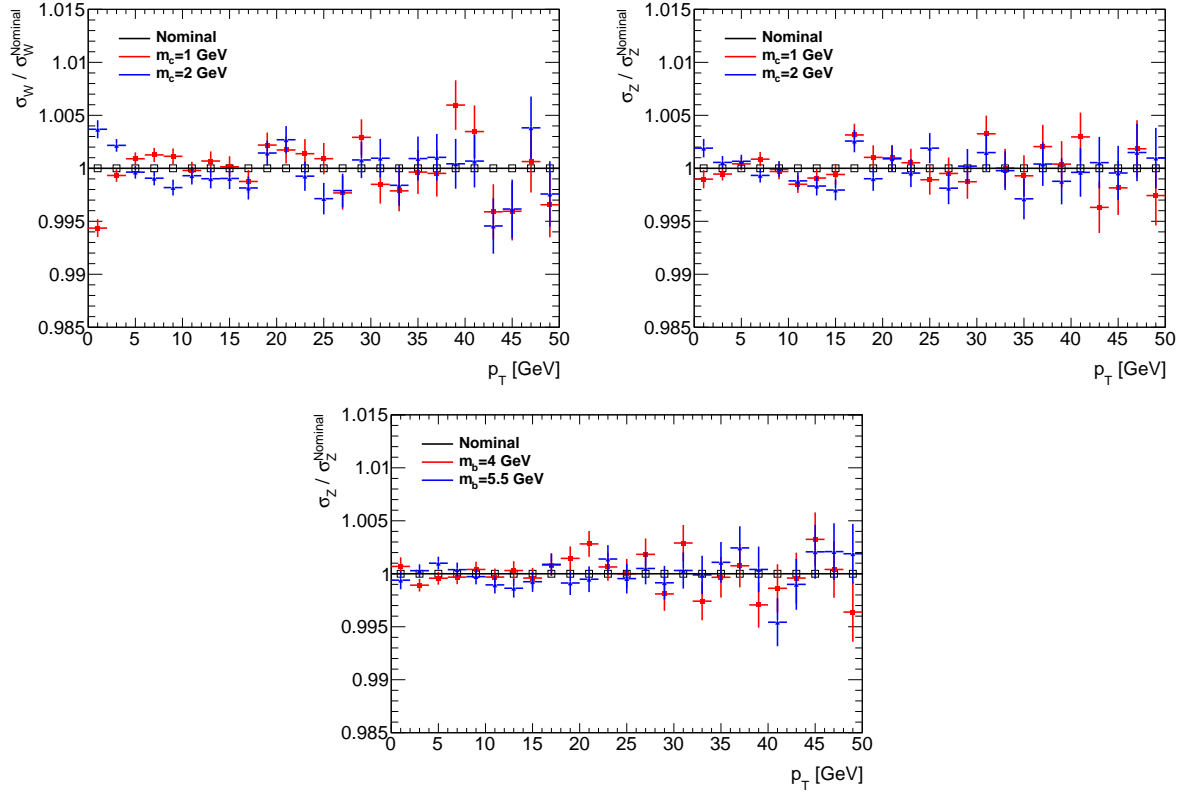


Figure 6.21: Top row : relative effect on the boson transverse momentum distribution of varying the charm quark mass for W^\pm (top) and Z (middle). Effect of varying the bottom quark mass for Z (bottom).

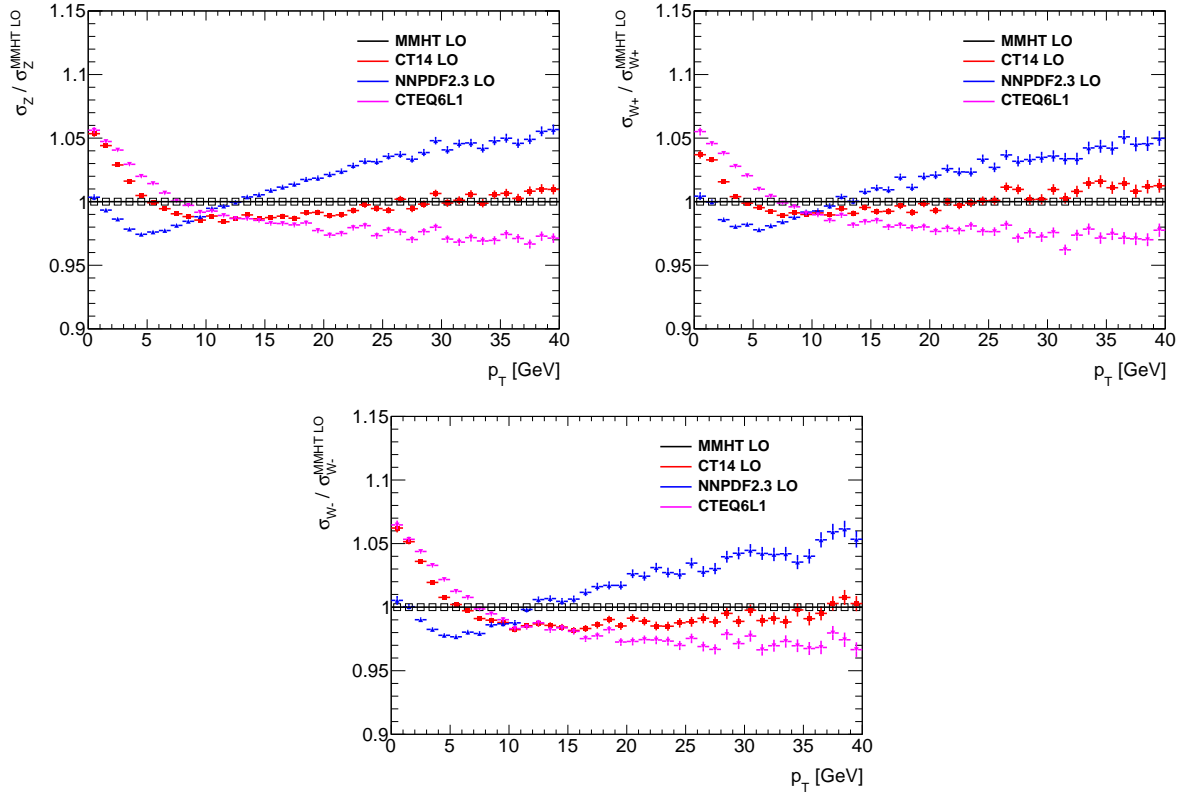


Figure 6.22: Relative effect on the boson transverse momentum distribution of varying the LO PDF in the parton shower, compared to MMHTLO, for Z (top), W^+ (middle), W^- (bottom).

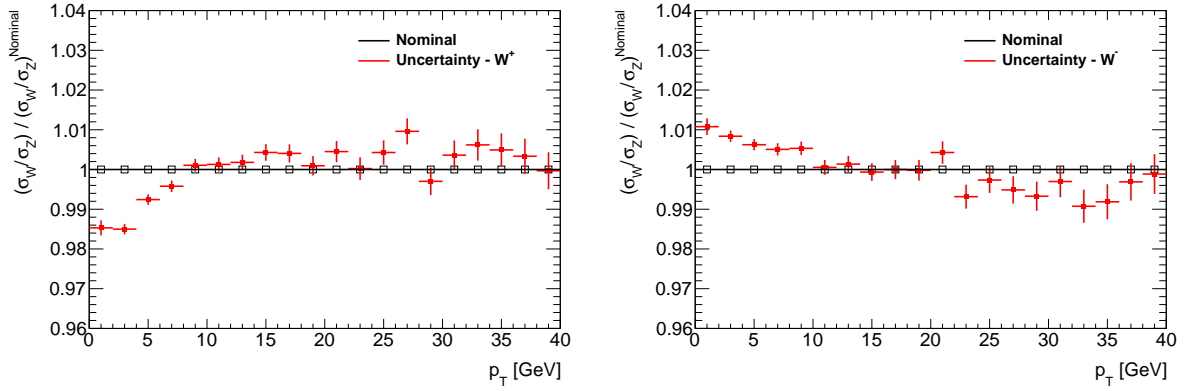


Figure 6.23: Uncertainty on the $p_T^{W^+}/p_T^Z$ and $p_T^{W^-}/p_T^Z$ distribution ratios from LO PDF variations. The uncertainty is defined from the CT14 LO PDF, as this PDF gives the strongest difference between the W^+ , W^- and Z p_T distributions

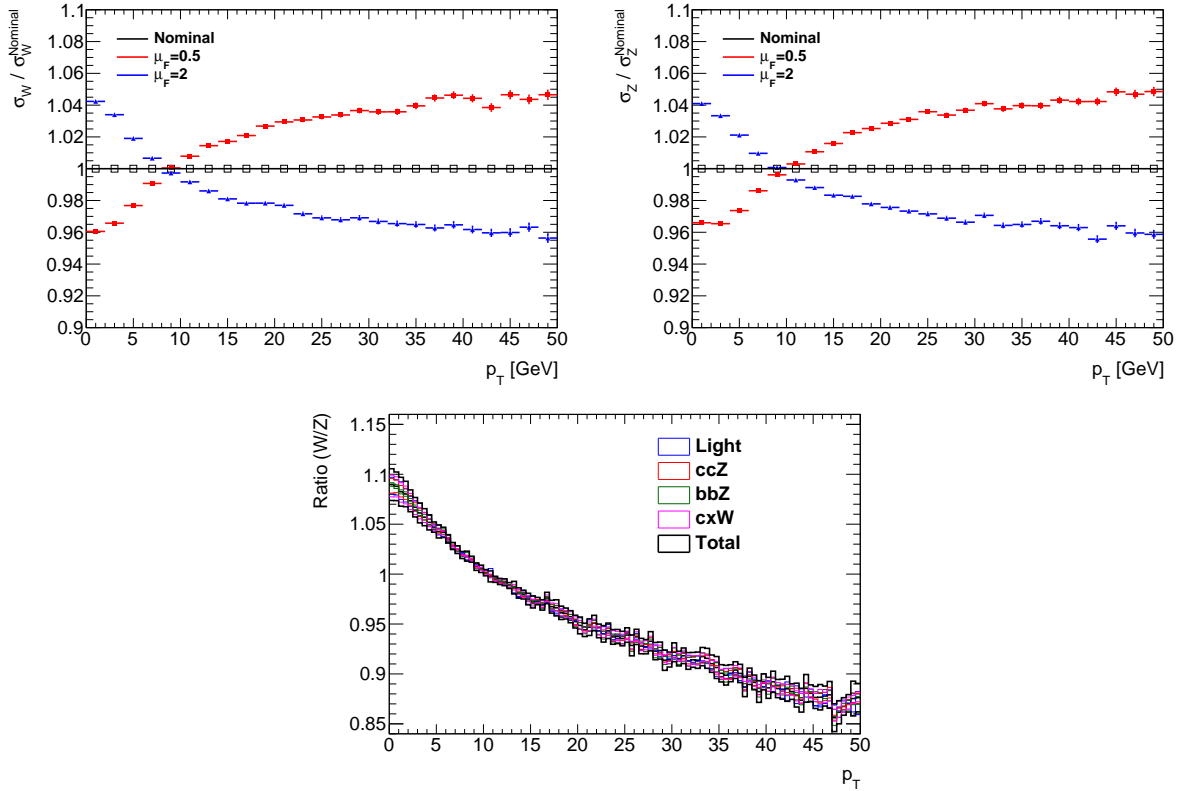


Figure 6.24: Relative effect on the boson transverse momentum distribution of varying the parton shower factorization scale, μ_F , for W^\pm (top) and Z (middle). Bottom: ratio of the W and Z p_T distributions varying the values of μ_F using the decorrelation model described in the text.

where W is the event weight, f are the CT10nnlo nominal PDFs, and f' the CT10nnlo uncertainty set variations. These variations are calculated for W and Z production, and the uncertainty in the p_T^W distribution is evaluated with the constraint that the p_T^Z distribution remains constant, since it is fixed by the data. This constraint is applied by defining the uncertainty variations as:

$$\left(\frac{d\sigma_W}{dp_T}\right)'_{\text{var}} = \left(\frac{d\sigma_W}{dp_T}\right)_{\text{var}} / \left[\left(\frac{d\sigma_Z}{dp_T}\right)_{\text{var}} / \left(\frac{d\sigma_Z}{dp_T}\right)_{\text{nom}} \right] \quad (6.18)$$

where “var” and “nom” on the r.h.s refer to the usual eigenset variations, and the primed variation on the l.h.s represents the p_T^Z -constrained uncertainty. Figure 6.25 illustrates the PDF-induced uncertainties on the p_T^W distribution, with and without the constraint. These variations will be included in the PDF uncertainties.

6.6 Propagation of QCD uncertainties to m_W

There are various sources of uncertainty affecting the QCD modeling of the Drell-Yan process, that can give rise to sizable uncertainties for the extraction of the mass of the W -boson at hadron colliders. They include PDF uncertainties, uncertainties on fundamental QCD parameters such as the value of the strong-coupling constant at the scale of the Z -boson mass, $\alpha_s(m_Z)$, and the values of the charm-quark and bottom-quark masses m_c and m_b , and uncertainties on the modeling of the angular coefficients. In order to reduce the uncertainties of the QCD modeling, precise measurements of the W - and Z -boson production can be used to constrain the parameters of the QCD models.

The incomplete knowledge of the parton density functions (PDFs) is an important source of uncertainty for the extraction of the W -boson mass, and it motivates a detailed discussion related to the sources of these large uncertainties. In particular, when m_W is determined from the transverse momentum spectrum of electrons and muons produced in the leptonic decay of the W boson, the PDFs uncertainty is expected to be among the dominant sources of theoretical uncertainties.

This section discusses the uncertainties on m_W resulting from the QCD modeling uncertainties discussed above. These uncertainties can be classified as PDF, p_T^W and polarization uncertainties. The first section below discusses a general method to reweight the vector boson kinematical distributions, that will be applied to evaluate the PDF, p_T^W and polarization uncertainties. The following sections discuss the uncertainties themselves.

6.6.1 Reweighting in (p_T, y, A_i) space

In order to estimate the QCD modeling uncertainties, all the event distributions have to be produced according to each parameter variation. However the direct reproduction of the MC samples is time-consuming process. However this can be achieved by reweighting an available prediction to another physics model. This section presents a fairly economical and sufficiently accurate method to perform this reweighting.

Equation 6.7 suggests that any prediction of the kinematic distributions of vector bosons and their decay products can be transformed into any other using a simple reweighting of the three-dimensional boson phase space distribution, followed by a reweighting of the decay angle distributions. Starting from the (p_T, y, M) distributions and tabulated values of the A_i coefficients for a source and a target generator prediction, the phase space weight is just a ratio of histograms, and the angular weight is defined as

$$w = \frac{1 + \cos^2 \theta + \sum_i A'_i f_i(\theta, \phi)}{1 + \cos^2 \theta + \sum_i A_i f_i(\theta, \phi)}. \quad (6.19)$$

where A'_i and A_i are the coefficients for the target and source generator respectively, and the $f_i(\theta, \phi)$ can be read off of Equation 6.7. This scheme is very flexible, as it is possible to study separately

the effect of each coefficient, by keeping $A'_i = A_i$ everywhere, except for the coefficient of interest. This method is used both to transmit the QCD predictions described in Sections 6.4-6.5 to the initial POWHEG distributions, and to evaluate the impact of the PDF and p_T^W uncertainties.

A simplification is introduced considering the fact that the boson invariant mass distribution is very peaked, and essentially insensitive to PDF variations (insensitivity of the mass distribution to initial state effects was also noted in Section 6.3.3). We therefore neglect this dimension, and base the reweighting on two-dimensional (p_T, y) phase space, and A_i coefficients tabulated accordingly. In practice the reweighting happens in two steps:

- the rapidity distribution is reweighted according to the $O(\alpha_s^2)$ predictions of Section 6.4;
- at given rapidity, the $p_T^{W,Z}$ distribution is reweighted to the AZ prediction (Section 6.5).

This procedure gives the desired $p_T^{W,Z}$ distribution without distorting the NNLO rapidity distribution.

6.6.2 PDF uncertainties

To estimate the PDF uncertainties, 25×2 nominal CT10nnlo uncertainty variations are calculated using DYTURBO¹, and used to generate pseudodata. Each pair corresponds to a $\pm 1\sigma$ variation of the corresponding fitted PDF parameter. The uncertainty on the W mass corresponding to each variation is estimated from template fits, comparing the mass obtained from the central CT10nnlo PDF and the one obtained for each PDF variation i : $\Delta m_W^i = m_W^i - m_W^0$. PDF variations are propagated, for each eigenset, *via* their impact on the rapidity distribution and the polarization coefficients.

Symmetric PDF uncertainties are defined taking the mean value of the up and down variation for each set, giving rise, in case of a single measurement, to a total uncertainty of

$$(\Delta m_W)^2 = \sum_{i=0}^{24} ((m_W^{2i+1} - m_W^{2i+2})/2)^2.$$

The effect of asymmetric eigenset variations was checked by calculating correspondingly asymmetric m_W uncertainties; after summing separately the negative and positive uncertainty contributions in quadrature, the overall uncertainty is still found symmetric within 0.2 MeV, and consistent with the symmetric estimate within the same amount. Therefore the simple symmetric treatment is kept.

The PDF-induced uncertainty on the p_T^W distribution is conservatively represented by a $\pm 2\%$ distortion of the distribution with respect to the central PDF prediction, over the range $0 < p_T^W < 30$ GeV. This uncertainty is taken fully correlated across $|\eta|$ and W boson charge, and contributes 10 MeV for the p_T fits, and 3 MeV for the m_T fits.

When the measurement is performed in several categories, the combined uncertainty can be derived as follows. The covariance matrix between 2 categories i and j is given by

$$E = Cov(m_W^i, m_W^j) = \sum_{k=0}^{24} \delta m_W^{i,k} \delta m_W^{j,k}.$$

The combined error is then computed using

$$\sigma^2 = \tilde{\alpha} E \alpha,$$

where α is the vector of the weighting factors given by

$$\alpha = E^{-1} U / (\tilde{U} E^{-1} U),$$

¹ DYTURBO is a fast tool for theory calculations developed by ATLAS members.

and U being the unity matrix.

Tables 6.7-6.8 summarize the PDF uncertainties on m_W for CT10nnlo. These numbers are estimated from p_T^l and m_T fits, and take into account the correlation between measurement categories. The CT10nnlo PDF uncertainty is in the range 25–35 MeV for each measurement category. Combining $|\eta|$ bins for a given boson charge brings this uncertainty down to about 17–10 MeV, depending on the observable. As expected, combining the electron and muon channels for a given boson charge does not bring much, but combining W^+ and W^- measurements improves further to about 14 MeV for p_T , and 10 MeV for m_T .

Channel	Uncertainty [MeV]	Channel	Uncertainty [MeV]
W^+ , $0.0 < \eta_\mu < 0.8$	28.4	W^- , $0.0 < \eta_\mu < 0.8$	31.0
W^+ , $0.8 < \eta_\mu < 1.4$	24.3	W^- , $0.8 < \eta_\mu < 1.4$	22.8
W^+ , $1.4 < \eta_\mu < 2.0$	29.1	W^- , $1.4 < \eta_\mu < 2.0$	23.8
W^+ , $2.0 < \eta_\mu < 2.4$	35.4	W^- , $2.0 < \eta_\mu < 2.4$	36.9
W^+ , $0.0 < \eta_e < 0.6$	28.5	W^- , $0.0 < \eta_e < 0.6$	31.7
W^+ , $0.6 < \eta_e < 1.2$	23.7	W^- , $0.6 < \eta_e < 1.2$	24.8
W^+ , $1.8 < \eta_e < 2.4$	28.4	W^- , $1.8 < \eta_e < 2.4$	26.9
$W^+ \rightarrow \mu\nu$ combined	15.8	$W^- \rightarrow \mu\nu$ combined	15.0
$W^+ \rightarrow e\nu$ combined	14.2	$W^- \rightarrow e\nu$ combined	12.7
All W^+ combined	14.2	All W^- combined	13.4
All combined		7.5	

Table 6.7: 68% CL PDF uncertainties on the m_W measurement with CT10nnlo using p_T^ℓ fits. The p_T^Z constraint is applied.

Channel	Uncertainty [MeV]	Channel	Uncertainty [MeV]
W^+ , $0.0 < \eta_\mu < 0.8$	28.9	W^- , $0.0 < \eta_\mu < 0.8$	31.3
W^+ , $0.8 < \eta_\mu < 1.4$	23.6	W^- , $0.8 < \eta_\mu < 1.4$	22.3
W^+ , $1.4 < \eta_\mu < 2.0$	27.4	W^- , $1.4 < \eta_\mu < 2.0$	23.3
W^+ , $2.0 < \eta_\mu < 2.4$	33.2	W^- , $2.0 < \eta_\mu < 2.4$	34.4
W^+ , $0.0 < \eta_e < 0.6$	29.0	W^- , $0.0 < \eta_e < 0.6$	31.9
W^+ , $0.6 < \eta_e < 1.2$	23.6	W^- , $0.6 < \eta_e < 1.2$	24.0
W^+ , $1.8 < \eta_e < 2.4$	27.6	W^- , $1.8 < \eta_e < 2.4$	28.6
$W^+ \rightarrow \mu\nu$ combined	16.0	$W^- \rightarrow \mu\nu$ combined	14.7
$W^+ \rightarrow e\nu$ combined	14.1	$W^- \rightarrow e\nu$ combined	13.8
All W^+ combined	14.6	All W^- combined	13.6
All combined		7.4	

Table 6.8: 68% CL PDF uncertainties on the m_W measurement with CT10nnlo using m_T fits.

6.6.3 Non-PDF uncertainties on the p_T^W distribution

For each variation of the p_T^W model parameters described in Section 6.5, pseudo-data are generated according to the variation and fitted to templates constructed using the nominal model. The resulting uncertainties in m_W are given in Table 6.9.

The quadratic sum of the eigentune, factorization scale and charm mass variations gives 11.7 MeV for the p_T fits, and 7.2 MeV for the m_T fits. These uncertainties are correlated between the electron and muon channels, W^+ and W^- processes, and measurement bins. The effect of the LO PDF variation is taken from the table, and is anticorrelated between W^+ and W^- .

Source	δm_W (p_T fits) [MeV]	δm_W (m_T fits) [MeV]
Eigentune variations	(+5 -7)	(+1.5 -2)
Factorization scale	9.8	7.0
Charm mass	2.5	0.8
LO PDF	+7.5 (W^+), -5.1 (W^-), +2.5 (W^\pm)	+1.9 (W^+), -1.3 (W^-), +0.6 (W^\pm)

Table 6.9: Summary of the sources of uncertainty in m_W from the p_T^W distribution. Except for the LO PDF case, the uncertainties apply identically for W^+ , W^- and W^\pm .

6.6.4 Non-PDF polarization uncertainties

The full set of polarization coefficients can only be measured accurately for Z events, although the W polarization states can be partly measured in data at high p_T^W [70]. Consequently we need to rely on Z data to identify a proper theoretical calculation, and assume its correctness for W production. We make use of the ATLAS Z polarization measurement performed using 8 TeV data [71] to identify this prediction and assign corresponding uncertainties.

According to the Z measurement results described in [71], the $O(\alpha_S^2)$ calculation of DYNNLO agrees with the data within its accuracy, except for A_2 . The uncertainty on the corresponding W predictions receives contributions from the Z A_i measurement uncertainties (essentially saying that the DYNNLO prediction is validated within the limits of the data accuracy), and from the discrepancy between data and theory for A_2 .

Figure 6.26, left, compares the Z data and the corresponding DYNNLO predictions, for A_0 – A_4 . With the exception of A_2 , the predictions agree everywhere with the data. For A_2 , a $\sim 20\%$ discrepancy develops starting about $p_T^Z \sim 25$ GeV. This discrepancy is parametrized using a second order polynomial and used to define the first source of uncertainty, as shown in the left column of plots. The same variation is shown for W DYNNLO predictions in the right column. The discrepancy observed for the Z process can be assumed to be representative of W production, since the NNLO-NLO corrections for this coefficient are very similar in both processes (and, if anything, slightly smaller for the latter), indicating that the missing corrections beyond NNLO, necessary to restore agreement with data, are of similar size as well.

The corresponding uncertainty on m_W is estimated as follows. Templates of the W decay lepton transverse momentum are built for different values of m_W and assuming the nominal DYNNLO prediction for the A_i 's, and pseudo-data distributions are defined by the parametrized A_i 's with the full differences between data and MC as measured on Z events. The fit of the pseudo-data by the templates gives a difference of 1.6 MeV compared to the nominal mass. This is taken as an uncertainty due to the measured discrepancy between data and DYNNLO for A_2 .

The second source of uncertainty is estimated propagating the Z data uncertainties as described below. Templates of the W transverse mass and of the decay lepton transverse momentum are built for different values of m_W and assuming the nominal DYNNLO prediction for the A_i 's, and pseudo-data distributions are defined by fluctuating the A_i 's within their uncertainties (statistical+systematics in the region $|y| < 2$) and preserving the correlations of the measurement uncertainties. The A_i uncertainties and correlations are illustrated in Figures 6.27–6.29. The typical measurement accuracy is at the level of 1% or below. For most coefficients, the measurement tend to be anti-correlated between neighboring p_T^Z bins. No correlations are observed among different coefficients at given p_T^Z . For each pseudo-data distribution, the W mass is fitted as described in Section 8.1.1, and the spread of the fit results defines the uncertainty.

Figure 6.30 shows the fitted mass difference wrt the nominal template (ΔM_W), using the decay lepton transverse momentum of W^+ , for each toy considering only the statistical uncertainties from the Z measurement on the left and the full uncertainties on the right. The quoted uncertainty is 6.2 MeV on the W mass measurement dominated by the correlated PDF systematic uncertainties

in p_T bins for A_0 . Similar results were obtained when fitting the W transverse mass.

In summary, a total uncertainty of 6.4 MeV on m_W is presently assigned from polarization uncertainties. The effect is dominated by the Z data accuracy. This estimate is thought to be conservative, as it allows for variations of all A_i coefficients by 0.5-1% near $p_T \sim 0$, where most coefficients should vanish up to small $O(\alpha_S^2)$ effects.

6.7 Summary

This chapter presents the physics of vector boson production and decay, its uncertainties and their impact on the m_W measurement. The samples used for the analysis are generated with POWHEG+PYTHIA8, completed by PHOTOS for QED final state corrections. While the latter part is accurately modeled, corrections need to be applied to the vector boson rapidity distribution, to the description of polarisation coefficients, and to the rapidity dependence of the vector boson p_T distribution. In addition, the effect of missing higher-order electroweak corrections needs to be evaluated. In the absence of a complete generator describing all physics effects needed for an accurate W mass measurement, a compound model has been constructed combining predictions from specialized tools.

Electroweak higher-order corrections were estimated using WINHAC, and found to contribute about 5.5 MeV when using the p_T^ℓ observable, and 2.5 MeV when using m_T . These uncertainties are presently sub-leading. For future measurements, they could be divided by a factor 2-3 by incorporating them in the simulation, using a suitable Monte Carlo program.

PDF uncertainties initially contribute about 7.5 and 7.4 MeV for lepton transverse momentum and transverse mass fits respectively, when using the nominal CT10 PDF for the estimation (with uncertainty variations scaled down to cover 68%CL). These uncertainties are expected to improve when reconsidering the profiled PDFs using the W, Z inclusive cross section measurements at 7 TeV. Performing the measurement in $|\eta|$ categories, and combining the W^+ and W^- measurements provides a factor 2–3 improvement compared to the single categories. In the future, additional W, Z cross section measurements, inclusive and in association with heavy quarks, should allow to further reduce these uncertainties.

Beyond PDFs, non-perturbative QCD effects and generally any parameter that affects the p_T^W distribution contributes uncertainty. These effects were addressed using resummation tools and parton shower programs, and the former were discarded due to unsatisfactory behaviour at low p_T^W . The PYTHIA parton shower was tuned to the available 7 TeV p_T^Z data, and the related m_W uncertainties were evaluated to about 11.7 MeV for p_T fits, and 7.2 MeV for m_T fits. Finally, polarization uncertainties contribute 6.4 MeV, with 6.2 MeV contributed by the Z data accuracy, and 1.6 MeV from the discrepancy observed for A_2 .

In summary, a total physics modeling uncertainty of about 16.2 MeV can be expected for the lepton transverse momentum fits. This number reduces to about 12.3 MeV when using the transverse mass. These numbers are indicative as they are estimated in the absence of other systematic uncertainties and for initial fitting range of $30 < p_T < 50$ GeV and $65 < m_T < 100$ GeV, and are evaluated in the full measurement context in the m_W measurement Section 8.

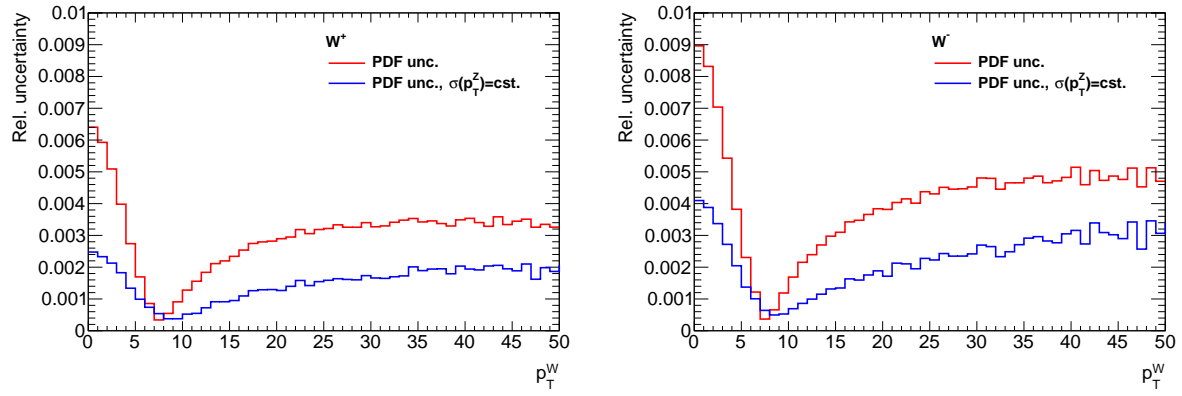


Figure 6.25: PDF-induced uncertainty on the the p_T^W distribution, with and without the p_T^Z constraint, for W^+ (left) and W^- (right).

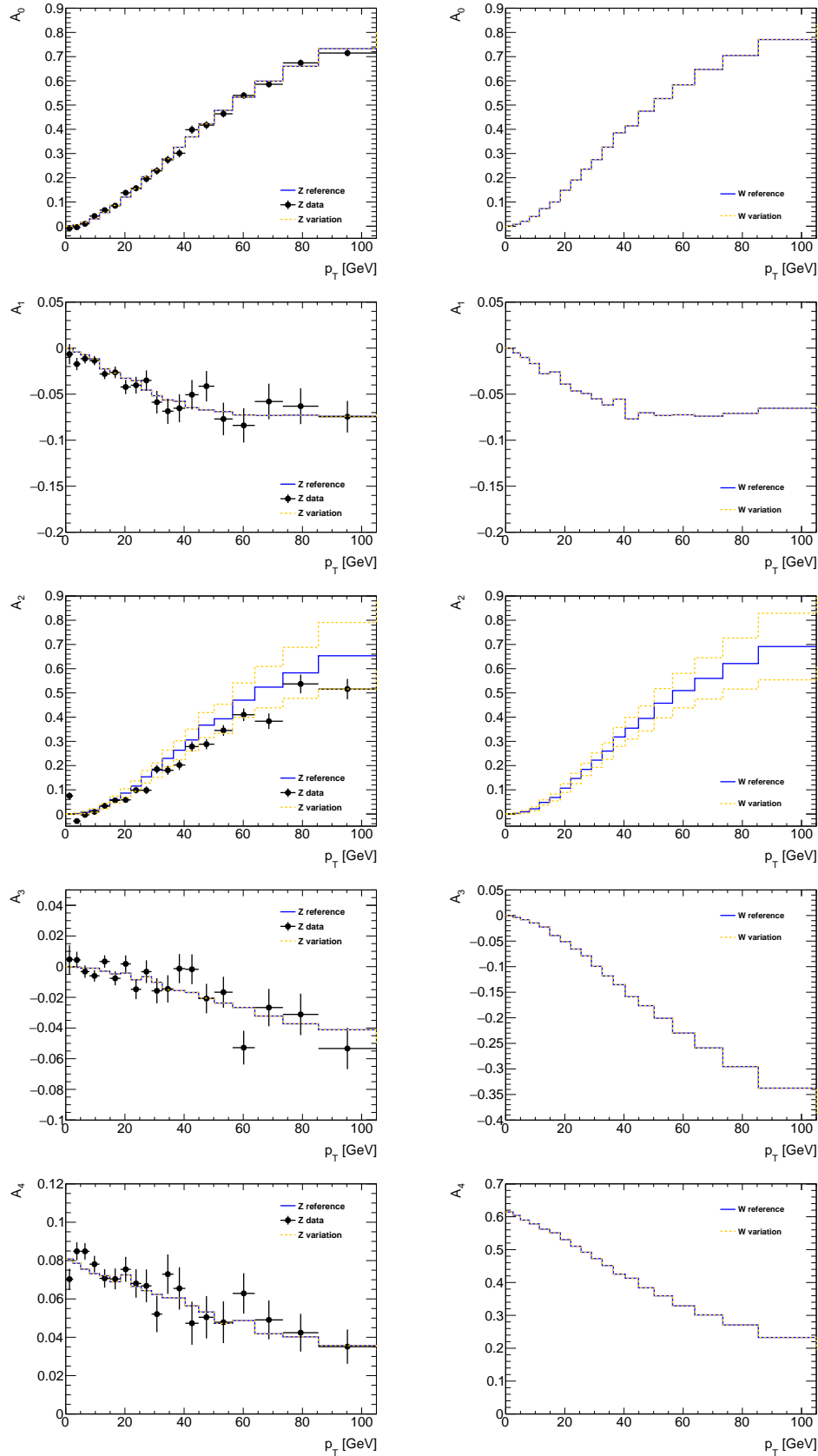


Figure 6.26: Left: comparison of the measured and predicted A_i coefficients, for Z production as a function of p_T^Z . In the case of A_2 , an uncertainty on the prediction is defined from a parametrization of the observed discrepancy with the data. Right: the corresponding predictions and uncertainties for W production.

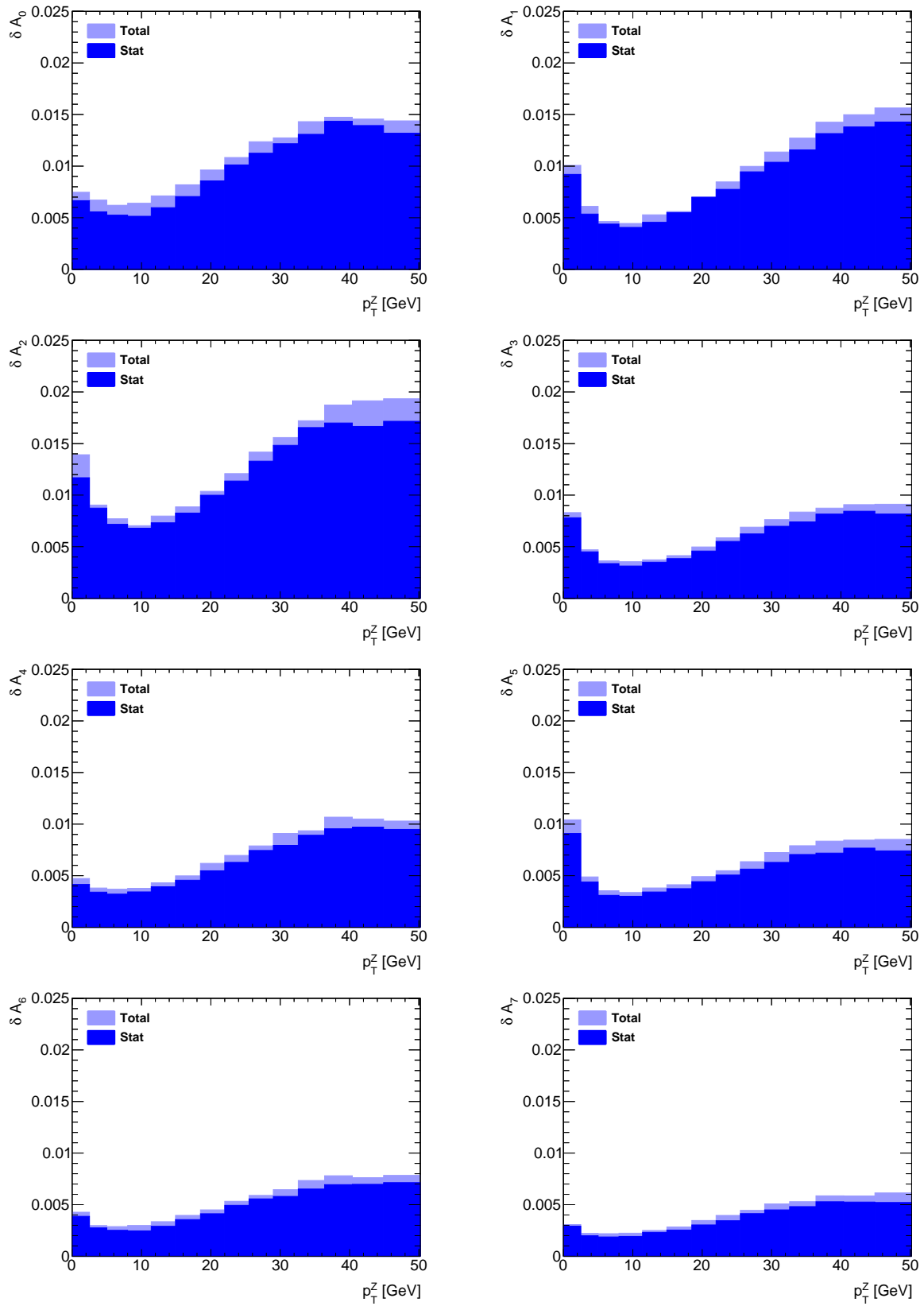


Figure 6.27: Measurement uncertainty on the A_i coefficients, as a function of p_T^Z [71].

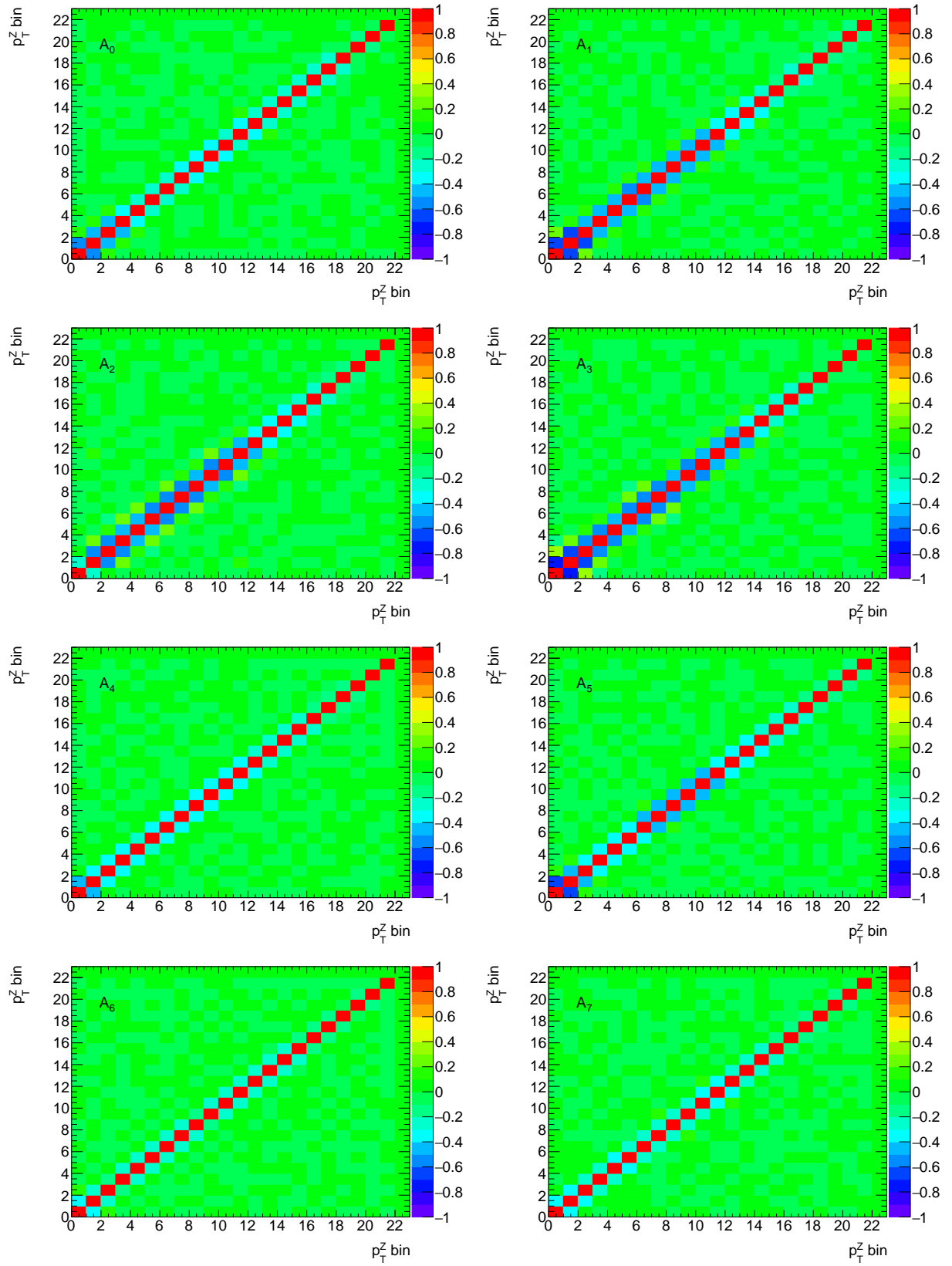


Figure 6.28: Correlations of given angular coefficient measurements across the p_T^Z range used for the measurement [71].

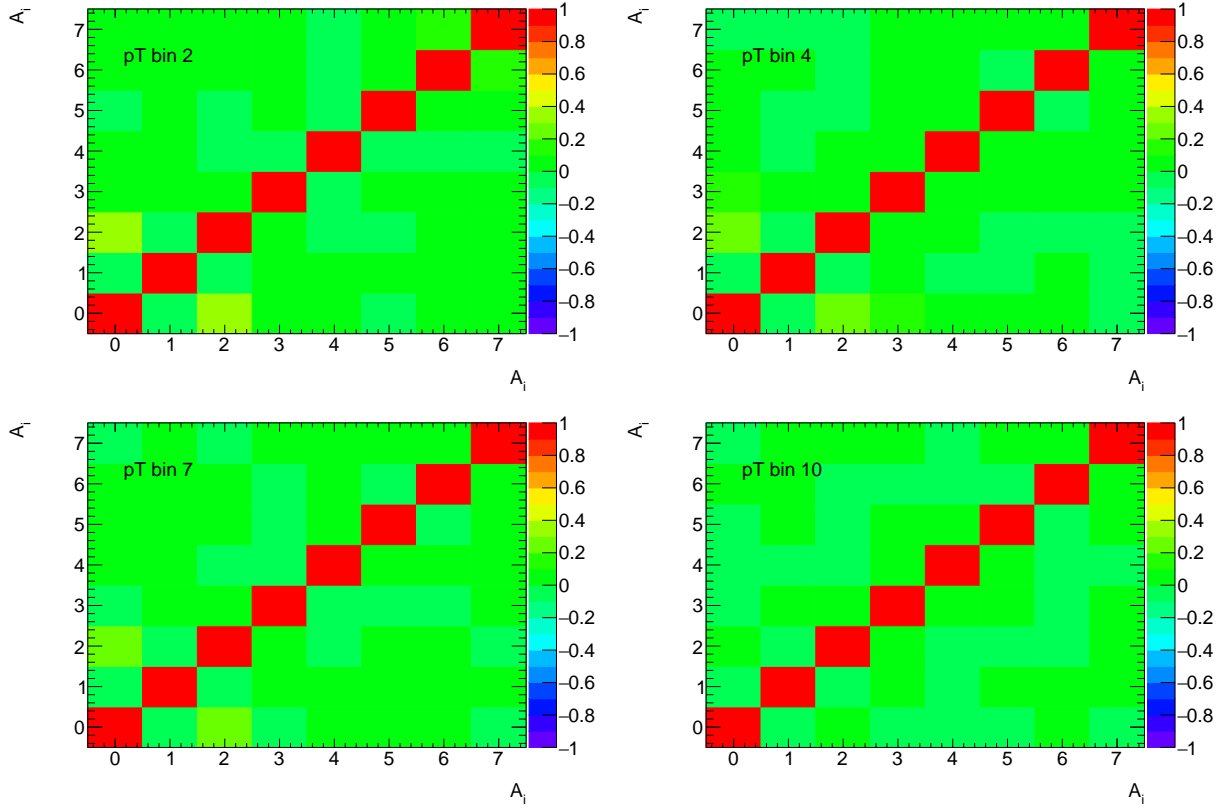


Figure 6.29: Correlations among the measured A_i coefficients, in a choice of fixed p_T^Z bins [71].

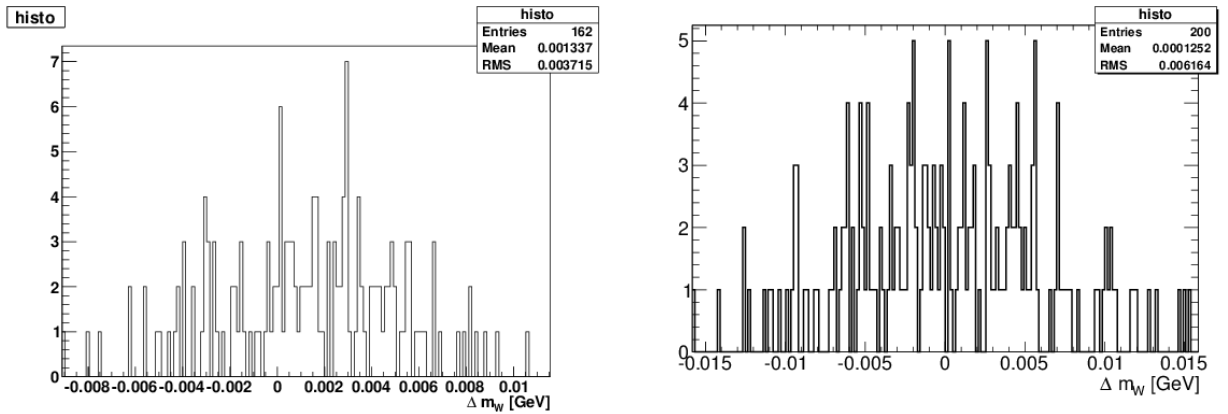


Figure 6.30: Toy MC error propagation. Left: considering only statistical uncertainty from the A_i measurement on Z data. Right: considering full (statistical+systematics) uncertainties from the A_i measurement on Z data.

Event selection and background determination

7.1 Data samples and Monte Carlo simulations

▷ Data samples

The measurement is performed with proton-proton collision data collected at center-of-mass energy of $\sqrt{s} = 7$ TeV with the ATLAS detector. The data is used for the analysis only if relevant sub-detectors were operational in normal conditions and magnet systems were on with nominal fields during data acquisition. This guarantees that the computed energies and momenta of the selected objects does not deviate from their expected behavior. After application of data quality requirements (see Section 2.2.5), the total integrated luminosity corresponds to $4.64 \pm 0.08 \text{ fb}^{-1}$ [72].

The muon candidates in this analysis are selected using a single muon trigger with requirements that have been changed with time of data acquisition. In the beginning the trigger with requirement on the transverse momenta of at least 18 GeV was used. A second part of data has been recorded with additional requirement on the muon isolation. The recorded electron candidates have been passed a single-medium-electron trigger with imposed requirements on the transverse momenta changed during the data acquisition: first $p_{\text{T}}^e > 20$ GeV, and later raised to $p_{\text{T}}^e > 22$ GeV. The looser versions of triggers were also used for the $W \rightarrow e\nu$ background studies.

▷ Monte Carlo samples

Monte Carlo samples for W and Z boson production at NLO and their decays in electron, muon and tau channels were generated with POWHEG framework [73] using CT10 parton distribution function (PDF) set [74]. The parton showering, hadronization and underlying event simulation were performed via the POWHEG interface to PYTHIA [75] with parameters set up according to the AUET2B tune [76]. The Photos program [58] was used to simulate the effect of final state radiation (FSR) and τ lepton decays were simulated with Tauola [77]. The masses of the W and Z bosons were assumed to be $M_W = 80385$ MeV and $M_Z = 91187$ MeV respectively for the nominal simulations.

Top quark pair and single top production were modeled using MC@NLO [78], and gauge boson pair production (WW, WZ, ZZ) were simulated using HERWIG. Both programs are interfaced to CT10 PDF set. The multijet background events, $pp \rightarrow b\bar{b}$ and $c\bar{c}$, that can lead to fake muons in final state, were simulated using PYTHIA. Both multijet background samples were used for the cross-checks with data-driven background estimation methods that have been used in the analysis.

All the simulated samples were processed through the GEANT4 based simulation [79] of the ATLAS detector. The events were reconstructed within the ATLAS software framework with the same analysis chain as data. The simulated samples were overlaid with additional proton-proton interactions ('pile-up') generated with PYTHIA and the appropriate ATLAS tune AMBT1 [80].

For the electroweak processes of vector boson production, considered as signal or background, the samples are normalized according to cross sections calculated at NNLO using the FEWZ program [81]. The uncertainties on the cross section are obtained to be about 5% and include the

uncertainties from the choice of PDF set used in computation ($\sim 3-4\%$), the choice of factorization and renormalization scales ($< 1\%$), and the uncertainty on the strong coupling constant ($\sim 2\%$). The cross sections on the vector boson pair production are also taken from [81] with relative uncertainty 7%. The $t\bar{t}$ cross section $\sigma_{t\bar{t}} = 177 \pm 11\text{pb}$ is calculated at NNLO with a top quark mass of 172.5 GeV. The single top cross sections are taken from [82]. Table 7.1 summarizes the simulated samples used in this analysis and their cross sections. The cross sections for the multijet $c\bar{c}$ and $b\bar{b}$ samples indicated in the table are computed using PYTHIA and used in the analysis only for their relative normalization to compare with data-driven methods of the multijet background estimates. The cross sections for the signal and background electroweak samples, as well as for top pair and single top samples, are used for their relative normalization that together with multijet background defines the distributions used for the W mass extraction. Moreover, these cross section are to estimate an amount of electroweak and top contaminations in a multijet control region (see later).

Process	Generator	$\sigma \times BR[\text{pb}]$	N_{evt}	$L_{\text{int}}[\text{fb}^{-1}]$
Signal Samples				
$W^+ \rightarrow \mu^+ \nu$	POWHEG+PYTHIA8	6344.9	$9.544 \cdot 10^7$	15.042
$W^- \rightarrow \mu^- \nu$	POWHEG+PYTHIA8	4376.5	$6.517 \cdot 10^7$	14.891
$W^+ \rightarrow e^+ \nu$	POWHEG+PYTHIA8	6344.9	$9.376 \cdot 10^7$	14.778
$W^- \rightarrow e^- \nu$	POWHEG+PYTHIA8	4376.5	$6.592 \cdot 10^7$	15.062
Background Samples				
$W^+ \rightarrow \tau^+(\rightarrow e^+, \mu^+) \nu$	POWHEG+PYTHIA8	930.04	$1.488 \cdot 10^7$	16.000
$W^- \rightarrow \tau^-(\rightarrow e^-, \mu^-) \nu$	POWHEG+PYTHIA8	603.63	$9.990 \cdot 10^6$	16.550
$Z \rightarrow \mu\mu$	POWHEG+PYTHIA8	990.3	$2.949 \cdot 10^7$	29.784
$Z \rightarrow e^+e^-$	POWHEG+PYTHIA8	990.3	$2.952 \cdot 10^7$	29.808
$Z \rightarrow \tau^+\tau^-(\rightarrow e, \mu)$	POWHEG+PYTHIA8	260.42	$5.871 \cdot 10^6$	22.543
WW	HERWIG	20.86	$2.457 \cdot 10^6$	11.781
ZZ	HERWIG	1.54	$2.478 \cdot 10^5$	160.883
WZ	HERWIG	6.97	$9.920 \cdot 10^5$	142.332
$t\bar{t}$	MC@NLO	101.51	$1.146 \cdot 10^7$	112.950
$st_{tchan_{e\nu}}$	MC@NLO	6.83	$1.758 \cdot 10^5$	25.737
$st_{tchan_{\mu\nu}}$	MC@NLO	6.82	$1.755 \cdot 10^5$	25.731
$st_{tchan_{\tau\nu}}$	MC@NLO	6.81	$1.748 \cdot 10^5$	25.670
$st_{schan_{e\nu}}$	MC@NLO	0.46	$2.512 \cdot 10^5$	546.170
$st_{schan_{\mu\nu}}$	MC@NLO	0.46	$2.513 \cdot 10^5$	546.370
$st_{schan_{\tau\nu}}$	MC@NLO	0.46	$2.514 \cdot 10^5$	546.608
st_{Wt}	MC@NLO	14.37	$7.897 \cdot 10^5$	54.954

Table 7.1: MC samples used in the analysis. The quoted cross-sections, except multijet samples, are used to normalize NNLO estimates of expected number of event.

▷ Applied corrections

The modeled MC samples do not take into account certain detector effects and they are simulated only according to certain theoretical models. The samples can be corrected to account for the detector effects and/or to desired physical model through reweighting procedure. The weights for physics corrections are applied at truth level.

The following corrections are applied:

- Pileup reweighting in $\langle \mu \rangle$ bins (described in Section 5.5.1) and primary vertex z reweighting

- Muon momentum scale and resolution corrections (described in Section 5.1)
- Muon reconstruction, identification, trigger and isolation efficiency corrections (described in Section 5.2)
- Electron energy scale and resolution corrections (described in Section 5.3.2)
- Electron reconstruction, identification, trigger and isolation efficiency corrections (described in Section 5.4)
- Recoil response corrections (described in Section 5.5)
- Boson p_T reweighting in boson rapidity bins (described in Section 6.5): Pythia8 AZ tune
- W polarization reweighting (described in Section 6.4.2): DYNNLO predictions
- PDF and parton shower corrections to CT10nnlo PDF set
- Lineshape correction

7.2 Definition of the signal region

▷ Muon selection

Muon candidates are selected using single-muon trigger with high muon transverse momenta that ensures good distribution of the $W \rightarrow \mu\nu$ events from background. The muon track parameters are reconstructed separately in ID and MS, the corresponding tracks are matched and muon parameters are statistically combined using Staco algorithm. The muon pseudorapidity cut $|\eta| < 2.4$ is imposed that corresponds to ID and trigger system coverage. Moreover, the selected muons are required to have a minimum number of hits in the ID. This ensures a high quality of reconstructed muons. The muon selection cuts are described in details in Section 3.4.1. Events are requested to pass Good Run List (GRL) requirements ensuring all subsystems were working properly. The events falling in period L3-L4 are rejected because of an RPC timing problem.

In addition, muon candidates are required to have a z position of muon track extrapolated to the beam axis with respect to the coordinate of the primary vertex to be $|z_{extr} - z_{PV}| < 10$ mm to reduce muons arising from cosmic and other non-collision backgrounds. The candidates are also required to satisfy a loose isolation criteria in order to suppress background from heavy-flavour decays. The isolation requires the scalar sum of momenta of ID tracks within a cone $\Delta R = \sqrt{\Delta\eta^2 + \Delta\phi^2} < 0.2$ around the muon candidate (excluding the muon candidate itself) to be less than 10% of the muon p_T .

▷ Electron selection

Electron candidates are built from clusters of energy deposited in the electromagnetic calorimeter that are associated with at least one well-reconstructed track angles η and ϕ in the ID (see Section 3.2). They are required to have $p_T > 15$ GeV and $|\eta| < 2.4$ excluding the calorimeter crack region $1.2 < |\eta| < 1.82$, and to pass the tight identification criterion of a cut-based discriminating variables. An event LAr veto is applied to veto events if a calorimeter jet falls in the vicinity of a LAr hole due to missing LAr FEBs. Furthermore, the electrons that involve the problematic regions (such as dead or noisy cells, dead readout boards) of the LAr calorimeter in the reconstruction were removed with the “LAr Error” flag.

In order to further reduce large background contributions, the various electron identification (ID) cuts are applied requiring electron to be 'tight', as described in Section 3.4.2. Besides, the two additional cuts are imposed on the track-based p_T^{cone40} and calorimeter-based E_T^{cone20} electron isolation variables, defined as

- track-based electron isolation p_T^{cone40} defined as the scalar sum of the p_T of tracks in a cone of $\Delta R < 0.4$ around the electron track, minus the p_T of the electron.
- calorimeter-based electron isolation E_T^{cone20} determined by the total E_T of energy deposits in the calorimeter within $\Delta R < 0.2$ around the electron track (centroid of EM cluster), minus E_T of EM cluster.

Unlike simple cut on muon isolation variable, the electron isolation cuts are p_T - and η -dependent maintaining a uniform isolation efficiency of 97% for track- and 98% for calorimeter-based variables across a wide range of p_T and η . In general, these cuts vary in the range of $p_T^{\text{cone40}} < 2.0..3.0$ GeV and $E_T^{\text{cone20}} < 2.5..4.5$ GeV.

▷ W boson selection

Events containing a W boson candidate are selected starting from selection of energetic leptons passing corresponding criteria explained above. The parameters (four-momenta) of selected muons used in this analysis are built from ID only, whereas the kinematics of the selected electrons are defined from the energy measured in the EM calorimeter, and from the associated track angles η and ϕ . The events with more than one selected lepton in the collection are rejected. The number of tracks associated with reconstructed primary vertex is required to be at least three.

Finally, the cuts on the W kinematics are the following

- Lepton transverse momentum: $p_T^\ell > 30$ GeV
- Hadronic recoil as a measure of p_T^W : $u_T < 30$ GeV
- Neutrino transverse momentum defined as missing energy: $E_T^{\text{miss}} > 30$ GeV
- W boson transverse mass: $m_T^W = \sqrt{2p_T^\ell E_T^{\text{miss}} \cdot (1 - \cos(\phi_\ell, \phi_{\text{miss}}))} > 60$ GeV

The selection requirements have been optimized to reduce the multi-jet background contribution, as well as to minimize model uncertainties on the W mass measurement.

The hadronic recoil, \vec{u} , is calculated from the vector sum of all cluster momenta measured in the calorimeter. Although the neutrino from the W boson decay leaves the detector unseen, its transverse momentum can be indirectly determined via the measured hadronic recoil and lepton transverse momentum as

$$\vec{p}_T^\nu = E_T^{\text{miss}} = -\vec{u} - \vec{p}_T^\ell \quad (7.1)$$

The definition and the calculation of the hadronic recoil observable and its importance for the W boson mass measurement is described in details in Section 3.3.

The resulting cut-flow in data and signal MC for both $W \rightarrow \mu\nu$ and $W \rightarrow e\nu$ channels, separated by charge, are shown in Table 7.3 and Table 7.2 respectively.

7.3 EW and top backgrounds

The W events with leptonic final states are contaminated with relatively low background. The expected background for the $W \rightarrow e\nu$ and $W \rightarrow \mu\nu$ channels results from $W \rightarrow \tau\nu$, $Z \rightarrow \ell\ell$, $Z \rightarrow \tau\tau$, as well as dibosons decays, top processes and multijet events. The electroweak and top

Cut	Data	$W^+ \rightarrow e\nu$	$W^- \rightarrow e\nu$
No cut	185039772	29129499 (100.000)	20092555 (100.000)
LarError	184421049	29129499 (100.000)	20092555 (100.000)
Good PV	184249665	28998609 (99.551)	20014265 (99.610)
GRL	167449232	28998609 (99.551)	20014265 (99.610)
Trigger	153832216	13838494 (47.507)	8929879 (44.444)
$p_T^e > 30$ GeV	129628319	6079159 (20.869)	4296406 (21.383)
Veto loose++	16051922	6075906 (20.858)	4294068 (21.371)
One tight++	16051922	6075906 (20.858)	4294068 (21.371)
Trigger Matching	16046360	6075769 (20.858)	4293961 (21.371)
Jet Cleaning	16029602	6073567 (20.850)	4292459 (21.363)
LAr simple veto	15986316	6067694 (20.830)	4287952 (21.341)
E_T^{cone20}	14072267	5996666 (20.586)	4236090 (21.083)
p_T^{cone40}	12702703	5864655 (20.133)	4144350 (20.626)
$p_T^W < 30$ GeV	8318577	4404741 (15.121)	3090396 (15.381)
$W_T > 60$ GeV	6606062	3699063 (12.699)	2637032 (13.124)
$E_T^{\text{miss}} > 30$ GeV	5812035	3278407 (11.255)	2335110 (11.622)

Table 7.2: Cut-flow in the $W \rightarrow e\nu$ channel in the signal region. Electrons are requested to be tight++. Numbers in brackets represent cumulative efficiency (in %) of the given cut.

processes ($t\bar{t}$, as well as single t production) are modeled with good accuracy: their respective cross-sections are measured with good agreement with the theoretical expectations, and Monte Carlo is used to implement them. The corresponding samples are described in Section 7.1. Table 7.6 reports the electroweak and the top background fractions with respect to the data. Total MC (signal + background) is normalised to the data with data driven multijet background subtracted. The level of the multijet background is given in the next section.

The impact of the uncertainty from the EW and top backgrounds has been evaluated by changing their normalization within uncertainty, rebuilding the templates accordingly, and comparing the corresponding fit results with the nominal results. A relative uncertainty of 2% on the $W \rightarrow \tau\nu$ background fraction is assumed, according to the experimental uncertainty on the ratio of the $W \rightarrow \tau\nu$ branching fraction relative to the electron and muons ones. For the $Z \rightarrow \ell\ell$ background the relative cross section with respect to the measured W^+ and W^- cross section is used. The relative uncertainty on the cross section is 1.8% and 2.25% for the W^+/Z and W^-/Z [55]. For the

Cut	Data	$W^+ \rightarrow \mu\nu$	$W^- \rightarrow \mu\nu$
No cut	154532753	29129499 (100.000)	20092555 (100.000)
GRL	140976111	29129499 (100.000)	20092555 (100.000)
Good PV	139003866	28956395 (99.406)	19991586 (99.497)
Trigger	116109480	14838771 (50.941)	9035835 (44.971)
Muon Sel.	43803081	12776948 (43.863)	7934334 (39.489)
$p_T^\mu > 20$ GeV	42951700	12713212 (43.644)	7903333 (39.335)
Muon veto	41153751	12713068 (43.643)	7903195 (39.334)
Trigger Matching	41044423	12710370 (43.634)	7901520 (39.326)
Jet Cleaning	40996618	12705864 (43.619)	7898825 (39.312)
LAr simple veto	40915645	12694963 (43.581)	7891061 (39.274)
LAr noise bursts	40801743	12694963 (43.581)	7891061 (39.274)
Muon $p_T \geq 30$ GeV AND remove periods L3+L4	16077674	7670767 (26.333)	5181689 (25.789)
$p_T^W < 30$ GeV	10811788	5814759 (19.962)	3894645 (19.384)
$W > 60$ GeV	8851402	4885304 (16.771)	3322739 (16.537)
$E_T^{\text{miss}} > 30$ GeV	7844778	4342572 (14.908)	2950049 (14.682)

Table 7.3: Cut-flow in the $W \rightarrow \mu\nu$ channel in the signal region. Muons are requested to have $p_{T\text{cone20}}/p_T < 0.1$. Numbers in brackets represent cumulative efficiency of the given cut.

$t\bar{t}$ cross section uncertainty of 3.9% is used [83] while for single top 12% samples is applied. For the diboson backgrounds, a relative normalization uncertainty of 5% is assumed. The results are summarised in Table 7.7. Tables 7.4 and 7.5 summarize the resulting cut-flow in background MC samples for both $W \rightarrow \mu\nu$ and $W \rightarrow e\nu$ channels.

It should be noted, that the veto of a second lepton in the events, requires the application of an MC correction scale-factor for the probability to not reconstruct the lepton if it is within the fiducial volume of the detector. This plays in particular a role for $Z \rightarrow \mu\mu$ events, having an impact of about 20%. The missing electron scale factor for $Z \rightarrow ee$ events is found to be about 4%.

The dominant background contribution in both decay channels is due to $Z \rightarrow \ell\ell$ events, when one lepton escapes detection and mimics missing transverse momentum. The production cross-section, as well as the kinematic distribution of Z boson events at the LHC is very well understood and hence the corresponding background contribution is estimated by MC predictions. The second largest background contribution is due to decays, where the τ decays further leptonically into electrons or muons. Table 7.6 reports the electroweak and the top background fractions with

Cut	$W \rightarrow \tau\nu$	$Z \rightarrow ee$	top	WW/WZ/ZZ	$Z \rightarrow \tau\tau$
No cut	7041098	4546477	871755	134852	1195589
LarError	7041098	4546477	871755	134852	1195589
Good PV	7003914	4525771	871377	134588	1191224
GRL	7003902	4525798	871377	134588	1191208
Trigger	848239	3163313	217990	44386	173267
$p_T^e > 30$ GeV	193216	1985745	127053	24958	46958
Veto loose++	192891	722570	119395	19886	44699
One tight++	192891	722570	119395	19886	44699
Trigger Matching	192886	719803	119365	19870	44683
Jet Cleaning	192805	721532	119246	19865	44629
LAr simple veto	192383	712095	117400	19715	44439
E_T^{cone20}	190418	702760	113485	19289	43960
p_T^{cone40}	186619	686673	105506	18454	43035
$p_T^W < 30$ GeV	106547	204069	11724	5829	17517
$W > 60$ GeV	67383	106894	10220	5038	8558
$E_T^{\text{miss}} > 30$ GeV	58459	81136	9223	4528	6967

Table 7.4: Cut-flow in the $W \rightarrow e\nu$ channel for background processes. The numbers represents number of events normalised according to the cross sections listed in Table 7.1 and normalised to the integrated luminosity of the data sample.

Cut	$W \rightarrow \tau\nu$	$Z \rightarrow \mu\mu$	top	WW/WZ/ZZ	$Z \rightarrow \tau\tau$
No cut	7041098	4546477	871755	134852	1195589
GRL	7041098	4546477	871755	134852	1195589
LarError	7003914	4519068	871377	134588	1191224
Trigger	1319622	3304329	230939	45372	249997
Muon Sel.	930906	3109210	181726	39130	183105
$p_T^\mu > 20$ GeV	912106	3102010	181127	38989	179908
Muon veto	912084	1423848	172580	34813	175628
Trigger Matching	911863	1369356	170252	34646	175123
Jet cleaning	911546	1365933	170045	34604	174768
LAr simple veto	910452	1364188	167347	34396	174181
LAr noise bursts	910452	1364188	167347	34396	174181
Muon $p_T \geq 30$ GeV AND remove L3+L4	242669	839816	118148	23370	54751
$p_T^W < 30$ GeV	142062	577069	13784	7688	22405
$W > 60$ GeV	90351	476111	11859	6652	10715
$E_T^{\text{miss}} > 30$ GeV	78674	420111	10666	5971	8721

Table 7.5: Cut-flow in the $W \rightarrow \mu\nu$ channel for background processes. The numbers represents number of events normalised according to the cross sections listed in Table 7.1 and normalised to the integrated luminosity of the data sample.

respect to number of the W candidates in data.

7.4 Multijet background estimation

7.4.1 Methodology

The signal $W \rightarrow \ell\nu$ events are accompanied by multijet background which contributes significantly due to its large cross-section. The multijet events become a background to the $W \rightarrow \mu\nu$

Channel	$W \rightarrow \tau\nu$	$Z \rightarrow ee$	$Z \rightarrow \mu\mu$	$Z \rightarrow \tau\tau$	WW, WZ, ZZ	top
$W \rightarrow e^+\nu$	0.99	1.23	–	0.11	0.06	0.11
$W \rightarrow e^-\bar{\nu}$	1.03	1.63	–	0.14	0.08	0.13
$W \rightarrow \mu^+\nu$	1.00	–	4.83	0.10	0.06	0.09
$W \rightarrow \mu^-\bar{\nu}$	1.01	–	6.12	0.13	0.07	0.11

Table 7.6: Electroweak and top background fractions (%) with respect to data candidate events selected in signal region in muon and electron channels, separately for W^+ and W^- .

	$W \rightarrow \tau\nu$	$Z \rightarrow \tau\tau$	$Z \rightarrow \ell\ell$	Diboson	top
Impact, $W \rightarrow e\nu$ [MeV]	∓ 2.2	∓ 0.5	± 0.5	± 0.2	± 0.3
Impact, $W \rightarrow \mu\nu$ [MeV]	∓ 2.2	∓ 0.5	± 2.0	± 0.2	± 0.3

Table 7.7: Impact of the EW and top background normalisation on the mass determination fitting the $p_T^{\ell\ell}$ distribution.

signal if they contain a real muon and a neutrino from either semileptonic decays of b - and c -quarks or in-flight decays of pions or kaons within the tracking region. Furthermore, long-lived hadrons passing through the calorimeter constitute an additional source of background as they can mimic a muon signal. The main sources of multijet background to the $W \rightarrow e\nu$ channel are semileptonic heavy-flavour decays, photon conversions, and hadrons misidentified as electrons where the missing energy is mismeasured by the detector.

While electroweak and top processes are well modeled with MC simulation, the multijet background cannot be simulated reliably. It is therefore necessary to use a data-driven method for the multijet background estimate in the signal region. In this method, the multijet background sample is constructed from a jet-enriched control region in data by reversing or relaxing some of the lepton isolation requirements. Such control region is assumed to provide a shape of the background for all variables which are used for the m_W extraction. The normalisation for the multijet sample is determined from the **fraction fit method** using another discriminating variable in a fitting region before applying some cuts to ensure significant contribution from the multijet background. The fraction fit method is based on binned maximum likelihood fit of the combination of all samples modeling in Monte Carlo (signal, multijet, top, electroweak backgrounds) to the observed candidate events from data. In this fit, the relative normalisation of all modeled in Monte Carlo samples (signal $W \rightarrow \ell\nu$ and backgrounds $W \rightarrow \tau\nu$, Z , $t\bar{t}$, ...), is fixed according to pp cross-sections, whereas the normalizations of the multijet background and total MC-based contributions are allowed to float. The normalization of multijet background that satisfies the fitting phase space is assumed to be global, i.e. the same in any phase space. This allows to estimate the amount of background events in signal region as the normalization times the number of multijet events extracted from the control region. After the fit is performed and multijet sample is normalized, a fraction of multijet background is calculated in the signal region as a ratio of the number of multijet events to the number of all selected events in data.

7.4.2 Fits to kinematical distributions in the muon channel

▷ Simple case of control region definition

The track-based muon isolation is effective discriminant between signal and multijet background due to the fact that the muons originating from semileptonic heavy-flavour decays are typically surrounded by tracks from other particles. Thus, in the muon channel, the multijet-enriched sample **control region** is created using data with the same $W \rightarrow \mu\nu$ signal selection requirements

as described in section 7.2, but the muon track in the ID is required to have an activity of $0.2 < \sum p_T^{trk}/p_T < 0.4$ (anti-isolation criteria) in a cone of $\Delta R \leq 0.2$ around the muon candidate. Such jet-enriched data sample is contaminated by W signal events, electroweak and top backgrounds. By applying the same selection criteria to MC samples, the contamination can be found according to corresponding integrated luminosity and subtracted. At this step, a 'pure' sample of multijet events is available. For simplicity, the sample with isolated muons is named **signal region** (SR) while the sample with anti-isolated muons is named **control region** (CR) (see Table 7.8).

At the next step, the normalisation of the pure multijet sample has to be found as its cross section is unknown in contrast to MC-based backgrounds. This is done with the fraction fit to the following discriminating variables:

- The E_T^{miss} distribution of the background events is peaked at lower value comparing to signal $W \rightarrow \mu\nu$ events.
- The W transverse mass m_T^W constructed using background events tends to be small.
- The ratio p_T^μ/m_T^W containing angular information between muon-like object and a neutrino. This distribution is peaked at 0.5 for well-balanced signal $W \rightarrow \mu\nu$ events, while the balance can be disregarded in multijet events leading to presence of tail in the distribution.

In order to give an access to multijet dominant regions for the fraction fits (low m_T^W and E_T^{miss} , high p_T^μ/m_T^W), the fitting region is constructed by removing the $E_T^{\text{miss}} > 30$ GeV and $m_T^W > 60$ GeV cuts (FR1). For the cross-check, another fitting region with additional relaxation of $p_T^W < 30$ GeV cut (FR2) is also considered providing significant discriminative power between the multijet background and $W \rightarrow \mu\nu$ signal. The Table 7.8 summarises the definitions of the signal region and all the control and fitting regions.

Cuts	Lepton isolation		E_T^{miss}	m_T^W	p_T^W
Selection	SR sample	CR sample			
Signal region			$E_T^{\text{miss}} > 30$ GeV	$m_T^W > 60$ GeV	$p_T^W < 30$ GeV
FR1	$Iso < 0.1$	$0.2 < Iso < 0.4$	-	-	$p_T^W < 30$ GeV
FR2			-	-	-

Table 7.8: Table which summarises the definitions of the signal region and all the control and fitting regions. 'Iso' corresponds to muon isolation $\sum p_T^{trk}/p_T$ variable.

An idea of the fraction fit method is the following (taking an example of fit to E_T^{miss} distribution in FR1):

- (1) Produce the SR sample for Data and total MC with isolated muons. Fill corresponding E_T^{miss} distributions in the FR1. This results in $N_{data}^{FR1-iso}$ events in data and $N_{mc}^{FR1-iso}$ events in MC. In parallel, fill the E_T^{miss} distributions in the signal region that results in N_{data}^{SR-iso} events in data and N_{mc}^{SR-iso} events in MC.
- (2) Produce the CR sample in Data and MC with anti-isolated muons. Fill corresponding E_T^{miss} distributions in the FR1. Subtract MC from Data. This results in $N_{jet}^{FR1-anti-iso} = N_{data}^{FR1-anti-iso} (1 - f_{MC}^{FR1-anti-iso})$ pure multijet events. Here $f_{MC}^{FR1,anti-iso}$ is a fraction of EW contamination. Repeat this step with all cuts applied corresponding to signal region. This results to $N_{jet}^{SR-anti-iso} = N_{data}^{SR-anti-iso} (1 - f_{MC}^{SR-anti-iso})$ pure multijet events.
- (3) Combine the multijet and MC E_T^{miss} distributions in order to match data in $FR1-iso$

$$T \cdot N_{jet}^{FR1-anti-iso} + \alpha \cdot N_{mc}^{FR1-iso} = N_{data}^{FR1-iso} \quad (7.2)$$

where T and α are free parameters. They are extracted from a binned likelihood fit of corresponding distribution. In general $\alpha \approx 1$ as expected as the MC sample is normalized according to cross sections. The parameter T represents a global transfer factor that scales the multijet sample. Since the fitting regions exist as isol and anti-isol variants, the *FR1-iso* is used to indicate this.

- (4) An amount of multijet background in SR is then calculated as

$$N_{jet}^{SR-iso} = T \cdot N_{jet}^{SR-anti-iso} \quad (7.3)$$

and the corresponding multijet fraction is calculated as $f_{jet} = N_{jet}^{SR-iso} / N_{data}^{SR-iso}$.

The steps introduced above can be repeated for fits to m_T^W and p_T^μ / m_T^W in the FR1 as well as FR2. Examples of the fits to E_T^{miss}, m_T^W and p_T^μ / m_T^W are shown in figures 7.1 and 7.2 respectively for $W \rightarrow \mu^+ \nu$ and $W \rightarrow \mu^- \bar{\nu}$ channels. The extracted T -values are indicated for each case.

Cut	Name	$N_{Data}^{Name-anti-iso}$	$f_{MC}^{Name} [\%]$	T	N_{jet}^{SR-iso}
Channel	$W^+ \rightarrow \mu\nu$				
$p_T^\ell > 30 \text{ GeV}$	FR2	1457290	0.6	0.71 ± 0.08	17287 ± 1948
$p_T^W < 30 \text{ GeV}$	FR1	181947	2.1	1.00 ± 0.01	24348 ± 243
$m_T^W > 60 \text{ GeV}$		37305	11.1	-	-
$E_T^{\text{miss}} > 30 \text{ GeV}$	SR	28148	13.5	-	-
Channel	$W^- \rightarrow \mu\nu$				
$p_T^\ell > 30 \text{ GeV}$	FR2	1424729	0.5	0.70 ± 0.07	16294 ± 1629
$p_T^W < 30 \text{ GeV}$	FR1	174374	2.5	0.97 ± 0.01	22579 ± 233
$m_T^W > 60 \text{ GeV}$		35128	9.3	-	-
$E_T^{\text{miss}} > 30 \text{ GeV}$	SR	26272	11.4	-	-

Table 7.9: Cutflow of the data selection and expected EW contamination in the $W^+ \rightarrow \mu\nu$ and $W^- \rightarrow \mu\nu$ channels, requiring muons to be anti-isolated within $0.1 < \sum p_T^{\text{trk}} / p_T < 0.4$. MC corresponds to simulated signal and background contamination normalized to their cross sections.

The Table 7.9 summarizes the cutflow of selected events in the control region sample and amount of corresponding EW contamination. The normalization value T of data-driven background sample is found from the multijet fit using three variables mentioned above. The column with $T \pm \Delta T$ is a spread found from the multijet fit using m_T^W , E_T^{miss} and p_T^μ / m_T^W variables in corresponding FR. The corresponding multijet yield in SR is calculated as $N_{jet}^{SR-iso} = T \cdot N_{Data}^{SR-anti-iso} (1 - f_{MC}^{SR-anti-iso})$ and uncertainty $\Delta N_{jet}^{SR-iso} = \Delta T \cdot N_{Data}^{SR-anti-iso} (1 - f_{MC}^{SR-anti-iso})$. The multijet yields derived from the fits to kinematical distributions in the FR1 are in a good agreement, giving 24348 ± 243 events for W^+ and 22579 ± 233 events for W^- channel. However the results are significantly spread for the FR2: 17287 ± 1948 events for W^+ and 16294 ± 1629 events for W^- . In addition, the background fractions have lower values with respect to FR1 results. Correspondingly, the Data/MC agreement is not perfect, with $O(5\%)$ discrepancy depending on the fitting variable (see ratio plots in figures 7.1 and 7.2).

The reason for this behavior is intrinsic to our definition of the hadronic recoil which, in short, consists of a vector sum of all calorimeter cluster energies in the event, excluding the clusters located in a cone of radius $\Delta R = 0.2$ around the leptons selected in the analysis. This removal is adapted for W and Z events where the leptons are typically isolated, and is needed to make the recoil insensitive to energy deposits by the leptons, making its response identical in all channels of interest ($W \rightarrow e\nu$, $W \rightarrow \mu\nu$, $Z \rightarrow ee$ and $Z \rightarrow \mu\mu$). This however implies that the recoil reconstructed in events with non-isolated leptons is biased along the lepton direction, as the energy present around the lepton

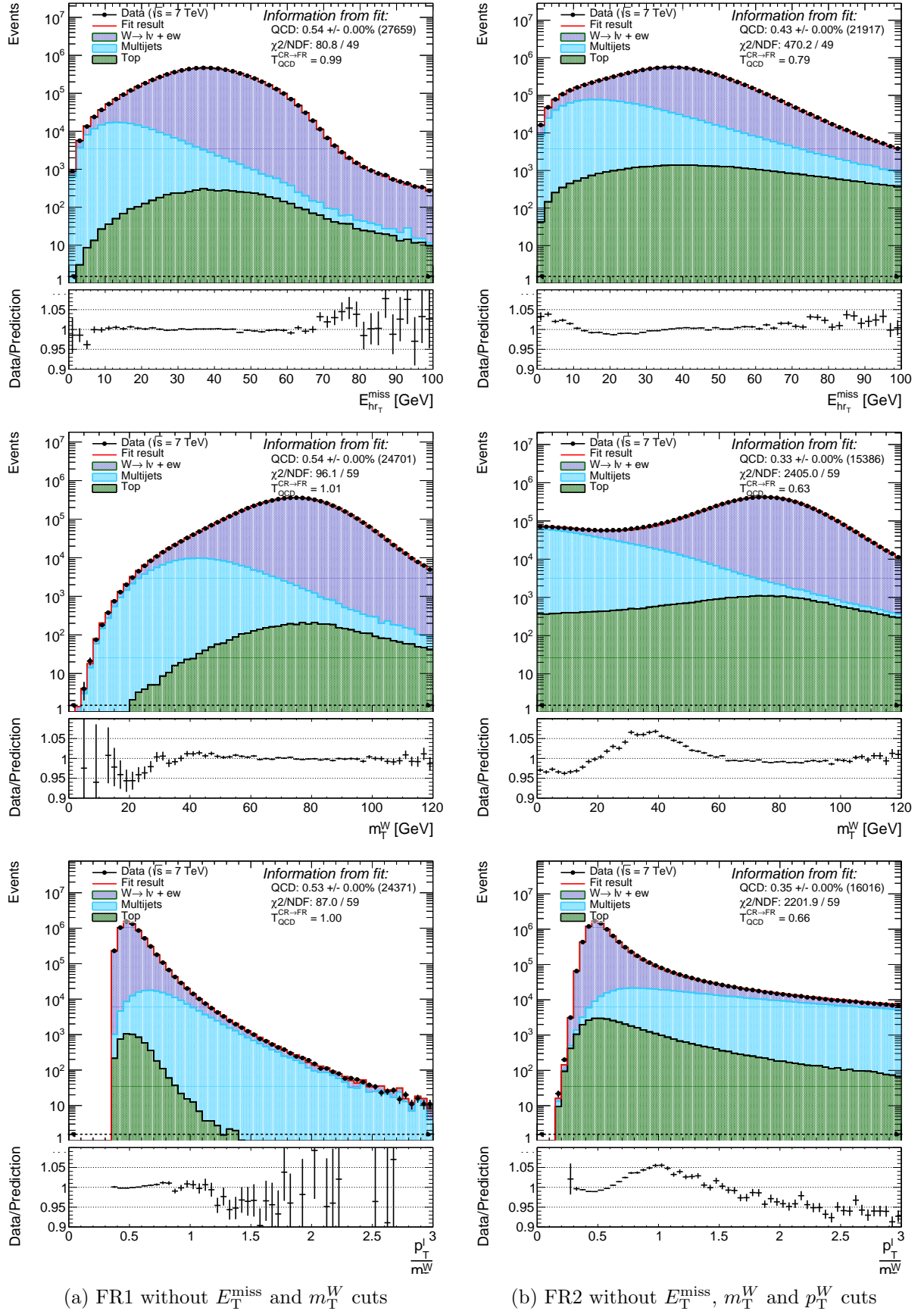


Figure 7.1: Example of multijet template fits of E_T^{miss} , m_T^W and p_T^W/m_T^W distributions in FR1 and FR2, for integrated $W^+ \rightarrow \mu^+ \bar{\nu}$ selection. Multijet distribution is extracted from $0.2 < \sum p_T^{\text{trk}}/p_T < 0.4$ region. The fitting range is indicated by the dashed arrow. The estimated multijet fraction in the SR is specified in the figure.

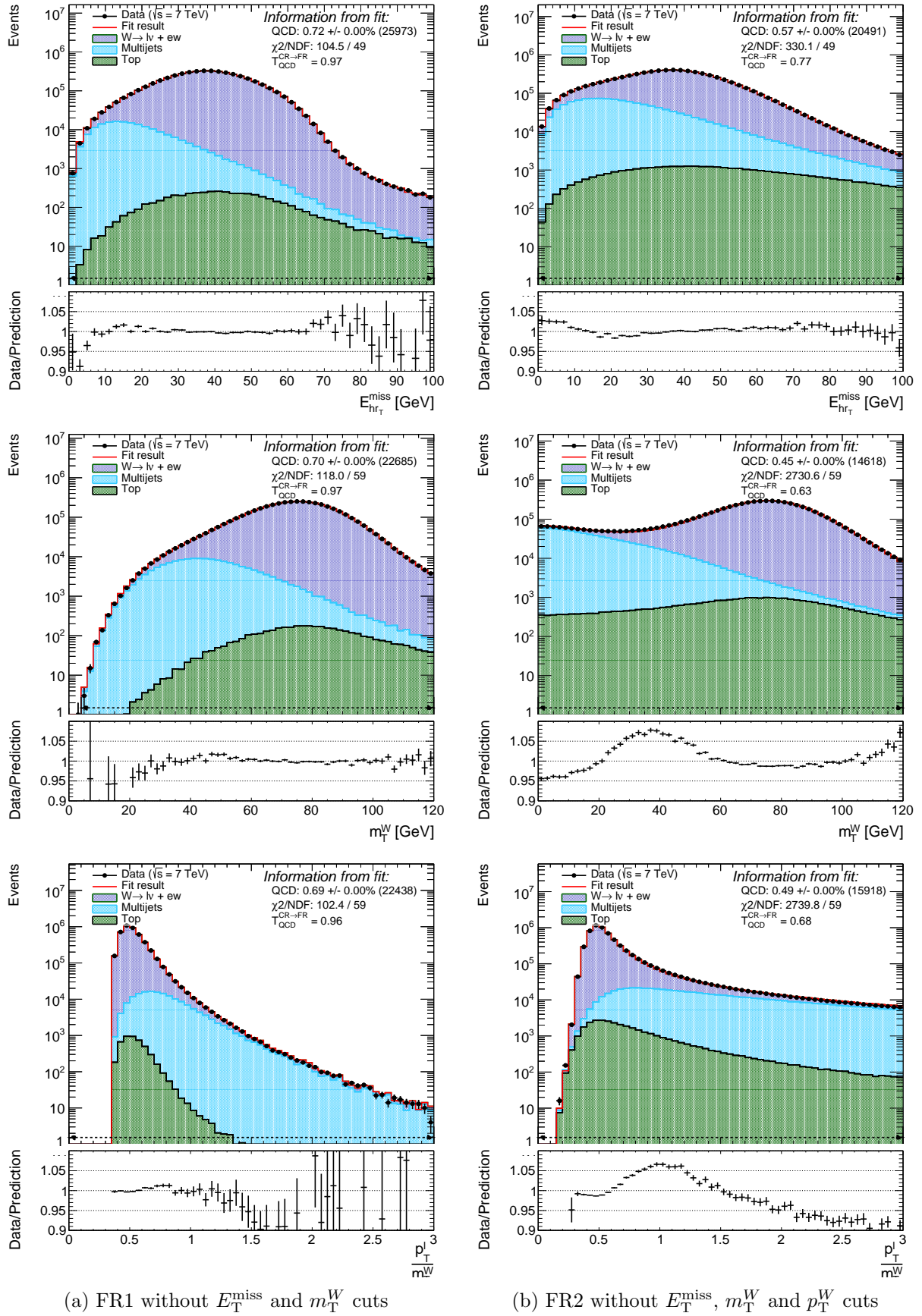


Figure 7.2: Example of multijet template fits of E_T^{miss} , m_T^W and p_T^W/m_T^W distributions in FR1 and FR2, for integrated $W^- \rightarrow \mu^- \nu$ selection. Multijet distribution is extracted from $0.2 < \sum p_{\text{T}}^{\text{trk}}/p_{\text{T}} < 0.4$ region. The fitting range is indicated by the dashed arrow. The estimated multijet fraction in the SR is given in the figure.

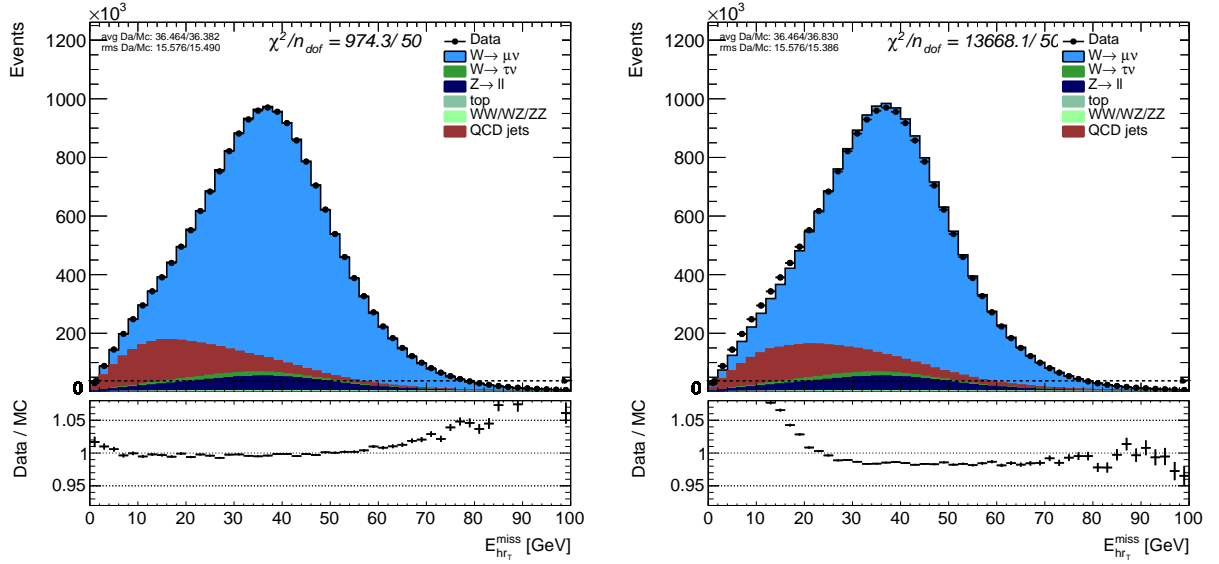


Figure 7.3: E_T^{miss} in data and simulation with multijet background injected with the same fraction, but extracted from different isolation regions: $0.10 < p_T^{\text{cone20}}/p_T^\mu < 0.13$ (left) and $0.37 < p_T^{\text{cone20}}/p_T^\mu < 0.40$ (right). The cuts $E_T^{\text{miss}} > 30$ GeV, $m_T^W > 60$ GeV and $p_T^W < 30$ GeV are removed in order to increase the impact of the multijet background.

in this case is underestimated in the present approach. As a result, the kinematic distributions that depend on the recoil (E_T^{miss} , m_T^W and p_T^μ/m_T^W) measured in the anti-isolated control regions do not exactly represent the actual background in the isolated signal region.

▷ Scanning of the isolation variable

Due to the problems explained above, an improved multijet background estimation method has been used which allows to reduce the spread of the results caused by the choice of fitting region or variable. The method consists in testing of different muon isolation slices as control regions by repeating the procedure explained above. The multijet distribution extracted from the isolation slice near the signal region is closer to the truth than that one which is extracted from high isolation region. Thus, the final multijet yield can be obtained by extrapolating the results extracted from different isolation slices to the signal region. Figure 7.3 shows the Data/MC for the E_T^{miss} distribution in the region with removed E_T^{miss} , m_T^W and p_T^W cuts for two isolation slices from which the multijet background is extracted. The data and MC distributions are the same, while only the shape of multijet background is different. The fraction of the multijet background in both cases is equal. As expected, the agreement is better when using the multijets from lower isolation values.

In Fig.7.4 the multijet background yield in the signal region is plotted versus the range of the isolation variable used to define the data-driven distributions. Each curve corresponding to different fitting region/variable is then extrapolated to the signal region. As can be seen, the curves converge when moving to the signal region. Good agreement using different fitting regions and variables (i.e. small spread between lines at zero isolation) is obtained. The fact that these curves match in the signal region confirms the validity of the method. The final background yield and its systematic uncertainty are estimated with the following procedure:

- Determine the lines that correspond to highest and lowest multi-jet yield at zero isolation $N_{\text{jet}}^{\text{max}}$ and $N_{\text{jet}}^{\text{min}}$.
- The central value of multi-jet background yield is calculated as $(N_{\text{jet}}^{\text{max}} + N_{\text{jet}}^{\text{min}})/2$ (center of ellipses in Fig.7.4)

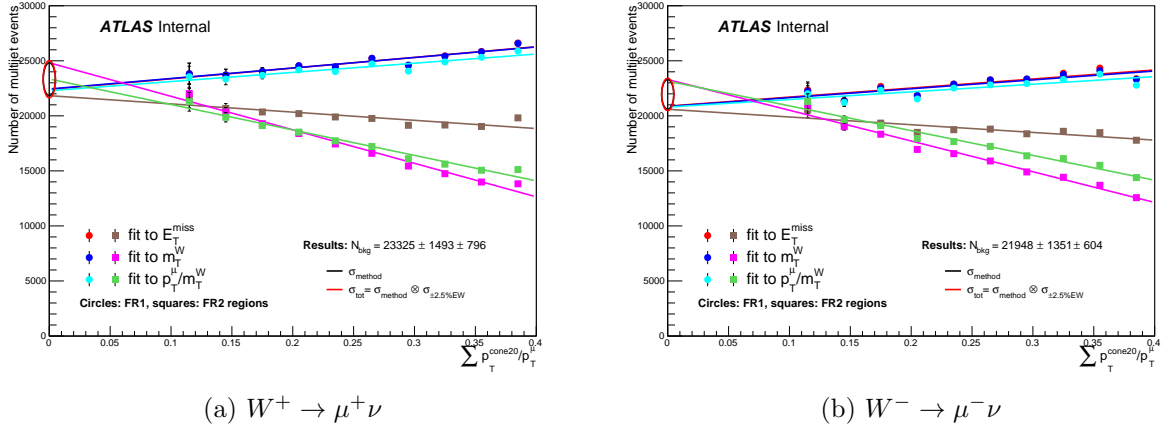


Figure 7.4: Fitted multijet background yield in the signal region plotted in bins of the isolation variable used to define the data-driven distributions. Error bars at each point are the combination of statistical uncertainty coming from the fraction fits and uncertainties due to $\pm 2.5\%$ variations of predicted non-multijet contamination in the CR. The center of black/red ellipse at $p_T^{\text{cone20}}/p_T^\mu \sim 0$ is the expected average isolation value of the multi-jet background in the signal region, while the radius of red (black) ellipse is equal to total (method) uncertainty.

- The uncertainty of multi-jet background yield is calculated as $\sigma_{\text{method}} = (N_{\text{jet}}^{\text{max}} - N_{\text{jet}}^{\text{min}})/2$ (major radius of black ellipse in Fig.7.4)
- Vary cross section for EW background by $\pm 2.5\%$ up or down and repeat the previous steps. Difference between old and new central value is taken as systematic uncertainty σ_{EW} coming from EW cross section variation.
- Add both types of uncertainty in quadrature to obtain the total uncertainty σ_{tot} (major radius of red ellipse in Fig.7.4)

The choice of 2.5% variation refers to W cross section measurement at 7 TeV.

The results are shown in Table 7.10 for the $W \rightarrow \mu^+ \nu$ and $W \rightarrow \mu^- \bar{\nu}$ channels separately. The multijet background is estimated with a relative precision of less than 10%. The error bars in each point in In Fig.7.4 correspond to the combined statistical \oplus systematic uncertainty. Systematic uncertainty comes from variation of predicted EW contamination in the CR by $\pm 2.5\%$. The systematic uncertainty coming from variations of fitting range for each variable is found to be small.

Channel	Multijet background fraction (%)	Multijet background yield
$W \rightarrow \mu^+ \nu$	0.51 ± 0.04	23325 ± 1692
$W \rightarrow \mu^- \bar{\nu}$	0.68 ± 0.05	21948 ± 1480

Table 7.10: Multijet background estimates using fits to kinematical distributions, for the $W \rightarrow \mu^+ \nu$ and $W \rightarrow \mu^- \bar{\nu}$ channels, inclusively in η and $< \mu >$.

7.4.3 Fits to kinematical distributions in the electron channel

Similar to muon channel, an electron-like object with large jet activity around its track is more like to be a background electron present in light- and heavy-flavour jets. Thereby a background dominated sample is selected with modified electron isolation criteria keeping the electron identification requirement as "tight". Unlike simple cut on muon isolation variable, the complex electron

isolation includes both the track-based p_T^{cone40} and calorimeter-based E_T^{cone20} electron isolation variables. Various control (anti-isolated) regions with enriched multijet background can be defined by requiring to fail one isolation cut and keep, remove or invert the requirement on another one. In this analysis, the nominal multijet background control region is chosen to be constructed by requiring $4\text{GeV} < p_T^{\text{cone40}} < 8\text{GeV}$ cut and removing E_T^{cone20} cut. Higher values of p_T^{cone40} are excluded as it is too far from the signal region which is within $p_T^{\text{cone40}} < 4\text{GeV}$. The signal and EW background contamination is taken into account using MC samples normalised to corresponding cross-sections.

Once the multijet sample is created, its normalisation can be found from the fraction fit using the following discriminating variables (similar to muon channel):

- The E_T^{miss} distribution of the background events is peaked at lower value comparing to signal $W \rightarrow e\nu$ events.
- The W transverse mass m_T^W constructed using background events tends to be small.
- The ratio p_T^e/m_T^W containing angular information between electron-like object and a neutrino. This distribution is peaked at 0.5 for well-balanced signal $W \rightarrow e\nu$ events, while the balance can be disregarded in multijet events leading to presence of tail in the distribution.

In order to give an access to multijet dominant regions for the background fits, the fitting region is constructed with removed $E_T^{\text{miss}} > 30$ GeV and $m_T^W > 60$ GeV cuts (FR1). For the cross-check, another fitting region with additional relaxation of $p_T^W < 30$ GeV cut (FR2) is also considered providing significant discriminative power between the multijet and EW templates. Examples of the fits are shown in figures 7.5 and 7.6 respectively for $W \rightarrow e^+\nu$ and $W \rightarrow e^-\bar{\nu}$ channels.

Cut	Name	$N_{Data}^{Name,anti-iso}$	$f_{MC}^{Name}[\%]$	T	$N_{jet}^{SR,iso}$
Channel	$W^+ \rightarrow e\nu$				
$p_T^\ell > 30$ GeV	FR2	475655	10.0	1.77 ± 0.11	26129 ± 1624
$p_T^W < 30$ GeV	FR1	143466	23.1	2.21 ± 0.06	32624 ± 886
$m_T^W > 60$ GeV		49677	55.3	-	-
$E_T^{\text{miss}} > 30$ GeV	SR	39365	62.5	-	-
Channel	$W^- \rightarrow e\nu$				
$p_T^\ell > 30$ GeV	FR2	1424729	7.6	1.77 ± 0.10	26593 ± 1502
$p_T^W < 30$ GeV	FR1	132930	18.0	2.20 ± 0.05	33054 ± 751
$m_T^W > 60$ GeV		42435	47.1	-	-
$E_T^{\text{miss}} > 30$ GeV	SR	32876	54.3	-	-

Table 7.11: Cutflow of the data selection and expected EW contamination in the $W^+ \rightarrow e\nu$ and $W^- \rightarrow e\nu$ channels, requiring electrons to be anti-isolated requiring $4\text{GeV} < p_T^{\text{cone40}} < 8\text{GeV}$ and removing E_T^{cone20} cuts. MC corresponds to simulated signal and background contamination normalized to their cross sections.

Table 7.11 summarizes the cutflow of selected events in the control region sample and amount of corresponding EW contamination. The column with $T \pm \Delta T$ is a spread found from the multijet fit using m_T^W , E_T^{miss} and p_T^μ/m_T^W variables in corresponding FR. The corresponding multijet yield in SR is calculated as $N_{jet}^{SR-iso} = T \cdot N_{Data}^{SR-anti-iso} (1 - f_{MC}^{SR-anti-iso})$ and uncertainty $\Delta N_{jet}^{SR-iso} = \Delta T \cdot N_{Data}^{SR-anti-iso} (1 - f_{MC}^{SR-anti-iso})$. Note that an amount of EW contamination f_{MC}^{Name} in the nominal control region is significantly higher than in the muon channel leading to larger the systematic uncertainty. The normalization value T is found from the multijet fit using three variables mentioned above. The results are different when using different fitting regions and this is traced to a correlation between the electron isolation and the recoil-based variables used

for the template fit, as discussed in the previous section. So the improved method of scanning isolation variable, introduced in the previous section, has to be used.

▷ Scanning of the isolation variable

The nominal control region has been split into subregions by means of p_T^{cone40} as shown in Fig.7.7. Each curve corresponding to different fitting region/variable is then extrapolated to the signal region. The central value of multijet yield and its total uncertainty are defined in the same way as for muon channel.

The results are shown in Table 7.12 for the $W \rightarrow e^+\nu$ and $W \rightarrow e^-\bar{\nu}$ channels separately. Good agreement using different fitting regions and variables is obtained. The multijet background is estimated with a relative precision of less than 10% and number of background events is compatible between W^+ and W^- channels. The error bars in each point correspond to the combined statistical \oplus systematic uncertainty. Systematic uncertainty comes from variation of predicted EW contamination in the CR by $\pm 2.5\%$. The systematic uncertainty coming from variations of fitting range for each variable is found to be small.

Channel	Multijet background fraction (%)	Multijet background yield
$W \rightarrow e^+\nu$	0.83 ± 0.09	27897 ± 3179
$W \rightarrow e^-\bar{\nu}$	1.21 ± 0.10	29477 ± 2496

Table 7.12: Multijet background estimates using fits to kinematical distributions, for the $W \rightarrow e^+\nu$ and $W \rightarrow e^-\bar{\nu}$ channels, inclusively in η and $< \mu >$.

▷ Cross-checks with other control regions

As mentioned above, the nominal multijet background control region in electron channel is chosen to be constructed by inverting p_T^{cone40} cut and removing E_T^{cone20} cut. However, various control regions can be defined by requiring to fail one isolation cut and keep, remove or invert the requirement on another one. In general, the scanning procedure for all of them has to lead to the same result of multijet yield in the signal region. This conclusion comes from the fact, that the method takes into account the evolution of each background component (type) when moving from high to low values of isolation variable without their separate consideration (evaluation).

Figure 7.8 illustrates the amount of multijet background with respect to total W event candidates in the charge-blinded signal region using three definitions of multijet control region. All of them converge to the same result of about 1% of multijet fraction.

7.4.4 Independent cross-check of the multijet background estimates with W and Z cross section analysis at $\sqrt{s} = 7$ TeV

To verify the multijet background estimates in the $W \rightarrow \mu\nu$ and $W \rightarrow e\nu$ analyses with an independent method, the signal region was extended to exactly the same phase space as in the W cross section measurement, i.e. $p_T^\ell > 25$ GeV, $E_T^{\text{miss}} > 25$ GeV, $m_T^W > 40$ GeV and no cut on the p_T^W . Moreover, the missing energy has been changed from HR-based to more complex calorimeter-based definition (MET ReFFinal). Despite careful synchronization, a few known minor differences remain between the analyses:

- Used $W \rightarrow \ell\nu$ signal MC samples, physics and detector corrections and calibrations are slightly different between the analyses

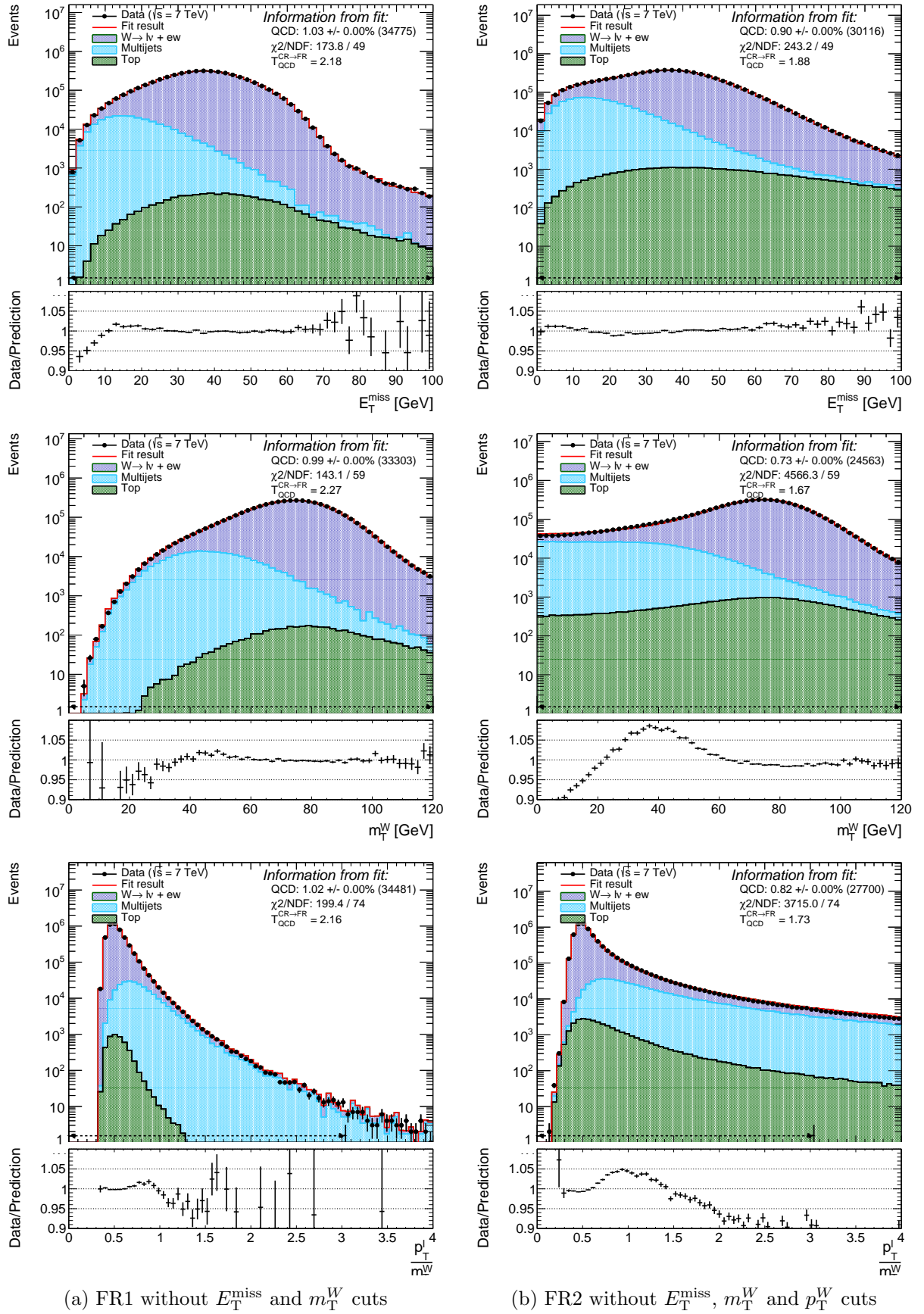


Figure 7.5: Example of multijet template fits of E_T^{miss} , m_T^W and p_T^W/m_T^W distributions in FR1 and FR2, for integrated $W^+ \rightarrow e^+ \bar{\nu}$ selection. Multijet background templates are derived from data using an anti-isolation requirement on the p_T^{cone40} variable, as described in the text. The fitting range is indicated by the dashed arrow. The estimated multijet fraction in the SR is given in the figure.

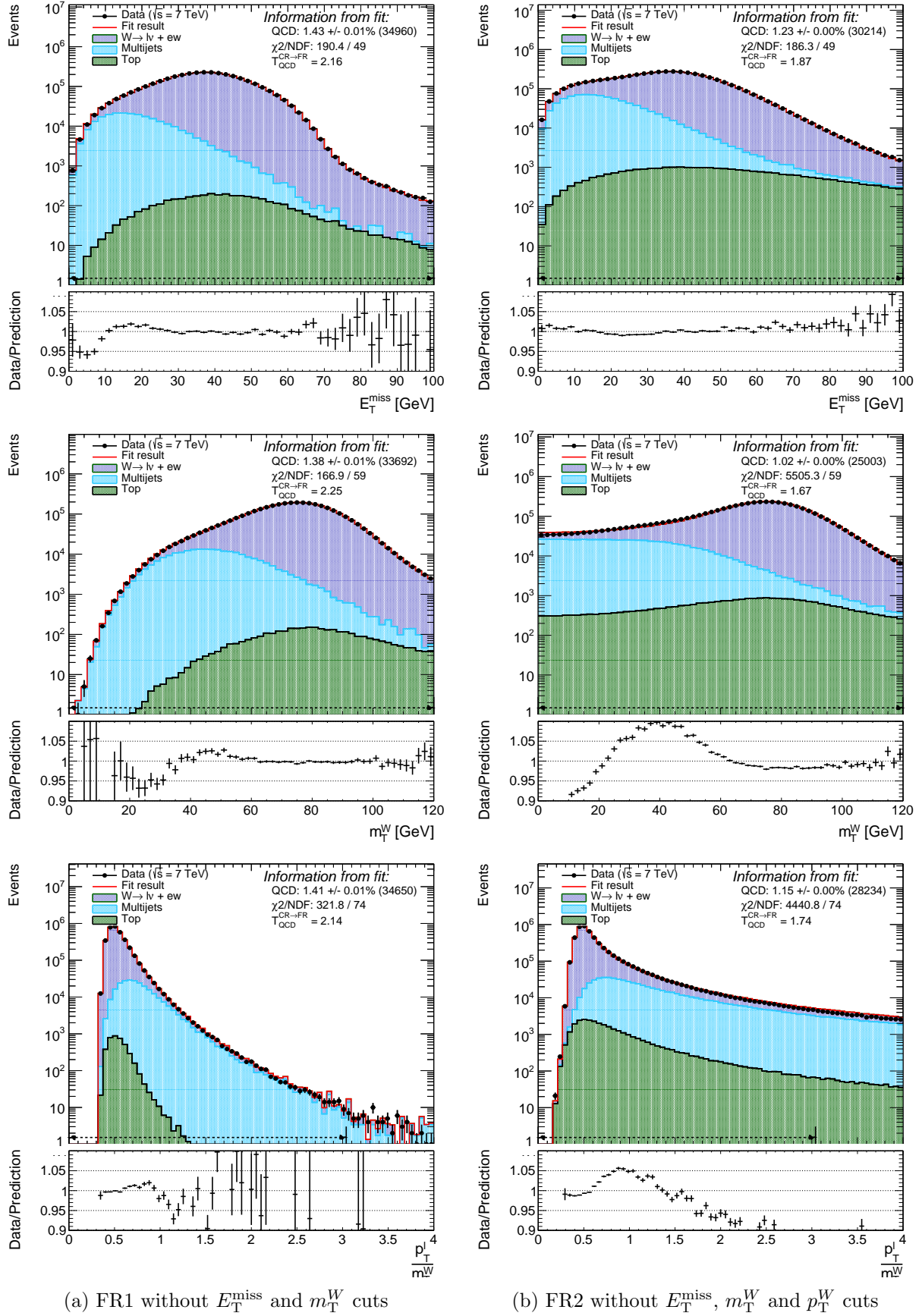


Figure 7.6: Example of multijet template fits of E_T^{miss} , m_T^W and p_T^W/m_T^W distributions in FR1 and FR2, for integrated $W^- \rightarrow e^- \nu$ selection. Multijet background templates are derived from data using an anti-isolation requirement on the p_T^{cone40} variable, as described in the text. The fitting range is indicated by the dashed arrow. The estimated multijet fraction in the SR is given in the figure.

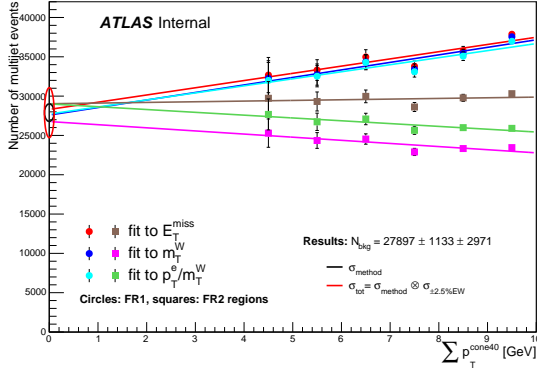
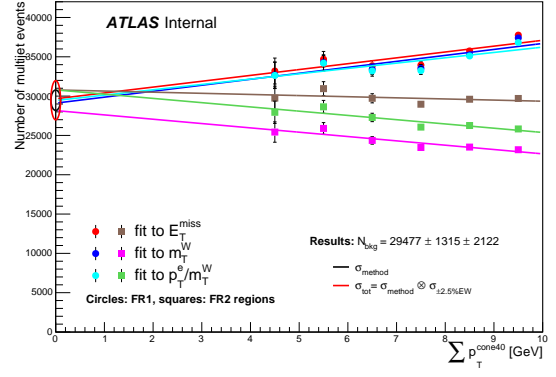
(a) $W^+ \rightarrow e^+ \nu$ (b) $W^- \rightarrow e^- \nu$

Figure 7.7: Fitted multijet background yield in the signal region plotted in bins of the isolation variable used to define the data-driven distributions. Error bars at each point are the combination of statistical uncertainty coming from the fraction fits and uncertainties due to $\pm 2.5\% \sigma$ variations of predicted non-multijet contamination in the CR. The center of black/red ellipse at $p_T^{\text{cone}20} \sim 0$ corresponds to the central value of multi-jet background, while the radius of red (black) ellipse is equal to total (method) uncertainty.

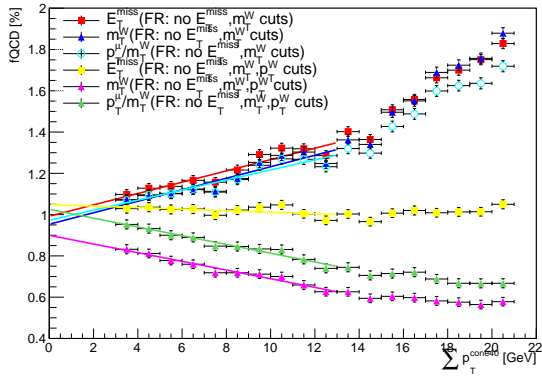
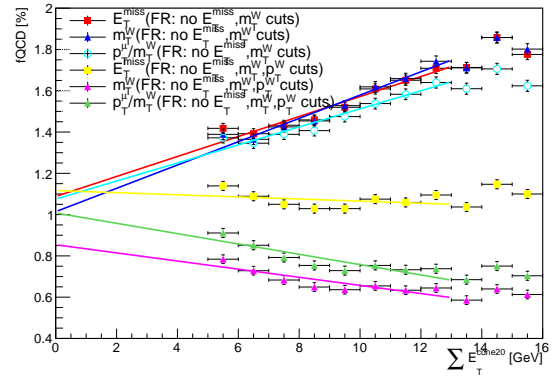
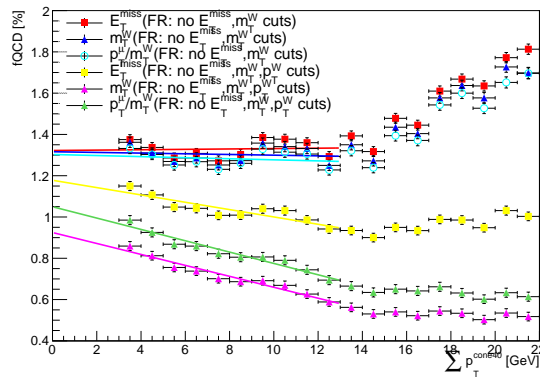
(a) $p_T^{\text{cone}40}$ cut inverted, $E_T^{\text{cone}20}$ cut removed(b) $p_T^{\text{cone}40}$ cut removed, $E_T^{\text{cone}20}$ cut inverted(c) Both $p_T^{\text{cone}40}$ and $E_T^{\text{cone}20}$ cuts inverted

Figure 7.8: Fitted multijet background fraction in the charge-blinded signal region using three definitions of multijet control region. The figure (a) corresponds to the nominal control region.

Cutflows were cross-checked on both data and MC and agreement to typically $\sim 1\%$ level was obtained. Given this level of good agreement, it is expected, that the amount of QCD multijet background expressed as fraction w.r.t. the selected data, f_{QCD} , can be directly compared between the analyses.

In short, the differences of the W cross section method compared to method presented here are:

- $W \rightarrow \mu\nu$
 - The method uses the fits to kinematical distribution, similar as in Section 7.4.2
 - The control region is defined to be within the muon isolation range $0.15 < \sum p_T^{\text{trk}}/p_T < 0.30$ which is quite close to signal region
- $W \rightarrow e\nu$
 - The control region is defined to have 'loose-not-medium' electron ID that pass some additional track cuts
 - The isolation requirement is dropped. Instead, require anti-isolation $E_T^{\text{cone30}}/E_T > 0.2$
 - The charge requirement is dropped. The same QCD templates are used for $W^+ +$ and W^-

The Figure 7.9 compares the measured QCD multijet background fractions f_{QCD} for the four channels $W^+ \rightarrow \mu\nu$, $W^- \rightarrow \mu\nu$, $W^+ \rightarrow e\nu$ and $W^- \rightarrow e\nu$ graphically. Both the integrated number (the first bin) and the numbers in several $|\eta^\ell|$ bins are given. For technical reasons the $\eta^{\ell\ell}$ bins different between cross section analysis and W mass analysis methods. The integrated numbers fully comparable and covers the same η^ℓ range. In the $W \rightarrow e\nu$ channel the agreement is satisfactory at the level of $\sim 1\sigma$. In the $W \rightarrow \mu\nu$ channel the agreement is excellent at the level of $< 0.5\sigma$ total uncertainty. The results obtained in $\eta^{\ell\ell}$ and inclusively are summarized in Table 7.13.

$ \eta $ range	0 – 0.8	0.8 – 1.4	1.4 – 2.0	2.0 – 2.4	Integrated
$W^\pm \rightarrow \mu\nu$	3.27 ± 0.15	2.81 ± 0.08	2.29 ± 0.04	1.81 ± 0.10	2.64 ± 0.08
$W^+ \rightarrow \mu\nu$	2.86 ± 0.13	2.40 ± 0.04	1.91 ± 0.06	1.47 ± 0.08	2.23 ± 0.07
$W^- \rightarrow \mu\nu$	3.81 ± 0.17	3.40 ± 0.14	2.86 ± 0.04	2.37 ± 0.12	3.24 ± 0.10
$ \eta $ range	0 – 0.6	0.6 – 1.2	-	1.8 – 2.4	Integrated
W^\pm	1.99 ± 0.12	2.88 ± 0.11	-	5.36 ± 0.67	3.62 ± 0.24
W^+	1.69 ± 0.12	2.51 ± 0.06	-	4.35 ± 0.56	2.96 ± 0.16
W^-	2.39 ± 0.14	3.51 ± 0.11	-	7.15 ± 0.90	4.23 ± 0.28

Table 7.13: Measured multijet background fractions (%) in the four channels $W^+ \rightarrow \mu\nu$, $W^- \rightarrow \mu\nu$, $W^+ \rightarrow e\nu$ and $W^- \rightarrow e\nu$

7.4.5 Multijet background estimation for W cross section measurement at $\sqrt{s} = 8$ TeV

The method of multijet background estimates explained in this section has been applied in the W cross section analysis in $W \rightarrow \mu\nu$ channel at center-of-mass energy of 8TeV. The signal region is defined to have $p_T^\ell > 25$ GeV, $E_T^{\text{miss}} > 25$ GeV, $m_T^W > 40$ GeV cuts and no cut on the p_T^W .

The three different definitions of the missing energy were tested:

- Track based E_T^{miss}
- Calorimeter based E_T^{miss}

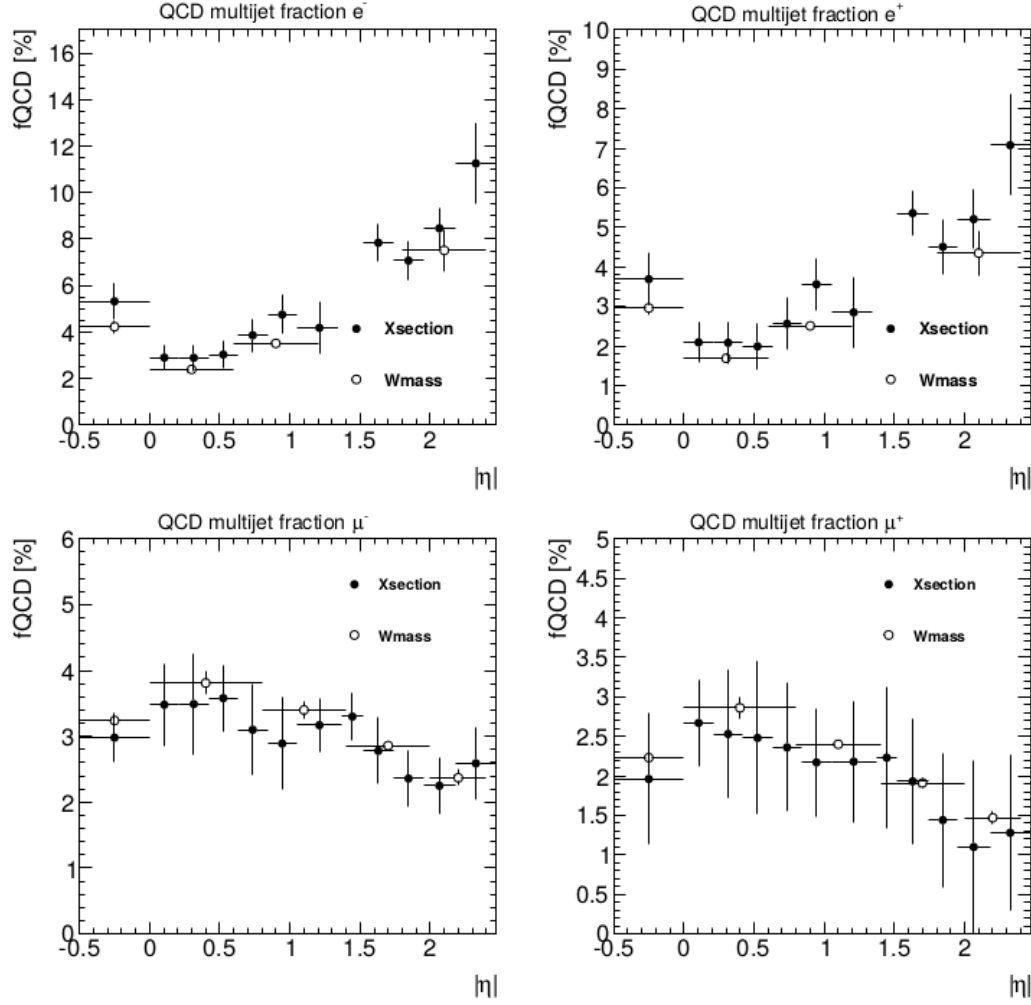


Figure 7.9: Comparison of measured QCD multijet background fractions in the four channels $W^+ \rightarrow \mu\nu$, $W^- \rightarrow \mu\nu$, $W^+ \rightarrow e\nu$ and $W^- \rightarrow e\nu$ obtained with the cross section analysis (full black dots) and W mass analysis (open circles) methods. The first point shown at $|\eta_l| < 0$ shows the value when integrating over the full η_l range.

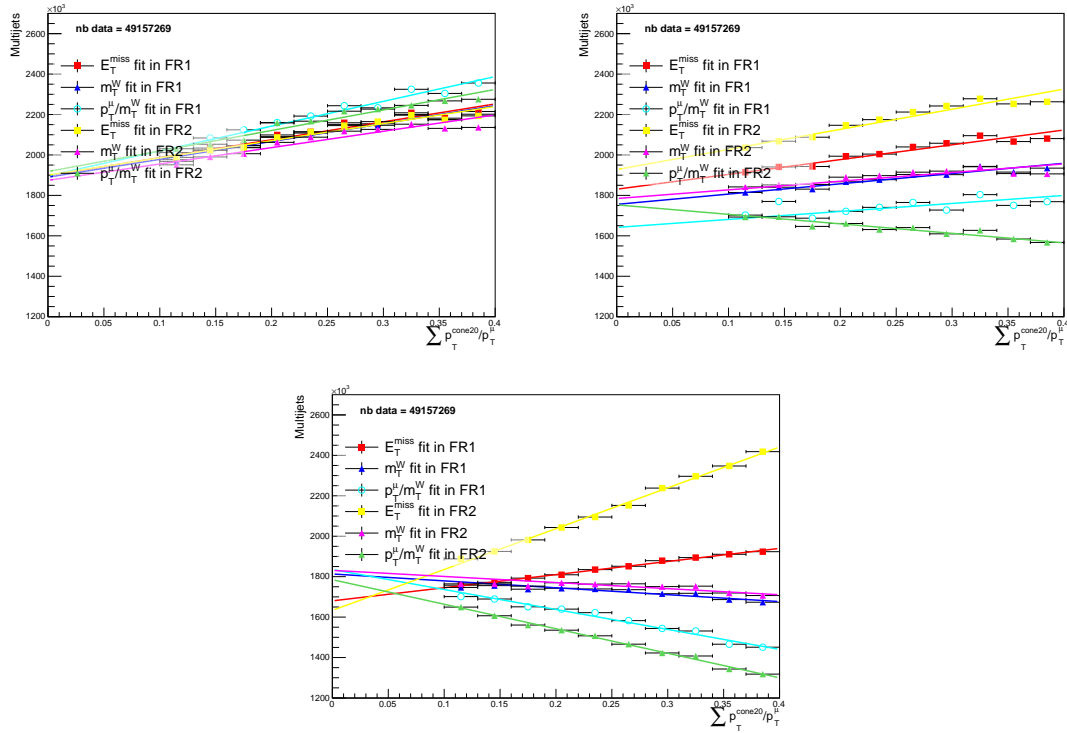


Figure 7.10: Comparison of measured multijet background yield in the $W^+ \rightarrow \mu\nu$ channel using three different missing energy definitions: track-based (left), calorimeter-based (middle) and HR-based (right) as used in W mass analysis.

- Hadronic recoil based E_T^{miss} (similar as for M_W analysis)

Usage of all of them gives similar multijet yield as shown in figures 7.10 and 7.11.

7.4.6 Multijet fractions in the measurement categories

Following the measurement categorisation introduced in section 8.2.2, the multijet background estimates are performed inclusively, separately for W^+ and W^- , as well as for each $\eta \times \mu$ bin. The background fractions are shown for standard signal selection in Tab. 7.14 for muon and Tab. 7.15 for electron channels.

7.4.7 Correction of the multijet background shapes

As described in the previous section, an amount of multijet background events is estimated by probing an evolution of the multijet distributions extracted from enriched control regions which are defined by changing the lepton isolation requirements towards the signal region. Such a method allows to obtain the background yield without an exact knowledge of the shape of multijet distribution in signal region. However, the W mass extraction relies on the precise modeling not only of the background yield, but also the shapes of relevant distributions. The shapes available in the control region not always represent the shapes in the signal region. Even if the control region is defined to be close to signal region, the shape mismodeling can introduce a bias to the extracted m_W value.

This section describes a method of multijet shapes correction using information about their evolution in background enriched control region. In order to quantify how each distribution ($p_T^e, m_T^W, E_T^{\text{miss}}, \eta_l$, recoil) changes over lepton isolation criteria, two control regions are defined: one is close to signal region (CR1) and one is further away (CR2). The ratio of these distributions is then used for the shape extrapolation to signal region (linear assumption).

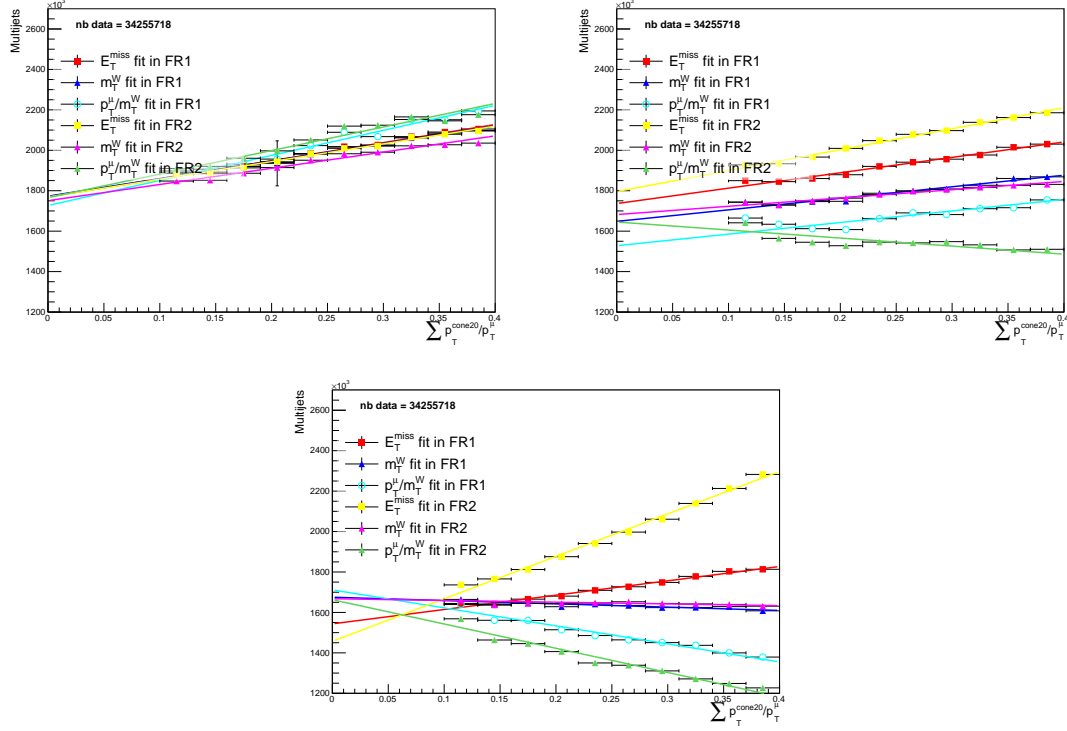


Figure 7.11: Comparison of measured multijet background yield in the $W^- \rightarrow \mu\nu$ channel using three different missing energy definitions: track-based (left), calorimeter-based (middle) and HR-based (right) as used in W mass analysis.

	$ \eta $ range	0 – 0.8	0.8 – 1.4	1.4 – 2.0	2.0 – 2.4	inclusive
μ -inclusive	W^\pm	0.72 ± 0.07	0.57 ± 0.04	0.51 ± 0.03	0.49 ± 0.03	0.58 ± 0.04
	W^+	0.66 ± 0.07	0.50 ± 0.04	0.44 ± 0.03	0.40 ± 0.03	0.51 ± 0.04
	W^-	0.79 ± 0.07	0.67 ± 0.05	0.62 ± 0.04	0.61 ± 0.04	0.68 ± 0.05
	$ \eta $ range	0 – 0.8	0.8 – 1.4	1.4 – 2.0	2.0 – 2.4	inclusive
$2.5 < \langle \mu \rangle < 6.5$	W^\pm	0.48 ± 0.03	0.37 ± 0.03	0.34 ± 0.02	0.33 ± 0.03	0.38 ± 0.03
	W^+	0.40 ± 0.03	0.35 ± 0.03	0.31 ± 0.03	0.28 ± 0.06	0.33 ± 0.02
	W^-	0.57 ± 0.05	0.40 ± 0.04	0.39 ± 0.03	0.43 ± 0.04	0.47 ± 0.04
	$ \eta $ range	0 – 0.8	0.8 – 1.4	1.4 – 2.0	2.0 – 2.4	inclusive
$6.5 < \langle \mu \rangle < 9.5$	W^\pm	0.66 ± 0.05	0.55 ± 0.03	0.50 ± 0.03	0.55 ± 0.06	0.57 ± 0.03
	W^+	0.65 ± 0.07	0.46 ± 0.04	0.39 ± 0.04	0.49 ± 0.09	0.50 ± 0.03
	W^-	0.64 ± 0.05	0.65 ± 0.05	0.69 ± 0.04	0.61 ± 0.10	0.66 ± 0.04
	$ \eta $ range	0 – 0.8	0.8 – 1.4	1.4 – 2.0	2.0 – 2.4	inclusive
$9.5 < \langle \mu \rangle < 16$	W^\pm	1.13 ± 0.06	0.89 ± 0.04	0.77 ± 0.03	0.67 ± 0.08	0.89 ± 0.04
	W^+	1.01 ± 0.09	0.74 ± 0.04	0.70 ± 0.04	0.49 ± 0.09	0.78 ± 0.03
	W^-	1.24 ± 0.07	1.06 ± 0.08	0.84 ± 0.07	0.80 ± 0.09	1.04 ± 0.05

Table 7.14: Measured multijet fractions (%) in $W \rightarrow \mu\nu$ channel as a function of muon pseudorapidity $|\eta|$ and pile-up μ obtained from fits to kinematical distributions by scanning of $p_T^{\text{cone20}}/p_T > 0.1$ control region.

Using the corrected multijet sample, a value of the m_W is extracted. In order to confirm that the shape correction procedure works properly, another method of the m_W extraction is used which has similar spirit with the method for the multijet background yield estimates. In this method, the values of m_W are extracted assuming different multijet shapes from different control regions which are defined by changing the lepton isolation requirements. For all cases the backgrounds are injected with the same fraction, so only an effect of its shape is probed. Then the fitted value of m_W is extrapolated to the signal region. The comparison of m_W results extracted using both methods is used as a cross check.

▷ Muon channel

To estimate how multijet distributions change over muon isolation criteria, two control regions are defined:

- CR1: muon isolation requirement is $0.1 < p_T^{\text{cone20}}/p_T^\mu < 0.25$;
- CR2: muon isolation requirement is $0.25 < p_T^{\text{cone20}}/p_T^\mu < 0.4$.

Examples of $p_T^\mu, m_T^W, E_T^{\text{miss}}$ and η_μ distributions are shown in Figure 7.12. The ratios CR1/CR2 are parametrized using functions of the following form:

$$R(x) = 1 + \sum_{i=1}^2 \frac{a_i}{(x - b_i)^i}.$$

These functions are evaluated with $x = p_T^\mu, m_T^W, E_T^{\text{miss}}$ and quantify the difference in the multijet distributions between $< p_T^{\text{cone20}}/p_T^\mu > \sim 0.325$ and $< p_T^{\text{cone20}}/p_T^\mu > \sim 0.175$. The correction is not interpolated as a function of η_μ . The corrected multijet distributions are obtained by multiplying the distributions observed in CR1 by $R^{\alpha=0.175/0.15}$, extrapolating the shape to the region $p_T^{\text{cone20}}/p_T^\mu \sim 0$. Here, 0.15 is the difference of the average isolation values of the two control regions ($CR1 \sim 0.175$; $CR2 \sim 0.325$), for which the shape difference is measured. The value 0.175 is the extrapolation from CR1 to the signal region.

▷ Electron channel

Similarly, the electron multijet background shape evolution is probed using two control regions:

- CR1: electron isolation requirement is $4 \text{ GeV} < p_T^{\text{cone40}} < 7 \text{ GeV}$, removed requirement on E_T^{cone20}
- CR2: electron isolation requirement is $7 \text{ GeV} < p_T^{\text{cone40}} < 12 \text{ GeV}$, removed requirement on E_T^{cone20}

Examples of $p_T^e, m_T^W, E_T^{\text{miss}}$ and η_e distributions are shown in Figure 7.13. The ratios CR1/CR2 are fitted as above. The averaged isolation values in CR1 and CR2 are about 5.3 GeV and 9.3 GeV respectively, so that the functions correspond to a shift of the isolation value by 4 GeV towards the signal region. Thus, the corrected multijet distributions are obtained as $R^{\alpha=5.3/4}$ times the reference distributions extracted from CR1. As can be seen from Figure 7.13, the multijet enriched control region in the electron channel has poor statistics with respect to the muon channel, which limits the precision of the jet background shape correction.

▷ Impact of shape corrections on m_W

The impact of the multijet shape correction on m_W is illustrated in Figures 7.14 and 7.15, for the muon and electron channels respectively. For both methods, the multijet shape correction and the direct, linear extrapolation of the fitted m_W value to the signal region lead to comparable

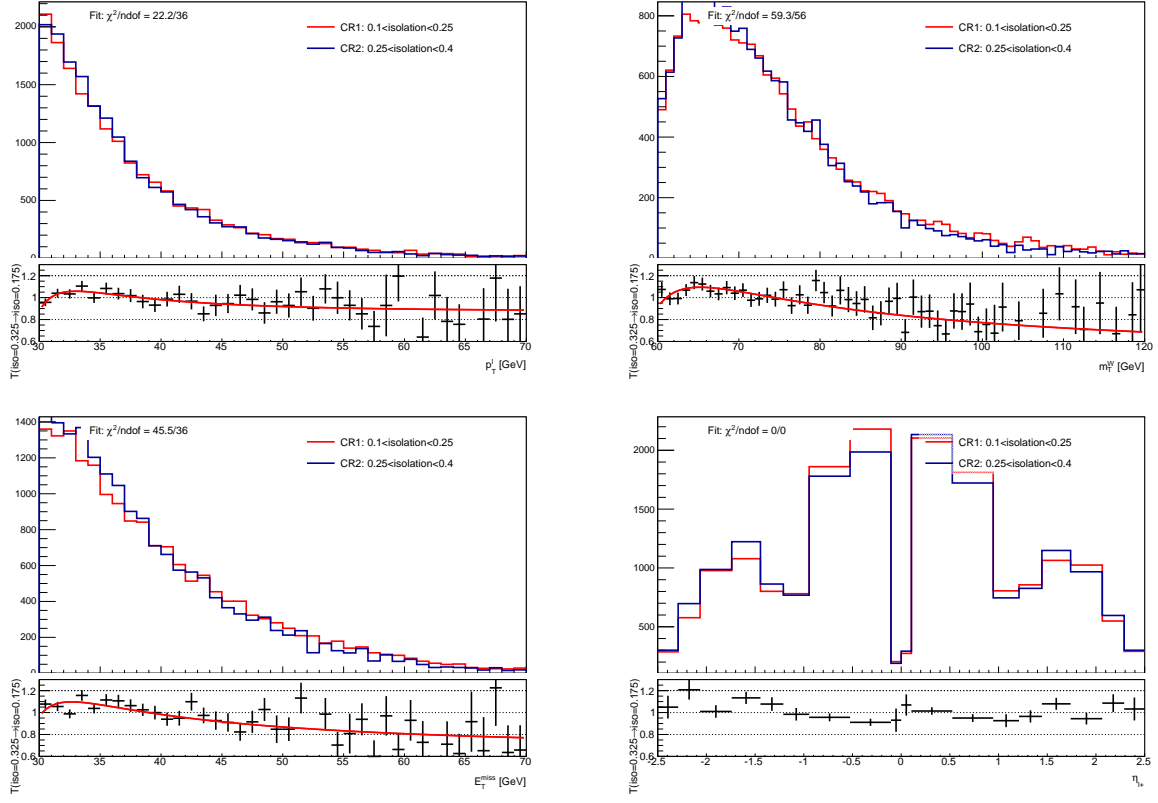


Figure 7.12: Examples of p_T^μ , m_W^W , E_T^{miss} and η_μ multijet distributions extracted from CR1 and CR2 and corresponding transfer functions (shown in the ratio) in the $W^+ \rightarrow \mu\nu$ channel.

results. Since the method uses data control regions as basic input, the corresponding statistical uncertainty on these methods needs to be evaluated.

For the direct extrapolation method (red points and line in Figures 7.14, 7.15), the straight line fit was rerun several times, each time removing a single point from the set. This procedure was repeated for all points in the set, and the spread of the corresponding line fit intercepts was taken as uncertainty.

For the shape extrapolation method, the error propagation was done using the Toy MC method : the “CR1” and “CR2” histogram bin contents were fluctuated within their statistical uncertainties, and the parametric fit was rerun on the resulting CR1/CR2 ratio. The result was then injected as MJ background distribution in the templates, and the m_W fit was rerun. This procedure was repeated 500 times, and the spread of the m_W fit result distribution was taken as uncertainty for this method.

The statistical uncertainties for both methods are represented as ellipses in Figures 7.14 and 7.15. The results of both methods overlap within uncertainties. Given the good compatibility between the two methods. Since the black ellipses always lead to larger uncertainties, we define the associated uncertainty only via the black ellipses and assign no further uncertainty.

The impact of the multijet correction on the m_W fit central value is summarized in Table 7.16. These values are taken from Figures 7.14 and 7.15 as m_W differences resulting from the injection of extrapolated shape (empty circular point) and nominal multijet shape (indicated by black lines) used before correction. As can be seen, the impact is larger for m_W^W distributions comparing to p_T^ℓ distributions. Such shape corrections lead to m_W values which are more compatible between m_W^W and p_T^ℓ fit results.

It should be noted, that we assume that the multi jet background shapes are the same for positive and negative charged lepton decay channels and hence combine the extracted shapes

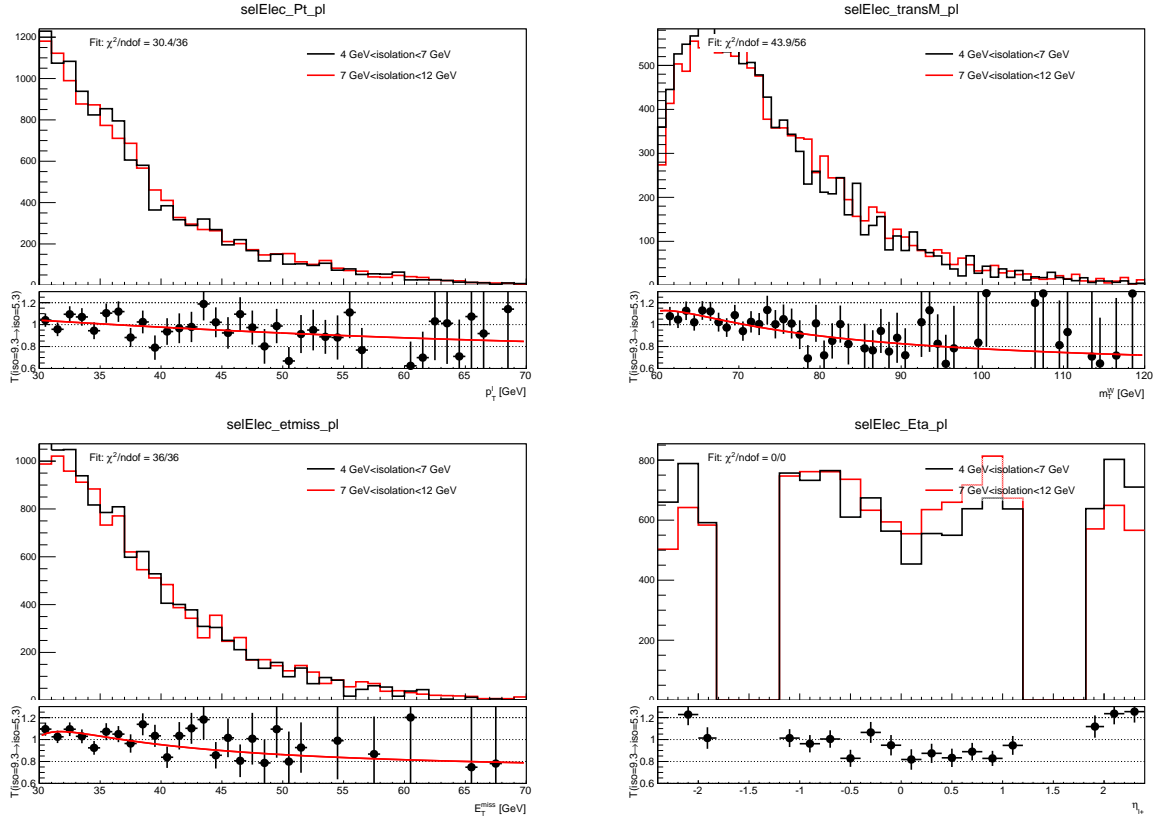


Figure 7.13: Examples of p_T^e , m_T^W , E_T^{miss} and η_e multijet distributions extracted from CR1 and CR2 and corresponding transfer functions (shown in the ratio) in the $W^+ \rightarrow e\nu$ channel.

to decrease statistical uncertainties. Once the multi jet background shapes are combined, i.e. charge-blind, we repeat the full procedure to extract the associated background estimates and uncertainties.

7.4.8 Impact of multijet background uncertainty on M_W

The multijet background fractions are summarized for standard signal selection in Tab. 7.14 for muon and Tab. 7.15 for electron channels. The spread of multijet fractions $f \pm \Delta f$ corresponds to the spread of the fitted lines extrapolated to signal region using different variables and fitting regions for multijet fit (see Figure 7.3). The central value of multijet yield corresponds to equidistant point from uppermost and bottommost. The total uncertainty includes the uncertainty from the method (radius of black ellipse on the MJ extrapolation plots) combined with the uncertainty from $\pm 2.5\%$ variation of the EW contamination in the control region.

Propagation of the MJ background uncertainty to the W mass measurement is performed by injecting the multijet background with fraction that corresponds to the central value and up (or down) variation. In each case the m_W is extracted from the W mass template fit and the uncertainty δm_W is taken as corresponding difference $|m_W(fQCD) - m_W(fQCD + \Delta fQCD)|$. The procedure is repeated for each measurement category in electron and muon channels and the results are summarized in Tables 7.17 and 7.18.

The uncertainty coming from the multijet background shapes modeling, as described in Section 7.4.7, injected into the distributions used for the W mass extraction are also summarized in Tables 7.17 and 7.18. The multijet fraction and shape uncertainties are then added in quadrature that yields to the total uncertainty on the multijet background modeling.

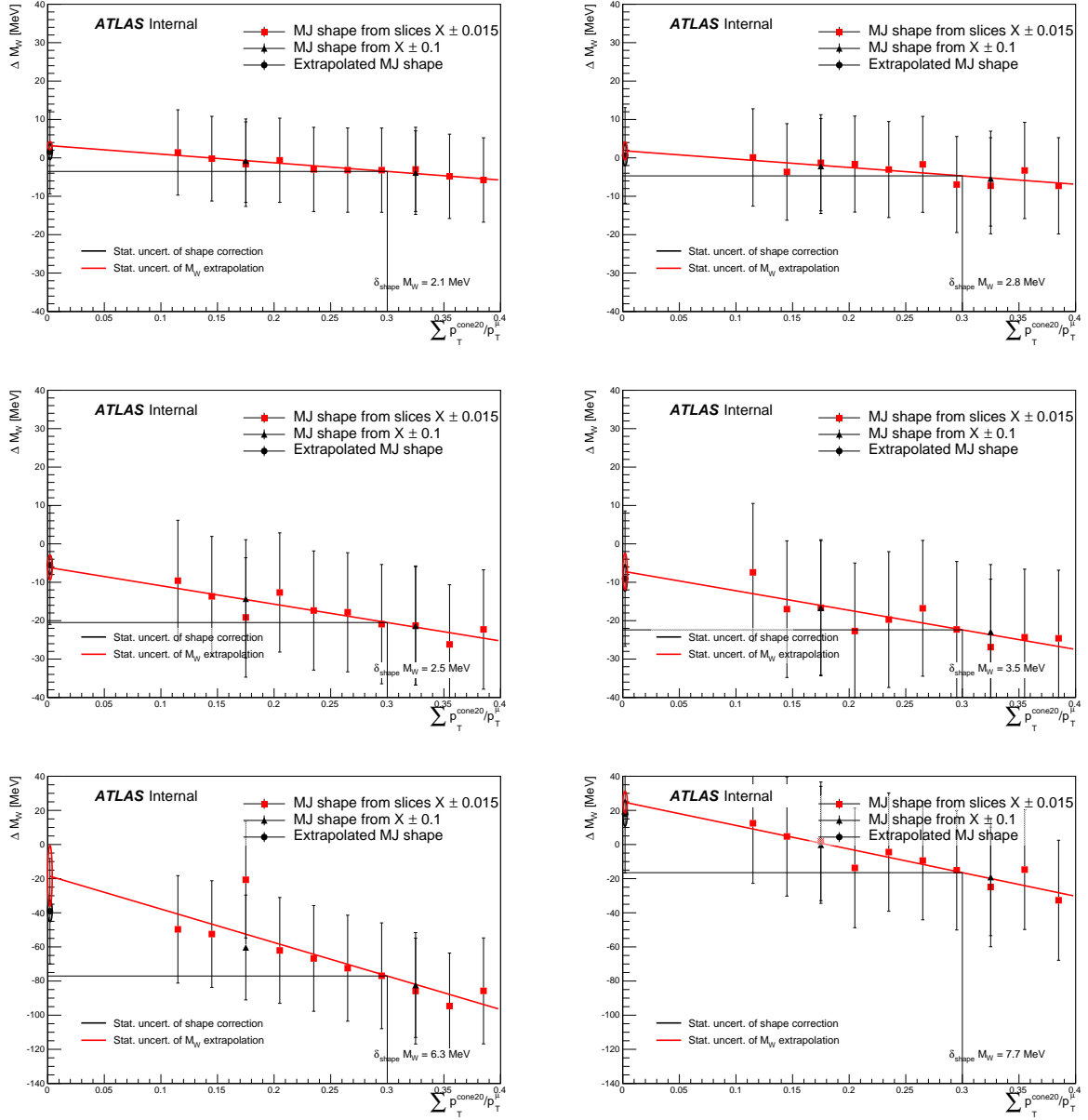


Figure 7.14: Extracted m_W values for different shapes of the multijet background using template fits on p_T^μ , m_T^W and E_T^{miss} distributions in $W^+ \rightarrow \mu\nu$ (left) and $W^- \rightarrow \mu\nu$ (right) channels. Error bars are statistical only. The values are plotted in bins of the isolation variable used to define the data-driven distributions. Two triangular points correspond to multijet shapes extracted from CR1 and CR2 described in the text. The m_W obtained after shape correction procedure is indicated by circular point. Red points correspond to shapes from smaller isolation slices, which are then extrapolated to the signal region with a linear fit.

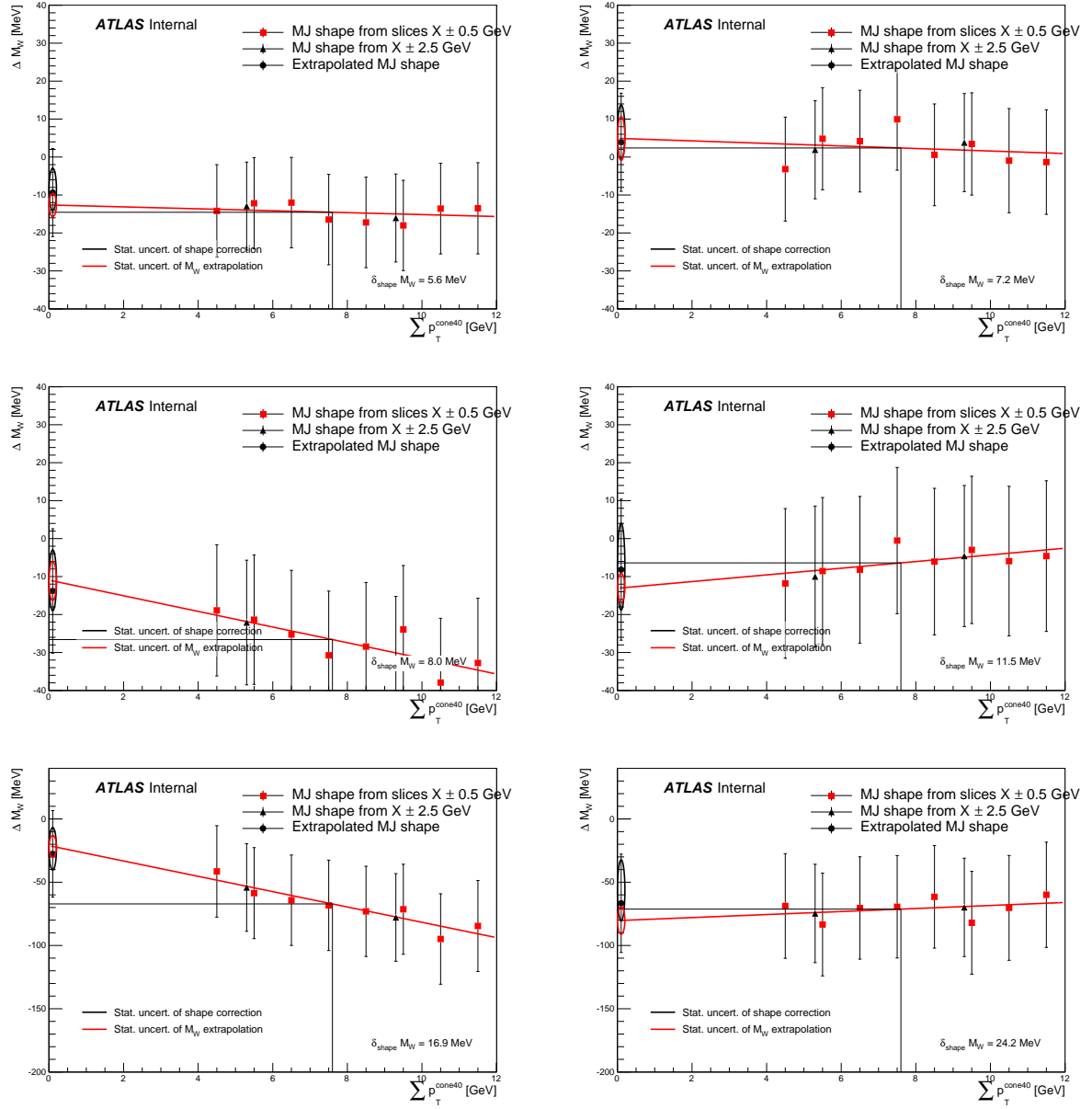


Figure 7.15: Extracted m_W values for different shapes of the multijet background using template fits on p_T^e (upper row), m_T^W (middle row) and E_T^{miss} (lower row) distributions in $W^+ \rightarrow e\nu$ (left) and $W^- \rightarrow e\nu$ (right) channels. Error bars are statistical only. The values are plotted in bins of the isolation variable used to define the data-driven distributions. Two triangular points correspond to multijet shapes extracted from CR1 and CR2 described in the text. The m_W obtained after shape correction procedure is indicated by circular point. Red points correspond to shapes from smaller isolation slices, which are then extrapolated to the signal region with a linear fit. It should be noted that the fully correct extrapolation point would be the average isolation value *for the jet background* in the signal region. Since there is currently no reliable method to estimate this, we extrapolate to 0 as it is simpler (i.e. well defined) and always conservative.

7.5 The distributions

Kinematic distributions for W candidate events passing the selection requirements described in Section 7.2 are presented in this section. The data and Monte Carlo samples used here are introduced in Section 7.1. The following correction procedure are applied on the signal (PowhegPythia) and background Monte Carlo samples:

- line-shape reweighting, incorporating EW corrections, to a blinded mass value: $m_W = 80399 + b$ MeV
- reweighting of the vector boson $p_T(V)$ in bins of $y(V)$ according to the ATLAS AZ tune. Keep in mind, that the rapidity distribution is unchanged by this reweighting
- reweight the rapidity distribution following a fixed order NNLO prediction (via an improved version of DNNLO) and the CT10 PDF Set
- reweight the QCD angular coefficients A_i in bins of $y(V)$, m and $p_T(V)$ according to our fixed order NNLO prediction
- vertex-reweighting
- all experimental corrections to the electron, muon and hadronic recoil described in Section 5

The distributions of the EW and top backgrounds are fully simulated and their normalizations fixed according to pp cross-sections. The multijet background is estimated with data-driven method as described in Section 7.4. All the distributions correspond to blinded W boson mass.

The distributions of the EW and top backgrounds are fully simulated and their relative normalization is fixed according to pp cross-sections. The multijet background is estimated with data-driven method as described above. All the signal distributions correspond to blinded W boson mass. All the χ^2 values shown on the plots include statistical and systematic uncertainties with no bin-to-bin correlations.

The lepton η , φ and transverse momentum distribution for both $W \rightarrow e\nu$ and $W \rightarrow \mu\nu$ channels with uncertainty bands are shown in Figures 7.16, 7.17, 7.18. Transverse mass, missing transverse energy, hadronic recoil with its parallel and perpendicular projection with respect to the lepton p_T are shown in Figures 7.19, 7.20, 7.21, 7.22 and 7.23. The distributions in different lepton $|\eta|$ categories are summarized in Appendix C.

Distributions that have worse Data/MC ratio are the lepton η and φ , particularly in the electron channel. The ratio of data/MC of the lepton η distribution in the electron channel is compatible between positively and negatively charged leptons ($\chi^2/ndf = 38/35$ including systematic uncertainties on the efficiencies). Similarly, m_W is fitted in the azimuthal bins of the lepton, and good agreement is found between the bins. Excluding the bins just around $\phi \sim -2$ (this bin has the largest discrepancy in the control plot) will have marginal impact on the fitted value of m_W . Hence, these imperfections are not relevant for the presented measurement.

Lepton transverse momentum, transverse mass, missing transverse energy, hadronic recoil with its parallel and perpendicular projection with respect to the lepton p_T for each η category are shown in Figures C.1 – C.24 of Appendix 5. The most prominent discrepancy is observed for the p_T^e distribution, with a dip in the distribution around $p_T^e \sim 41$ GeV and an excess at higher values. To understand this feature, cross checks were performed on all the components of the analysis corrections and uncertainties:

- electron performance : energy resolution and efficiency scale factors (reconstruction, identifications, isolation, trigger);
- multijet background uncertainties;

- physics corrections: polarization effects; and the influence of the electron pseudorapidity distribution.

For all these effects, the corrections were varied within their uncertainties, or entirely switched off. No obvious explanation was found.

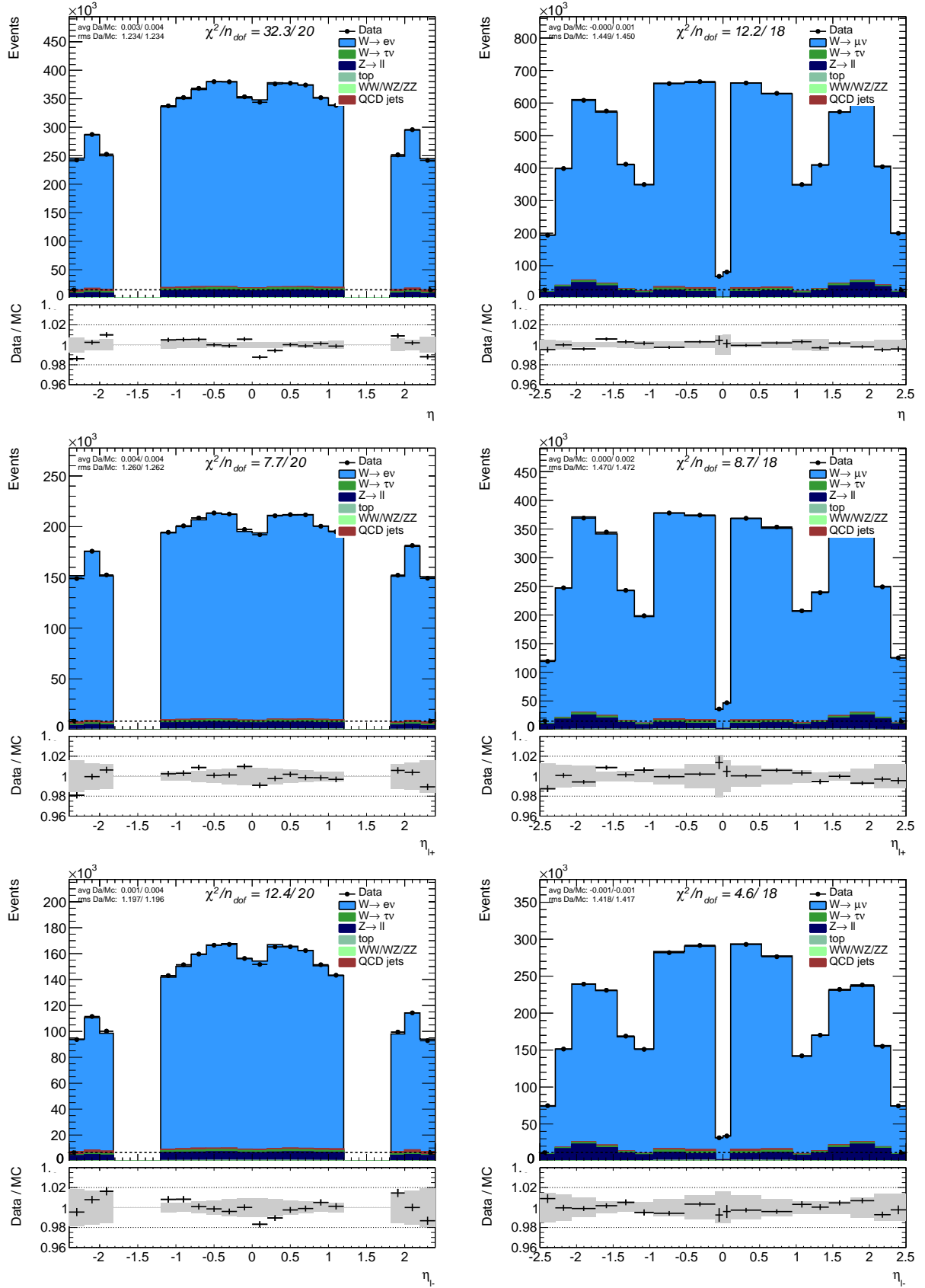


Figure 7.16: Lepton pseudorapidity distribution from $W \rightarrow e\nu$ (left) and $W \rightarrow \mu\nu$ (right); $W^+ \rightarrow e\nu$ (left) and $W^+ \rightarrow \mu\nu$ (right); $W^- \rightarrow e\nu$ (left) and $W^- \rightarrow \mu\nu$ (right). (W^\pm : upper row, W^+ : middle row, W^- : lower row).

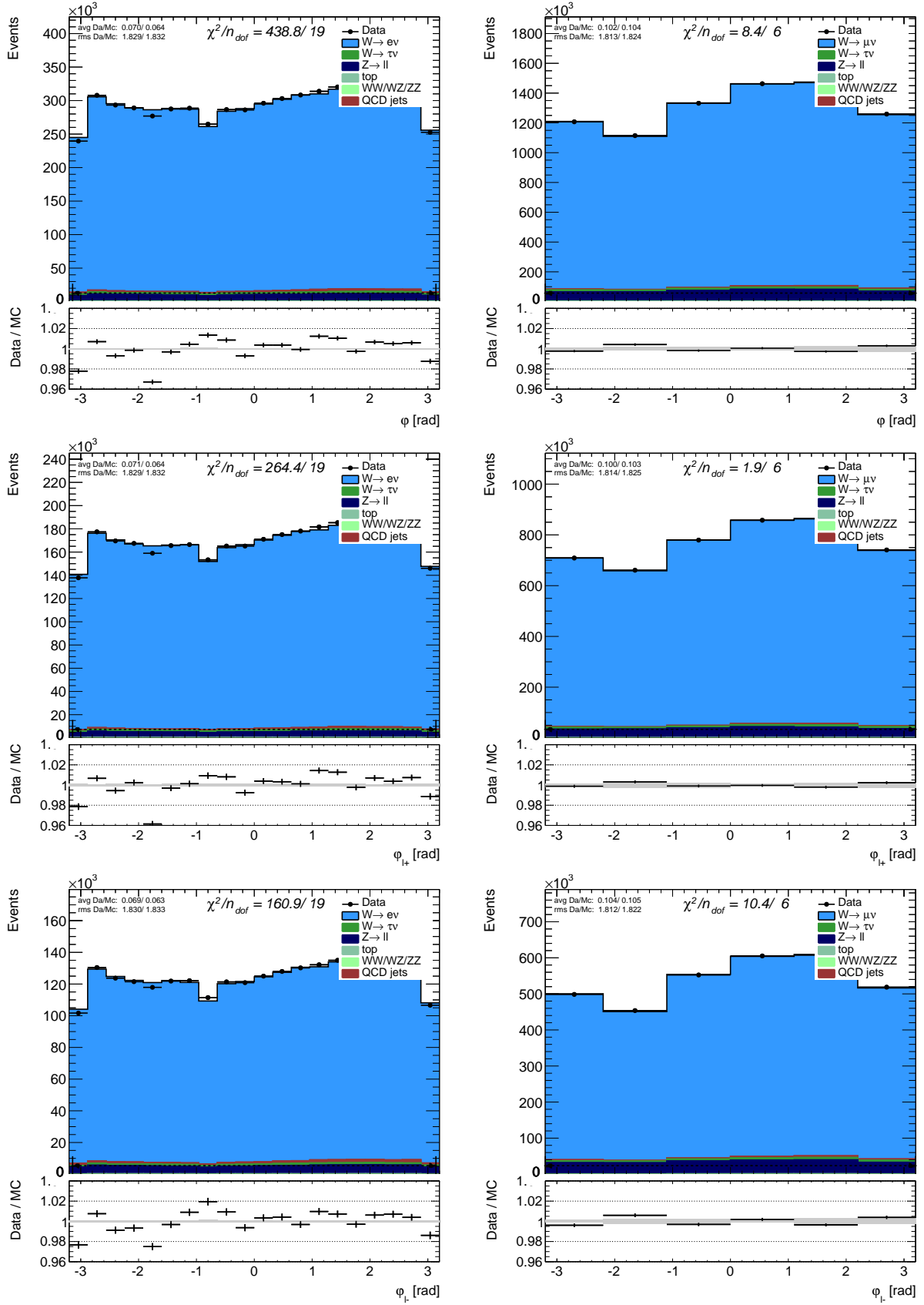


Figure 7.17: Lepton ϕ distribution from $W \rightarrow e\nu$ (left) and $W \rightarrow \mu\nu$ (right); $W^+ \rightarrow e\nu$ (left) and $W^+ \rightarrow \mu\nu$ (right); $W^- \rightarrow e\nu$ (left) and $W^- \rightarrow \mu\nu$ (right). (W^\pm : upper row, W^+ : middle row, W^- : lower row)

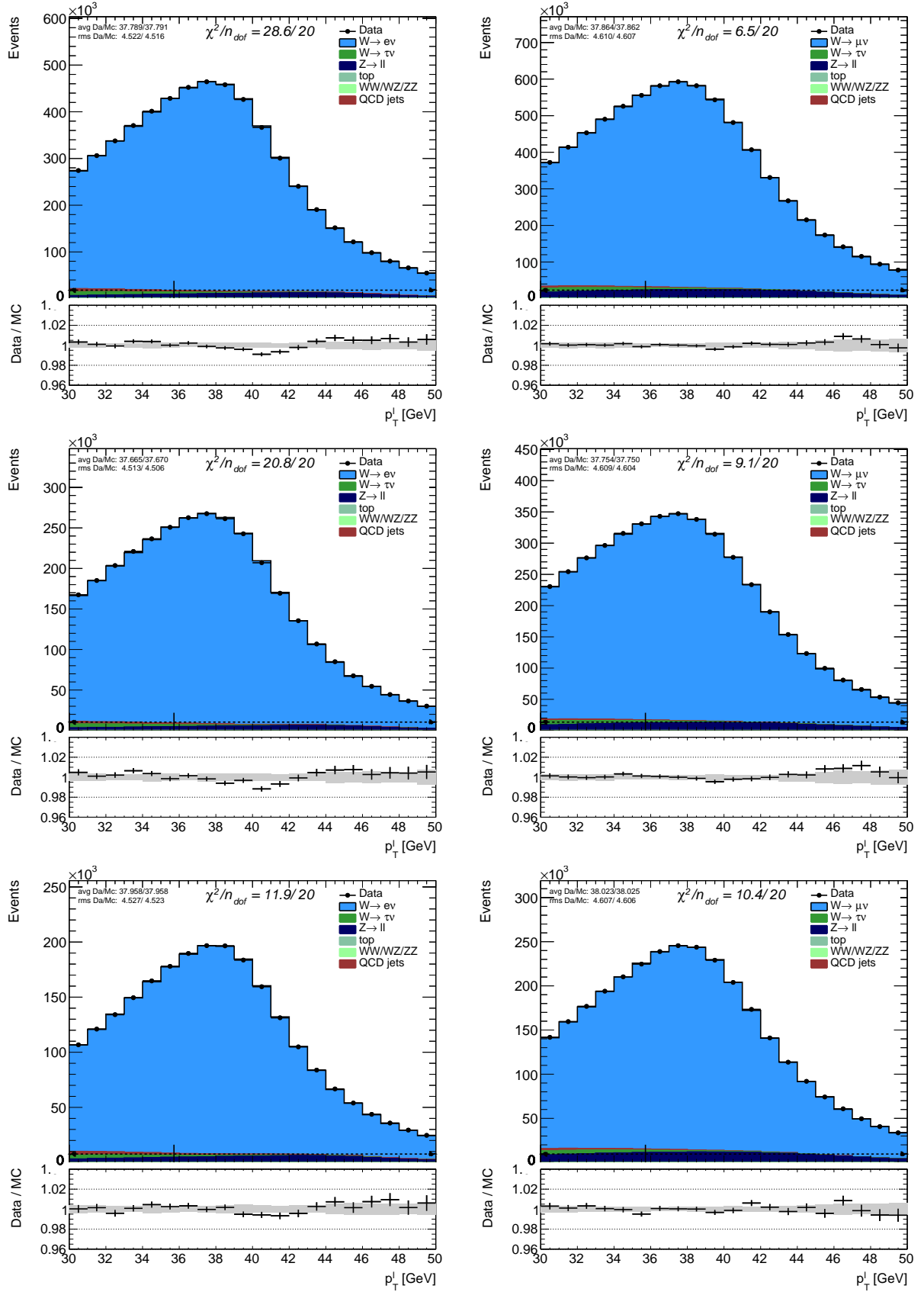


Figure 7.18: Lepton p_T^ℓ distribution from $W \rightarrow e\nu$ (left) and $W \rightarrow \mu\nu$ (right); $W^+ \rightarrow e\nu$ (left) and $W^+ \rightarrow \mu\nu$ (right); $W^- \rightarrow e\nu$ (left) and $W^- \rightarrow \mu\nu$ (right) with the best mass fit template for each category. (W^\pm : upper row, W^+ : middle row, W^- : lower row)

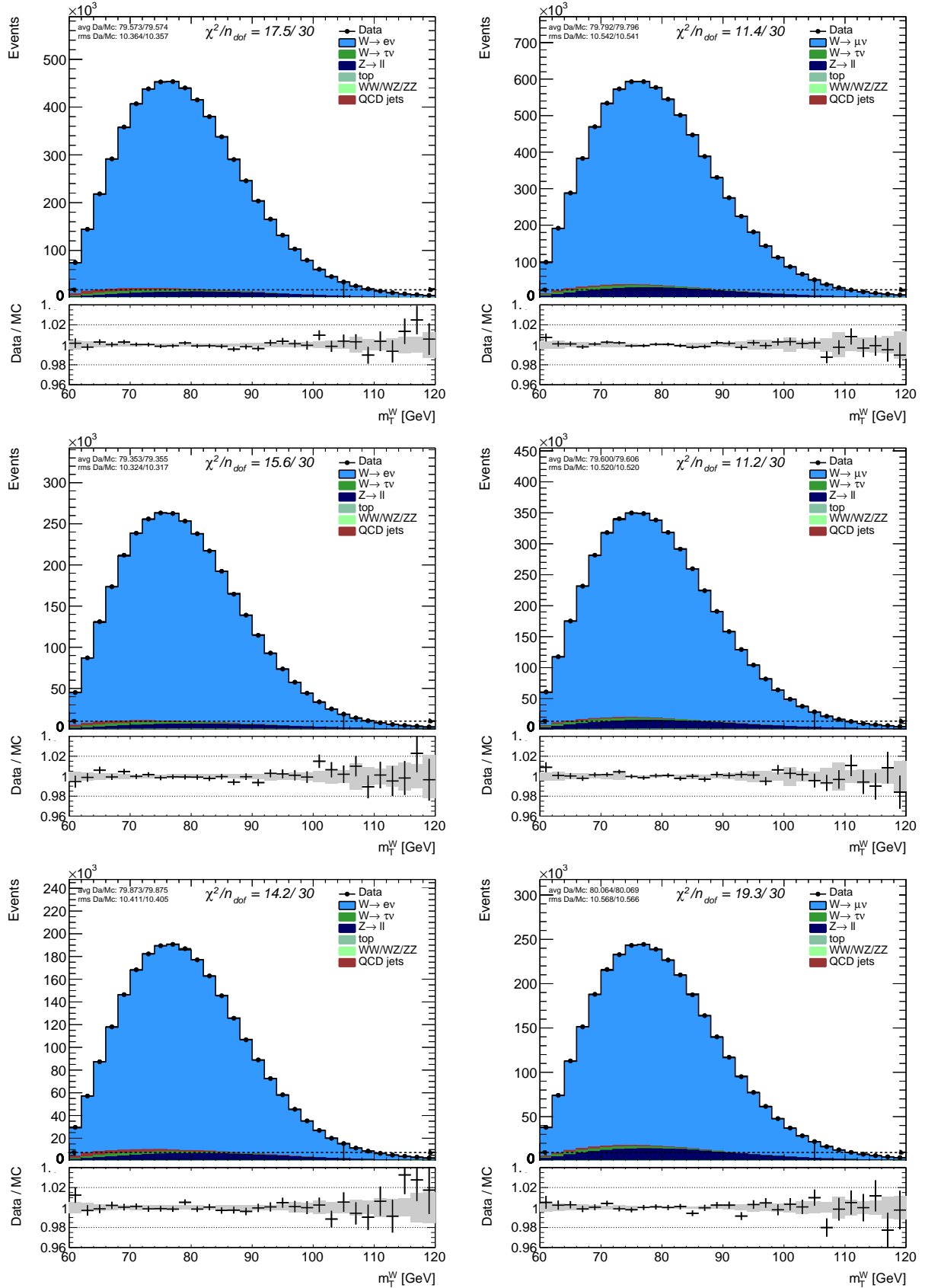


Figure 7.19: Transverse mass distribution from $W \rightarrow e\nu$ (left) and $W \rightarrow \mu\nu$ (right); $W^+ \rightarrow e\nu$ (left) and $W^+ \rightarrow \mu\nu$ (right); $W^- \rightarrow e\nu$ (left) and $W^- \rightarrow \mu\nu$ (right) with the best mass fit template for each category. (W^\pm : upper row, W^+ : middle row, W^- : lower row)

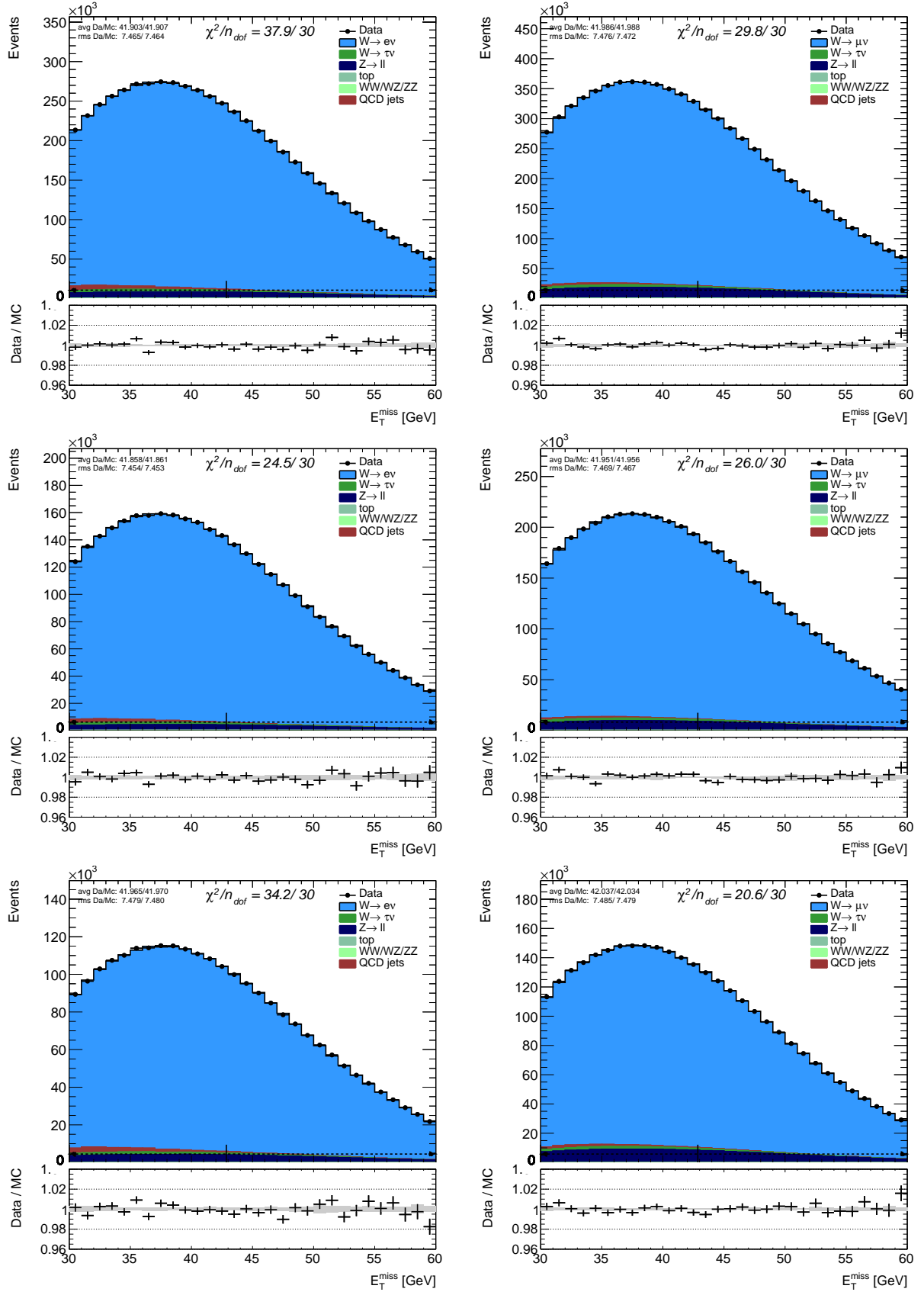


Figure 7.20: Missing transverse energy distribution from $W \rightarrow e\nu$ (left) and $W \rightarrow \mu\nu$ (right); $W^+ \rightarrow e\nu$ (left) and $W^+ \rightarrow \mu\nu$ (right); $W^- \rightarrow e\nu$ (left) and $W^- \rightarrow \mu\nu$ (right) with the best mass fit template for each category. (W^\pm : upper row, W^+ : middle row, W^- : lower row)

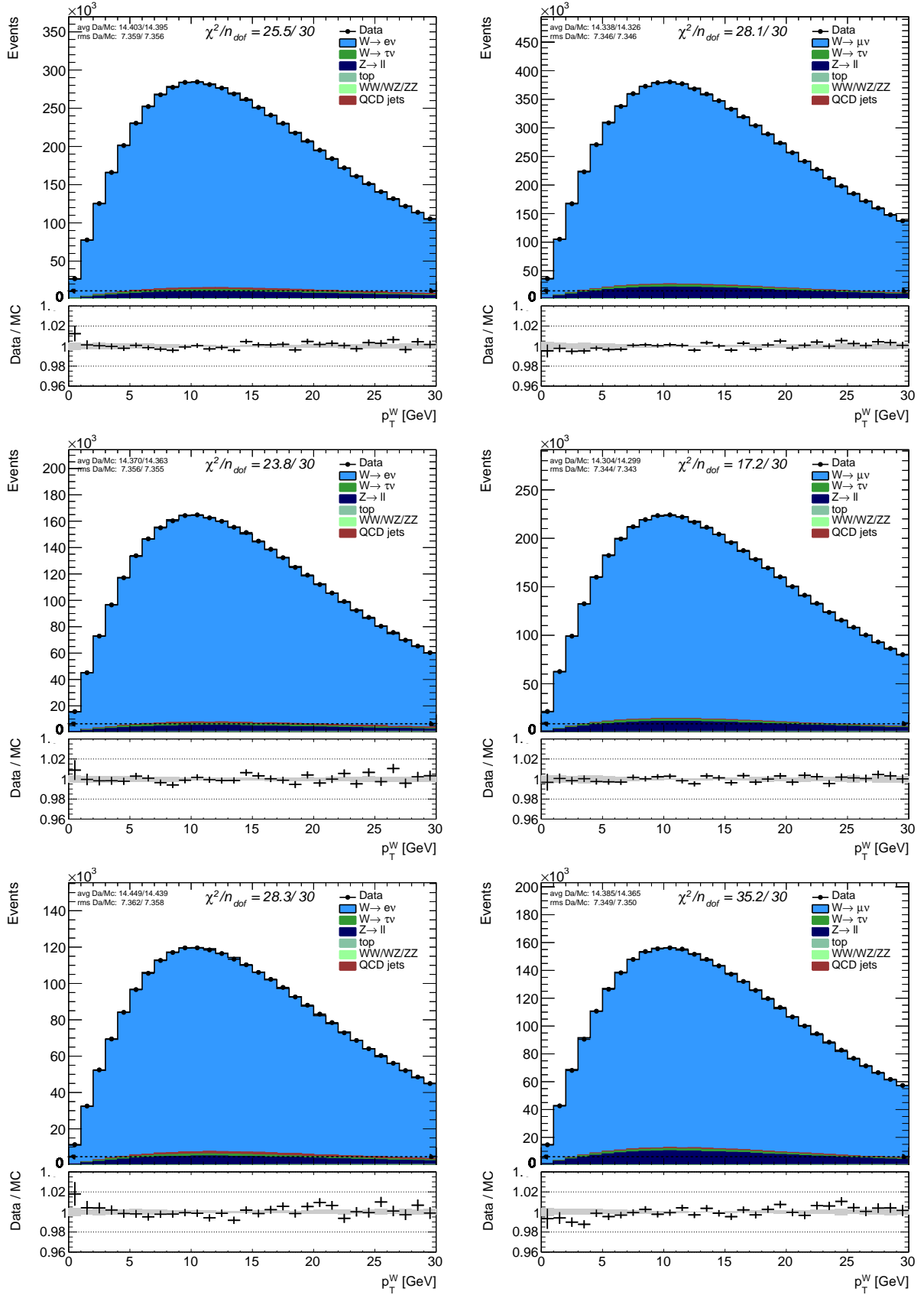
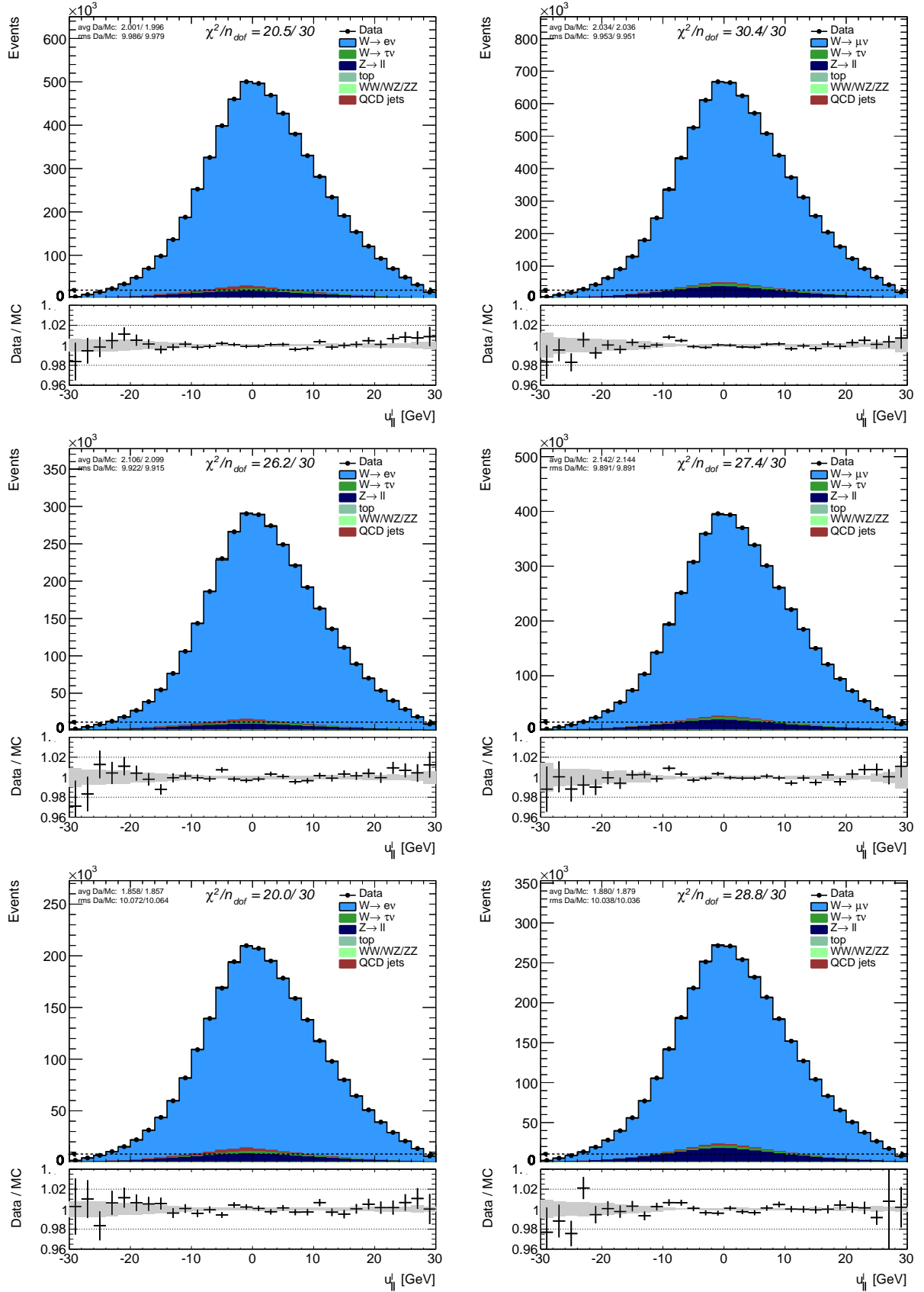


Figure 7.21: Hadronic recoil distribution from $W \rightarrow e\nu$ (left) and $W \rightarrow \mu\nu$ (right); $W^+ \rightarrow e\nu$ (left) and $W^+ \rightarrow \mu\nu$ (right); $W^- \rightarrow e\nu$ (left) and $W^- \rightarrow \mu\nu$ (right). (W^\pm : upper row, W^+ : middle row, W^- : lower row)



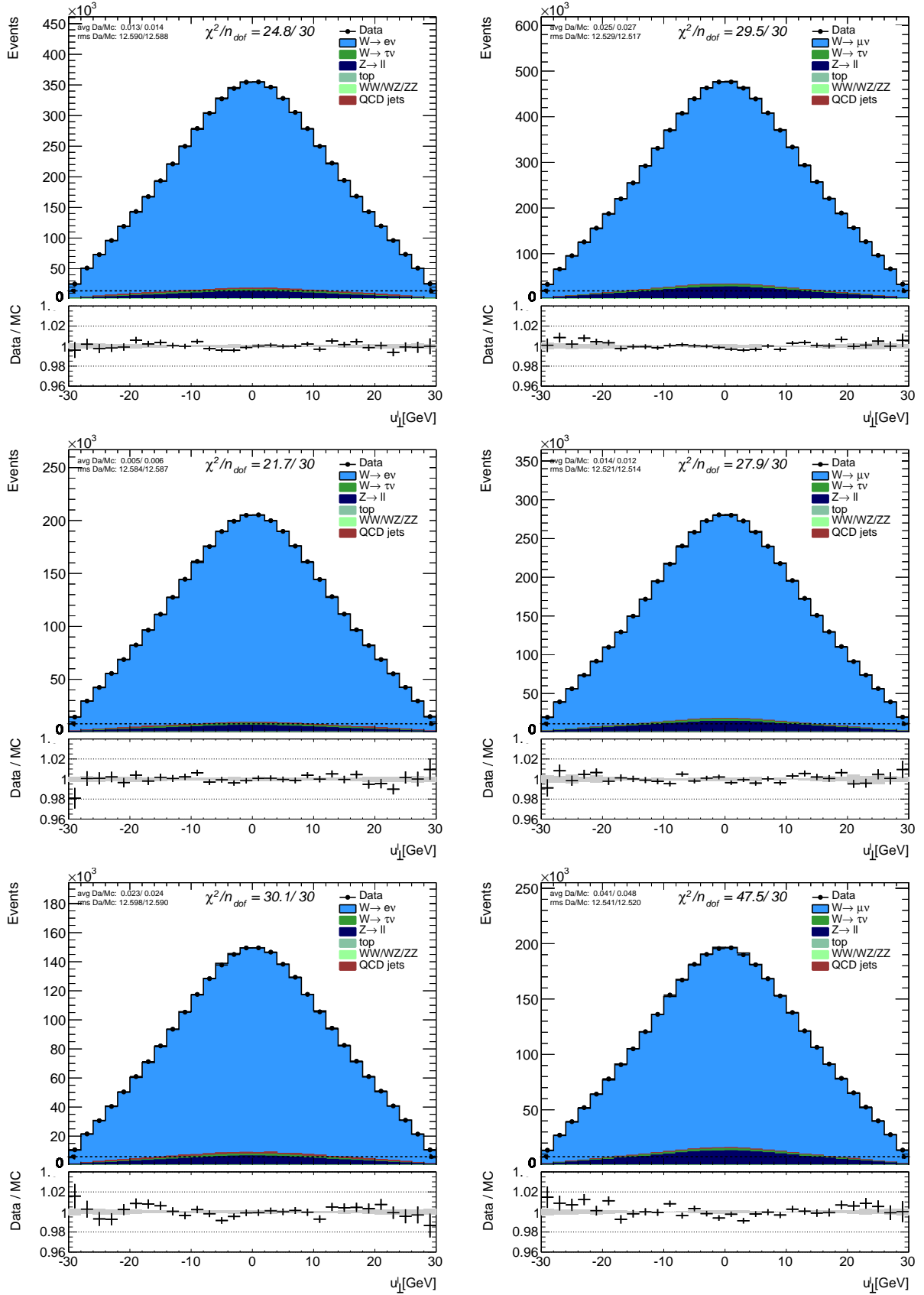


Figure 7.23: Perpendicular projection of hadronic recoil distribution with respect to lepton p_T from $W \rightarrow e\nu$ (left) and $W \rightarrow \mu\nu$ (right); $W^+ \rightarrow e\nu$ (left) and $W^+ \rightarrow \mu\nu$ (right); $W^- \rightarrow e\nu$ (left) and $W^- \rightarrow \mu\nu$ (right). (W^\pm : upper row, W^+ : middle row, W^- : lower row)

	$ \eta $ range	0 – 0.6	0.6 – 1.2	1.8 – 2.4	inclusive
μ -inclusive	W^\pm	0.58 ± 0.08	0.76 ± 0.09	1.73 ± 0.19	0.99 ± 0.10
	W^+	0.47 ± 0.08	0.67 ± 0.09	1.36 ± 0.19	0.83 ± 0.09
	W^-	0.73 ± 0.09	0.90 ± 0.09	2.33 ± 0.18	1.21 ± 0.10
	$ \eta $ range	0 – 0.6	0.6 – 1.2	1.8 – 2.4	inclusive
$2.5 < \langle \mu \rangle < 6.5$	W^\pm	0.41 ± 0.08	0.50 ± 0.09	1.29 ± 0.11	0.68 ± 0.09
	W^+	0.34 ± 0.09	0.44 ± 0.10	0.94 ± 0.12	0.53 ± 0.09
	W^-	0.54 ± 0.08	0.63 ± 0.10	1.82 ± 0.13	0.88 ± 0.10
	$ \eta $ range	0 – 0.6	0.6 – 1.2	1.8 – 2.4	inclusive
$6.5 < \langle \mu \rangle < 9.5$	W^\pm	0.51 ± 0.08	0.69 ± 0.09	1.12 ± 0.23	0.82 ± 0.11
	W^+	0.36 ± 0.10	0.63 ± 0.12	0.83 ± 0.23	0.64 ± 0.11
	W^-	0.75 ± 0.10	0.82 ± 0.08	1.63 ± 0.19	1.07 ± 0.10
	$ \eta $ range	0 – 0.6	0.6 – 1.2	1.8 – 2.4	inclusive
$9.5 < \langle \mu \rangle < 16$	W^\pm	0.93 ± 0.10	1.25 ± 0.11	3.20 ± 0.20	1.61 ± 0.12
	W^+	0.90 ± 0.13	1.15 ± 0.13	2.71 ± 0.22	1.45 ± 0.12
	W^-	0.97 ± 0.14	1.44 ± 0.14	3.94 ± 0.19	1.83 ± 0.12

Table 7.15: Measured multijet fractions (%) in $W \rightarrow e\nu$ channel as a function of electron pseudo-rapidity $|\eta|$ and pile-up μ obtained from fits to kinematical distributions by scanning of the p_T^{cone40} variable in control region with removed E_T^{cone20} cut.

m_W shift [MeV]						
muons						
$ \eta $ range		(0 – 0.8)	(0.8 – 1.4)	(1.4 – 2.0)	(2.0 – 2.4)	Inclusive
W^\pm	p_T^ℓ	6.8	13.6	3.2	-7.2	5.4
W^+		7.9	13.0	3.4	-1.3	5.0
W^-		8.2	15.4	7.4	-10.2	6.7
W^\pm	m_T	18.6	23.1	13.8	3.2	12.5
W^+		23.5	19.1	10.6	17.4	12.9
W^-		15.3	32.8	22.9	-10.5	14.0
electrons						
$ \eta $ range		(0 – 0.6)	(0.6 – 1.2)	–	(1.8 – 2.4)	Inclusive
W^\pm	p_T^ℓ	3.2	3.5	–	28.0	5.9
W^+		5.5	-0.9	–	28.0	7.2
W^-		0.6	7.6	–	26.5	2.5
W^\pm	m_T	-9.8	3.2	–	36.0	6.4
W^+		4.0	5.2	–	54.3	12.8
W^-		-17.9	-3.2	–	0.7	-1.8

Table 7.16: Impact of the multijet shape correction on the fitted value of m_W .

δm_W [MeV]						
muons: uncertainty on the jet fraction						
$ \eta $ range		(0 – 0.8)	(0.8 – 1.4)	(1.4 – 2.0)	(2.0 – 2.4)	Inclusive
W^\pm	p_T^ℓ	4.1	2.0	1.2	1.6	3.0
W^+		3.5	1.8	1.9	2.2	2.3
W^-		3.7	2.8	2.6	3.6	3.1
W^\pm	m_T	5.9	4.8	1.9	2.3	4.6
W^+		6.2	3.0	2.9	3.1	3.6
W^-		6.0	4.3	3.9	5.1	4.7
muons: uncertainty on the jet shape						
$ \eta $ range		(0 – 0.8)	(0.8 – 1.4)	(1.4 – 2.0)	(2.0 – 2.4)	Inclusive
W^\pm	p_T^ℓ	2.7	2.8	3.0	5.5	1.7
W^+		3.5	3.9	4.1	7.6	2.1
W^-		4.0	5.2	6.0	11.1	2.8
W^\pm	m_T	3.6	4.1	4.2	9.9	2.1
W^+		4.9	6.2	5.9	8.8	2.5
W^-		6.2	9.2	7.7	19.9	3.5

Table 7.17: The propagated multijet background uncertainties on the W mass in $W \rightarrow \mu\nu$ channel.

δm_W [MeV]						
electrons: uncertainty on the jet fraction						
$ \eta $ range		(0 – 0.6)	(0.6 – 1.2)	–	(1.8 – 2.4)	Inclusive
W^\pm	p_T^ℓ	4.5	3.9	–	4.0	3.8
W^+		4.5	3.8	–	3.2	3.3
W^-		5.1	4.2	–	3.9	4.1
W^\pm	m_T	7.1	8.2	–	16.3	8.9
W^+		7.3	8.7	–	16.0	8.2
W^-		7.7	7.6	–	16.2	8.7
electrons: uncertainty on the jet shape						
$ \eta $ range		(0 – 0.6)	(0.6 – 1.2)	–	(1.8 – 2.4)	Inclusive
W^\pm	p_T^ℓ	5.0	5.7	–	10.7	4.2
W^+		5.7	7.5	–	14.2	5.6
W^-		8.1	8.0	–	21.1	7.3
W^\pm	m_T	8.0	9.0	–	19.5	6.6
W^+		9.0	12.5	–	19.7	8.0
W^-		13.3	13.9	–	36.5	11.4

Table 7.18: The propagated multijet background uncertainties on the W mass in $W \rightarrow e\nu$ channel.

W boson mass measurement

8.1 Methodology

8.1.1 Introduction to the template fit method

The W boson is an unstable particle and it decays either to jets or to lepton-neutrino pair. While the energy resolution of the reconstructed jets suffers from high hadron activity at hadron colliders, the energetic leptons can be reconstructed with a high precision that makes the leptonic channel to be convenient for the W boson studies. In contrast to the Z boson, one of the W boson decay products, the neutrino, leaves the detector unseen that makes the reconstruction of the invariant mass impossible. However the magnitude and direction of the neutrino momentum in the transverse plane with respect to the beam direction, \vec{p}_T^ν , can be determined from momentum imbalance of the visible particles in an event. All the kinematic variables are thus considered in the transverse plane.

Although the invariant mass of the W boson is not reconstructable, the transverse distributions of its decay products carry all information needed for the W mass extraction. The most important observables, which depend on the mass of the W boson are

- Transverse momentum of the charged lepton p_T^ℓ
- Missing transverse energy $E_T^{\text{miss}} = p_T^\nu$
- Transverse mass of the lepton-neutrino system $m_T^W = \sqrt{2p_T^\ell E_T^{\text{miss}} \cdot (1 - \cos(\phi_\ell, \phi_T^{\text{miss}}))}$

The determination of the W boson mass exploits the kinematic peaks of these distributions. In particular, in the rest frame of decaying W, the charged lepton and the neutrino are back-to-back, so the lepton transverse momentum and missing transverse energy spectra have Jacobian peaks at $p_T = m_W/2$, whilst the transverse mass spectrum peaks at $m_T^W = m_W$. In reality, these peaks are 'smeared' out by non-zero p_T^W distribution (see Section 1.4.3) and by detector effects. Therefore, the accurate modeling of the p_T^W and precise understanding of the detector performance is required.

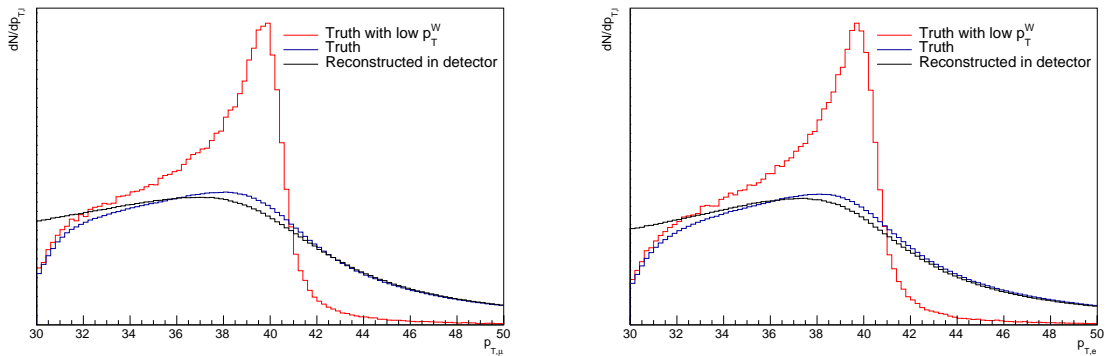


Figure 8.1: The p_T^ℓ spectra in muon (left) and electron (right) channels at truth level with and without requirement on low p_T^W values, and with detector effects.

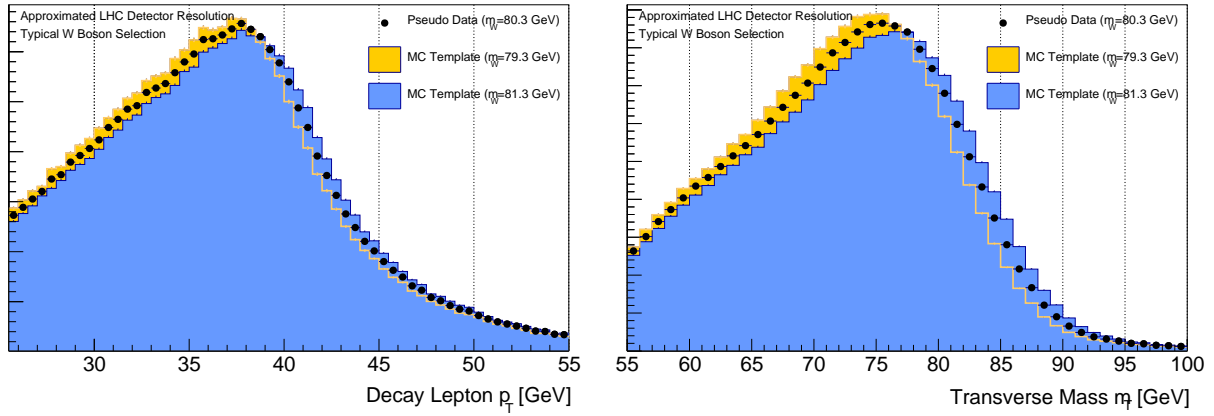


Figure 8.2: Templates of the p_T^ℓ (left) and m_T^W (right) distributions for three different assumed M_W masses using a typical LHC detector response.

The basic idea of the m_W determination is to use the correlation between the W boson mass and the resulting energy and momentum of its decay products. Technically this is realised by a so-called template fit approach. For different assumed W boson masses, the expected final state distributions, i.e. templates, which would be measured in the detector are calculated and compared to the actual measurement. The minimal residual difference between the different simulated m_W hypotheses and the measurement then provides a handle on the actual W boson mass. This basic principle is illustrated in Figure 8.2 where p_T^ℓ and m_T^W templates for three significantly different masses $M_W = 79.3, 80.3, 81.3$ GeV are compared.

Due to the large statistics required, a single mass point is simulated, namely $m_W = 80.399$ GeV. The analysis then exploits the natural width of the W resonance to reweight the boson invariant mass distribution from a given mass point to another, using the formalism described in Section 6.2. The reweighting is performed analytically. This reweighting can also be extended to introduce different W boson width values (Γ_W), i.e. allow for a combined variation of m_W and Γ_W . However, in this first analysis, the width of the W boson is kept fixed to its Standard Model prediction. The uncertainty on this prediction is 1-2 MeV, which has a negligible impact on the measurement. Therefore, the fully simulated MC events, can be reweighted to any given value of m_W within the width of m_W .

The comparison of each template distribution with the observed distribution in data is performed through the χ^2 -test. For each χ^2 -test, both the data histogram h_1 and the template histogram h_2 are normalized to unity, and the χ^2 is calculated as follows:

$$\chi^2 = \sum_{i=1}^N \frac{(f_{1,i} - f_{2,i})^2}{\sigma_{f_{1,i}}^2 + \sigma_{f_{2,i}}^2} \quad (8.1)$$

with $f_{1,i}$ being the number of entries in bin i of h_1 , $f_{2,i}$ the number of entries in bin i of h_2 . The quantities $\sigma_{f_{1,i}}$ and $\sigma_{f_{2,i}}$ are the uncertainties on bin i in h_1 and h_2 , respectively. Then the χ^2 is plotted against the M_W of the corresponding template.

Since the templates are only produced for disjunct points in parameter space, interpolation has to be done to find the global minimum of the χ^2 curve, as shown in Figure 8.3c. For this interpolation, the fact is used that the χ^2 curve can be approximated by a parabola close to its minimum. The equations used is

$$\chi^2 \approx \chi_{min}^2 + (M_W^{temp} - M_W)^2 \quad (8.2)$$

where χ_{min}^2 denotes the minimum value of χ^2 and M_W is the measured W boson mass value where the minimum is reached. The total statistical uncertainty is estimated from the width of the parabola and corresponds to deviation from measured M_W to M_W^{temp} with $\chi_{min}^2 + 1$.

This method relies on fully simulated samples described in Section 7.1 to predict histograms of several observables — lepton p_T , m_T^W and E_T^{miss} . All known detector data/MC corrections and all known model corrections are applied.

The method has been used in previous experiments, e.g. by CDF and D0 at the Tevatron collider, for the W boson mass determination. In contrast to more sophisticated approaches, e.g. profiled measurements, it has the advantage to allow a detailed study of the impact of different experimental and model dependent systematic uncertainties.

8.1.2 Consistency Test

To test the consistency of the template fit method, the signal MC sample with central $M_W = 80.399$ GeV is split into two disjunct samples, A and B , of equal size. One of these samples is treated as data, the other as MC. Then the templates were generated from the MC sample using M_W reweighting procedure and the template fit method described above has been applied. Figure (8.3) shows a sample of control plots for the fits of subsample A vs B using three kinematical variables $p_T^\ell, m_T^W, E_T^{\text{miss}}$. The mass fitting ranges were chosen $30 \text{ GeV} < p_T^\ell < 50 \text{ GeV}$, $30 \text{ GeV} < E_T^{\text{miss}} < 50 \text{ GeV}$ and $65 \text{ GeV} < m_T^W < 100 \text{ GeV}$. The χ^2 was interpolated with a parabola close to its minimum and corresponding value of the W mass was extracted. As summarized in Table 8.1, the result of the fit agree with the truth value within statistical uncertainty.

It is visible that E_T^{miss} has a much smaller sensitivity to M_W than the other two observables, as it directly depends on the measurement of all other particles in the detector, that is complicated at hadron colliders. In contrast, the highest statistical sensitivity is seen for the p_T^ℓ observable that is due to excellent lepton reconstruction with the ATLAS detector at these energies.

Observable	p_T^ℓ	m_T^W	E_T^{miss}
Extracted W mass [MeV]	80399	80399	80399
Statistical error [MeV]	7	12	15

Table 8.1: Extracted W mass value and expected statistical uncertainty in the consistency test of the template fit method.

8.2 Measurement strategy

8.2.1 Introduction

Due to the relatively limited resolution of E_T^{miss} on the transverse momentum of the neutrino, it is expected that a fit in this observable has only a limited sensitivity on m_W . In contrary, the experimental resolution on the p_T of the charged decay leptons is excellent and hence a high sensitivity on m_W is expected. While the experimental resolutions have the smallest impact on m_W for the p_T distributions, the model uncertainties due to the PDF uncertainties and the modeling of the transverse momentum of the W boson plays the largest role. The statistical sensitivity of m_T^W observable is worse than the p_T , but at the same time it has the advantage that its spectrum is less sensitive to the boson p_T dynamics ($\sim q_T^2/M_W^2$).

In order to test the consistency and the understanding of experimental and - in particular - model uncertainties, the fit of m_W is performed not only inclusively but also in several disjunct kinematic categories and channels. The m_W measurement is performed for four channels $W^+ \rightarrow e^+\nu$, $W^- \rightarrow e^-\nu$, $W^+ \rightarrow \mu^+\nu$ and $W^- \rightarrow \mu^-\nu$. The usage of both lepton decay channels, allows for the test of consistencies of experimental uncertainties, A consistent charge dependency of m_W would point to a problem of the underlying physics model, while the agreement of m_W^+ and m_W^- in the muon channel but not in the electron channel, would point to an experimental problem.

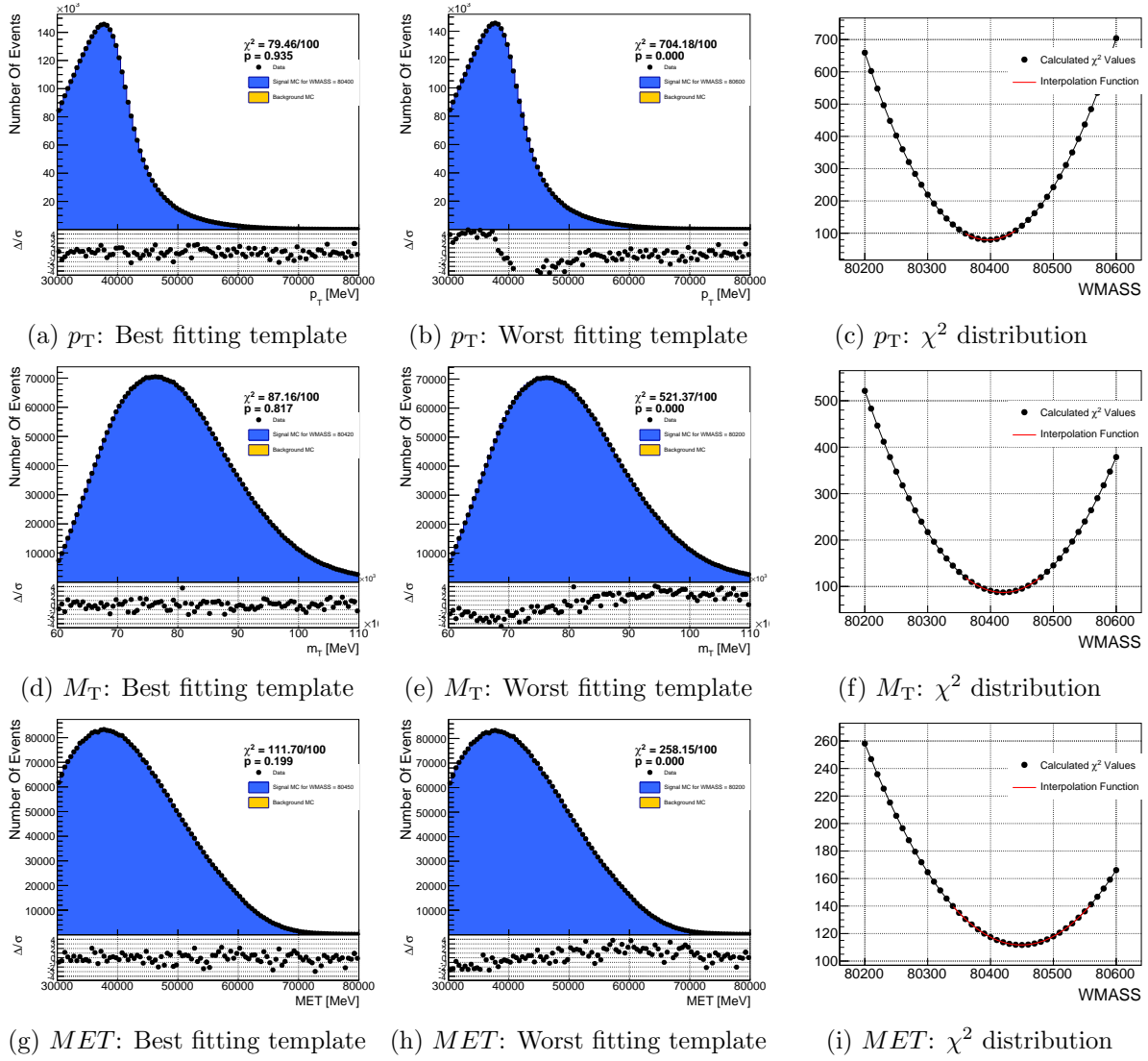


Figure 8.3: Selected control plots from the consistency tests. The 'best' fitting template corresponds to the template which leads to the minimal χ^2 value, while the 'worst' fitting template leads to the highest tested χ^2 value in the given fitting range of m_W .

In addition, these four measurements are performed in 3-4 bins for different lepton η regions, which allows to test the consistency for PDF and A_i QCD coefficient uncertainties. The stability against the pile-up environment and also the impact of the modeling of the W boson transverse momentum on m_W is tested, by performing the fits also in bins of the hadronic recoil and the number of interactions per bunch-crossing. A detailed description of the different measurement categories is given in the next Section 8.2.2.

In addition, the W mass measurement procedure and the applied corrections for the detector effects can be validated by performing the measurements of the Z boson mass M_Z , which is well-known. A measurement based on the lepton pair invariant mass directly tests the consistency of the lepton energy calibration. The p_T^ℓ -based measurement tests the p_T -dependent efficiency corrections, the Z boson transverse momentum and polarization models. The test of recoil calibration can also be performed using pseudo observables E_T^{miss} and m_T^Z , which can be defined treating one of the decay leptons as a neutrino.

Finally, the measurement results for both M_W and M_Z in bins of lepton azimuth angle allows to test the corresponding detector performance. In addition, the stability of the fit result against the fitting range is also tested. The choice of the nominal fitting range is based on the balance

between statistical and systematic uncertainties.

8.2.2 Measurement categories

The measurement introduced above is performed in signal region defined in Section 7.2 for four channels: $W^+ \rightarrow e^+\nu_e$, $W^- \rightarrow e^-\bar{\nu}_e$, $W^+ \rightarrow \mu^+\nu_\mu$, and $W^- \rightarrow \mu^-\bar{\nu}_\mu$. It comes in several variations:

- Inclusively, in the following phase space: one category per channel:
 - lepton transverse momentum: $p_T^\ell > 30$ GeV;
 - lepton pseudo-rapidity: $0 < |\eta| < 1.2$ or $1.8 < |\eta| < 2.4$ in the electron channels, and $0 < |\eta| < 2.4$ in the muon channels;
 - transverse mass: $M_T^W > 60$ GeV;
 - recoil: $u < 30$ GeV.
 - Two alternative selections: $E_T^{\text{miss}} > 30$ GeV, or no cut on E_T^{miss} .
- Separately in the following pseudo-rapidity bins: 3 (4) independent measurements in the electron (muon) channels:
 - $0 < |\eta| < 0.6$, $0.6 < |\eta| < 1.2$ and $1.8 < |\eta| < 2.4$ in the electron channels;
 - $0 < |\eta| < 0.8$, $0.8 < |\eta| < 1.4$, $1.4 < |\eta| < 2.0$ and $2.0 < |\eta| < 2.4$ in the muon channels;
 - two alternative selections: $E_T^{\text{miss}} > 30$ GeV, or no cut on E_T^{miss} ;
 - other cuts as in the inclusive measurement.
- Separately in the following pseudo-rapidity and recoil bins: 18 (24) independent measurements in the electron (muon) channels:
 - $|\eta|$ ranges as above;
 - $0 < u < 15$ GeV, $15 < u < 30$ GeV;
 - pile-up categories: $2.5 < \langle \mu \rangle < 6.5$, $6.5 < \langle \mu \rangle < 9.5$, $9.5 < \langle \mu \rangle < 16$;
 - two alternative selections: $E_T^{\text{miss}} > 30$ GeV, or no cut on E_T^{miss} ;
 - other cuts as in the inclusive measurement.

Number of selected W candidate events in data in different $|\eta|$ vs μ categories are summarized in Tab.8.2 for muon channel and Tab.8.3 for electron channel.

	$ \eta $ range	0 – 0.8	0.8 – 1.4	1.4 – 2.0	2.0 – 2.4	inclusive
$W^+ \rightarrow \mu^+\nu$	μ -inclusive	1283332	1063131	1377773	885582	4609818
$W^- \rightarrow \mu^-\bar{\nu}$		1001592	769876	916163	547329	3234960
$W^+ \rightarrow \mu^+\nu$	$2.5 < \langle \mu \rangle < 6.5$	601431	489215	627327	403488	2121461
$W^- \rightarrow \mu^-\bar{\nu}$		470382	354059	416797	249015	1490253
$W^+ \rightarrow \mu^+\nu$	$6.5 < \langle \mu \rangle < 9.5$	354451	297637	388891	249892	1290871
$W^- \rightarrow \mu^-\bar{\nu}$		275880	215022	258688	154340	903930
$W^+ \rightarrow \mu^+\nu$	$9.5 < \langle \mu \rangle < 16$	326670	275660	360718	231653	1194701
$W^- \rightarrow \mu^-\bar{\nu}$		254719	200290	240125	143636	838770

Table 8.2: Data statistics in the $|\eta|$ vs $\langle \mu \rangle$ categories in $W \rightarrow \mu\nu$ channel.

	$ \eta $ range	0 – 0.6	0.6 – 1.2	1.8 – 2.4	inclusive
$W^+ \rightarrow e^+ \nu$	μ -inclusive	1233960	1207136	956620	3397716
$W^- \rightarrow e^- \bar{\nu}$		969170	908327	610028	2487525
$W^+ \rightarrow e^+ \nu$	$2.5 < \langle \mu \rangle < 6.5$	502383	491697	397090	1391170
$W^- \rightarrow e^- \bar{\nu}$		394395	368783	251819	1014997
$W^+ \rightarrow e^+ \nu$	$6.5 < \langle \mu \rangle < 9.5$	368292	360155	283949	1012396
$W^- \rightarrow e^- \bar{\nu}$		289498	271419	180856	741773
$W^+ \rightarrow e^+ \nu$	$9.5 < \langle \mu \rangle < 16$	362571	354631	275074	992276
$W^- \rightarrow e^- \bar{\nu}$		284740	267635	177010	729385

Table 8.3: Data statistics in the $|\eta|$ vs μ categories in $W \rightarrow e\nu$ channel.

8.3 Validation on Z boson mass measurement

The $Z \rightarrow ll$ sample constitutes a powerful cross-check for the $W \rightarrow l\nu$ analysis. It allows to test the template fitting technique used for high precision M_W measurement, as the Z decay lepton momenta p_T are very similar to those from the W decay. Moreover, it provides a consistency check of the lepton and recoil calibration, efficiency corrections as well as the relevant physics corrections applied to the $W \rightarrow l\nu$ events. The remaining differences not covered by Z are the selection criteria, the backgrounds and residual physics corrections. With about ten times less statistics but two leptons per event, the statistical accuracy of these tests is expected to be only about factor two worse than that of the W sample.

8.3.1 Z boson selection

The event selection used for $Z \rightarrow ll$ analysis follows the W selection as described in Section 7.2. The main differences are:

- Select two leptons with opposite charge instead of one
- The cuts on the lepton $p_T > 25$ GeV are lower than in the W analysis to account for smaller m_W
- The requirement on the dilepton momentum is imposed $p_T^{\ell\ell} < 30$ GeV in order to select events kinematically closer to the W selection, which requires a cut on the hadronic recoil of 30 GeV
- Tight invariant mass cut is applied $81 \text{ GeV} < m_{\ell\ell} < 101 \text{ GeV}$

This analysis is based on the same data and Monte Carlo samples used for the W selection as described in Section 7.1. Here the modeled signal samples refer to $Z \rightarrow ll$ ($l = e, \mu$) processes and background samples to $Z \rightarrow \tau\tau$, dibosons, $t\bar{t}$ + single top, $W \rightarrow l\nu$ and heavy flavour production. The amount of background arising from top and electroweak processes is estimated using MC simulation. The fraction of events passing the selections is normalized to the theoretical cross section calculated at NNLO accuracy. The amount of multijet background in muon channel is estimated with $b\bar{b}/c\bar{c} \rightarrow \mu + X$ MC samples and normalized using the corresponding LO cross sections to the integrated luminosity. With the tight invariant mass cut the amount of the multijet background found to be negligible. In the electron channel, a data-driven multijet background estimate is performed. The background distribution is taken from the data, applying the usual kinematic selections but inverting the identification cuts, requiring the selected electrons to satisfy the loose identification at most. The fraction is estimated from the multijet background fit of the E_T^{cone30}/E_T variable and found to be less than 0.1% that corresponds to a few MeV impact of the mass fits. Table 8.4 summarizes the number of selected events in $Z \rightarrow ll$ in data and MC.

Sample	Data	$Z \rightarrow ll$	$Z \rightarrow \tau\tau$	$W \rightarrow l\nu$	$W \rightarrow \tau\nu$	top	$WW/WZ/Z$	Multijet
μ -channel	1045561	1020211	98.5	8.8	1.8	186.5	995.7	119.6
e -channel	447159	429077	32.2	2.4	0.3	78.1	410.4	447.16

Table 8.4: Number of selected $Z \rightarrow ll$ ($l = \mu, e$) events in data and MC. MC predictions are scaled to to the integrated luminosity in data and theoretical cross sections.

8.3.2 Lepton-pair distributions

Kinematical distributions for Z candidate events passing the selection requirements in both channels described in Section 8.2.2 are presented in this section. Figure 8.4 shows the invariant di-lepton mass, the transverse momentum and the rapidity of the Z boson distributions for $Z \rightarrow ee$ and $Z \rightarrow \mu\mu$. The good agreement in the invariant mass plots show the accuracy of the energy calibration reached for both muons and electrons. The good agreement in p_T^Z is obtained using the AZNLO tune described in Section 6. In addition, the polarization coefficients A_i ($i = 1..3$) are reweighted from nominal Powheg+Pythia8 values to the DYNNLO predictions at NNLO accuracy. The A_4 coefficient kept to remain as in the DYNNLO it is predicted from leading-order relation $\sin^2\theta_W = 1 - M_W^2/M_Z^2$, while POWHEG+PYTHIA8 uses the effective mixing angle measured at LEP $\sin^2\theta_W^{eff}$. This configuration is found to better follow data distributions and is taken as baseline in the W analysis.

8.3.3 Lepton momentum, W-like recoil and transverse mass distributions

After applying the physics corrections described in previous section, the modeled lepton transverse momentum distributions describe data with a good accuracy in both decay channels. The p_T^{l+} and p_T^{l-} distributions are shown in Fig.8.5 and Fig.8.6 for muons and electrons respectively. In order to construct the W-like distributions, the hadronic recoil u has been reconstructed following Section 3.3 and calibrated following Section 5.5. For the recoil, the u_{\parallel}^Z , u_{\perp}^Z are its projections on the axes parallel and perpendicular to the Z boson momentum vector as reconstructed from the final state lepton pair. The value of the transverse mass $m_T^Z(l)$ is calculated separately for positive and negative lepton in the event, using kinematical information of the given lepton and the measured recoil in the event. The corresponding distributions are shown in Fig.8.5 and Fig.8.6 for muons and electrons respectively, with all performance and physics corrections applied. A similar methodology was employed in Ref. [84].

8.3.4 Z boson mass fit results

To determine the value of the Z boson mass, a χ^2 profile as a function of m_Z is evaluated by comparing the $m_{\ell\ell}$, p_T^l and $m_T^Z(l)$ distributions in data to a set of templates built by varying the mass in steps of 2 MeV within ± 100 MeV of the reference mass value fixed to the world average $m_Z = 91187.6$ MeV. The interpolation between the different steps is done by fitting the χ^2 profile with a parabolic function. The minimum of the χ^2 function gives the value of the extracted mass, the difference of this mass with respect to the reference mass is defined as ΔM_Z .

The fitting ranges used are 80 – 100 GeV for $m_{\ell\ell}$, 30 – 55 GeV for p_T^l and 40 – 120 GeV for $m_T^Z(l)$. The results of the fits are summarised in Figure 8.7 for different steps: before energy/momentum corrections (see Section 5); after sagitta bias corrections in muon channel, after polarisation reweighting of all coefficients; and after polarisation reweighting of all coefficients except for A_4 (see Section 6). In the electron channel, the mass fit results are also reported before and after isolation cuts, applied in final selection.

After energy corrections, the electron transverse momentum results are compatible among each other, but biased with respect to the invariant mass fit by about 70 MeV. In the muon channel,

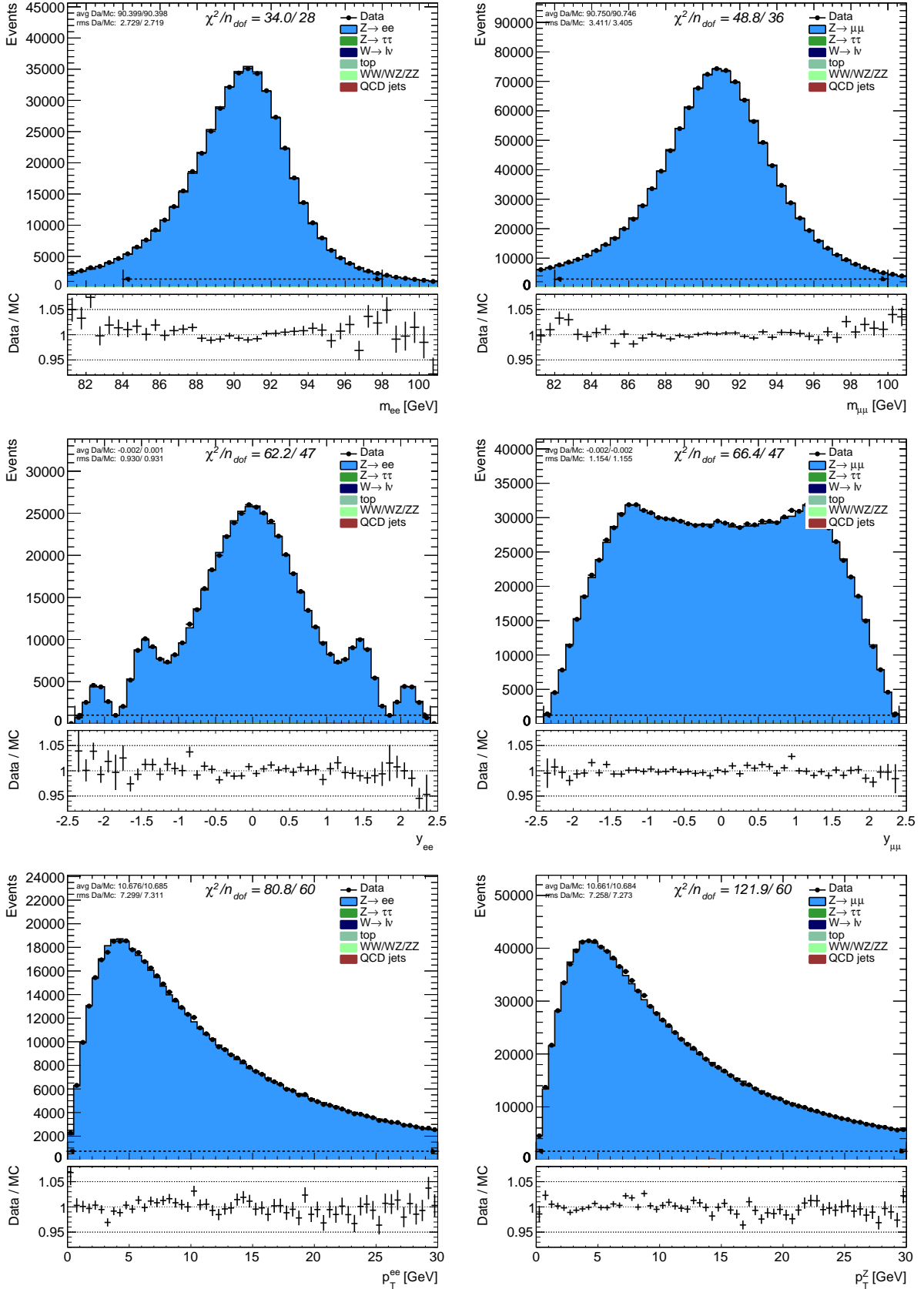


Figure 8.4: $m_{\ell\ell}$ (top), $y_{\ell\ell}$ (middle) and $p_{T\ell\ell}$ (bottom) distributions after all experimental corrections and after polarisation reweighting from Powheg+Pythia8 to DYNLO except A4. The electron and muon channels are shown on the left and on the right, respectively. The dashed line indicates the range over which the averages, RMS and χ^2 values are computed.

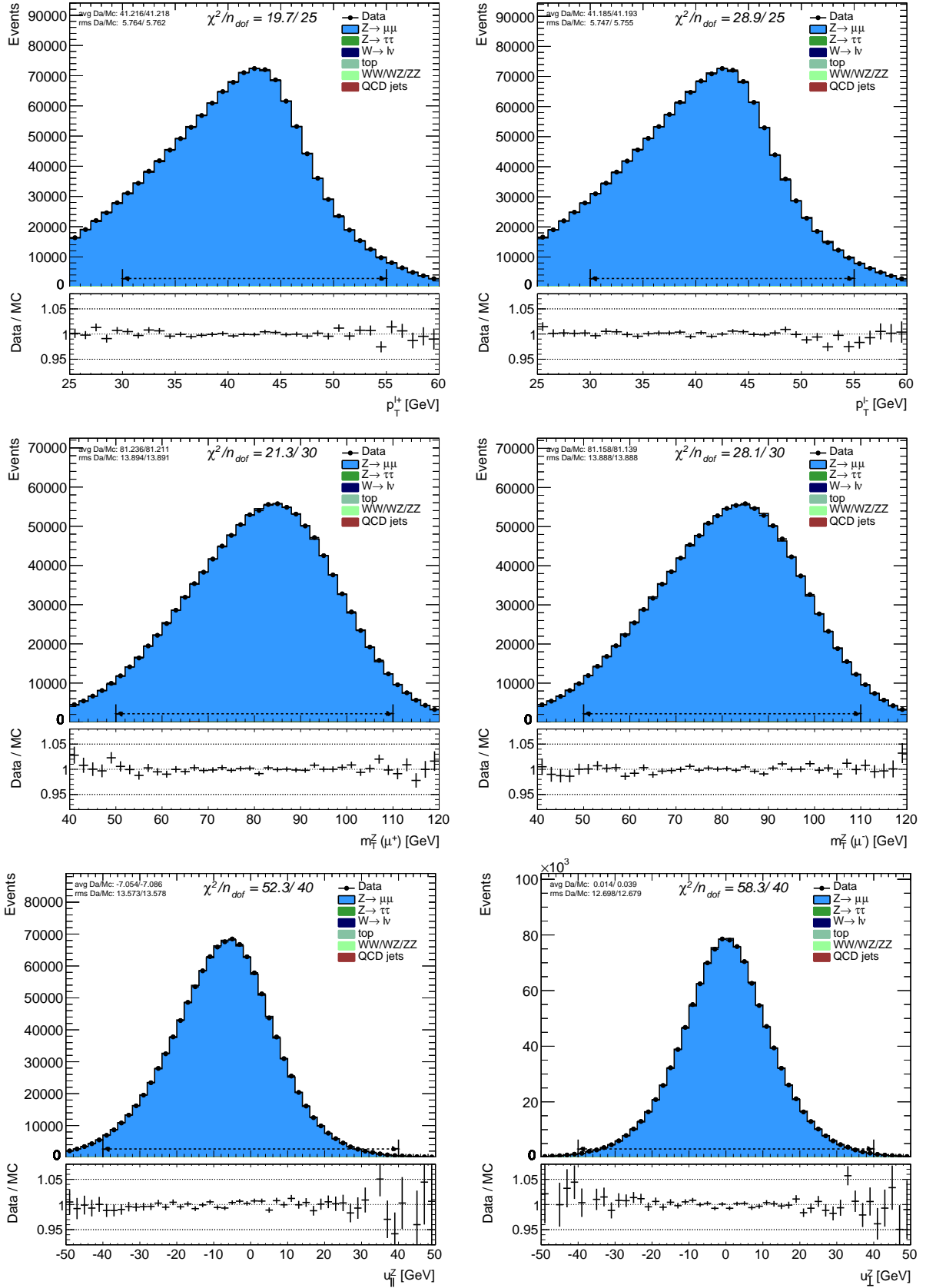


Figure 8.5: p_T^μ and $M_T^Z(\mu)$ distributions in pseudo $W^+ \rightarrow \mu^+ \nu$ (left) and $W^- \rightarrow \mu^- \nu$ (right) channels as well as parallel u_{\parallel} and perpendicular u_{\perp} projections of the recoil on the p_T^Z direction after all corrections applied. The dashed line indicates the range over which the averages, RMS and χ^2 values are computed.

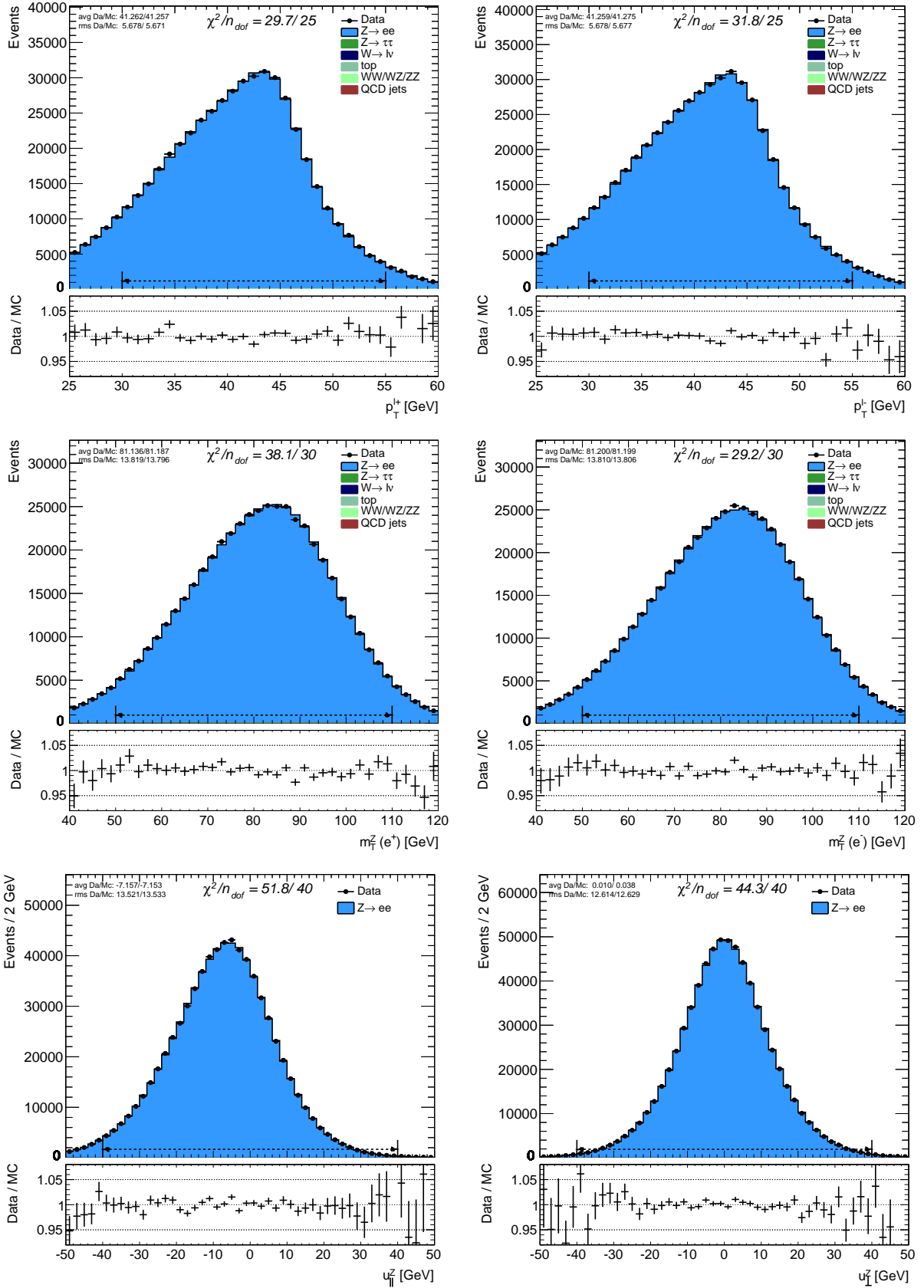


Figure 8.6: p_T^e and $M_T^Z(e)$ distributions in pseudo $W^+ \rightarrow e^+\nu$ (left) and $W^- \rightarrow e^-\nu$ (right) channels as well as parallel u_{\parallel} and perpendicular u_{\perp} projections of the recoil on the p_T^Z direction after all corrections applied. The dashed line indicates the range over which the averages, RMS and χ^2 values are computed.

the momentum scale corrections bring the compatibility between invariant mass and the charge-combined p_T^μ fits at the same level as in the electron channel; however, the positive and negative muons are apart by about 200 MeV. Good compatibility between $p_T^{\mu+}$ and $p_T^{\mu-}$ is obtained only after the sagitta bias corrections. The invariant mass and transverse momentum fits are reconciled after the polarization corrections.

For each channel and observable, the mass fits performed for positively and negatively charged leptons are expected to be correlated as they use the same samples. In the case of the p_T^ℓ fits, the two observables are measured independently, but the Z decay induces a kinematical correlation between the p_T^{l+} and p_T^{l-} distributions. This kinematical correlation is present also in the case of m_T ; in addition the hadronic recoil is common to $m_T^Z(l+)$ and $m_T^Z(l-)$ so that the two observables are also experimentally correlated.

The correlation is evaluated by building two-dimensional histograms of the p_T^{l+} , p_T^{l-} and $m_T^Z(l+)$, $m_T^Z(l-)$ distributions, and creating pseudo-data samples by fluctuating the bin contents of these distributions within their uncertainties. For each pseudo-data sample, the two-dimensional distribution is projected along the l^+ and l^- axes and the mass fits are repeated. The correlation between the p_T^{l+} and p_T^{l-} fit results is found to be -6.9%, and that between the $m_T^Z(l+)$ and $m_T^Z(l-)$ results is -12.4%.

The final fit results are also given in Tables 8.5 and 8.6 separately for the electron and muon channels, and after statistical combination including the above correlation. The final p_T^ℓ fits after the above mentioned corrections give a mass value compatible within 1σ with the reference mass value. The difference between the combined p_T^{l+} and p_T^{l-} fits is compatible with 0 within 1.4 standard deviations; for $m_T^Z(l+, l-)$, the compatibility is at the 1.2σ level. For the $m_T^Z(l\pm)$ fits, the compatibility with the reference mass is at the level of 1.8 standard deviations.

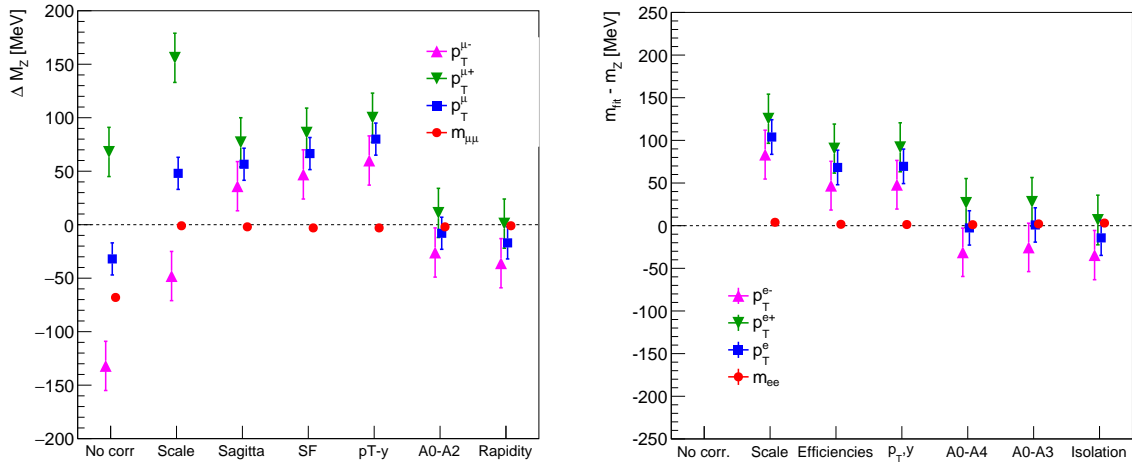


Figure 8.7: Summary of the p_T^ℓ -based mass fits results for muons (left) and electrons (right). The error bars are statistical only.

Finally, the $|\eta|$ dependence of the lepton p_T fits for both channels is summarized in Figure 8.8. The $|\eta|$ dependence of the $m_T^Z(l)$ fits is shown in Figure 8.9.

8.4 Uncertainty determination

The advantage of the template fit method introduced in Section 8.1.1 is that it allows a detailed study of the impact of different experimental and model dependent systematic uncertainties. With this technique, a systematic uncertainties can be assessed by their effect on MC and background templates. Some uncertainties only affect background distribution, such as the multijet background

Channel	$\delta m_Z : p_T^{l+}$ [MeV]	$\delta m_Z : p_T^{l-}$ [MeV]	$\delta m_Z : p_T^{l\pm}$ [MeV]
Electron	13 ± 31	-20 ± 31	-3 ± 21
Muon	1 ± 22	-36 ± 22	-17 ± 14
Combined	5 ± 18	-31 ± 18	-12 ± 12

Table 8.5: Z boson mass fit results in the electron and muon channels, after all corrections are applied. The $p_T^{l+,l-,l\pm}$ distributions are used. Shown are the differences between the $m_{\ell\ell}$ and p_T^ℓ fit results, as the $m_{\ell\ell}$ fits agree with m_Z by construction and the compatibility between the invariant mass and transverse momentum observables is tested here. The combined results are also shown. The uncertainties quoted are statistical only.

Channel	$\delta m_Z : m_T^Z(l+)$ [MeV]	$\delta m_Z : m_T^Z(l-)$ [MeV]	$\delta m_Z : m_T^Z(l\pm)$ [MeV]
Electron	-93 ± 38	4 ± 38	-45 ± 27
Muon	-35 ± 28	-1 ± 27	-18 ± 19
Combined	-58 ± 23	1 ± 22	-29 ± 16

Table 8.6: Z boson mass fit results in the electron and muon channels, after all corrections are applied. The $m_T^Z(l+,l-,l\pm)$ distributions are used. Shown are the differences between the $m_{\ell\ell}$ and m_T^ℓ fit results, as the $m_{\ell\ell}$ fits agree with m_Z by construction and the compatibility between the invariant mass and transverse mass observables is tested here. The combined results are also shown. The uncertainties quoted are statistical only.

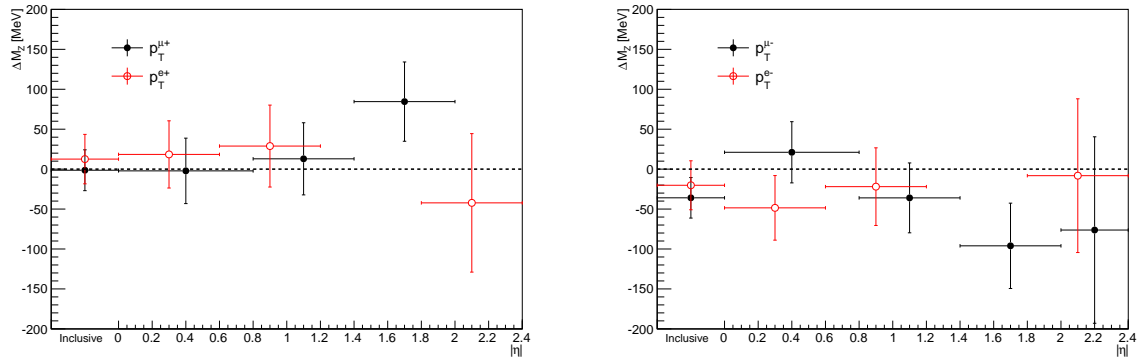


Figure 8.8: $|\eta|$ dependence of the lepton p_T fit results. The error bars are statistical only.

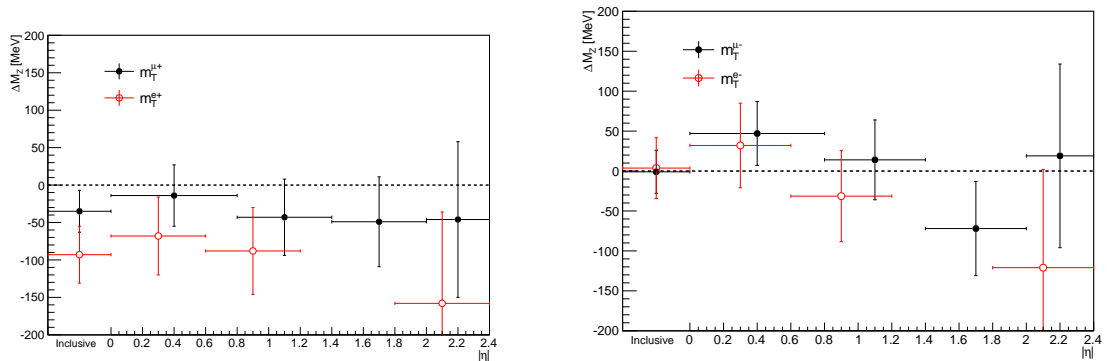


Figure 8.9: $|\eta|$ dependence of the lepton m_T fit results. The error bars are statistical only.

estimation or limited knowledge of other backgrounds modeled by MC. Others affect only signal sample, such as the PDF uncertainties.

The propagation of the uncertainties from background templates is performed by replacing the nominal background template with varied background templates and assessing the effect on the boson mass fit result. The propagation of the uncertainties from the MC templates can be performed in two ways:

- **Full Template method:** In the full template method, for each uncertainty source, a new set of MC templates is produced. The fitting is then performed for each combination of data and MC / background template.
- **Pseudo-Data method:** In this method, pseudo-data templates are produced from MC for each uncertainty source. In the fitting procedure, the fit is performed for each combination of the pseudo-data and the nominal MC template.

There are different types of systematic uncertainties which need to be treated differently:

- **Paired:** Paired systematics consist of associated up and down variations. There are cases, in which several paired systematics have to be combined for a total paired systematic. For example, the total uncertainty for the Parton Density Functions (PDF) consist of several eigenvector uncertainties. In general, several paired systematics are combined following ref. [85]. The symmetrized form is used here. The resulting equations read as:

$$\Delta^+ = \sqrt{\sum_{i=1}^N \max(X_{up,i} - X_{base}, X_{down,i} - X_{base}, 0)^2} \quad (8.3)$$

$$\Delta^- = \sqrt{\sum_{i=1}^N \max(X_{base} - X_{up,i}, X_{base} - X_{down,i}, 0)^2} \quad (8.4)$$

$$\Delta = \frac{1}{2} \sqrt{\sum_{i=1}^N (X_{up,i} - X_{down,i})^2} \quad (8.5)$$

- **Shifts:** In some cases, only a number of shifts with respect to the baseline setting is supplied. This is, for example, the case for the hadronic recoil correction, where the uncertainty estimation originates from three variations with respect to the nominal setting. The resulting uncertainty for the error source is combined by quadratical addition of the different shifts according to:

$$\Delta = \sqrt{\sum_{i=1}^N (X_{s,i} - X_{base})^2} \quad (8.6)$$

- **Toy MCs:** Uncertainties can be estimated with Toy MCs. Consider for example a correction with a set of Scale Factors (SF) for each bin. The connected uncertainty can be estimated by performing an up and down variation with $\widetilde{SF} = SF \pm 1\sigma$. A better way is to produce combined Toy Monte Carlos, where in each Toy Monte Carlo i the Scale Factors for each bin k are modified as

$$\widetilde{SF}_i^k = SF^k + \Delta SF_{\text{stat+uncorr}}^k \cdot g_i^k + \sum_{s=1}^S \Delta SF_{\text{cor},s}^k \cdot g_{i,s} \quad (8.7)$$

Here g is defined with $g \in \text{Gauss}(0,1)$. Note that $g_{i,s}$ is the same random number for all bins k in a given Toy Monte Carlo i . In this way, bin-to-bin correlated and uncorrelated

uncertainties are correctly taken into account. The resulting uncertainty stemming from the Scale Factors on the parameter is now estimated using the empirical standard deviation:

$$\Delta = \sqrt{\frac{1}{n-1} \sum_{i=1}^N (X_{s,i} - \overline{X_s})^2} \quad (8.8)$$

Different uncertainty sources can always be combined using the quadratic sum.

8.5 Blinded fit results

The W boson mass results extracted with the template fit method introduced in Section 8.1.1. The p_T^l and m_T observables, which are most sensitive to the mass of the W boson, were used in the template fits. All data/MC and physics modeling corrections have been applied. In order to be sensitive to the Jacobian peak, and at the same time minimizing a possible bias from misprediction of the multijet background, the fitting ranges are chosen to be 30 – 50 GeV for p_T^l and 65 – 100 GeV for m_T . All the W mass fit results presented here are blinded, i.e. all the distributions are modeled with injected offset b to the W mass, where b is a random value within range [-100 MeV, 100 MeV].

The p_T^l and m_T fit results as a function of lepton pseudorapidity are shown on Figures 8.10 for electron and muon channels. The first point corresponds to η inclusive result. The error bars correspond to statistical uncertainties only. Already without taking into account systematic uncertainties, a very good compatibility across channels and categories can be seen.

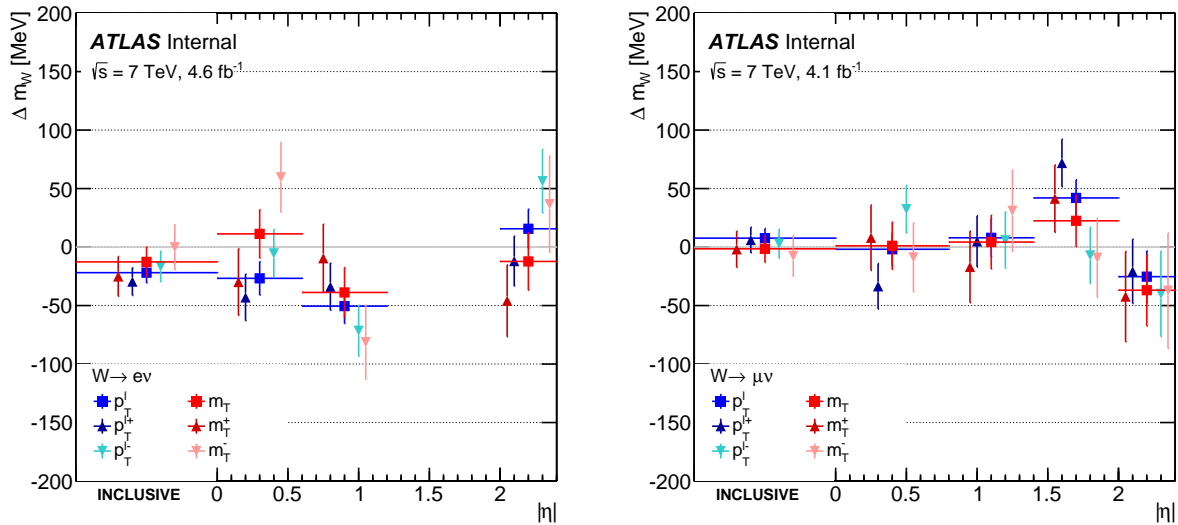


Figure 8.10: Blinded p_T^l and m_T fit results as a function of lepton pseudorapidity for electron (left) and muon (right) channel, with the nominal event selection. Error bars are statistical only. The result is given as a shift with respect to the assumed value of m_W in the MC, plus an unknown offset.

8.5.1 Correlations between W boson observables

A study is performed to assess the level of statistical correlation between the m_W value as obtained using a fit to the p_T^l distribution and to the m_T distribution. This is necessary input for the combination of the m_W value obtained from the two measurements. The study uses 1000 pseudo-datasets, which are created from $W \rightarrow \mu\nu$ Monte Carlo events. A pseudo-dataset is obtained by weighting each Monte Carlo event by a random sample from a Poisson distribution

		δm_W [MeV]								
		electron channel				muon channel				
$ \eta $ range		(0 – 0.6)	(0.6 – 1.2)	(1.8 – 2.4)	Inclusive	(0 – 0.8)	(0.8 – 1.4)	(1.4 – 2.0)	(2.0 – 2.4)	Inclusive
$< \mu >$ inclusive										
W^\pm	p_T^ℓ	-27 ± 14	-50 ± 15	16 ± 17	-22 ± 9	-2 ± 14	8 ± 16	42 ± 16	-25 ± 22	8 ± 8
W^+		-43 ± 20	-34 ± 20	-12 ± 21	-30 ± 12	-34 ± 19	5 ± 22	72 ± 20	-21 ± 27	6 ± 11
W^-		-5 ± 21	-72 ± 22	56 ± 27	-17 ± 13	32 ± 20	6 ± 24	-7 ± 24	-40 ± 37	3 ± 12
W^\pm	m_T	11 ± 21	-39 ± 21	-12 ± 25	-13 ± 13	1 ± 20	4 ± 23	22 ± 22	-37 ± 31	-2 ± 12
W^+		-30 ± 29	-10 ± 29	-46 ± 31	-25 ± 17	8 ± 28	-17 ± 31	41 ± 29	-42 ± 39	-2 ± 15
W^-		60 ± 30	-81 ± 32	37 ± 41	0 ± 19	-9 ± 29	31 ± 35	-9 ± 34	-37 ± 49	-8 ± 18

Table 8.7: Blinded fit results (in MeV) for the p_T^ℓ and m_T -based m_W measurement with only statistical uncertainty. The result is given as a shift with respect to the assumed value of m_W in the MC, plus an unknown offset.

with mean 1. Figure 8.11 plots the m_W value as obtained using the m_T against the m_W value as obtained using the p_T^ℓ fit, for each of the 1000 pseudo-datasets.

One can see qualitatively that there is positive correlation between the two fitting distributions, as expected. The sample correlation coefficient r , between sample pairs (X_i, Y_i) is defined in Equation 8.9:

$$r = \frac{\sum_{i=1}^N (X_i - \bar{X})(Y_i - \bar{Y})}{\sqrt{\sum_{i=1}^N (X_i - \bar{X})^2} \sqrt{\sum_{i=1}^N (Y_i - \bar{Y})^2}} \quad (8.9)$$

The value of r obtained using the sample pairs in Figure 8.11 is 0.51 ± 0.02 , where the uncertainty arises from the limited number of pseudo-datasets. The corresponding histograms for fits in different lepton $|\eta|$ ranges are given in Figure 8.12. Note that both the pseudo-datasets and the MC used for fitting have the requirement on $|\eta|$ made.

A further study performed was to investigate how much can be gained in statistical precision from the combination of the m_W value from the p_T^ℓ and m_T fits. The motivation is that a second measurement can appear to be decorrelated from the first, without adding additional information (called here ‘fake decorrelation’). The extreme example would be a measurement of p_T^ℓ (X) and of p_T^ℓ plus a noise term (Y). In this scenario the correlation r would be equal to σ_X/σ_Y , but the uncertainty on the combination would be no smaller than σ_X .

The two methods used to estimate the statistical uncertainty on the combination are now described and are found to give consistent results. Note that in the following the m_W value from the p_T^ℓ and m_T fits are denoted as A and B respectively and their combined value is denoted as C . The first method involves calculating σ_C directly using the standard formulae given in Equations 8.10 to 8.12 [?]. The value of C is given by Equation 8.10

$$C = wA + (1 - w)B, \quad (8.10)$$

where w is a weight to be determined.

The error on C squared, σ_C^2 , is given in Equation 8.11:

$$\sigma_C^2 = w^2 \sigma_A^2 + 2rw(1 - w)\sigma_A \sigma_B + (1 - w)^2 \sigma_B^2, \quad (8.11)$$

where r is the correlation value calculated previously.

Equation 8.11 can be minimised to get the value of w which gives the smallest uncertainty on the combination (Equation 8.12).

$$w = \frac{\sigma_B^2 - r\sigma_A \sigma_B}{\sigma_A^2 - 2r\sigma_A \sigma_B + \sigma_B^2} \quad (8.12)$$

The example calculation used here is for the $0.0 < |\eta| < 2.4$ category, where $r = 0.524$, $\sigma_A = 3.93$ MeV (p_T^ℓ fit) and $\sigma_B = 4.83$ MeV (m_T fit). Therefore $w = 0.71$ and $\sigma_C = 3.727$.

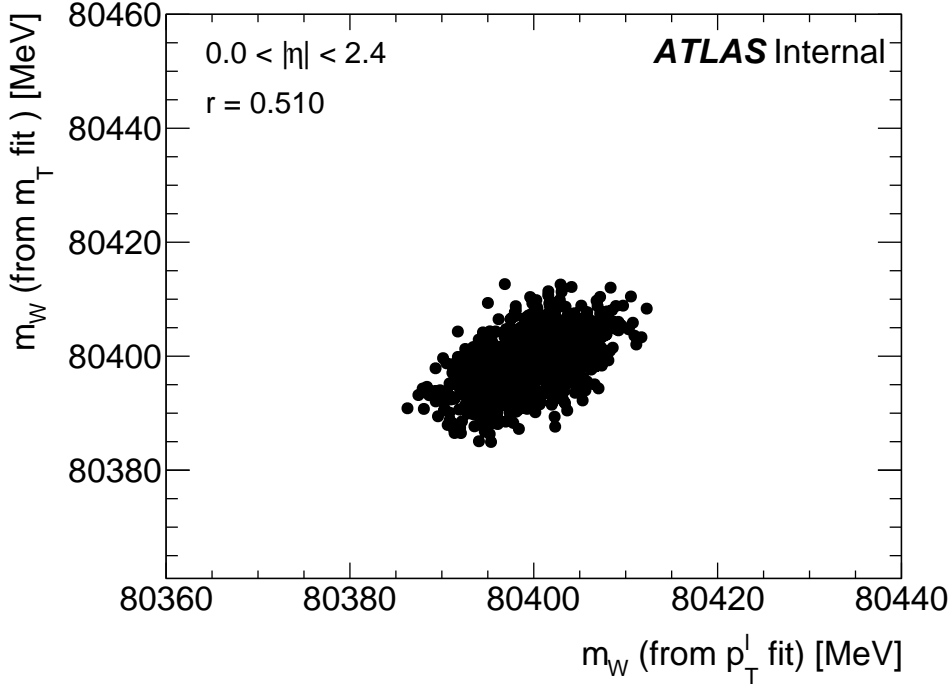


Figure 8.11: The m_W value obtained from a fit to the m_T distribution against the m_W value obtained from a fit to the p_T^ℓ distribution for 1000 pseudo-datasets.

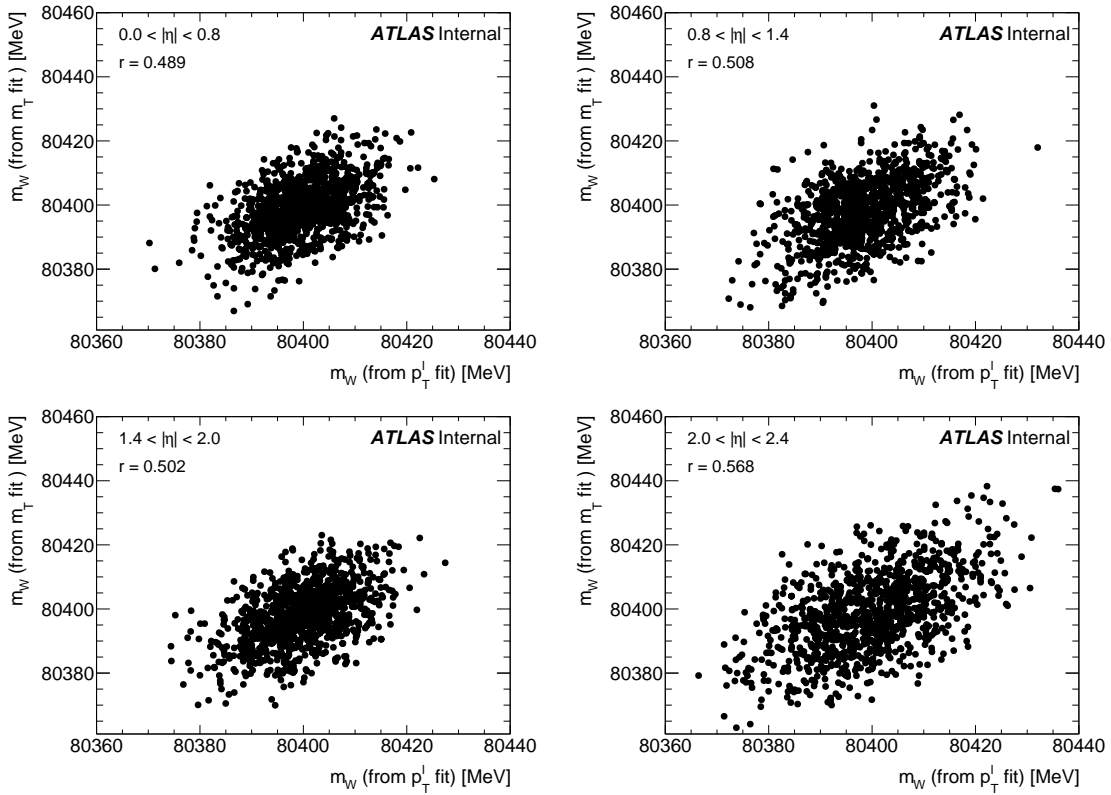


Figure 8.12: The m_W value obtained from a fit to the m_T distribution against the m_W value obtained from a fit to the p_T^ℓ distribution for 1000 pseudo-datasets. Each plot corresponds to a different selection requirement on the lepton $|\eta|$ (the range is indicated on each plot).

A second way of calculating the value of σ_C is to again create a set of 1000 pseudo-datasets from $W \rightarrow \mu\nu$ MC events and to combine the values of A and B for each pseudo-dataset. This creates a set of 1000 combined values. There are two possible choices for the values of σ_A and σ_B in this case, the first being the statistical uncertainty on the fit to each pseudo-dataset. However since some events are lost when the Poisson weight is set to 0, this is larger than the statistical uncertainty on the nominal MC. Therefore a better value to use is the RMS of the 1000 pseudo-datasets.

An estimate for σ_C is given by the RMS of the set of 1000 values of C . Using again the same $|\eta|$ category (and therefore with the same value of w as above) - the RMS of the set of 1000 values of C is 3.721, which is very similar to the direct calculation obtained above.

The conclusion of this study is that a reduction in the statistical uncertainty from 3.93 (taking the result from the p_T^ℓ fit only) to 3.72 (from the combination of the p_T^ℓ and m_T fits) is perhaps less than might be hoped for, given a correlation, r , of only $\approx 50\%$. This suggests there is indeed some (smaller) level of fake decorrelation between the p_T^ℓ and m_T fits.

8.5.2 Combination Procedure and Correlations

8.5.2.1 χ^2 definition and least squares solution

The method described here is referred to as the BLUE method, documented for example in the Particle data review [86] or in the paper by A. Valassi [87]. It is summarized here for the case of N independent measurements of a single physical parameters. The χ^2 to be minimized is defined as:

$$\chi^2 = (X - \bar{X})^T C^{-1} (X - \bar{X}) \quad (8.13)$$

where the vector $X = \{X_1^e, \dots, X_m^e; X_1^\mu, \dots, X_n^\mu\}$ represents the measured values of m_W in the $m + n = N$ electron and muon channels and categories; $\bar{X} = \{\bar{X}, \dots, \bar{X}\}$ contains N times the average value to be determined, and C is the full $N \times N$ covariance matrix.

The χ^2 minimization and combined uncertainty calculation is performed analytically. The solution is:

$$\bar{X} = (H^T C^{-1} H)^{-1} H^T C^{-1} X, \quad (8.14)$$

where H is, in the case of a single parameter of interest, a unit vector of size N :

$$H = \begin{pmatrix} 1 \\ \vdots \\ 1 \end{pmatrix} \quad (8.15)$$

Finally, the combined covariance matrix is:

$$\bar{C} = (H^T C^{-1} H)^{-1}. \quad (8.16)$$

8.5.2.2 Construction of the covariance matrices

The total covariance matrix can be written

$$C = C^{\text{stat}} + \sum_{\alpha} C^{\alpha}. \quad (8.17)$$

C^{stat} is a diagonal matrix containing the measurements statistical uncertainties, *i.e.* $C_{k,k}^{\text{stat}} = \delta X_k$, and $C_{k \neq l}^{\text{stat}} = 0$. The C^{α} are systematic uncertainty contributions.

Most systematic sources are described by a single nuisance parameter, which can affect one or a larger subset of the measurements X_k . In this case, the covariance matrix is constructed from the differences

$$\delta X_k^{\alpha} = X_k^{\alpha} - X_k^{\text{nom}}, \quad (8.18)$$

where α labels the sources of uncertainty and k the measurements, and δX_k^α reflects the impact of the uncertainty variation α on measurement k . Finally,

$$C_{k,l}^\alpha = \delta X_k^\alpha \times \delta X_l^\alpha \quad (8.19)$$

describes the covariance of measurements k, l under this variation.

In some special cases, where a given class of uncertainty source involves a large number of nuisance parameters, it is more practical to propagate the uncertainties with the toy Monte Carlo method, where all nuisance parameters of the class are varied simultaneously. The random variations follow a gaussian distribution of mean 0 and width equal to the nuisance parameters uncertainties, and preserve correlations among them if applicable. The uncertainty on each measurement is estimated from the spread of the measurement results under the toy variations, and the covariance is calculated explicitly:

$$C_{k,l}^\alpha = \frac{1}{n_{\text{toys}}} \sum_{i=1}^{n_{\text{toys}}} (X_k^{\alpha,i} - X_k^{\text{nom}})(X_l^{\alpha,i} - X_l^{\text{nom}}). \quad (8.20)$$

8.5.2.3 Sources of uncertainty and correlations

While electron and muon measurement uncertainties are specific to each channel, the recoil scale and resolution systematics are assumed fully correlated between the two channels. Multijet, electroweak and top background uncertainties are discussed in Section 7 and considered correlated across channels and rapidity bins.

FSR theoretical uncertainties, and smaller effects such as fermion pair radiation, ISR/FSR interference corrections and pure higher-order weak (non QED) corrections are taken fully correlated between all categories. Finally, the experimental uncertainty on m_Z contributes *via* the energy/momentum calibration. The associated uncertainty is taken fully correlated across measurement categories.

PDF uncertainties are taken from the CT10 NNLO set and are propagated to the boson angular coefficients and rapidity distribution. In addition, the W boson mass fits have been performed, using the CT14 NNLO and the MMHT NNLO pdf sets as baseline. The maximal difference between the fitted m_W values using these alternative pdf-sets to the nominal pdf-set is taken as additional PDF uncertainty for the overall combined m_W value. It should be noted, that when varying the PDF, we also change the matrix element PDF in the $p_T(W)/p_T(Z)$ prediction, as discussed in the following.

Strong interaction uncertainties not related to PDFs further affect the W transverse momentum distribution and angular coefficients. As discussed in [87], the PYTHIA parton shower is used to model the boson p_T distributions, differentially in rapidity. The parton shower parameters are constrained using the measured p_T^Z distribution at 7 TeV, and the fitted parameter uncertainties, which reflect the p_T^Z data accuracy, constitute a first source of uncertainty in the p_T^W distribution. In addition, the uncertainty in the p_T^W/p_T^Z distribution ratio is estimated from variations of the parton shower factorization scale, of the c and b quark masses, and from different choices of the LO PDF used for the parton shower evolution. Finally, uncertainty in the theoretical modeling of the boson angular coefficients is estimated using the Z angular coefficients measurement performed at 8 TeV. All these sources are counted as uniform as a function of p_T , fully correlated across all measurement categories.

The overall measurement includes 117 separate sources of uncertainty.

8.5.3 Results with initial fitting range

The measurement combination is performed in several ways:

- combining all measurement categories, separately for p_T and m_T fits;

- combining the electron and muon channel results separately;
- combining all W^+ and W^- results separately;
- combining all measurement categories, including p_T and m_T fits.

The correlation between p_T and m_T is taken from Sec. 7.3. The fitted m_W values are given always with respect to the MC W boson mass plus an unknown blinding value b , i.e. $80399 + b$ MeV. The fit-results for all individual categories and channels, including all uncertainties are given in Table 8.8 and illustrated in Figure 8.13. Here, the BLUE-Combination method has been used. In addition, these results were verified by using the X-fitter framework for the combination. Both combinations yield equivalent results with $\chi^2/ndf = 30.5/27$, i.e. a very good agreement of all individual measurements is observed. While the PDF uncertainties for each individual measurement are in the order of 20-35 MeV, a significant reduction in the combined fit can be observed, coming from different impacts of PDF uncertainty eigenvectors in the different categories and fit-observables.

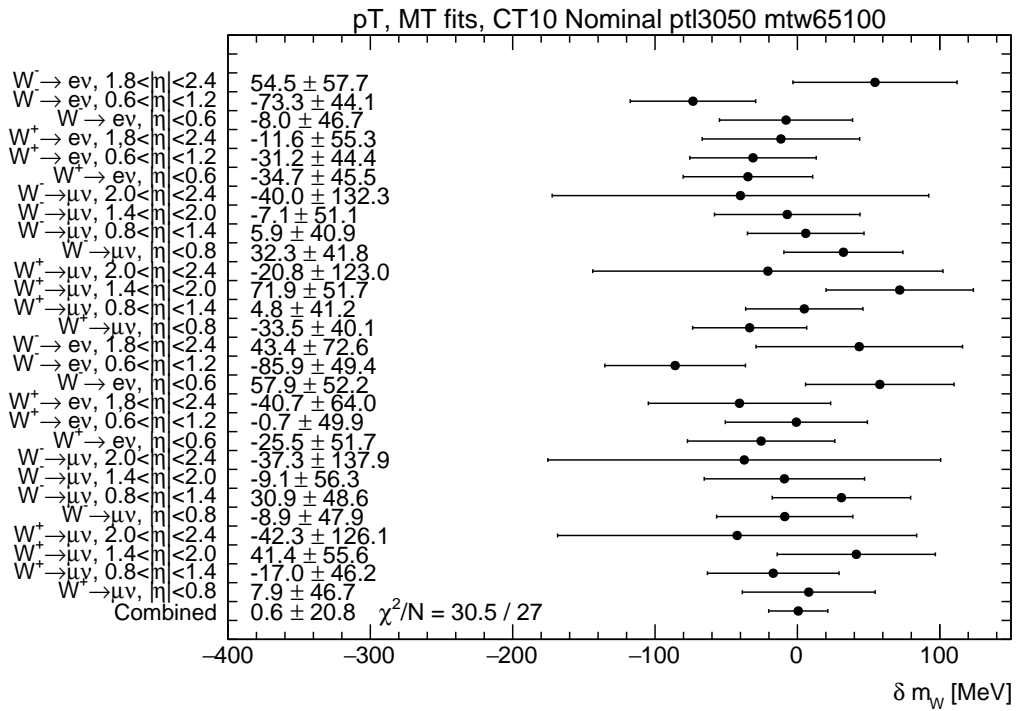


Figure 8.13: Combination of all p_T^1 fit results (upper half) and m_T fit results (lower half) in all channels and categories using the CT10 PDF set. The full uncertainties of each individual fit are indicated. The result is given as a shift with respect to the assumed value of m_W in the MC, plus an unknown offset.

In order to test the compatibility of all channels, fit-observables and categories further, we combined several combinations individually, shown in Table 8.9. All individual combinations, e.g. combined all m_T -fits in the W^+ decay channels, lead to very good χ^2/ndf values, all close to one σ deviation. Moreover, all combined values are consistent with each other. The good consistency between the electron and the muon channel results indicate a correct modeling of the detector response, while the agreement between the results for W^+ and W^- are an additional confirmation of the underlying physics modeling. The agreement between the p_T and m_T based tests both physics and the detector response modeling. Several combinations are illustrated in Figures 8.14, 8.15, 8.16, 8.17 and 8.18.

The effect of PDF uncertainties on m_W was under long discussion in the past. Table 8.10 shows the difference of the m_W -fit results, including uncertainties, based on p_T - and m_T -templates

Channel m_T -Fit	Value [MeV]	Stat. Unc.	Muon Calib.	Elec. Calib.	Recoil Calib.	Back- grd.	QCD	EWK	PDF's	Total Unc.
$W^+ \rightarrow \mu\nu, \eta < 0.8$	7.9	28.0	13.6	0.0	14.3	7.4	10.0	3.4	28.9	46.7
$W^+ \rightarrow \mu\nu, 0.8 < \eta < 1.4$	-17.0	30.6	19.4	0.0	11.1	6.1	9.7	3.4	23.6	46.2
$W^+ \rightarrow \mu\nu, 1.4 < \eta < 2.0$	41.4	28.8	34.4	0.0	13.5	6.6	9.4	3.4	27.4	55.6
$W^+ \rightarrow \mu\nu, 2.0 < \eta < 2.4$	-42.3	38.7	113.9	0.0	13.7	9.0	8.5	3.4	33.2	126.1
$W^- \rightarrow \mu\nu, \eta < 0.8$	-8.9	29.5	12.8	0.0	10.6	7.7	9.6	3.4	31.3	47.9
$W^- \rightarrow \mu\nu, 0.8 < \eta < 1.4$	30.9	34.8	19.5	0.0	10.8	6.7	9.9	3.4	22.3	48.6
$W^- \rightarrow \mu\nu, 1.4 < \eta < 2.0$	-9.1	34.0	34.8	0.0	10.1	6.8	9.9	3.4	23.3	56.3
$W^- \rightarrow \mu\nu, 2.0 < \eta < 2.4$	-37.3	49.4	122.8	0.0	11.0	9.9	9.9	3.4	34.4	137.9
$W^+ \rightarrow e\nu, \eta < 0.6$	-25.5	28.2	0.0	22.7	13.4	15.2	10.0	3.4	29.0	51.7
$W^+ \rightarrow e\nu, 0.6 < \eta < 1.2$	-0.7	29.1	0.0	24.4	14.2	13.4	9.7	3.4	23.6	49.9
$W^+ \rightarrow e\nu, 1.8 < \eta < 2.4$	-40.7	30.9	0.0	32.7	14.0	32.2	8.5	3.4	27.6	64.0
$W^- \rightarrow e\nu, \eta < 0.6$	57.9	30.1	0.0	19.3	10.1	14.8	9.6	3.4	31.9	52.2
$W^- \rightarrow e\nu, 0.6 < \eta < 1.2$	-85.9	31.5	0.0	22.8	9.8	12.0	9.9	3.4	24.0	49.4
$W^- \rightarrow e\nu, 1.8 < \eta < 2.4$	43.4	40.9	0.0	36.2	11.4	35.0	9.9	3.4	28.6	72.6
p_T -Fit										
$W^+ \rightarrow \mu\nu, \eta < 0.8$	-33.5	19.4	13.0	0.0	1.2	6.0	13.4	6.0	28.4	40.1
$W^+ \rightarrow \mu\nu, 0.8 < \eta < 1.4$	4.8	21.9	19.5	0.0	0.6	5.1	13.5	6.0	24.3	41.2
$W^+ \rightarrow \mu\nu, 1.4 < \eta < 2.0$	71.9	20.3	34.6	0.0	1.0	5.3	12.6	6.0	29.1	51.7
$W^+ \rightarrow \mu\nu, 2.0 < \eta < 2.4$	-20.8	27.5	113.9	0.0	0.6	4.3	10.4	6.0	35.4	123.0
$W^- \rightarrow \mu\nu, \eta < 0.8$	32.3	20.5	12.2	0.0	1.4	5.8	12.1	6.0	31.0	41.8
$W^- \rightarrow \mu\nu, 0.8 < \eta < 1.4$	5.9	24.2	18.9	0.0	0.9	5.4	12.2	6.0	22.8	40.9
$W^- \rightarrow \mu\nu, 1.4 < \eta < 2.0$	-7.1	24.1	35.2	0.0	1.3	5.5	12.5	6.0	23.8	51.1
$W^- \rightarrow \mu\nu, 2.0 < \eta < 2.4$	-40.0	36.6	120.5	0.0	1.8	8.2	13.0	6.0	36.9	132.3
$W^+ \rightarrow e\nu, \eta < 0.6$	-34.7	19.7	0.0	24.4	1.1	7.9	13.4	5.3	28.5	45.5
$W^+ \rightarrow e\nu, 0.6 < \eta < 1.2$	-31.2	20.0	0.0	27.1	1.6	7.8	13.5	5.3	23.7	44.4
$W^+ \rightarrow e\nu, 1.8 < \eta < 2.4$	-11.6	21.3	0.0	37.9	1.4	15.0	10.4	5.3	28.4	55.3
$W^- \rightarrow e\nu, \eta < 0.6$	-8.0	20.5	0.0	22.8	1.6	8.0	12.1	5.3	31.7	46.7
$W^- \rightarrow e\nu, 0.6 < \eta < 1.2$	-73.3	21.8	0.0	24.7	1.6	7.7	12.2	5.3	24.8	44.1
$W^- \rightarrow e\nu, 1.8 < \eta < 2.4$	54.5	27.1	0.0	38.2	1.6	14.4	13.0	5.3	26.9	57.7
Combined	0.6	5.7	7.6	6.6	3.8	5.5	11.8	5.0	9.4	20.8

Table 8.8: Fitted mass values v , given by $m_W = 80399 + b \pm v$ MeV, where b is an unknown blinding value. The m_W fit is performed in the electron and muon decay channel, in different η lepton categories using the p_T and m_T observables (nominal fitting range). In addition to the statistical uncertainties, all experimental uncertainties, i.e. the muon, the electron and the hadronic recoil calibration uncertainties as well as the background related uncertainties on m_W are given. Also the model uncertainties, due to EWK corrections, QCD corrections (scales, PS, A_i coefficient modeling) and PDFs are given. All uncertainties are given in MeV.

Combination of	Value [MeV]	Stat. Unc.	Muon Calib.	Elec. Calib.	Recoil Calib.	Back-grd.	QCD	EWK	PDF's	Total Unc.	χ^2/ndf of Comb.
m_T -Fit (W^+)	-7.1	11.8	8.7	7.3	13.3	9.2	9.6	3.4	16.7	30.3	2.1/6
m_T -Fit (W^-)	1.1	13.3	9.2	7.0	10.5	9.4	9.8	3.4	16.0	29.6	8.6/6
m_T -Fit (W^\pm)	-1.0	9.4	8.2	5.6	11.6	8.2	9.7	3.4	9.6	24.2	14.4/13
p_T -Fit (W^+)	-11.5	8.5	7.4	9.4	1.1	5.5	12.6	5.7	16.5	26.7	3.8/6
p_T -Fit (W^-)	6.0	9.5	8.0	8.9	1.2	5.7	12.4	5.7	15.5	26.4	8.0/6
p_T -Fit (W^\pm)	-1.1	6.5	7.4	7.1	1.1	5.2	12.6	5.8	9.4	21.3	16.6/13
p_T -Fit (el)	-22.0	8.8	0	17.6	1.4	6.8	12.5	5.3	9.1	26.5	6.4/5
m_T -Fit (el)	-9.9	12.9	0	15.8	12.0	13.1	9.7	3.4	10.2	30.7	11.5/5
p_T -Fit (μ)	6.4	8.8	11.4	0	1.0	4.7	12.7	6.0	11.1	23.5	4.2/7
m_T -Fit (μ)	2.8	12.5	11.9	0	11.6	5.9	9.8	3.4	10.7	26.2	2.2/7

Table 8.9: Combined fit results for different selected m_W fits. The result is given as a shift with respect to the assumed value of m_W in the MC, plus an unknown offset. In addition to the statistical uncertainties, all experimental uncertainties, i.e. the muon, the electron and the hadronic recoil calibration uncertainties as well as the background related uncertainties on m_W are given. Also the model uncertainties, due to EWK corrections, QCD corrections (scales, PS, A_i coefficient modeling) and PDFs are given. All uncertainties are given in MeV.

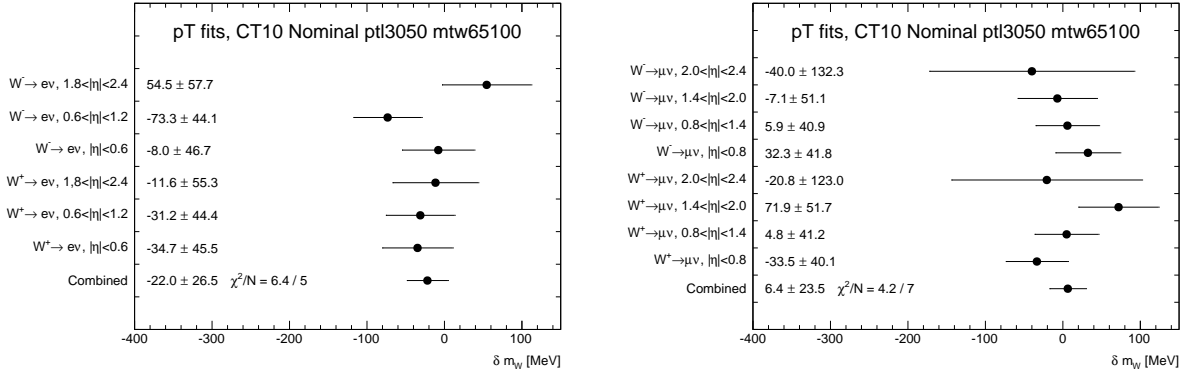


Figure 8.14: Combination of all p_T^ℓ fit results in electron (left) and muon (right) channels. The result is given as a shift with respect to the assumed value of m_W in the MC, plus an unknown offset.

for the CT14 and MMHT PDF set in comparison to the baseline of CT10. The alternative PDF sets have been used for the full physics modeling, in particular the rapidity distribution and the angular coefficients, except the modeling of the $p_T(W)$ spectrum. The latter already was already studied separately for different PDF sets. As it can be seen, all fits agree within the given PDF uncertainties. The MMHT pdf-set has a 25% smaller PDF uncertainty compared to CT10, in agreement with independent studies [48]. As an additional uncertainty due to the different results for different PDF sets, we treat half of the maximal observed difference (7.5/2 MeV) as additional uncertainty on the combined value of m_W , to be added in quadrature.

In summary, we measure the mass of the W boson to be

$$\begin{aligned}
 m_W &= 80399 + 0.6 + b \pm 5.7 \text{ MeV(stat.)} \pm 12.0 \text{ MeV(exp.sys.)} \pm 16.3 \text{ MeV(mod.sys.)} \\
 &= 80399 + 0.6 + b \pm 21.0 \text{ MeV,}
 \end{aligned}$$

where the unblinding parameter $b = [-100, 100] \text{ MeV}$ is yet unknown for the initial fitting range (30 – 50 GeV for p_T^ℓ and 65 – 100 GeV for m_T). The indicated uncertainties correspond to statistical, experimental systematic and physics-modelling systematic components.

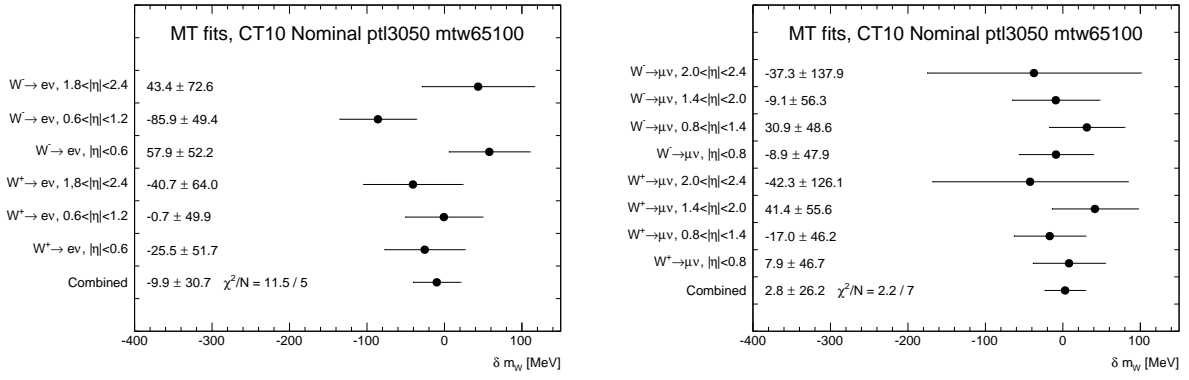


Figure 8.15: Combination of all m_T fit results in electron (left) and muon (right) channels. The result is given as a shift with respect to the assumed value of m_W in the MC, plus an unknown offset.

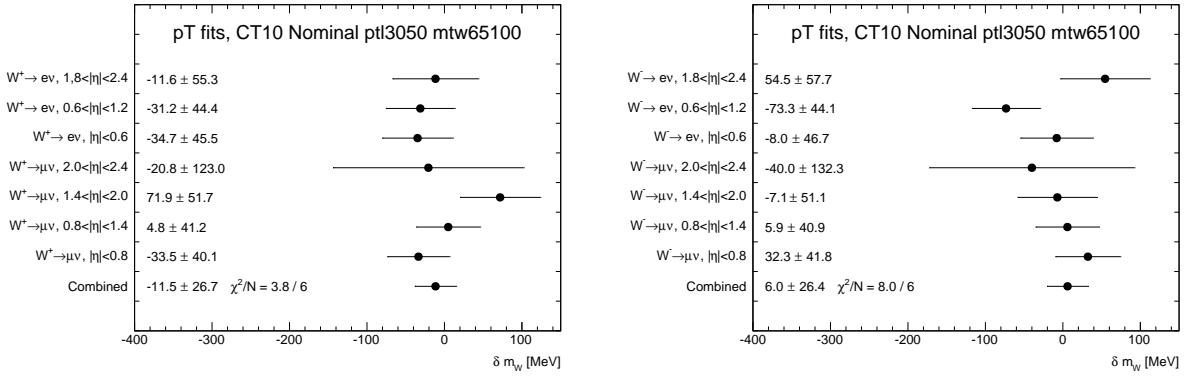


Figure 8.16: Combination of all p_T^l fit results in electron and muon channels for W^+ (left) and W^- (right). The result is given as a shift with respect to the assumed value of m_W in the MC, plus an unknown offset.

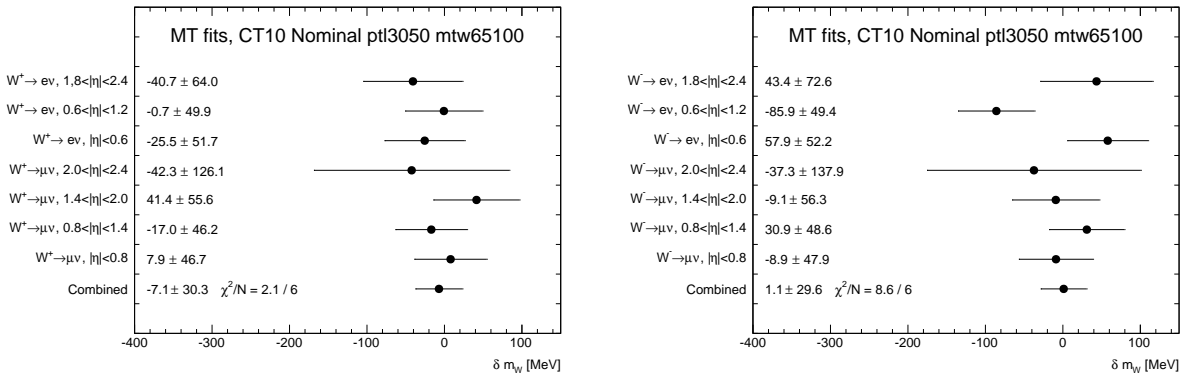


Figure 8.17: Combination of all m_T fit results in electron and muon channels for W^+ (left) and W^- (right). The result is given as a shift with respect to the assumed value of m_W in the MC, plus an unknown offset.

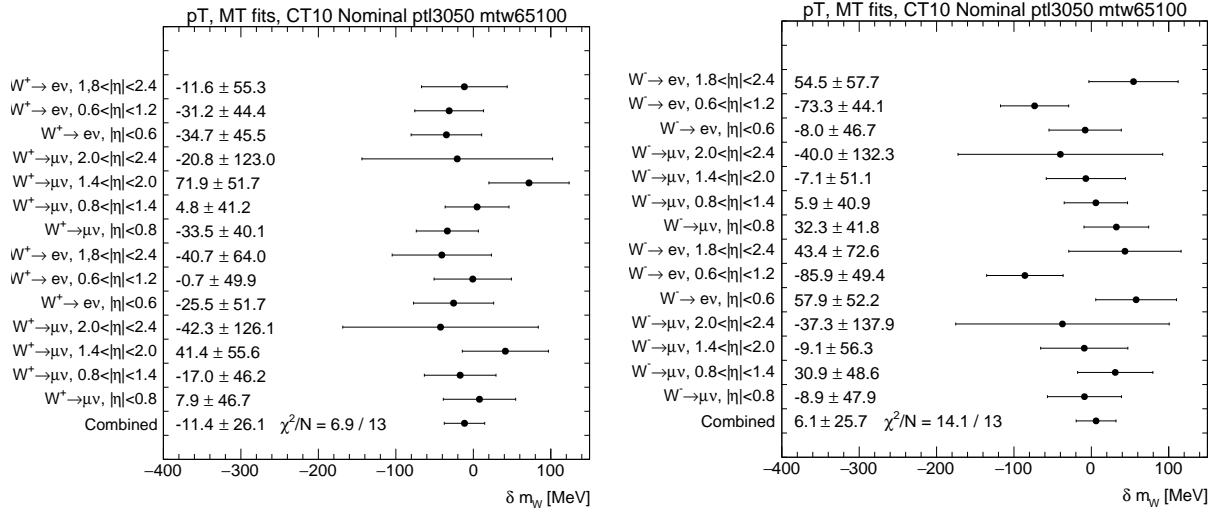


Figure 8.18: Combination of all fit results in electron and muon channels for W^+ (left) and W^- (right). The result is given as a shift with respect to the assumed value of m_W in the MC, plus an unknown offset.

PDF-Set	Value [MeV]	Total Unc.	PDF. Unc
p_T and m_T Fits:			
CT14-CT10	2.9	19.2	10.3
MMHT-CT10	7.5	18.8	9.5
p_T Fits:			
CT14-CT10	4.3	20.3	11.8
MMHT-CT10	8.5	19.8	11.1
m_T Fits:			
CT14-CT10	1.5	22.2	9.2
MMHT-CT10	7.6	21.9	8.6

Table 8.10: Combined fit results for different PDF sets in comparison to the nominal CT10-PDF Set, including total uncertainties and pdf-related uncertainties intrinsic to the given PDF set. All uncertainties are given in MeV.

8.5.4 Stability of m_W measurement with different fitting ranges

The stability of the m_W for different fitting ranges has been also studied, by changing the upper and lower fit-ranges of p_T^ℓ and m_T by up to 5 GeV in steps of 1 GeV. The extreme cases are therefore

- p_T^ℓ -fit ranges (nominal 30 – 50 GeV): 30 – 45 GeV...35 – 50 GeV
- m_T -fit ranges (nominal 65 – 100 GeV): 65 – 90 GeV...70 – 100 GeV

To compare the results obtained from different fitting ranges, the uncertainty on the difference needs to be evaluated. This is done by calculating, for each source of uncertainty, the quadratic difference between the two results for the statistical, polarisation and multi-jet shape and the linear difference for all other sources, and then summing quadratically over all sources:

$$\delta(m_W^i - m_W^j) = \left(\sum_k \left[(\delta m_W^{i,k})^2 - (\delta m_W^{j,k})^2 \right] + \sum_l \left[(\delta m_W^{i,l}) - (\delta m_W^{j,l}) \right]^2 \right)^{1/2} \quad (8.21)$$

where i, j label fit ranges, k the uncertainty sources for statistical, polarisation and multi-jet shape, and l the other uncertainty sources.

It should be noted, that highly asymmetric fitting ranges, e.g. $30-45$ GeV in p_T^ℓ , are unnatural, as they potentially enhance effects which would otherwise affect symmetrically the Jacobian peak of the distributions.

The full scan of the fitting ranges is shown in Appendix ?? on Figures ?? – ?. For all the fitting ranges the fully combined measurement result is within $\approx 1.6\sigma$ with respect to the nominal value. The dominating source of uncertainty is from the p_T^W which is becoming smaller when reducing the p_T^ℓ range as can be observed on the left plot of Figure 8.24.

The smallest value of the total uncertainty for the symmetric ranges is found to be ≈ 18.6 MeV for p_T^ℓ range $[34, 45]$ for all m_T ranges. The fully combined measurement for the p_T^ℓ range $[34, 45]$ and m_T range $[66, 99]$ is giving -9.8 ± 18.6 MeV with $\chi^2/NDF = 28.1/27$, while for the nominal fit-range we measure 0.6 ± 20.8 MeV with $\chi^2/NDF = 30.5/27$. The optimal fitting range (p_T^ℓ range $[34, 45]$ and m_T range $[66, 99]$) is chosen as a reference for comparing the differences between the different fitting ranges.

8.5.4.1 Muon Channel

The resulting m_W values for the different fitting ranges of p_T^ℓ and m_T are shown in Figure 8.19 for the muon decay channel. The statistical and systematic uncertainties are only partly correlated between the different fitting ranges, hence we expected a certain variation of the resulting m_W results. In order to judge, if these variations are consistent within the uncertainties, we illustrated the uncorrelated statistical uncertainties for each measurement range in green and the total uncorrelated uncertainty in blue always in comparison to the optimal fit range; the latter has therefore no indicated uncertainties. For each source we take the quadratic or linear difference of the errors for the two cut points (i.e. ranges) and then sum quadratically all uncertainty contributions. The observed variations in muon channel are fully covered by the assigned uncertainties.

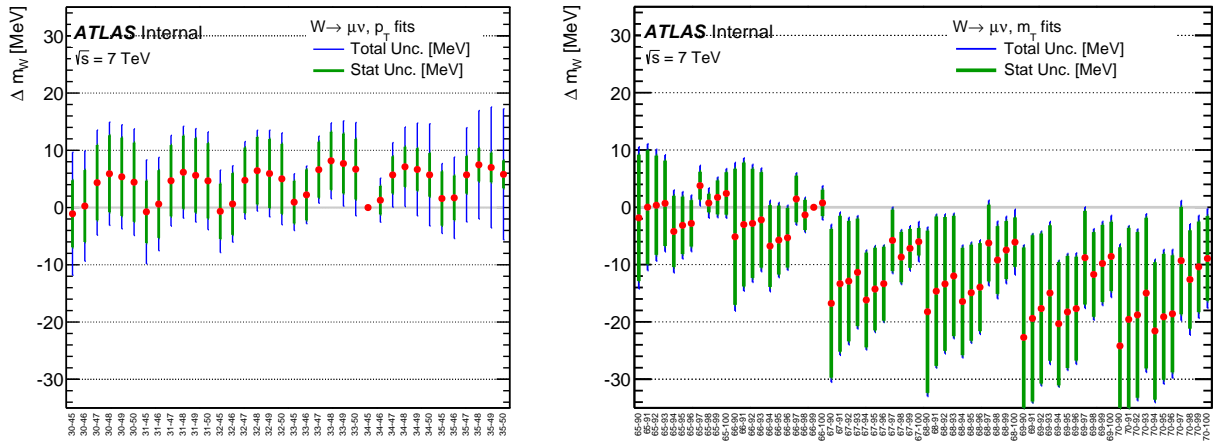


Figure 8.19: Fit results for different fitting ranges using the p_T^ℓ distribution (left) and m_T distribution (right) in the muon channel. The uncorrelated statistical uncertainties are indicated in green, the total uncorrelated uncertainties between the different fitting ranges are shown as blue line. As reference, the nominal fitting range is chosen.

The dependence on the individual uncertainties for the different fitting ranges is shown in Figure 8.20, where the largest variation is due to the statistical uncertainties for the m_T fits, while for the p_T^ℓ fit results the biggest contribution is coming from p_T^W uncertainty.

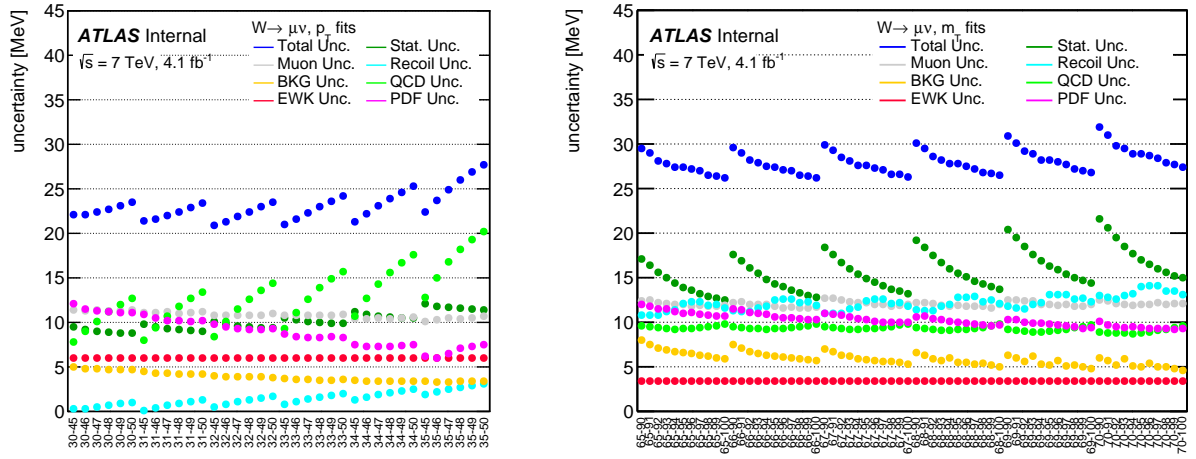


Figure 8.20: Dependence of the statistical and systematic uncertainties on the fitting ranges in the p_T^ℓ distribution (left) and m_T distribution (right) in the muon channel.

8.5.4.2 Electron Channel

Similar to the muon channel, the resulting m_W values for the different fitting ranges of p_T^ℓ and m_T are shown in Figure 8.21 for the electron decay channel. Again, the uncertainties are indicated. The associated dependence of the uncertainties is shown in Figure 8.22.

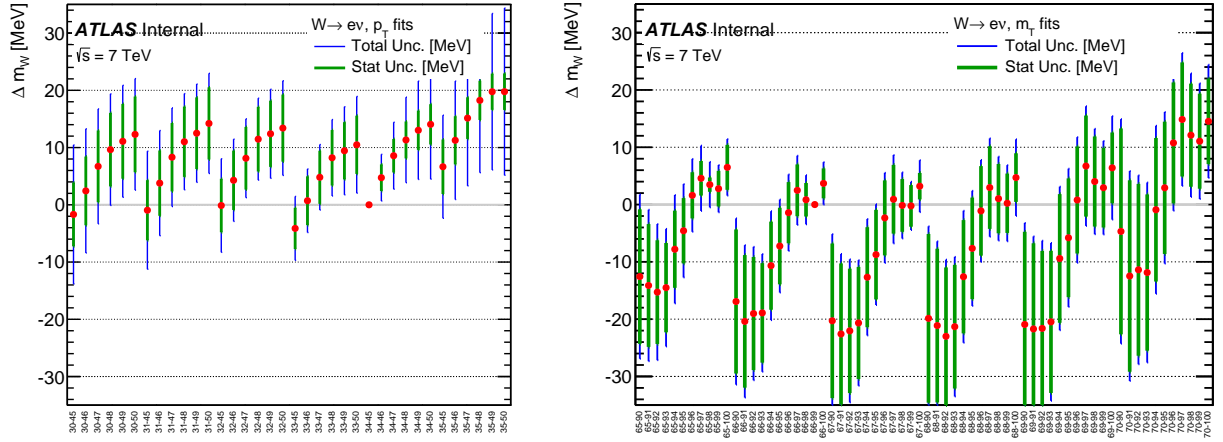


Figure 8.21: Fit results for different fitting ranges using the p_T^ℓ distribution (left) and m_T distribution (right) in the electron channel. The uncorrelated statistical uncertainties are indicated in green, the total uncorrelated uncertainties between the different fitting ranges are shown as blue line. As reference, the nominal fitting range is chosen.

In contrast to the muon channel, we observe here a significant dependence on the chosen fitting range. Several things have to be noted: First of all, the fit results are stable when we apply a symmetric variation of the fitting range, i.e. going from $[30, 50]$ to e.g. $[32, 48]$. This scenario seems to be the most relevant one, as potential resolution effects are expected to similarly impact both sides of the p_T distribution. In addition, this scenarios always keep the peak position and therefore the most sensitive area in the center of the fitting range. In addition, we observe that the fit stability is also within expected uncertainties when raising the lower bound of the fitting range by up to 5 GeV. Therefore, the only remaining effect comes from the decrease of the upper

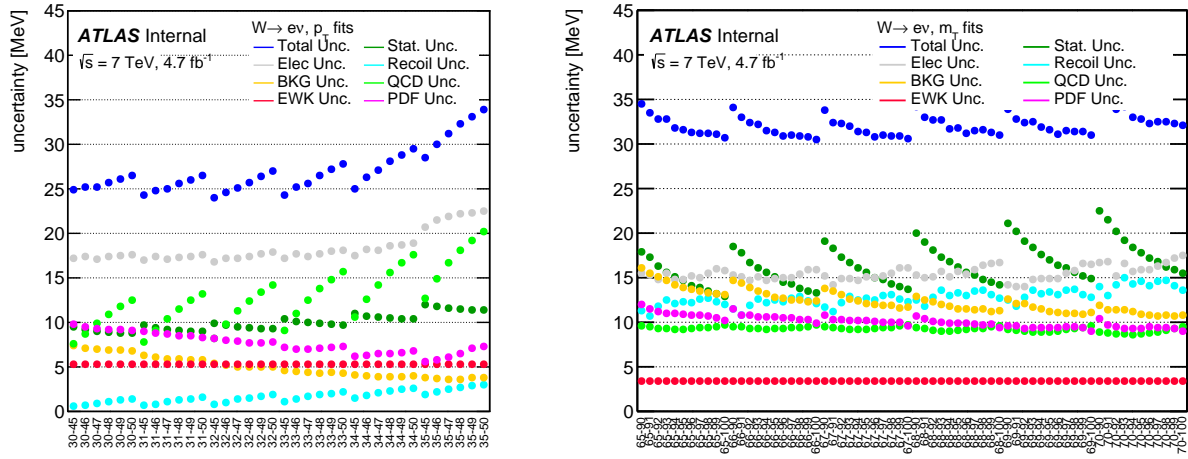


Figure 8.22: Dependence of the statistical and systematic uncertainties on the fitting ranges in the p_T^ℓ distribution (left) and m_T distribution (right) in the electron channel.

fitting range, leading to an $\approx 1.6\sigma$ tension of the most extreme fitting ranges $[30 - 45 \text{ GeV}]$ and $[60 - 90 \text{ GeV}]$.

8.5.4.3 Combined fitting range scans

The results for the fitting range scans with the fully combined measurement is shown on Figures 8.23 and Figures 8.24 when only p_T^ℓ range and m_T range is varied. The dominating source of uncertainty is from the p_T^ℓ which is becoming smaller when reducing the p_T^ℓ range as can be observed on the left plot of Figure 8.24.

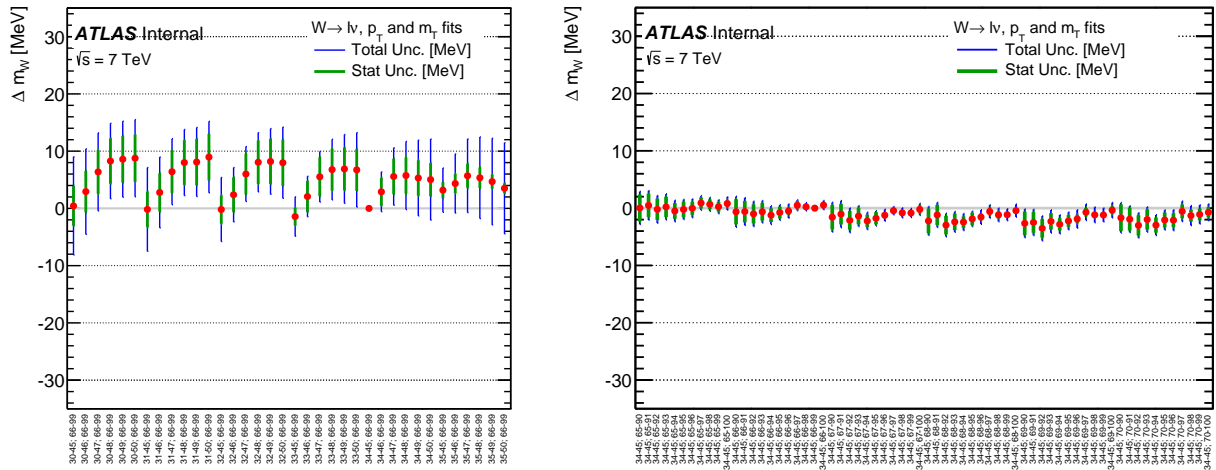


Figure 8.23: Fit results for different fitting ranges when only p_T^ℓ range (left) and m_T range (right) is varied for the combination. The uncorrelated statistical uncertainties are indicated in green, the total uncorrelated uncertainties between the different fitting ranges are shown as blue line. As reference, the nominal fitting range is chosen.

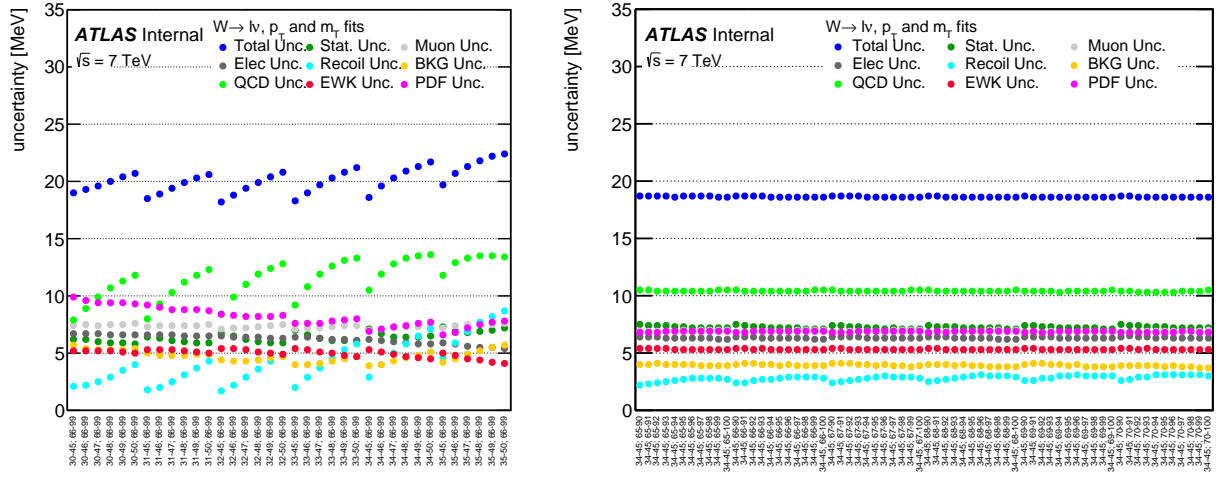


Figure 8.24: Dependence of the statistical and systematic uncertainties on the fitting ranges for the combination when only p_T^l range (left) and when only m_T range is varied (right).

8.5.5 Results with optimal fitting range

In this section combined fit results with optimal fitting range are shown, several combinations are illustrated in Figures 8.25, 8.26, 8.27, 8.28, 8.29, 8.30 and 8.31. The optimal fitting range in which the total uncertainty is minimized is found to be 32 – 45 GeV for p_T^ℓ and 66 – 99 GeV for m_T^W . The extracted m_W values with corresponding uncertainties in different measurement categories are summarized in Table 8.11. In summary, we measure the mass of the W boson to be:

$$\begin{aligned} m_W &= 80399 - 10.0 + b \pm 6.7 \text{ MeV}(\text{stat.}) \pm 10.7 \text{ MeV}(\text{exp.sys.}) \pm 13.6 \text{ MeV}(\text{mod.sys.}) \\ &= 80399 - 10.0 + b \pm 18.6 \text{ MeV}, \end{aligned}$$

where the unblinding parameter $b = [-100, 100] \text{ MeV}$. The indicated uncertainties correspond to statistical, experimental systematic and physics-modelling systematic components. The PDF envelope uncertainty from Table 8.10 is also taken into account.

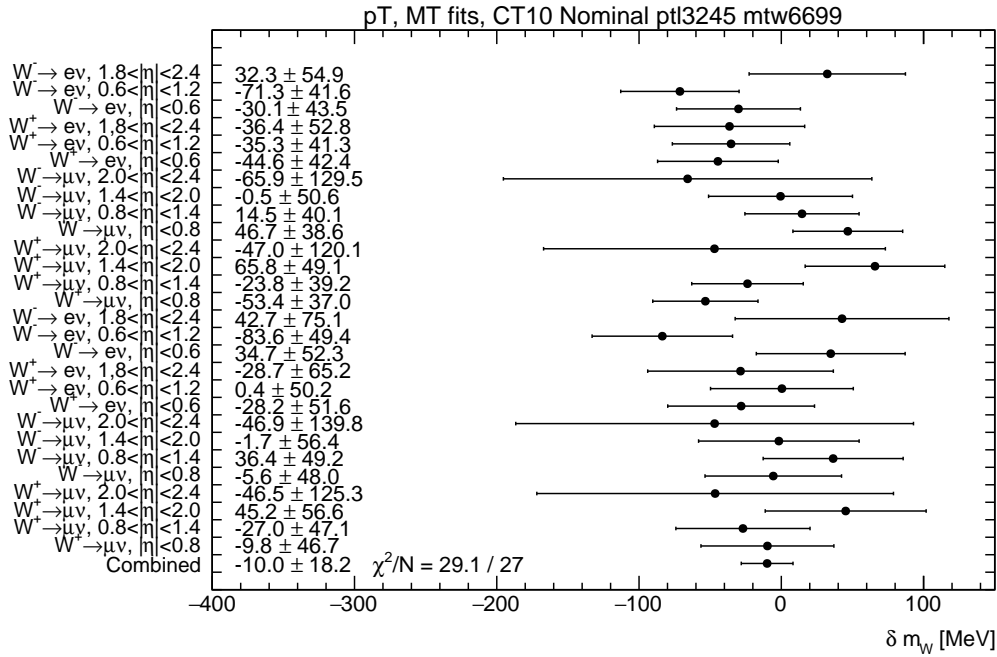


Figure 8.25: Combination of all p_T^ℓ fit results (upper half) and m_T fit results (lower half) in all channels and categories using the CT10 PDF set with the optimal fitting range. The full uncertainties of each individual fit are indicated. The result is given as a shift with respect to the assumed value of m_W in the MC, plus an unknown offset.

8.5.6 Additional Cross-Checks

Several additional cross-checks have been performed to validate the m_W fits, in particular testing its stability for different selections, different fit observables and fitting ranges.

- **Fits of m_W using Missing Transverse Energy.** Even though the final combination of m_W depends only of the fits of p_T^ℓ and m_T , the consistency of the m_W -fit was tested using the observed E_T^{miss} distributions. The results are shown in Figure 8.32 and in Table ?? for the electron and muon channel, where only statistical uncertainties are shown, the correction of the multijet shape is taken into account. A good consistency is observed.
- **Dependence on Pile-Up.** In order to test the fit stability for different pile-up conditions, the signal selection was separated in three independent $\langle \mu \rangle$ categories, i.e. $[2.5 - 6.5]$,

Channel m_T -Fit	Value [MeV]	Stat. Unc.	Muon Calib.	Elec. Calib.	Recoil Calib.	Back- grd.	QCD	EWK	PDF's	Total Unc.
$W^+ \rightarrow \mu\nu, \eta < 0.8$	-9.8	29.2	12.7	0.0	14.6	7.5	9.9	3.4	28.1	46.7
$W^+ \rightarrow \mu\nu, 0.8 < \eta < 1.4$	-27.0	32.1	19.4	0.0	12.3	6.1	9.6	3.4	22.9	47.1
$W^+ \rightarrow \mu\nu, 1.4 < \eta < 2.0$	45.2	30.2	35.2	0.0	13.7	6.5	9.3	3.4	26.9	56.6
$W^+ \rightarrow \mu\nu, 2.0 < \eta < 2.4$	-46.5	40.9	112.4	0.0	13.8	8.4	8.4	3.4	32.5	125.3
$W^- \rightarrow \mu\nu, \eta < 0.8$	-5.6	30.6	11.7	0.0	12.4	7.4	9.5	3.4	30.3	48.0
$W^- \rightarrow \mu\nu, 0.8 < \eta < 1.4$	36.4	36.4	18.5	0.0	11.5	6.5	9.7	3.4	21.8	49.2
$W^- \rightarrow \mu\nu, 1.4 < \eta < 2.0$	-1.7	35.6	33.9	0.0	9.6	6.9	9.7	3.4	22.7	56.4
$W^- \rightarrow \mu\nu, 2.0 < \eta < 2.4$	-46.9	52.4	123.8	0.0	10.8	9.3	9.9	3.4	33.8	139.8
$W^+ \rightarrow e\nu, \eta < 0.6$	-28.2	29.4	0.0	22.7	12.4	14.9	9.9	3.4	28.2	51.6
$W^+ \rightarrow e\nu, 0.6 < \eta < 1.2$	0.4	30.4	0.0	24.2	14.5	12.7	9.6	3.4	23.1	50.2
$W^+ \rightarrow e\nu, 1.8 < \eta < 2.4$	-28.7	32.4	0.0	32.9	15.9	32.6	8.4	3.4	27.0	65.2
$W^- \rightarrow e\nu, \eta < 0.6$	34.7	31.3	0.0	19.1	11.0	14.3	9.5	3.4	31.0	52.3
$W^- \rightarrow e\nu, 0.6 < \eta < 1.2$	-83.6	33.0	0.0	21.3	10.3	11.4	9.7	3.4	23.5	49.4
$W^- \rightarrow e\nu, 1.8 < \eta < 2.4$	42.7	42.8	0.0	39.8	12.1	34.6	9.9	3.4	27.8	75.1
p_T -Fit										
$W^+ \rightarrow \mu\nu, \eta < 0.8$	-53.4	22.1	12.3	0.0	0.8	4.8	9.0	6.0	24.3	37.0
$W^+ \rightarrow \mu\nu, 0.8 < \eta < 1.4$	-23.8	25.1	19.0	0.0	0.5	4.3	8.9	6.0	20.2	39.2
$W^+ \rightarrow \mu\nu, 1.4 < \eta < 2.0$	65.8	23.9	33.2	0.0	0.6	4.5	8.2	6.0	24.8	49.1
$W^+ \rightarrow \mu\nu, 2.0 < \eta < 2.4$	-47.0	34.5	110.1	0.0	0.3	6.1	6.7	6.0	31.5	120.1
$W^- \rightarrow \mu\nu, \eta < 0.8$	46.7	23.3	11.8	0.0	0.8	4.8	8.1	6.0	26.1	38.6
$W^- \rightarrow \mu\nu, 0.8 < \eta < 1.4$	14.5	27.9	18.4	0.0	0.2	4.6	8.0	6.0	19.3	40.1
$W^- \rightarrow \mu\nu, 1.4 < \eta < 2.0$	-0.5	28.1	35.2	0.0	0.9	4.6	8.0	6.0	20.2	50.6
$W^- \rightarrow \mu\nu, 2.0 < \eta < 2.4$	-65.9	45.5	116.2	0.0	0.9	6.8	8.3	6.0	32.4	129.5
$W^+ \rightarrow e\nu, \eta < 0.6$	-44.6	22.2	0.0	24.0	0.5	5.9	9.0	5.3	24.2	42.4
$W^+ \rightarrow e\nu, 0.6 < \eta < 1.2$	-35.3	22.8	0.0	25.2	0.9	6.3	8.9	5.3	20.1	41.3
$W^+ \rightarrow e\nu, 1.8 < \eta < 2.4$	-36.4	24.0	0.0	38.0	1.0	11.7	6.7	5.3	23.7	52.8
$W^- \rightarrow e\nu, \eta < 0.6$	-30.1	23.1	0.0	23.3	0.9	5.8	8.1	5.3	26.3	43.5
$W^- \rightarrow e\nu, 0.6 < \eta < 1.2$	-71.3	24.9	0.0	23.7	1.1	6.0	8.0	5.3	20.5	41.6
$W^- \rightarrow e\nu, 1.8 < \eta < 2.4$	32.3	30.1	0.0	37.4	1.1	10.7	8.3	5.3	22.3	54.9
Combined	-10.0	6.7	7.1	6.5	1.7	4.4	8.4	5.4	8.4	18.2

Table 8.11: Fitted mass values v , given by $m_W = 80399 + b \pm v$ MeV, where b is an unknown blinding value for the optimal fitting range. The m_W fit is performed in the electron and muon decay channel, in different η lepton categories using the p_T and m_T observables (optimal fitting range). In addition to the statistical uncertainties, all experimental uncertainties, i.e. the muon, the electron and the hadronic recoil calibration uncertainties as well as the background related uncertainties on m_W are given. Also the model uncertainties, due to EWK corrections, QCD corrections (scales, PS, A_i coefficient modeling) and PDFs are given. All uncertainties are given in MeV.

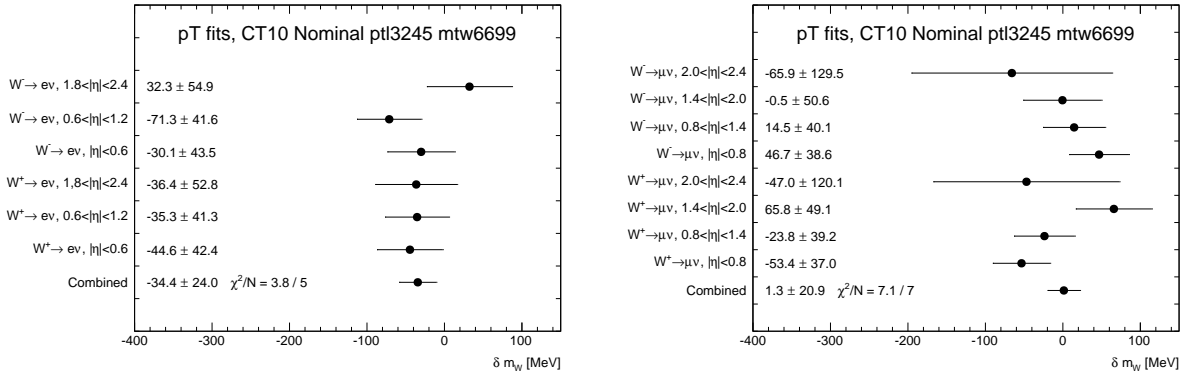


Figure 8.26: Combination of all p_T fit results in electron (left) and muon (right) channels with the optimal fitting range. The result is given as a shift with respect to the assumed value of m_W in the MC, plus an unknown offset.

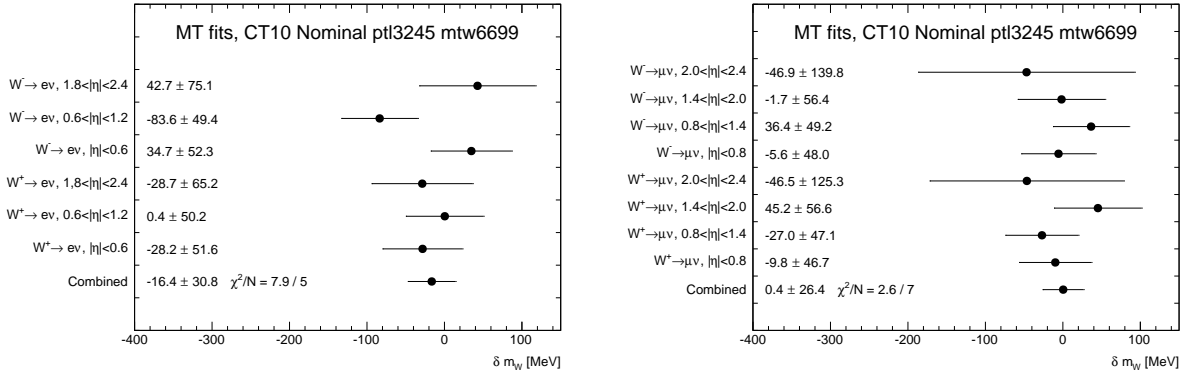


Figure 8.27: Combination of all m_T fit results in electron (left) and muon (right) channels with the optimal fitting range. The result is given as a shift with respect to the assumed value of m_W in the MC, plus an unknown offset.

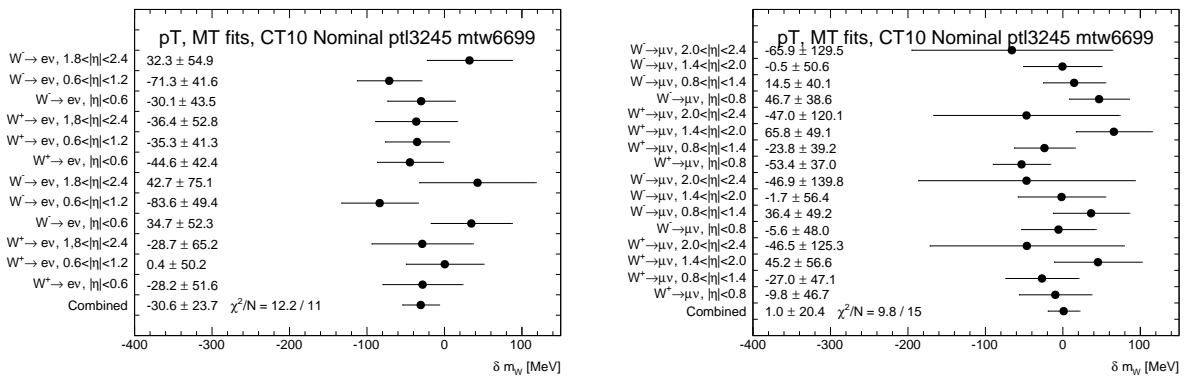


Figure 8.28: Combination of all fit results in electron (left) and muon (right) channels with the optimal fitting range. The result is given as a shift with respect to the assumed value of m_W in the MC, plus an unknown offset.

[6.5 – 9.5] and [9.5 – 16], and performed m_W fits using the p_T^ℓ and m_T observables. It should be noted that this categorization also tests the stability of m_W vs. time, as the pileup

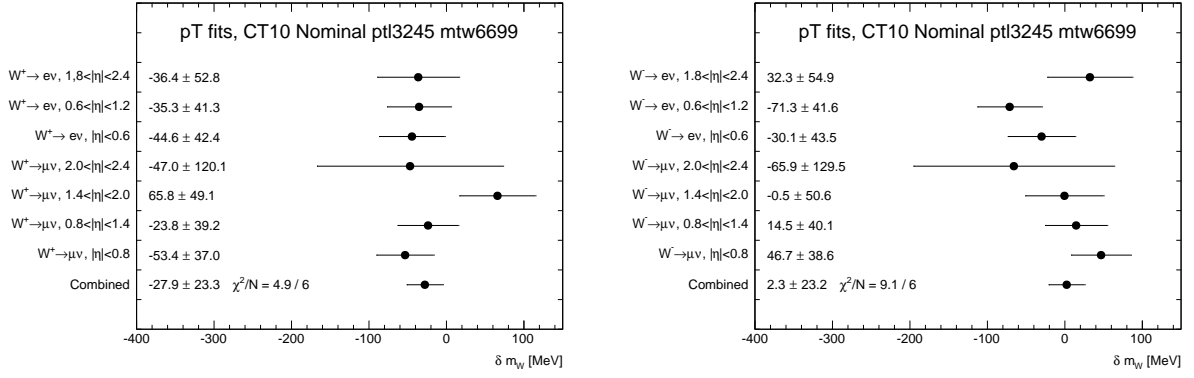


Figure 8.29: Combination of all p_T fit results in electron and muon channels for W^+ (left) and W^- (right) with the optimal fitting range. The result is given as a shift with respect to the assumed value of m_W in the MC, plus an unknown offset.

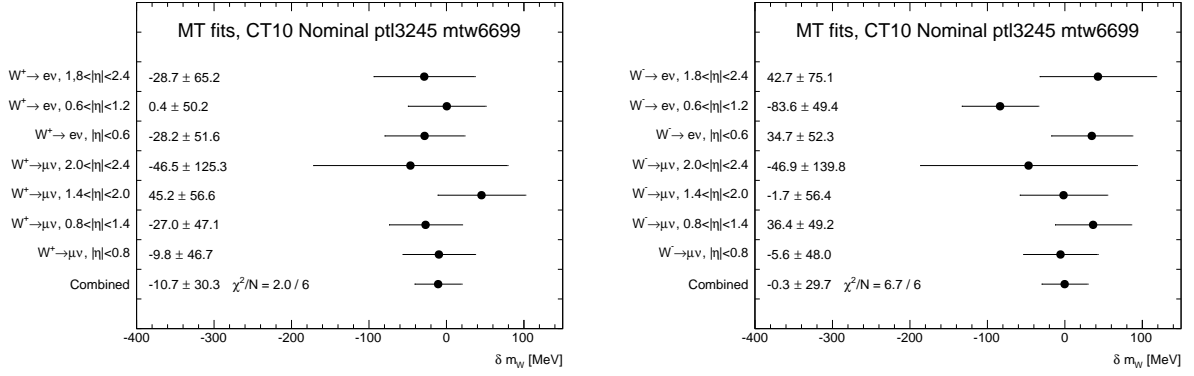


Figure 8.30: Combination of all m_T fit results in electron and muon channels for W^+ (left) and W^- (right) with the optimal fitting range. The result is given as a shift with respect to the assumed value of m_W in the MC, plus an unknown offset.

conditions change during the year due to the increasing LHC performance. The results are shown in Figure 8.33 for the electron and muon channel, where only statistical uncertainties are shown. A good consistency is observed.

- **Dependence on measured hadronic recoil.** In order to test the experimental modeling of the hadronic recoil response as well as the modeling of the $p_T(W)$, we performed also m_W fits in two bins of the hadronic recoil ($0 < u < 15$ GeV and $15 < u < 30$ GeV), as well as in two regions of $u_{||}$ ($0 < u_{||}$ and $u_{||} < 0$), i.e. the parallel component of the measured recoil projected on the decay lepton. The results are shown for the electron and muon channel in Figure 8.34 and 8.35 where only statistical uncertainties are shown.
- **Removed E_T^{miss} cut from W selection.** The systematic uncertainties associated to the recoil calibration on the p_T^ℓ -based m_W -fits are significantly reduced when no cut on E_T^{miss} is performed. Thus, the stability of the m_W fits for a signal selection without a requirement on E_T^{miss} is also performed (see Table 8.12).

The consistency tests for the m_W measurement are summarized in Table 8.12 for the η -inclusive measurements using p_T^ℓ and m_T -fits in the electron and muon decay channel. Only statistical uncertainties are shown. A very good agreement between all performed measurements is observed.

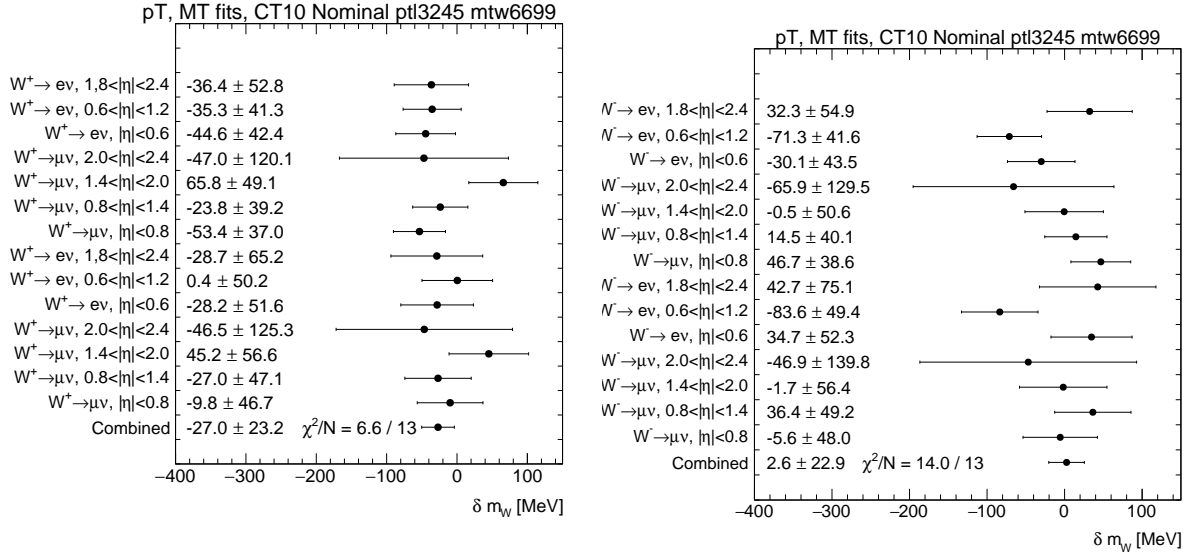


Figure 8.31: Combination of all fit results in electron and muon channels for W^+ (left) and W^- (right) with the optimal fitting range. The result is given as a shift with respect to the assumed value of m_W in the MC, plus an unknown offset.

Measurement Category	$W \rightarrow e\nu$ p_T^ℓ -Fit	$W \rightarrow e\nu$ m_T -Fit	$W \rightarrow e\nu$ E_T^{miss} -Fit	$W \rightarrow \mu\nu$ p_T^ℓ -Fit	$W \rightarrow \mu\nu$ m_T -Fit	$W \rightarrow \mu\nu$ E_T^{miss} -Fit
nominal	-27 ± 9	-28 ± 13	-44 ± 26	3 ± 8	-14 ± 12	-41 ± 23
no E_T^{miss} -cut	-13 ± 9	-29 ± 13	-44 ± 26	13 ± 8	-20 ± 12	-41 ± 23
$0 < p_T(W) < 15 \text{ GeV}$	-27 ± 11	-36 ± 13	-52 ± 20	8 ± 10	-6 ± 12	-34 ± 17
$15 < p_T(W) < 30 \text{ GeV}$	-17 ± 15	-28 ± 24	-35 ± 62	-1 ± 14	-32 ± 22	32 ± 56
$u_{ } < 0 \text{ GeV}$	-19 ± 15	-8 ± 17	-31 ± 23	6 ± 13	-13 ± 16	-43 ± 20
$u_{ } > 0 \text{ GeV}$	-36 ± 10	-27 ± 14	-37 ± 21	-9 ± 10	-4 ± 13	7 ± 19
$\langle \mu \rangle$ in $[2.5, 6.5]$	-19 ± 14	-14 ± 18	-27 ± 35	-19 ± 12	-14 ± 16	-23 ± 28
$\langle \mu \rangle$ in $[6.5, 9.5]$	-33 ± 16	-22 ± 23	-43 ± 49	15 ± 15	-22 ± 22	-45 ± 45
$\langle \mu \rangle$ in $[9.5, 16]$	-28 ± 16	-25 ± 27	-90 ± 60	28 ± 16	21 ± 26	-16 ± 60

Table 8.12: Summary of consistency tests of m_W -fits in several measurement categories. The blinded fit results (in MeV) for the p_T^ℓ and m_T -based fits in the electron and muon decay channel is given. Uncertainties are statistical only. The result is given as a shift with respect to the assumed value of m_W in the MC, plus an unknown offset.

8.6 Unblinding

Since a very good compatibility between the electron and muon channels, as well as W^+ and W^- for the two observables in the different η and $\langle \mu \rangle$ categories is observed for blinded W boson mass, validating the experimental calibration procedure and physics modeling, the analysis can be unblinded. The random off-set parameter is found to be

$$b = -17.9 \text{ MeV}, \quad (8.22)$$

leading to the final results:

$$\begin{aligned} m_W &= 80371.1 \pm 6.7 \text{ MeV}(\text{stat.}) \pm 10.7 \text{ MeV}(\text{exp.sys.}) \pm 13.6 \text{ MeV}(\text{mod.sys.}) \\ &= 80371.1 \pm 18.6 \text{ MeV}, \end{aligned}$$

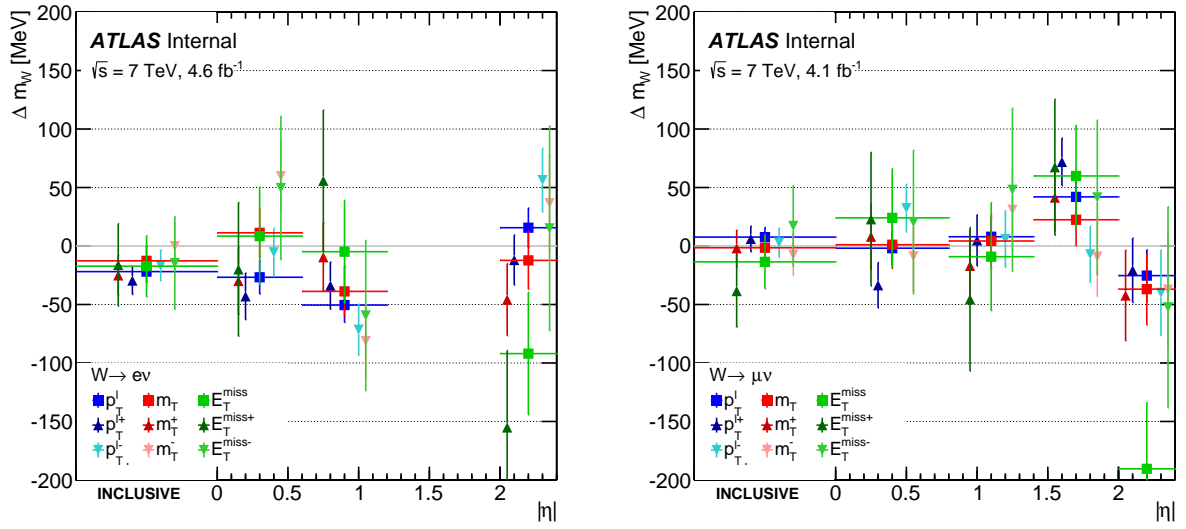


Figure 8.32: Fit results using p_T^ℓ , m_T and E_T^{miss} for the electron channel (left) and the muon channel (right) for different η regions.

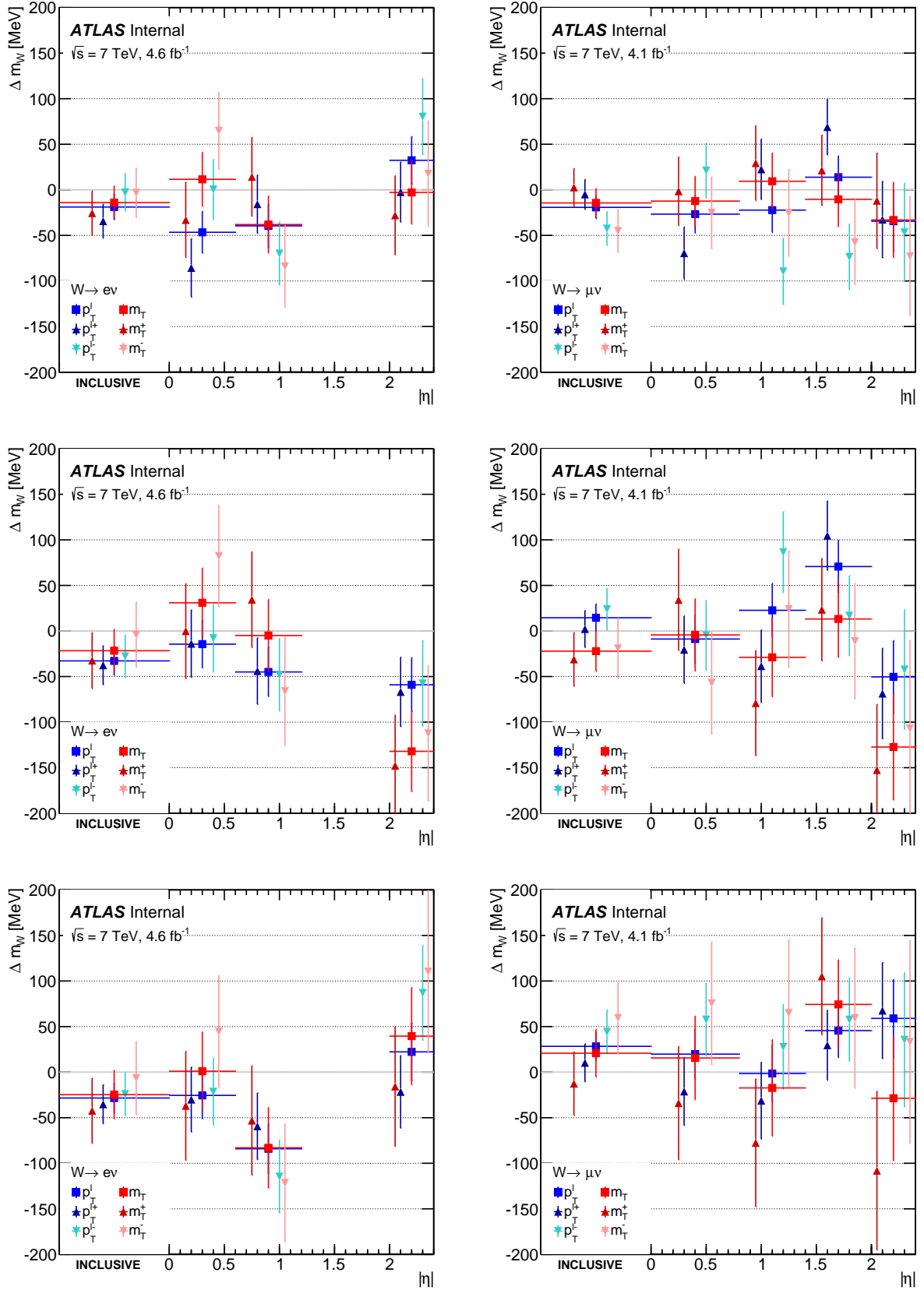


Figure 8.33: Fit results using p_T^ℓ and m_T for the electron channel (left) and the muon channel (right) for different regions in $\langle \mu \rangle$ (upper-row: 2.5-6.5, middle-row: 6.5-9.5, lower row: 9.5-16).

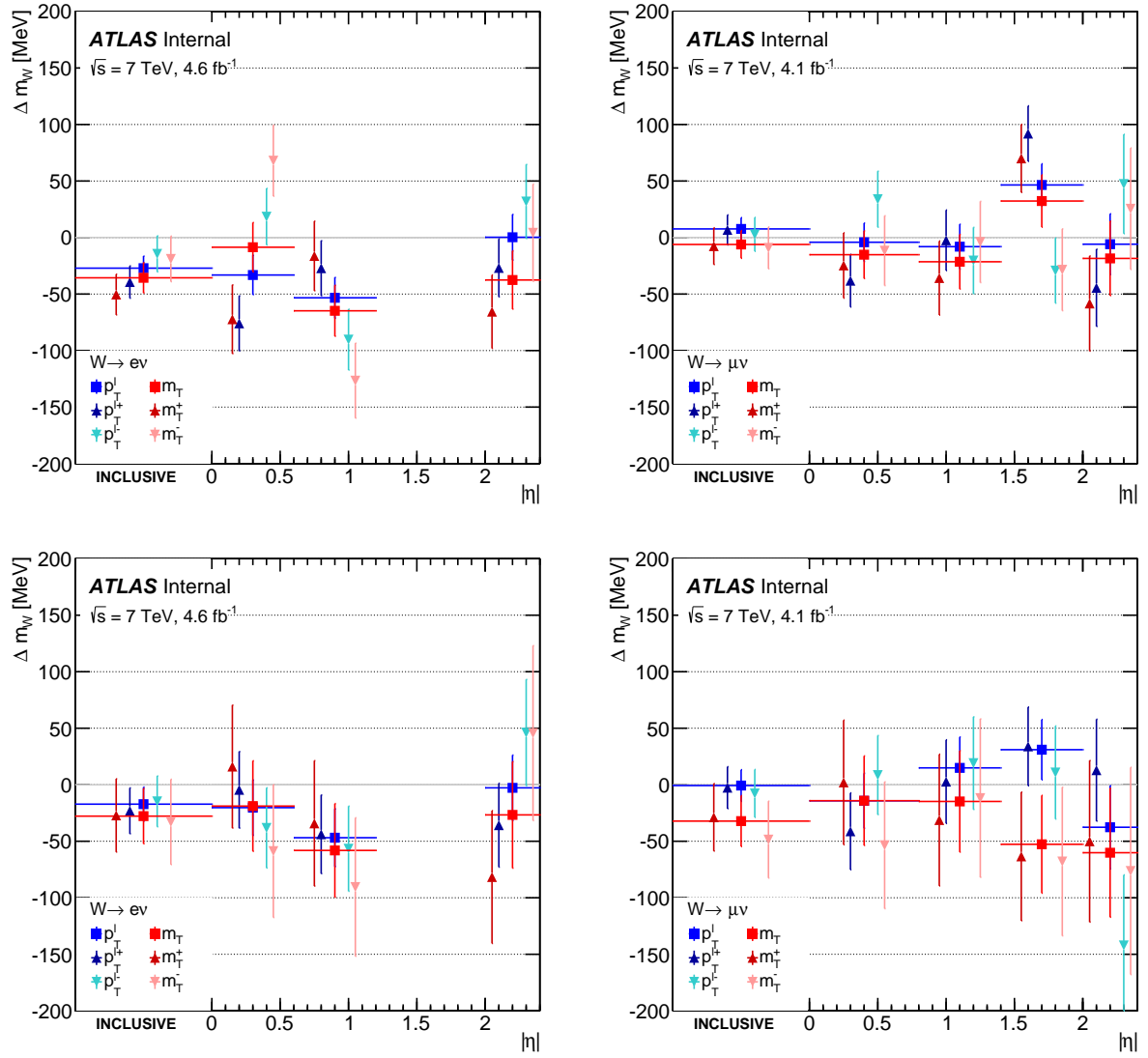


Figure 8.34: Fit results using p_T^ℓ and m_T or the electron channel (left) and the muon channel (right) for events with $0 < u < 15$ GeV (upper row) and $15 < u < 30$ GeV (lower row)

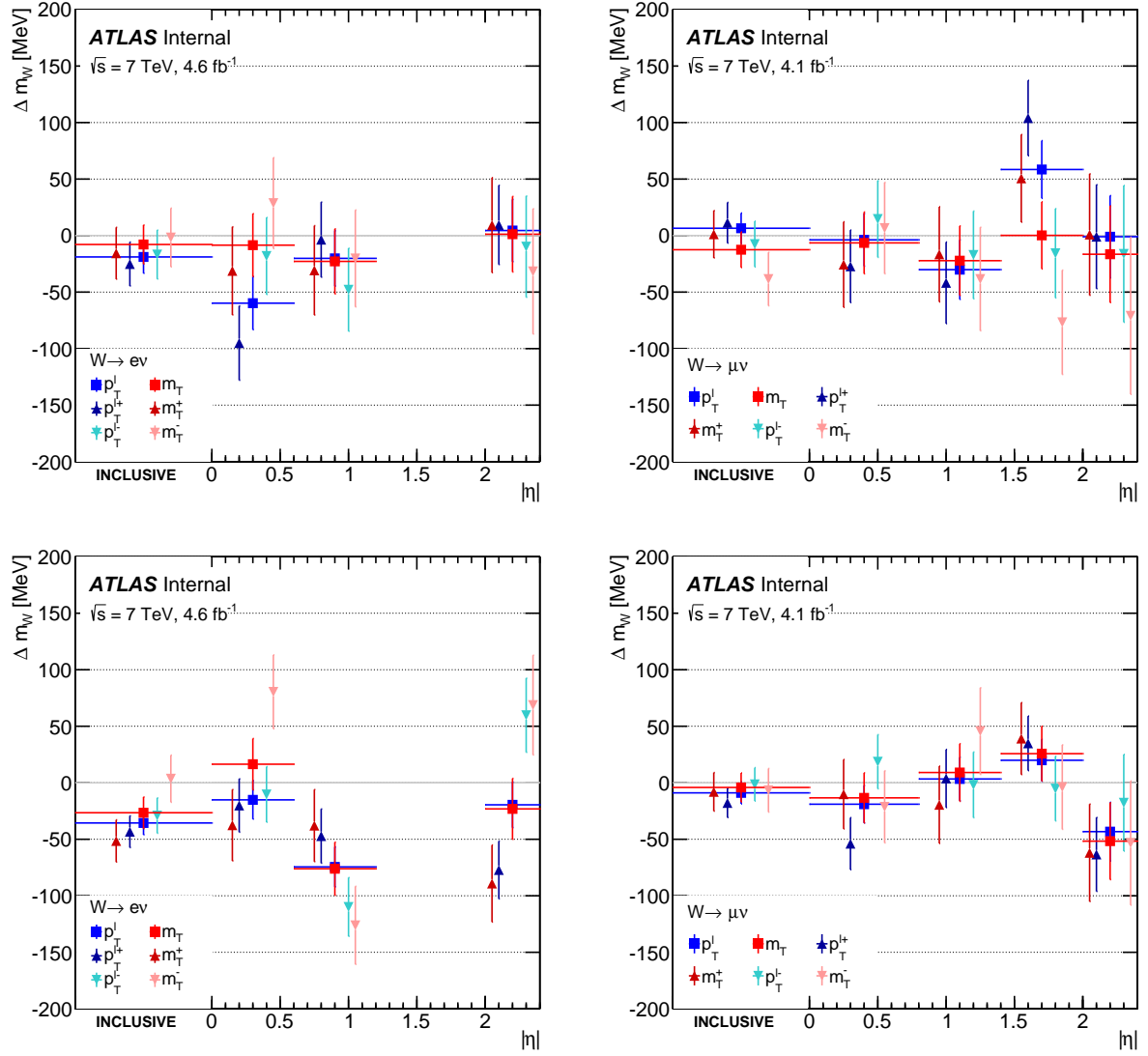


Figure 8.35: Fit results using p_T^ℓ and m_T for the electron channel (left) and the muon channel (right) for events with $u_{||} < 0$ (upper row) and $0 < u_{||}$ (lower row).

Summary and conclusions

This thesis describes the W boson mass measurement with the ATLAS detector based on the 2011 data-set recorded by ATLAS at a centre-of-mass energy of $\sqrt{s} = 7$ TeV, and corresponding to 4.6 fb^{-1} of integrated luminosity. Measurements are performed through template fits to transverse momentum distributions of charged leptons as well as to transverse mass distributions of the W boson in electron and muon decay modes in various kinematic categories. Measurement through the template fit to missing energy distribution was also performed for the cross-check. The precise detector calibration relies on the study of Z boson events, leading to precise modelling of the electron, muon and hadronic recoil. Simulated samples of the W -boson signal relies on the NLO MC generator POWHEG, interfaced to PYTHIA8 for the parton shower. The signal samples are supplemented with several additional physics modeling corrections which allows for the inclusion of higher-order QCD and electroweak corrections, and for improvements of the modelling of the lepton kinematic distributions. The physics modeling and the detector calibrations were cross-checked on the W -like fits of the Z boson mass. All the individual measurements are found to be consistent and their combination after unblinding leads to a value of

$$\begin{aligned} m_W &= 80371.1 \pm 6.7 \text{ MeV}(\text{stat.}) \pm 10.7 \text{ MeV}(\text{exp.sys.}) \pm 13.6 \text{ MeV}(\text{mod.sys.}) \\ &= 80371.1 \pm 18.6 \text{ MeV}, \end{aligned}$$

This result corresponds to the m_W extraction in the optimal fitting range ($34 - 45 \text{ GeV}$ for p_T^ℓ and $66 - 99 \text{ GeV}$ for m_T).

The measured value of the W boson mass is compatible to the current world average of $m_W = 80385 \pm 15 \text{ MeV}$. The uncertainty is competitive to the current most precise measurements performed by the CDF and D0 collaborations. An overview of the different experimental m_W measurements, including the prediction of the global electroweak fit, is shown in Figure 8.36. The measured value is consistent with the SM expectation of $m_W = 80358 \pm 8 \text{ MeV}$ obtained from the electroweak fit as illustrated in Figures 8.37 and 8.38. Further improvements of m_W measurement are expected after inclusion of the PDF profiling described in Appendix B.

In addition, the results are presented on the study of the EM calorimeter performance. In particular, a method was developed and implemented for estimation of the cross-talk in the EM calorimeter using its response to muons. Also the calorimeter misalignment and deformations were spotted, which are also visible in the m_W analysis. These were corrected using effective approach. However, further work is required in order to obtain and implement the correction from first principles.

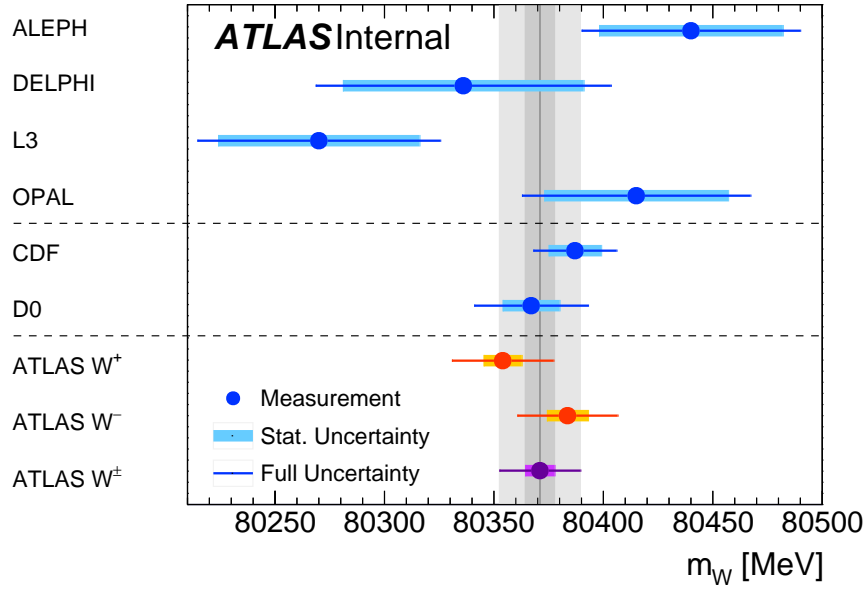


Figure 8.36: Comparison of the results of this analysis (violet dot) with other published results for m_W . This includes the most precise measurements from LEP including ALEPH, DELPHI, L3 and OPAL and from the Tevatron collider experiments D0, and CDF. The light and dark grey bands show the statistical and total uncertainties of the ATLAS measurement, the blue bands and blue lines show the statistical and total uncertainties of the other published results. Measured values of m_W for positively- and negatively-charged W bosons are also shown (red dots).

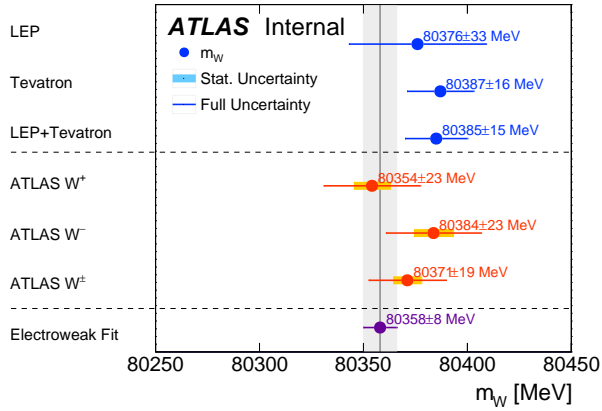


Figure 8.37: The measured values of m_W (red dots) are compared to the SM prediction from the electroweak fit (violet dot), and to the combined values of m_W measured at LEP and at the Tevatron collider (blue dots). The light grey band shows the uncertainty of the SM prediction from the electroweak fit, assuming $m_t = 173.34 \pm 0.76$ GeV and $m_H = 125.09 \pm 0.24$ GeV.

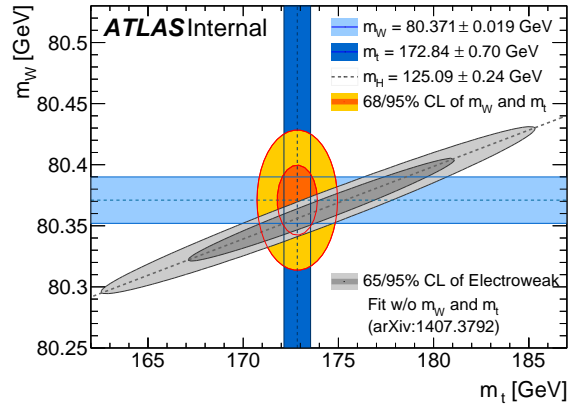


Figure 8.38: The 68% and 95% confidence level contours of the m_W and m_t indirect determination from the global electroweak fit [12] (grey ellipses) are compared to the 68% and 95% confidence level contours of the ATLAS measurements of the top-quark and W boson masses (red and orange ellipses). The determination from the electroweak fit uses as input the LHC measurement of the Higgs boson mass, $m_H = 125.09 \pm 0.24$ GeV. The light and dark blue bands indicate the uncertainties on the ATLAS measurements of m_W and m_t .

Bibliography

- [1] C. N. Yang and R. L. Mills, *Conservation of Isotopic Spin and Isotopic Gauge Invariance*, Phys. Rev. **96** (Oct, 1954) 191–195. <http://link.aps.org/doi/10.1103/PhysRev.96.191>.
- [2] S. L. Glashow, *Partial Symmetries of Weak Interactions*, Nucl. Phys. **22** (1961) 579–588.
- [3] S. Weinberg, *A Model of Leptons*, Phys. Rev. Lett. **19** (1967) 1264–1266.
- [4] A. Salam, *Weak and Electromagnetic Interactions*, Conf. Proc. **C680519** (1968) 367–377.
- [5] G. Arnison et al., *Experimental observation of isolated large transverse energy electrons with associated missing energy at $s=540$ GeV*, Physics Letters B **122** (1983) no. 1, 103 – 116. <http://www.sciencedirect.com/science/article/pii/0370269383911772>.
- [6] P. Bagnaia et al., *Evidence for $Z_0 \rightarrow e^+e^-$ at the CERN pp collider*, Physics Letters B **129** (1983) no. 1, 130 – 140. <http://www.sciencedirect.com/science/article/pii/037026938390744X>.
- [7] ATLAS Collaboration, G. Aad et al., *Observation of a new particle in the search for the Standard Model Higgs boson with the ATLAS detector at the LHC*, Phys. Lett. **B716** (2012) 1–29, [arXiv:1207.7214](https://arxiv.org/abs/1207.7214) [hep-ex].
- [8] CMS Collaboration, S. Chatrchyan et al., *Observation of a new boson at a mass of 125 GeV with the CMS experiment at the LHC*, Phys. Lett. **B716** (2012) 30–61, [arXiv:1207.7235](https://arxiv.org/abs/1207.7235) [hep-ex].
- [9] C. S. Wu, E. Ambler, R. W. Hayward, D. D. Hoppes, and R. P. Hudson, *Experimental Test of Parity Conservation in Beta Decay*, Phys. Rev. **105** (Feb, 1957) 1413–1415. <http://link.aps.org/doi/10.1103/PhysRev.105.1413>.
- [10] M. Veltman, *Limit on mass differences in the Weinberg model*, Nuclear Physics B **123** (1977) no. 1, 89 – 99. <http://www.sciencedirect.com/science/article/pii/055032137790342X>.
- [11] M. Awramik, M. Czakon, A. Freitas, and G. Weiglein, *Precise prediction for the W boson mass in the standard model*, Phys. Rev. **D69** (2004) 053006, [arXiv:hep-ph/0311148](https://arxiv.org/abs/hep-ph/0311148) [hep-ph].
- [12] Gfitter Group Collaboration, M. Baak, J. Cuth, J. Haller, A. Hoecker, R. Kogler, K. Monig, M. Schott, and J. Stelzer, *The global electroweak fit at NNLO and prospects for the LHC and ILC*, Eur. Phys. J. **C74** (2014) 3046, [arXiv:1407.3792](https://arxiv.org/abs/1407.3792) [hep-ph].
- [13] S. Heinemeyer, *Higgs/Electroweak in the SM and the MSSM*, [arXiv:1301.7197](https://arxiv.org/abs/1301.7197) [hep-ph].
- [14] M. A. Thomson, *Measurement of the W-boson mass at LEP*, . <https://cds.cern.ch/record/504968>.
- [15] The ALEPH, DELPHI, L3, OPAL Collaborations, the LEP Electroweak Working Group, *Electroweak Measurements in Electron-Positron Collisions at W-Boson-Pair Energies at LEP*, Phys. Rept. **532** (2013) 119, [arXiv:1302.3415](https://arxiv.org/abs/1302.3415) [hep-ex].
- [16] CDF, D0 Collaboration, T. A. Aaltonen et al., *Combination of CDF and D0 W-Boson Mass Measurements*, Phys. Rev. **D88** (2013) no. 5, 052018, [arXiv:1307.7627](https://arxiv.org/abs/1307.7627) [hep-ex].

- [17] T. D. H. Project, *Online PDF plotting and calculation*, .
<http://hepdata.cedar.ac.uk/pdf/pdf3.html>.
- [18] J. M. Campbell, J. W. Huston, and W. J. Stirling, *Hard Interactions of Quarks and Gluons: A Primer for LHC Physics*, *Rept. Prog. Phys.* **70** (2007) 89, [arXiv:hep-ph/0611148 \[hep-ph\]](#).
- [19] F. Halzen, Y. S. Jeong, and C. S. Kim, *Charge Asymmetry of Weak Boson Production at the LHC and the Charm Content of the Proton*, *Phys. Rev.* **D88** (2013) 073013, [arXiv:1304.0322 \[hep-ph\]](#).
- [20] W. S. R.K. Ellis and B. Webber, *QCD and collider physics*. Cambridge university press, 2003.
- [21] J. M. Campbell, R. K. Ellis, and D. L. Rainwater, *Next-to-leading order QCD predictions for $W + 2$ jet and $Z + 2$ jet production at the CERN LHC*, *Phys. Rev.* **D68** (2003) 094021, [arXiv:hep-ph/0308195 \[hep-ph\]](#).
- [22] G. A. Ladinsky and C. P. Yuan, *The Nonperturbative regime in QCD resummation for gauge boson production at hadron colliders*, *Phys. Rev.* **D50** (1994) R4239, [arXiv:hep-ph/9311341 \[hep-ph\]](#).
- [23] C. Balazs and C. P. Yuan, *Soft gluon effects on lepton pairs at hadron colliders*, *Phys. Rev.* **D56** (1997) 5558–5583, [arXiv:hep-ph/9704258 \[hep-ph\]](#).
- [24] F. Landry, R. Brock, P. M. Nadolsky, and C. P. Yuan, *Tevatron Run-1 Z boson data and Collins-Soper-Sterman resummation formalism*, *Phys. Rev.* **D67** (2003) 073016, [arXiv:hep-ph/0212159 \[hep-ph\]](#).
- [25] T. Sjostrand, S. Mrenna, and P. Z. Skands, *PYTHIA 6.4 Physics and Manual*, *JHEP* **05** (2006) 026, [arXiv:hep-ph/0603175 \[hep-ph\]](#).
- [26] G. Corcella, I. G. Knowles, G. Marchesini, S. Moretti, K. Odagiri, P. Richardson, M. H. Seymour, and B. R. Webber, *HERWIG 6: An Event generator for hadron emission reactions with interfering gluons (including supersymmetric processes)*, *JHEP* **01** (2001) 010, [arXiv:hep-ph/0011363 \[hep-ph\]](#).
- [27] T. Gleisberg, S. Hoeche, F. Krauss, M. Schonherr, S. Schumann, F. Siegert, and J. Winter, *Event generation with SHERPA 1.1*, *JHEP* **02** (2009) 007, [arXiv:0811.4622 \[hep-ph\]](#).
- [28] P. Z. Skands, *Tuning Monte Carlo Generators: The Perugia Tunes*, *Phys. Rev.* **D82** (2010) 074018, [arXiv:1005.3457 \[hep-ph\]](#).
- [29] *Measurement of the W-boson P_T distribution in $p\bar{p}$ collisions at $\sqrt{s} = 1.8$ TeV*, .
- [30] D0 Collaboration, B. Abbott et al., *Measurement of the shape of the transverse momentum distribution of W bosons produced in $p\bar{p}$ collisions at $\sqrt{s} = 1.8$ TeV*, *Phys. Rev. Lett.* **80** (1998) 5498–5503, [arXiv:hep-ex/9803003 \[hep-ex\]](#).
- [31] ATLAS Collaboration, G. Aad et al., *Measurement of the Transverse Momentum Distribution of W Bosons in pp Collisions at $\sqrt{s} = 7$ TeV with the ATLAS Detector*, *Phys. Rev.* **D85** (2012) 012005, [arXiv:1108.6308 \[hep-ex\]](#).
- [32] *Luminosity Determination Using the ATLAS Detector*, .
- [33] S. White, R. Alemany-Fernandez, H. Burkhardt, and M. Lamont, *First Luminosity Scans in the LHC*, . <https://cds.cern.ch/record/1271694>.

- [34] A. collaboration, G. Aad, et al., *The ATLAS Experiment at the CERN Large Hadron Collider*, 2008. <http://dx.doi.org/10.1088/1748-0221/3/08/S08003>.
- [35] ATLAS Collaboration Collaboration, *ATLAS inner detector: Technical Design Report, 1*. Technical Design Report ATLAS. CERN, Geneva, 1997. <https://cds.cern.ch/record/331063>.
- [36] ATLAS Collaboration, G. Aad et al., *The ATLAS Inner Detector commissioning and calibration*, *Eur. Phys. J.* **C70** (2010) 787–821, [arXiv:1004.5293 \[physics.ins-det\]](#).
- [37] *Alignment of the ATLAS Inner Detector and its Performance in 2012*, Tech. Rep. ATLAS-CONF-2014-047, CERN, Geneva, Jul, 2014. <http://cds.cern.ch/record/1741021>.
- [38] T. G. Cornelissen, N. Van Eldik, M. Elsing, W. Liebig, E. Moyse, N. Piacquadio, K. Prokofiev, A. Salzburger, and A. Wildauer, *Updates of the ATLAS Tracking Event Data Model (Release 13)*, Tech. Rep. ATL-SOFT-PUB-2007-003. ATL-COM-SOFT-2007-008, CERN, Geneva, Jun, 2007. <https://cds.cern.ch/record/1038095>.
- [39] ATLAS Collaboration, G. Aad et al., *Performance of the ATLAS Trigger System in 2010*, *Eur. Phys. J.* **C72** (2012) 1849, [arXiv:1110.1530 \[hep-ex\]](#).
- [40] T. Golling, H. S. Hayward, P. U. E. Onyisi, H. J. Stelzer, and P. Waller, *The ATLAS Data Quality Defect Database System*, *Eur. Phys. J.* **C72** (2012) 1960, [arXiv:1110.6119 \[physics.ins-det\]](#).
- [41] ATLAS Collaboration, G. Aad et al., *Topological cell clustering in the ATLAS calorimeters and its performance in LHC Run 1*, [arXiv:1603.02934 \[hep-ex\]](#).
- [42] W. Lampl, S. Laplace, D. Lelas, P. Loch, H. Ma, S. Menke, S. Rajagopalan, D. Rousseau, S. Snyder, and G. Unal, *Calorimeter clustering algorithms: Description and performance*, .
- [43] G. Barrand et al., *GAUDI - A software architecture and framework for building HEP data processing applications*, *Comput. Phys. Commun.* **140** (2001) 45–55.
- [44] F. Hubaut, P. Pralavorio, B. Dekhissi, J. E. Derkaoui, A. El-Kharrim, and F. Maaroufi, *Crosstalk in production modules of the Electromagnetic Endcap Calorimeter*, .
- [45] F. Hubaut, *Crosstalk Measurements in the EM Barrel Module 0 from 99', May 00' and July 00' Beam Tests*, .
- [46] ATLAS Collaboration, G. Aad et al., *Electron and photon energy calibration with the ATLAS detector using LHC Run 1 data*, *Eur. Phys. J.* **C74** (2014) no. 10, 3071, [arXiv:1407.5063 \[hep-ex\]](#).
- [47] Y. Nakahama and J.-B. de Vivie, *Calorimeter - Tracker Inter-Alignment*, .
- [48] G. Bozzi, L. Citelli, and A. Vicini, *Parton density function uncertainties on the W boson mass measurement from the lepton transverse momentum distribution*, *Phys. Rev.* **D91** (2015) no. 11, 113005, [arXiv:1501.05587 \[hep-ph\]](#).
- [49] ATLAS Collaboration, G. Aad et al., *Measurement of the muon reconstruction performance of the ATLAS detector using 2011 and 2012 LHC proton-proton collision data*, *Eur. Phys. J.* **C74** (2014) no. 11, 3130, [arXiv:1407.3935 \[hep-ex\]](#).
- [50] J.-B. Blanchard, J.-B. de Vivie, and P. Mastrandrea, *In situ scales and smearings from Z and J/ψ events*, .

- [51] ATLAS Collaboration, G. Aad et al., *Electron reconstruction and identification efficiency measurements with the ATLAS detector using the 2011 LHC proton-proton collision data*, *Eur.Phys.J.* **C74** (2014) no. 7, 2941, [arXiv:1404.2240 \[hep-ex\]](#).
- [52] L. Devroye, *"Non-Uniform Random Variate Generation"*. Springer-Verlag, 1986.
Available at <http://www.eirene.de/Devroye.pdf>.
- [53] S. D. Drell and T.-M. Yan, *Massive Lepton Pair Production in Hadron-Hadron Collisions at High-Energies*, *Phys. Rev. Lett.* **25** (1970) 316–320. [Erratum: *Phys. Rev. Lett.* 25,902(1970)].
- [54] ATLAS Collaboration, G. Aad et al., *Measurement of the transverse momentum and ϕ_η^* distributions of Drell-Yan lepton pairs in proton-proton collisions at $\sqrt{s} = 8$ TeV with the ATLAS detector*, *Eur. Phys. J.* **C76** (2016) no. 5, 291, [arXiv:1512.02192 \[hep-ex\]](#).
- [55] K. Bachas, M. Bellomo, F. Ballester, S. Camarda, A. Cooper-Sarkar, J. Dassoulas, R. S. Hickling, F. Ellinghaus, C. Issever, C. T. Jeske, D. Froidevaux, L. Ionomidou-Fayard, A. Glazov, T. Guillemin, A. Kapliy, M. Karnevskiy, M. Klein, U. Klein, J. Kretzschmar, T. Kono, A. Lewis, K. Lohwasser, M. Lisovsky, T. Matsushita, J. Maurer, P. Onyisi, E. Richter-Was, E. Rizvi, V. Radescu, P. Sommer, G. Sedov, T. Serre, A. Schaffer, S. Schmitt, J. Sendler, M. Shochet, J. Tseng, M. Vincet, M. Wielers, and E. Yatsenko, *Measurement and QCD Analysis of Differential Inclusive $W^+ \pm \rightarrow \ell \nu$ and $Z/\gamma^* \rightarrow \ell \ell$ Production and Leptonic Decay Cross Sections with ATLAS*, .
<https://cds.cern.ch/record/1517987>.
- [56] ATLAS Collaboration, G. Aad et al., *Measurement of the angular coefficients in Z-boson events using electron and muon pairs from data taken at $\sqrt{s} = 8$ TeV with the ATLAS detector*, *JHEP* **08** (2016) 159, [arXiv:1606.00689 \[hep-ex\]](#).
- [57] D. Y. Bardin, A. Leike, T. Riemann, and M. Sachwitz, *Energy Dependent Width Effects in $e^+ e^-$ Annihilation Near the Z Boson Pole*, *Phys.Lett.* **B206** (1988) 539–542.
- [58] P. Golonka and Z. Was, *PHOTOS Monte Carlo: A Precision tool for QED corrections in Z and W decays*, *Eur. Phys. J.* **C45** (2006) 97–107, [arXiv:hep-ph/0506026 \[hep-ph\]](#).
- [59] G. Nanava, Q. Xu, and Z. Was, *Matching NLO parton shower matrix element with exact phase space*, *Eur.Phys.J.* **C70** (2010) 673–688, [arXiv:0906.4052 \[hep-ph\]](#).
- [60] G. Nanava and Z. Was, *How to use SANC to improve the PHOTOS Monte Carlo simulation of bremsstrahlung in leptonic W boson decays*, *Acta Phys.Polon.* **B34** (2003) 4561–4570, [arXiv:hep-ph/0303260 \[hep-ph\]](#).
- [61] A. Andonov, A. Arbuzov, D. Bardin, S. Bondarenko, P. Christova, et al., *SANCScope - v.1.00*, *Comput.Phys.Comm.* **174** (2006) 481–517, [arXiv:hep-ph/0411186 \[hep-ph\]](#).
- [62] L. Barze, G. Montagna, P. Nason, O. Nicrosini, and F. Piccinini, *Implementation of electroweak corrections in the POWHEG BOX: single W production*, *JHEP* **04** (2012) 037, [arXiv:1202.0465 \[hep-ph\]](#).
- [63] L. Barze, G. Montagna, P. Nason, O. Nicrosini, F. Piccinini, and A. Vicini, *Neutral current Drell-Yan with combined QCD and electroweak corrections in the POWHEG BOX*, *Eur. Phys. J.* **C73** (2013) no. 6, 2474, [arXiv:1302.4606 \[hep-ph\]](#).
- [64] D. Bardin, S. Bondarenko, S. Jadach, L. Kalinovskaya, and W. Placzek, *Implementation of SANC EW corrections in WINHAC Monte Carlo generator*, *Acta Phys. Polon.* **B40** (2009) 75–92, [arXiv:0806.3822 \[hep-ph\]](#).

- [65] S. Dulat, T.-J. Hou, J. Gao, M. Guzzi, J. Huston, P. Nadolsky, J. Pumplin, C. Schmidt, D. Stump, and C. P. Yuan, *New parton distribution functions from a global analysis of quantum chromodynamics*, *Phys. Rev.* **D93** (2016) no. 3, 033006, [arXiv:1506.07443 \[hep-ph\]](#).
- [66] L. A. Harland-Lang, A. D. Martin, P. Motylinski, and R. S. Thorne, *Parton distributions in the LHC era: MMHT 2014 PDFs*, *Eur. Phys. J.* **C75** (2015) no. 5, 204, [arXiv:1412.3989 \[hep-ph\]](#).
- [67] S. Catani, L. Cieri, G. Ferrera, D. de Florian, and M. Grazzini, *Vector boson production at hadron colliders: a fully exclusive QCD calculation at NNLO*, *Phys. Rev. Lett.* **103** (2009) 082001, [arXiv:0903.2120 \[hep-ph\]](#).
- [68] S. Catani, B. R. Webber, and G. Marchesini, *QCD coherent branching and semiinclusive processes at large x* , *Nucl. Phys.* **B349** (1991) 635–654.
- [69] NNPDF Collaboration, R. D. Ball et al., *Parton distributions for the LHC Run II*, *JHEP* **04** (2015) 040, [arXiv:1410.8849 \[hep-ph\]](#).
- [70] ATLAS Collaboration, G. Aad et al., *Measurement of the polarisation of W bosons produced with large transverse momentum in pp collisions at $\sqrt{s} = 7$ TeV with the ATLAS experiment*, *Eur. Phys. J.* **C72** (2012) 2001, [arXiv:1203.2165 \[hep-ex\]](#).
- [71] A. J. Armbruster, M. B. Balcerak, A. Ezhilov, O. Fedin, D. Froidevaux, M. Lisovyi, E. Richter-Was, B. Ryniec, K. Schmieden, and M. Vincet, *Probing QCD dynamics with precise measurements of the polarisation angular coefficients using electron and muon pairs from Z -boson decays with the ATLAS detector at the LHC*, .
<https://cds.cern.ch/record/2053182>.
- [72] ATLAS Collaboration Collaboration, *Improved Luminosity Determination in pp Collisions at $\sqrt{s} = 7$ TeV using the ATLAS Detector at the LHC*, Tech. Rep. ATLAS-CONF-2012-080, CERN, Geneva, Jul, 2012. <https://cds.cern.ch/record/1460392>.
- [73] S. Alioli, P. Nason, C. Oleari, and E. Re, *A general framework for implementing NLO calculations in shower Monte Carlo programs: the POWHEG BOX*, *JHEP* **06** (2010) 043, [arXiv:1002.2581 \[hep-ph\]](#).
- [74] H.-L. Lai, M. Guzzi, J. Huston, Z. Li, P. M. Nadolsky, J. Pumplin, and C. P. Yuan, *New parton distributions for collider physics*, *Phys. Rev.* **D82** (2010) 074024, [arXiv:1007.2241 \[hep-ph\]](#).
- [75] T. Sjostrand, S. Mrenna, and P. Z. Skands, *A Brief Introduction to PYTHIA 8.1*, *Comput. Phys. Commun.* **178** (2008) 852–867, [arXiv:0710.3820 \[hep-ph\]](#).
- [76] *ATLAS tunes of PYTHIA 6 and PYTHIA 8 for MC11*, Tech. Rep. ATL-PHYS-PUB-2011-009, CERN, Geneva, Jul, 2011.
<https://cds.cern.ch/record/1363300>.
- [77] S. Jadach, J. H. Kühn, and Z. Was, *TAUOLA—a library of Monte Carlo programs to simulate decays of polarized τ leptons*, *Computer Physics Communications* **64** (1991) no. 2, 275–299.
- [78] S. Frixione and B. R. Webber, *Matching NLO QCD computations and parton shower simulations*, *JHEP* **06** (2002) 029, [arXiv:hep-ph/0204244 \[hep-ph\]](#).
- [79] S. Agostinelli, J. Allison, K. a. Amako, J. Apostolakis, H. Araujo, P. Arce, M. Asai, D. Axen, S. Banerjee, G. Barrand, et al., *Geant4 simulation toolkit*, *Nuclear instruments and methods in physics research section A: Accelerators, Spectrometers, Detectors and Associated Equipment* **506** (2003) no. 3, 250–303.

- [80] ATLAS Collaboration, G. Aad et al., *Charged-particle multiplicities in pp interactions measured with the ATLAS detector at the LHC*, *New J. Phys.* **13** (2011) 053033, [arXiv:1012.5104 \[hep-ex\]](#).
- [81] J. Butterworth, E. Dobson, U. Klein, B. M. Garcia, T. Nunnemann, J. Qian, D. Rebuzzi, and R. Tanaka, *Single boson and diboson production cross sections in pp collisions at $\sqrt{s} = 7$ TeV*, ATLAS Internal Communication ATL-COM-PHYS-2010-695 (2010) .
- [82] *Top group's MC11(a,b,c) Samples For 2011 Data Analyses*, .
- [83] ATLAS Collaboration, G. Aad et al., *Measurement of the $t\bar{t}$ production cross-section using $e\mu$ events with b -tagged jets in pp collisions at $\sqrt{s} = 7$ and 8 TeV with the ATLAS detector*, *Eur. Phys. J.* **C74** (2014) no. 10, 3109, [arXiv:1406.5375 \[hep-ex\]](#).
- [84] CMS Collaboration, *W-like measurement of the Z boson mass using dimuon events collected in pp collisions at $\sqrt{s} = 7$ TeV*, Tech. Rep. CMS-PAS-SMP-14-007, CERN, Geneva, 2016. <https://cds.cern.ch/record/2139655>.
- [85] G. Watt and R. Thorne, *Study of Monte Carlo approach to experimental uncertainty propagation with MSTW 2008 PDFs*, *JHEP* **1208** (2012) 052, [arXiv:1205.4024 \[hep-ph\]](#).
- [86] Particle Data Group Collaboration, K. Olive et al., *Review of Particle Physics*, *Chin.Phys.* **C38** (2014) 090001.
- [87] A. Valassi, *Combining correlated measurements of several different physical quantities*, *Nucl. Instrum. Meth.* **A500** (2003) 391–405.
- [88] H. Paukkunen and P. Zurita, *PDF reweighting in the Hessian matrix approach*, *JHEP* **1412** (2014) 100, [arXiv:1402.6623 \[hep-ph\]](#).
- [89] HERAFitter developers' Team Collaboration, S. Camarda et al., *QCD analysis of W- and Z-boson production at Tevatron*, [arXiv:1503.05221 \[hep-ph\]](#).
- [90] S. Alekhin, O. Behnke, P. Belov, S. Borroni, M. Botje, et al., *HERAFitter, Open Source QCD Fit Project*, [arXiv:1410.4412 \[hep-ph\]](#).
- [91] H1 Collaboration, F. Aaron et al., *Measurement of the Inclusive ep Scattering Cross Section at Low Q^2 and x at HERA*, *Eur. Phys. J. C* **63** (2009) 625–678, [arXiv:0904.0929 \[hep-ex\]](#).

Cross-talk calculations

A.1 Middle-Strip crosstalk

Consider energy distribution deposited by projective muons in $\Delta\phi \times \Delta\eta = 1 \times 5$ cluster of strip or middle layer. Define its most probable energy as

$$S = MPV(E_{-2} + E_{-1} + E_0 + E_{+1} + E_{+2}) \quad (\text{A.1})$$

This value does not depend on the horizontal crosstalk between cells of the same layer as it contains total energy profile and is compensated by the summation. Then a real muon energy deposit S^0 in strip layer and muon energy deposit S taking into account the longitudinal crosstalk are connected by the following equation:

$$S_{strip} = S_{strip}^0 - \chi_{1 \rightarrow 2} S_{strip}^0 + 4\chi_{2 \rightarrow 1} S_{middle}^0 \quad (\text{A.2})$$

where $\chi_{1 \rightarrow 2}$ corresponds to part of energy that flows from strip to middle layer due to crosstalk and $\chi_{2 \rightarrow 1}$ corresponds to part of energy that flows from middle to strip layer through the same $\Delta\phi \times \Delta\eta$ area; factor 4 comes from cells granularity in ϕ direction. By assuming that energy flows between layers for both directions are equal, one can get middle-strip crosstalk

$$\chi_{2 \rightarrow 1} = \frac{S_{strip} - S_{strip}^0}{4S_{middle}^0 - S_{strip}^0} \quad (\text{A.3})$$

A.2 Strip-strip crosstalk

Denote E_0 as most probable energy deposit of a projective muon in the crossed cell, $E_{\pm 1}$ as most probable energy deposits in its first neighbour $\eta - 1$ and $\eta + 1$ cells, $E_{\pm 2}$ in its second neighbour $\eta - 2$ and $\eta + 2$ cells. A real muon energy deposit E_{-1}^0 in left neighbour cell of strip layer and muon energy deposit E_{-1} taking into account crosstalk effect are connected by (see Fig.4.3)

$$E_{-1} = E_{-1}^0 - (\chi_{\eta \rightarrow \eta-1} + \chi_{\eta \rightarrow \eta+1} + \chi_{\eta \rightarrow \eta-2} + \chi_{\eta \rightarrow \eta+2} + \chi_{1 \rightarrow 2})E_{-1}^0 + \chi_{\eta \rightarrow \eta-1}E_0^0 + \chi_{\eta \rightarrow \eta+1}E_{-2}^0 + \chi_{\eta \rightarrow \eta-2}E_{+1}^0 + 1.32\chi_{1 \rightarrow 2}E_{0,middle}^0 \quad (\text{A.4})$$

where negative terms represent energy migration from the considered cell to all possible directions and the positive terms represent energy migration to considered cell. Similar equation can be written for second neighbour cell of strip layer:

$$E_{-2} = E_{-2}^0 - (\chi_{\eta \rightarrow \eta-1} + \chi_{\eta \rightarrow \eta+1} + \chi_{\eta \rightarrow \eta-2} + \chi_{\eta \rightarrow \eta+2} + \chi_{1 \rightarrow 2})E_{-2}^0 + \chi_{\eta \rightarrow \eta-1}E_{-1}^0 + \chi_{\eta \rightarrow \eta-2}E_0^0 + 1.32\chi_{1 \rightarrow 2}E_{0,middle}^0 \quad (\text{A.5})$$

Here $\chi_{1 \rightarrow 2}$ corresponds to middle-strip crosstalk found in Appendix 1; $\chi_{\eta \rightarrow \eta \pm 1}$ corresponds to strip-strip crosstalk and $\chi_{\eta \rightarrow \eta \pm 2}$ corresponds to strip-2nd strip crosstalk. For simplicity we assume that energy migration between strips in both directions is equal

$$\begin{aligned} \chi_{\eta \rightarrow \eta-1} &\approx \chi_{\eta \rightarrow \eta+1} \\ \chi_{\eta \rightarrow \eta-2} &\approx \chi_{\eta \rightarrow \eta+2} \end{aligned} \quad (\text{A.6})$$

one can get from (A.4) and (A.5):

$$\chi_{\eta \rightarrow \eta \pm 1} = \frac{\frac{E_{\pm 1} - E_{\pm 1}^0 - 1.32\chi_{21}E_{0,mid}^0}{E_{\mp 1}^0 - 2E_{\pm 1}^0} - \frac{E_{\pm 2} - E_{\pm 2}^0 - 1.32\chi_{21}E_{0,mid}^0}{E_0^0 - 2E_{\pm 2}^0}}{\frac{E_0^0 + E_{\pm 2}^0 - 2E_{\pm 1}^0}{E_{\mp 1}^0 - 2E_{\pm 1}^0} - \frac{E_{\pm 1}^0 - 2E_{\pm 2}^0}{E_0^0 - 2E_{\pm 2}^0}} \quad (\text{A.7})$$

and

$$\chi_{\eta \rightarrow \eta \pm 2} = \frac{\frac{E_{\pm 1} - E_{\pm 1}^0 - 1.32\chi_{21}E_{0,mid}^0}{E_0^0 + E_{\pm 2}^0 - 2E_{\pm 1}^0} - \frac{E_{\pm 2} - E_{\pm 2}^0 - 1.32\chi_{21}E_{0,mid}^0}{E_{\pm 1}^0 - 2E_{\pm 2}^0}}{\frac{E_{\mp 1}^0 - 2E_{\pm 1}^0}{E_0^0 + E_{\pm 2}^0 - 2E_{\pm 1}^0} - \frac{E_0^0 - 2E_{\pm 2}^0}{E_{\pm 1}^0 - 2E_{\pm 2}^0}} \quad (\text{A.8})$$

A.3 Middle-Middle crosstalk

Consider energy deposits of projective muons in the middle layer. Denote E_0 as most probable energy deposit of a projective muon in the crossed cell with coordinate η , $E_{\pm 1}$ as most probable energy deposits in first neighbour $\eta - 1$ and $\eta + 1$ cells, $E_{\pm 2}$ in second neighbour $\eta - 2$ and $\eta + 2$ cells. Taking into account lateral and horizontal energy leakage, a detected energy E_{-1} in the left neighbour cell and full energy deposited by the muon in this cell are connected by the following expression:

$$E_{-1} = [1 - 8\chi_{21} - \chi_{\eta \rightarrow \eta - 1} - \chi_{\eta \rightarrow \eta + 1}]E_{-1}^0 + \chi_{\eta \rightarrow \eta - 1}E_0^0 + \chi_{\eta \rightarrow \eta + 1}E_{-2}^0 \quad (\text{A.9})$$

And similarly for opposite neighbour cell:

$$E_{+1} = [1 - 8\chi_{21} - \chi_{\eta \rightarrow \eta - 1} - \chi_{\eta \rightarrow \eta + 1}]E_{+1}^0 + \chi_{\eta \rightarrow \eta + 1}E_0^0 + \chi_{\eta \rightarrow \eta - 1}E_{+2}^0 \quad (\text{A.10})$$

After solving the system of linear equations (A.10) and (A.9), the middle-middle crosstalk is given by

$$\chi_{\eta \rightarrow \eta \pm 1} = \frac{\frac{E_{\pm 1} - E_{\pm 1}^0(1 - 8\chi_{21})}{E_{\pm 1}^0 - E_{\pm 2}^0} - \frac{E_{\mp 1} - E_{\mp 1}^0(1 - 8\chi_{21})}{E_0^0 - E_{\mp 1}^0}}{\frac{E_0^0 - E_{\pm 1}^0}{E_{\pm 1}^0 - E_{\pm 2}^0} - \frac{E_{\mp 1}^0 - E_{\mp 2}^0}{E_0^0 - E_{\mp 1}^0}} \quad (\text{A.11})$$

The latter can be simplified taking into account that the $E_{\pm 2} \approx 0$ GeV:

$$\chi_{\eta \rightarrow \eta \pm 1} = \frac{\frac{E_{\pm 1} - E_{\pm 1}^0(1 - 8\chi_{21})}{E_{\pm 1}^0} - \frac{E_{\mp 1} - E_{\mp 1}^0(1 - 8\chi_{21})}{E_0^0 - E_{\mp 1}^0}}{\frac{E_0^0 - E_{\pm 1}^0}{E_{\pm 1}^0} - \frac{E_{\mp 1}^0}{E_0^0 - E_{\mp 1}^0}} \quad (\text{A.12})$$

PDF profiling

B.0.0.1 Profiling of PDF and resummation parameters

Existing PDF sets can be updated using data from newer measurements using a profiling procedure [88, 89]. The procedure can be extended to include additional theoretical uncertainties such as α_S . The profiling is performed using a χ^2 function which includes both the experimental uncertainties and the theoretical uncertainties arising from PDF variations and extra sources:

$$\begin{aligned} \chi^2(\beta_{\text{exp}}, \beta_{\text{th}}) = & \sum_{i=1}^{N_{\text{data}}} \frac{\left(\sigma_i^{\text{exp}} + \sum_j \Gamma_{ij}^{\text{exp}} \beta_{j,\text{exp}} - \sigma_i^{\text{th}} - \sum_k \Gamma_{ik}^{\text{th}} \beta_{k,\text{th}} \right)^2}{\Delta_i^2} \\ & + \sum_j \beta_{j,\text{exp}}^2 + \sum_k \beta_{k,\text{th}}^2. \end{aligned} \quad (\text{B.1})$$

The correlated experimental and theoretical uncertainties are included using the nuisance parameter vectors β_{exp} and β_{th} , respectively. Their influence on the data and theory predictions is described by the Γ_{ij}^{exp} and Γ_{ik}^{th} matrices. The index i runs over all N_{data} data points, whereas the index j (k) corresponds to the experimental (theoretical) uncertainty nuisance parameters. The measurements and the uncorrelated experimental uncertainties are given by σ_i^{exp} and Δ_i , respectively, and the theory predictions are σ_i^{th} . The χ^2 function of Eq. B.1 can be generalised to account for asymmetric uncertainties, as described in Ref. [89].

The value at the minimum of the χ^2 function provides a compatibility test of the data and theory. In addition, the values at the minimum of the nuisance parameters $\beta_{k,\text{th}}^{\text{min}}$ can be interpreted as optimisation (“profiling”) of PDFs and additional theoretical sources to describe the data. Explicitly, the profiled central PDF set f'_0 is given by

$$f'_0 = f_0 + \sum_k \beta_{k,\text{th}}^{\text{min}} \left(\frac{f_k^+ - f_k^-}{2} - \beta_{k,\text{th}}^{\text{min}} \frac{f_k^+ + f_k^- - 2f_0}{2} \right), \quad (\text{B.2})$$

where f_0 is the original central PDF set. f_k^\pm stands for up and down PDF variations for the PDF nuisance parameters and sources which are correlated to PDFs (such as α_S and heavy-quark masses, m_b and m_c), while for sources uncorrelated with PDFs (such as DYRES NP parameter) $f_k^+ = f_k^- = f_0$.

The profiling procedure is used in this analysis as implemented in the HERAFitter package [90] (trunk version, revision 1814).

The profiled PDFs have reduced uncertainties which are a mixture of the original PDF and additional theoretical sources. The dimension of the vector space describing the uncertainties is increased by the number of extra sources. In general, the shifted PDF eigenvectors are no longer orthogonal, but can be transformed to an orthogonal representation using a standard diagonalisation procedure, as in Ref. [91], which can be extended to asymmetric uncertainties [89]. The diagonalization procedure is not unique and can be followed by additional orthogonal transformations of the eigenvector basis. These additional transformations can be arranged such that one selected profiled eigenvector follows the direction of the corresponding original eigenvector, the second is a linear combination of the two original eigenvectors and so on, e.g. the transformation matrix from the original to the profiled bases has a diagonal form with all elements above the main

diagonal equal to zero. For the W -boson mass measurement, the direction of non-perturbative parameter has been chosen to be preserved in the profiling while the α_S variation is chosen to be described by the two profiled eigenvectors.

The profiling procedure produces reliable results only in the vicinity of the minimum where quadratic approximation of Eq. B.1 can be applied. First indication of the validity of the procedure is a good χ^2/dof value at the minimum which implies moderate shifts of the theory nuisance parameters. It is also important to perform a closure test by calculating the predictions using the profiled PDFs and additional theoretical uncertainty sources, and compare with the predictions resulting from the minimization procedure, calculated in terms of the initial PDF and nuisance parameter shifts. If sizable non-closure is observed, the procedure can be iterated.

The profiling uses $\Delta\chi^2 = 1$ criterion while the global PDF sets such as CT10 and CT14 use a two-tier tolerance with $\Delta\chi^2 > 1$ to account for inconsistency of data sets and other sources of theoretical uncertainties. The increased tolerance for the PDF fits is due to discrepancies among different data sets and between data sets and theory predictions. Thus profiling may have different impact on PDFs compared to a full fit. Since the systematic uncertainties for the Z_{pT} data are well understood it is probably not an issue (and even good) that for the purposes of the ATLAS W -boson mass measurement the ATLAS data enter with higher weight. However the profiled PDF set should be used with care for other purposes. In any case, the uncertainties of the CT10 set are re-scaled from the quoted 90% to 68% CL.

Eq. B.1 assumes that the Γ_{ik}^{th} factors are determined with negligible statistical uncertainty. Significant statistical noise for them may cause artificial profiling of the corresponding nuisance parameters. For this reason, the numerical accuracy of the predictions used for the profiling has been greatly improved by using fast integration techniques as discussed below.

B.0.0.2 Profiling results

The profiling of the PDFs was performed on the W , Z inclusive cross-section 2011 data excluding the low mass Z which is badly described. The central-central and central-forward on peak Z rapidity data are combined with the high mass central-central and central-forward Z rapidity data. In addition the W lepton rapidity is considered separately by charge. Three sets of PDFs were compared: CT10 nnlo, CT14 nnlo and MMHT.

The result of the profiling on the gluon, valence and sea PDFs are shown in Figs. B.1, B.2 and B.3 for CT10 nnlo, CT14 nnlo and MMHT PDFs. The differential cross section as a function of rapidity for Z 2011 data is shown in Fig. B.4 before and after profiling of the CT10 nnlo PDF for different Z mass ranges. The agreement between the prediction and the data is improved after profiling.

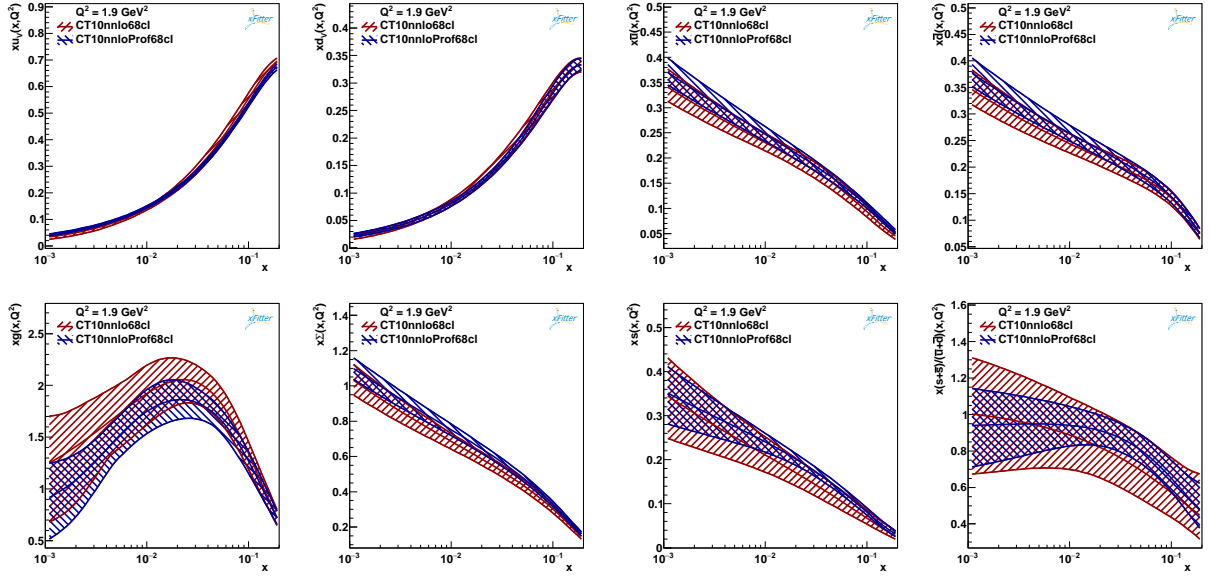


Figure B.1: Results of the profiling on the gluon (g), valence (u_V , d_V), and sea (\bar{u} , \bar{d} and s) CT10nnlo PDFs. Σ represents the sum of the sea quarks PDFs.

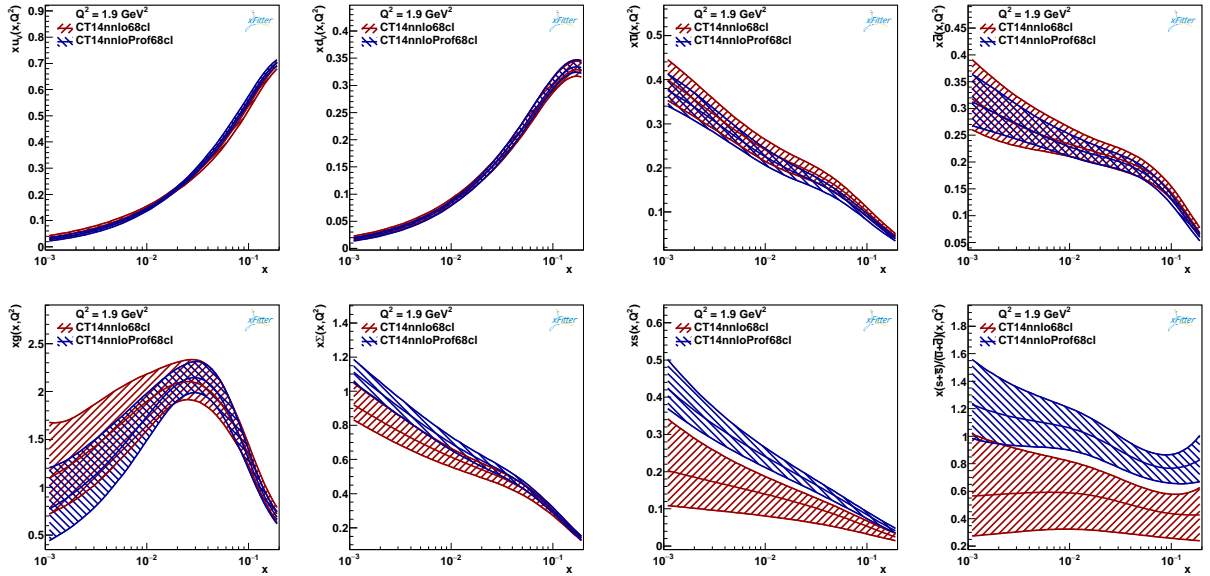


Figure B.2: Results of the profiling on the gluon (g), valence (u_V , d_V), and sea (\bar{u} , \bar{d} and s) CT14nnlo PDFs. Σ represents the sum of the sea quarks PDFs.

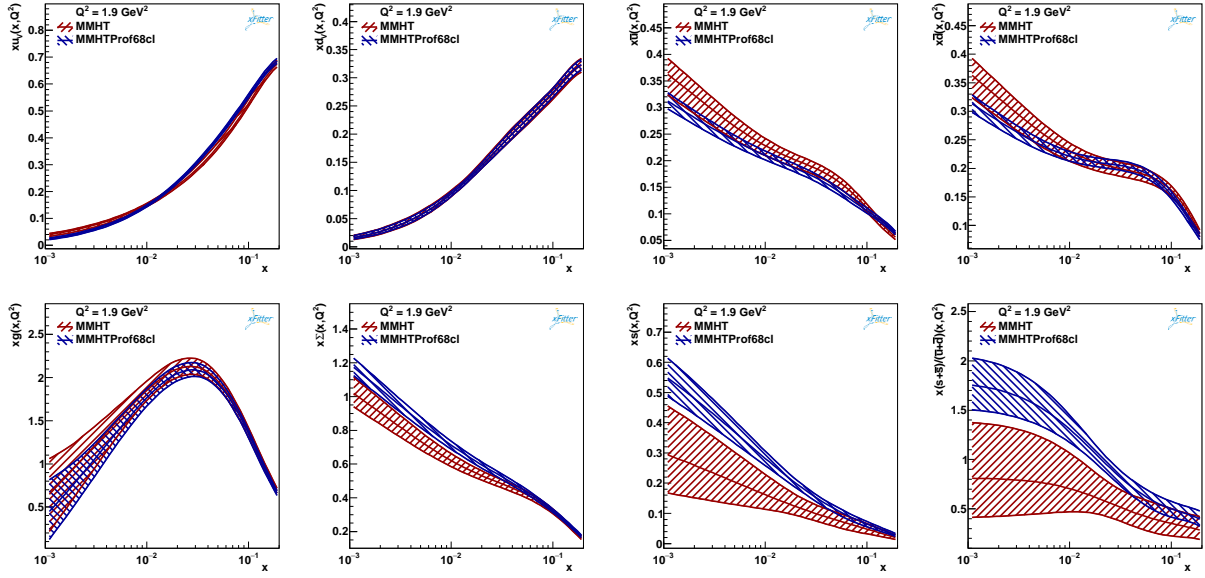


Figure B.3: Results of the profiling on the gluon (g), valence (u_V , d_V), and sea (\bar{u} , \bar{d} and s) MMHT PDFs. Σ represents the sum of the sea quarks PDFs.

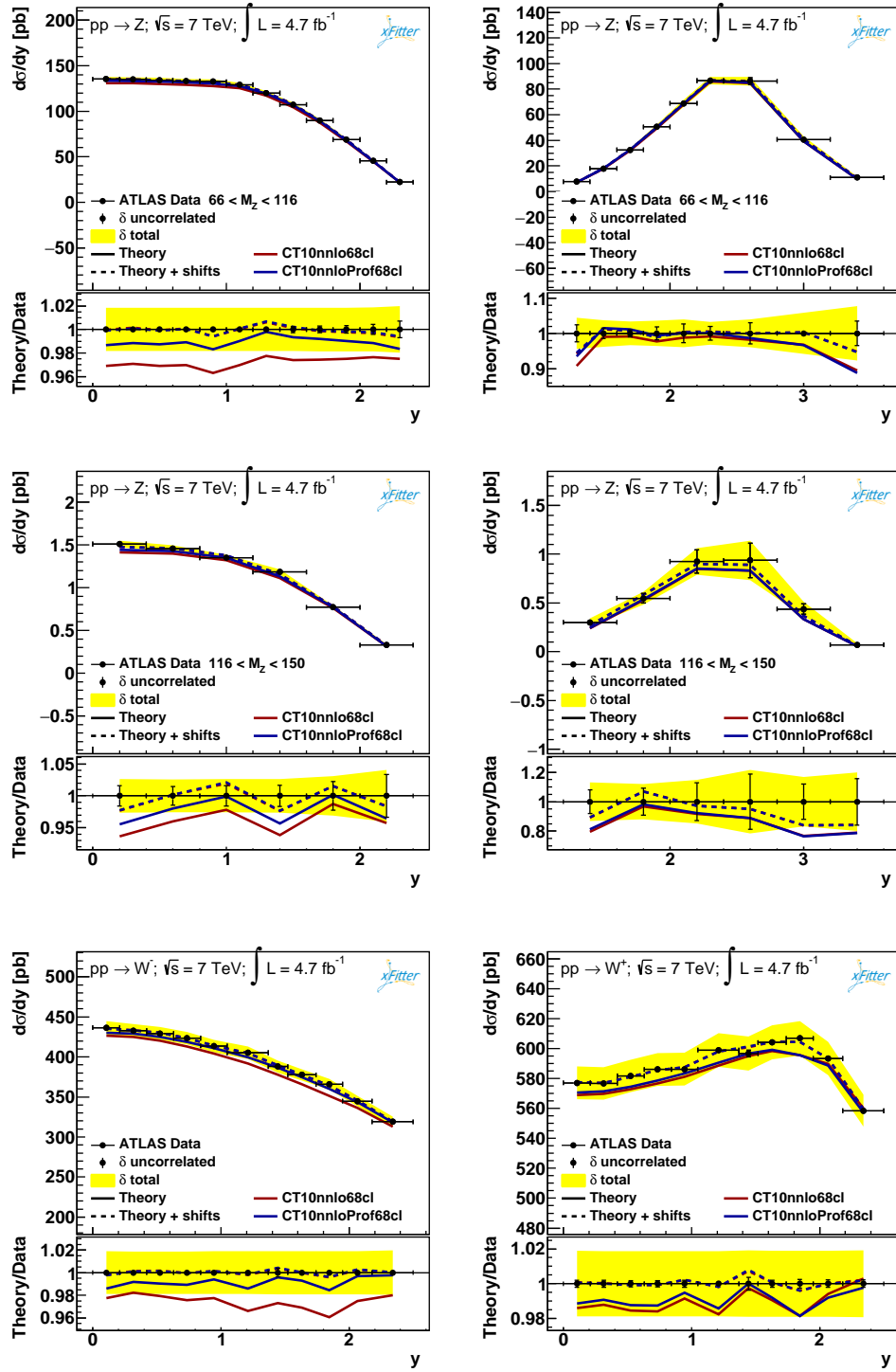


Figure B.4: Differential cross section as a function of rapidity for 2011 Z data before and after profiling of the CT10nnlo PDF

Distributions in lepton $|\eta|$ categories

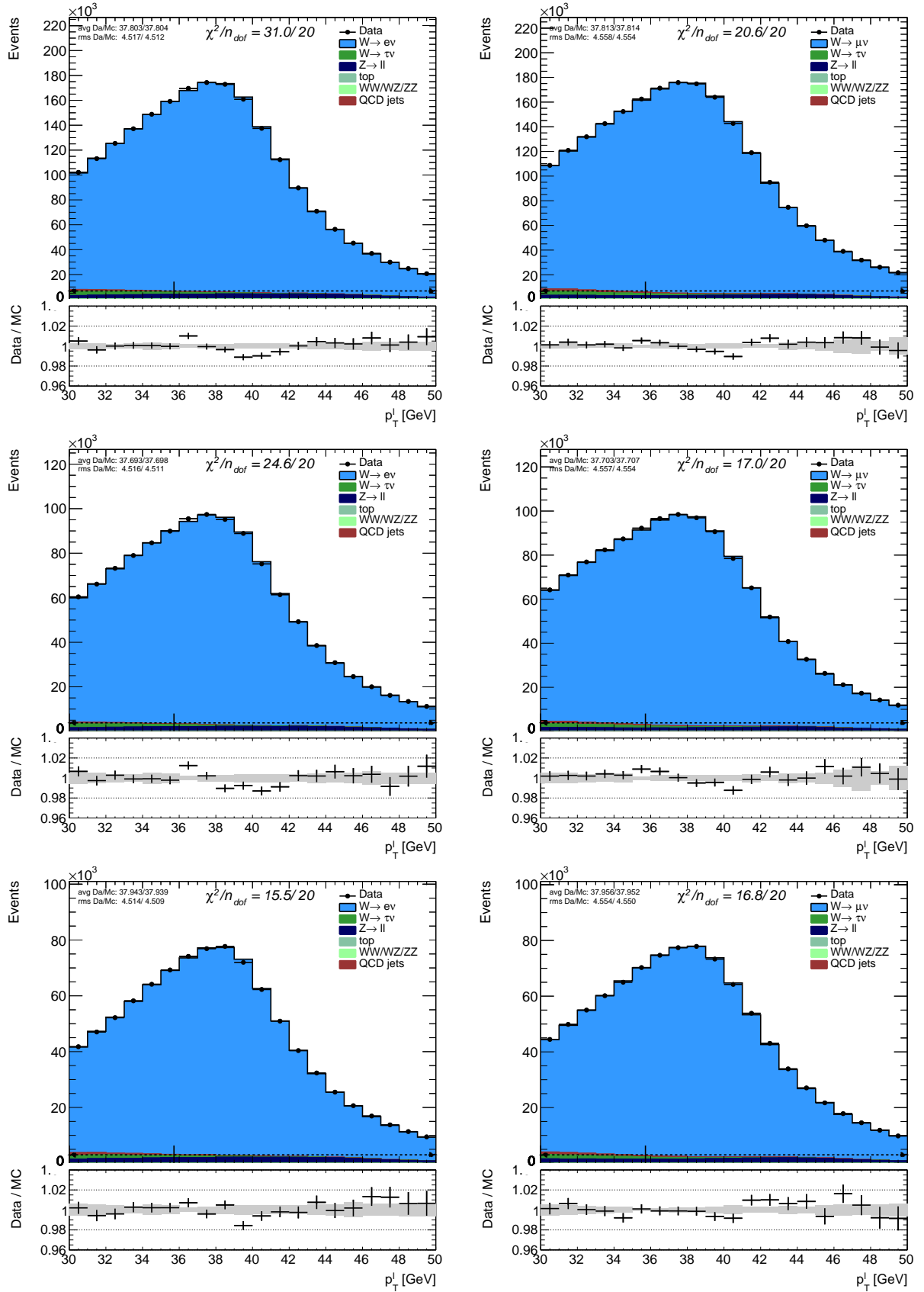


Figure C.1: Lepton p_T distribution from $W \rightarrow e\nu$ (left) and $W \rightarrow \mu\nu$ (right); $W^+ \rightarrow e\nu$ (left) and $W^+ \rightarrow \mu\nu$ (right); $W^- \rightarrow e\nu$ (left) and $W^- \rightarrow \mu\nu$ (right), for $|\eta| < 0.6$ in electron channel and $|\eta| < 0.8$ in muon channel with the best mass fit template for each category. (W^\pm : upper row, W^+ : middle row, W^- : lower row)

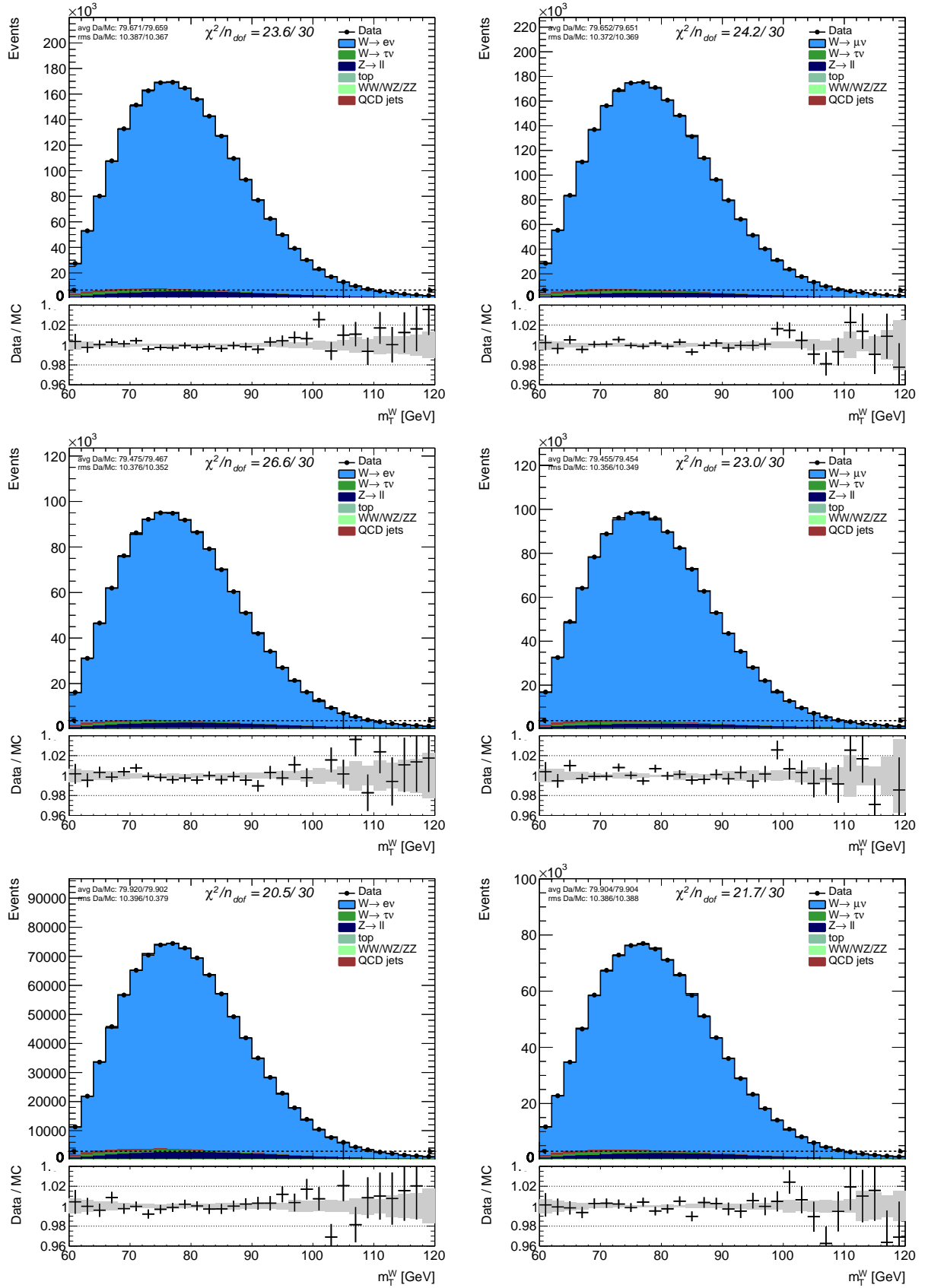


Figure C.2: Transverse mass distribution from $W \rightarrow e\nu$ (left) and $W \rightarrow \mu\nu$ (right); $W^+ \rightarrow e\nu$ (left) and $W^+ \rightarrow \mu\nu$ (right); $W^- \rightarrow e\nu$ (left) and $W^- \rightarrow \mu\nu$ (right), for $|\eta| < 0.6$ in electron channel and $|\eta| < 0.8$ in muon channel with the best mass fit template for each category. (W^\pm : upper row, W^+ : middle row, W^- : lower row)

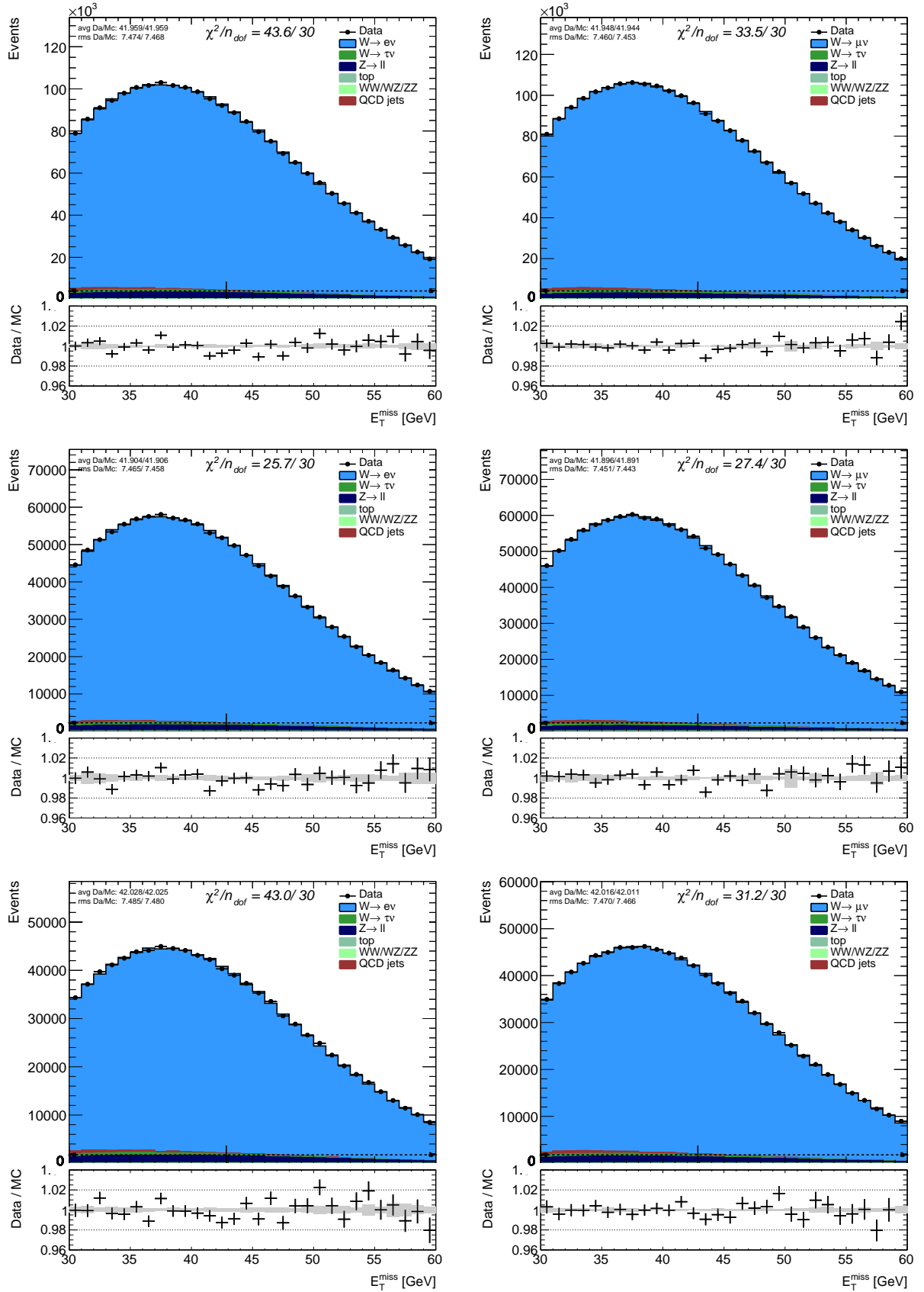


Figure C.3: Missing transverse energy distribution from $W \rightarrow e\nu$ (left) and $W \rightarrow \mu\nu$ (right); $W^+ \rightarrow e\nu$ (left) and $W^+ \rightarrow \mu\nu$ (right); $W^- \rightarrow e\nu$ (left) and $W^- \rightarrow \mu\nu$ (right), for $|\eta| < 0.6$ in electron channel and $|\eta| < 0.8$ in muon channel with the best mass fit template for each category. (W^\pm : upper row, W^+ : middle row, W^- : lower row)

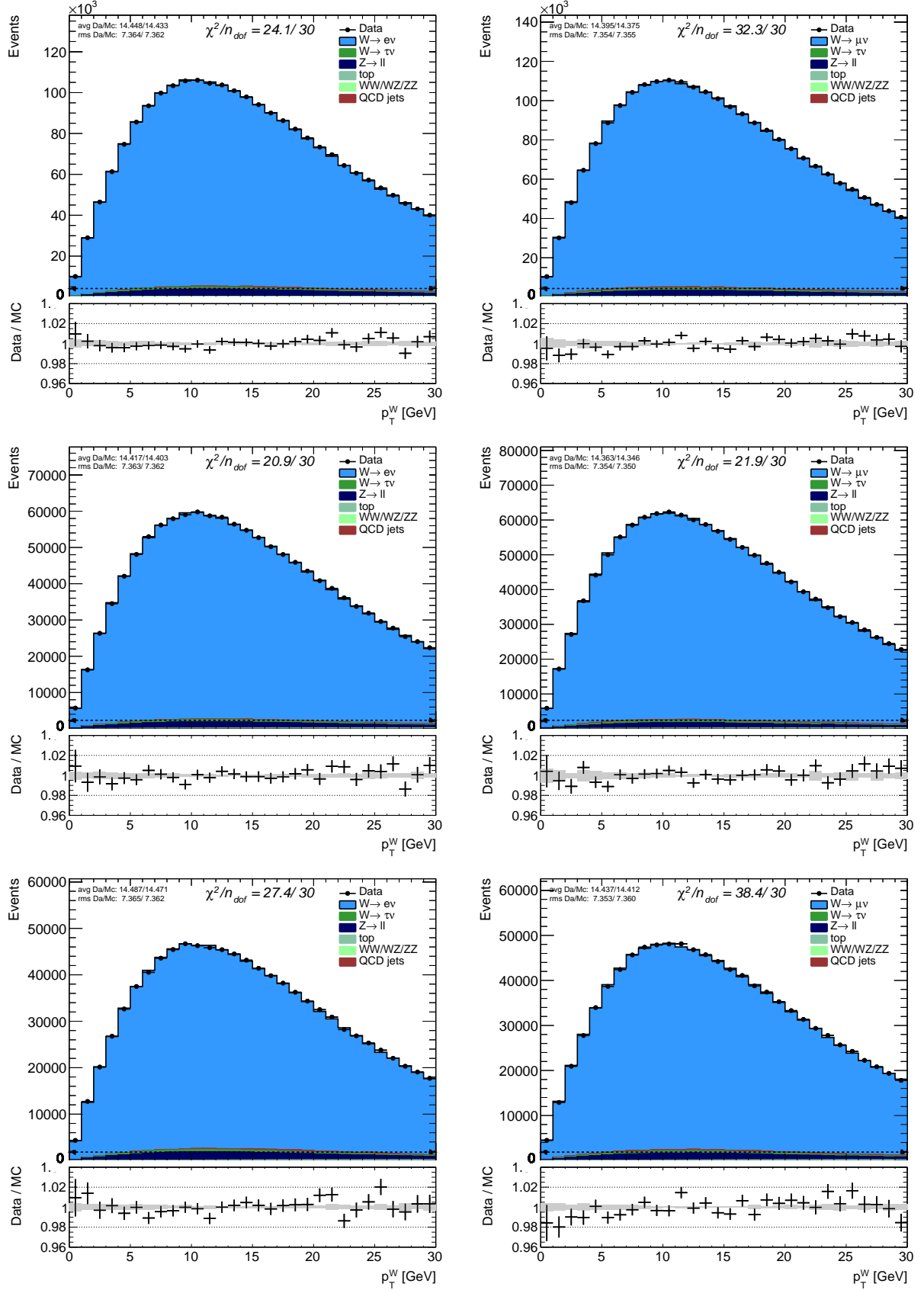


Figure C.4: Hadronic recoil distribution from $W \rightarrow e\nu$ (left) and $W \rightarrow \mu\nu$ (right); $W^+ \rightarrow e\nu$ (left) and $W^+ \rightarrow \mu\nu$ (right); $W^- \rightarrow e\nu$ (left) and $W^- \rightarrow \mu\nu$ (right), for $|\eta| < 0.6$ in electron channel and $|\eta| < 0.8$ in muon channel. (W^\pm : upper row, W^+ : middle row, W^- : lower row)

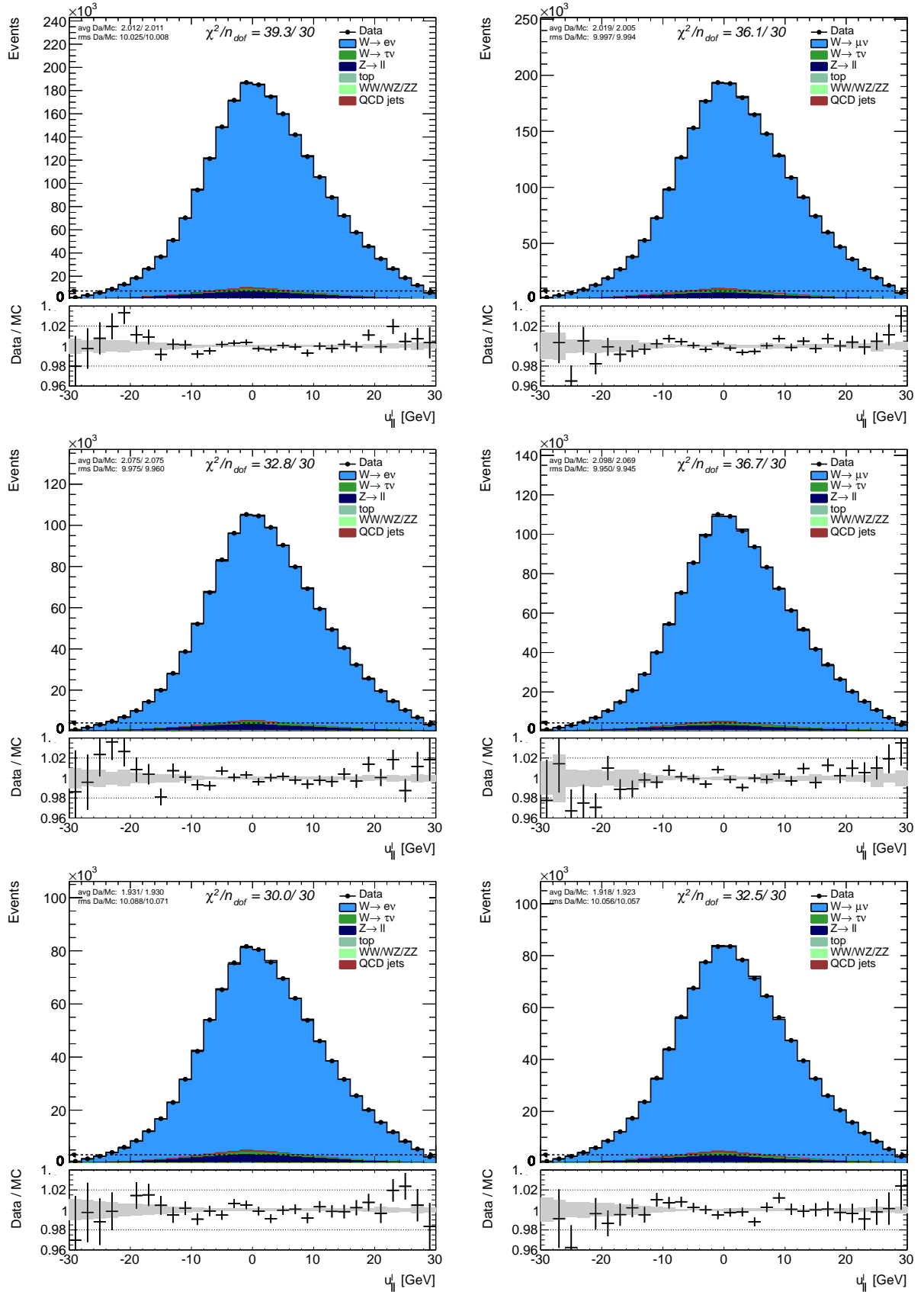
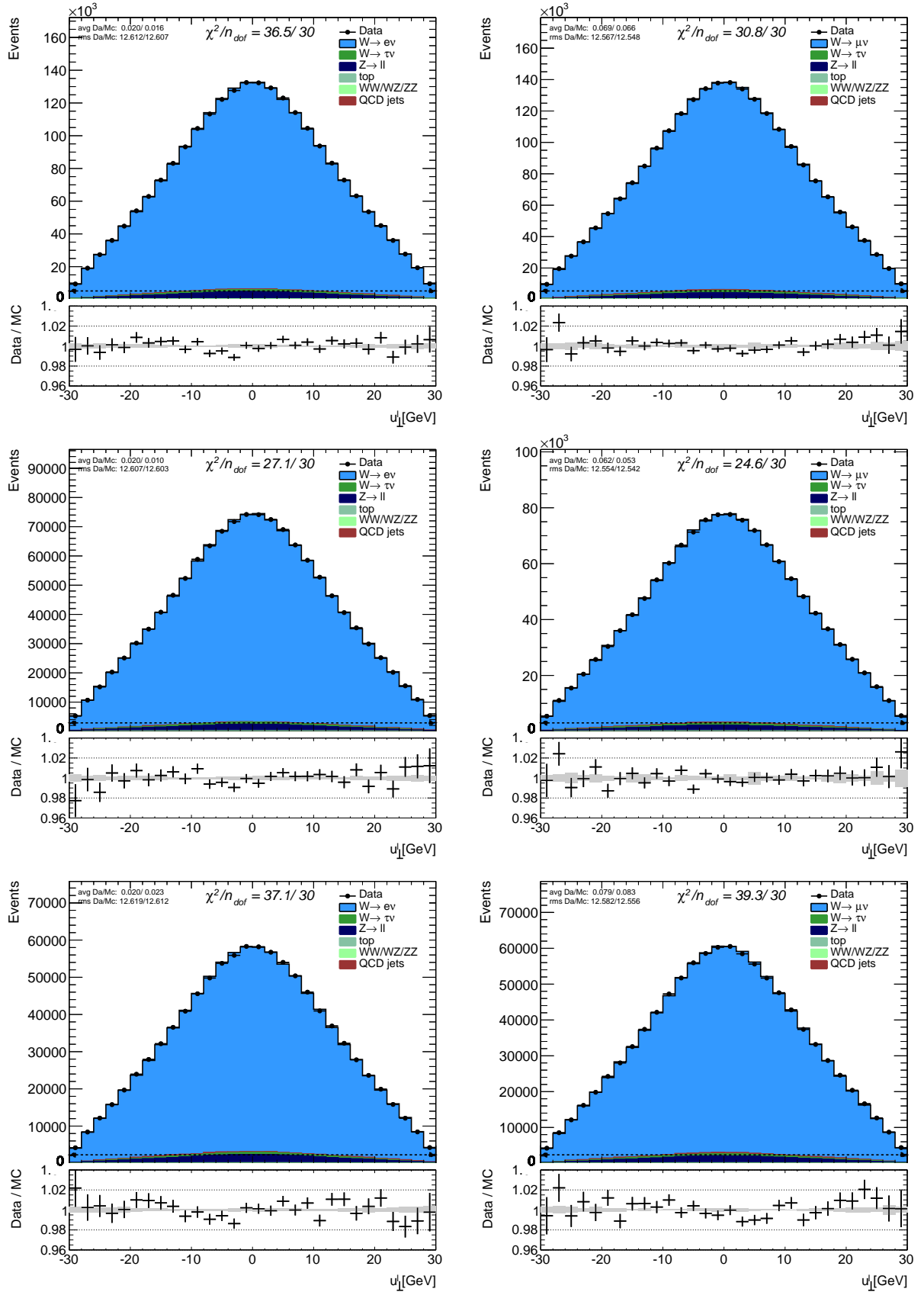


Figure C.5: Parallel projection of hadronic recoil distribution with respect to lepton p_T from $W \rightarrow e\nu$ (left) and $W \rightarrow \mu\nu$ (right); $W^+ \rightarrow e\nu$ (left) and $W^+ \rightarrow \mu\nu$ (right); $W^- \rightarrow e\nu$ (left) and $W^- \rightarrow \mu\nu$ (right), for $|\eta| < 0.6$ in electron channel and $|\eta| < 0.8$ in muon channel. (W^\pm : upper row, W^+ : middle row, W^- : lower row)



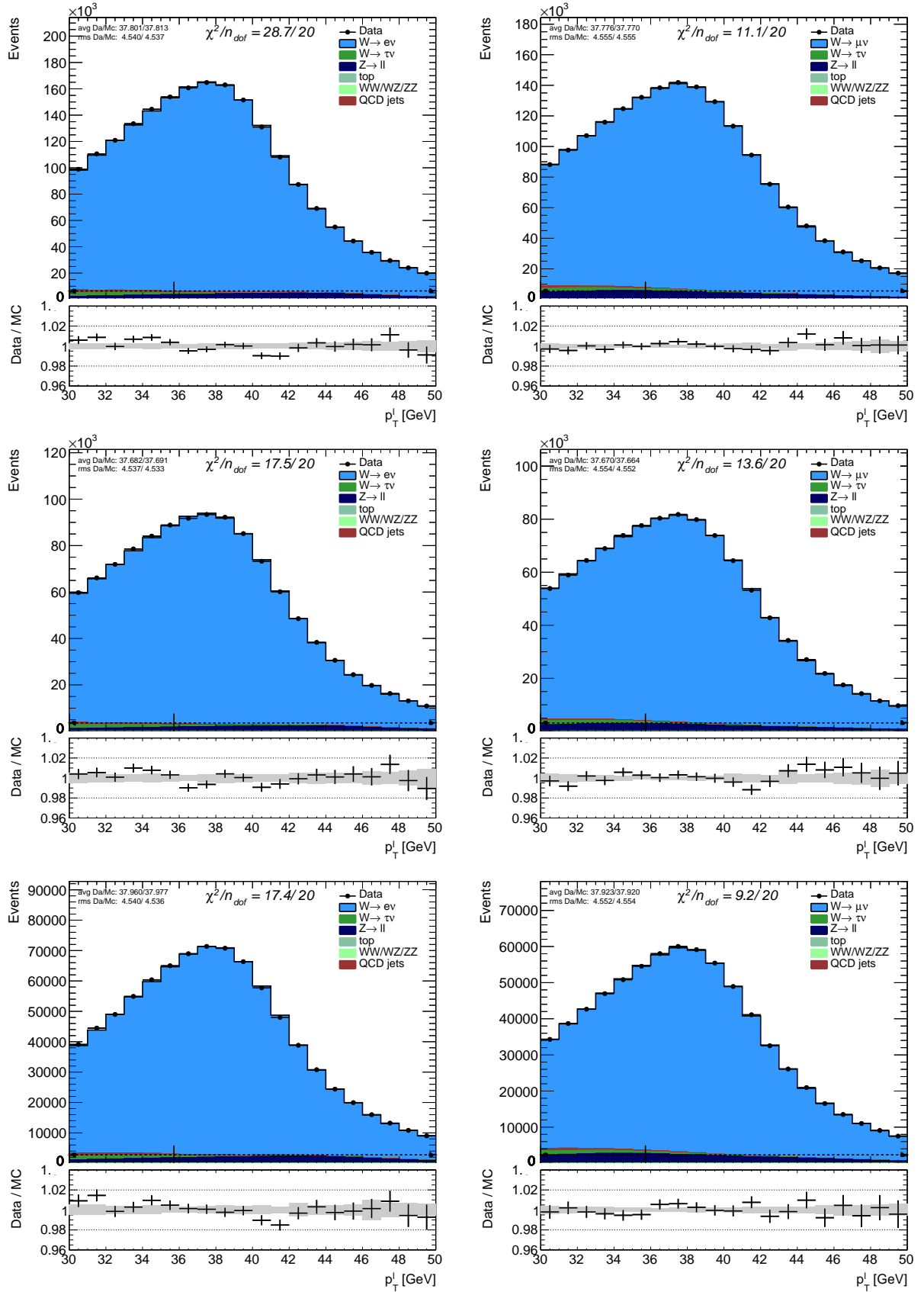


Figure C.7: Lepton p_T distribution from $W \rightarrow e\nu$ (left) and $W \rightarrow \mu\nu$ (right); $W^+ \rightarrow e\nu$ (left) and $W^+ \rightarrow \mu\nu$ (right); $W^- \rightarrow e\nu$ (left) and $W^- \rightarrow \mu\nu$ (right), for $0.6 < |\eta| < 1.2$ in electron channel and $0.8 < |\eta| < 1.4$ in muon channel with the best mass fit template for each category. (W^\pm : upper row, W^+ : middle row, W^- : lower row)

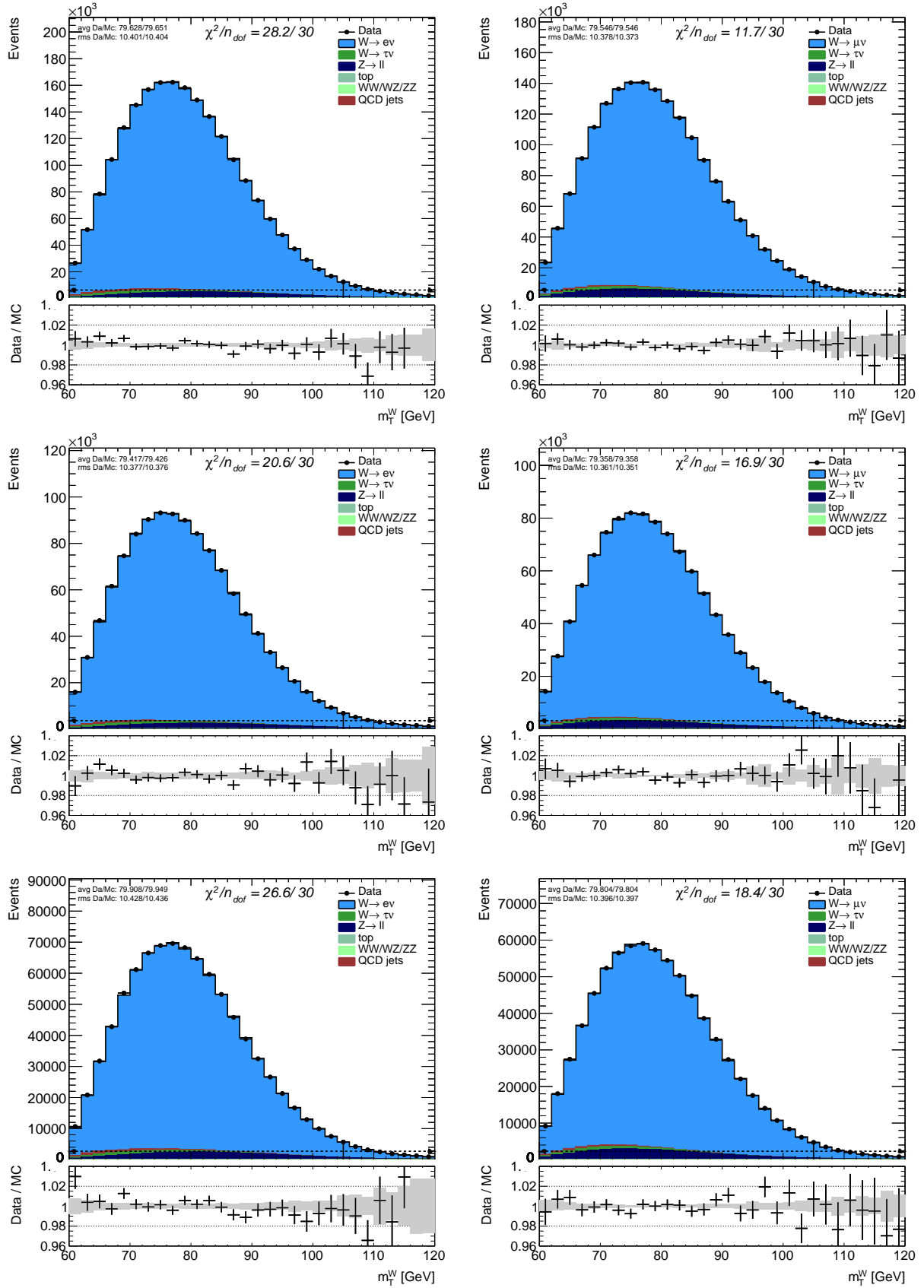


Figure C.8: Transverse mass distribution from $W \rightarrow e\nu$ (left) and $W \rightarrow \mu\nu$ (right); $W^+ \rightarrow e\nu$ (left) and $W^+ \rightarrow \mu\nu$ (right); $W^- \rightarrow e\nu$ (left) and $W^- \rightarrow \mu\nu$ (right), for $0.6 < |\eta| < 1.2$ in electron channel and $0.8 < |\eta| < 1.4$ in muon channel with the best mass fit template for each category. (W^\pm : upper row, W^+ : middle row, W^- : lower row)

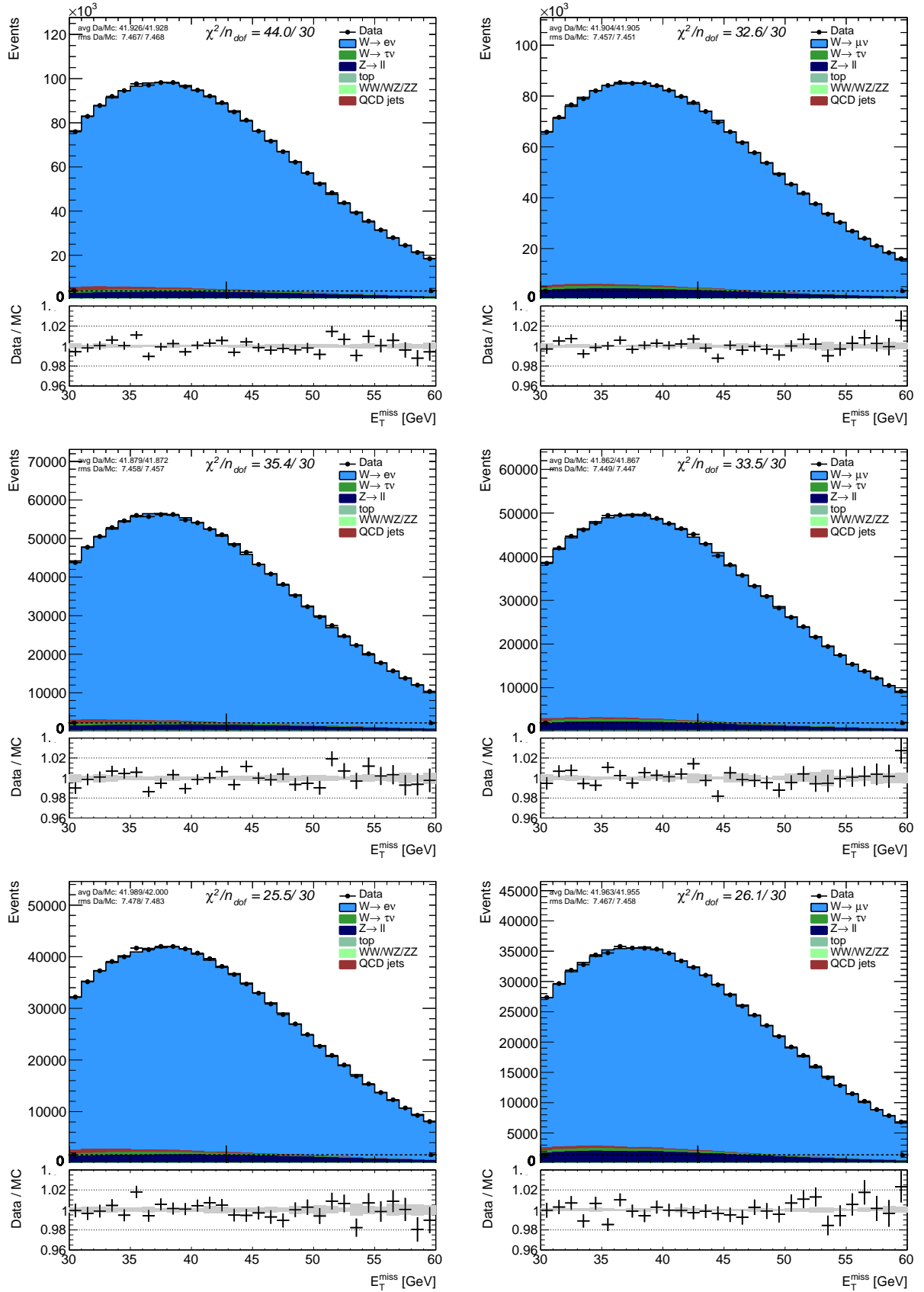


Figure C.9: Missing transverse energy distribution from $W \rightarrow e\nu$ (left) and $W \rightarrow \mu\nu$ (right); $W^+ \rightarrow e\nu$ (left) and $W^+ \rightarrow \mu\nu$ (right); $W^- \rightarrow e\nu$ (left) and $W^- \rightarrow \mu\nu$ (right), for $0.6 < |\eta| < 1.2$ in electron channel and $0.8 < |\eta| < 1.4$ in muon channel with the best mass fit template for each category. (W^\pm : upper row, W^+ : middle row, W^- : lower row)

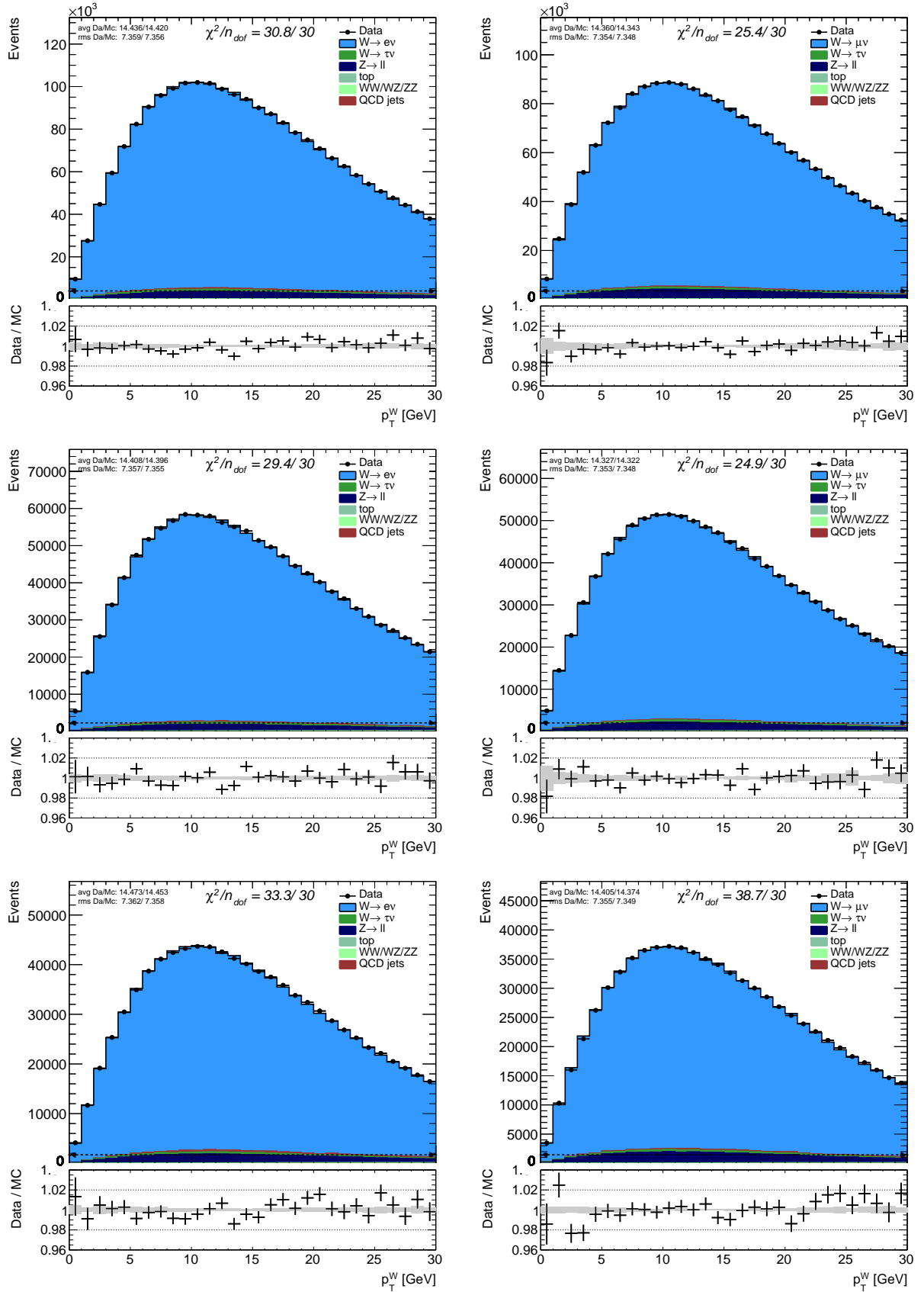


Figure C.10: Hadronic recoil distribution from $W \rightarrow e\nu$ (left) and $W \rightarrow \mu\nu$ (right); $W^+ \rightarrow e\nu$ (left) and $W^+ \rightarrow \mu\nu$ (right); $W^- \rightarrow e\nu$ (left) and $W^- \rightarrow \mu\nu$ (right), for $0.6 < |\eta| < 1.2$ in electron channel and $0.8 < |\eta| < 1.4$ in muon channel. (W^\pm : upper row, W^+ : middle row, W^- : lower row)

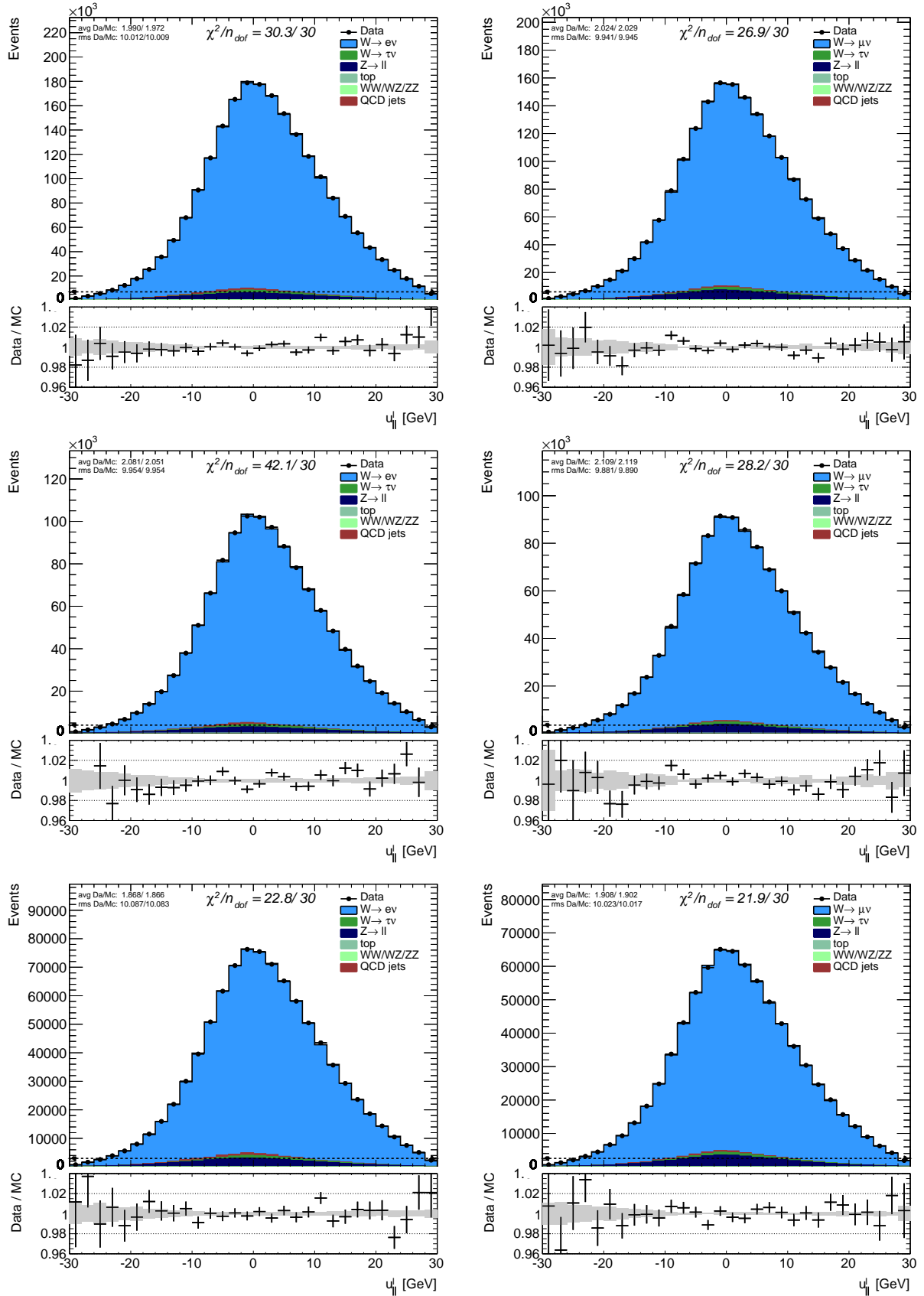
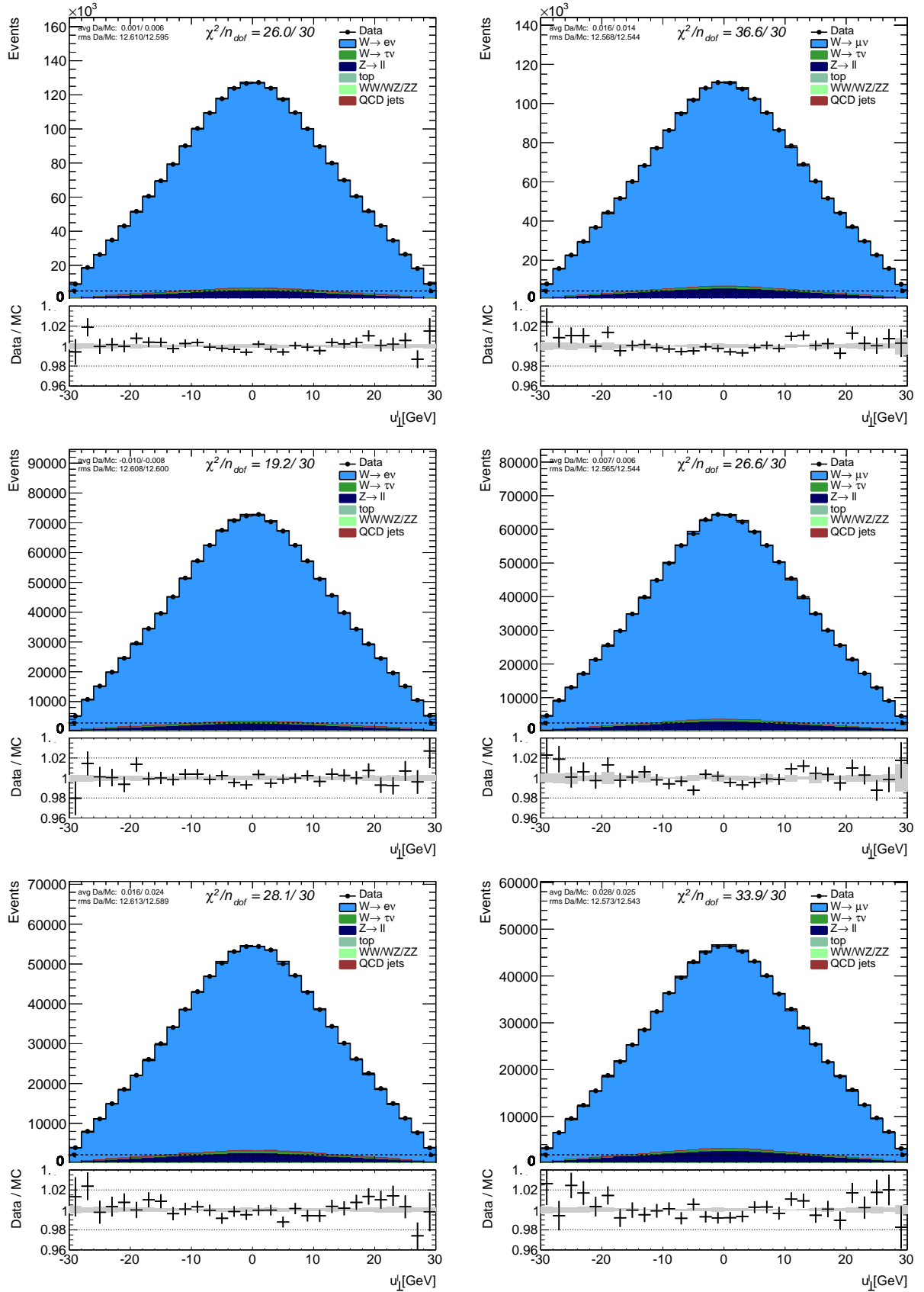


Figure C.11: Parallel projection of hadronic recoil distribution with respect to lepton p_T from $W \rightarrow e\nu$ (left) and $W \rightarrow \mu\nu$ (right); $W^+ \rightarrow e\nu$ (left) and $W^+ \rightarrow \mu\nu$ (right); $W^- \rightarrow e\nu$ (left) and $W^- \rightarrow \mu\nu$ (right), for $0.6 < |\eta| < 1.2$ in electron channel and $0.8 < |\eta| < 1.4$ in muon channel. (W^\pm : upper row, W^+ : middle row, W^- : lower row)



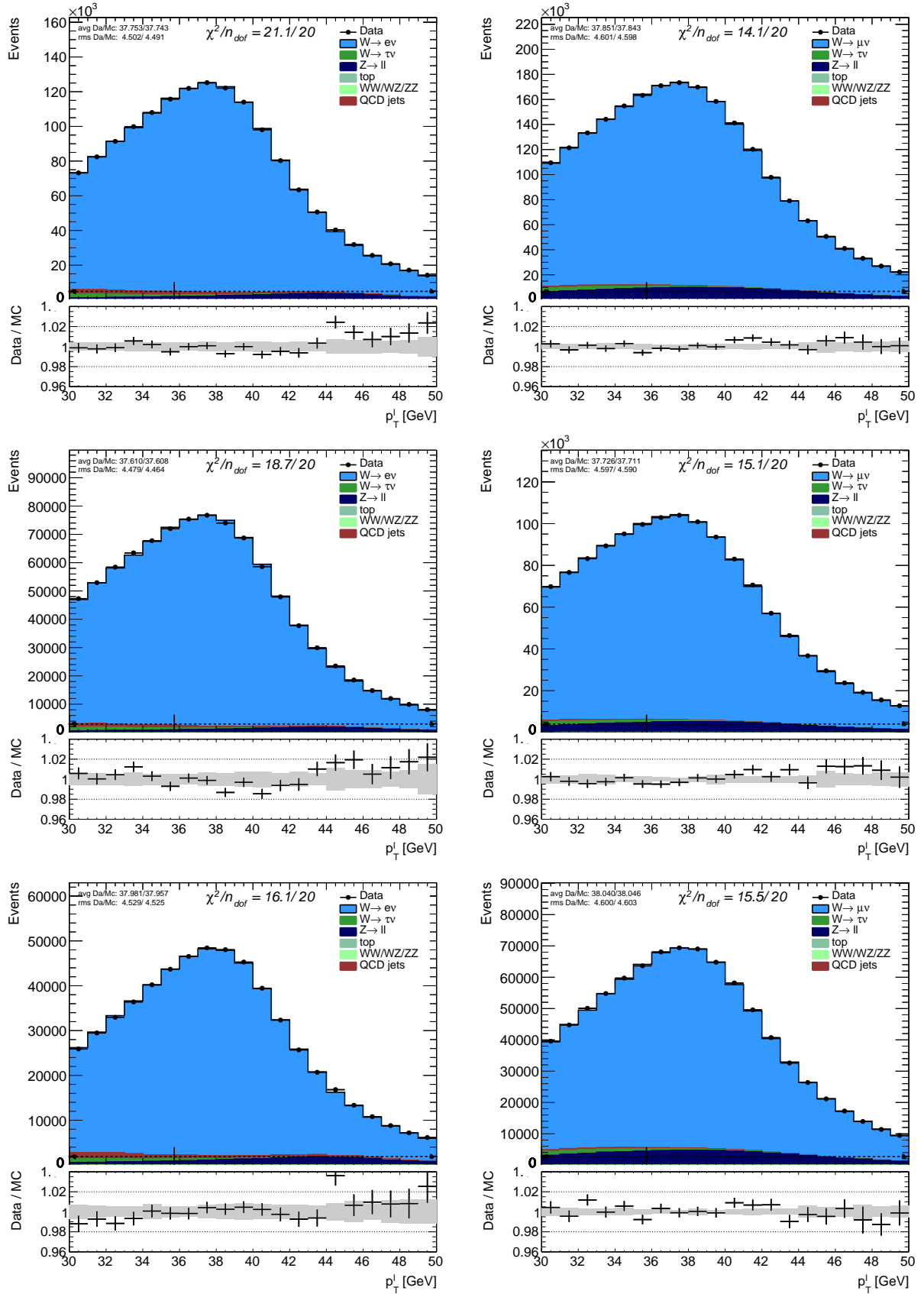


Figure C.13: Lepton p_T distribution from $W \rightarrow e\nu$ (left) and $W \rightarrow \mu\nu$ (right); $W^+ \rightarrow e\nu$ (left) and $W^+ \rightarrow \mu\nu$ (right); $W^- \rightarrow e\nu$ (left) and $W^- \rightarrow \mu\nu$ (right), for $1.8 < |\eta| < 2.4$ in electron channel and $1.4 < |\eta| < 2.0$ in muon channel with the best mass fit template for each category. (W^\pm : upper row, W^+ : middle row, W^- : lower row)

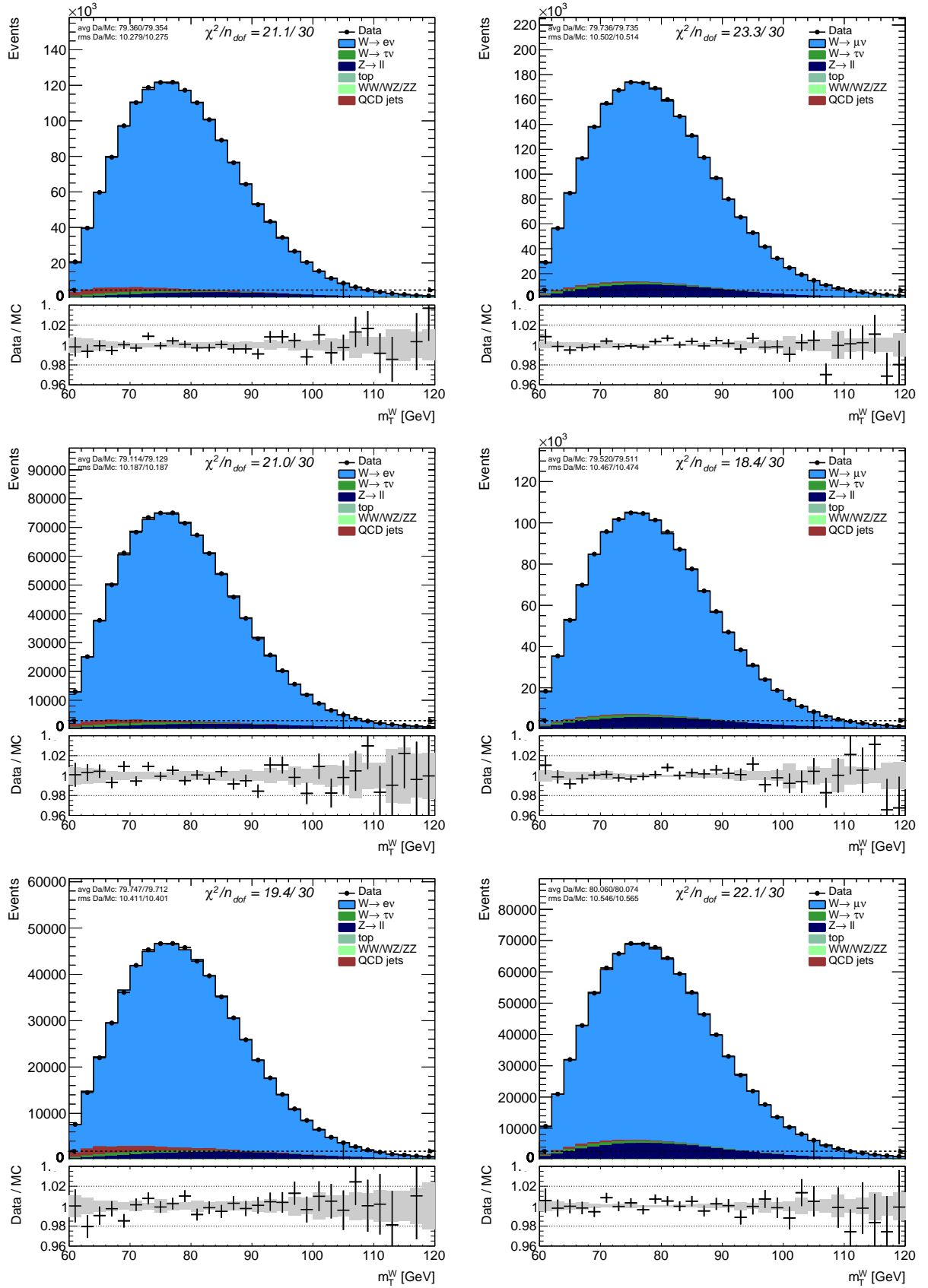


Figure C.14: Transverse mass distribution from $W \rightarrow e\nu$ (left) and $W \rightarrow \mu\nu$ (right); $W^+ \rightarrow e\nu$ (left) and $W^+ \rightarrow \mu\nu$ (right); $W^- \rightarrow e\nu$ (left) and $W^- \rightarrow \mu\nu$ (right), for $1.8 < |\eta| < 2.4$ in electron channel and $1.4 < |\eta| < 2.0$ in muon channel with the best mass fit template for each category. (W^\pm : upper row, W^+ : middle row, W^- : lower row)

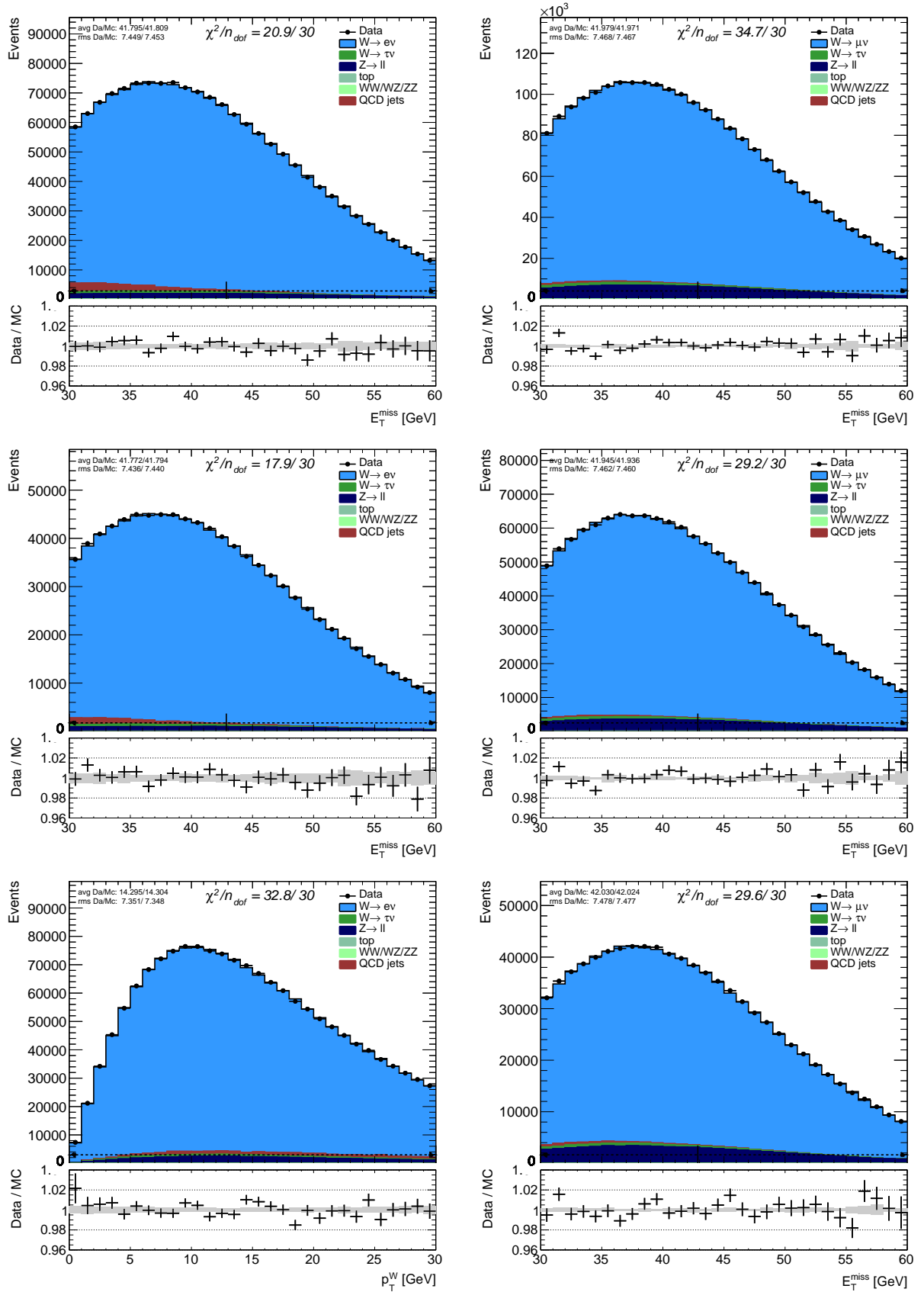


Figure C.15: Missing transverse energy distribution from $W \rightarrow e\nu$ (left) and $W \rightarrow \mu\nu$ (right); $W^+ \rightarrow e\nu$ (left) and $W^+ \rightarrow \mu\nu$ (right); $W^- \rightarrow e\nu$ (left) and $W^- \rightarrow \mu\nu$ (right), for $1.8 < |\eta| < 2.4$ in electron channel and $1.4 < |\eta| < 2.0$ in muon channel with the best mass fit template for each category. (W^\pm : upper row, W^+ : middle row, W^- : lower row)

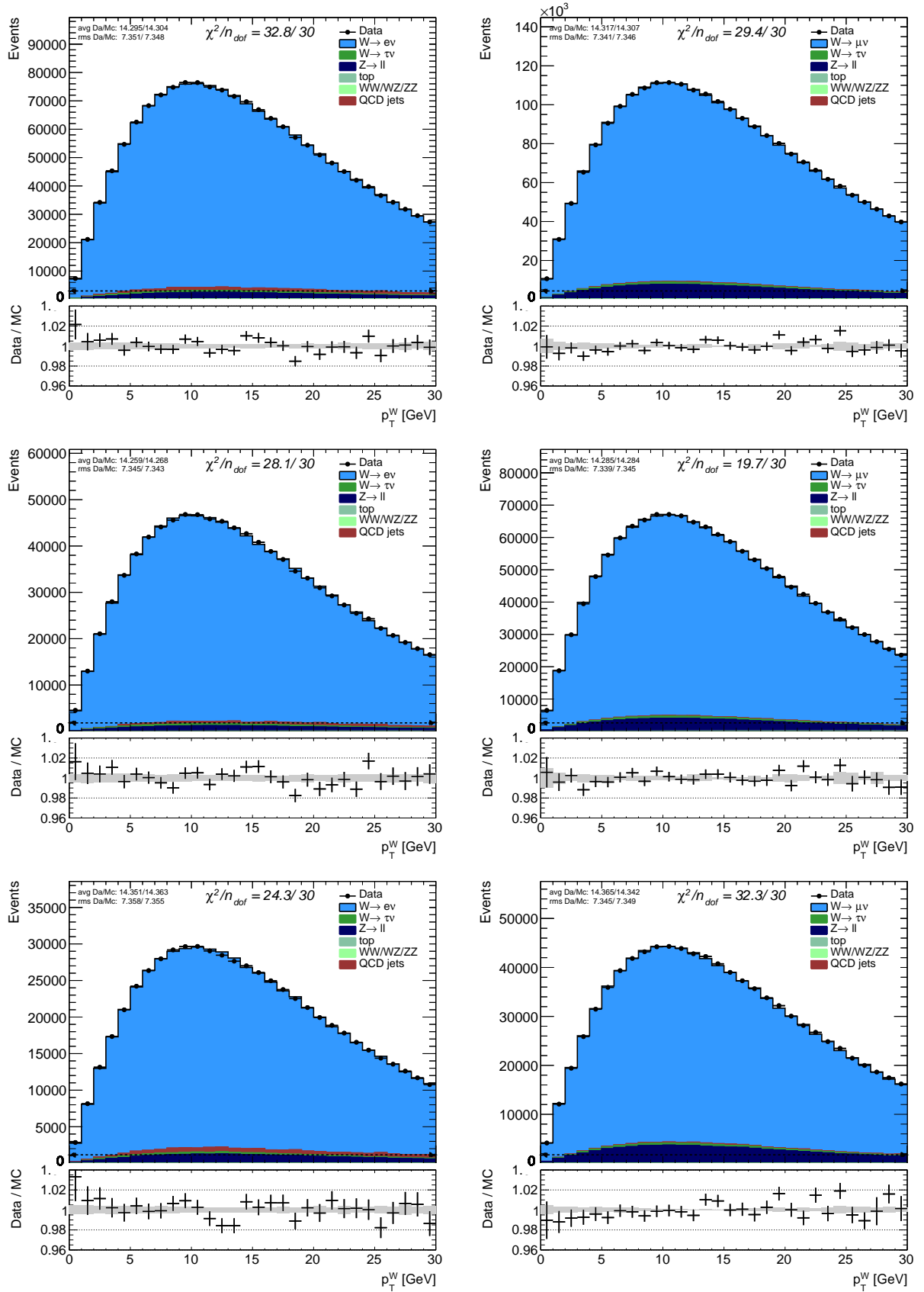


Figure C.16: Hadronic recoil distribution from $W \rightarrow e\nu$ (left) and $W \rightarrow \mu\nu$ (right); $W^+ \rightarrow e\nu$ (left) and $W^+ \rightarrow \mu\nu$ (right); $W^- \rightarrow e\nu$ (left) and $W^- \rightarrow \mu\nu$ (right), for $1.8 < |\eta| < 2.4$ in electron channel and $1.4 < |\eta| < 2.0$ in muon channel. (W^\pm : upper row, W^+ : middle row, W^- : lower row)

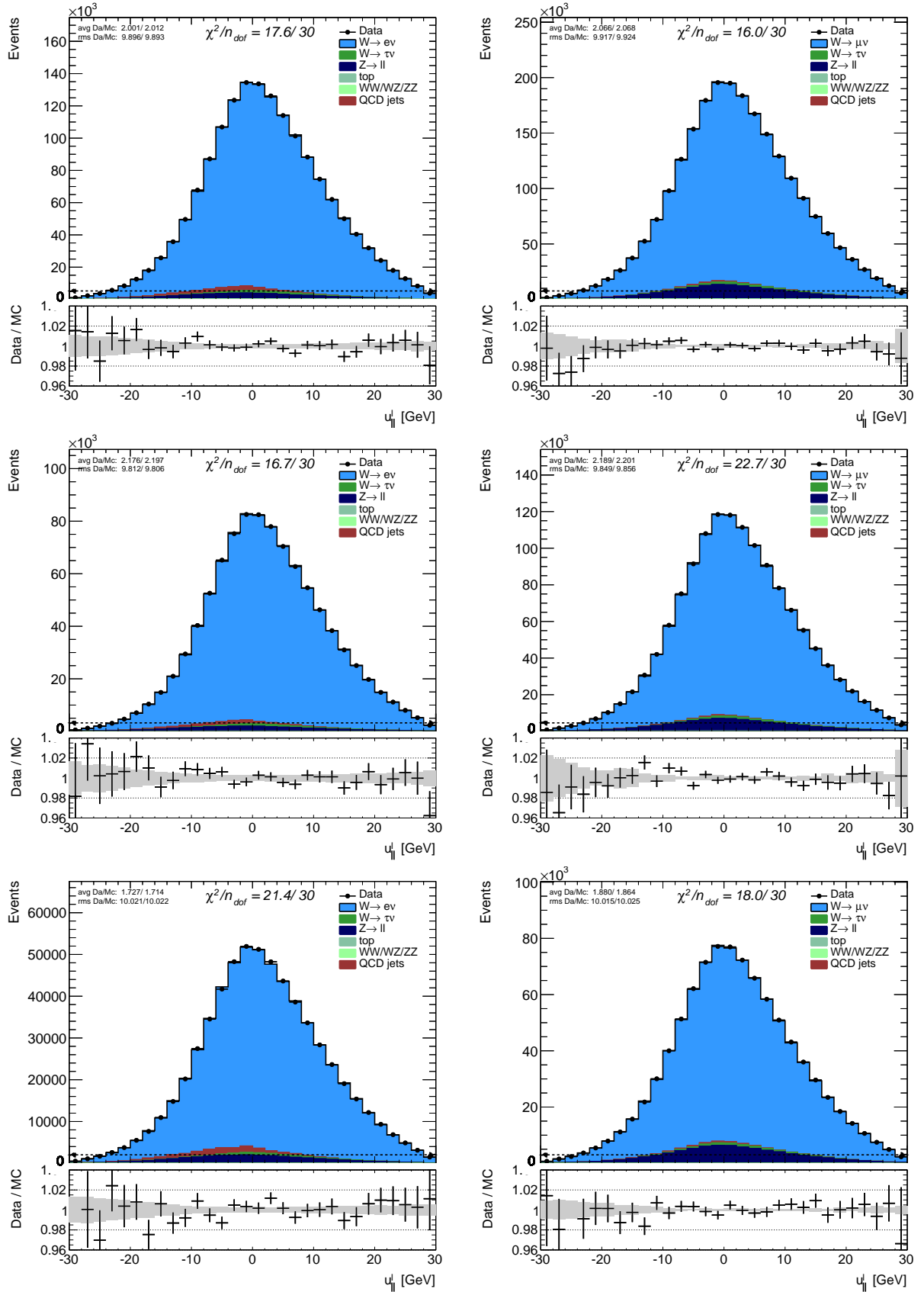
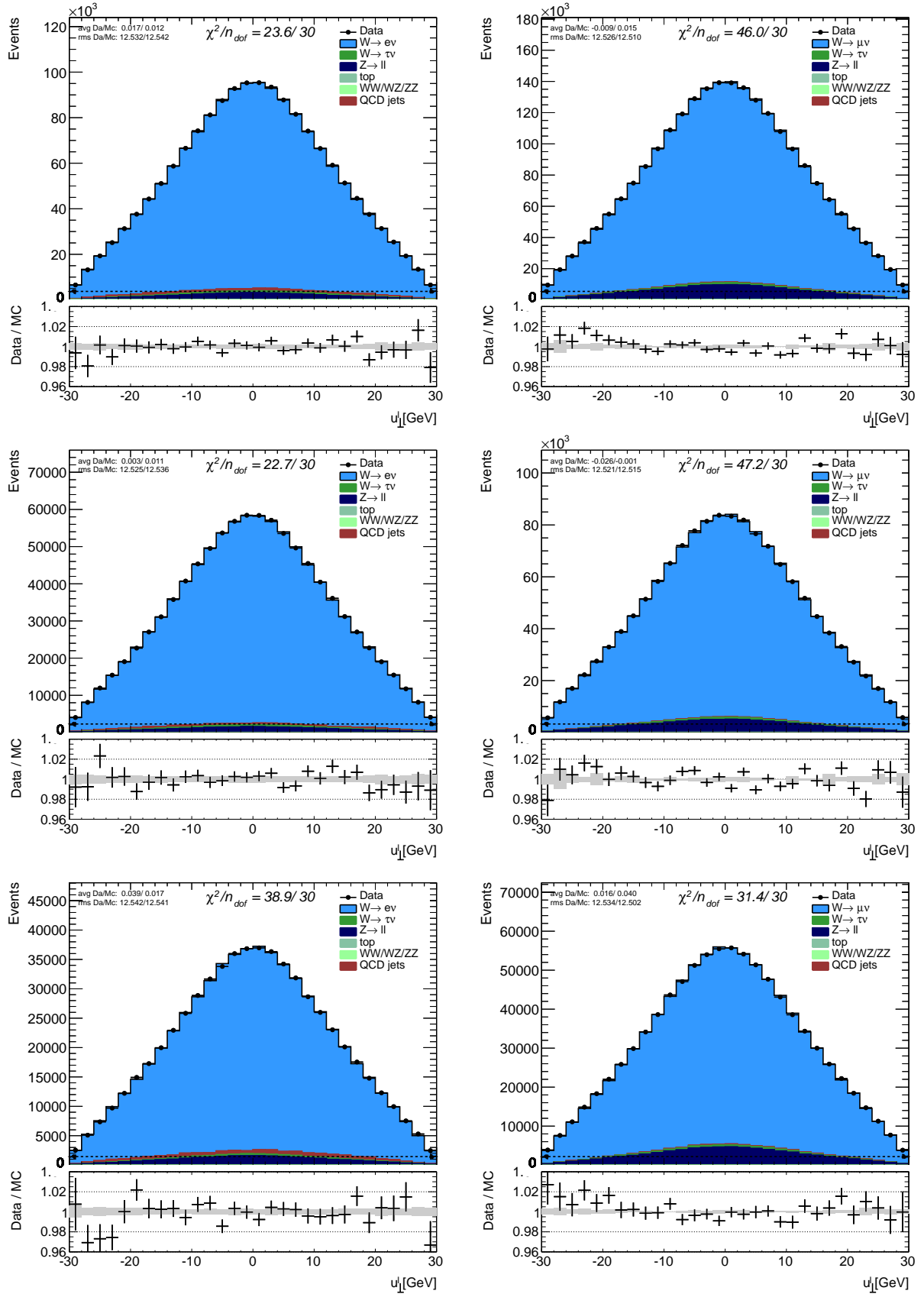


Figure C.17: Parallel projection of hadronic recoil distribution with respect to lepton p_T from $W \rightarrow e\nu$ (left) and $W \rightarrow \mu\nu$ (right); $W^+ \rightarrow e\nu$ (left) and $W^+ \rightarrow \mu\nu$ (right); $W^- \rightarrow e\nu$ (left) and $W^- \rightarrow \mu\nu$ (right), for $1.8 < |\eta| < 2.4$ in electron channel and $1.4 < |\eta| < 2.0$ in muon channel. (W^\pm : upper row, W^+ : middle row, W^- : lower row)



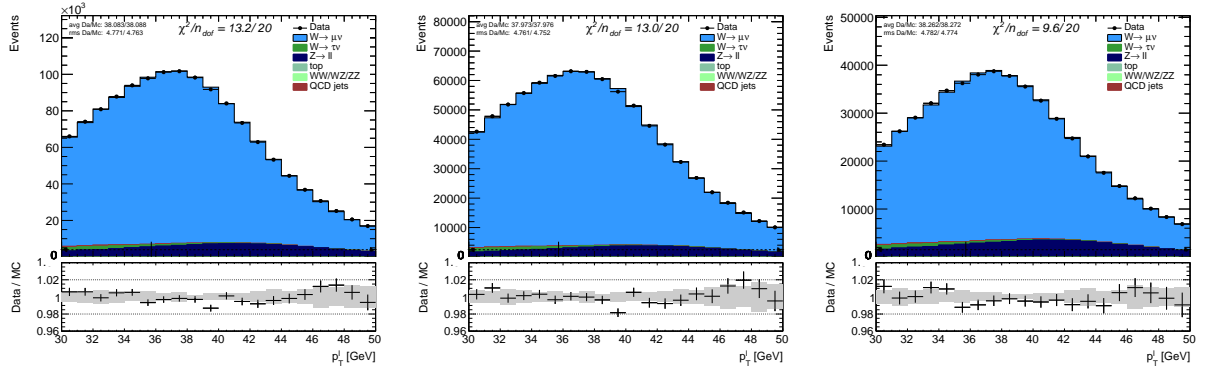


Figure C.19: Lepton p_T distribution from $W \rightarrow \mu\nu$; $W^+ \rightarrow \mu\nu$ (left) and $W^- \rightarrow \mu\nu$ (right), for $2.0 < |\eta| < 2.4$ with the best mass fit template for each category.

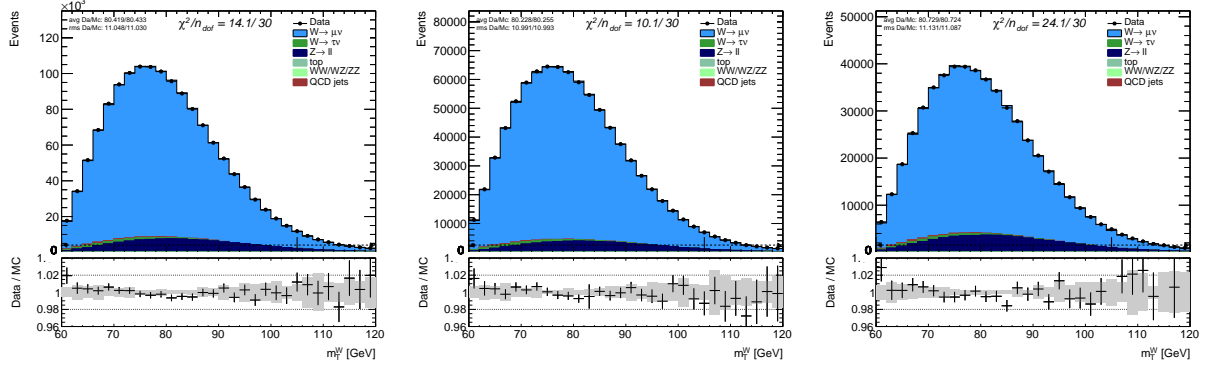


Figure C.20: Transverse mass distribution from $W \rightarrow \mu\nu$; $W^+ \rightarrow \mu\nu$ (left) and $W^- \rightarrow \mu\nu$ (right), for $2.0 < |\eta| < 2.4$ with the best mass fit template for each category.

ACKNOWLEDGEMENTS

First of all, I would like to express my deepest gratitude to my advisor, Maarten Boonekamp, for his support of my PhD studies. Oftentimes his suggestions moved me out of the stalemates and inspired me for new ideas. I can not imagine having better advisor, I really enjoyed all our discussions. I also would like to thank Philippe Schwemling, with whom I started to work on my qualification task in ATLAS, for giving me first knowledge and skills.

I also thank all of the members of my jury, for reviewing my work: Reza Ansari, Daniel Froidevaux, Luca Malgeri, Fulvio Piccinini, Boris Tuchming.

Besides, I am very thankful to everyone from the W mass group for appreciating my work. In particular, thanks to Matthias, Raimund, Nenad, Jean-Baptiste, Nancy, Chris, Stefano for many useful comments and great ideas. Special thanks to Aleksandra for her patience as I worked with her more than with all. Thanks to Remie for enduring me during two years.

Thanks to everyone in CEA/SPP for their companionship: Laurent, Jean-Francois, Pierre-Francois, Ahmimed, Frederic, Nathalie, Claude, Joao, Witold, Philippe. Big thanks to Romain, Remie and Fabrice for their frequent help in administration procedures.

Thanks to students at CEA for all the good times we spent: Marta, Romain, Eloi, Laura, Matthias, Arthur, Maria. Thank to Denys for taking the coffee breaks with me.

It was a great pleasure working with all of you.

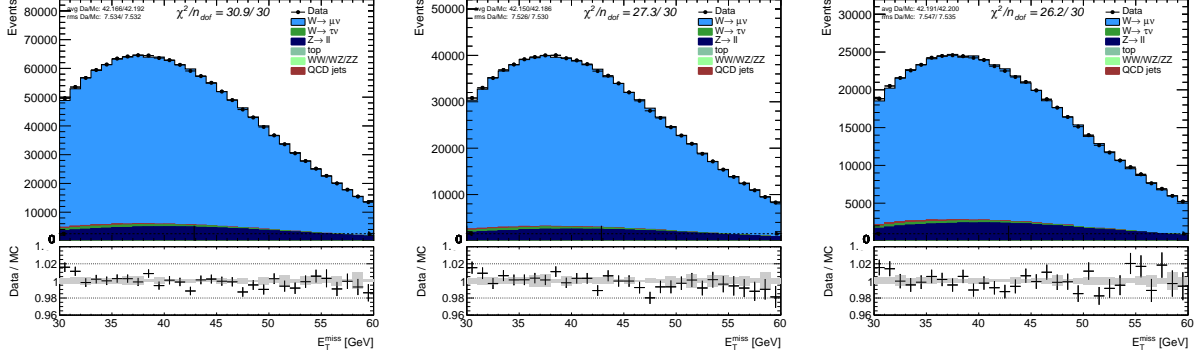


Figure C.21: Missing transverse energy distribution from $W \rightarrow \mu\nu$; $W^+ \rightarrow \mu\nu$ (left) and $W^- \rightarrow \mu\nu$ (right), for $2.0 < |\eta| < 2.4$ with the best mass fit template for each category.

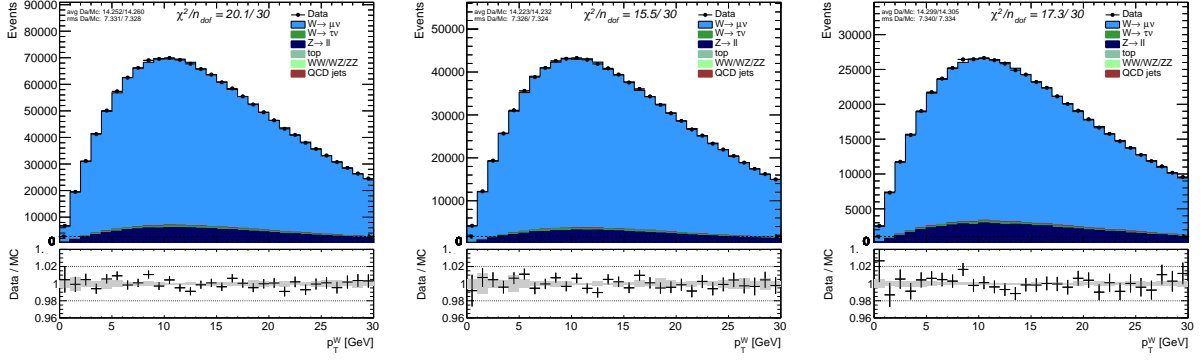


Figure C.22: Hadronic recoil distribution from $W \rightarrow \mu\nu$; $W^+ \rightarrow \mu\nu$ (left) and $W^- \rightarrow \mu\nu$ (right), for $2.0 < |\eta| < 2.4$.

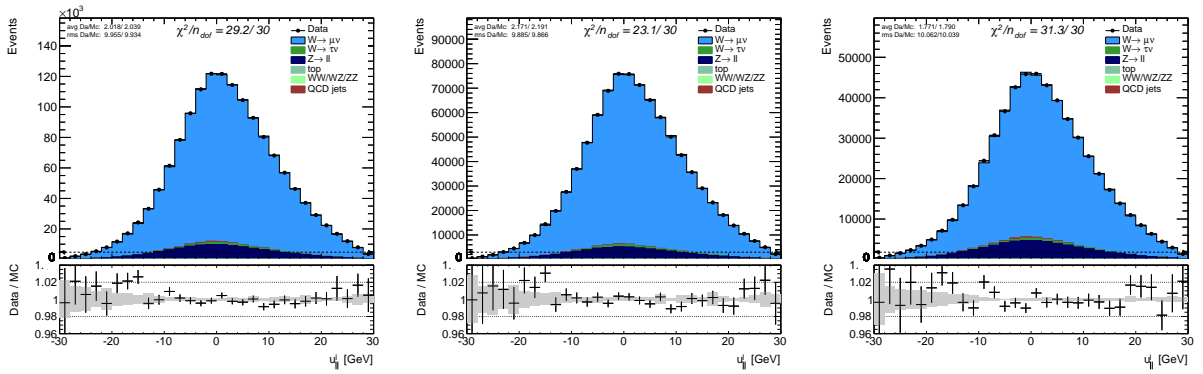


Figure C.23: Parallel projection of hadronic recoil distribution with respect to the p_T from $W \rightarrow \mu\nu$; $W^+ \rightarrow \mu\nu$ (left) and $W^- \rightarrow \mu\nu$ (right), for $2.0 < |\eta| < 2.4$.

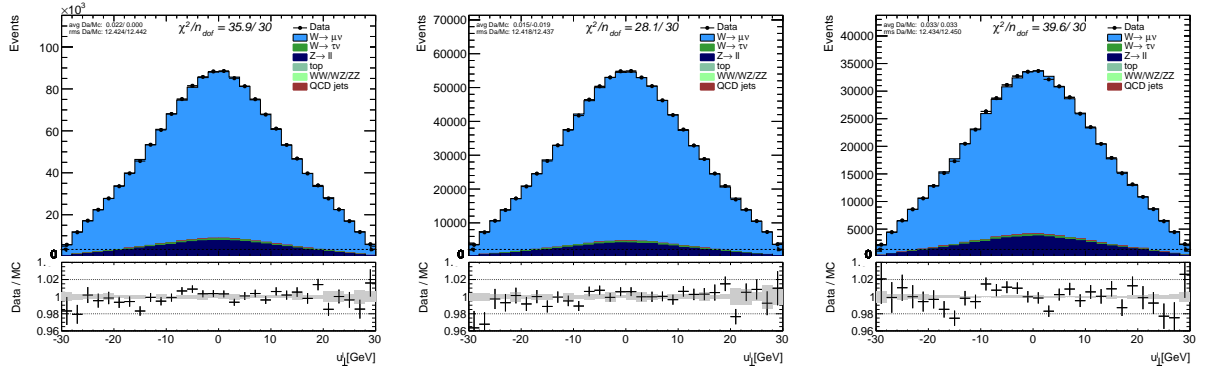


Figure C.24: Perpendicular projection of hadronic recoil distribution with respect to the p_T from $W \rightarrow \mu\nu$; $W^+ \rightarrow \mu\nu$ (left) and $W^- \rightarrow \mu\nu$ (right), for $2.0 < |\eta| < 2.4$.

List of Figures

1.1	Prediction of M_W as a function of m_t as obtained from electroweak fit, including (blue contour) and excluding (grey contour) Higgs boson mass M_H , as compared to the direct measurement (vertical and horizontal green bands and black dot). . . .	8
1.2	Prediction of M_W as a function of m_t . The green region corresponds to parameter scan within MSSM model. The red strip indicates the overlap region of the SM and the MSSM, with $M_H^{SM} = 125.6 \pm 0.7$ GeV.	9
1.3	<i>Left:</i> combined LEP W^+W^- cross-section measurements as a function of the center-of-mass energy compared with the SM predictions using $M_W = 80.35$ GeV. <i>Right:</i> Measurements of the W-boson mass by the LEP and Tevatron experiments. The world-average uncertainty (15 MeV) is indicated by the yellow band.	10
1.4	The CT14 parton distribution functions at $Q = 2$ GeV and $Q = 100$ GeV for $u, \bar{u}, d, \bar{d}, s = \bar{s}$ and g [17].	12
1.5	Standard model cross sections as predicted at the Tevatron (first vertical green line) and LHC (second vertical green line) colliders. The second vertical line corresponds to designed LHC energy of $\sqrt{s} = 14$ TeV.	13
1.6	The rapidity distribution of the differential cross sections for W^+, W^- and Z boson productions at $\sqrt{s} = 7$ TeV.	14
1.7	Differential cross section as a function of rapidity (<i>left</i>) and transverse momentum (<i>right</i>) for W^+ boson for different initial parton flavours.	15
2.1	Illustration of the LHC accelerator complex.	18
2.2	The total integrated luminosity recorded by ATLAS detector during 2011 data-taking period.	21
2.3	<i>Left:</i> Cut-away view of the ATLAS inner detector. <i>Right:</i> Illustration of the ID sensors and structural elements traversed by a charged track in the barrel inner detector ($ \eta = 0.3$)	22
2.4	The $R - z$ view of individual ATLAS Inner Detector components	23
2.5	<i>Left:</i> Illustration of the parameterised track [38]. <i>Right:</i> Amount of material traversed by a particle, in units of radiation length X_0 , as a function of $ \eta $	24
2.6	Three-dimensional view of the ATLAS calorimetry.	25
2.7	Segmentation of the barrel EM calorimeter showing the corresponding thickness in radiation length (upstream material included).	26
2.8	Read-out granularity and accordion shape of the EM calorimeter.	27
2.9	Side view of one quadrant (<i>left</i>) and transverse view (<i>right</i>) of the muon spectrometer.	28
2.10	Mechanical structure of a MDT chamber (<i>left</i>) and transverse cross section of the MDT tube (<i>right</i>).	29
3.1	Illustration of the muon track reconstruction and sagitta definition in the Muon Spectrometer.	31
3.2	Illustration of the track reconstruction in the Inner Detector	32
3.3	The pulse shape in the ATLAS LAr calorimeters. The unipolar triangular pulse is the current pulse in the liquid argon generated by fast ionising particles. t_d represents the drift time. The shaped pulse is superimposed with circles indicating 25 ns intervals. [41].	33
3.4	Projection of Hadronic Recoil on vector boson for the definition of $u_{ }$ and u_{\perp}	36
3.5	Definition of different zones in the calculation of the cluster-based hadronic recoil.	37

4.1	Average energies in central cell and its neighbour cells deposited by muons traversing central cell of middle (<i>left</i>) and strip (<i>right</i>) layer.	40
4.2	Block-scheme showing the strategy used for the crosstalk analysis.	41
4.3	Schematic illustration of muon energy deposits in cells of strip and middle layers of the EM calorimeter.	41
4.4	Comparison of the z_0 impact parameter distributions of selected muons in data and MC.	42
4.5	Average number of pileup interactions μ in data and MC.	42
4.6	Energy spectra deposited by muon in crossed cell E_0 , in the left neighbouring cell E_{-1} and in second neighbouring cell E_{-2} of middle layer in data. The central cell corresponds to $0 < \eta < 0.025$. Energy distributions are fitted with Gauss-Landau convolution. The center of the Gauss distribution (magenta colour) that corresponds to the noise is fixed at zero. The landau distribution (red line, shown only for central cell) represents the energy deposited by muon.	43
4.7	Energy spectra deposited by muon in crossed cell E_0 , in the left neighbouring cell E_{-1} and in second neighbouring cell E_{-2} of strip layer in data. The central cell corresponds to $0 < \eta < 0.003$. Energy distributions are fitted with Gauss-Landau convolution(plus additional gauss term in central cell). The center of the Gauss distribution (magenta colour) that corresponds to the noise is fixed at zero. The landau distribution (red line) represents the energy deposited by muon. The additional gaussian term in central cell (green) is needed to model the low energy tail caused by strip displacement (taken as distribution from the left strip).	44
4.8	Most probable energy distributions E_0 , E_{-1} , E_{+1} , E_{-2} and E_{+2} of strip layer in muon's rapidity bins respectively. The distributions are shown for data and all MC samples. The error bars correspond to the statistical uncertainty.	45
4.9	Most probable energy distributions E_0 , E_{-1} , E_{+1} , E_{-2} and E_{+2} of middle layer in muon's rapidity bins respectively. The distributions are shown for data and all MC samples. The error bars correspond to the statistical uncertainty.	46
4.10	Most probable energy distributions $S = MPV(E_{-2} + E_{-1} + E_0 + E_{+1} + E_{+2})$ in middle and strip samplings as a function of muon η . The distributions are shown for data and all MC samples. The error bars correspond to the statistical uncertainty.	47
4.11	The crosstalk map in barrel EM calorimeter used in athena and reconstructed from MC $E_\mu = 40$ GeV simulations. The $middle \rightarrow strip$, $middle \rightarrow middle + 1$, $strip \rightarrow strip + 1$ and $strip \rightarrow strip + 2$ crosstalks are shown. The results for $middle \rightarrow middle - 1$, $strip \rightarrow strip - 1$ and $strip \rightarrow strip - 2$ are similar and thus omitted here. The error bars correspond to the statistical uncertainty.	48
4.12	The estimated pile-up contribution using Eq.(4.4) in MeV in data and MC as a function of η observed in second neighbour cells (low signal) of middle (<i>left</i>) and strip (<i>right</i>) layers. Mismodeling of the pile-up contribution is observed to be about 3 MeV in middle and about 0.6 MeV in strip layers.	49
4.13	The W_1 (<i>left</i>) and W_0 (<i>right</i>) pile-up correction factors in strip layer extracted from MC (see Eq.(4.2)).	49
4.14	The W_1 (<i>left</i>) and W_0 (<i>right</i>) pile-up correction factors in middle layer extracted from MC (see Eq.(4.2)).	50
4.15	Ratio $E_{data/MC} = MPV(E_{data})/MPV(E_{MC})$ as a function of η in strip (<i>left</i>) and middle (<i>right</i>) layers.	50
4.16	The L1/L2 layer intercalibration scale factor $\alpha_{1/2}$	50
4.17	The global energy correction applied to data to equalize the total muon energy deposits in Data and MC.	51

4.18	The comparison of the MPV distributions in first neighbour cells extracted from strip sampling. The left side corresponds to data and the right side corresponds to MC. Distributions are shown after pile-up subtraction and energy scale corrections in data.	52
4.19	Impact of muon z_0 impact parameter shifts on the energy deposits in neighbour cell of strip layer.	52
4.20	Schematic illustration of cell displacement. Black arrow represents a muon direction crossing the calorimeter.	53
4.21	Profile of the deposited energy in strip cell crossed by muon as a function of $\Delta\eta$ between muon track and expected cell center position in data and MC. The muon pseudorapidity is required to have $-0.15 < \eta_\mu < -0.10$	53
4.22	Observed displacement of strip cells in terms of $\Delta\eta$ with respect to expected position as a function of η . The displacements are parametrized using Eq.4.9 and summarized in Table 4.1.	54
4.23	Observed displacement of strip cells in terms of $\Delta\eta$ as a function of azimuth in $0.55 < \eta < 0.6$ region. The horizontal line indicates the ϕ -integrated $\Delta\eta$ displacement that corresponds to Figure 4.22.	56
4.24	Example of fits with ϕ -dependent model introduced in equation (4.12). The following components are shown: <i>black</i> line represents ϕ -integrated A_0 coefficient; <i>blue</i> line represents effect of X_c, Y_c -shifts and tilts(A_1, B_1); <i>green-dashed</i> line represents the pear-shape deformation.	56
4.25	Comparisons of ΔR calorimeter deformation observed in survey and extracted from $Z \rightarrow \mu\mu$ analysis. The survey has been performed at a warm temperature.	57
4.26	The pear-shape deformation in (X, Y) plane in different η regions.	57
4.27	Impact of the pear-shape deformation of the calorimeter on the W boson mass extraction using electrons. The M_W values are plotted with respect to reference value.	57
4.28	The comparison of the MPV distributions in first neighbour cells extracted from strip sampling after correction of the position of strip cells.	58
4.29	The <i>middle</i> \rightarrow <i>strip</i> crosstalk in barrel EM calorimeter used in athena, reconstructed from MC $Z \rightarrow \mu\mu$ simulation and from data after all corrections are applied. The errors are statistical only.	58
4.30	The crosstalk map as a function of η in barrel EM calorimeter used in athena, reconstructed from MC $Z \rightarrow \mu\mu$ simulation and from data after all corrections are applied. The <i>middle</i> \rightarrow <i>middle</i> - 1, <i>middle</i> \rightarrow <i>middle</i> + 1, <i>strip</i> \rightarrow <i>strip</i> - 1, <i>strip</i> \rightarrow <i>strip</i> + 1, <i>strip</i> \rightarrow <i>strip</i> - 2 and <i>strip</i> \rightarrow <i>strip</i> + 2 crosstalks are shown. The errors are statistical only.	59
4.31	Difference <i>Data</i> - <i>MC</i> of energies collected in three strips, in central strip only and in neighbour strips only.	60
4.32	Impact of muon energy scale variation on the <i>middle</i> \rightarrow <i>middle</i> , <i>strip</i> \rightarrow <i>strip</i> and <i>strip</i> \rightarrow 2^{nd} <i>strip</i> cross-talk derivation in MC as a function of η	60
5.1	Combined values of $\delta_{sagitta}$ from E/p and $Z \rightarrow \mu\mu$ measurements.	65
5.2	Muon momentum scale corrections (a) and additional curvature resolution term (b) obtained from the $Z \rightarrow \mu\mu$ events. The resulting scale corrections are shown as function of η . The shown uncertainties are statistical.	66
5.3	Azimuthal dependence of the momentum calibration, before and after the ϕ -dependent correction. The plot corresponds to $-2.0 < \eta < -1.4$ bin.	67
5.4	Illustration of the Tag-and-Probe method. One strongly selected muon candidate in a $Z \rightarrow \mu\mu$ event is used as tag, while the other is used as a probe to investigate the reconstruction, trigger and isolation efficiencies, respectively.	68

5.5	Determined reconstruction efficiency by the tag- and probe-method for Data and MC.	69
5.6	Determined trigger efficiency by the tag- and probe-method for Data and MC. . .	69
5.7	Isolation efficiencies for Powheg, $p_T^{\text{cone20}}/p_T < 0.1$. From left to right, top to bottom: η , ϕ , p_T , $u_{ }^l$	70
5.8	Comparison of the data and MC distribution for positive (left) and negative (right) charged muons vs. η (top) and ϕ (bottom) in $Z \rightarrow \mu\mu$ events with applying all corrections factors to the muon reconstruction, muon isolation cut and muon trigger efficiencies.	71
5.9	The dielectron invariant mass distributions reconstructed in data and MC after complete electron calibration procedure.	72
5.10	(a) Azimuthal dependence of the energy calibration in $-1.2 < \eta_e < -0.6$ region, before and after the m_{ee} -based correction described in the text; (b) Azimuthal dependence of the E/p distribution mean in $-1.2 < \eta_e < -0.6$ region, after the m_{ee} -based correction described in the text.	73
5.11	Relative difference between the E/p profiles for positrons and electrons, as a function of $ \eta $, before (<i>left</i>) and after sagitta bias corrections (<i>right</i>). The empty region $1.4 < \eta < 1.82$ corresponds to the crack region in the calorimeter.	74
5.12	Azimuthal dependence of the E/p distribution mean, used to the define the ϕ intercalibration correction. The points represent the mean of the E/p distribution, calculated within the range $0.6 < E/p < 1.5$ for $Z \rightarrow ee$ events. The 12 ϕ bins cover $-\pi < \phi < \pi$ in bins of size $\pi/6$. The η bins are, from top left to bottom right, $-2.4 < \eta < -1.8$, $-1.2 < \eta < -0.6$, $-0.6 < \eta < 0$, $0 < \eta < 0.6$, $0.6 < \eta < 1.2$, $1.8 < \eta < 2.4$	75
5.13	Measured value of m_W as a function of ϕ_e , before (left) and after (right) the intercalibration correction based on E/p	76
5.14	Comparison of the E/p distribution in data and simulation, for $W \rightarrow e\nu$ and $Z \rightarrow ee$ events.	76
5.15	Comparison of the E/p distribution in $Z \rightarrow ee$ data and simulation, for electrons with and without TRT hits associated to the nominal track.	77
5.16	E/p distributions in $Z \rightarrow ee$ simulation, for the nominal ATLAS geometry (s1718) and geometries with Inner Detector material distortions described in the text (from top left to bottom right: s1814, s1816 barrel region, s1816 endcap region, s1895 and s1818). Since s1816 contains two independent material variations located in the barrel and in the endcap respectively, the comparison with the nominal geometry is performed separately for barrel and endcap electrons. The ratio panels show the ratio between the distorted geometry and the nominal geometry.	78
5.17	Top row: geometrical view of the “LAr hole” in W events (left) and Z (right) events taken during periods E-H. Middle and bottom rows: electron η and ϕ distributions for the data affected (left) or not (right) by the EM calorimeter failure.	80
5.18	Comparison of the data and MC distribution as a function of electrons pseudorapidity η (<i>left</i>) and ϕ (<i>right</i>) in $Z \rightarrow ee$ events after applying all efficiency correction factors. The calorimeter crack region $1.2 < \eta < 1.8$ has been excluded.	82
5.19	(a) Mean number of interactions per bunch crossing, (b) number of vertices, (c) ΣE_T distribution and (d) $\Sigma E_T - u$ distribution in Data (points) and MC (solid line) after pile-up reweighting and rescaling the $\langle \mu \rangle$ distribution by 1.1.	84
5.20	An example of the Smirnov transform procedure for $\Sigma E_T - u$ distribution for the bin $10 < p_T(Z) < 20$ GeV.	85
5.21	$\Sigma E_T - u$ distribution in Data and MC before and after the transformation as described in the text, where MC T in the legend denotes the transformed $\Sigma E_T - u$ distribution. The transformation is defined in bins of p_T^Z	85

5.22	Hadronic recoil distribution in Data (points) and MC (solid line) in $Z \rightarrow \mu^+\mu^-$ events: (a) x -component of the hadronic recoil, (b) y -component of the hadronic recoil, (c) φ distribution of the hadronic recoil. Distributions are obtained after the pile-up reweighting and rescaling the $\langle \mu \rangle$ distribution by 1.1.	86
5.23	Mean of u_X and u_Y distributions in Data (black points) and MC (blue points) in $Z \rightarrow \mu^+\mu^-$ events: (a) and (b) as a function of $\Sigma E_T - u$, (c) and (d) as a function of φ of the di-muon system. Distributions are obtained after the pile-up reweighting and rescaling the $\langle \mu \rangle$ distribution by 1.1.	87
5.24	Hadronic recoil distribution in Data (points) and MC (solid line) in $Z \rightarrow \mu^+\mu^-$ events: (a) parallel projection of the hadronic recoil on the transverse momentum of the vector boson, (b) sum of parallel projection of the hadronic recoil and the vector boson p_T^Z , (c) perpendicular projection of the hadronic recoil on the transverse momentum of the vector boson, (d) hadronic recoil distribution. Distributions are obtained after the pile-up reweighting, rescaling the $\langle \mu \rangle$ distribution by 1.1 and applying the u_X and u_Y correction.	88
5.25	Schematic view of the correction procedure: resolution of u_\perp as a function of $\Sigma E_T - u$. There are three resolution curves: Data in dotted red (σ_{Data}), MC in solid black (σ_{MC}) and MC as a function of $(\Sigma E_T - u)^{tr}$ in dotted black (σ'_{MC}). Step 1 \rightarrow 2 represents the transformation of $\Sigma E_T - u$ in MC; step 2 \rightarrow 3 is the actual resolution correction (difference in resolution between Data and MC for a given value of $(\Sigma E_T - u)^{tr}$	89
5.26	The RMS of u_\perp as a function of $\langle \mu \rangle$ in Z boson events for Data and MC. . . .	89
5.27	Hadronic recoil distribution in Data and MC before and after the hadronic recoil corrections in $Z \rightarrow \mu^+\mu^-$ events inclusive in $\langle \mu \rangle$. (a) Projection of the hadronic recoil to the parallel to the transverse momentum of the vector boson. (b) Sum of parallel projection of the hadronic recoil to the transverse momentum of the vector boson and the transverse momentum of the vector boson. (c) Projection of the hadronic recoil to the perpendicular to the transverse momentum of the vector boson. (d) Hadronic recoil distribution.	91
5.28	Hadronic recoil distribution in Data and MC before and after the hadronic recoil corrections in $Z \rightarrow e^+e^-$ events inclusive in $\langle \mu \rangle$. (a) Projection of the hadronic recoil to the parallel to the transverse momentum of the vector boson. (b) Sum of parallel projection of the hadronic recoil to the transverse momentum of the vector boson and the transverse momentum of the vector boson. (c) Projection of the hadronic recoil to the perpendicular to the transverse momentum of the vector boson. (d) Hadronic recoil distribution.	92
5.29	Hadronic recoil distribution in W^\pm (a), W^+ (b) and W^- (c) for inclusive $\langle \mu \rangle$ after recoil corrections with systematics uncertainties due to variation of all corrections. . . .	93
5.30	Perpendicular component of hadronic recoil distribution in (left) data and MC for Z events and (right) MC for Z, W^+ and W^- events, after ΣE_T reweighting. . . .	93
6.1	FSR treatment as applied in ATLAS using PHOTOS. The dot represents the matrix element for a single photon emission. After each photon emission, the outgoing lepton lines (right of the dashed line) are considered by PHOTOS again for further photon emissions, in an interactive way.	97
6.2	Comparison of the electron pair invariant mass distribution (left) and the muon transverse momentum distribution (right) at various levels of QED corrections. “No FSR” refers to Born-level leptons; “approx ME” and “exact ME” refer to the implementations of references [60] and [59] (see text).	98

6.3	Ratios between the “exact ME” and “approx ME” predictions (“Exp+ME/Exp” in the plots), for $W \rightarrow e\nu$ (left) and $W \rightarrow \mu\nu$ (right). The observables shown are charged lepton p_T (top), neutrino p_T (middle), and transverse mass (bottom). Events were generated using POWHEG+PYTHIA, interfaced to PHOTOS.	99
6.4	Ratios between the “exact ME” and “approx ME” predictions (“Exp+ME/Exp” in the plots), for $Z \rightarrow ee$ (left) and $Z \rightarrow \mu\mu$ (right). The observables shown are negatively charged lepton p_T (top), positively charged lepton p_T (middle), and lepton pair invariant mass (bottom). Events were generated using POWHEG+PYTHIA, interfaced to PHOTOS.	100
6.5	Ratios between the “Exp+PE” and “Exp” predictions, for $W \rightarrow e\nu$ (left) and $W \rightarrow \mu\nu$ (right). The observables shown are leading charged lepton p_T (top), neutrino p_T (middle) and transverse mass (bottom). No selection is applied except to require that $ \eta < 2.4$ for the leading charged lepton. Events were generated using PYTHIA+PHOTOS.	101
6.6	Ratios between the “Exp+PE” and “Exp” predictions, for $Z \rightarrow ee$ (left) and $Z \rightarrow \mu\mu$ (right). The observables shown are leading negatively charged lepton p_T (top), leading positively charged lepton p_T (middle) and leading lepton pair invariant mass (bottom). No selection is applied except to require that $ \eta < 2.4$ for the leading charged leptons. Events were generated using PYTHIA+PHOTOS.	102
6.7	Examples of pair emission in Drell-Yan process: virtual pair (left) or real pair (right) NLO correction.	102
6.8	Contribution of pair emission to the NLO QED corrections shown as $\delta = \frac{\sigma^{NLO} - \sigma^{Born}}{\sigma^{Born}}$ as a function of the $\mu^- p_T$ in $Z \rightarrow \mu^+ \mu^-$ events. For the estimation of σ^{NLO} the electron pair emission only has been switched on, there is no photonic radiation.	103
6.9	FSR, full QED and full NLO EW corrections from WINHAC, in absence of QCD radiations effects (i.e. the parton shower is switched off), for $W \rightarrow \mu\nu$ events using bare kinematics. Left column: the ratios are taken to the Born distributions; right column: the ratio is taken to the FSR-corrected distribution.	105
6.10	FSR, full QED and full NLO EW corrections from WINHAC, with QCD corrections from the PYTHIA parton shower, for $W \rightarrow \mu\nu$ events using bare kinematics. Left column: the ratios are taken to the Born distributions; right column: the ratio is taken to the FSR-corrected distribution.	106
6.11	Effect of QCD corrections on the muon-neutrino invariant mass distribution. Left column: effect of switching the parton shower on and off in WINHAC, on the Born-level distribution (top), on the distribution after FSR (middle), and for the NLO EW distribution (bottom). Right column: effect of switching the $O(\alpha_S)$ correction on and off in POWHEG, while keeping the parton shower active. Born-level distribution (top), distribution after FSR (middle), and NLO EW distribution (bottom).	108
6.12	Comparison of the EW-corrected kinematic distributions, in the G_μ and α_0 schemes, to the FSR-corrected predictions, using WINHAC. Left: without parton shower; right: with parton shower.	109
6.13	Differential cross section of W^+ (left) and W^- (right) production as a function of rapidity for the CT10nnlo PDF set. The blue line and the red line show predictions to the W^- and Z -boson rapidity measurements, respectively. The shadowed bands correspond to the PDF uncertainty.	111
6.14	Ratio of differential cross section of W^+ (left) and W^- (right) production as a function of rapidity for the CT10nnlo (blue), CT14nnlo (red), and MMHT2014nnlo (green) PDF sets. The shadowed bands correspond to the PDF uncertainty.	111

6.15	(a) Differential Z -boson cross-section as a function of boson rapidity, and (b) differential W^+ and W^- cross-sections as a function of charged decay-lepton pseudorapidity at $\sqrt{s} = 7\text{ TeV}$ [55]. The measured cross sections are compared to the DNNLO predictions using the CT10nnlo PDF set. The vertical bars show the total experimental uncertainties, including luminosity uncertainty, and the bands show the PDF uncertainties of the predictions.	112
6.16	Angular coefficients for the Z , W^+ and W^- bosons for POWHEG+PYTHIA8, DNNLO NLO and DNNLO NNLO	114
6.17	p_T distributions of the Z boson (left) and decay lepton (right) at the truth level before and after polarisation reweighting of the angular coefficients from POWHEG to DNNLO.	115
6.18	The (a) A_0 and (b) A_2 angular coefficients in Z -boson events as a function of p_T . The measured coefficients are compared to the DNNLO predictions using the CT10nnlo PDF set. The vertical bars show the total experimental uncertainties, and the bands show the uncertainties assigned to the theoretical predictions.	115
6.19	Measured differential cross section of $p_T(Z)$ (left) and the differential cross-section ratio of $\sigma(W)/\sigma(Z)$ vs. $p_T(V=W,Z)$ (right) compared to the POWHEG+PYTHIA prediction, reweighted to the AZ tune. Statistical and experimental systematic uncertainties are indicated.	116
6.20	Ratio between the p_T^W distribution obtained from the tune variations ($1\pm$, $2\pm$, $3\pm$) and the nominal tune.	117
6.21	Top row : relative effect on the boson transverse momentum distribution of varying the charm quark mass for W^\pm (top) and Z (middle). Effect of varying the bottom quark mass for Z (bottom).	119
6.22	Relative effect on the boson transverse momentum distribution of varying the LO PDF in the parton shower, compared to MMHTLO, for Z (top), W^+ (middle), W^- (bottom).	119
6.23	Uncertainty on the $p_T^{W^+}/p_T^Z$ and $p_T^{W^-}/p_T^Z$ distribution ratios from LO PDF variations. The uncertainty is defined from the CT14 LO PDF, as this PDF gives the strongest difference between the W^+ , W^- and Z p_T distributions	120
6.24	Relative effect on the boson transverse momentum distribution of varying the parton shower factorization scale, μ_F , for W^\pm (top) and Z (middle). Bottom: ratio of the W and Z p_T distributions varying the values of μ_F using the decorrelation model described in the text.	120
6.25	PDF-induced uncertainty on the the p_T^W distribution, with and without the p_T^Z constraint, for W^+ (left) and W^- (right).	126
6.26	Left: comparison of the measured and predicted A_i coefficients, for Z production as a function of p_T^Z . In the case of A_2 , an uncertainty on the prediction is defined from a parametrization of the observed discrepancy with the data. Right: the corresponding predictions and uncertainties for W production.	127
6.27	Measurement uncertainty on the A_i coefficients, as a function of p_T^Z [71].	128
6.28	Correlations of given angular coefficient measurements across the p_T^Z range used for the measurement [71].	129
6.29	Correlations among the measured A_i coefficients, in a choice of fixed p_T^Z bins [71].	130
6.30	Toy MC error propagation. Left: considering only statistical uncertainty from the A_i measurement on Z data. Right: considering full (statistical+systematics) uncertainties from the A_i measurement on Z data.	130

- 7.1 Example of multijet template fits of E_T^{miss} , m_T^W and p_T^μ/m_T^W distributions in FR1 and FR2, for integrated $W^+ \rightarrow \mu^+\bar{\nu}$ selection. Multijet distribution is extracted from $0.2 < \sum p_T^{\text{trk}}/p_T < 0.4$ region. The fitting range is indicated by the dashed arrow. The estimated multijet fraction in the SR is specified in the figure. 141
- 7.2 Example of multijet template fits of E_T^{miss} , m_T^W and p_T^μ/m_T^W distributions in FR1 and FR2, for integrated $W^- \rightarrow \mu^-\nu$ selection. Multijet distribution is extracted from $0.2 < \sum p_T^{\text{trk}}/p_T < 0.4$ region. The fitting range is indicated by the dashed arrow. The estimated multijet fraction in the SR is given in the figure. 142
- 7.3 E_T^{miss} in data and simulation with multijet background injected with the same fraction, but extracted from different isolation regions: $0.10 < p_T^{\text{cone20}}/p_T^\mu < 0.13$ (*left*) and $0.37 < p_T^{\text{cone20}}/p_T^\mu < 0.40$ (*right*). The cuts $E_T^{\text{miss}} > 30$ GeV, $m_T^W > 60$ GeV and $p_T^W < 30$ GeV are removed in order to increase the impact of the multijet background. 143
- 7.4 Fitted multijet background yield in the signal region plotted in bins of the isolation variable used to define the data-driven distributions. Error bars at each point are the combination of statistical uncertainty coming from the fraction fits and uncertainties due to $\pm 2.5\%\sigma$ variations of predicted non-multijet contamination in the CR. The center of black/red ellipse at $p_T^{\text{cone20}}/p_T^\mu \sim 0$ is the expected average isolation value of the multi-jet background in the signal region, while the radius of red (black) ellipse is equal to total (method) uncertainty. 144
- 7.5 Example of multijet template fits of E_T^{miss} , m_T^W and p_T^e/m_T^W distributions in FR1 and FR2, for integrated $W^+ \rightarrow e^+\bar{\nu}$ selection. Multijet background templates are derived from data using an anti-isolation requirement on the p_T^{cone40} variable, as described in the text. The fitting range is indicated by the dashed arrow. The estimated multijet fraction in the SR is given in the figure. 147
- 7.6 Example of multijet template fits of E_T^{miss} , m_T^W and p_T^μ/m_T^W distributions in FR1 and FR2, for integrated $W^- \rightarrow e^-\nu$ selection. Multijet background templates are derived from data using an anti-isolation requirement on the p_T^{cone40} variable, as described in the text. The fitting range is indicated by the dashed arrow. The estimated multijet fraction in the SR is given in the figure. 148
- 7.7 Fitted multijet background yield in the signal region plotted in bins of the isolation variable used to define the data-driven distributions. Error bars at each point are the combination of statistical uncertainty coming from the fraction fits and uncertainties due to $\pm 2.5\%\sigma$ variations of predicted non-multijet contamination in the CR. The center of black/red ellipse at $p_T^{\text{cone20}} \sim 0$ corresponds to the central value of multi-jet background, while the radius of red (black) ellipse is equal to total (method) uncertainty. 149
- 7.8 Fitted multijet background fraction in the charge-blinded signal region using three definitions of multijet control region. The figure (a) corresponds to the nominal control region. 149
- 7.9 Comparison of measured QCD multijet background fractions in the four channels $W^+ \rightarrow \mu\nu$, $W^- \rightarrow \mu\nu$, $W^+ \rightarrow e\nu$ and $W^- \rightarrow e\nu$ obtained with the cross section analysis (full black dots) and W mass analysis (open circles) methods. The first point shown at $|\eta| < 0$ 151
- 7.10 Comparison of measured multijet background yield in the $W^+ \rightarrow \mu\nu$ channel using three different missing energy definitions: track-based (left), calorimeter-based (middle) and HR-based (right) as used in W mass analysis. 152
- 7.11 Comparison of measured multijet background yield in the $W^- \rightarrow \mu\nu$ channel using three different missing energy definitions: track-based (left), calorimeter-based (middle) and HR-based (right) as used in W mass analysis. 153

7.12	Examples of $p_T^\mu, m_T^W, E_T^{\text{miss}}$ and η_μ multijet distributions extracted from CR1 and CR2 and corresponding transfer functions (shown in the ratio) in the $W^+ \rightarrow \mu\nu$ channel.	155
7.13	Examples of $p_T^e, m_T^W, E_T^{\text{miss}}$ and η_e multijet distributions extracted from CR1 and CR2 and corresponding transfer functions (shown in the ratio) in the $W^+ \rightarrow e\nu$ channel.	156
7.14	Extracted m_W values for different shapes of the multijet background using template fits on p_T^μ, m_T^W and E_T^{miss} distributions in $W^+ \rightarrow \mu\nu$ (<i>left</i>) and $W^- \rightarrow \mu\nu$ (<i>right</i>) channels. Error bars are statistical only. The values are plotted in bins of the isolation variable used to define the data-driven distributions. Two triangular points correspond to multijet shapes extracted from CR1 and CR2 described in the text. The m_W obtained after shape correction procedure is indicated by circular point. Red points correspond to shapes from smaller isolation slices, which are then extrapolated to the signal region with a linear fit.	157
7.15	Extracted m_W values for different shapes of the multijet background using template fits on p_T^e (upper row), m_T^W (middle row) and E_T^{miss} (lower row) distributions in $W^+ \rightarrow e\nu$ (<i>left</i>) and $W^- \rightarrow e\nu$ (<i>right</i>) channels. Error bars are statistical only. The values are plotted in bins of the isolation variable used to define the data-driven distributions. Two triangular points correspond to multijet shapes extracted from CR1 and CR2 described in the text. The m_W obtained after shape correction procedure is indicated by circular point. Red points correspond to shapes from smaller isolation slices, which are then extrapolated to the signal region with a linear fit. It should be noted that the fully correct extrapolation point would be the average isolation value *for the jet background* in the signal region. Since there is currently no reliable method to estimate this, we extrapolate to 0 as it is simpler (i.e. well defined) and always conservative.	158
7.16	Lepton pseudorapidity distribution from $W \rightarrow e\nu$ (left) and $W \rightarrow \mu\nu$ (right); $W^+ \rightarrow e\nu$ (left) and $W^+ \rightarrow \mu\nu$ (right); $W^- \rightarrow e\nu$ (left) and $W^- \rightarrow \mu\nu$ (right). (W^\pm : upper row, W^+ : middle row, W^- : lower row).	161
7.17	Lepton φ distribution from $W \rightarrow e\nu$ (left) and $W \rightarrow \mu\nu$ (right); $W^+ \rightarrow e\nu$ (left) and $W^+ \rightarrow \mu\nu$ (right); $W^- \rightarrow e\nu$ (left) and $W^- \rightarrow \mu\nu$ (right). (W^\pm : upper row, W^+ : middle row, W^- : lower row)	162
7.18	Lepton p_T^ℓ distribution from $W \rightarrow e\nu$ (left) and $W \rightarrow \mu\nu$ (right); $W^+ \rightarrow e\nu$ (left) and $W^+ \rightarrow \mu\nu$ (right); $W^- \rightarrow e\nu$ (left) and $W^- \rightarrow \mu\nu$ (right) with the best mass fit template for each category. (W^\pm : upper row, W^+ : middle row, W^- : lower row)	163
7.19	Transverse mass distribution from $W \rightarrow e\nu$ (left) and $W \rightarrow \mu\nu$ (right); $W^+ \rightarrow e\nu$ (left) and $W^+ \rightarrow \mu\nu$ (right); $W^- \rightarrow e\nu$ (left) and $W^- \rightarrow \mu\nu$ (right) with the best mass fit template for each category. (W^\pm : upper row, W^+ : middle row, W^- : lower row)	164
7.20	Missing transverse energy distribution from $W \rightarrow e\nu$ (left) and $W \rightarrow \mu\nu$ (right); $W^+ \rightarrow e\nu$ (left) and $W^+ \rightarrow \mu\nu$ (right); $W^- \rightarrow e\nu$ (left) and $W^- \rightarrow \mu\nu$ (right) with the best mass fit template for each category. (W^\pm : upper row, W^+ : middle row, W^- : lower row)	165
7.21	Hadronic recoil distribution from $W \rightarrow e\nu$ (left) and $W \rightarrow \mu\nu$ (right); $W^+ \rightarrow e\nu$ (left) and $W^+ \rightarrow \mu\nu$ (right); $W^- \rightarrow e\nu$ (left) and $W^- \rightarrow \mu\nu$ (right). (W^\pm : upper row, W^+ : middle row, W^- : lower row)	166
7.22	Parallel projection of hadronic recoil distribution with respect to lepton p_T from $W \rightarrow e\nu$ (left) and $W \rightarrow \mu\nu$ (right); $W^+ \rightarrow e\nu$ (left) and $W^+ \rightarrow \mu\nu$ (right); $W^- \rightarrow e\nu$ (left) and $W^- \rightarrow \mu\nu$ (right). (W^\pm : upper row, W^+ : middle row, W^- : lower row)	167

7.23	Perpendicular projection of hadronic recoil distribution with respect to lepton p_T from $W \rightarrow e\nu$ (left) and $W \rightarrow \mu\nu$ (right); $W^+ \rightarrow e\nu$ (left) and $W^+ \rightarrow \mu\nu$ (right); $W^- \rightarrow e\nu$ (left) and $W^- \rightarrow \mu\nu$ (right). (W^\pm : upper row, W^+ : middle row, W^- : lower row)	168
8.1	The p_T^ℓ spectra in muon (left) and electron (right) channels at truth level with and without requirement on low p_T^W values, and with detector effects.	171
8.2	Templates of the p_T^ℓ (left) and m_T^W (right) distributions for three different assumed M_W masses using a typical LHC detector response.	172
8.3	Selected control plots from the consistency tests. The 'best' fitting template corresponds to the template which leads to the minimal χ^2 value, while the 'worst' fitting template leads to the highest tested χ^2 value in the given fitting range of m_W . . .	174
8.4	$m_{\ell\ell}$ (top), $y_{\ell\ell}$ (middle) and $p_{T\ell\ell}$ (bottom) distributions after all experimental corrections and after polarisation reweighting from Powheg+Pythia8 to DYNNLO except A4. The electron and muon channels are shown on the left and on the right, respectively. The dashed line indicates the range over which the averages, RMS and χ^2 values are computed.	178
8.5	p_T^μ and $M_T^Z(\mu)$ distributions in pseudo $W^+ \rightarrow \mu^+\nu$ (left) and $W^- \rightarrow \mu^-\nu$ (right) channels as well as parallel u_\parallel and perpendicular u_\perp projections of the recoil on the p_T^Z direction after all corrections applied. The dashed line indicates the range over which the averages, RMS and χ^2 values are computed.	179
8.6	p_T^e and $M_T^Z(e)$ distributions in pseudo $W^+ \rightarrow e^+\nu$ (left) and $W^- \rightarrow e^-\nu$ (right) channels as well as parallel u_\parallel and perpendicular u_\perp projections of the recoil on the p_T^Z direction after all corrections applied. The dashed line indicates the range over which the averages, RMS and χ^2 values are computed.	180
8.7	Summary of the p_T^ℓ -based mass fits results for muons (left) and electrons (right). The error bars are statistical only.	181
8.8	$ \eta $ dependence of the lepton p_T fit results. The error bars are statistical only. . . .	182
8.9	$ \eta $ dependence of the lepton m_T fit results. The error bars are statistical only. . .	182
8.10	Blinded p_T^l and m_T fit results as a function of lepton pseudorapidity for electron (left) and muon (right) channel, with the nominal event selection. Error bars are statistical only. The result is given as a shift with respect to the assumed value of m_W in the MC, plus an unknown offset.	184
8.11	The m_W value obtained from a fit to the m_T distribution against the m_W value obtained from a fit to the p_T^ℓ distribution for 1000 pseudo-datasets.	186
8.12	The m_W value obtained from a fit to the m_T distribution against the m_W value obtained from a fit to the p_T^ℓ distribution for 1000 pseudo-datasets. Each plot corresponds to a different selection requirement on the lepton $ \eta $ (the range is indicated on each plot).	186
8.13	Combination of all p_T^l fit results (upper half) and m_T fit results (lower half) in all channels and categories using the CT10 PDF set. The full uncertainties of each individual fit are indicated. The result is given as a shift with respect to the assumed value of m_W in the MC, plus an unknown offset.	189
8.14	Combination of all p_T^l fit results in electron (left) and muon (right) channels. The result is given as a shift with respect to the assumed value of m_W in the MC, plus an unknown offset.	191
8.15	Combination of all m_T fit results in electron (left) and muon (right) channels. The result is given as a shift with respect to the assumed value of m_W in the MC, plus an unknown offset.	192

8.16	Combination of all p_T^1 fit results in electron and muon channels for W^+ (left) and W^- (right). The result is given as a shift with respect to the assumed value of m_W in the MC, plus an unknown offset.	192
8.17	Combination of all m_T fit results in electron and muon channels for W^+ (left) and W^- (right). The result is given as a shift with respect to the assumed value of m_W in the MC, plus an unknown offset.	192
8.18	Combination of all fit results in electron and muon channels for W^+ (left) and W^- (right). The result is given as a shift with respect to the assumed value of m_W in the MC, plus an unknown offset.	193
8.19	Fit results for different fitting ranges using the p_T^ℓ distribution (left) and m_T distribution (right) in the muon channel. The uncorrelated statistical uncertainties are indicated in green, the total uncorrelated uncertainties between the different fitting ranges are shown as blue line. As reference, the nominal fitting range is chosen. . .	194
8.20	Dependence of the statistical and systematic uncertainties on the fitting ranges in the p_T^ℓ distribution (left) and m_T distribution (right) in the muon channel. . . .	195
8.21	Fit results for different fitting ranges using the p_T^ℓ distribution (left) and m_T distribution (right) in the electron channel. The uncorrelated statistical uncertainties are indicated in green, the total uncorrelated uncertainties between the different fitting ranges are shown as blue line. As reference, the nominal fitting range is chosen. . .	195
8.22	Dependence of the statistical and systematic uncertainties on the fitting ranges in the p_T^ℓ distribution (left) and m_T distribution (right) in the electron channel. . . .	196
8.23	Fit results for different fitting ranges when only p_T^ℓ range (left) and m_T range (right) is varied for the combination. The uncorrelated statistical uncertainties are indicated in green, the total uncorrelated uncertainties between the different fitting ranges are shown as blue line. As reference, the nominal fitting range is chosen. . .	196
8.24	Dependence of the statistical and systematic uncertainties on the fitting ranges for the combination when only p_T^ℓ range (left) and when only m_T range is varied (right). .	197
8.25	Combination of all p_T^1 fit results (upper half) and m_T fit results (lower half) in all channels and categories using the CT10 PDF set with the optimal fitting range. The full uncertainties of each individual fit are indicated. The result is given as a shift with respect to the assumed value of m_W in the MC, plus an unknown offset. . . .	198
8.26	Combination of all p_T^1 fit results in electron (left) and muon (right) channels with the optimal fitting range. The result is given as a shift with respect to the assumed value of m_W in the MC, plus an unknown offset.	200
8.27	Combination of all m_T fit results in electron (left) and muon (right) channels with the optimal fitting range. The result is given as a shift with respect to the assumed value of m_W in the MC, plus an unknown offset.	200
8.28	Combination of all fit results in electron (left) and muon (right) channels with the optimal fitting range. The result is given as a shift with respect to the assumed value of m_W in the MC, plus an unknown offset.	200
8.29	Combination of all p_T^1 fit results in electron and muon channels for W^+ (left) and W^- (right) with the optimal fitting range. The result is given as a shift with respect to the assumed value of m_W in the MC, plus an unknown offset.	201
8.30	Combination of all m_T fit results in electron and muon channels for W^+ (left) and W^- (right) with the optimal fitting range. The result is given as a shift with respect to the assumed value of m_W in the MC, plus an unknown offset.	201
8.31	Combination of all fit results in electron and muon channels for W^+ (left) and W^- (right) with the optimal fitting range. The result is given as a shift with respect to the assumed value of m_W in the MC, plus an unknown offset.	202
8.32	Fit results using p_T^ℓ , m_T and E_T^{miss} for the electron channel (left) and the muon channel (right) for different η regions.	203

8.33	Fit results using p_T^ℓ and m_T for the electron channel (left) and the muon channel (right) for different regions in $\langle \mu \rangle$ (upper-row: 2.5-6.5, middle-row: 6.5-9.5, lower row: 9.5-16).	204
8.34	Fit results using p_T^ℓ and m_T for the electron channel (left) and the muon channel (right) for events with $0 < u < 15$ GeV (upper row) and $15 < u < 30$ GeV (lower row))	205
8.35	Fit results using p_T^ℓ and m_T for the electron channel (left) and the muon channel (right) for events with $u_{ } < 0$ (upper row) and $0 < u_{ }$ (lower row).	206
8.36	Comparison of the results of this analysis (violet dot) with other published results for m_W . This includes the most precise measurements from LEP including ALEPH, DELPHI, L3 and OPAL and from the Tevatron collider experiments D0, and CDF. The light and dark grey bands show the statistical and total uncertainties of the ATLAS measurement, the blue bands and blue lines show the statistical and total uncertainties of the other published results. Measured values of m_W for positively- and negatively-charged W bosons are also shown (red dots).	208
8.37	The measured values of m_W (red dots) are compared to the SM prediction from the electroweak fit (violet dot), and to the combined values of m_W measured at LEP and at the Tevatron collider (blue dots). The light grey band shows the uncertainty of the SM prediction from the electroweak fit, assuming $m_t = 173.34 \pm 0.76$ GeV and $m_H = 125.09 \pm 0.24$ GeV.	208
8.38	The 68% and 95% confidence level contours of the m_W and m_t indirect determination from the global electroweak fit [12] (grey ellipses) are compared to the 68% and 95% confidence level contours of the ATLAS measurements of the top-quark and W boson masses (red and orange ellipses). The determination from the electroweak fit uses as input the LHC measurement of the Higgs boson mass, $m_H = 125.09 \pm 0.24$ GeV. The light and dark blue bands indicate the uncertainties on the ATLAS measurements of m_W and m_t	208
B.1	Results of the profiling on the gluon (g), valence (u_V , d_V), and sea (\bar{u} , \bar{d} and s) CT10nnlo PDFs. Σ represents the sum of the sea quarks PDFs.	219
B.2	Results of the profiling on the gluon (g), valence (u_V , d_V), and sea (\bar{u} , \bar{d} and s) CT14nnlo PDFs. Σ represents the sum of the sea quarks PDFs.	219
B.3	Results of the profiling on the gluon (g), valence (u_V , d_V), and sea (\bar{u} , \bar{d} and s) MMHT PDFs. Σ represents the sum of the sea quarks PDFs.	220
B.4	Differential cross section as a function of rapidity for 2011 Z data before and after profiling of the CT10nnlo PDF	221
C.1	Lepton p_T distribution from $W \rightarrow e\nu$ (left) and $W \rightarrow \mu\nu$ (right); $W^+ \rightarrow e\nu$ (left) and $W^+ \rightarrow \mu\nu$ (right); $W^- \rightarrow e\nu$ (left) and $W^- \rightarrow \mu\nu$ (right), for $ \eta < 0.6$ in electron channel and $ \eta < 0.8$ in muon channel with the best mass fit template for each category. (W^\pm : upper row, W^+ : middle row, W^- : lower row)	224
C.2	Transverse mass distribution from $W \rightarrow e\nu$ (left) and $W \rightarrow \mu\nu$ (right); $W^+ \rightarrow e\nu$ (left) and $W^+ \rightarrow \mu\nu$ (right); $W^- \rightarrow e\nu$ (left) and $W^- \rightarrow \mu\nu$ (right), for $ \eta < 0.6$ in electron channel and $ \eta < 0.8$ in muon channel with the best mass fit template for each category. (W^\pm : upper row, W^+ : middle row, W^- : lower row)	225
C.3	Missing transverse energy distribution from $W \rightarrow e\nu$ (left) and $W \rightarrow \mu\nu$ (right); $W^+ \rightarrow e\nu$ (left) and $W^+ \rightarrow \mu\nu$ (right); $W^- \rightarrow e\nu$ (left) and $W^- \rightarrow \mu\nu$ (right), for $ \eta < 0.6$ in electron channel and $ \eta < 0.8$ in muon channel with the best mass fit template for each category. (W^\pm : upper row, W^+ : middle row, W^- : lower row)	226

C.4	Hadronic recoil distribution from $W \rightarrow e\nu$ (left) and $W \rightarrow \mu\nu$ (right); $W^+ \rightarrow e\nu$ (left) and $W^+ \rightarrow \mu\nu$ (right); $W^- \rightarrow e\nu$ (left) and $W^- \rightarrow \mu\nu$ (right), for $ \eta < 0.6$ in electron channel and $ \eta < 0.8$ in muon channel. (W^\pm : upper row, W^+ : middle row, W^- : lower row)	227
C.5	Parallel projection of hadronic recoil distribution with respect to lepton p_T from $W \rightarrow e\nu$ (left) and $W \rightarrow \mu\nu$ (right); $W^+ \rightarrow e\nu$ (left) and $W^+ \rightarrow \mu\nu$ (right); $W^- \rightarrow e\nu$ (left) and $W^- \rightarrow \mu\nu$ (right), for $ \eta < 0.6$ in electron channel and $ \eta < 0.8$ in muon channel. (W^\pm : upper row, W^+ : middle row, W^- : lower row)	228
C.6	Perpendicular projection of hadronic recoil distribution with respect to lepton p_T from $W \rightarrow e\nu$ (left) and $W \rightarrow \mu\nu$ (right); $W^+ \rightarrow e\nu$ (left) and $W^+ \rightarrow \mu\nu$ (right); $W^- \rightarrow e\nu$ (left) and $W^- \rightarrow \mu\nu$ (right), for $ \eta < 0.6$ in electron channel and $ \eta < 0.8$ in muon channel. (W^\pm : upper row, W^+ : middle row, W^- : lower row)	229
C.7	Lepton p_T distribution from $W \rightarrow e\nu$ (left) and $W \rightarrow \mu\nu$ (right); $W^+ \rightarrow e\nu$ (left) and $W^+ \rightarrow \mu\nu$ (right); $W^- \rightarrow e\nu$ (left) and $W^- \rightarrow \mu\nu$ (right), for $0.6 < \eta < 1.2$ in electron channel and $0.8 < \eta < 1.4$ in muon channel with the best mass fit template for each category. (W^\pm : upper row, W^+ : middle row, W^- : lower row)	230
C.8	Transverse mass distribution from $W \rightarrow e\nu$ (left) and $W \rightarrow \mu\nu$ (right); $W^+ \rightarrow e\nu$ (left) and $W^+ \rightarrow \mu\nu$ (right); $W^- \rightarrow e\nu$ (left) and $W^- \rightarrow \mu\nu$ (right), for $0.6 < \eta < 1.2$ in electron channel and $0.8 < \eta < 1.4$ in muon channel with the best mass fit template for each category. (W^\pm : upper row, W^+ : middle row, W^- : lower row)	231
C.9	Missing transverse energy distribution from $W \rightarrow e\nu$ (left) and $W \rightarrow \mu\nu$ (right); $W^+ \rightarrow e\nu$ (left) and $W^+ \rightarrow \mu\nu$ (right); $W^- \rightarrow e\nu$ (left) and $W^- \rightarrow \mu\nu$ (right), for $0.6 < \eta < 1.2$ in electron channel and $0.8 < \eta < 1.4$ in muon channel with the best mass fit template for each category. (W^\pm : upper row, W^+ : middle row, W^- : lower row)	232
C.10	Hadronic recoil distribution from $W \rightarrow e\nu$ (left) and $W \rightarrow \mu\nu$ (right); $W^+ \rightarrow e\nu$ (left) and $W^+ \rightarrow \mu\nu$ (right); $W^- \rightarrow e\nu$ (left) and $W^- \rightarrow \mu\nu$ (right), for $0.6 < \eta < 1.2$ in electron channel and $0.8 < \eta < 1.4$ in muon channel. (W^\pm : upper row, W^+ : middle row, W^- : lower row)	233
C.11	Parallel projection of hadronic recoil distribution with respect to lepton p_T from $W \rightarrow e\nu$ (left) and $W \rightarrow \mu\nu$ (right); $W^+ \rightarrow e\nu$ (left) and $W^+ \rightarrow \mu\nu$ (right); $W^- \rightarrow e\nu$ (left) and $W^- \rightarrow \mu\nu$ (right), for $0.6 < \eta < 1.2$ in electron channel and $0.8 < \eta < 1.4$ in muon channel. (W^\pm : upper row, W^+ : middle row, W^- : lower row)	234
C.12	Perpendicular projection of hadronic recoil distribution with respect to lepton p_T from $W \rightarrow e\nu$ (left) and $W \rightarrow \mu\nu$ (right); $W^+ \rightarrow e\nu$ (left) and $W^+ \rightarrow \mu\nu$ (right); $W^- \rightarrow e\nu$ (left) and $W^- \rightarrow \mu\nu$ (right), for $0.6 < \eta < 1.2$ in electron channel and $0.8 < \eta < 1.4$ in muon channel. (W^\pm : upper row, W^+ : middle row, W^- : lower row)	235
C.13	Lepton p_T distribution from $W \rightarrow e\nu$ (left) and $W \rightarrow \mu\nu$ (right); $W^+ \rightarrow e\nu$ (left) and $W^+ \rightarrow \mu\nu$ (right); $W^- \rightarrow e\nu$ (left) and $W^- \rightarrow \mu\nu$ (right), for $1.8 < \eta < 2.4$ in electron channel and $1.4 < \eta < 2.0$ in muon channel with the best mass fit template for each category. (W^\pm : upper row, W^+ : middle row, W^- : lower row)	236
C.14	Transverse mass distribution from $W \rightarrow e\nu$ (left) and $W \rightarrow \mu\nu$ (right); $W^+ \rightarrow e\nu$ (left) and $W^+ \rightarrow \mu\nu$ (right); $W^- \rightarrow e\nu$ (left) and $W^- \rightarrow \mu\nu$ (right), for $1.8 < \eta < 2.4$ in electron channel and $1.4 < \eta < 2.0$ in muon channel with the best mass fit template for each category. (W^\pm : upper row, W^+ : middle row, W^- : lower row)	237

C.15 Missing transverse energy distribution from $W \rightarrow e\nu$ (left) and $W \rightarrow \mu\nu$ (right); $W^+ \rightarrow e\nu$ (left) and $W^+ \rightarrow \mu\nu$ (right); $W^- \rightarrow e\nu$ (left) and $W^- \rightarrow \mu\nu$ (right), for $1.8 < \eta < 2.4$ in electron channel and $1.4 < \eta < 2.0$ in muon channel with the best mass fit template for each category. (W^\pm : upper row, W^+ : middle row, W^- : lower row)	238
C.16 Hadronic recoil distribution from $W \rightarrow e\nu$ (left) and $W \rightarrow \mu\nu$ (right); $W^+ \rightarrow e\nu$ (left) and $W^+ \rightarrow \mu\nu$ (right); $W^- \rightarrow e\nu$ (left) and $W^- \rightarrow \mu\nu$ (right), for $1.8 < \eta < 2.4$ in electron channel and $1.4 < \eta < 2.0$ in muon channel. (W^\pm : upper row, W^+ : middle row, W^- : lower row)	239
C.17 Parallel projection of hadronic recoil distribution with respect to lepton p_T from $W \rightarrow e\nu$ (left) and $W \rightarrow \mu\nu$ (right); $W^+ \rightarrow e\nu$ (left) and $W^+ \rightarrow \mu\nu$ (right); $W^- \rightarrow e\nu$ (left) and $W^- \rightarrow \mu\nu$ (right), for $1.8 < \eta < 2.4$ in electron channel and $1.4 < \eta < 2.0$ in muon channel. (W^\pm : upper row, W^+ : middle row, W^- : lower row)	240
C.18 Perpendicular projection of hadronic recoil distribution with respect to lepton p_T from $W \rightarrow e\nu$ (left) and $W \rightarrow \mu\nu$ (right); $W^+ \rightarrow e\nu$ (left) and $W^+ \rightarrow \mu\nu$ (right); $W^- \rightarrow e\nu$ (left) and $W^- \rightarrow \mu\nu$ (right), for $1.8 < \eta < 2.4$ in electron channel and $1.4 < \eta < 2.0$ in muon channel. (W^\pm : upper row, W^+ : middle row, W^- : lower row)	241
C.19 Lepton p_T distribution from $W \rightarrow \mu\nu$; $W^+ \rightarrow \mu\nu$ (left) and $W^- \rightarrow \mu\nu$ (right), for $2.0 < \eta < 2.4$ with the best mass fit template for each category.	242
C.20 Transverse mass distribution from $W \rightarrow \mu\nu$; $W^+ \rightarrow \mu\nu$ (left) and $W^- \rightarrow \mu\nu$ (right), for $2.0 < \eta < 2.4$ with the best mass fit template for each category.	242
C.21 Missing transverse energy distribution from $W \rightarrow \mu\nu$; $W^+ \rightarrow \mu\nu$ (left) and $W^- \rightarrow \mu\nu$ (right), for $2.0 < \eta < 2.4$ with the best mass fit template for each category. . .	243
C.22 Hadronic recoil distribution from $W \rightarrow \mu\nu$; $W^+ \rightarrow \mu\nu$ (left) and $W^- \rightarrow \mu\nu$ (right), for $2.0 < \eta < 2.4$	243
C.23 Parallel projection of hadronic recoil distribution with respect to the p_T from $W \rightarrow \mu\nu$; $W^+ \rightarrow \mu\nu$ (left) and $W^- \rightarrow \mu\nu$ (right), for $2.0 < \eta < 2.4$	243
C.24 Perpendicular projection of hadronic recoil distribution with respect to the p_T from $W \rightarrow \mu\nu$; $W^+ \rightarrow \mu\nu$ (left) and $W^- \rightarrow \mu\nu$ (right), for $2.0 < \eta < 2.4$	244

List of Tables

1.1	Generations of quarks and leptons with their masses and charges.	2
1.2	The Standard Model bosons with their masses and ‘charges’, and corresponding interaction types.	3
2.1	Summary of the main characteristics of the three ATLAS ID sub-detectors [37]. .	23
2.2	Typical resolutions for track parameter with $p_T > 30\text{GeV}$ [36].	24
2.3	Rapidity coverage and granularity of the EM calorimeter.	26
2.4	Parameters of the four sub-systems of the muon detector.	29
3.1	Definition of variables used for loose, medium and tight electron identification cuts.	35
4.1	The temperature expansion coefficients in the calorimeter and z -shifts of different compartments extracted from the fit of data.	55
5.1	Impact of muon performance corrections on the m_W measurement uncertainties. .	67
5.2	Comparison of Z and W boson mass fit results with and without E/p cut, before and after the corresponding recalibration. The shown results are differences with respect to a blinded reference value of m_W , and are given in MeV.	77
5.3	Comparison of the W mass fit results for data taken during periods E-H and outside of these periods. The shown results are differences with respect to a blinded reference value of m_W , and are given in MeV.	79
5.4	Impact of electron performance corrections on the m_W measurement uncertainties.	81
5.5	Impact of recoil performance corrections on the m_W measurement uncertainties. .	93
5.6	Summarised results of total uncertainty from the hadronic recoil corrections. The systematics on m_W are given in MeV.	93
6.1	Gauge coupling constants, fermion vector and axial-vector coupling factors, and generation mixing terms in the Standard Model.	96
6.2	From the comparison between Exp and Exp+PE versions of PHOTOS, shift on the vector boson mass induced by not taking into account final state lepton pair emission, for the different tested distributions and with the two definitions of boson decay leptons, either bare or dressed. The uncertainties are from the finite size of the generated samples.	103
6.3	Systematic effect on the m_W measurement (in MeV) from EW corrections beyond FSR, in the G_μ and α_0 schemes.	110
6.4	Relative systematic uncertainties on the energy and momentum scale measurement, from higher-order EW corrections in $Z \rightarrow \ell\ell$ events. The table entries express relative energy scale uncertainties. The dashes indicate cases where the effect is negligibly small.	110
6.5	Systematic uncertainties on the m_W measurement (in MeV), from higher-order EW corrections in $W \rightarrow l\nu$ events, in MeV. The dashes indicate cases where the effect is negligibly small.	110
6.6	Summary of the sources of uncertainty in the p_T^W distribution.	118
6.7	68% CL PDF uncertainties on the m_W measurement with CT10nnlo using p_T^ℓ fits. The p_T^Z constraint is applied.	123
6.8	68% CL PDF uncertainties on the m_W measurement with CT10nnlo using m_T fits.	123
6.9	Summary of the sources of uncertainty in m_W from the p_T^W distribution. Except for the LO PDF case, the uncertainties apply identically for W^+ , W^- and W^\pm	124

7.1	MC samples used in the analysis. The quoted cross-sections, except multijet samples, are used to normalize NNLO estimates of expected number of event.	132
7.2	Cut-flow in the $W \rightarrow e\nu$ channel in the signal region. Electrons are requested to be tight++. Numbers in brackets represent cumulative efficiency (in %) of the given cut.	135
7.3	Cut-flow in the $W \rightarrow \mu\nu$ channel in the signal region. Muons are requested to have $p_{T\text{cone20}}/p_T < 0.1$. Numbers in brackets represent cumulative efficiency of the given cut.	136
7.4	Cut-flow in the $W \rightarrow e\nu$ channel for background processes. The numbers represents number of events normalised according to the cross sections listed in Table 7.1 and normalised to the integrated luminosity of the data sample.	137
7.5	Cut-flow in the $W \rightarrow \mu\nu$ channel for background processes. The numbers represents number of events normalised according to the cross sections listed in Table 7.1 and normalised to the integrated luminosity of the data sample.	137
7.6	Electroweak and top background fractions (%) with respect to data candidate events selected in signal region in muon and electron channels, separately for W^+ and W^-	138
7.7	Impact of the EW and top background normalisation on the mass determination fitting the p_T^{ell} distribution.	138
7.8	Table which summarises the definitions of the signal region and all the control and fitting regions. 'Iso' corresponds to muon isolation $\sum p_T^{\text{trk}}/p_T$ variable.	139
7.9	Cutflow of the data selection and expected EW contamination in the $W^+ \rightarrow \mu\nu$ and $W^- \rightarrow \mu\nu$ channels, requiring muons to be anti-isolated within $0.1 < \sum p_T^{\text{trk}}/p_T < 0.4$. MC corresponds to simulated signal and background contamination normalized to their cross sections.	140
7.10	Multijet background estimates using fits to kinematical distributions, for the $W \rightarrow \mu^+\nu$ and $W \rightarrow \mu^-\bar{\nu}$ channels, inclusively in η and $< \mu >$	144
7.11	Cutflow of the data selection and expected EW contamination in the $W^+ \rightarrow e\nu$ and $W^- \rightarrow e\nu$ channels, requiring electrons to be anti-isolated requiring $4\text{GeV} < p_T^{\text{cone40}} < 8\text{GeV}$ and removing E_T^{cone20} cuts. MC corresponds to simulated signal and background contamination normalized to their cross sections.	145
7.12	Multijet background estimates using fits to kinematical distributions, for the $W \rightarrow e^+\nu$ and $W \rightarrow e^-\bar{\nu}$ channels, inclusively in η and $< \mu >$	146
7.13	Measured multijet background fractions (%) in the four channels $W^+ \rightarrow \mu\nu$, $W^- \rightarrow \mu\nu$, $W^+ \rightarrow e\nu$ and $W^- \rightarrow e\nu$	150
7.14	Measured multijet fractions (%) in $W \rightarrow \mu\nu$ channel as a function of muon pseudo-rapidity $ \eta $ and pile-up μ obtained from fits to kinematical distributions by scanning of $p_T^{\text{cone20}}/pt > 0.1$ control region.	153
7.15	Measured multijet fractions (%) in $W \rightarrow e\nu$ channel as a function of electron pseudo-rapidity $ \eta $ and pile-up μ obtained from fits to kinematical distributions by scanning of the p_T^{cone40} variable in control region with removed E_T^{cone20} cut.	169
7.16	Impact of the multijet shape correction on the fitted value of m_W	169
7.17	The propagated multijet background uncertainties on the W mass in $W \rightarrow \mu\nu$ channel.	170
7.18	The propagated multijet background uncertainties on the W mass in $W \rightarrow e\nu$ channel.	170
8.1	Extracted W mass value and expected statistical uncertainty in the consistency test of the template fit method.	173
8.2	Data statistics in the $ \eta $ vs $\langle \mu \rangle$ categories in $W \rightarrow \mu\nu$ channel.	175
8.3	Data statistics in the $ \eta $ vs μ categories in $W \rightarrow e\nu$ channel.	176

8.4	Number of selected $Z \rightarrow ll$ ($l = \mu, e$) events in data and MC. MC predictions are scaled to the integrated luminosity in data and theoretical cross sections. . . .	177
8.5	Z boson mass fit results in the electron and muon channels, after all corrections are applied. The $p_T^{l+, l-, l\pm}$ distributions are used. Shown are the differences between the $m_{\ell\ell}$ and p_T^ℓ fit results, as the $m_{\ell\ell}$ fits agree with m_Z by construction and the compatibility between the invariant mass and transverse momentum observables is tested here. The combined results are also shown. The uncertainties quoted are statistical only.	182
8.6	Z boson mass fit results in the electron and muon channels, after all corrections are applied. The $m_T^Z(l+, l-, l\pm)$ distributions are used. Shown are the differences between the $m_{\ell\ell}$ and m_T^ℓ fit results, as the $m_{\ell\ell}$ fits agree with m_Z by construction and the compatibility between the invariant mass and transverse mass observables is tested here. The combined results are also shown. The uncertainties quoted are statistical only.	182
8.7	Blinded fit results (in MeV) for the p_T^ℓ and m_T -based m_W measurement with only statistical uncertainty. The result is given as a shift with respect to the assumed value of m_W in the MC, plus an unknown offset.	185
8.8	Fitted mass values v , given by $m_W = 80399 + b \pm v$ MeV, where b is an unknown blinding value. The m_W fit is performed in the electron and muon decay channel, in different η lepton categories using the p_T and m_T observables (nominal fitting range). In addition to the statistical uncertainties, all experimental uncertainties, i.e. the muon, the electron and the hadronic recoil calibration uncertainties as well as the background related uncertainties on m_W are given. Also the model uncertainties, due to EWK corrections, QCD corrections (scales, PS, A_i coefficient modeling) and PDFs are given. All uncertainties are given in MeV.	190
8.9	Combined fit results for different selected m_W fits. The result is given as a shift with respect to the assumed value of m_W in the MC, plus an unknown offset. In addition to the statistical uncertainties, all experimental uncertainties, i.e. the muon, the electron and the hadronic recoil calibration uncertainties as well as the background related uncertainties on m_W are given. Also the model uncertainties, due to EWK corrections, QCD corrections (scales, PS, A_i coefficient modeling) and PDFs are given. All uncertainties are given in MeV.	191
8.10	Combined fit results for different PDF sets in comparison to the nominal CT10-PDF Set, including total uncertainties and pdf-related uncertainties intrinsic to the given PDF set. All uncertainties are given in MeV.	193
8.11	Fitted mass values v , given by $m_W = 80399 + b \pm v$ MeV, where b is an unknown blinding value for the optimal fitting range. The m_W fit is performed in the electron and muon decay channel, in different η lepton categories using the p_T and m_T observables (optimal fitting range). In addition to the statistical uncertainties, all experimental uncertainties, i.e. the muon, the electron and the hadronic recoil calibration uncertainties as well as the background related uncertainties on m_W are given. Also the model uncertainties, due to EWK corrections, QCD corrections (scales, PS, A_i coefficient modeling) and PDFs are given. All uncertainties are given in MeV.	199
8.12	Summary of consistency tests of m_W -fits in several measurement categories. The blinded fit results (in MeV) for the p_T^ℓ and m_T -based fits in the electron and muon decay channel is given. Uncertainties are statistical only. The result is given as a shift with respect to the assumed value of m_W in the MC, plus an unknown offset.	202

Titre : Mesure de la masse du boson W avec le détecteur ATLAS

Mots clefs : LHC, ATLAS, masse du boson W, Modele Standard

Résumé : Cette thèse décrit une mesure de la masse du boson W avec le détecteur ATLAS. La mesure exploite les données enregistrées par ATLAS en 2011, à une énergie dans le centre de masse de 7 TeV et correspondant à une luminosité intégrée de 4.6 inverse femtobarn. Les mesures sont faites par ajustement aux données de distributions en énergie transverse des leptons chargés et en masse transverse du boson W obtenues par simulation dans les canaux electron et muon, et dans plusieurs catégories cinématiques. Les

différentes mesures sont en bon accord et leur combinaison donne une valeur de

$$m_W = 80371.1 \pm 18.6 \text{ MeV},$$

La valeur mesurée est compatible avec la moyenne mondiale des mesures existantes, $m_W = 80385 \pm 15 \text{ MeV}$, et l'incertitude obtenue est compétitive avec les mesures les plus précises réalisées par les collaborations CDF et D0.

Title : Measurement of the W boson mass with the ATLAS detector

Keywords : LHC, ATLAS, W boson mass, Standard Model.

Abstract : This thesis describes a measurement of the W boson mass with the ATLAS detector based on the data-set recorded by ATLAS in 2011 at a centre-of-mass energy of 7 TeV, and corresponding to 4.6 inverse femtobarn of integrated luminosity. Measurements are performed through template fits to the transverse momentum distributions of charged leptons and to transverse mass distributions of the W boson, in electron and muon decay modes in various kinematic categories. The

individual measurements are found to be consistent and their combination leads to a value of

$$m_W = 80371.1 \pm 18.6 \text{ MeV},$$

The measured value of the W boson mass is compatible with the current world average of $m_W = 80385 \pm 15 \text{ MeV}$. The uncertainty is competitive with the current most precise measurements performed by the CDF and D0 collaborations.